Lecture Notes in Mechanical Engineering

Monica Carfagni · Rocco Furferi ·
Paolo Di Stefano · Lapo Governi ·
Francesco Gherardini *Editors*

Design Tools and Methods in Industrial Engineering III

Proceedings of the Third International Conference on Design Tools and Methods in Industrial Engineering, ADM 2023, September 6–8, 2023, Florence, Italy, Volume 1

Springer

Lecture Notes in Mechanical Engineering

Lecture Notes in Mechanical Engineering (LNME) publishes the latest developments in Mechanical Engineering—quickly, informally and with high quality. Original research reported in proceedings and post-proceedings represents the core of LNME. Volumes published in LNME embrace all aspects, subfields and new challenges of mechanical engineering.

To submit a proposal or request further information, please contact the Springer Editor of your location:

Europe, USA, Africa: Leontina Di Cecco at Leontina.dicecco@springer.com
China: Ella Zhang at ella.zhang@springer.com
India: Priya Vyas at priya.vyas@springer.com
Rest of Asia, Australia, New Zealand: Swati Meherishi at swati.meherishi@springer.com

Topics in the series include:

- Engineering Design
- Machinery and Machine Elements
- Mechanical Structures and Stress Analysis
- Automotive Engineering
- Engine Technology
- Aerospace Technology and Astronautics
- Nanotechnology and Microengineering
- Control, Robotics, Mechatronics
- MEMS
- Theoretical and Applied Mechanics
- Dynamical Systems, Control
- Fluid Mechanics
- Engineering Thermodynamics, Heat and Mass Transfer
- Manufacturing Engineering and Smart Manufacturing
- Precision Engineering, Instrumentation, Measurement
- Materials Engineering
- Tribology and Surface Technology

Indexed by SCOPUS, EI Compendex, and INSPEC.

All books published in the series are evaluated by Web of Science for the Conference Proceedings Citation Index (CPCI).

To submit a proposal for a monograph, please check our Springer Tracts in Mechanical Engineering at https://link.springer.com/bookseries/11693.

Monica Carfagni · Rocco Furferi ·
Paolo Di Stefano · Lapo Governi ·
Francesco Gherardini
Editors

Design Tools and Methods in Industrial Engineering III

Proceedings of the Third International Conference on Design Tools and Methods in Industrial Engineering, ADM 2023, September 6–8, 2023, Florence, Italy, Volume 1

Springer

Editors
Monica Carfagni
Department of Industrial Engineering
University of Florence
Florence, Italy

Rocco Furferi
Department of Industrial Engineering
University of Florence
Florence, Italy

Paolo Di Stefano
Department of Industrial and Information
Engineering and Economics
University of L'Aquila
L'Aquila, Italy

Lapo Governi
Department of Industrial Engineering
University of Florence
Florence, Italy

Francesco Gherardini
Department of Engineering "Enzo Ferrari"
University of Modena and Reggio Emilia
Modena, Italy

ISSN 2195-4356 ISSN 2195-4364 (electronic)
Lecture Notes in Mechanical Engineering
ISBN 978-3-031-52074-7 ISBN 978-3-031-52075-4 (eBook)
https://doi.org/10.1007/978-3-031-52075-4

This Springer imprint is published by the registered company Springer Nature Switzerland AG
The registered company address is: Gewerbestrasse 11, 6330 Cham, Switzerland

Foreword

It is a great honor and pleasure to welcome you to the ADM 2023 International Conference promoted by ADM, the Italian Association of Design Methods and Tools for Industrial Engineering, held in Florence, Italy September 6–8, 2023. The conference, hosted by the University of Florence, a world-renowned university, provides a forum for researchers and students from industry and academia to share their latest findings and challenges and promote sustainable research.

First, I wish to thank all members of the ADM Executive Board and of the Scientific Council, especially the Coordinator, Prof. Paolo di Stefano, whose support made the organization of the ADM2023 International Conference possible.

A special thanks goes to the Conference Program Chair, Prof. Monica Carfagni, and to the members of the Organizing Committee for their tremendous efforts in making this conference successful and attractive.

The number of papers submitted was significant, and I also would like to thank all the authors and all the international and Italian reviewers for their continuous collaboration and commitment that led to the publication of this book of high scientific quality consisting of two volumes.

Finally, the conference is a great opportunity to meet all together and establish new collaborations and strengthen existing ones, and this is also thanks to all ADM members for their active engagement and support, which are essential to promote and organize these initiatives.

Caterina Rizzi
ADM President

Letters to the Authors

These volumes collect the interventions carried out at the ADM 2023 International Conference of the Italian Association of Design Methods and Tools for Industrial Engineering, held in Florence, Italy, September 6–8, 2023.

ADM is an association of researchers, mainly universities, who are at the service of scientific innovation in industry and the knowledge economy. Knowledge is a strategic resource for businesses and society; whoever possesses it can gain a competitive advantage, especially in a context where the ability to innovate, design in time for the market, and generate high-quality products is essential to continue to exist in the markets.

The conference ADM represents a regular event that has been repeated for almost 50 years. The conference aims to discuss the latest advances in research and share knowledge, experience, and progress in advanced methods for the design and development of industrial products, providing links between educators, industry, and academic research. Its proceedings are the acme of cultural evolution and evidence of state-of-the-art technologies for the design and development of industrial products.

The documents presented here combine the contributions of the congressmen, collected in some sections according to a criterion of homogeneity, and include a wide variety of topics concerning design and manufacturing. About 10% of the contributions come from non-Italian research groups. It is a collection of papers rich in scientific speculations, all oriented, each in a different way, to the real needs of the professions and industry. It constitutes a cultural product and confirms a tangible link between industry and academia.

To introduce new research topics or fields of application of traditional methods and promote the continued evolution of the conference, following the development of new technology, five special sessions have been proposed in this edition of the ADM 2023 International Conference. In these sessions, 32 works have been presented at the conference and are now published in these volumes.

I want to thank all the authors and colleagues for the important scientific contribution they gave to the conference with their valuable work. The ADM association exists as long as there are motivated and qualified members with high scientific qualities; today, ADM is particularly vital! I also want to thank the reviewers of the papers who, with their work, have been the guarantors of the quality of the conference and of these volumes, which are the testimony for future memory. Special thanks to the members of the Organizing Committee for their efforts in making this conference possible and for their hospitality in Florence, and to the President of the ADM, Prof. Caterina Rizzi, for supporting the initiative.

September 2023 Paolo Di Stefano

Preface

This volume, together with Volume 2, collects the proceedings of the ADM 2023 International Conference, entitled "Design Tools and Methods in Industrial Engineering III" held in Florence, Italy, September 6–8, 2023.

The conference is organized and hosted by the Department of Industrial Engineering of Florence which, for the three days of the conference, we had the honor to represent.

Florence, a city renowned for its artistic heritage, rich history, and timeless charm, provided the perfect backdrop for our journey into the world of design methods. The picturesque streets and iconic landmarks of this cultural treasure inspired us all as we delve into the realms of research, innovation, and collaboration.

Throughout the conference days, our event served as a platform to exchange ideas, showcase breakthroughs, and foster connections that transcend borders and disciplines. Together, we explored the evolving landscape of the ADM compelling research field.

Almost 200 researchers joined the conference with an overall number of 183 papers arranged in the two volumes. More than 230 authors' authored papers were accepted at the conference, and more than 150 reviewers were involved to help the Scientific Committee in revising, scoring, and selecting accepted contributions. All papers were presented in 30 oral sessions which included also keynote speakers and session chairs.

The main topics covered in this volume are Design for Additive Manufacturing, Engineering Methods in Medicine, Human-Related and User-Centered Design, Industrial Design and Ergonomics, Design for Sustainability and EcoDesign, Engineering Education, Experimental Methods in Product Development, Geometrical Product Specification, Geometric and Functional Characterization of Products, Integrated Methods for Product and Process Design, Simulation, Analysis and Optimization.

We wish to thank the President of ADM Prof. Caterina Rizzi and Prof. Paolo di Stefano, coordinator of the Scientific Council of the ADM.

We also thank the whole Organizing Committee, with special thanks to Prof. Francesco Gherardini and Prof. Giuseppe Marannano for the management of the paper review procedure and to Eng. Francesco Buonamici for the precious help in organizing the conference sessions. Special thanks to Doriano Giannelli and Patrizia Cecchi for the administrative and logistics management of the conference and side events. We wish to thank also all the colleagues who have supported us as members of the Scientific Committee and as reviewers and all the authors who gave their valuable contribution to the conference with their research.

Last but not least, the publisher Springer Nature honored us by publishing the two volumes proceedings of this third edition in the series "Lecture Notes in Mechanical Engineering."

September 2023

Monica Carfagni
Rocco Furferi
Conference Program Chairs

Organization

ADM2023 is organized by ADM—Italian Association of Design Methods and Tools for Industrial Engineering, in cooperation with the Department of Industrial Engineering of the University of Florence, Italy.

Organizing Committee

Monica Carfagni (Conference Chair)	Università di Firenze
Rocco Furferi (Conference Program Chair)	Università di Firenze
Francesco Gherardini	Università di Modena e Reggio Emilia
Giuseppe Marannano	Università di Palermo
Emanuele Guardiani	Università dell'Aquila
Francesco Buonamici	Università di Firenze
Patrizia Cecchi	Università di Firenze
Doriano Giannelli	Università di Firenze

Scientific Committee

Caterina Rizzi (ADM President)	Università degli Studi di Bergamo, Italy
Michele Germani (ADM Board)	Università Politecnica delle Marche, Italy
Salvatore Gerbino (ADM Board)	Università degli Studi della Campania, Italy
Lapo Governi (ADM Board)	Università degli Studi di Firenze, Italy
Tommaso Ingrassia (ADM Board)	Università degli Studi di Palermo, Italy
Francesco Leali (ADM Board)	Università degli Studi di Modena e Reggio Emilia, Italy
Maurizio Muzzupappa (ADM Board)	Università della Calabria, Italy
Armando Viviano Razionale (ADM Board)	Università degli Studi di Pisa, Italy
Enrico Vezzetti (ADM Board)	Politecnico di Torino, Italy
Paolo Di Stefano (ADM Scientific Committee Coordinator)	Università degli Studi dell'Aquila, Italy
Giovanni Berselli (ADM Scientific Committee)	Università degli Studi di Genova, Italy

Giorgio Colombo (ADM Scientific Committee)	Politecnico di Milano, Italy
Alfredo Liverani (ADM Scientific Committee)	Università degli Studi di Bologna, Italy
Massimo Martorelli (ADM Scientific Committee)	Università di Napoli Federico II, Italy
Antonio Emmanuele Uva (ADM Scientific Committee)	Politecnico di Bari, Italy
Valerio Villa (ADM Scientific Committee)	Università degli Studi di Brescia, Italy
Francesco Buonamici (ADM Scientific Committee)	Università degli Studi di Firenze, Italy
Luca Puggelli	Università degli Studi di Firenze, Italy
Michaela Servi	Università degli Studi di Firenze, Italy
Antonio Marzola	Università degli Studi di Firenze, Italy
David Ranz Angulo (INGEGRAF)	University of Zaragoza, Spain
Ismael Lengüa Lengüa (INGEGRAF)	Universitat Politècnica de València, Spain
Rikardo Minguez Gabiña (INGEGRAF)	Faculty of Engineering—Bilbao, Spain
Daniel Moreno Nieto (INGEGRAF)	Universidad de Cádiz, Spain
Ramón Miralbés Buil (INGEGRAF)	Universidad de Zaragoza, Spain
Stephan Odenwald	Technical University of Chemnitz, Germany
Lars Penter	Technical University of Dresden, Germany
Pasquale Franciosa	University of Warwick, UK
Marco Montemurro (S.mart)	École Nationale Supérieure d'Arts et Métiers, France
Raffaele De Amicis	Oregon State University, USA
Cosimo Della Santina	Technical University of Delft, The Netherlands
Linda Weisheit	Fraunhofer-IWU, Germany
Arvid Hellmich	Fraunhofer-IWU, Germany
Gabriele Guidi	Indiana University Bloomington, USA

Reviewers

Alessandri Giulia
Ambu Rita
Aruanno Beatrice
Bacciaglia Antonio
Baggetta Mario
Barberi Emmanuele
Barbieri Loris
Becattini Niccolò
Beltrami Daniele
Berni Aurora

Bianconi Francesco
Boccaccio Antonio
Brunzini Agnese
Buonocore Sara
Buttarazzi Massimo Generoso
Calì Michele
Califano Rosaria
Caporaso Teodorico
Cappelletti Federica
Cappetti Nicola
Caragiuli Manila
Cardilicchio Antimo
Caruso Giandomenico
Cattaneo Andrea
Ciccone Francesco
Cicconi Paolo
Conti Paolo
Cristofolini Ilaria
Dalle Mura Francesco
Dastan Mine
De Crescenzio Francesca
De Crescenzo Chiara
De Giglio Vito
De Napoli Luigi
Di Angelo Luca
Di Gironimo Giuseppe
Evangelista Alessandro
Favi Claudio
Filippi Stefano
Fiorenitno Michele
Furferi Rocco
Gattullo Michele
Gherardini Francesco
Gianvincenzi Mattia
Graziosi Serena
Greco Alessandro
Guardiani Emanuele
Haid Daniel Matthias
Ihlenfeldt Steffen
Lagudi Antonio
Lanzotti Antonio
Magherini Roberto
Maltauro Mattia
Mandolini Marco
Manghisi Vito Modesto
Manuguerra Luca
Marconi Marco
Marzullo Domenico
Massanova Nicola
Mencarelli Marta
Meneghello Roberto
Moos Sandro
Morabito Anna Eva
Moreno Nieto Daniel
Morosi Federico
Motyl Barbara
Mozzillo Rocco
Mussi Elisa
Naddeo Alessandro
Neri Paolo
Occhiuto Enrico
Paoli Alessandro
Papallo Ida
Pascoletti Giulia
Perfetto Donato
Peruzzini Margherita
Pigazzi Riccardo
Pini Fabio
Profili Andrea
Raffaeli Roberto
Rega Andrea
Regazzoni Daniele
Renzi Cristina
Ricotta Vito
Rotini Federico
Sanseverino Giuseppe
Schwanitz Stefan
Severino Umberto
Sfravara Felice
Spreafico Christian
Stomaci Tommaso
Tamburrino Francesco
Tarallo Andrea
Uccheddu Francesca
Vaiani Lorenzo
Zago Marco
Zanini Alessio
Zoppoli Andrea

Contents

Human-Related and User-Centered Design

Industrial Design and Ergonomics

Design for Sustainability and EcoDesign

Experimental Methods in Product Development

Geometrical Product Specification, Geometric and Functional Characterization of Products

Integrated Methods for Product and Process Design, Simulation, Analysis and Optimization

Design for Additive Manufacturing

FDM Printing Time Prediction Tuning Through a DOE Approach

Antonio Bacciaglia(✉), Alessandro Ceruti, Francesco Ciccone, and Alfredo Liverani

Department of Industrial Engineering (DIN), University of Bologna, Viale del Risorgimento 2, 40132 Bologna, Italy
antonio.bacciaglia2@unibo.it

Abstract. Additive Manufacturing is widely applied in aerospace, automotive and marine engineering. Indeed, large-scale components are often required in these applications, such as for non-structural parts of aircraft, spare parts or small lots of cars or marine components. Fused Deposition Modelling is one of the Additive Manufacturing processes used to affordably convert digital models into mockups, prototypes, and functional parts: a slicing software converts the object's digital model into a list of instructions for the machine. However, commercial slicing software packages often fail to accurately estimate the time required to produce models, especially when their size is significant: the errors could be up to several hours, which cannot be adequate in a real-life industrial context where production must be scheduled in a precise way. This manuscript compares the build time estimation of several commercial slicing software considering a real-life part. Furthermore, the evaluation of the manufacturing setting mainly affects the error in estimating the build time achieved through a Design of Experiment approach. The more time-impacting printing parameters have been detected, allowing fine helpful tuning to increase the accuracy of the build time in commercial slicing software. A case study included in the manuscript supports the analyses. Proper setting of the commercial slicing software can significantly improve the accuracy of the printing time.

Keywords: Additive Manufacturing · Fused Deposition Modelling · Slicing · Time Estimation · Design of Experiment

1 Introduction

Nowadays, a wide range of structures and complex geometries are fabricated from 3D digital models using Additive Manufacturing (AM) techniques. The method entails consecutive manufacturing layers of materials on top of one another, contrary to traditional approaches based on removing raw materials. Charles Hull pioneered this technology in 1986 using Stereolithography (SLA) [1]. The AM panorama was enriched in the following decades by additional advancements, including Powder Bed Fusion (PBF), Direct Metal Laser Sintering (DMLS) and Fused Deposition Modelling (FDM). Biomedical,

M. Carfagni et al. (Eds.): ADM 2023, LNME, pp. 3–12, 2024.
https://doi.org/10.1007/978-3-031-52075-4_1

automotive, and aerospace fields are just a few fields that have extensively benefited AM approaches [2]. The increased use of AM instead of traditional methods leads to various gains, including highly accurate manufacture of complicated geometry, maximum material savings, design freedom, reduction of time-to-market, and individual customisation [3].

FDM is one of the most well-known AM approaches characterised by reduced costs and is particularly suitable for prototyping applications [4]. FDM is currently the most cost-effective AM technique for thermoplastic materials: introducing carbon filament or metal-charged wires also allows for high-strength parts. In the FDM process, a raw polymer filament is fed, melted, and extruded through an hotend before being deposited following preset patterns.

In AM, a 3D digital model must be divided into layers, and a printhead path must be computed to deposit materials for each layer, up to obtaining the whole part. A slicing software typically operates by intersecting a plane with the 3D model at fixed-step Z-heights and figuring out the boundary segments on each layer. The printhead's motion is then calculated to infill the area inside each layer's boundary, considering the manufacturing settings chosen by the user [5]. The printer profile can be defined as the set of process variables, such as printing temperatures, printing speed, build orientation, layer thickness, infill density, and pattern the user chooses before processing the 3D model and slicing it. These settings can significantly influence the manufactured components' characteristics and quality [6]. Thus, the slicing software can convert the 3D digital model into a path specified in a G-code that lists the machine's instructions to obtain the intended shape [7].

In the last decades, the research community's primary focus on FDM related to the optimisation of the building time [8], the computation of the support volume [9], and the evaluation of the production cost [10]: this effort aimed at improving FDM further and make it a viable substitute for conventional manufacturing processes. Among them, estimating the proper build time in relation to the manufacturing settings is of particular interest [11]. Though commercial slicing software packages frequently roughly quote the Estimated Time of Manufacturing (ETM) required to produce 3D models. This error could be magnified by the scale of the models that must be produced; the error could reach several hours, which is unacceptable in an industrial context.

To solve this challenge, the scientific community proposed some algorithms to guess the build time estimation with promising results [12, 13, 14]. However, these methods are still not implemented in commercial software; thus, relatively high estimation errors could affect the manufacturing time evaluation in commercial codes.

Compared to the existing literature, this paper proposes a methodology applicable to precisely understand the significance and effect of some definite slicing parameters on the ETM through a statistically helpful approach to reduce the number of printing configurations to test. At first, the article examines the ETM and estimated filament weight provided by a set of commercial slicing software packages using a scaled 3D model representing an aircraft mockup for wind tunnel tests. Afterwards, the most reliable software was selected for tests to determine which manufacturing parameters significantly impact the ETM. A Design of Experiment (DOE) methodology [15] and the Minitab software [16] have been used. This research suggests a way to find the more crucial process factors that influence how accurately the build time is estimated in commercial slicing software. Using the proposed approach, the user can correct the most ETM-impacting default settings of the commercial slicing software, and the build time estimation can be improved by far. The user can understand which settings deserve attention for an accurate ETM evaluation. This way, the requirements, time planning and production scheduling in an industrial environment can be respected.

The article is structured as follows. Section 2 describes the printer profile used for tests and the case study chosen to evaluate commercial slicing software accuracy on the ETM. In the following, Sect. 3 shows how to apply the Design of Experiment approach to analyse the importance of some selected process variables on the ETM. Section 4 discusses the results achieved with the DOE methodology and summarises the article with conclusions and future developments.

2 Estimated Time of Manufacturing: A Comparative Analysis

In this Section, the authors evaluate five - commercial and free - slicing software to compare their build time and weight estimation accuracy. A realistic component has been chosen to achieve this task.

In recent years, AM has seen a rise in its use, particularly in producing structural parts for the automotive and aerospace sectors. In the latter case, particular attention has been given to structural components, such as the UAV's mainframe of multi-copter fuselage and fixed-wing aircraft's aerodynamic surfaces. Moreover, FDM technology has been applied to produce mockup models for wind tunnel tests to evaluate the aerodynamic loads of conceptual aerospace configurations [17]. This research considers a down-scaled mockup model of a civil transport aircraft to be used for wind tunnel tests. Post-processes [18] to smooth the external surface of the model are not considered, even if required to decrease the roughness of parts which is generally higher when using FDM than conventional technologies.

The Boeing X-48B is a NASA-supported experimental aircraft designed to study the properties of Blended Wing Body (BWB) transport aircraft [19]. The BWB is a fixed-wing aircraft with blended fuselage and wings. This configuration shows advantages in drag reduction and is studied to reduce commercial aviation's environmental impact.

A 0.75% down-scaled 3D model of the conceptual 73m span design has been used for the purpose of this research. The 3D model has bounding box dimensions of 0.547x 0.306 x 0.061m. A Modix Big60v2 FDM machine equipped with a 0.6mm diameter nozzle has been used to manufacture the prototype as a single piece in PLA material, thanks to its 0.216 m^3 working volume. A printing profile already used successfully for printing parts is chosen as a starting point for this research (Table 1). Cura software estimated 30 h and 34 min to build the X-48 scaled mode.

Moreover, the slicing software estimated the % of the time required to manufacture some features of the project: 31% for infill; 18% for support; 17% for skin; 10% for inner walls; 9% for support interface; 8% for outer wall and 7% for other features. The actual manufacturing time needed to build the 3D model was recorded as 31 h and 49 min (see Fig. 1), and the overall model weight is 795g. A PLA filament from the FiloAlfa manufacturer has been chosen as the raw material for the model. An FDM machine requires a G-code file with instructions to manufacture the desired object. This file has been previously prepared using the Cura Ultimaker slicing software and implementing the manufacturing settings collected in Table 1. The ETM was compared with the actual manufacturing time to evaluate the estimation accuracy. Secondly, the same 3D model has been sliced using four different free slicing software, as reported in Table 2. The differences between the ETM and the real printing time are listed in the bar chart shown in Fig. 2a, while a similar comparison is made for the estimated model weight (Fig. 2b).

Table 1. Slicing printing settings used for PLA filament.

Parameter	Unit	Value	Parameter	Unit	Value
Layer Height	mm	0.22	Travel Speed	mm/s	100
Initial Layer Height	mm	0.25	Infill Print Speed	mm/s	60
Line Width	mm	0.65	Wall Print Speed	mm/s	40
Initial Layer Line Width factor	%	110	Retraction distance	mm	2
N° of bottom and top layers	–	3	Retraction Speed	mm/s	30
Wall Line Count	–	3	Fan Speed	%	100
Infill Density	%	30	Regular Fan Speed at Height	mm	0.22
Infill Topology		Cubic	Support Structure	–	True
Nozzle Temperature	°C	210	Support Type	–	Build Plate
Build Plate Temperature	°C	60	Support Pattern	–	Zig Zag
Flow	%	105	Support Density	%	15
Initial Layer Flow	%	110	Overhang Angle	°	50
Print Speed	mm/s	50	Adhesion Type	–	Raft
Initial Layer Print speed	mm/s	15	Raft Margin	mm	8

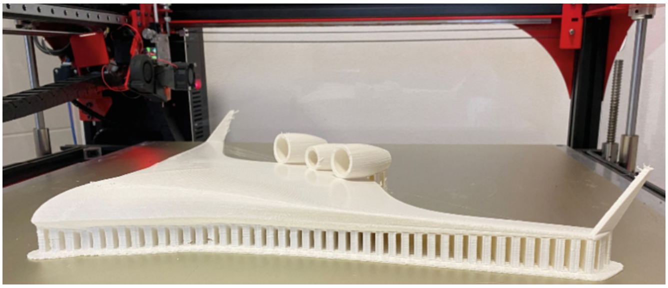

Fig. 1. Down-scaled X-48B model manufactured with a Modix Big60v2 FDM machine.

The data presented in Fig. 2a and 2b show that Cura Ultimaker provides more accurate estimations of the manufacturing time and final model weight than its analysed

Table 2. Slicing software comparison in terms of ETM.

Slicing software	ETM [days]	ETM [hours]	Filament Weight [g]
Cura	1.27	30.57	822
PrusaSlicer	1.58	38.08	920
ideaMaker	1.37	32.88	644
IceSL	1.58	38.23	749
Kiri	1.39	33.37	716

competitors. As a result, this slicing software will be utilised as the reference in future analyses.

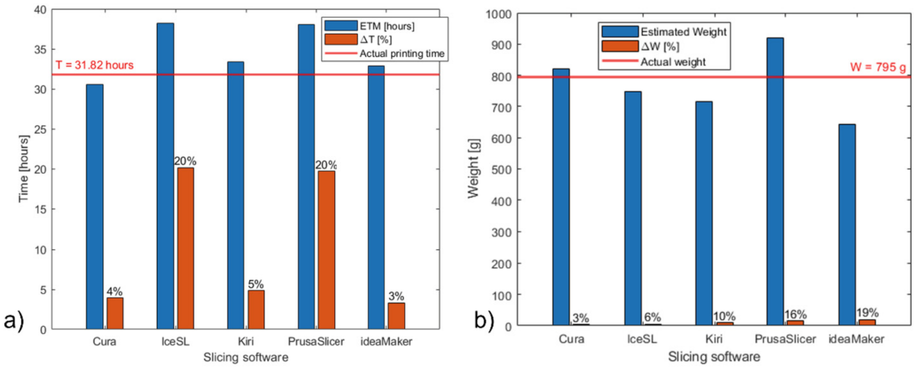

Fig. 2. a) A bar chart highlighting the ETM values (in blue) and the absolute % errors (in orange) compared to the actual manufacturing time (red horizontal line) for the specific case study; b) a similar bar chart compares the estimated and actual weight of the model.

It is important to highlight that the settings of the printing profile shown in Table 1 have been used for each slicing software. However, the exact replication of the slicing settings is not straightforward: every software has a different nomenclature for printing configurations; some settings are missing, and their value cannot be accessed. Just to cite some examples, in the former case, Cura names the number of outlines of the model's wall 'Wall line count', while PrusaSlicer calls them 'Perimeters'. In the latter case, Cura allows fine-tuning the raft options with external margin width, while Kiri enables only turning on or off the raft option as the build plate adhesion method. Nevertheless, the authors tried maintaining similar settings when shifting between different slicing packages by profoundly analysing the slicing software documentation to find the corresponding arrangements. Such meticulous analysis has been done to avoid possible effects on selecting the best slicing software for the following DOE analysis.

3 Design of Experiment Analysis

The DOE technique can be considered a formal statistical strategy built up to evaluate the influence of variables (referred to as factors) that have some values within a range (referred to as level) affecting the output of a particular system. The more conventional DOE analysis is known as a 2k-factorial architecture, where each of the k factors only has two levels, with a total of 2^k potential combinations. For the specific case study described in the previous section, it has been demonstrated that most of the time, the FDM machine is occupied with deposing new material to build the infill, the support or the outer skin of the model. For this reason, the authors selected the factors that could highly influence the ETM based on their experience in AM. Seven factors with two levels have been chosen (Table 3), set within the tested printing profile (Table 1).

The impact of these seven slicing parameters ($k = 7$) has been examined to determine which variables and which variables' interactions most influence the response, namely the ETM, through the statistical software Minitab [16]. Cura slicing software has been chosen to simulate the different runs required from Minitab to build the model based on the results shown in the previous section.

Table 3. Summary table of the seven factors and two levels analysed.

Slicing Factor	Level A	Level B	Unit
Layer Height	0.22	0.25	mm
Wall Line Count	3	5	–
Top/Bottom Layer Count	3	5	–
Infill Density	30	50	%
Infill Speed	30	60	mm/s
Wall Speed	25	50	mm/s
Support Speed	20	50	mm/s

The DOE approach is advantageous in predicting the response of a system when the level of a set of parameters is changed without simulating all the possible combinations. DOE offers several advantages, such as decreasing the time and cost required for experimentation, enhancing comprehension and regulation of the process, and improving the quality and performance of the product. In this case study, the possible slicing parameter combinations are 128, a large set of configurations to be simulated. Thus, Minitab gives the possibility to analyse just a randomly generated small group of runs to estimate the behaviour of the entire process. Randomisation is a technique used to balance the effect of extraneous or uncontrollable conditions that can impact the results of an experiment.

To understand the interaction of the first-order mixed terms on the output (ETM), Minitab requires 30 possible combinations not to saturate the model's degrees of freedom. Indeed, to have at least a Degree of Freedom (DF) on the residuals (DF_{res}), the following equation should be verified [16]:

$$DF_{res} = DF_{total} - \left(\sum_{i=1}^{k} DF_{main} + \sum_{j=1}^{l} DF_{inter} \right) > 0 \quad (1)$$

where the terms identify these parameters:

DF_{total}: Total Degree of Freedom, equal to the total number of experiment runs minus one;
DF_{main}: Degree of Freedom of a single k factor, equal to the number of factor levels minus one. In the case of 2k factorial design, $DF_{main} = 2 - 1 = 1$;
DF_{inter}: Degree of Freedom of a single j interaction term, equal to the DF for component factors, multiplied by each other.

The possible first-order combinations of 7 factors are $C_{7,2} = 21$; thus, for the specific case with seven factors and first-order term interest, it is possible to obtain that the required runs x not to saturate the model are: $0 < (x - 1) - (7 + 21) \overset{yields}{\rightarrow} x > 29$. Therefore, the first integer number of runs that satisfies the equation is 30. These combinations, not reported due to brevity, are listed on Minitab's worksheet, and the user is responsible for entering data of ETM in the output column. Therefore, by applying DOE, it is possible to simulate 23% of possible configurations to understand which printing setting and first-order setting interaction mainly affect the ETM, saving a lot of time. The factorial regression analysis is done once the statistical DOE testing is configured. The Pareto graph is the first result, which compares the principal and interaction effects' relative magnitude and statistical significance. A factor's contribution to the output is insignificant for the studied process if the P-value is less than a significance level, which has been set to 5%. The outcomes are simpler to comprehend when these terms are ignored (such as the Wall Line Count and most interaction terms) (Fig. 3a and 3b). After some iterations to remove the irrelevant factors, the standard error of the estimated S-value returned by Minitab shows a good fit of the model to the available data. The final model has a coefficient of determination value of $R^2 = 99.89\%$.

The residual plots confirm a good fit of the model to the available data once non-relevant terms are neglected. Moreover, factorial plots are available to the user better to comprehend the model's behaviour (Fig. 4). It is possible to see that a change in both Infill Density and Speed has a much higher influence (plot with greater slope) on the ETM compared to differences on the Wall Speed parameter (almost horizontal segment). Similar considerations may be obtained by observing Fig. 3b, where the more impacting factors are better highlighted.

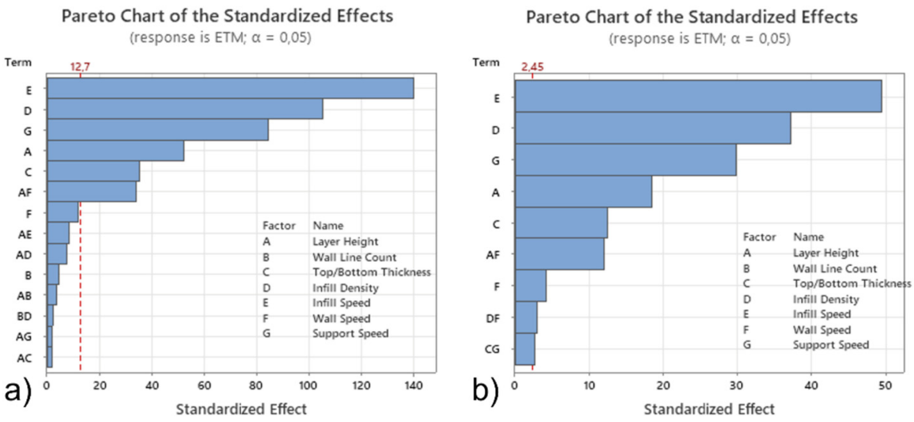

Fig. 3. a) Initial Pareto chart of slicing factors' effects on the output; b) Pareto graph when only the relevant factors are isolated.

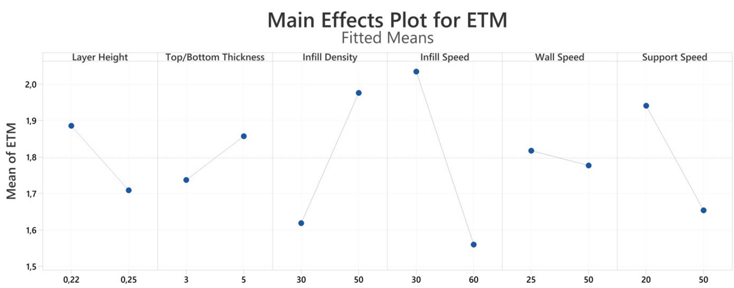

Fig. 4. The main effect plot shows the magnitude of changes of the ETM for each main factor level: the more the line is inclined, the greater the influence on the system's response.

4 Discussion and Conclusions

This research aims to understand which printing parameters primarily affect the Estimated Manufacturing Time in commercial slicing software packages. DOE improves process comprehension and reduces the need for time and costly tests; in this study, 23% of possible printing profile configurations have been tested. Thus, this manuscript proposes a helpful methodology to guide the end user in focusing on the most critical settings that impact a correct evaluation of the printing time. Through a DOE analysis, it is possible to build a model relating the response (ETM) to the main printing profile variables. As a secondary result, the authors investigated the accuracy of five free commercial slicing software for FDM technology available in the market. Cura Ultimaker demonstrated encouraging results for the time and weight estimation, respectively, with 4% and 3% errors if compared with the experimental tests.

The results shown in the previous Sections confirm high variability in estimating the manufacturing time and weight using different slicing software. On the one hand, Cura, Kiri and ideaMaker return a good agreement (≅5%) if compared with the required time to manufacture the 3D model, while IceSL and PrusaSlicer overestimated the ETM by about 20%. Conversely, Cura and IceSL estimated the model's weight accurately, while the others returned a coarse estimation (up to 19% error). This result could be blamed on a non-perfect matching of the printing profile settings due to a non-uniform nomenclature between the tested software. However, selecting a specific slicing software (including the possible bias produced by a different nomenclature) does not affect the proposed statistical approach.

A DOE 2k factorial analysis demonstrated that the infill density and speed mostly influence the ETM for the specific case study, where 31% of the total manufacturing time is spent on the infill. At the same time, the wall line count does not influence the model and can be ignored. Thus, for the model herein considered, a simple strategy to lower the printing time error is to decrease the infill density % and speed up the material deposition to manufacture it. It is straightforward that the printing settings are also tailored to the project's requirements: a higher infill density is necessary for a stiff object, even if the manufacturing time is longer.

The results collected in this manuscript are case study-dependent. Still, they could give some practical advice on selecting and modifying the more impacting printing parameters, which drive the accurate estimation of the build time in commercial slicing software. Moreover, this manuscript shows how to design a simple DOE analysis to efficiently plan the manufacturing process and speed up the design-to-manufacturing cycle. In the future, additional tests with different geometries will be carried out to outline more precise guidelines to reduce the printing time related to FDM technology, considering parts with different support and infill requirements.

References

1. Guo, N., Leu, M.C.: Additive manufacturing: technology, applications and research needs. Front. Mech. Eng. **8**, 215–243 (2013)
2. Abdulhameed, O., et al.: Additive manufacturing: challenges, trends, and applications. Adv. Mech. Eng. **11**, 1687814018822880 (2019)
3. 3DHubs: Additive manufacturing trend report 2021 (2021)
4. Ferretti, P., et al.: Production readiness assessment of low cost, multi-material, polymeric 3D printed moulds. Heliyon. **8**, e11136 (2022)
5. McPherson, J., Zhou, W.: A chunk-based slicer for cooperative 3D printing. RPJ. **24**, 1436–1446 (2018)
6. Ferretti, P., et al.: Relationship between FDM 3D printing parameters study: parameter optimisation for lower defects. Polymers **13**, 2190 (2021)
7. Krishnanand, S.S., Nayak, A., Taufik, M.: Generation of tool path in fused filament fabrication. In: Agrawal, R., Jain, J.K., Yadav, V.S., Manupati, V.K., Varela, L. (eds.) Recent Advances in Smart Manufacturing and Materials. LNME, pp. 153–161. Springer, Singapore (2021). https://doi.org/10.1007/978-981-16-3033-0_14
8. Komineas, G., et al.: Build time estimation models in thermal extrusion additive manufacturing processes. Procedia Manuf. **21**, 647–654 (2018)
9. Di Angelo, L., Di Stefano, P., Guardiani, E.: Search for the optimal build direction in additive manufacturing technologies: a review. JMMP. **4**, 71 (2020)
10. Dinda, S., et al.: Expediting build time, material, and cost estimation for material extrusion processes to enable mobile applications. In: Volume 2A: 43rd Design Automation Conference. American Society of Mechanical Engineers, Cleveland, Ohio, USA (2017)

11. Srivastava, M., Maheshwari, S., Kundra, T.K., Rathee, S., Yashaswi, R.: experimental investigation of process parameters for build time estimation in FDM process using RSM technique. In: Mandal, D.K., Syan, C.S. (eds.) CAD/CAM, Robotics and Factories of the Future. LNME, pp. 229–241. Springer, New Delhi (2016). https://doi.org/10.1007/978-81-322-2740-3_23
12. Di Angelo, L., et al.: A reliable build orientation optimisation method in additive manufacturing: the application to FDM technology. Int. J. Adv. Manuf. Technol. **108**, 263–276 (2020)
13. Zhang, Y., et al.: Fast adaptive modeling method for build time estimation in additive manufacturing. CIRP J. Manuf. Sci. Technol. **10**, 49–60 (2015)
14. Han, W., Jafari, M.A., Seyed, K.: Process speeding up via deposition planning in fused deposition-based layered manufacturing processes. Rapid Prototyping J. **9**, 212–218 (2003)
15. Jiju, A.: Design of Experiments for Engineers and Scientists. Elsevier (2003)
16. Minitab. https://www.minitab.com/en-us/. Accessed 05 Mar 2023
17. Sivamani, S., et al.: Analysis of cross axis wind turbine blades designed and manufactured by FDM based additive manufacturing. Mater. Today: Proc. **33**, 3504–3509 (2020)
18. Singh, J., Singh, R., Singh, H.: Investigations for improving the surface finish of FDM based ABS replicas by chemical vapor smoothing process: a case study. AA. **37**, 13–21 (2017)
19. NASA: NASA-Boeing X-48. https://www.nasa.gov/centers/dryden/research/X-48B/index.html. Accessed 15 Feb 2023

Comparative Assessment of Simulation Tools in Design for Additive Manufacturing Process

Alessio Zanini[1](✉), Marco Marconi[1], and Marco Mandolini[2]

[1] Università degli Studi della Tuscia, Largo dell'Università, 01100 Viterbo, Italy
alessio.zanini@unitus.it

[2] Università Politecnica delle Marche, Via Brecce Bianche 12, 60131 Ancona, Italy

Abstract. Additive manufacturing (AM) is a flexible technology allowing designers to produce highly customized and complex shapes. The design phase can be supported by Design for AM (DfAM) tools in order to reduce material waste, design time and economic resources. This paper aims to evaluate the functionality of four commercial tools for simulating the powder bed fusion (PBF) deposition process using quantitative and qualitative evaluation metrics. An AM process simulation workflow has been defined to facilitate the tools evaluation. For a complete evaluation, three different case studies were analyzed. Simulation carried out with the tools have the same critical zones relative to the three mechanical components, but with different maximum distortion values. Qualitative metrics show differences in workflow complexity and support provided by tools during the simulation setup phase. In the industrial field, these aspects can affect the choice of one tool over another.

Keywords: Additive Manufacturing · Design for Additive Manufacturing · DfAM tools · Simulation · PBF deposition process

1 Introduction and Research Background

Additive Manufacturing (AM) includes a wide range of technologies that allow to create physical components from virtual 3D models with a layer-by-layer process [1]. One of the advantages of AM is the ability to use robust Design for Additive Manufacturing (DfAM) methods and tools that allow designers to predict the technical response of systems and automate the design process. DfAM aims to maximize product performance while simultaneously considering the shape, manufacturing process and functionality of components, without the production constraints of traditional methods [2].

Powder bed fusion (PBF) is a printing technology approved by the ISO/ASTM 52900 standard [3]. This technique uses thermal energy to melt and solidify a region of powder bed layer by layer. Selective laser melting (SLM) is a PBF additive manufacturing technology, based on the melting of atomized metal powder by laser [4]. The power of the laser can produce negative thermal effects causing distortion of parts and cracks [5]. Therefore, the evaluation of distortions represents a fundamental focus to prevent the occurrence of such phenomena. A "trial and error" process is not recommended

M. Carfagni et al. (Eds.): ADM 2023, LNME, pp. 13–20, 2024.
https://doi.org/10.1007/978-3-031-52075-4_2

because it involves a waste of material, time and costs. In recent years, several DfAM methodologies and tools have been investigated to support designers in evaluating and setting the parameters of the deposition process [6, 7].

In this context, the present study aims to preliminarily compare the functionalities of four DfAM commercial tools aimed at supporting the deposition process simulation. Among the different existing computational approaches this work adopted a macro-scale approach that is the most used in the industrial field [8]. The final goal is to support designers in choosing the most appropriate DfAM tool based on their needs. In order to facilitate the assessment, an evaluation protocol has been defined starting from the pre-processing phase (part orientation, printing parameters) up to the post-processing operations (removal of the part from the printing plate and supports).

2 Method

To carry out an objective assessment of the four analyzed DfAM tools, an evaluation protocol consisting of the main phases (Sect. 2.1) of the workflow has been defined. Comparison between the various tools is facilitated by some quantitative and qualitative metrics (Sect. 2.2) that will be applied to the case studies.

2.1 Evaluation Protocol

The definition of an evaluation protocol (Fig. 1) is essential for carrying out a systematic assessment and allows to analyze all the main steps and their sequentiality.

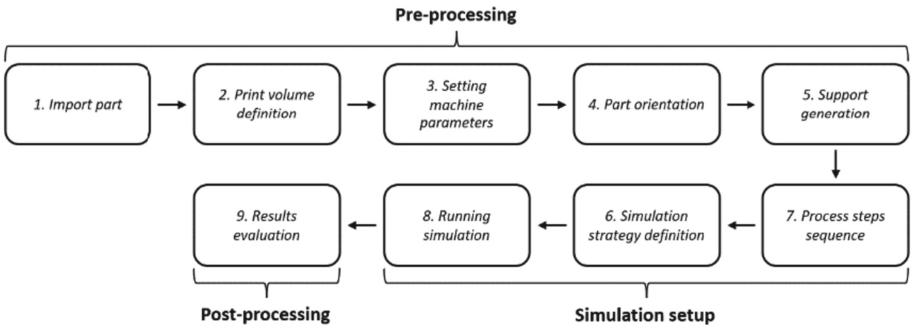

Fig. 1. Steps of the simulation process.

The simulation process consists of 9 consecutive steps grouped into 3 main phases: i) *Pre-processing*, that represents all the simulation preliminary settings; ii) *Simulation setup*, that includes the simulation settings and steps sequence; iii) *Post-processing*, that consists of observing the results.

2.2 Metrics

A mix of quantitative and qualitative metrics have been adopted to make a systematic and objective assessment of the tools.

Quantitative metrics allow an assessment of results from a technical point of view and the main ones are: i) *Maximum total deformation*; ii) *Recoater impacts* with the previously solidified layer; iii) *STL of the deformed and compensated geometry*, defined as the number of facets.

Qualitative metrics aim to assess the functionality and features of the tools analyzed. In this study are as follows: i) *Workflow complexity*, defined as the number of clicks required to set up the simulation; ii) *Flexibility* and *customization of the simulation*, that represent the heat treatment customization, the presence of a help window, the possibility of visualizing the mesh and the print time estimation; iii) *AM process wizard* presence.

3 Case Studies

3.1 Components

This section shows three components that will undergo the simulation of the printing process. The choice of components is based on their geometric complexity, functionality, and field of application. The three components selected for the study are: i) *Gas turbine blade*; ii) *Drone frame*; iii) *Wall bracket* topologically optimized.

To make a consistent evaluation, the same simulation parameters were set in all DfAM tools (Table 1). The orientation of the components was set on the optimization of the printing time to evaluate the deformation effects generated.

Table 1. Components and simulation settings.

Component		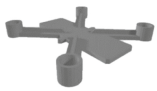	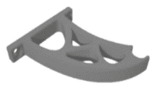
Mesh size	3 mm	1.6 mm	1.6 mm
Material		Inconel 718	
Support type		Block support	
Layer thickness		40 µm	
Baseplate temperature		80°C	
Heat treatment		800°C	
Laser power		290 W	
Laser scan speed		1000 mm/s	
Recoating time		12 s	

3.2 DfAM Tools

Through a careful analysis of the state of the art referring to the simulation of the PBF process, four commercial tools used in industry and research were selected [9–11]: i) *Ansys Additive Print 2021 R1*, a stand-alone software tools; ii) *Ansys Additive Suite 2021 R1*, that allows to perform a thermomechanical simulation; iii) *Siemens NX 19.0*, equipped with a PBF simulation module; iv) *Autodesk Netfabb Ultimate 2023*.

4 Results and Discussion

This section shows the results obtained from simulations performed with the DfAM tools. Parts orientation was chosen optimizing the printing time. Results are shown in Sects. 4.1 and 4.2. Section 4.3 provides a critical discussion on the obtained results.

4.1 Quantitative Metrics

Figures 2, Fig. 3 and Fig. 4 show the total deformations of the case studies obtained from the simulations of the printing process performed with the four tools, while the respective quantitative metrics are shown in Table 2.

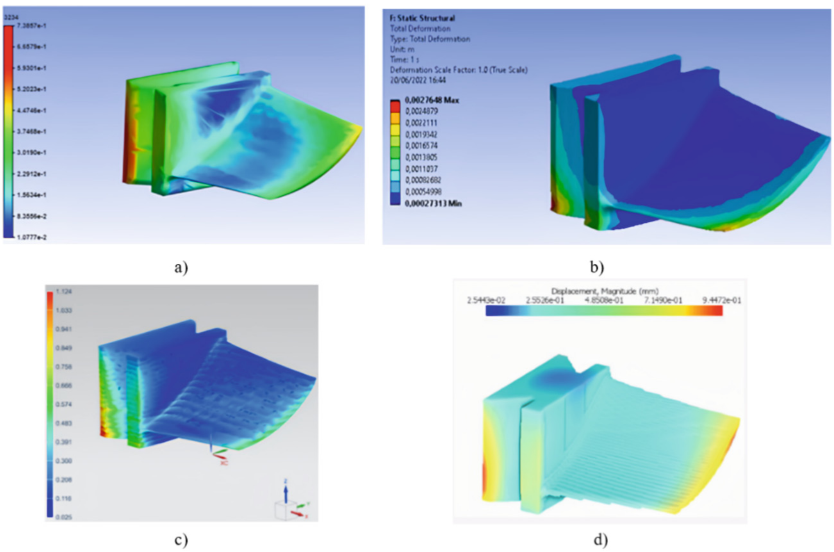

Fig. 2. Total deformations of turbine blade: a) Ansys Additive Print; b) Ansys Additive Suite; c) Siemens NX; d) Autodesk Netfabb.

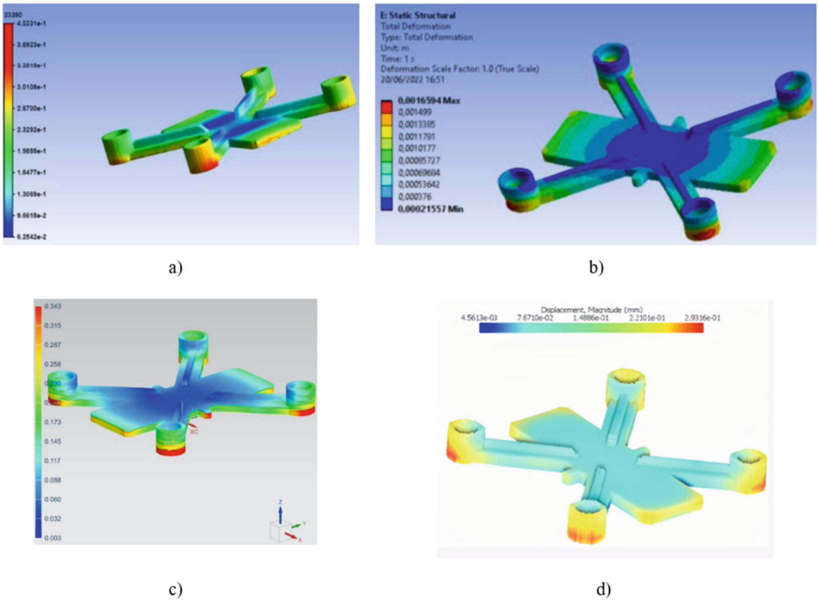

Fig. 3. Total deformations of drone frame: a) Ansys Additive Print; b) Ansys Additive Suite; c) Siemens NX; d) Autodesk Netfabb.

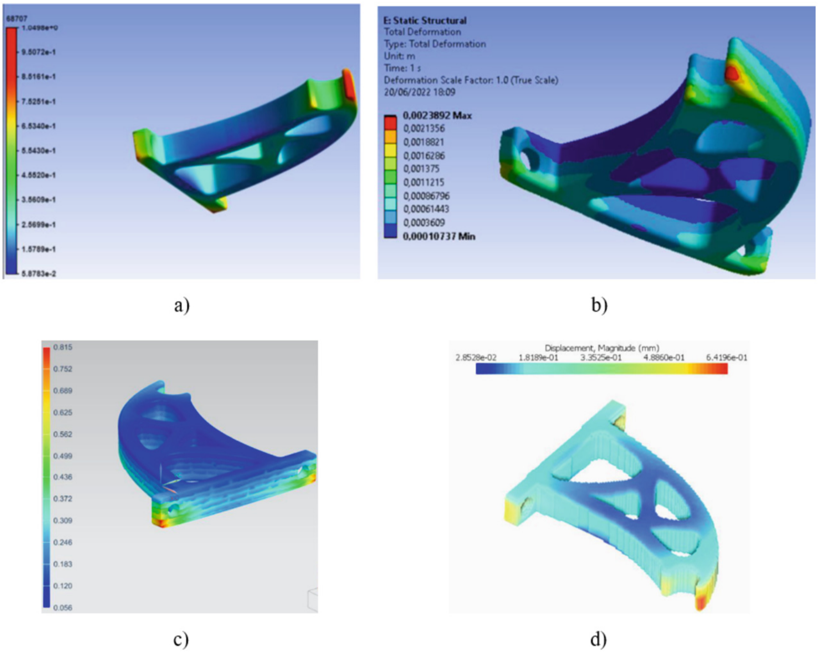

Fig. 4. Total deformations of wall bracket: a) Ansys Additive Print; b) Ansys Additive Suite; c) Siemens NX; d) Autodesk Netfabb.

Table 2. Quantitative metrics of the three components.

DfAM tool	Deformation [mm]	Recoater impacts	Deformed STL facets	Compensated STL facets
TURBINE BLADE				
Ansys Additive Print	0.738	16	6636	6464
Ansys Additive Suite	2.764	23	355120	355120
Siemens NX	1.124	12	34078	34078
Netfabb Ultimate	0.945	14	218462	220288
DRONE FRAME				
Ansys Additive Print	0.403	6	49528	47892
Ansys Additive Suite	1.659	11	332728	332728
Siemens NX	0.343	4	33628	33628
Netfabb Ultimate	0.293	3	82820	82904
WALL BRACKET				
Ansys Additive Print	1.045	9	149212	149150
Ansys Additive Suite	2.389	13	131992	131992
Siemens NX	0.815	7	87052	87052
Netfabb Ultimate	0.642	5	211526	214716

4.2 Qualitative Metrics

Workflow complexity is evaluated by the number of clicks from the part import phase until the results are obtained at the end of the simulation (i.e., from step 1 to step 8 of the evaluation protocol shown in Fig. 1). The simulation procedure is the same for each part regardless of its geometry, and for this reason the number of clicks for each software is equivalent for all three case studies. Table 3 shows the qualitative metrics.

4.3 Discussion

From the simulation results, the maximum deformations obtained by the four tools for each component are in the same critical areas.

Regarding the quantitative metrics of the turbine blade, shown in Table 2, the deformations recorded in Siemens NX and Autodesk Netfabb have comparable values to each other, while Ansys Additive Print has lower deformations. In contrast, Ansys Additive Suite has higher deformations than the other tools. In addition, a considerable number of impacts were found with the printer recoater due to the extension of the geometry in the vertical direction (printing direction). It is worth noting how the number of facets in the STL file of the deformed and compensated geometry remains unchanged in simulations with Ansys Additive Suite and Siemens NX. In Ansys Additive Print the number of

Table 3. Qualitative metrics of the various DfAM tools analyzed.

Qualitative metric	Ansys Additive Print	Ansys Additive Suite	Siemens NX	Autodesk Netfabb
Workflow complexity	96	194	73	61
AM process wizard	No	Yes	No	No
Heat treatment customization	No	Yes	Yes	Yes
Help window	Yes	Yes	No	No
Mesh visualization	No	Yes	Yes	Yes
Print time estimation	No	No	No	Yes

facets of the compensated geometry is less than that of the deformed geometry, while in Autodesk Netfabb there is the opposite situation.

The deformations obtained from the drone frame simulations performed with Ansys Additive Print, Siemens NX and Autodesk Netfabb assume extremely comparable values between them, as shown in Table 2. Again, Ansys Additive Suite has higher total deformations compared to other tools. The same trend can be appreciated in the impacts with the printer recoater, where Ansys Additive Suite recorded more impacts due to the higher geometry deformation. Siemens NX and Ansys Additive Suite have the same number of facets in the STL file of the deformed and compensated geometry. In contrast, Ansys Additive Print provides more facets of the deformed geometry than the compensated geometry, while Autodesk Netfabb has fewer facets of the deformed geometry than the compensated geometry.

About the wall bracket simulations, the maximum total deformation and the number of recoater impacts obtained with Ansys Additive Suite are significantly higher than their counterparts. Like the previous two case studies, Ansys Additive Print, Siemens NX, and Autodesk Netfabb have very similar deformation values between them. In relation to the number of facets of the deformed and compensated geometry, the same considerations drawn from the previous two cases can be inferred.

Concerning qualitative metrics and observing the Table 3, it appears that Ansys Additive Print and Siemens NX have comparable workflow complexity, while Autodesk Netfabb has lower complexity. Instead, Ansys Additive Suite has higher workflow complexity than the others, despite being the only DfAM tool to have a wizard that supports the simulation setup phase.

Ansys Additive Print is the only tool that does not allow customizing the heat treatment of the simulation. In addition, during the simulation setup phase it does not allow to visualize the mesh, and this aspect could be very disadvantageous in case it is necessary to visualize any changes in some mesh and supports parameters.

Siemens NX and Autodesk Netfabb do not have a help window that makes it easier to understand the input parameters for the simulation, while only Autodesk Netfabb provides an estimate of the printing time based also on the characteristics of the machine used.

5 Conclusions

The comparative evaluation showed that all tools are able to identify the same critical areas in terms of deformation. Ansys Additive Suite is the tool that allows a more advanced customization of the simulation than the others, providing also extensive support during setup but with a higher workflow complexity. The other tools present comparable results from a technical point of view. Regarding qualitative metrics, Ansys Additive Print provides limited support during simulation and does not allow for customization of heat treatment, while Siemens NX and Autodesk Netfabb have similar qualitative metrics, with the last one that is the only tool that estimates printing times.

Future developments could regard an increase in case studies and tools, as well as metrics, with the aim of having a more comprehensive evaluation. In addition, a mesh sensitivity analysis should be performed to verify how the outputs are influenced. The realization of a physical prototype could be crucial to establish the reliability of the different simulations. Finally, a usability assessment could be also done.

References

1. Ngo, T.D., Kashani, A., Imbalzano, G., Nguyen, K.T.Q., Hui, D.: Additive manufacturing (3D printing): a review of materials, methods, applications and challenges. Compos. B Eng. **143**, 172–196 (2018)
2. Diegel, O., Nordin, A., Motte, D.: A Practical Guide to Design for Additive Manufacturing. 1st edn. Springer, Singapore (2019). https://doi.org/10.1007/978-981-13-8281-9
3. Calignano, F., et al.: Overview on additive manufacturing technologies. Proc. IEEE **105**(4), 593–612 (2017)
4. Gibson, I., Rosen, D., Stucker, B.: Additive Manufacturing Technologies – 3D Printing, Rapid Prototyping, and Direct Digital Manufacturing. 2nd Edition, Springer, New York (2015). https://doi.org/10.1007/978-1-4939-2113-3
5. Hajnys, J., Pagáč, M., Měsíček, J., Petru, J., Król, M.: Influence of scanning strategy parameters on residual stress in the SLM process according to the bridge curvature method for AISI 316L stainless steel. Materials **13**, 1659 (2020)
6. Alammar, A., Kois, J.C., Revilla-León, M., Att, W.: Additive manufacturing technologies: current status and future perspectives. J. Prosthodont. **31**, 4–12 (2022)
7. Kumke, M., Watschke, H., Hartogh, P., et al.: Methods and tools for identifying and leveraging additive manufacturing design potentials. Int. J. Interact. Des. Manuf. **12**, 481–493 (2018)
8. Daryadel, S., Behroozfar, A., Minary-Jolandan, M.: A microscale additive manufacturing approach for in situ nanomechanics. Mater. Sci. Eng. A **767**, 138441 (2019)
9. Wiberg, A., Persson, J., Ölvander, J.: Design for additive manufacturing – a review of available design methods and software. Rapid Prototyping J. **25**(6), 1080–1094 (2019)
10. Sbrugnera Sotomayor, N.A., Caiazzo, F., Alfieri, V.: Enhancing design for additive manufacturing workflow: optimization. Des. Simul. Tools. Appl. Sci. **11**, 6628 (2021)
11. Moreno Nieto, D., Moreno Sanchez, D.: Design for additive manufacturing: tool review and a case study. Appl. Sci. **11**, 1571 (2021)

Investigation About the Impact of Nozzle and Chamber Temperatures and Infill Orientation on the Mechanical Behavior of 3D Printed PEEK Specimens

Alessandro Greco[1](✉), Raffaele Sepe[2], and Salvatore Gerbino[1]

[1] Department of Engineering, University of Campania Luigi Vanvitelli, via Roma 29, 81031 Aversa, (CE), Italy
alessandro.greco@unicampania.it
[2] Department of Industrial Engineering, University of Salerno, via G. Paolo II 132, 84084 Fisciano, (SA), Italy

Abstract. Polyether Ether Ketone (PEEK) is a high-performance polymer widely used in several fields due to its excellent material and chemical strength properties also at high operating temperatures. The processing conditions used to fabricate PEEK parts can significantly influence the crystallinity and, hence, mechanical properties. Manufacturing difficulties are further amplified when PEEK is produced by Additive Manufacturing (AM), since it requires high processing temperatures, which only a few 3D printers available on the market can guarantee.

In this paper, a Design of Experiment (DoE) was employed to investigate the mechanical properties of PEEK produced by Fused Filament Fabrication (FFF). Nozzle Temperature (390 °C and 420 °C), Chamber Temperature (80 °C and 100 °C) and Infill orientations (0° and 45°) were involved in the experiment through a 2-level full factorial DoE. Young's modulus, Yield Stress, Ultimate Tensile Stress and elongation at fracture were investigated.

Through ANOVA analysis it was found that the three parameters do not influence Young modulus (2.6 ÷ 3.2 GPa), while their combinations influence yield stress (36 ÷ 46 MPa), tensile strength (45 ÷ 74 MPa) and elongation at fracture (2.1 ÷ 16%). As expected, the optimal values for the best mechanical properties are the highest levels of nozzle and chamber temperatures and 0° infill orientation.

Keywords: Design for AM · Fused Filament Fabrication · PEEK · Design of Experiment · Tensile Test

1 Introduction

PolyEther Ether Ketone (PEEK) is a linear, aromatic, semi-crystalline thermoplastic polymer and an important member of Poly Aryl Ether Ketone (PAEK) family. It offers excellent thermal stability, chemical resistance and mechanical properties, making PEEK a popular choice for engineering applications [1]. Among the family members, PEEK is the most widely used 3D printing material due to its easy of machining and unique

M. Carfagni et al. (Eds.): ADM 2023, LNME, pp. 21–30, 2024.
https://doi.org/10.1007/978-3-031-52075-4_3

combination of mechanical properties, including high temperature and combustion resistance, good dielectric performance, and resistance to wear, fatigue, and creep. Thanks to its biocompatibility, PEEK is also widely used in biomedical applications [2], as well as in aerospace, automotive, electrical, and other fields where it can replace metals [3].

There are various modes of producing PEEK, such as injection molding, machining, extrusion, etc., but AM processes, particularly Fused Filament Fabrication (FFF), offers a cost-effective solution with greater shape complexity, higher customization, and flexibility. FFF process consists of layer-by-layer building, and, in recent years, it has been so innovative that it allows the manufacture of advanced polymers, such as PEEK, which typically have very high glass transition temperatures. To ensure good mechanical and aesthetical properties, AM produced PEEK requires nozzle temperatures exceeding 400 °C and chamber temperatures exceeding 150 °C [4].

Currently, AM fabrication of PEEK faces significant challenges, primarily attributable to its semi-crystalline characteristics and its elevated melting temperature. These properties render PEEK highly sensitive to alteration in processing conditions, leading to observed inconsistencies in the material's ultimate performance. Consequently, the utilization of FFF printing for PEEK remains not yet sufficiently suitable in applications where ensuring high standard and consistent results are utmost importance. Studying in depth how the 3D printing process parameters affect the performance of AM products is crucial in the Design for AM processes. Although many studies have been done on polymers, printable with FFF technologies, about PEEK several aspects still need to be investigated.

In recent years, various research studies have examined the effect of printing parameters on the performance of the 3D-printed PEEK parts since residual stress, accumulated during layer-by-layer manufacturing, lead to warping and interlayer delamination. These problems are more pronounced in AM process and can significantly affect dimensional accuracy and mechanical properties.

Among numerous process parameters, the most important researches are focused on layer thickness, chamber, nozzle and bed temperatures, as well as raster angles. In a study conducted by Wang et al. [5], the influence of nozzle diameter and printing layer thickness on the physical and mechanical properties of PEEK was investigated. The findings indicated minimal changes in density and tensile strength of PEEK when printed using a 0.4 mm nozzle diameter. However, when larger diameter nozzles were employed, the tensile strength of PEEK deteriorated, particularly with an increase in layer thickness. The authors suggested that interlayer bonding strength was compromised for layers thicker exceeding 0.35 mm. Additionally, Wu et al. [6] found that PEEK exhibited optimal tensile, flexural, and compressive strength when printed with a layer thickness of 0.3 mm.

Concerning temperatures, several authors have investigated their influence on the mechanical and crystallinity properties of PEEK. The mechanical properties of PEEK are significantly influenced by the chamber temperature. Increasing the ambient temperature results higher percentage of crystalline phase, leading to notable enhancement in Young's Modulus and Ultimate Tensile Stress [4, 7]. In terms of nozzle, insufficient printing temperature can lead to issues such as nozzle clogging and delamination between deposited layers. Conversely, excessively high temperatures can cause thermal degradation of PEEK, and result in dimensional inaccuracies due to significant changes in viscosity [8]. It is recommended to maintain a nozzle temperature range of 420–440 °C.

Bed temperature controls the quality of the manufact. Tseng et al. [9] measured the coefficient of adhesion friction (μs) for polymers, and for PEEK it was observed a high value. Nonetheless, excessively high temperatures can compromise the adhesion process by causing inadequate solidification of the polymer layer. Taking these factors into account, the authors suggest a bed temperature of 280 °C as the optimal value for printing PEEK samples.

From the literature, it is possible finding the recommended values for 3D printing of PEEK, as reported in [4], which are summarized in Table 1.

Table 1. Recommended value for FFF 3D-printing of PEEK [4].

Parameter	Value
Raster angle	0°
Layer thickness	0.1 ÷ 0.3 mm
Chamber temperature	150 ÷ 200 °C
Nozzle temperature	410 ÷ 440 °C
Printing speed	20 mm/s
Infill	100%

It should be emphasized that these values are primarily derived from tensile mechanical performance of the specimens. Nevertheless, achieving satisfactory structural performance often involves a trade-off with the aesthetic requirements of the artefacts, making it important to strike a balance by setting the process parameters appropriately. Technically speaking, the optimization of the difference between the nozzle and bed/chamber temperature in 3D-printers is the most critical aspect. This is because minimizing thermal gradients across the beads is necessary for producing parts that exhibit desirable mechanical performance and dimensional stability.

Moreover, not all FFF systems on the market, considered suitable for PEEK printing, guarantee operation in the optimal temperature ranges.

In collaboration with 3DnA Srl (Italy), this article presents the results of an experimental campaign that aimed to investigate the impact of infill orientation, nozzle and chamber temperatures, and their combinations, on the tensile properties of 3D printed PEEK specimens. To achieve this objective, a full factorial Design of Experiment (DoE) was employed, and all specimens were subjected to tensile test. This paper marks represents an advancement in the existing literature by contributing to a more comprehensive understanding of the behavior of this complex material. Specifically, it sheds light on the challenges encountered when attempting to achieve optimum print settings under less than ideal conditions.

2 Materials and Methods

The experimental campaign was carried out in collaboration with 3DnA Srl (Italy) and based on a two-level full-factorial DoE. Three critical FFF process parameters were considered as input:

- Nozzle temperature;
- Chamber temperature;
- Infill orientation.

The DoE structure and the combinations are reported in Tables 2 and 3 respectively.

Table 2. DoE structure.

Parameter	Levels	
Nozzle Temperature	390 °C	420 °C
Chamber temperature	80 °C	100 °C
Infill Orientation	0 deg	45 deg

Table 3. DoE combinations.

Series	Nozzle temperature [°C]	Chamber temperature [°C]	Infill orientation [deg]
A	420	80	45
B	420	100	45
C	390	80	45
D	390	80	0
E	390	100	45
F	420	80	0
G	420	100	0
H	390	100	0

A total number of 24 specimens, three specimens for each configuration, were manufactured according to ASTM D638 requirements (Fig. 1) by Selltek D3-XP 3D printer [10] with fixed printing parameters reported in Table 4. The specimens were made of TreeD Natural PEEK 1.75 mm diameter filament [11]. The filament datasheet [11] reports a 3.8 GPa Young Modulus and 97 MPa Ultimate Tensile Stress. Figure 2 shows the first repetition of the specimens series labeled according to Table 3.

All the specimens were subjected to tensile tests by MTS Insight 30 Electromechanical Testing Machine equipped with a load cell of 30 kN. Strains were gathered through an MTS Axial Extensometer having a 50 mm gauge length.

Table 4. Fixed 3D printing parameters.

Parameter	Value
Layer thickness	0.2 mm
Nozzle diameter	0.4 mm
Infill density	100%
Infill pattern	linear
Specimen orientation	Flat
Number of perimeters	2
Printing speed	15 mm/s
Bed temperature	120 °C

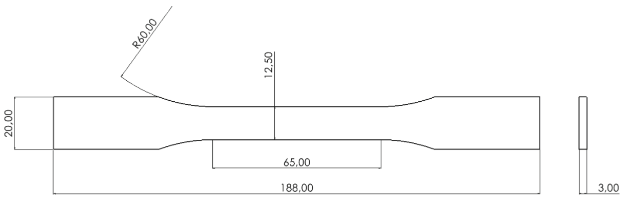

Fig. 1. Specimen geometry in accordance with the Standard ASTM-D638.

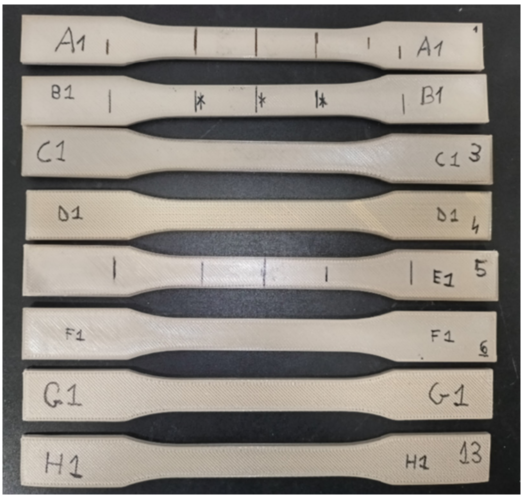

Fig. 2. Printed specimens series (label 1 stands for "first repetition").

3 Results Analysis and Discussion

Figure 3 shows the stress-strain curves, while Table 5 reports the average values and standard deviation of the evaluated tensile properties for each series of specimens: Young's modulus, Yield Stress, Ultimate Tensile Stress (UTS), Elongation at fracture.

Table 4 displays the average mechanical properties of all the series, which are found to be inconsistent with the filament technical datasheet. Notably, the Young's modulus values differ from the producer's reference value (3.8 GPa) by 22% (series C) and 28% (series A). Similarly, about UTS, values are significantly lower than those provided by the company (97 MPa), varying from 29% (series G) to 45.5% (series E).

To further investigate the effect of parameters and their interaction on tensile properties, ANOVA analysis was performed at significance level of $\alpha = 0.05$.

Pareto charts revealed that none of the parameters, whether considered individually or with interaction, had a significant influence on the Young's Modulus values, as they are enough consistent between them.

About Yield stress, it is influenced by the interaction of the three parameters, with B and D series exhibiting the highest and the lowest values respectively.

As expected, the G series, printed at the highest nozzle and chamber temperature and a 0 deg infill orientation angle, represents the best combination in terms of mechanical properties and repeatability of data.

However, by comparing the results with those available in the literature it is important to know that the mechanical performance of 3D printed PEEK is still considerably lower to that of molded PEEK., typically characterized by 4 GPa Young's modulus and 120 MPa UTS. Moreover, as anticipated, the selected parameters combination still returns lower values of Young's modulus and UTS even than those reported for the used filament (3.8 GPa and 98 MPa respectively). Nevertheless, a direct comparison with other result published in the literature was made. Table 6 presents a comparison of Young's modulus and UTS reported in other articles, which carried out a similar experimentations.

From the comparison it emerges that, at the similar conditions for nozzle temperature, infill orientation, nozzle diameter and others, the lower tensile performance, for both Young's Modulus and UTS, seems to be strongly dependent on the chamber temperature. This agrees with the statement in Sect. 1, which highlights the crucial role played by chamber temperature in the mechanical properties of printed PEEK. Indeed, as already stated, increasing the ambient temperature results higher percentage of crystalline phase, leading to notable enhancement in Young's Modulus and UTS [4, 7]. It is noteworthy that the Selltek 3D-XP printer does not guarantee a chamber temperature above 120 °C, not comparable with glass transition temperature (around 143 °C for PEEK) which may explain the observed lower tensile performance. This might suggest that the material's behaviour tends to be amorphous.

It is no wonder that, from the Table 6, UTS value is similar to that obtained in [6], where the used homemade printer probably does not provide chamber temperature control, so its value is assumed to be comparable to the one in this study. However, a further comparison can be made with values reported in [15], which investigates parameters setting similar to this study and reports similar results in terms of Young's modulus and UTS, based on comparison also with filaments from different manufacturers.

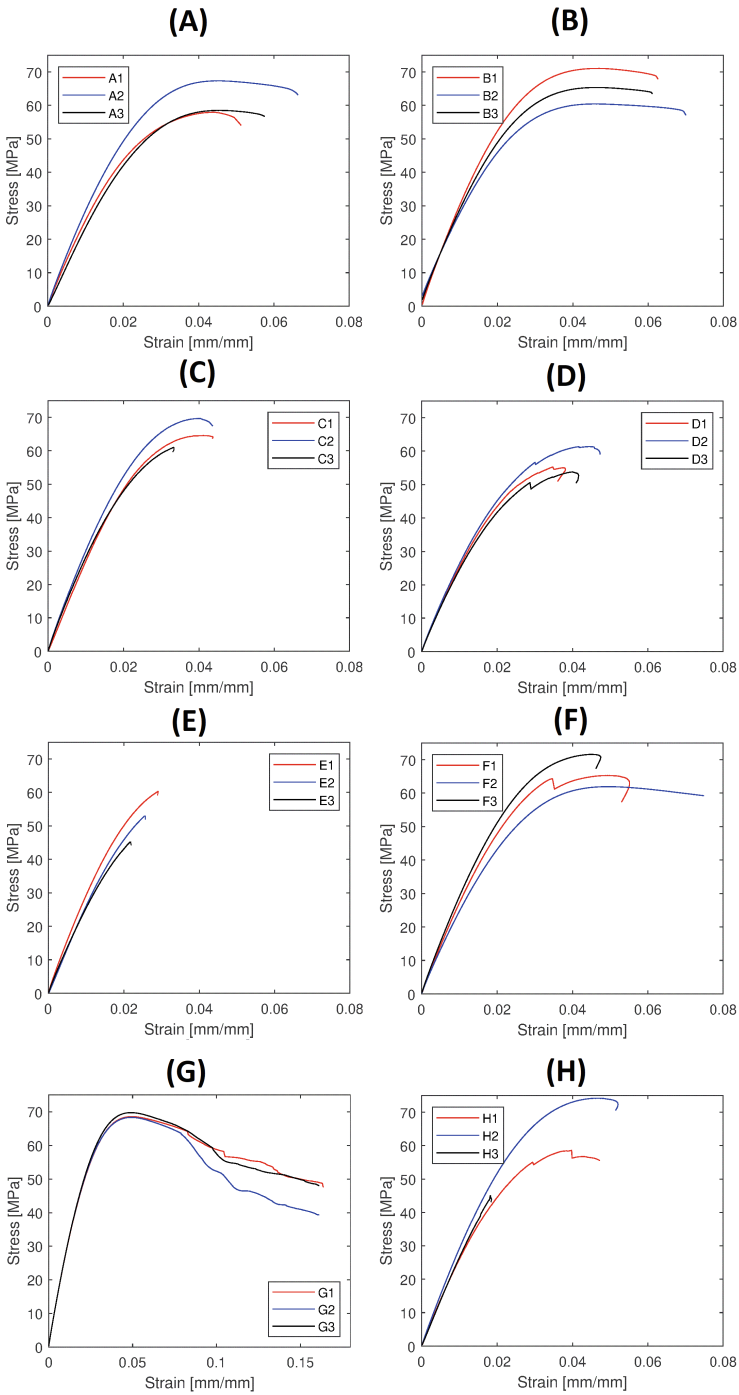

Fig. 3. Stress-strain curves grouped by series.

Table 5. Average values of mechanical properties.

Series	Young's modulus [GPa]	Yield Stress [MPa]	Elongation at fracture [%]	UTS [MPa]
A	2.711 ± 0.30	39.129 ± 2.40	5.79 ± 0.70	61.249 ± 5.27
B	2.885 ± 0.27	44.728 ± 0.38	6.45 ± 0.47	65.591 ± 5.31
C	2.973 ± 0.20	43.683 ± 3.66	4.01 ± 0.59	65.062 ± 4.33
D	2.680 ± 0.09	36.462 ± 1.78	4.23 ± 0.45	56.790 ± 4.01
E	2.819 ± 0.23	40.217 ± 3.21	2.54 ± 0.37	52.819 ± 7.55
F	2.823 ± 0.21	41.235 ± 4.21	7.25 ± 3.70	66.237 ± 4.88
G	2.860 ± 0.001	41.869 ± 0.43	16.06 ± 0.11	68.867 ± 0.75
H	2.824 ± 0.13	43.135 ± 3.67	3.9 ± 1.83	59.245 ± 14.57

Table 6. Comparison with similar studies in literature.

Author	3D Printer	Main FFF parameters	Young's Modulus [GPa]	UTS [MPa]
Present work	Selltek D3-XP	see Table 3 and Table 4	2.68 ÷ 2.88	52 ÷ 69
Zerean et al. [12]	Kumovis R1	0 deg raster angle; 4 mm nozzle diameter; 250 °C chamber temp.; 100% infill; flat orientation	3.29	89.381
Arif et al. [13]	Indmatec HPP 155	0.1 mm layer height; 410 °C nozzle temp.; 100% infill; flat orientation; 100 °C bed temp	3.8	82.6
Wu et al. [6]	Custom-built	0.2 mm layer thickness; 0 deg raster angle; flat orientation; 0.4 mm nozzle diameter	–	56.6
Ding et al. [14]	Custom-built	0.4 mm nozzle diameter.; flat orientation; 270 °C bed temp.; 0.2 mm layer thickness; 390–410 °C nozzle temp	–	81 ÷ 83

4 Conclusions

The aim of this paper was to examine the impact of some FFF process parameters, including nozzle and chamber temperatures and infill orientation, on tensile properties of PEEK specimens fabricated with Selltek 3D-XP printer.

Tensile tests indicated that, as expected, the best results are achieved with the series of specimens printed at the highest considered nozzle and chamber temperature (420 °C and 100 °C respectively) and infill orientation at 0° (filament deposited along the same direction as the applied load). However, the resulting performance, especially in terms of both Young's modulus and UTS, was lower than not only the reference values of molded PEEK but also other similar studies in the literature.

These findings suggest that the Selltek 3D-XP printer is certainly capable of printing PEEK, which can eventually be used for the production of non-structural parts, avoiding its use as metal-replacement.

For future researches, we plan to conduct additional investigations to better understand the behavior of the material. These will involve the exploration of potential post-treatments, such as annealing, that could enhance the material's mechanical performance. Additionally, we will perform geometrical inspections to assess any distortions that may arise. By incorporating these elements into our research, we aim to gain a comprehensive understanding of the material's behavior and identify strategies to improve its properties.

Acknowledgments. The authors would like to acknowledge 3DnA Srl (Italy) for contributing to this research by providing the AM PEEK specimens. This research is supported by the project TOTEM (ML-based predicTive mOdel for besT pErforMance of AM parts) at the University of Campania Luigi Vanvitelli (IT).

References

1. Wang, J.: Polyether Ether Ketone. In: Handbook of Engineering and Speciality Thermoplastics. pp. 55–95. Wiley, Hoboken (2011). https://doi.org/10.1002/9781118104729.ch3
2. Zheng, J., et al.: Additively-manufactured PEEK/HA porous scaffolds with highly-controllable mechanical properties and excellent biocompatibility. Mater. Sci. Eng. C **128**, 112333 (2021). https://doi.org/10.1016/j.msec.2021.112333
3. Dua, R., Rashad, Z., Spears, J., Dunn, G., Maxwell, M.: Applications of 3D-printed PEEK via fused filament fabrication: a systematic review. Polymers (Basel). **13**, 4046 (2021). https://doi.org/10.3390/polym13224046
4. Zanjanijam, A.R., Major, I., Lyons, J.G., Lafont, U., Devine, D.M.: Fused filament fabrication of PEEK: a review of process-structure-property relationships. Polymers (Basel). **12**, 1665 (2020). https://doi.org/10.3390/polym12081665
5. Wang, P., Zou, B., Xiao, H., Ding, S., Huang, C.: Effects of printing parameters of fused deposition modeling on mechanical properties, surface quality, and microstructure of PEEK. J. Mater. Process. Technol. **271**, 62–74 (2019). https://doi.org/10.1016/j.jmatprotec.2019.03.016
6. Wu, W., Geng, P., Li, G., Zhao, D., Zhang, H., Zhao, J.: Influence of layer thickness and raster angle on the mechanical properties of 3D-printed PEEK and a comparative mechanical study between PEEK and ABS. Materials. **8**, 5834–5846 (2015). https://doi.org/10.3390/ma8095271

7. Yang, C., Tian, X., Li, D., Cao, Y., Zhao, F., Shi, C.: Influence of thermal processing conditions in 3D printing on the crystallinity and mechanical properties of PEEK material. J. Mater. Process. Technol. **248**, 1–7 (2017). https://doi.org/10.1016/j.jmatprotec.2017.04.027
8. Vaezi, M., Yang, S.: Extrusion-based additive manufacturing of PEEK for biomedical applications. Virtual Phys Prototyp. **10**, 123–135 (2015). https://doi.org/10.1080/17452759.2015.1097053
9. Tseng, J.-W., et al.: Screw extrusion-based additive manufacturing of PEEK. Mater. Des. **140**, 209–221 (2018). https://doi.org/10.1016/j.matdes.2017.11.032
10. Selltek 3D-XP. https://www.selltek.it/stampanti-3d-professionali-selltek/. Accessed 23 Feb 2023
11. TreeD Natural PEEK filament. https://treedfilaments.com/product/peek-natural-175o-750gr-spool/. Accessed 14 Feb 2023
12. Zarean, P., et al.: Effect of printing parameters on mechanical performance of material-extrusion 3D-printed PEEK specimens at the point-of-care. Appl. Sci. **13**, 1230 (2023). https://doi.org/10.3390/app13031230
13. Arif, M.F., Kumar, S., Varadarajan, K.M., Cantwell, W.J.: Performance of biocompatible PEEK processed by fused deposition additive manufacturing. Mater. Des. **146**, 249–259 (2018). https://doi.org/10.1016/j.matdes.2018.03.015
14. Ding, S., Zou, B., Wang, P., Ding, H.: Effects of nozzle temperature and building orientation on mechanical properties and microstructure of PEEK and PEI printed by 3D-FDM. Polym. Test. **78**, 105948 (2019). https://doi.org/10.1016/j.polymertesting.2019.105948
15. Das, A., et al.: Current understanding and challenges in high temperature additive manufacturing of engineering thermoplastic polymers. Addit. Manuf. **34**, 101218 (2020). https://doi.org/10.1016/j.addma.2020.101218

Assessment of the Achievable Dimensional Tolerances in 17-4PH Stainless Steel Parts Fabricated by Metal Binder Jetting

M. Zago(✉) and I. Cristofolini

Department of Industrial Engineering, University of Trento, Via Sommarive 9, 38123 Trento, Italy
marco.zago-1@unitn.it

Abstract. This work aims at evaluating the dimensional precision and the accuracy achievable through the Metal Binder Jetting Additive Manufacturing process. An artifact was designed, and 36 replicates were produced using a 17-4PH stainless steel powder aiming at evaluating different feature sizes. The dimensions of the samples were measured by a coordinate measuring machine (CMM) before and after sintering.

At green state, the distribution of measured dimensions parallel to the building direction was centered on the nominal dimension, while the distribution of measured dimensions parallel to the building plane was shifted from the nominal ones. Dimensions of cavities were found to be significantly smaller than nominal ones (*Z* position for fundamental deviation), whereas the dimensions of outer features were larger than the nominal sizes probably on the reason of excessive binder saturation. The dimensional precision ranged from IT9 to IT11.

After sintering, the inaccuracy increased with the distance of samples from the building plane, in turn related to non-uniform shrinkage on sintering. Additionally, sintering determined worsening in the dimensional precision, which ranged from IT11 to IT15.

Keywords: Metal Binder Jetting · Design for AM · Dimensional Precision and Accuracy

1 Introduction

Metal Binder Jetting (MBJ) process has the potential to be widely used thanks to the promising high cost-effectiveness production. Among Additive Manufacturing (AM) technique, MBJ has the ability to process any powders at high production rate and lower cost compared to laser powder bed fusion (L-PBF) and electron beam melting (EBM) processes. The MBJ process involves five steps: printing, curing, de-powdering, de-binding and sintering. To effectively design MBJ products, it is necessary to have a thorough understanding of the process workflow and the variations in product properties and shape that occur during each step, particularly sintering, which can cause significant anisotropic dimensional change and even distortion. These changes can negatively

M. Carfagni et al. (Eds.): ADM 2023, LNME, pp. 31–40, 2024.
https://doi.org/10.1007/978-3-031-52075-4_4

impact the quality of the final product if not properly accounted for in the design process. Several studies investigated the dimensional and geometrical accuracy of product fabricated by Binder jetting (BJ) technique in order to assess the precision capability of the process. Most works focused on green product obtained by ceramic powders. Kim and Oh observed the poor quality of a BJ product in comparison with the same benchmark fabricated with other AM techniques (stereo lithography, fused deposition modeling, poly-jet, selective laser melting, laminated object manufacturing) [1]. In addition, the authors observed a wide distribution of deviation, far away from normal gaussian distribution. Dimitrov et al. confirm the poor precision and accuracy of BJ by the fabrication of a benchmark made of: starch-based, plaster-based and epoxy-based powders. Their analysis highlights precision capability in the range IT9 - IT16 [2]. Islam and Sacks reported similar results (IT13-IT15) for a benchmark fabricated by calcium sulphate hemihydrate [3]. Recently, Modi and Sahu obtained a tolerance grade between IT3 and IT10 in the fabrication of porous bone scaffold by two types of calcium sulphate hemihydrate [4]. The authors attributed the drastic improvement to the selection of optimized material and process parameters. The research of optimal printing parameters is currently under investigation. Several works studied the effect of metal powders and printing parameters by DoE approach [5–7]. In addition, the effect of sintering parameters is studied in-depth since the anisotropic dimensional change significantly affects product precision [8].

Calves et al. studied the repeatability of product precision through 18 months of production, discovering a strong impact of printhead speed and trajectory on the accuracy and precision of green and sintered products. In addition, the analysis highlighted that the tendency observed at green state are not always representative of the tendency at sintered state [9]. Currently, literature lacks of guideline on precision capability of MBJ. On the basis of previous studies [10, 11], this work aims at assessing the dimensional precision achievable by MBJ Additive Manufacturing process. A benchmark was designed, whose geometry includes several features. Green and sintered dimensions were measured by a coordinate measuring machine (CMM). Experimental data were compared with nominal dimensions, and deviation was statistically analyzed in terms of accuracy and precision. Results are shown in terms of fundamental deviation and IT grade classes in order to provide straightforward information to the designers.

2 Materials and Method

This study aims at investigating the achievable dimensional accuracy and precision of MBJ process. A benchmark was designed, including different features: edge, fillet, bulk and hollow cylinders and freeform surface. A code number in the sample surface allowed to recognize sample position and orientation in the building chamber, after de-powdering. Figure 1 shows the axonometric view of the artifact, and the orientation with respect to the printing reference system (X: Binder injection direction, Y: powder spreading direction, Z: building direction). Actual size of the features cannot be disclosed, according to the confidential agreement with the company partner.

36 samples were fabricated, uniformly distributed in the building box at four height levels; on each plane 9 samples were equally spaced in the printing box. A 17-4PH steel powder was employed, samples were printed in one batch by Digital Metal Printing

machine (P1701) according to the process parameters reported in Table 1. The building box measured 178, 189.5 and 66.95 mm along X, Y and Z direction. The saturation level was controlled defining a Dark 3, which corresponds to the saturation of 69% of the pixels [12].

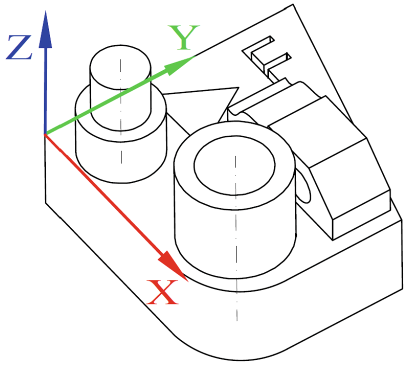

Fig. 1. Axonometric view of the benchmark investigated in this study.

Table 1. Printing parameters.

Layer thickness	Resolution	Bed temperature	Printing speed
42 μm	1200 dpi	80 °C	200 mm/s

After printing, de-powdering and curing, products were thermally de-binded. Then the batch was sintered at 1385 °C for 210 min in a belt furnace under controlled atmosphere. For each sample, the dimensions and geometrical features were measured by a coordinate measuring machine (CMM) before and after sintering process. On the basis of required dimensions at sintered state, the dimensions of the green part were defined using scaling factors proposed by the printing machine producer. The measurements were compared with the nominal dimensions expected at green and sintered state, to evaluate the precision and accuracy.

The dimensional accuracy was determined computing the difference between the average of the measured dimensions and the related nominal dimensions. Results were then provided by the fundamental deviation code system defined in standard system UNI EN ISO 286-1, reporting the letters used for dimensional tolerances positioning (from $a(A)$ to $z_c(Z_c)$).

Dimensional precision was assessed by the standard deviation of the set of measured dimensions. The resulting 6-sigma interval was correlated to the equivalent IT grade class established by the standard code of UNI EN ISO 286-1.

Finally, the fundamental deviation and IT grade tolerances were grouped considering the intervals of dimensions: 0 ÷ 3, 3 ÷ 6, and 10 ÷ 18 mm. Dimensions parallel to the building direction were analyzed separately with respect to dimensions parallel to the building plane; additionally, the results were distinguished considering the four construction levels. This description aims at highlighting the effect of printing and sintering processes on the origin of inaccuracy and lack of precision.

3 Results and Discussion

The precision and accuracy of artifacts are presented at both green and sintered state. Firstly, the dimensional accuracy is shown through the fundamental deviation. Secondly, the dimensional precision is discussed as a function of IT grades. The results are discussed highlighting the contribution of the process workflow to the origin of dimensional errors. The analysis aims at deriving a corrective approach that can improve production quality. The data are presented as grouped by nominal size intervals to provide designers with a ready-to-use guideline for determining process capability.

3.1 Dimensional Accuracy

The dimensional accuracy is analyzed in terms of fundamental deviation, which is calculated by the difference between the average of the measured dimensions and the related nominal dimensions. Figure 2, 3 and Fig. 4 show the fundamental deviation obtained in the intervals of $0 \div 3$, $3 \div 6$ and $10 \div 18$ mm, respectively. Figures report data in the green (G) and sintered (S) state for dimensions parallel to the building plane. Color boxes refer to the different features.

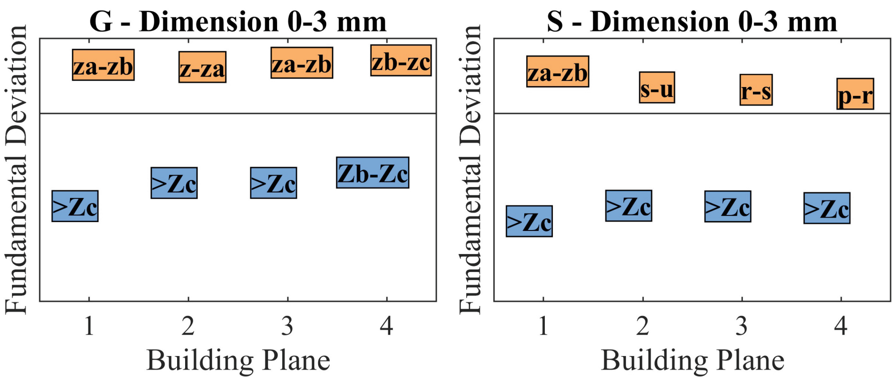

Fig. 2. Fundamental deviation resulting at (G) green and (S) sintered state. Dimensions interval 0 and 3 mm – dimensions parallel to the building plane.

At green state, the measured dimensions are almost unaffected by the fabrication levels, and by the nominal size. The distribution of measured dimensions is characterized by a constant offset, highlighted analyzing feature by feature. For holes, and in general for small dimensions ($0 \div 6$ mm), the deviation from nominal dimension is exceptionally high, over z and Z positions. In case of holes, the presence of residual powders, as a consequence of difficult complete de-powdering in so small holes, might significantly affect

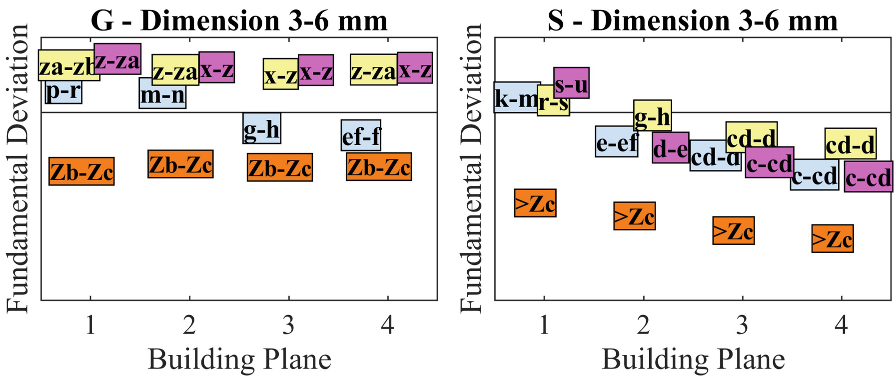

Fig. 3. Fundamental deviation resulting at (G) green and (S) sintered state. Dimensions interval 3 and 6 mm – dimensions parallel to the building plane.

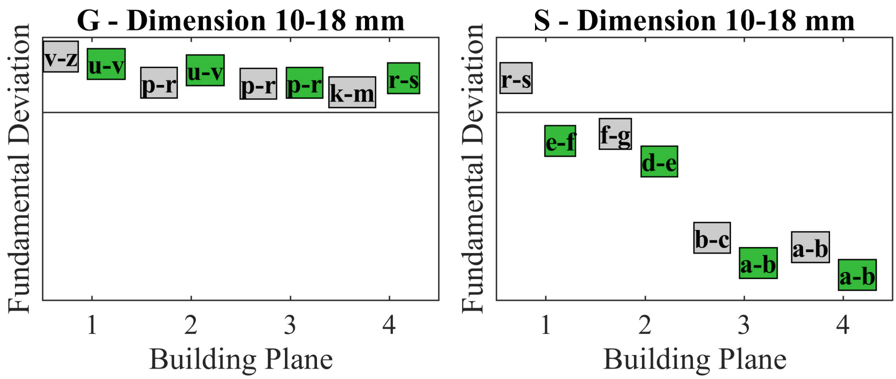

Fig. 4. Fundamental deviation resulting at (G) green and (S) sintered state. Dimensions interval 10 and 18 mm – dimensions parallel to the building plane.

the measurement results, so that measured holes diameters result smaller. For external features, instead, the positive deviation could be related to improper control of binder saturation [13]. The authors assumed that excessive binder was injected, producing a blurring effect. Further work will investigate the influence of binder saturation to prove such hypothesis.

At sintered state, inaccuracy significantly increases on increasing the height level (distance from the building plane). Additionally, the trend becomes more evident on increasing feature size. The results are related to the larger linear shrinkage (and volumetric shrinkage) observed on increasing the fabrication level. As described in literature, non-uniform shrinkage could be ascribed to variation of green density [7] or binder content [14]. Further work will clarify the causes of non-uniform shrinkage to propose a correct tuning of scaling factors.

Figure 5 displays the outcome of heights, which are the dimensions aligned with building direction. At green state, deviations are randomly spread around nominal dimensions, confirming the proper tuning of the process parameters with respect of dimensions aligned with building direction. Conversely, at sintered state, the accuracy shows similar trend as the other features, also highlighting the effect of building level.

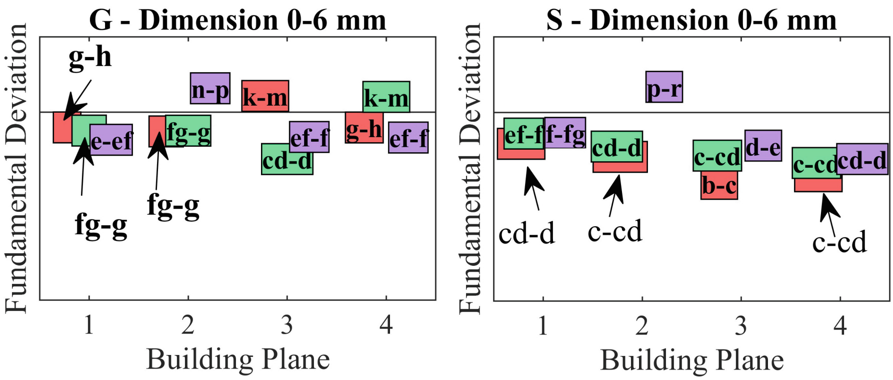

Fig. 5. Fundamental deviation resulting at (G) green and (S) sintered state. Dimensions interval 0 and 6 mm – dimensions parallel to the building plane.

3.2 Dimensional Precision

The dimensional precision is discussed as a function of the IT grades, which are computed using the 6-sigma interval of the measurements. Figures 6, 7 and Fig. 8 compare the precision at the green (G) and sintered (S) state in the dimensional range of: 0 ÷ 3, 3 ÷ 6 and 10 ÷ 18 mm, respectively. Within main intervals, bars are ordered from left to right increasing the nominal size of the features. As stated in the previous section, results are distinguished according to the four building levels, and fifth bar column (all) summarizes the average results for each feature across all building planes. Figure 6, 7 and Fig. 8 shows dimensions parallel the construction plane, whereas height dimensions (parallel to the building direction) are reported in Fig. 9.

At green state, precision varies between IT9 and IT15, mostly in the range IT11-IT12. Same results are shown for height dimensions in Fig. 9. Generally, increasing the nominal size leads to higher dimensional precision. No correlation can be highlighted with nominal dimension or construction plane in dimensions smaller than 3 mm. Higher precision (IT9) occurred in the highest construction plane considering the interval 3 ÷ 6 mm, whereas the interval 10 ÷ 18 exhibits higher precision (IT11) in the first construction plane. According to this description, interval 3 ÷ 6 seems to be the optimal dimensional range for fabricating MBJ products. Further investigation did not reveal any trend ascribable to binder spreading direction or powder spreading direction. Small inner dimensions can be probably affected by de-powdering source of errors, see column blue in Fig. 6 and orange in Fig. 7, related to small holes. Conversely, larger dimensions

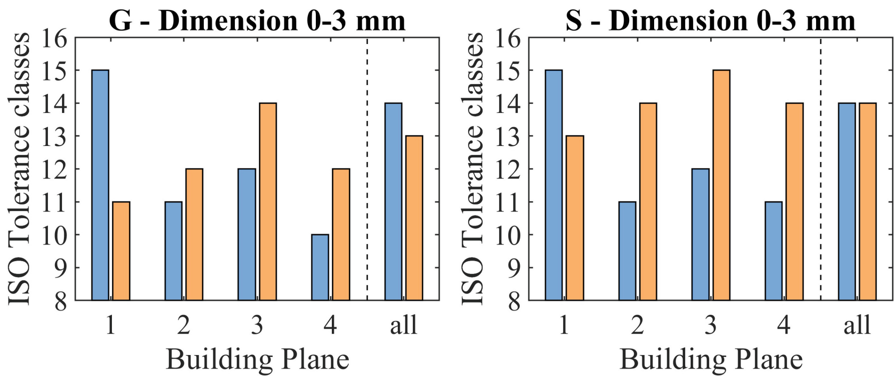

Fig. 6. IT grade tolerance classes resulting at (G) green and (S) sintered state. Dimensions interval 0 and 3 mm – dimensions parallel to the building plane.

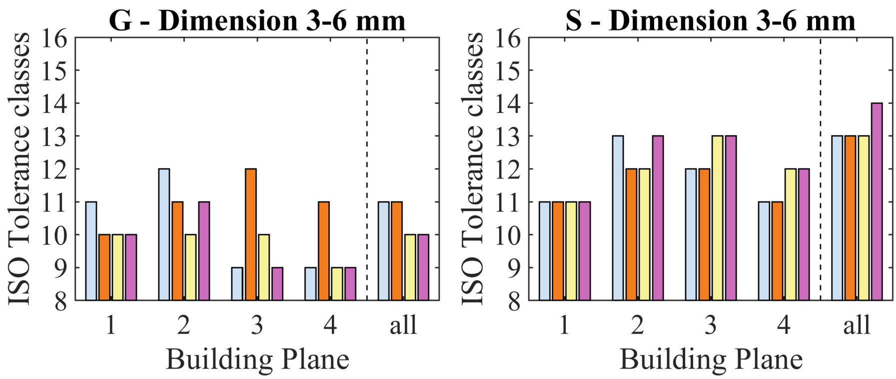

Fig. 7. IT grade tolerance classes resulting at (G) green and (S) sintered state. Dimensions interval 3 and 6 mm – dimensions parallel to the building plane.

might derive by the superposition of different process-induced defects as well as binder fluctuation and layer shifting.

At sintered state, precision significantly lowers in all feature dimensions, both aligned with plane and with building direction. Tolerance classes were shifted in the range between IT11 and IT15, showing a worsening from 1 up to 3 IT grades in comparison with green state condition. The data show poor precision in comparison with metal injection molding reference, which is characterized by an average error of IT11 [15].

An in-depth analysis of sintering results shows a decrease of precision as a function of the building level. The widening of the standard deviation of measured dimensions has not been completely understood yet. According to literature, a small variation of binder saturation [14] and powder particle size [16] can cause significant variation in the dimensional change on sintering. Nevertheless, no influence of building level has been currently reported in literature. Summarizing, though sintering negatively affects the dimensional quality of products, printing process is essentially the main cause of

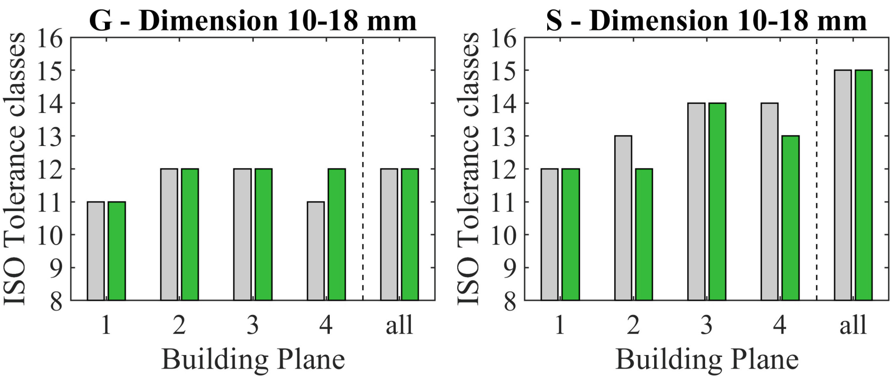

Fig. 8. IT grade tolerance classes resulting at (G) green and (S) sintered state. Dimensions interval 10 and 18 mm – dimensions parallel to the building plane.

the poor precision in final products. Therefore, future studies will optimize the printing process to improve product quality.

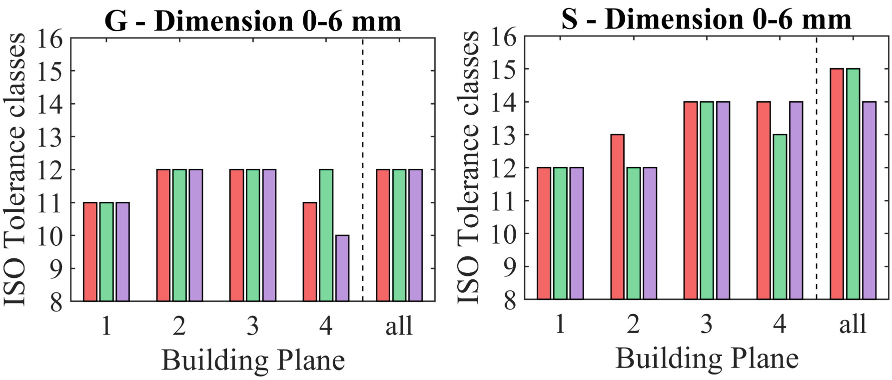

Fig. 9. IT grade tolerance classes resulting at (G) green and (S) sintered state. Dimensions interval 0 and 6 mm – dimensions parallel to the building plane.

4 Conclusions

This study investigated the dimensional accuracy and precision of artifacts fabricated by Metal Binder Jetting process. The samples were measured by means of a CMM before and after the sintering process. The dimensional accuracy was evaluated by fundamental deviation, while dimensional precision was estimated by IT tolerance grades, according to the UNI EN ISO 286-1. The analysis of dimensional accuracy highlights that:

- At green state,

   - o Inner features presented negative deviation (fundamental deviation over Z) likely due to incomplete de-powdering.
   - o External features had positive deviation which is attributed to the excessive binder saturation set-up.
   - o Fundamental deviations of height features were randomly distributed around target position.

- At sintered state:

   - o Fundamental deviation increased with the distance from the building plane. Results are attributed to the increase of linear shrinkage caused by a gradient of green density, or by binder saturation.

The analysis of dimensional precision shows that:

- At the green state: IT grades ranged from IT11 and IT12. Higher error occurred in smaller features.
- At the sintered state, IT grades ranged from of IT11 and IT15. Accuracy decreases with the increase of the distance by the building plane. The reason will be investigated in future work.

Acknowledgements. The project is financed by Provincia Autonoma di Trento, L.P. 13/12/1999, n. 6, Art. 5: Aiuti per la promozione della ricerca e sviluppo. Authors are grateful to dr. Matteo Perina and the whole staff of Mimest s.p.a. for producing the samples and fruitfully cooperating.

References

1. Kim, G.D., Oh, Y.T.: A benchmark study on rapid prototyping processes and machines: Quantitative comparisons of mechanical properties, accuracy, roughness, speed, and material cost. In: Proceedings of the Institution of Mechanical Engineers, Part B: Journal of Engineering Manufacture, pp. 201–215 (2008)
2. Dimitrov, D., Van Wijck, W., Schreve, K., De Beer, N.: Investigating the achievable accuracy of three dimensional printing. Rapid Prototyp. J. **12**, 42–52 (2006)
3. Islam, M.N., Sacks, S.: An experimental investigation into the dimensional error of powder-binder three-dimensional printing. Int. J. Adv. Manuf. Technol. **82**, 1371–1380 (2016)
4. Modi, Y.K., Sahu, K.K.: Process capability analysis of binder jetting 3D printing process for fabrication of calcium sulphate based porous bone scaffolds. Aust. J. Mech. Eng. **00**, 1–9 (2020)
5. Chen, H., Zhao, Y.F.: Process parameters optimization for improving surface quality and manufacturing accuracy of binder jetting additive manufacturing process. Rapid Prototyp. J. **22**, 527–538 (2016)
6. Shrestha, S., Manogharan, G.: Optimization of binder jetting using Taguchi method. Jom. **69**, 491–497 (2017)
7. Barthel, B., Janas, F., Wieland, S.: Powder condition and spreading parameter impact on green and sintered density in metal binder jetting. Powder Metall. 0, 1–9 (2021)
8. Wang, Y., Zhao, Y.F.: Investigation of sintering shrinkage in binder jetting additive manufacturing process. Procedia Manuf. **10**, 779–790 (2017)

9. Calves, P., Robert, M., Verquin, B.: Evaluation of the dimensional repeatability for metal binder jetting : method and results. Proc. WorldPM2022 Congr. Exhib. (2022)
10. Zago, M., Lecis, N.F.M., Vedani, M., Cristofolini, I.: Geometrical issues in design for binder jetting – the effect of anisotropic dimensional change on sintering. In: Rizzi, C., Campana, F., Bici, M., Gherardini, F., Ingrassia, T., Cicconi, P. (eds.) Design Tools and Methods in Industrial Engineering II, pp. 410–421. Springer International Publishing, Cham (2022)
11. Zago, M., Lecis, N., Mariani, M., Uçak, O.U., Cristofolini, I.: Influence of shape distortion on the precision of holes in parts fabricated by Metal Binder Jetting. Int. J. Interact. Des. Manuf. (2023)
12. Dahmen, T., et al.: Densification, microstructure, and mechanical properties of heat-treated MAR-M247 fabricated by Binder Jetting. Addit. Manuf. **39** (2021)
13. Crane, N.B.: Impact of part thickness and drying conditions on saturation limits in binder jet additive manufacturing. Addit. Manuf. **33** (2020)
14. Jiang, R., Monteil, L., Kimes, K., Mostafaei, A., Chmielus, M.: Influence of powder type and binder saturation on binder jet 3D–printed and sintered Inconel 625 samples. Int. J. Adv. Manuf. Technol. **116**, 3827–3838 (2021)
15. Vervoort, P., Martens, M.: 8 - Secondaries for metal injection molding (MIM). In: Heaney, D.F. (ed.) Handbook of Metal Injection Molding (Second Edition), pp. 173–194. Woodhead Publishing (2019)
16. Lee, Y., Gurnon, A.K., Bodner, D., Simunovic, S.: Effect of particle spreading dynamics on powder bed quality in metal additive manufacturing. Integr. Mater. Manuf. Innov. **9**, 410–422 (2020)

Effects of Printing Speed and Thermal Post-processing Treatments on the Mechanical Properties of PEEK Processed by Fused Deposition Modeling

Francesco Tamburrino(✉), Beatrice Aruanno, Alessandro Paoli, and Armando Viviano Razionale

Department of Civil and Industrial Engineering, University of Pisa, Largo L, Lazzarino 1, 56122 Pisa, Italy
francesco.tamburrino@unipi.it

Abstract. Polyether ether ketone (PEEK) is a thermoplastic polymer that presents notable thermal resistance, high mechanical strength, biocompatibility, durability, chemical resistance, and low density. PEEK can be additively manufactured by Power Bed Fusion (PBF) and Material Extrusion (ME) techniques. However, the latter is easier to operate and less expensive than the first solution. Printing parameters and thermal post-processing are fundamental aspects to improve the mechanical and thermal properties of the printed part. In the present study, the effects of two distinct thermal post-processing treatments and three different printing speeds on the mechanical properties of PEEK samples produced by ME were investigated. 45 specimens were manufactured, 15 for each printing speed and 5 for each thermal treatment. The results demonstrated that for the as-printed condition, higher printing speeds produced the greatest outcomes in terms of ultimate tensile strength and elastic modulus, whereas the lowest printing speed produced the maximum strain at break. The thermal post-processing treatments revealed that the one carried out at lower temperatures resulted in negligible changes, while the other significantly improved the mechanical performance of the material. The study's findings provide a solid foundation for printing and post-processing a cutting-edge polymer like PEEK to maximize its potential.

Keywords: PEEK · Material Extrusion · Printing Speed · Thermal Post-Processing · Mechanical Properties

1 Introduction and Background

Polyether ether ketone (PEEK) is a thermoplastic polymer with outstanding thermal and mechanical properties. These material's properties make it appealing for a wide range of industrial applications, including medical, aerospace, electronics, and chemical industries. Unreinforced and reinforced PEEK is increasingly being used to replace metals such as aluminum, magnesium and even steel in some cases, because of its

M. Carfagni et al. (Eds.): ADM 2023, LNME, pp. 41–49, 2024.
https://doi.org/10.1007/978-3-031-52075-4_5

excellent thermal resistance, high mechanical strength, durability, chemical resistance, and low density. As well, this material can be an excellent alternative to titanium, which is more expensive and has a higher density, for orthopedic and dental applications due to its biocompatibility and bone-like mechanical properties [1].

PEEK can be additively manufactured by using two technologies: Powder Bed Fusion (PBF), and in particular Selective Laser Sintering (SLS); and Material Extrusion (ME). SLS is a technique that uses laser beam thermal energy to selectively melt sections of a powder bed together, to form a solid component layer by layer. The ME technique employs a feeder motor to load a filament into the printing system. The filament is then heated to a semi-liquid state before being extruded through a nozzle and printed on a bed one layer at a time, until the entire geometry is produced. In some cases, SLS machines can outperform ME systems in terms of resolution. They are, however, very expensive when compared to ME machines. Furthermore, ME is widely preferred over SLS because it is easier to operate and there is a wide availability of machines that have a large enough printing volume to produce large components [2]. ME should use a machine with a heated and controlled temperature chamber, as well as a nozzle and bed capable of reaching high temperatures, when additively manufacturing PEEK. Furthermore, printing parameters must be correctly set to prevent warping and delamination, and thermal post-processing may be required to improve the mechanical and thermal properties of the printed material [3, 4].

In the present study, the effects of two distinct thermal post-processing treatments (renamed hereafter TT1 and TT2) and three different printing speeds (10 mm/s, 15 mm/s, and 20 mm/s) on the mechanical properties of PEEK samples produced by ME were investigated. The printing speed affects the mechanical properties of the part, such as its strength and stiffness. A higher printing speed may result in a higher number interlayer voids and a more porous structure [5]. Furthermore, it may influence the thermal gradients across extrusion rasters and lead to lower mechanical properties. On the other hand, a slower printing speed can result in a higher mechanical strength, but also a longer printing time. Therefore, it's important to find a tradeoff between printing speed and mechanical properties [6–8]. Thermal post-processing can significantly improve the mechanical properties of the PEEK parts produced by ME. It can increase the crystallinity of the polymer chains, which in turn can improve the mechanical properties of the part. This can be achieved through various methods, such as annealing, or hot-isostatic pressing (HIP). The annealing process consists in bringing the material to high temperatures to favor its crystallization, keeping it at that temperature for a defined time and then gradually cooling it. HIP is a process which simultaneously applies heat and isostatic pressure. The type of material to be treated determines the extent of the temperatures and pressures used. This method has the purpose of reducing internal porosity, and it is primarily utilized with metals produced using additive manufacturing. The thermal post-processing temperature and time play an important role in determining the final properties of the part [9, 10].

In this work, 45 specimens were manufactured, 15 for each printing speed and 5 for each condition (i.e., as-printed, thermal post-processing treatment 1 and thermal post-processing treatment 2). All the specimens were designed and tested according to the ISO 527-1 and ISO 527-2 [11, 12], which specify the testing conditions for determining the tensile properties of plastic materials. Elastic modulus, ultimate tensile strength, and strain at break were determined. Furthermore, the stress-strain curves of the tested specimens were analyzed to determine how the three different printing speeds and the two distinct thermal post-processing treatments affect the mechanical behavior of the material. The study's findings provide a solid foundation for printing and post-processing a cutting-edge polymer like PEEK to maximize its potential.

2 Materials and Methods

The Luvocom 3F 9581 PEEK (Polyether Ether Ketone) filament, supplied by Prima SELECT™, was 3D printed by the CreatBot F430 printing machine. This 3D printer has two direct drive extruders, a closed and heated chamber with a maximum temperature of 70 °C, a maximum bed temperature of 120 °C, and a maximum nozzle temperature of 420 °C. The dog-bone specimen geometry (see Fig. 1) and testing conditions were chosen in compliance with UNI ISO 527–2:2012 (specimen type 5-A). This standard specifies the test conditions for determining the tensile properties of moulding and extrusion plastics. Tensile tests were carried out at room temperature using a Schenck Universal Testing machine, equipped with a load cell of 2 kN and an MTS extensometer with a gauge length of 10 mm. Cross-head speed and data collection rate, instead, were set at 1 mm/min and 25 Hz, respectively. Two grips were used to clamp and test the specimens.

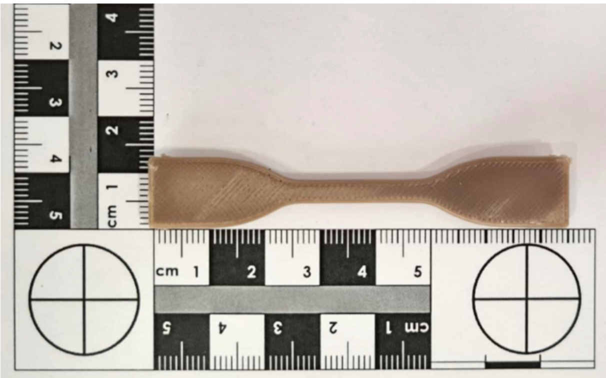

Fig. 1. Dog-bone specimen geometry, specimen type 5-A.

45 specimens were fabricated and included 15 specimens for each of the three conditions that were taken into consideration: as-printed, thermal post-processing treatment 1, and thermal post-processing treatment 2. The process parameters were determined based on early experimental tests and on the instructions provided by the filament manufacturer, to ensure the material's printability. All printing parameters were held constant, except for the printing speed. Table 1 lists the main parameters that were used, while the printing speeds tested are as follows: 10 mm/s, 15 mm/s and 20 mm/s. For each speed, 15 specimens were produced (Fig. 2).

Table 1. Main process parameters used.

Layer height	0,15 mm
Infill density	100%
Extrusion temperature	418 °C
Bed temperature	120 °C
Chamber temperature	65 °C

Two thermal post-processing treatments were considered, one with a maximum temperature of 150 °C and another with a maximum temperature of 200 °C.

The first temperature of 150° was determined by taking into account some previous published studies and PEEK's glass transition temperature (145–155 °C) [13, 14]. However, a semi-crystalline polymer, as PEEK, requires to be brought and maintained at a temperature that is close or even above its glass transition temperature to increase its crystallinity and fully utilize the mechanical properties. For this reason, a second maximum temperature of 200 °C was chosen. The thermal treatments were performed using a Metal 3D printing Starter furnace supplied by Sapphire 3D. The furnace has a heated chamber of 152 × 152 × 159 mm^3 and can reach a maximum temperature of 1370 °C (±1 °C of temperature control accuracy). Figure 3 reports the two thermal treatments that were planned and executed. The two thermal treatments were applied to 30 of the 45 total specimens, 15 for each treatment and thus 5 for the three printing speeds studied. The specimens were packed and placed into an alumina powder-filled crucible during the treatments to prevent direct heat and ensure that the specimens were uniformly heated during the thermal cycles.

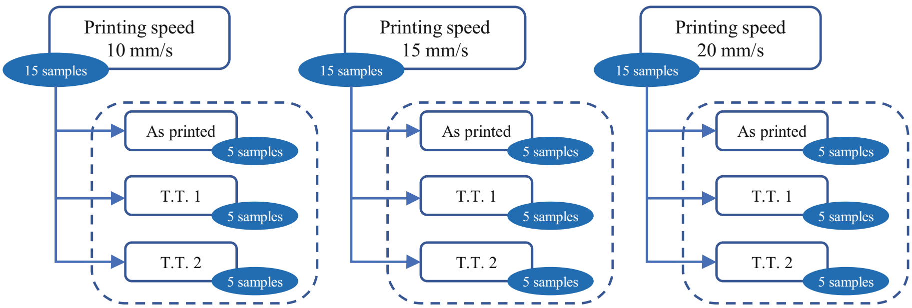

Fig. 2. Plan of the experimental tests.

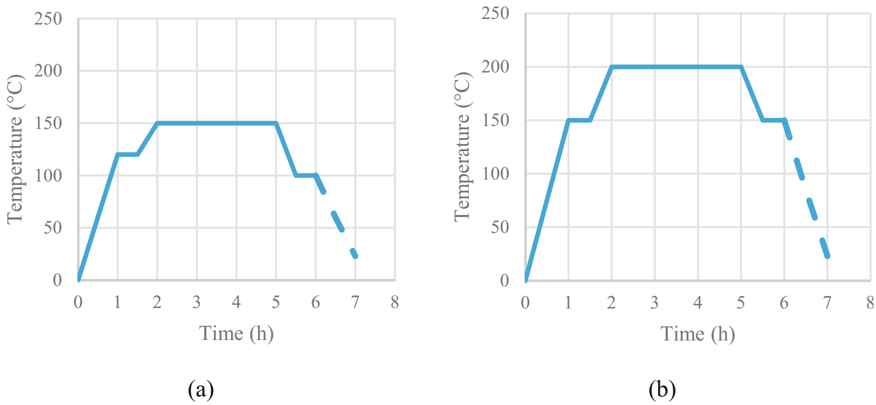

Fig. 3. Thermal post-processing treatments TT1 (a) and TT2 (b)

3 Results and Discussions

Figure 4 reports the results obtained for the tensile tests. Representative stress-strain curves for each printing speed and each condition (as-printed, TT1 and TT2) have been plotted. It is clear that after TT2 the material becomes stiffer and its strength increases. TT1, instead, not always produces significant changes. It is worth noting that the printing speed of 10 mm/s gives the lowest strength and stiffness. However, this set also provides the most noticeable improvement after TT2. The strain at break for all specimens is generally about 3%, with the exceptionof two tested conditions (as-printed and TT1) for printing speed of 10 mm/s, where the strain is higher.

The results retrieved for ultimate tensile strength, elastic modulus and strain reached at break are reported in Fig. 5. TT2 causes an increase in the elastic modulus, which always results greater than 4 GPa. This could be ascribed to a decrease in the delamination and an increase in the polymer's crystallinity. The ultimate tensile strength, after TT2, always increases, becoming higher than 80 MPa (between 83.3 and 85.6 MPa). This specific thermal treatment appears to level the effects of the different printing speeds, which is instead visible by analyzing the results obtained for the as-printed samples. The TT1, on the other hand, does not appear to produce appreciable variations with respect to the as-printed condition, as it also occurred for the elastic modulus. This could be ascribed to maximum temperature of the TT1, which is just above the glass transition temperature, thus preventing adequate crystallization of the material. The strains reached at break are greater for the as-printed condition, while decrease after heat treatment. Minor delaminations that occur after thermal post-processing are likely to result in more brittle mechanical behavior. Overall, the samples manufactured with a printing speed of 10 mm/s exhibit the greatest deformations. Finally, it is noteworthy to highlight that the implementation of both heat treatment methods does not yield any observable manifestations of dimensional and geometric variations. This finding is consistent with expected results, because PEEK is a polymer recognized for its intrinsic capacity to endure high temperatures.

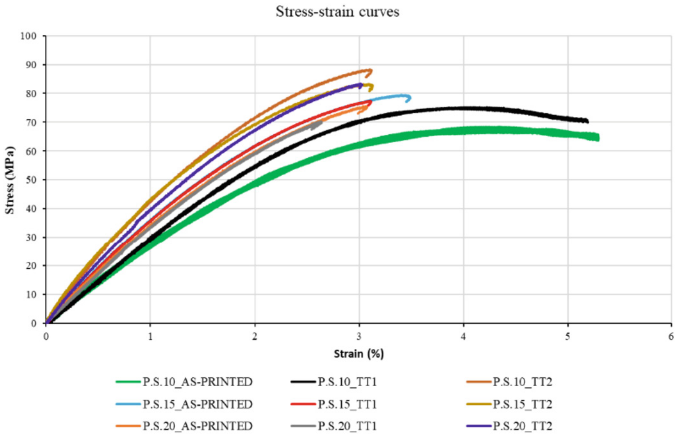

Fig. 4. Stress-strain curves for each printing speed (P.S.10, P.S.15 and P.S.20) and for all the experimented conditions (as-printed, TT1 and TT2).

The current study's findings are interesting also because the printing device employed was not specifically developed for the additive manufacturing of PEEK. For instance, some features, such as maximum chamber and build plate temperatures, may be too low for a material like PEEK. Although the 3D printers used in many similar studies have better technical characteristics, the tensile properties are lower or similar to those found in this study [15, 16]. The maximum tensile strength in the best cases is close to 90 MPa, which is slightly higher than the value determined in this study. However, even after annealing treatments, the elastic modulus values reach a maximum of about 3.6 GPa, which is lower than our findings. In the present study, the elastic modulus is always greater than 4 GPa after annealing, with a maximum value of 4.8 GPa. Chamber temperatures up to 160 °C, for instance, are used in [1, 4]. However, the ultimate tensile strengths achieved (90–95 MPa) are slightly higher than those reported in the present study. In particular, [4] shows that the higher the values of the nozzle, bed, and chamber temperatures, the higher the mechanical properties of 3D printed PEEK. Nonetheless, the greatest elastic modulus observed is 3.1 GPa, which is significantly lower than the value reported in the current study. Finally, another significant result in the study is that TT2 can produce high strength and elastic modulus regardless of printing speed. From an industrial standpoint, this can result in faster production and lower costs.

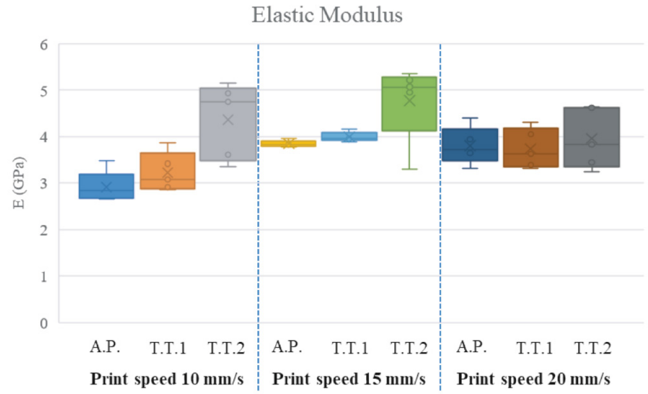

(a)

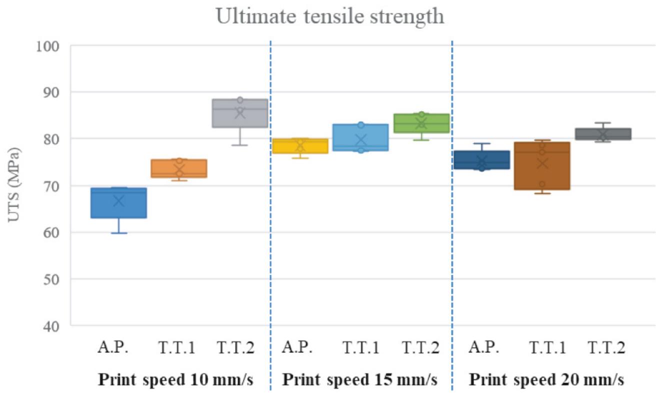

(b)

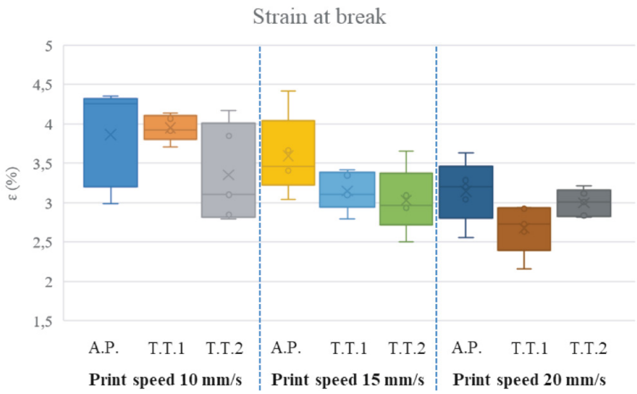

(c)

Fig. 5. Boxplot representation of elastic modulus (a), ultimate tensile strength (b) and strain at break (c) for each printing speed and for all the experimented conditions..

4 Conclusions

The results reported in the present study highlight the importance to correctly set and perform thermal post-processing treatments when PEEK is additively manufactured by ME technology. The effect of three printing speed on tensile properties are also tested.

The main findings that can be retrieved are:

– the printing speed 10 mm/s gives the worst results in terms of strength and elastic modulus, but the highest strains reached at break;
– TT1 does not produce significant changes with respect to the as-printed condition;
– TT2 produces a significant enhancement in terms of tensile strength and elastic modulus with respect to the as-printed condition;
– The specimens annealed using the TT2 at three different printing speeds show no significant changes in tensile strength and partly for the elastic modulus. This is noteworthy because it means that under the same treatment, the material's properties do not vary significantly depending on the adopted printing speed;
– Strain values reached at break decrease when thermal post-processing treatments (in particular for TT2) are carried out.

In conclusion, the study showed that PEEK after TT2 has excellent mechanical properties even at the highest value of the evaluated printing speeds, allowing for reduced printing times and costs. Future studies could be oriented at studying the effects of new printing parameters and different post-processing treatments (e.g., mechanical or chemical), to make the properties of the material even higher and not only in relation to its degree of crystallinity.

References

1. Park, S.J., Lee, J.E., Park, J., Lee, N.K., Son, Y., Park, S.H.: High-temperature 3D printing of polyetheretherketone products: perspective on industrial manufacturing applications of super engineering plastics. Mater Design 211 (2021)
2. Dua, R., Rashad, Z., Spears, J., Dunn, G., Maxwell, M.: Applications of 3D-printed PEEK via fused filament fabrication: a systematic review. Polymers-Basel **13** (2021)
3. El Magri, A., El Mabrouk, K., Vaudreuil, S., Chibane, H., Touhami, M.E.: Optimization of printing parameters for improvement of mechanical and thermal performances of 3D printed poly (ether ether ketone) parts. J. Appl. Polym. Sci. **137** (2020)
4. Sikder, P., Challa, B.T., Gummadi, S.K.: A comprehensive analysis on the processing-structure-property relationships of FDM-based 3-D printed polyetheretherketone (PEEK) structures. Materialia **22** (2022)
5. Cardoso, P.H.M., Coutinho, R.R.T.P., Drummond, F.R., da Conceicao, M.D., Thire, R.M.D.M.: Evaluation of Printing Parameters on Porosity and Mechanical Properties of 3D Printed PLA/PBAT Blend Parts. Macromol Symp 394 (2020)
6. Wang, Y.Q., Muller, W.D., Rumjahn, A., Schwitalla, A.: Parameters influencing the outcome of additive manufacturing of tiny medical devices based on PEEK. Materials **13** (2020)
7. Tseng, J.W., et al.: Screw extrusion-based additive manufacturing of PEEK. Mater Design **140**, 209–221 (2018)
8. Arif, M.F., Kumar, S., Varadarajan, K.M., Cantwell, W.J.: Performance of biocompatible PEEK processed by fused deposition additive manufacturing. Mater Design **146**, 249–259 (2018)

9. Regis, M., Bellare, A., Pascolini, T., Bracco, P.: Characterization of thermally annealed PEEK and CFR-PEEK composites: structure-properties relationships. Polym. Degrad. Stabil. **136**, 121–130 (2017)
10. Liaw, C.Y., Tolbert, J.W., Chow, L.W., Guvendiren, M.: Interlayer bonding strength of 3D printed PEEK specimens. Soft Matter **17**, 4775–4789 (2021)
11. ISO 527-1:2019. Plastics - Determination of tensile properties - Part 1: General principles
12. ISO 527-2:2012. Plastics - Determination of tensile properties - Part 2: Test conditions for moulding and extrusion plastics
13. Zhao, Y.C., Zhao, K., Li, Y.C., Chen, F.: Mechanical characterization of biocompatible PEEK by FDM. J. Manuf. Process. **56**, 28–42 (2020)
14. Wang, Z., Runzi, M., Gilchrist, M., Gong, H.: Mechanical Properties of High-Performance Plastic Polyether-ether-ketone (PEEK) Printed by Fused Deposition Modeling. In: Solid Freeform Fabrication 2021: Proceedings of the 32nd Annual International Solid Freeform Fabrication Symposium – An Additive Manufacturing Conference
15. Francis, J.N., Banerjee, I., Chugh, A., Singh, J.: Additive manufacturing of polyetherether-ketone and its composites: a review. Polym Composite **43**, 5802–5819 (2022)
16. Moby, V., Dupagne, L., Fouquet, V., Attal, J.P., Francois, P., Dursun, E.: Mechanical Properties of Fused Deposition Modeling of Polyetheretherketone (PEEK) and Interest for Dental Restorations: A Systematic Review. Materials 15 (2022)

Designing a 3D Printed Personal Protective Equipment for a Binocular Indirect Ophthalmoscopy

Puggelli Luca[1](✉), Giansanti Fabrizio[2], Volpe Yary[1], and Buonamici Francesco[1]

[1] Department of Industrial Engineering, University of Florence, via di Santa Marta, 3, 50139 Florence, Italy
{luca.puggelli,yary.volpe,francesco.buonamici}@unifi.it
[2] NEUROFARBA - University of Florence, Viale Pieraccini, 6 - 50139 Florence, Italy
fabrizio.giansanti@unifi.it

Abstract. This research addresses the need for a protective device during binocular indirect ophthalmoscopy (BIO) exams, where traditional face shields cannot be used due to the presence of the instrument and the need for continuous manual interaction. The study aimed to design a device that is easy to fabricate using a 3D printer, usable with different models of ophthalmoscopes, and easy to apply and use. Three possible designs were produced, and the most promising one was further developed into a prototypal level. The article describes the design phase, testing of the prototype, and possible applications of design for additive principles to improve manufacturability. The study is part of the SafEye project, financed by the Tuscany Region with the Covid-19 Tuscany Research Grant, which fostered actions towards the prevention of the spread of the pandemic at all levels. The resulting device is a general-purpose personal protective equipment (PPE) for BIO that can be easily 3D printed and used worldwide, even in underdeveloped countries.

Keywords: 3D printing in medicine · 3D printing · Additive manufacturing · personal protective equipment · binocular indirect ophthalmoscopy

1 Introduction

The use of personal protective equipment (PPE) in ophthalmology is crucial to prevent the spread of infectious diseases [1, 2]. The level of exposure to various infectious agents suffered by ophthalmologists during their routine practice is significant due to the type of interaction established during ophthalmology exams; the use of PPE can help reduce the risk of transmission to themselves, their patients, and other healthcare workers. In particular, the use of indirect binocular ophthalmoscopes requires special attention.

The indirect binocular ophthalmoscope is commonly used for a comprehensive eye exam, and its use involves close proximity between the doctor and the patient's face [3]. This proximity can increase the risk of transmission of infectious agents from the

M. Carfagni et al. (Eds.): ADM 2023, LNME, pp. 50–57, 2024.
https://doi.org/10.1007/978-3-031-52075-4_6

patient to the ophthalmologist or vice versa. Therefore, the use of PPE, such as face masks and eye shields, is essential to protect against droplets or aerosols generated during the examination. Other PPE, such as gowns and gloves, are used to prevent direct contact, while face masks and eye shields or goggles are used to prevent the entry of droplets or aerosols into the eyes, nose, or mouth.

While most of such PPE equipment is typically observed during the ophthalmoscopy practice, the use of face/eye shield can impose severe limitations to the execution of the indirect binocular ophthalmoscopy exam. Most face shields need access to the forehead of the doctor to be positioned in place; the presence of the medical instrument, which needs to be used as showed in Fig. 1, prevent this possibility. Moreover, depending on the positioning of the hypothetical protective screen in front of the doctor's face, the user might have problems with accessing the controls for operating the instrument.

In order to solve this problem, this study aimed at the development of a customized solution for protecting the face of the doctors performing exams using a binocular ophthalmoscope from aerosols and droplets. The study was carried out taking into consideration the need of developing a solution that could be: i) used globally – this activity was financed by a grant issued by the Tuscany Region to foster actions to cope with the emergency established by the Covid-19 pandemic; accordingly it is important that the resulting device had the characteristics to guarantee the widest applicability to maximize the impact of the proposed solution; ii) used on any binocular indirect ophthalmoscope. This second point is fundamental as the devices that could be useful by different clinicians could differ in geometry, characteristics, position of the control interfaces. Accordingly, the designed PPE should be usable with any type of ophthalmoscope – so not to limit the usefulness of the designed solution. To this end, the idea is to realize the proposed PPE by means of Additive Manufacturing technology, in particular FFF. Sharing the PPE stl file on a website platform (such as [4]) will speed up its distribution, allowing a hospital in a far-off location to create a PPE duplicate in just a few hours (i.e. the time required for a 3D print to complete). As a result, there will be less chance of shortages like those experienced during the COVID-19 pandemic [5–7].

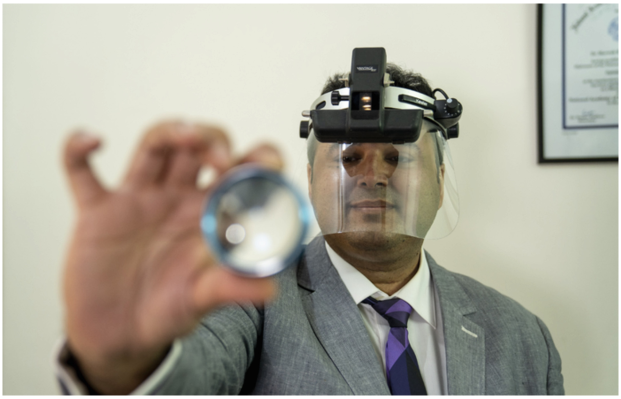

Fig. 1. Binocular Indirect Ophthalmoscope used by an ophthalmologist. It can be noticed that the shield (PPE) is positioned between user's eyes and device, thus limiting usability.

2 PPE Design

The design activity started with the study of the geometry of different models of binocular indirect ophthalmoscopes in order to understand their functioning, their mechanical features. Thanks to the collaboration with the Careggi hospital of Florence, the authors have been granted access to two different BIO models (Omega 500 produced by Heine [8], Vantage Plus produced by Keeler [9]), which present a similar architecture but with notable small differences. In order to speed up the design process, the geometries of the two devices were acquired using an optical handheld 3D scanner – i.e. Artec Eva. This allowed a reconstruction of the surfaces of interest that, once digitalized, were imported into a 3D CAD environment (i.e. Dassault Systèmes SolidWorks) to drive the design of the PPE device. The result of the geometry acquisition phase is visible in Fig. 2, where the 3D data acquired on the device is depicted along with the functional surfaces of the device, reconstructed using CAD surfaces. The CAD reconstruction process was carried out within a reverse engineering dedicated software, i.e. Geomagic Design X.

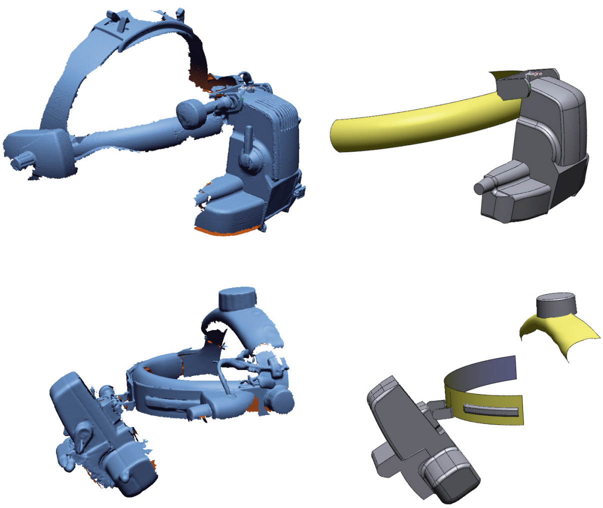

Fig. 2. Result of the 3D scanning and CAD reconstruction

Subsequently, an embodiment design phase was carried out to identify possible alternatives for the development of a custom PPE able to sustain a plastic transparent screen in front of the face of the medic while using a BIO. Additional design constraints were identified talking with the Ophthalmology department of the Careggi Hospital; clinicians have expressed the following needs: i) a protective screen, placed in front of the BIO; ii) access to the lateral and inferior part of the BIO, the areas where the controls of the device are located, which during the use of the device, are positioned directly in front of the eyes and forehead of the medic. iii) a device easy to be applied to the BIO and easy to be removed at the end of the use, without damaging the BIO.

Starting from these design constraints and considering the global goal pursued in the study, three different solutions were drafted to discuss possible strengths and drawbacks with the clinicians. The three sketches of the alternatives are depicted in Fig. 3.

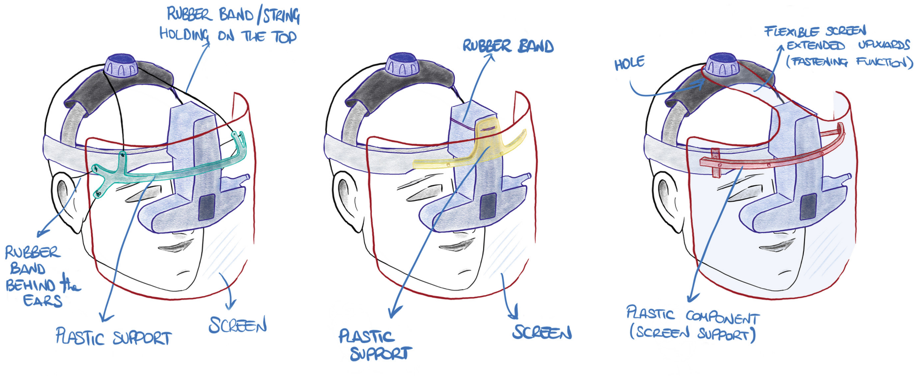

Fig. 3. 3 design ideas.

The three designs propose a similar solution to hold the screen, as in all cases the screen is connected to a plastic component by a set of pin/holes. Major differences are observed on how the screen/plastic component is connected to the BIO itself or is hold in place with respect to the user. The first solution (green one in Fig. 3) hypothesizes two holding points with the user – and not with the BIO: one behind the ears, thanks to a rubber band or a piece of string, and one on the top, exploiting a plastic knob that is positioned in all BIO models on a band running through the head. The second solution (yellow in Fig. 3) considers the possibility of connecting the PPE device with the central component of the BIO thanks to a rubber band. The third solution (red in Fig. 3) hypothesizes the use of the plastic screen also as structural element to connect it to the BIO, exploiting the top knob; moreover, the plastic component is equipped with supports that extend towards the forehead of the user to touch the metal strip that crosses the forehead of the user so to provide a support to the screen. The three solutions were analyzed and the yellow one was selected to continue the design, which was brought up to a detailed level.

A first version of the device was developed within SolidWorks to a detailed stage. The resulting geometry is depicted in Fig. 4. As previously mentioned, the transparent screen is kept in place using a series of snap-fit pins positioned at regular intervals on a plastic bow, responsible also for shaping the protective screen. The central part of the device was designed to connect with the BIO mainly through the use of one or more plastic bands. This choice, although rudimental, is the most economic and straightforward one and guarantees that the device can be applied to different BIO models without the use of fancy equipment; accordingly, it seemed the most promising solution also to maximize the applicability of the PPE even in underdeveloped countries. As a result of this choice, the central part was equipped with a series of holes and anchor points to allow different configurations of connection with the BIO. Mockups of the two BIOs were 3D printed to have physical replicas of the devices to perform preliminary tests. Several strategies were tested to identify possible configurations to hold the device in place firmly. Figure 5 presents some of the configurations tested in this phase.

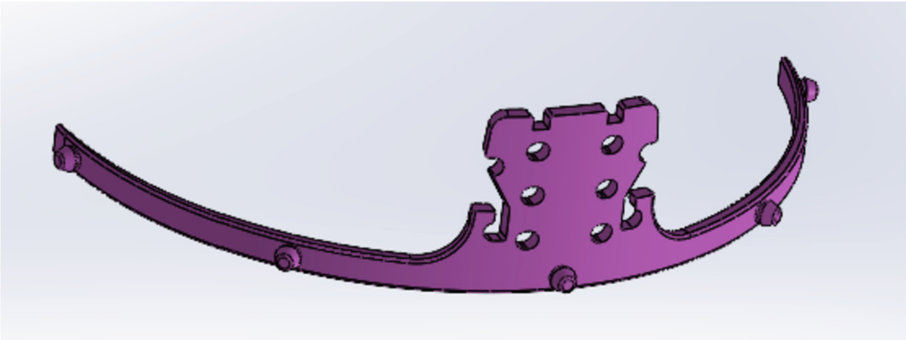

Fig. 4. PPE device to hold the protective screen in place.

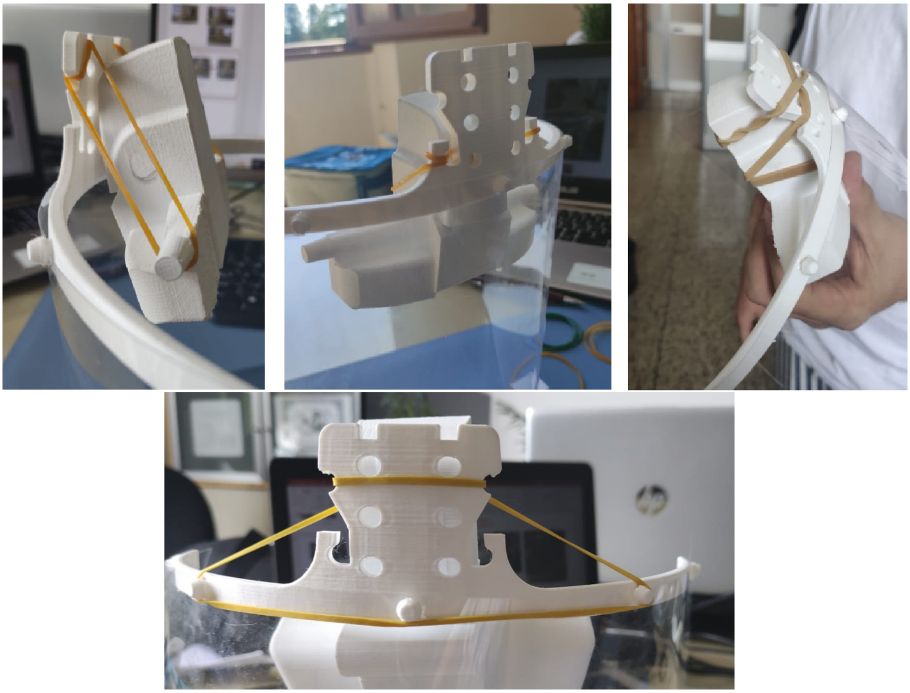

Fig. 5. Alternative configurations to hold the PPE device in place

During this phase, the authors experimented with the use of Velcro strips to improve the adhesion between the plastic support and the BIO. They were considered beneficial to the overall connection strength and they offer a good adaptability to different BIO models; all the BIO models present a solid body directly in front of the medic's forehead which offer an area for positioning the Velcro strip. These connections can be easily applied or removed without damaging the medical device. Accordingly, their use was considered overall an improvement; practical tests (Fig. 5) confirmed the usefulness of this additional connection.

After a series of tests performed with the plastic mockups, the prototype of the PPE was tested on the real devices (Fig. 6).

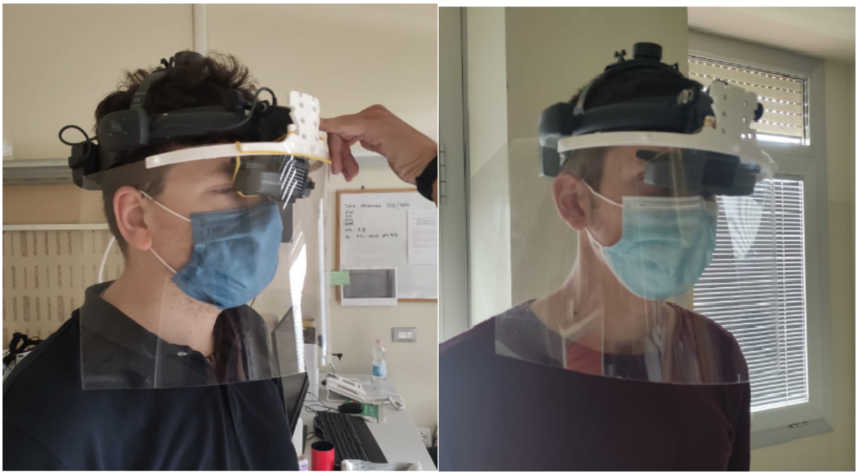

Fig. 6. Test of the PPE prototype on the real devices

The test highlighted possible areas for improvement, mainly due to the limited access that the protective screen grants to the device controls. To solve this issue, an improved version was conceived; the updated version presents the same geometry to connect with the BIOs, but introduces a gap between the area where the protective screen is positioned and the BIO itself. This solution (Fig. 7) creates a free area that can be used by the medic to access the device. The final configuration of the device was tested in a new round of practical tests on the BIO models, which confirmed the final shape of the device.

Comparing the proposed device with existing commercial solutions (e.g. Keeler BIO Breath Shield, proposed by Keeler, Windsor UK), they are designed to be mounted on a specific BIO. This leads to an optimal coupling with that specific device and the mounting operation results fast and intuitive. Conversely, the proposed one can be easily fitted on different BIO models, at the cost of a cumbersome assembly operation.

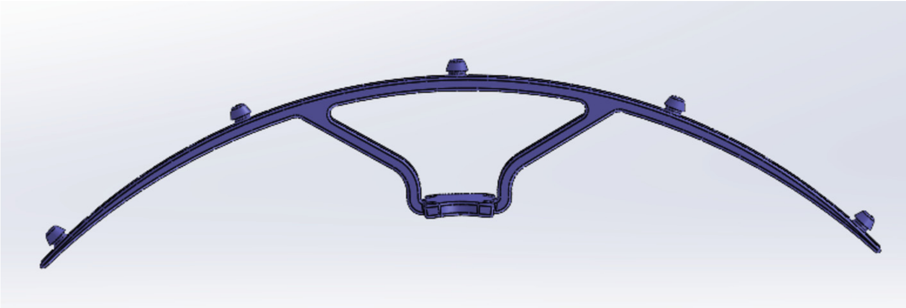

Fig. 7. Final version of the PPE

3 Conclusions

This study allowed the design of a PPE device that can be used during BIO exams to protect medics from spatter of liquid drops and aerosols. The solution was designed considering its simplicity as its main feature; this produced a PPE device that is easy to be fabricated, installed and used. Accordingly, the final result is a device that can be easily 3D printed with practically any type of low-end FFF printer. This result is important as it can allow the spread of the use of the device everywhere. To maximize this goal, the 3D models of the device will be made available online to be freely accessible from everywhere. 3D printing technology has the potential to revolutionize modern medicine by enabling the manufacturing of medical devices in third world countries, where access to such devices may be limited. In this specific case, the device was designed to be applied to any type of BIO available in the market, to further increase the usefulness of the device itself. Table 1 reports a synthetic list of requirements that this research activity aimed at guaranteeing for the PPE device and the solution/validation that was achieved.

Table 1. BIO PPE device functional requirements and solutions.

Requirement	Solution
General purpose, applicable to a generic BIO	Generic arch-shape, tested on two different BIO models
Easy to fabricate	Fabrication process: FFF process (desktop machine)
Ergonomic	Shape optimized thanks to clinicians' feedbacks. Validated by physicians
Not affecting the BIO inspection	Validated by physicians
Inexpensive	Printed using low-grade FFF filaments (PLA)

Future work will be oriented towards the development of an updated version of the PPE device which will be further optimized for FFF production, applying "design for additive manufacturing" rules and principles. Moreover, the authors are considering the development of versions of the PPE device for a specific type of BIO; although this choice would reduce the number of devices that could benefit from the protection, it could maximize the performances of the object (ergonomics, ease of installation, reduced dimensions) for a specific BIO model. Accordingly, the development of three or four different version, tuned for the most widespread BIO models, could allow the same coverage in terms of possible users while maximizing also the performances of the PPE device.

References

1. Safadi, K., et al.: Ophthalmology practice during the COVID-19 pandemic. BMJ Open Ophthalmol. **5**(1) (2020). https://doi.org/10.1136/BMJOPHTH-2020-000487
2. Bello, N.R., Nelson, L.B., Gunton, K.B.: Practice patterns of pediatric ophthalmologists during the COVID-19 pandemic. J. Pediatr. Ophthalmol. Strabismus **59**(3), 145–150 (2022). https://doi.org/10.3928/01913913-20210921-01
3. Shah, P.K., Narendran, V., Saravanan, V.R., Raghuram, A., Chattopadhyay, A., Kashyap, M.: Screening for retinopathy of prematurity - a comparison between binocular indirect ophthalmoscopy and RetCam 120. Indian J. Ophthalmol.Ophthalmol. **54**(1), 35–38 (2006). https://doi.org/10.4103/0301-4738.21612
4. Ultimaker. (n.d.). Thingiverse web site. https://www.thingiverse.com/
5. Ranney, M.L., Griffeth, V., Jha, A.K.: Critical supply shortages — the need for ventilators and personal protective equipment during the Covid-19 pandemic. N. Engl. J. Med. **382**(18), e41 (2020). https://doi.org/10.1056/NEJMP2006141
6. Choong, Y.Y.C., et al.: The global rise of 3D printing during the COVID-19 pandemic. Nature Reviews Materials. Nature Research, 1 September 2020. https://doi.org/10.1038/s41578-020-00234-3
7. Livingston, E., Desai, A., Berkwits, M.: Sourcing personal protective equipment during the COVID-19 pandemic. JAMA – J. Am. Med. Assoc. **323**(19), 1912–1914 (2020). https://doi.org/10.1001/JAMA.2020.5317
8. Heine. (n.d.). Heine web site. https://www.heine.com/en/products/indirect-ophthalmoscope/detail/23908-heine-omega-500-led-binocular-indirect-ophthalmoscope
9. Keeler. (n.d.). Keeler web site. https://www.keeler.co.uk/vantage-plus-indirect-ophthalmoscope.html

FDM Technology: Overhangs versus Layer Height Printability Performance Correlation

Giampiero Donnici, P. Ferretti, A. Montalti(✉), D. Francia, and Alfredo Liverani

ALMA MATER STUDIORUM – University of Bologna, Risorgimento, 2, 40136 Bologna, Italy
{patrich.ferretti2,andrea.montalti8}@unibo.it

Abstract. FDM (Fused Deposition Modelling) is the most popular 3D printing technology worldwide due to its simplicity and low costs. One of the key points of FDM is the need for supporting material to realize the overhanging features. In general, however, both in the case of printing supports with the same material as the part and in the case of printing with soluble supports, there is a high waste of material and a significant increase in the printing time to get the finished part.

One of the fundamental parameters for generating supports within the slicer software is the so-called "support overhang angle", which consists of the maximum achievable angle beyond which the slicer generates supports. The other key parameter in FDM printing is the "layer height", which directly determines both the quality of the final part, its strength, and the printing time itself.

This paper will therefore attempt to investigate the relationship present between "layer height" and "support overhang angle", bringing some examples of how with proper layer height one can significantly reduce support generation, wasted material and in some cases also printing time.

Keywords: Overhangs · FDM · Layer Height

1 Introduction to Fused Deposition Modelling (FDM)

Fused Deposition Modeling (FDM) also know as FFF (Fused Filament Fabrication) is the most popular type of 3D printing technology used for creating physical objects from digital designs. FDM is for its ease of use, affordability, and versatility, making it a popular choice for hobbyists, engineers, and designers alike [1].

The FDM process involves melting a thermoplastic filament and extruding it through a nozzle. The nozzle moves along a predetermined path created in a specific slicing software, laying down the melted plastic in thin layers to build up the object. As the plastic cools and solidifies, it bonds to the layer beneath it, creating a strong and durable part [2].

One of the advantages of this technology is the wide variety of materials that can be used for printing. There are many different types of filaments available, including basic thermoplastics like ABS (Acrylonitrile butadiene styrene) and PLA (polylactic acid) [3], as well as more advanced materials like Nylons [4], carbon fiber-infused filaments,

M. Carfagni et al. (Eds.): ADM 2023, LNME, pp. 58–65, 2024.
https://doi.org/10.1007/978-3-031-52075-4_7

flexible filaments, high temperature polymers like PEEK (polyetheretherketone) [5] and even metal-infused filaments.

This allows designers and engineers to choose the best material for their specific application, whether it be for a prototype or a final product. Overall, FDM and its range of materials offer a powerful tool for creating complex and functional 3D objects.

FDM technology is widely used in many industries, including aerospace [6,7], healthcare [8], automotive [9], naval [10] because it is relatively inexpensive, fast, and can produce complex shapes with high accuracy.

1.1 Overhangs in FDM (Fused Deposition Modelling)

Maximum overhang angle [11] and layer height [12] are two important factors to consider when using FDM 3D printing technology.

Overhangs refer to the portions of a 3D object that extend outward at an angle from the horizontal plane. These areas can be difficult to print using FDM technology because the molten plastic tends to droop or sag as it cools, resulting in poor quality or even failed prints. To address this issue, support structures can be added to the design to provide a temporary scaffold for the overhanging areas during printing [13]. Once the print is complete, the support structures can be removed, leaving the finished object.

Layer height refers to the thickness of each layer of material deposited during the 3D printing process. This parameter affects the surface quality, strength, and speed of the print. A smaller layer height results in a smoother surface finish, but it also takes longer to print and requires more material. Conversely, a larger layer height can be printed faster and with less material, but the surface quality may be rougher.

$$S_{layer} = LH(W - LH) + \pi \left({}^{LH}/_{2} \right)^2 \tag{1}$$

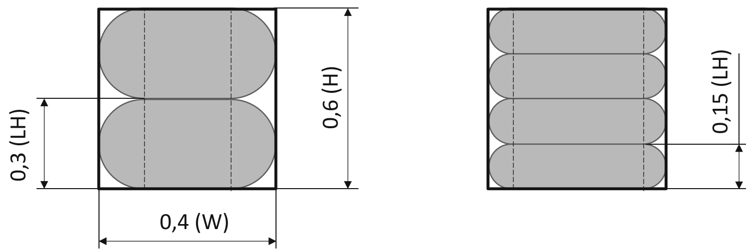

Fig. 1. Cross-section of the deposition of overlapping layers: (a) layer height 0.3mm with 83.9% section fill (b) layer height 0.15mm with 91.9% section fill.

The section of the individual line is thus schematized as the union of a rectangle and two semi-circles, whose diameter corresponds to the layer height.

Considering Fig. 1, a high layer height results in poor filling for a given volume, but lower layer heights result in better filling of the section.

Choosing the appropriate layer height for a particular print job depends on a variety of factors, including the complexity of the design, the desired level of detail, and the time and material constraints. In general, a layer height of 0.1mm to 0.3mm is a good starting point for most FDM prints, considering a standard nozzle dimension of 0.4mm. By reducing the layer height, each layer is thinner and has less weight, and less material and it cools down faster which can help to improve the bridging [14] and overhangs performance of the material and reduce the amount of sagging or drooping. In general, using a smaller layer height can achieve better quality prints. Reducing the layer height can also increase print time and material usage, so it's important to balance print quality with these factors when adjusting the layer height. It's interesting to evaluate the mathematical relation between layer height and maximum value of overhang.

2 Methodology

The following analysis is only true under the following hypotheses:

- only the layer height, overhang angle and line width parameters are taken into account, with all other parameters (e.g. cooling fan speed, flow, printing seed, etc.) remaining unchanged;
- this analysis focuses on the behavior of intermediate layers of the printed component; it is not applicable to the first layers;
- the line width is set at 0.4mm, which is equal to the nozzle size. It is considered constant in each layer and cannot be enlarged much due to cooling and mass overhang problems.

To be able to find a relationship that somehow links the layer height to the limiting angle beyond which to generate supports, it is necessary to parameterize the individual printed line. A possible parameterization is proposed in Fig. 2. This involves the use of two basic geometrical parameters: layer height and line width.

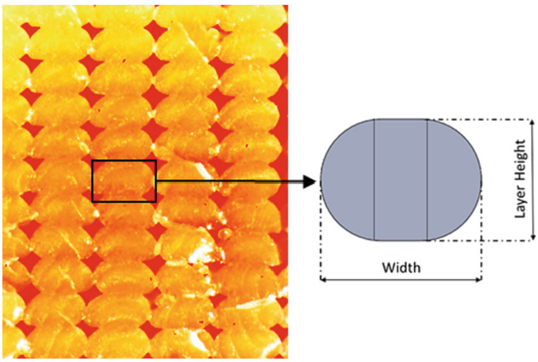

Fig. 2. Section of a printed specimen and parametrization

In Fig. 3 is possible to see the effect of the layer height on a given value of overhang. Considering an overhang of 45°, with a layer height of 0.15mm, no supports are needed, conversely if a layer height of 0.3mm is used, some lines are completely suspended in the air and need supports. This results in the partial or total elimination of the printing time advantages of a higher layer height.

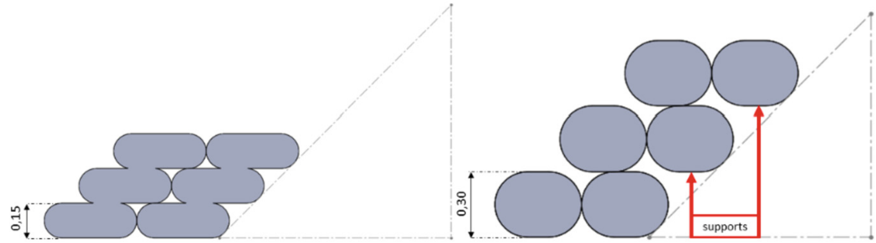

Fig. 3. Comparison between a layer height of 0,15mm and a layer height of 0,30mm on 45° overhang

2.1 Optimum Printability Condition of an Overhang

By exploiting the parameterization proposed in Fig. 2 and considering a pair of lines placed one above the other, in which the center of gravity of the upper line falls exactly at the boundary of the flat area of the lower layer. Considering two layers at a time, the first layer can be assumed to be a rigid body; to be able to deposit the next layer, the equilibrium condition must be met without considering the adhesion effect of the material, assuming a perfect cooling condition.

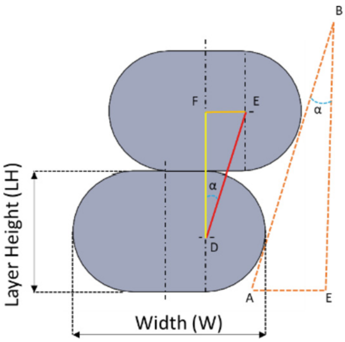

Fig. 4. Diagram used for parameterisation of the overhangs angle.

α is the angle defined between the tangent to the layers and the vertical and defines the support overhang angle. The triangle (DEF) equivalent to the triangle (ABE) is used to obtain Eq. 2:

$$\alpha = arctg \frac{\frac{W}{2} - \frac{LH}{2}}{LH} \tag{2}$$

By varying the value of the layer height, it is possible to obtain the respective overhang value realizable in this configuration (Fig. 5). This type of configuration can be considered as a condition of "optimal printability". That is, the maximum overhang that can be printed, where the overhang is well defined regardless of the material used to print the model. The condition obtained analytically by applying the equation is verified because it is consistent with the parameters usually used in slicers. This is thanks to the fact that the only half of the printed line is hanging in the air and the theoretical center of gravity let the line to be stable.

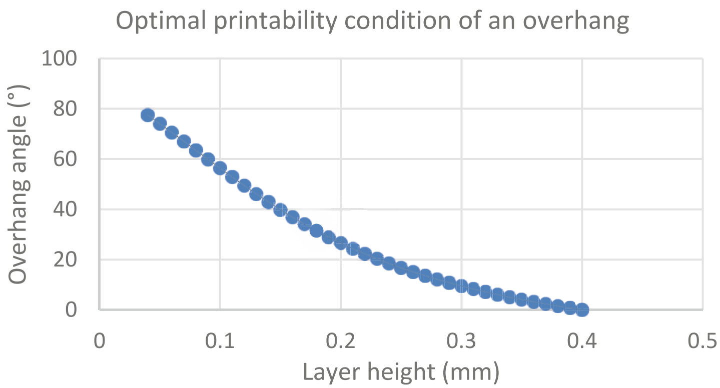

Fig. 5. Overhang angle vs layer height in the case of "optimal printability condition"

2.2 Printability Limit Condition: Maximum Achievable Overhang

Taking the condition shown in Fig. 4 to the limit, i.e. placing the ideal contact area between one layer and the next, results in a single point of contact as can be seen in Fig. 6. This condition represents the upper limit, beyond which supports must be made, otherwise the layer will be printed in the air and collapse on the previous layer, leaving a very inaccurate surface on the overhangs.

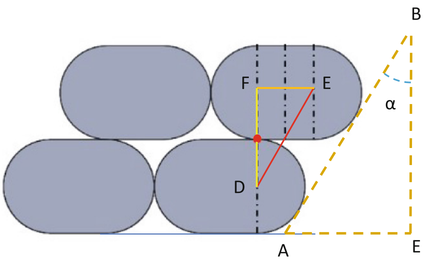

Fig. 6. Maximum value of overhang

In this specific case the Eq. 2 can be rewritten as follow:

$$\alpha = arctg\frac{W - LH}{LH} \tag{3}$$

A comparison between the printability limit value and the good printability value can be seen in Fig. 7. The delta between the two values and the possibility of reaching the printability limit value is highly dependent on the type of filament chosen and whether active cooling can be operated during printing.

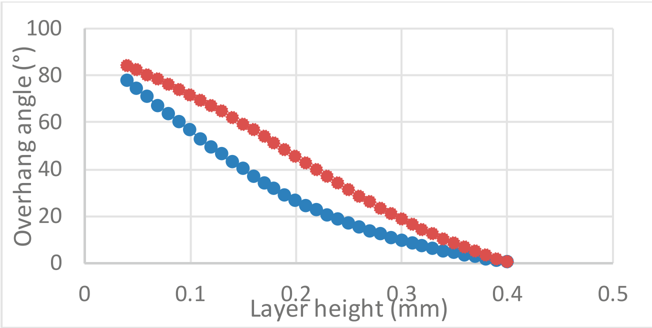

Fig. 7. Comparison between the optimal and the maximum achievable overhang condition

The curves identified define the maximum limit for which supports can be avoided. In general, increasing the layer height reduces the printing time, but increases the need for supports because it is related to the maximum protrusion angle. This results in post-processing for the removal of support structures. Conversely, reducing the layer height reduces the need for support because of the maximum protrusion angle, resulting in less post-processing. This leads to an increase in printing time. A low layer height results in the use of more material in the component and fewer supports, while a high layer height results in the use of less material in the component and more supports.

3 Case Study

Let us consider as a case study, for example, a component with complex geometries such as those obtainable through topological optimization (Fig. 7), which require extensive use of supports to be printed correctly.

In Fig. 8, it can be seen that by varying the layer height and consequently the maximum angle that can be reached in the case of the "maximum achievable overhang" condition, the amount of supports increases considerably.

If we consider keeping all the printing parameters unchanged, except for the layer height and the maximum overhang value, taking advantage of the preview obtained in the slicer, we get the results shown in Table 1, in terms of time and amount of material used.

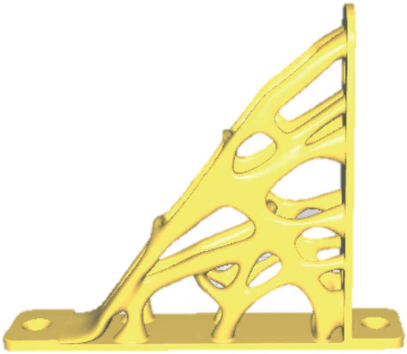

Fig. 8. Topology optimized bracket support.

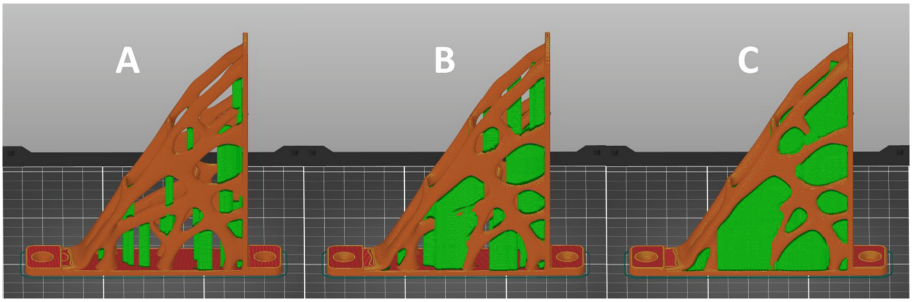

Fig. 9. (A) Layer height 0.15, overhang angle: 60°, (B) layer height 0.20, overhang angle: 45°, (C) layer height 0.3, overhang angle: 20°.

Table 1. Comparison of material and printing time with different layer height and overhang angle

CASE:	Printing Time (h - min)	Part material (g)	Support material (g)	Total material (g)
A	9 – 9	55.1	3.7	58.8
B	8 – 11	55.0	9.8	64.8
C	7 – 9	54.7	18.7	73.4

4 Conclusion

The case study in Fig. 9 and Table 1 allows us to establish that between conditions A and C there is a 20% variation in terms of material used and a 22% variation in printing time required compared to case C. Case A is therefore convenient when the cost of the material used is very high and when the final quality of the component must be maximized. Case C allows the component to be obtained more quickly, with the need to remove a large volume of support and with a great waste of material. The possibility of having a correlation between maximum overhang angle and layer height can lead to an optimization of the printed component to reduce the amount of wasted material, maximize quality and avoid the removal of a large number of supports. Furthermore, for particularly complex components, it may be advantageous to reduce the number of supports to be generated to avoid complications during post-processing.

Compared to recently developed tree supports, classical supports still prove to be superior in certain applications as they offer greater stability and rigidity to the component, allowing for improved precision and surface finish.

References

1. Frizziero, L., Donnici, G., Galiè, G., Pala, G., Pilla, M., Zamagna, E.: QFD and SDE methods applied to autonomous minibus redesign and an innovative mobile charging system (MBS). Inventions **8**(1), 1 (2023). https://doi.org/10.3390/inventions8010001
2. Solomon, I.J., Sevvel, P., Gunasekaran, J.: A review on the various processing parameters in FDM. Mater. Today: Proc. **37**, 509–514 (2021)
3. Alessandri G., et al.: Virtual surgical planning, 3D-Printing and customized bone allograft for acute correction of severe genu varum in children **12**(12), 2051 (2022)
4. Ramesh, M., Panneerselvam, K.: Mechanical investigation and optimization of parameter selection for Nylon material processed by FDM. Mater. Today: Proc. **46**, 9303–9307 (2021)
5. Zhao, Y., Zhao, K., Li, Y., Chen, F.: Mechanical characterization of biocompatible PEEK by FDM. J. Manuf. Process. **56**, 28–42 (2020)
6. Gebisa, A.W., Lemu, H.G.: Investigating effects of fused-deposition modeling (FDM) processing parameters on flexural properties of ULTEM 9085 using designed experiment. Materials **11**(4), 500 (2018)
7. Bacciaglia, A., Ceruti, A., Liverani, A.: Towards large parts manufacturing in additive technologies for aerospace and automotive applications. Procedia Comput. Sci. **200** (2022)
8. Alessandri, G., Santi, G.M., Martelli, P., et al.: 3D-printing of porous structures for reproduction of a femoral bone [version 1; peer review: awaiting peer review]. F1000 Research **12**, 17 (2023). https://doi.org/10.12688/f1000research.129267.1
9. Frizziero, L., et al.: IDeS method applied to an innovative motorbike. Appl. Topol. Optim. Augmented Reality (2022)
10. Liverani, A., Bacciaglia, A., Nisini, E., Ceruti, A.: Conformal 3D material extrusion additive manufacturing for large moulds. Appl. Sci. **13**(3), 1892 (2023). https://doi.org/10.3390/app13031892
11. Sammaiah, P., Krishna, D.C., Mounika, S.S., Reddy, I.R., Karthik, T.: Effect of the support structure on flexural properties of fabricated part at different parameters in the FDM process. In: IOP Conference Series: Materials Science and Engineering, vol. 981, no. 4, p. 042030. IOP Publishing (2020)
12. Bintara, R.D., Lubis, D.Z., Pradana, Y.R.A.: The effect of layer height on the surface roughness in 3D Printed Polylactic Acid (PLA) using FDM 3D printing. In: IOP Conference Series: Materials Science and Engineering, vol. 1034, no. 1, p. 012096. IOP Publishing (2021)
13. Gaynor, A.T., Meisel, N.A., Williams, C.B., Guest, J.K.: Topology optimization for additive manufacturing: considering maximum overhang constraint. In: 15th AIAA/ISSMO Multidisciplinary Analysis and Optimization Conference, p. 2036 (2014)
14. Sun, L., et al.: X-Bridges: designing tunable bridges to enrich 3D printed objects' deformation and stiffness. Assoc. Comput. Mach. **20**, 1–12 (2022). https://doi.org/10.1145/3526113.3545710

Prototyping a Mechanical Mounting System for the Photogrammetric Use of USB Microscopes

Sara Antinozzi[1], Andrea di Filippo[1], Sara Morena[2], Anna Sanseverino[3], and Francesco Villecco[4(✉)]

[1] Department of Civil Engineering, University of Salerno, via Giovanni Paolo II 132, 84084 Fisciano (SA), Italy

[2] Department of Architecture, University of Palermo, Piazza Marina 61, 90133 Palermo (PA), Italy

[3] Department of Civil Engineering and Architecture, University of Pavia, c.so Strada Nuova 65, 27100 Pavia (PV), Italy

[4] Department of Industrial Engineering, University of Salerno, via Giovanni Paolo II 132, 84084 Fisciano (SA), Italy

fvillecco@unisa.it

Abstract. The widespread and diversified use of portable devices with high magnification power at relatively low-cost, i.e., the so-called USB digital microscopes, has revealed the possibility of employing their photographic output in Structure from Motion processes for sub-millimetric digitisation. However, USB microscopes, born for two-dimensional inspection – if used without specific accessories, designed *ad-hoc* for the photogrammetric capture phase – can pose some difficulties for the surveyor in managing capture operations. Thus, this study suggests prototyping a low-cost, complete, and portable mounting compatible with the most common USB microscopes for image scanning. This system makes it possible to use portable USB microscopes for three-dimensional modelling at a low-cost, as it is easy to replicate both in terms of construction and the materials used. Therefore, through the interaction of several skills, the work shows how the photogrammetric process can also be made accessible to devices that were not initially designed for such application, paving the way for new paths in representation engineering research.

Keywords: Structure from Motion · Additive Manufacturing · Fast Survey

1 Towards the Micro-photogrammetric Use of USB Microscopes

For those requesting to produce and disseminate digital models of small items, particularly concerning sub-millimetre resolution applications, there is an ever-increasing need for accessible, efficient, and reasonably priced three-dimensional acquisition systems.

Although the large-scale dissemination of digital photography and its photogrammetric applications can provide a successful response, close-range activities have only

M. Carfagni et al. (Eds.): ADM 2023, LNME, pp. 66–76, 2024.
https://doi.org/10.1007/978-3-031-52075-4_8

recently gained recognition; therefore, to date, the appropriate applications for the rigorous description of small objects and their 3D virtual representation (digitisation) are still being studied and explored [1]. This could be due to the inherent difficulty of obtaining the expected result with known alternatives – such as photogrammetry – which are relatively cheaper than less versatile techniques. Indeed, CMM systems, laser triangulation, conoscopic holography, interferometry, X-ray computed axial tomography, confocal microscopy, etc. [2, 3], are generally unaffordable equipment being developed in highly specialistic fields, e.g., for applications in dimensional inspection, quality control, industrial design, testing, and reverse-engineering of micro components [4].

However, the image-based alternative requires a not negligible technical rigour. The challenges that 'very' close-range photogrammetry poses to the surveyor have recently been regarded as inherent in customising dedicated accessories to ensure adequate and verifiable accuracy, precision, and an optimised process [5–7]. Some of the primary studies available in the literature [8–15], dealing with the acquisition of small objects with necessarily high levels of detail and accuracy (hundredths and tenths of a millimetre, respectively), focus on streamlining photogrammetric workflows while maintaining high metric reliability [11]. Namely, these studies focus on adopting different solutions based on camera stabilisation, rotating bases, coded targets and greater control of camera settings and lighting, highlighting improvements in model quality, and emphasising the advantage of more controlled protocols.

Therefore, if these expedients significantly improve the outputs[1], they can make a significant difference in the case of more entry-level devices. Furthermore, it would mean that the design of *ad-hoc* configurations for a series of new photographic devices – now available on the market at affordable prices – could potentially allow for their incorporation into complex photogrammetric processes.

Thus, alongside the widespread use of compact and lightweight cameras[2], we now find another type of portable and affordable device in the panorama of macro-photography [13, 14]. Said devices are USB portable microscopes – created for inspection and two-dimensional metrological analysis – and are already popular in the manufacturing industry for quality control and in the medical field [16]. They consist of small, handy optical zooms designed to display image output directly on the monitor. Despite their resolution (usually up to 5MP) and small sensor size (about 1/4″), the images produced are to be considered high quality for the commercial segment in which they fit. However, not being designed as instruments for image-based three-dimensional reconstructions, these USB microscopes – albeit simple and intuitive – can be pretty challenging to use. Due in part to the absence of accessory components, such as mounts and calibrators, to adapt them for photogrammetric purposes, applications concerning the use of USB portable microscopes for three-dimensional reconstructions of the entire volume of a test specimen are sporadic. Less unusual, however, are partial modelling of objects whose two-dimensionality is prevalent [17].

[1] In the case of instruments whose effectiveness is 'established' for good quality macro-photogrammetric results, such as when using full-frame cameras combined with macro optics.

[2] In addition to the single-board computers which are around the size of a credit card (Raspberry Pi) and can be combined with both entry-level and professional photographic sensors and optical bodies.

The literature offers a few examples of the imaged-based set-up design involving USB microscopes.

In 2011, Graham proposed a 2D vision-based measurement system to convert USB microscopes, which were still considered hardly more than toys, into metrological tools [18]. This study takes a step forward in the metrological use of the instruments but proposes a set-up applicable only to two-dimensional measurements.

Subsequently, Maté-González et al. [19] conducted a micro-photogrammetric characterisation of cut marks on bones from USB microscope captures. Although it is not specified which mounts and systems were used for the acquisitions, this study demonstrates that the converging capture scheme increases the quality of the models, albeit they were excessively noisy and of poor quality. At the same time, Zitek et al. [20], using an Arduino Uno controller board, a stepping motor, and a self-designed 3D printed stage, stabilised the microscope while enabling a 360-degree rotation of the object, thus clarifying how to structure an inexpensive system (360 euros) to obtain convergent captures of objects smaller than 1 cm. However, their tests involved using a common stand that allowed the microscope to be held at a single fixed angle for the entire rotation; therefore, there was no way to add additional turns at different inclinations. Moreover, the object always had to be inside the framing field: had it been even a little larger, it would not have been possible to translate the object or the microscope reciprocally to achieve a parallel, as well as a convergent, overlap between several shots.

These examples found in the literature led us to a series of observations concerning the photogrammetric employment of USB microscope captures, noticing that the utilisation of specially designed components would be motivated by additional specific factors. Among the main reasons for the development of mounts to adapt USB microscopes for photogrammetric purposes are: limiting vibrations during shooting; ensuring sufficient framing for the overlap required to achieve a successful reconstruction despite the extremely narrow field of view; performing acquisitions while ensuring convergence of captures, i.e., management and control of the reciprocal positions of the optical system and the object; and the large number of shots to be taken in a short time.

Therefore, intending to keep costs down, this study proposes prototyping an initial low-cost, complete, and portable configuration based on the use of USB microscopes for image-based scanning, additionally verifying the possibility of gathering the different hardware components in one system.

2 Accessory Photogrammetric Component Design

To facilitate and speed up the acquisition process and to appropriately integrate USB digital microscopes into the photogrammetric workflow, an initial prototype was assembled for the systematisation of a real low-cost digitisation system based on the photogrammetric paradigm, i.e., the "3DINO SYSTEM". It consists of a series of mechanical supports whose frame is entirely 3D printed and supplemented with standard components readily available on the market. The design of the prototype is based on the idea of modularity, which allows the structure to be broken down into three main parts, properly connected and movable; they may also be used independently: the base (see Fig. 1 at numbers 1–5); the rib (7–10); the specimen holder (6).

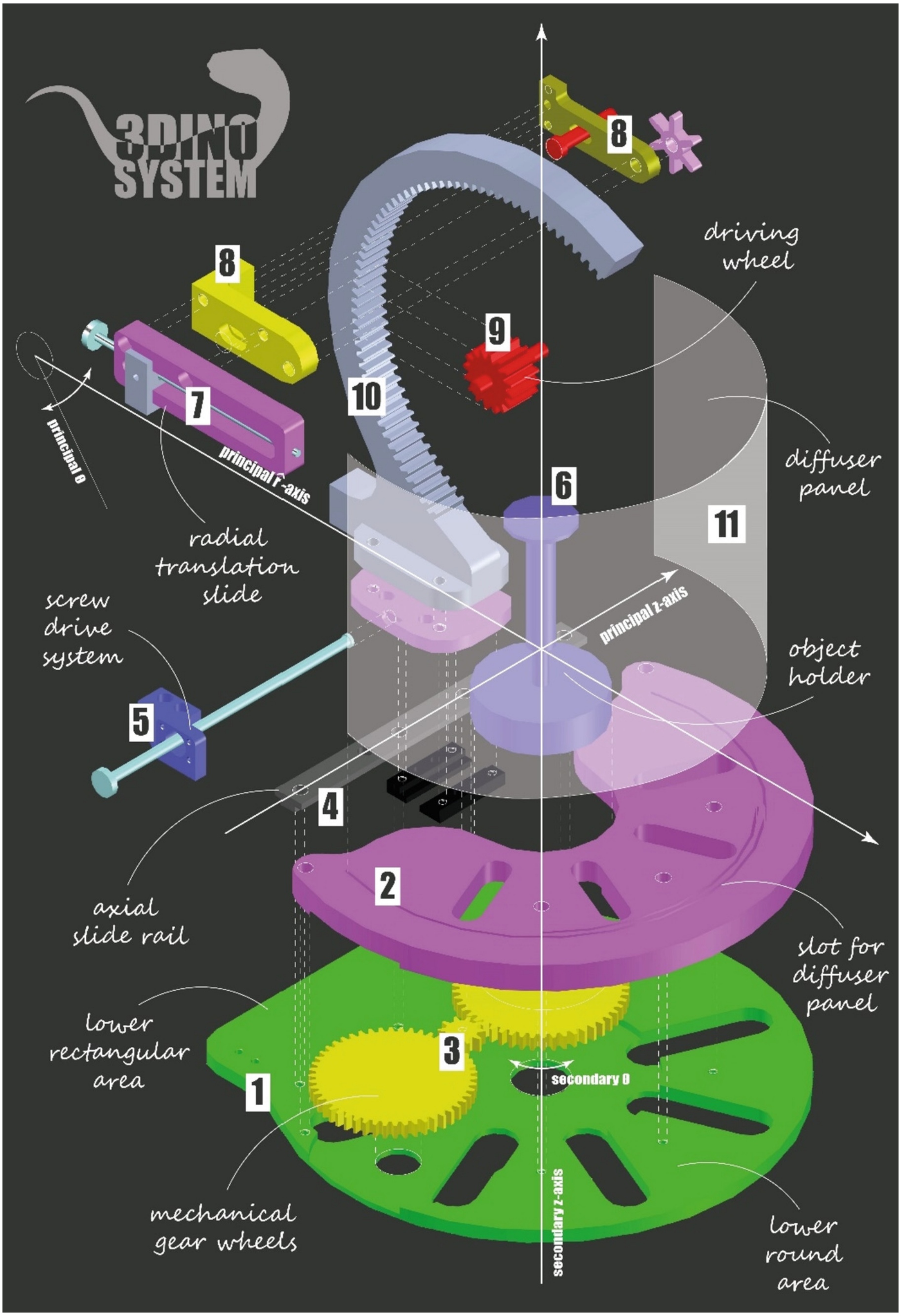

Fig. 1. Diagrams (exploded axonometric view) of the first prototype of the 3DINO SYSTEM based on the photogrammetric use of USB microscopes. The different parts, the base (numbers 1 to 5), the rib (7 to 10) and the holder (6), can be connected and moved independently.

These three controllers work together to obtain converging captures always orthogonal to the surface of the object, i.e., the axis of the camera is orthogonal to the plane tangent to the surface of the object in relation to the trace of the axis itself, which is the best condition from a photogrammetric point of view (see Fig. 2 and Fig. 3). Although the system was designed for small size photographic sensors, the modularity conception also makes it possible to utilise it in the case of photogrammetric sets for SLR cameras.

Regarding USB microscopes, due to their lightweight and small size, the entire optical system can be tilted against the object to be scanned. Tilts are ensured by the C-shaped rib, to which a micrometric slide is also fixed in order to accommodate the microscope, allowing it to move radially towards the centre of the system. Hence, we associate a "principal r-axis" with the radial movement of the optics, whose inclination – corresponding to the sensor's tilt – is referred to as an angle called the "θ-principal". Instead, the object is placed on a central support to be adjusted in height for the vertical alignment of the centre of the frame with respect to the object along the "secondary z-axis". Conversely, horizontal alignment is ensured by translating the optical system (rather than the object) along another axis defined as the "principal z-axis".

Thanks to a joint placed in the base, the tested specimen can also rotate 360 degrees around the "secondary z-axis" in increments of a specified "θ secondary" angle, enabling a complete revolution for each camera tilt.

The design of the individual areas of the 3DINO SYSTEM is thoroughly analysed as follows. The support base consists of two parts: a lower parallelepiped (see Fig. 1 at number 1, Fig. 2 and Fig. 3 referring to the green element), which houses a slide (4, in grey) constrained to slide along a guide in a longitudinal direction (according to the principal z-axis). The movement of the slide is via a mechanical gear (5, in purple and cyan) of the worm-worm type (also known as nut-worm). The transmission ratio of this type of gear is equal to:

$$\frac{2mm}{rotation} \Leftrightarrow \frac{2mm}{2\pi\, rad} \tag{1}$$

The nut of this gear is secured to the base using a screwed-on bracket; on the other hand, the worm gear is bound axially at the end of the slide, allowing the rotational freedom of the same screw to be maintained. The toothed rib is fixed on the slide via threads and constitutes the equipment's main part (10, in grey, described below). The base, consisting of two concentric parts (1 in green and 2 in pink), covers a circular area with a radius of 180 mm. In between, there is a technical compartment accommodating three toothed wheels (3, in yellow) with module 2 (the parameter on which the dimensioning of the gear is based, defined as the ratio between the primitive diameter[3] and the number of teeth of the wheel) with a transmission ratio (ratio between the two angular speeds) almost equal to one. The first (positioned in the centre of the system) and the third (projecting to the right) wheels, which allow for the rotation at the base of the central support (6, in purple), are partially visible. The tolerances of this gear are related to the accuracy of the 3D printing technology used during the prototyping phase (down to 0.2 mm).

[3] The diameter associated with the circumference along which the contact of the gear pair takes place, corresponding to the fictitious friction wheel capable of transmitting motion [21].

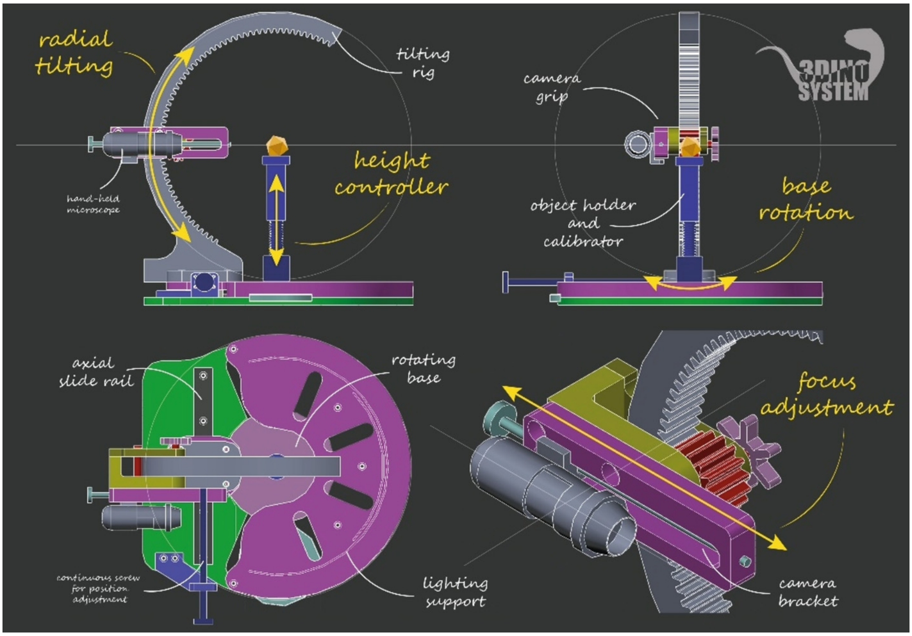

Fig. 2. Diagrams of the first prototype of the 3DINO SYSTEM: side and top views, axonometric detail (bottom right) of the optics housing structure.

As specified, the central wheel's rotation axis will be referred to as the secondary z-axis, and its rotation angle represents the secondary θ-coordinate. A support (6, in violet) can be attached at the centre of this wheel, with adjustable height (right along the secondary z-axis).

At the circular edge of the base, a small channel is envisaged for inserting a diffuser panel (11, in semi-transparent white).

The already mentioned rib is composed of a half-wheel with internal toothing having a primitive radius of 150 mm and a small, toothed drive wheel (9, in red) to which is connected a slide (7, in pink) suitable for the radial translation of the optics. To this radial translation, we associated the principal r-axis; instead, the angle that the optics slide forms with the horizon will represent the main θ-coordinate. The modulus of these gear wheels is similar to the previous one (equal to 2).

The equipment ultimately has three degrees of freedom for the optics and two degrees for the surveyed object. The principal θ-coordinate is related to the rotation of the small driving gear (9, in red), the pinion:

$$\theta = \frac{pinion\ radius}{150\ mm} \cdot 2\pi \cdot (pinion's\ rotation) \quad (2)$$

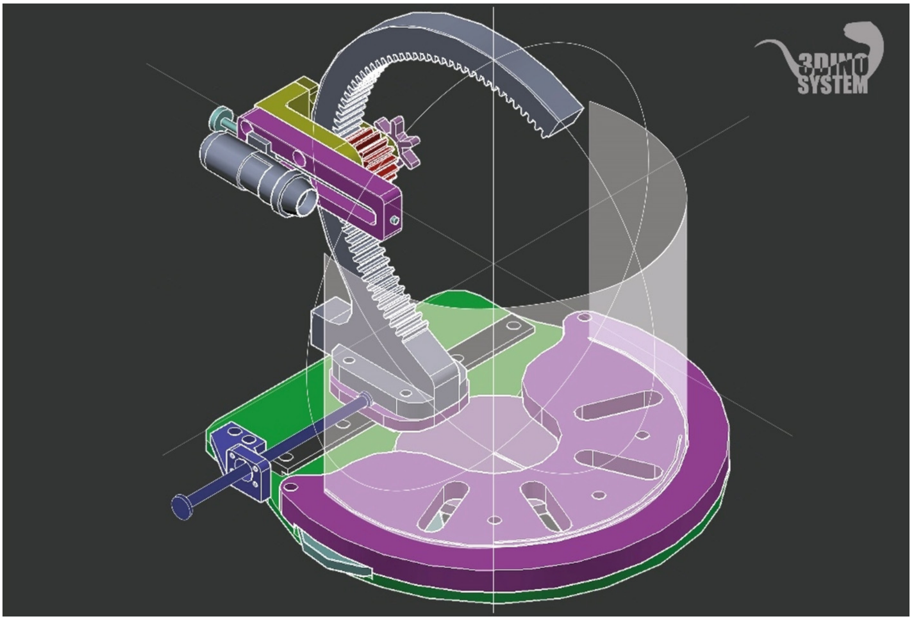

Fig. 3. Diagrams of the first prototype of the 3DINO SYSTEM: axonometry of assembled components with the addition of a diffuser panel for lighting.

The rationale underlying the sizing of the components is due to the constraints associated with performing movements compatible with the area framed by the microscope. Generally, the appropriate field of view for making acquisitions is an area of approximately 20 × 15 mm, which means moving the microscope and the object with millimetre precision. Furthermore, since the specimen housing area is designed as a detachable module, it must be large enough to accommodate up-to-15 cm objects for them to be acquired even with the sensor of a smartphone or, possibly, a conventional camera (dispensing with the utilisation of the rib).

3 Prototyping with Prusa I3 MK2.5S

The single parts were manufactured by FDM (Fused Deposition Modeling) technology using a Cartesian printer, the Prusa i3 MK2.5S [22].

In the additive manufacturing process, a three-dimensional object is produced by heating a thermoplastic filament to its melting point and then extruding it; layers of material are then deposited to shape the required components (see Fig. 4). It is worth noting that additional vertical support structures could be required for this type of 3D prototyping technique to sustain overhanging pieces during the printing process.

The filaments used are PLA (Polylactic Acid) for the auxiliary parts and ABS (Acrylonitrile Butadiene Styrene) for the structural-mechanical components, as they are subjected to higher stresses. PLA is a plastic of organic origin and is relatively affordable and easy to use in 3D printing. Although it comes with some disadvantages that limit its use, it is suitable for rapid prototyping. It combines high printing speed with sharp edges well, provided the material is properly cooled. It also benefits from a very good surface finish and low thermal expansion. In addition, the resulting parts tend to present very low deformability.

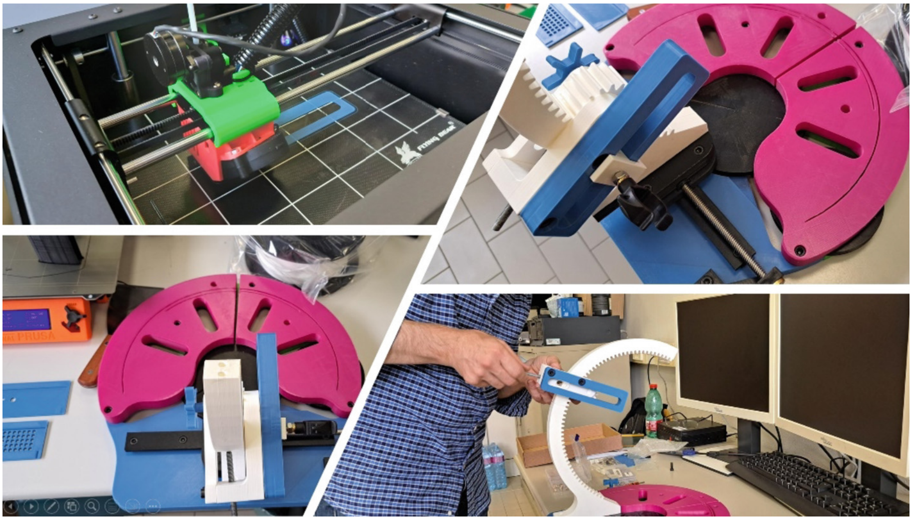

Fig. 4. 3DINO SYSTEM prototype manufacturing and assembling.

However, solid prototypes made from PLA are not designed to be subjected to mechanical stress, as the material is hard and brittle, nor to be exposed to intense heat sources (there would be a softening process over 60°C), and it does not withstand exposure to the atmospheric agents well.

Therefore, ABS – known for its toughness and impact resistance, producing durable components that can endure higher levels of use and wear – was used for the parts subjected to stress, even though it is harder to print. Indeed, ABS is a plastic material that shrinks in contact with air, often causing the 3D-printed elements to warp (or deform) and thus detach from the plate.

The diameter of the filaments, dictated by the printer's specifications, was 1.75 mm for both materials used. The printing specifications are listed as follows: extrusion (hot-end) temperature of 210°C and heat-bed temperature of 60°C for PLA and 100°C for ABS; layer height of 0.15 mm; 10% honeycomb pattern infill; the average print speed was equal to 60 mm/s. These values resulted in a total printing time of approximately 7 days (including finishing).

4 First Conclusions

Early uses of the prototype revealed some imperfections and limitations.

From the perspective of components production, the printer bed's size did not allow printing objects larger than 20 cm in diameter; this resulted in larger components being split into several pieces. Although these parts can be glued or otherwise fixed together at a later stage, this is never done precisely enough or even as accurately as if they had been printed in one piece. While this is considered to be acceptable in prototyping, it highlights the need for larger printing plates and even the possibility of excluding FDM 3D printing from final production. In addition, specifically for future prototyping, the deformation of the pieces should be taken into account; it is due to uneven temperature distribution within the printing chamber or between the areas of the piece directly in contact with the plate and those that are layering above it. Shrinkage of the material during cooling should also be managed by ensuring appropriate printing conditions, explicitly checking that the surrounding temperature is not too low: the faster the part is cooled, the greater the stress on the model. This is why working with closed printing chambers or at least ones sealed off from the environment would be advisable. Anyhow, in our case, the size of the elemental components and their orientation relative to the laying plate also played a disadvantageous role in terms of deformation, as large models are more susceptible to deformation.

To overcome many of the present issues, a new prototype is currently being developed that will be manufactured using selective laser sintering technology. This process, employing polymer powder, provides numerous improvements over FDM solutions. First of all, printing takes place in a controlled environment, thus overcoming the problem of deformations. The maximum size of the printable components is larger, allowing to reduce the number of joints between the sub-parts. Finally, the absence of supports will make it possible to redesign the axial slide rail and recess it inside the base itself, thereby giving the support greater stability. Conversely, it will most likely be necessary to perform a surface treatment on the new prototype, as the outputs of this technology are characterised by high porosity, which could adversely affect some elements' ability to slide over each other.

Another improvement will concern the weight of the base, which must be increased for higher durability of the system and vibration limitation. Indeed, despite the overall performance of the components being good, we are still far from ensuring sufficient vibration control. However, considering that the tested specimen rotates once the inclination of the chamber is fixed, this can be resolved by limiting the interaction between base and rib and rebalancing the components' weight.

Future developments will also include the general streamlining of the massive components, such as the fastening system for the micrometric slide of the optics to the rib. In addition, the movement of the rib, which is determined by a nut-screw mechanism that pushes the system along a T-shaped track, is sometimes tiring for the operator. Indeed, introducing a ball screw could increase precision, ease the operator's task and solve the asymmetry and instability caused by the overhang of the current screw. This would also allow the mechanism to be recessed into the base's thickness to lower the system's centre of gravity and hide the track.

Further adjustments could be implemented on the rib mechanism, which, although valid in its current state, would benefit from more precise axial tightening and a smoother sliding mechanism.

References

1. Galantucci, L.M., Guerra, M.G., Lavecchia, F.: Photogrammetry applied to small and micro scaled objects: a review. In: Ni, J., Majstorovic, V.D., Djurdjanovic, D. (eds.) AMP 2018. LNME, pp. 57–77. Springer, Cham (2018). https://doi.org/10.1007/978-3-319-89563-5_4
2. Parrinello, S., Dell'Amico, A., Galasso, F.: Arsinoe 3D. La narrazione digitale di uno scavo Archeologico/Arsinoe 3D. A project for the digital narration of an archaeological excavation. In Dialoghi. Visioni e visualità. In: Battini C., Bistagnino E. (eds.) Dialoghi. Visioni e Visualità. Atti del 43° Convegno Internazionale dei Docenti Delle Discipline Della Rappresentazione/Dialogues. Visions and visuality. Proceedings of the 43° International Conference of Representation Disciplines Teachers, pp. 881–902. FrancoAngeli, Milan, Italy (2022)
3. Parrinello, S., Dell'Amico, A.: Experience of documentation for the accessibility of widespread cultural heritage. Heritage **2**, 1032–1044 (2019)
4. Brown, D., Laurie, J.F.: Portable Metrology. In: Harding, K. (ed.) Handbook of Optical Dimensional Metrology, pp. 265–286. Taylor & Francis Group, Boca Raton, FL, United States (2013)
5. Barba, S., Mage, M.A.: Evaluación ex-ante y ex-post de la precisión de un proyecto fotogramétrico. In: Lomonaco H.C., Barba S. (eds.) Proceedings of the EGraFIA, V Congreso Internacional de Expresión Gráfica en Ingeniería, Arquitectura y Carreras afines, pp. 548–557. CUES, Fisciano, Salerno, Italy (2014)
6. Gujski, L.M., di Filippo, A., Limongiello, M.: Machine learning clustering for point clouds optimisation via feature analysis in cultural heritage. Int. Arch. Photogram., Remote Sens. Spatial Inf. Sci. XLVI-2/W1–2022, 245–251 (2022)
7. Alonso, B.M., Barba, S., Tordesillas, A.Á.: Documentación del Patrimonio Cultural. Método basado en la fusión de técnicas fotogramétricas y de escaneado óptico de triangulación. EGA Expresión Gráfica Arquitectónica **21**(28), 236–245 (2016)
8. Collins, T., Woolley, S.I., Gehlken, E., Ch'ng, E.: Automated low-cost photogrammetric acquisition of 3D models from small form-factor artefacts. Electronics **8**, 1441–1458 (2019)
9. Menna, F., Nocerino, E., Morabito, D., Farella, E.M., Perini, M.; Remondino, F.: An open-source low-cost automatic system for image-based 3D digitisation. Int. Arch. Photogram., Remote Sens. Spatial Inf. Sci. XLII-2/W8, 155–162 (2017)
10. Doria, E., Picchio, F.: Techniques for mosaics documentation through photogrammetry data acquisition. The Byzantine mosaics of the nativity church. ISPRS Ann. Photogram., Remote Sens. Spatial Inf. Sci. V-2–2020, 965–972 (2020)
11. Filippo, A., Villecco, F., Cappetti, N., Barba, S.: A methodological proposal for the comparison of 3D photogrammetric models. In: Rizzi, C., Campana, F., Bici, M., Gherardini, F., Ingrassia, T., Cicconi, P. (eds.) ADM 2021. LNME, pp. 930–937. Springer, Cham (2021). https://doi.org/10.1007/978-3-030-91234-5_94
12. De Paolis, L.T., De Luca, V., Gatto, C., D'Errico, G., Paladini, G.I. Photogrammetric 3D reconstruction of small objects for a real-time fruition. In: Proceedings of 7th International Conference Augmented and Virtual Reality, and Computer Graphics (AVR 2020), pp. 375–394, Springer, Berlin, Germany (2020).https://doi.org/10.1007/978-3-030-58465-8_28
13. Antinozzi, S.; Ronchi, D.; Barba, S.: Macro and micro photogrammetry for the virtualization of the Orphic Foil (V-IV BC) of National Museum of Vibo Valentia. In: Arena, A., et al. (eds.) Connettere. Un disegno per Annodare e Tessere. Atti del 42° Convegno Internazionale dei Docenti Delle Discipline Della Rappresentazione/Connecting. Drawing for Weaving Relationships. Proceedings of the 42° International Conference of Representation Disciplines Teachers, pp. 1538–1555. Franco Angeli, Milan, Italy (2020)
14. Antinozzi, S., Ronchi, D., Barba, S.: 3Dino system, shortening distances in precision surveys. In: Arena, A., Arena, M., Mediati, D., Raffa, P. (eds.) Connettere. Un disegno per annodare e

tessere. Atti del 42° Convegno Internazionale dei Docenti Delle Discipline Della Rappresentazione/Connecting. Drawing for Weaving Relationships. Proceedings of the 42° International Conference of Representation Disciplines Teachers, pp. 1922–1941. Franco Angeli, Milan, Italy (2021)
15. Eastwood, J., Sims-Waterhouse, D., Piano, S., Weir, R., Leach, R.: Towards automated photogrammetry. In: Proceedings of the 21st International conference of the European Society for Precision Engineering and Nanotechnology (euspen). Technical University of Denmark, Copenhagen, Denmark (2021)
16. Antinozzi, S., Fiorillo, F., Surdi, M.: Cuneiform tablets micro-surveying in an optimized photogrammetric configuration. Heritage **5**, 3133–3164 (2022)
17. Esmaeili, F., Ebadi, H.: Handy microscopic close-range videogrammetry. Int. Arch. Photogram., Remote Sens. Spatial Inf. Sci. XLII-4, 65–67 (2017)
18. Graham, L.L.: Repurposing Technology: An Innovative Low-cost Two-Dimensional Noncontact Measurement Tool. Arizona State University, Tempe, Arizona, USA (2011)
19. Maté González, M.A., Yravedra, J., González-Aguilera, D., Palomeque-González, J.F., Domínguez-Rodrigo, M.: Micro-photogrammetric characterization of cut marks on bones. J. Archaeol. Sci. **62**, 128–142 (2015)
20. Zitek, A., Mayrhofer, B., Oehm, J., Irrgeher, J., Prohaska, T.: Affordable 3D scanning of small otoliths for improved shape analysis by photogrammetry techniques. In: Morales-Nin, B., Geffren, A.J. (eds.) ICES/CIEM, Book of Abstracts of the 5th International Otolith Symposium 2014 (IOS2014), pp. 287–290. ICES/CIEM, Peguera, Spain (2015)
21. Pidatella, C., Ferrari Aggradi, G., Pidatella, D.: Corso di Meccanica. Zanichelli, Bologna, Italy (2010)
22. Prusa, J.: 3D Printing Handbook-Prusa Research a.s. Czech Republic, Prague (2020)

Design of Additive Manufactured Devices with Tailored Properties: Tackling Biomedical Challenges

Ida Papallo(✉), Antonio Gloria, and Massimo Martorelli

Department of Industrial Engineering, Fraunhofer JL IDEAS, University of Naples Federico II, Naples, Italy
ida.papallo@unina.it

Abstract. The design of advanced devices is a paramount goal in the biomedical field. Current challenges include the development of customized devices with improved and tailored properties according to the specific application. Accordingly, the aim of the study was to report some recent efforts in the design of advanced biomedical devices, especially focusing on dental implants and hybrid structures for cranioplasty.

Keywords: Additive Manufacturing · Design for Additive Manufacturing · Biomedical Applications

1 Introduction

In the biomedical applications, the paramount goal is the design of advanced devices to restore, maintain, or improve tissue functions *in vivo*, which may also be employed in many cases as 3D morphologically-controlled structures for the production of whole functional organs. Over the last three decades, many efforts have been made in the fabrication of multifunctional substitutes capable of reproducing specific functions of tissues and organs [1]. As a result of such progresses, the application area of biomedical engineering has strongly broadened from the fabrication of simple standardized prosthetic implants towards being an answer to current challenges, including the design and development of customized devices with tailored properties according to the specific application. To properly understand the achieved results and the current trends in the field, it should be important to look backward and analyse the evolution of the field, with a special focus on the design methodologies and technological advances that have been continuously introduced to meet the clinical and biological needs [1–3] as well as the structural and functional requirements [1, 4–6]. At the onset, the area of biomedical engineering found its driving force in the mechanical engineering, chemistry, materials science and biology, due to its multidisciplinary feature [1]. Pioneers of the field manufactured what can be defined as the first generation of prostheses and scaffolds for tissue engineering, especially aimed at detecting the cross-talk among materials, geometric and architectural features, biological cues, cell-cell and cell-material interactions

M. Carfagni et al. (Eds.): ADM 2023, LNME, pp. 77–83, 2024.
https://doi.org/10.1007/978-3-031-52075-4_10

[1]. Researchers frequently underlined how design and fabrication methods were not suitable to ensure neither the precise control of geometric/architectural aspects nor the functional performances of the prosthetic devices [1]. Consequently, the repeatability of the design procedures and experimental analyses resulted low, and the comparisons of the results obtained in different studies were not possible. This clearly led to the development of several manufacturing techniques and to the adaptation of old methodologies to the novel needs [1, 7].

The introduction of additive manufacturing technologies provided the greatest contribution in developing 3D structures with precise and controlled architectural features [1, 7].

A new research era was then characterised by the development of functional devices with tailored and improved properties, benefiting from suitable design methodologies (i.e., design for additive manufacturing).

In this scenario, it is well known that a good level of tissue-implant integration and stability depends on several factors whose inappropriate control can negatively influence functional and structural connection between the living tissue and the surface of the load-bearing device [8–13].

Many works have dealt with the analysis of the relationship between the geometric features and microstructure of prosthetic implants for several biomedical applications. The design of advanced implants represents one of the key factors influencing the resultant stress at the tissue-implant interface [8–13]. The design of 3D lattice structures with tailored porosity and architectures has been considered as a strategy for the reduction of the implant stiffness, in many cases favouring tissue ingrowth and the stability of the tissue-implant interface [14]. Metallic and polymeric foams with suitable properties (e.g., strength, stiffness) have been potentially developed for different applications [15, 16]. Design criteria have been employed for realizing different kinds of cellular materials, also deeply analysing the deformation of porous structures [15, 16].

The number of nodes and struts play a fundamental role in the unit cell, leading to several classes of unit cells, which can be considered the building blocks in developing cellular materials [15, 16].

Furthermore, strategies in designing advanced devices can also benefit from topology optimization (TO), which is considered a very powerful tool for the designer.

TO allows for providing the optimal material distribution in a defined design space consistently with the given loads and constraints, the aim being to maximize the design performance [17–20].

Accordingly, the current work reports some recent efforts based on specific methodological approaches for the design of advanced biomedical devices, with a special focus on dental implants and hybrid structures for cranioplasty.

2 Design of Dental Implants with Optimized Properties

Today, the dentists would expect to find the optimal solutions in terms of dental implants according to the needs of the patients. The osseointegration level and the consequent bone-implant anchorage are influenced by many factors. As an example, the surface area of the bone-implant contact clearly affects the stress transfer mechanism along the interface.

For this reason, the research has been frequently driven towards the development of 3D porous lattice structures with modulated architectures, the aim being to reduce the implant stiffness and to favour bone ingrowth as well as the stabilization of the implant [21].

In a previous study [21], several approaches were preliminarily considered for the development of novel dental implants, also providing technical suggestions for re-design guidelines. A further insight was provided into the design criteria, first considering a screw implant. A commercially available screw implant was topologically optimized for the given loading condition, constraints and boundary conditions. Different concepts of dental implants were developed considering the commercial screw implant as a starting point: i) implants characterized by a lattice shell surrounding a solid core, without thread (marked as LS-C implants); ii) implants with lattice structure (marked as LS implants).The strategy involved the compliance minimization (volume fraction of 0.50) [21]. The first step was to consider the basic principles in designing the octet-truss lattice, focusing on its properties. The relative density ($\overline{\rho}_{La}$) was related to the density of the lattice material and that of the material (Ti6Al4V) selected for the fabrication of the lattice, as well as to the geometric features [14, 15, 21].

Based on several considerations concerning the relative and effective mechanical properties as well as the yield strength of the selected material, $\overline{\rho}_{La} \geq 0.020$ was found according to critical conditions from a mechanical point of view [21]. In the study, $\overline{\rho}_{La}$ ranged from 0.11 to 0.50 [21].

The lower extreme of the range (i.e., 0.11) was properly selected as the idea was first to employ a value of the Young's modulus equal to that of the trabecular bone. Interesting information were obtained from finite element analysis (FEA) on the different models of bone-implant, concerning stress distributions in cortical and trabecular bone [21].

Figure 1 reports some examples of the findings obtained from the lattice TO (see Fig. 1).

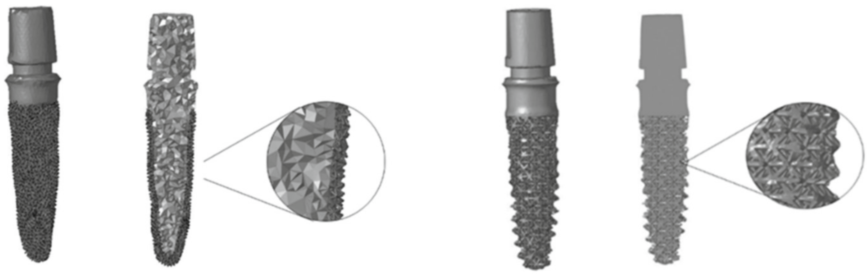

Fig. 1. Examples of implants from lattice TO: LS-C (left) and LS (right). The image was adapted from [21].

The concept developed for $\overline{\rho}_{La} = 0.11$ was not considered as in the lattice part the maximum stress was higher than yield strength for the lattice. With regard to the other cases, when LS-C and LS implants were considered, the values of maximum stress increased in the trabecular and cortical bone, if compared to the results obtained from the use of a commercially available screw implant (i.e., starting point) [21].

The theoretical analysis (i.e., FEA) highlighted how the presence of a lattice structure (i.e., LS-C and LS implants) may enhance the stress transfer to the surrounding bone. Specifically, the lattice structure may act as an "interface zone" with tailored properties and a lower Young's modulus, which may allow a better stress transfer. Little differences found among the different concepts of implant were ascribed to the adopted design criteria [21].

3 Design of 3D Advanced Structures for Cranioplasty

Over the past years, the attention has been focused on a huge range of materials for the repair or regeneration of cranial defects, involving polymeric and composite biomaterials, as well as several design strategies [7].

From a materials science point of view, some studies reported the use of poly(methyl methacrylate) (PMMA)-based bone cements and their modifications by means of the inclusion of copper doped tricalcium phosphate (Cu-TCP) particles [22].

In addition, the use of aliphatic polyesters (e.g., poly(ε-caprolactone) – PCL, polylactic acid - PLA) has also been considered for the fabrication of 3D scaffolds for cranial bone tissue engineering. In this scenario, a previous study [7] reported a strategy in designing and fabricating customized hybrid devices for the repair of large cranial defects. In particular, a hybrid device was developed in the form of a 3D additive manufactured polyester structure with an interconnected pore network characterized by specific lay-down patterns, which was infiltrated with a modified cement (i.e., PMMA/Cu-TCP 97.5/2.5 w/w). Reverse engineering was integrated with additive manufacturing (i.e., Fused Deposition Modeling), the aim being to develop customized devices with enhanced and tailored morphological, mechanical and functional features [7]. Briefly, starting from a 3D virtual model of a skull with a large cranial defect, a CAD system was employed to design 3D customized models of porous devices for cranioplasty. 3D porous models were developed from non-porous geometrical models. A porosity of 50% was selected for allowing the cement infiltration (see Fig. 2).

Temperature profiles and peak temperatures were suitably analyzed in the different kinds of hybrid structures based on PCL and PLA, as the heat released during the exothermic reaction represents a great drawback, if an *in situ* application of a PMMA-based bone cement is considered, especially in the case of large defects [7].

The validation of the feasibility of the technical solutions was demonstrated by means of both virtual and physical models. FEA was also caried out on the entire head model simulating severe impact conditions for people with the customized hybrid device, as a rigid sphere was considered impacting the implant region of the head [7]. This clearly represented an important research step since it would seem that until then none of the existing finite element models had taken into consideration the impact-related features for people using prosthetic devices in the case of large defects.

The geometry of an adult human head was considered, and the modeling of the anatomical components was performed also consistently with their properties [7].

The obtained findings gave information on the several model components. Even though the failure of some elements of the external layer of the cement was evident, the underneath PCL structure infiltrated with the cement was not significantly altered [7].

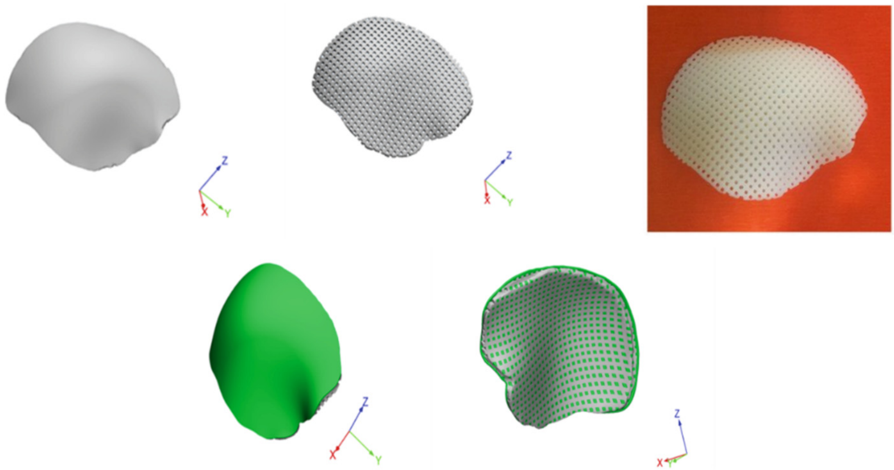

Fig. 2. Design and development of the proposed device: 3D geometrical non-porous model and porous model (top left); 3D additive manufactured device (top right); two views of 3D geometrical models related to a customized hybrid device highlighting the external cement layer and the cement infiltration in the pore network, where green colour was employed for the identification of the cement (bottom). The image was adapted from [7].

The results would suggest an increase in the ability of the designed device to absorb energy and to deform before failure.

4 Conclusions

Over the past years, great efforts have been carried out to make available tools for modeling complex geometries, while considering the manufacturing constraints.

In this scenario, many approaches based on different concepts and criteria have been proposed for the development of advanced biomedical devices [23–27].

With regard to the design of biomedical implants, the optimization of porous lattice structures has been frequently stressed in the literature [7, 21, 27–30], with a special focus on both mechanical and biological features.

It was already demonstrated how triply periodic minimal surfaces structures (i.e., gyroid) may allow to develop advanced porous orthopaedic implants and to fine-tune the mechanical properties for successful long-term performance [27]. The effects of the design parameters were also described [27].

However, even though the gyroid may be easily employed to reproduce the structure of the natural bone and it results stronger and stiffer in comparison to strut-based lattices, the design of octet-truss lattices was also proposed for the development of dental implants by means of several optimization strategies, providing interesting results [21]. In particular, the results evidenced that the potential of modulating the properties of the interface lattice structure may provide a better stress transfer from the implant to the bone [21]. Moreover, initial concepts based on functionally graded materials were previously introduced in designing dental implants, where the properties efficiently varied according to specific patterns for matching the biomechanical features at different zones in the bone [28]. Critical issues were first explored and the obtained results were analysed with a special focus on bone remodeling [28].

During the years, the research emphasis has also been on the development of technical solutions for cranioplasty, concerning the design of novel customized devices [7], as well as innovative methodologies relying on a planning phase, with the aim to guide the surgeon in the definition of the surgical approach and the optimization of the implant [29]. The methodological approach was successfully tested in a case study where high risk factors were identified [29].

Polymer-based prostheses have often been investigated and proposed as alternatives to the high-cost titanium mesh plates. Accordingly, the use of low-cost 3D printers has generated great opportunities to help the patients [30]. In this context, a novel customized hybrid device was developed [7]. The obtained findings highlighted how an appropriate design for additive manufacturing of the PCL structure embedded in the cement may provide a great contribution in terms of the overall mechanical behavior of the device, specifically creating a toughening effect [7].

Finally, it is worth noting that the investigations reported in Sects. 2 and 3 can be considered as first steps of a research devoted to a multi-objective design optimization of the proposed devices. An integrated strategy will be defined to find a set of optimal solutions for designers working in the field.

References

1. Celikkin, N., et al.: Tackling current biomedical challenges with frontier biofabrication and organ-on-a-chip technologies. Front. Bioeng. Biotechnol. **9**, 732130 (2021)
2. Kim, B.-S., Baez, C.E., Atala, A.: Biomaterials for tissue engineering. World J. Urol. **18**, 2–9 (2000)
3. Kaul, H., Ventikos, Y.: On the genealogy of tissue engineering and regenerative medicine. Tissue Eng. B: Rev. **21**, 203–217 (2015)
4. Peluso, V., et al.: Impact of magnetic stimulation on periodontal ligament stem cells. Int. J. Mol. Sci. **23**(1), 188 (2022)
5. Russo, T., et al.: Combination design of time-dependent magnetic field and magnetic nanocomposites to guide cell behavior. Nanomaterials **10**(3), 577 (2020)
6. Stocco, E., et al.: Development of two-layer hybrid scaffolds based on oxidized polyvinyl alcohol and bioactivated chitosan sponges for tissue engineering purposes. Int. J. Mol. Sci. **23**(20), 12059 (2022)
7. De Santis, R., Russo, T., Rau, J.V., Papallo, I., Martorelli, M., Gloria, A.: Design of 3D additively manufactured hybrid structures for cranioplasty. Materials **14**(1), 181 (2021)
8. Kayabaşı, O., Yüzbasıoğlu, E., Erzincanlı, F.: Static, dynamic and fatigue behaviors of dental implant using finite element method. Adv. Eng. Softw. **37**(10), 649–658 (2006)
9. Liang-jian, C., Hao, H., Yi-min, L., Ting, L., Xiao-ping, G., Rui-fang, W.: Finite element analysis of stress at implant−bone interface of dental implants with different structures. Trans. Nonferrous Metals Soc. China **21**, 1602–1610 (2011)
10. Ausiello, P., Franciosa, P., Martorelli, M., Watts, D.C.: Effects of thread features in osseo-integrated titanium implants using a statistics-based finite element method. Dent. Mater. **28**(8), 919–927 (2012)

11. Calì, M., et al.: Influence of thread shape and inclination on the biomechanical behaviour of plateau implant systems. Dent. Mater. **34**, 460–469 (2018)
12. Massoumi, F., Taheri, M., Mohammadi, A., Amelirad, O.: Evaluation of the effect of buccolingual and apicocoronal positions of dental implants on stress and strain in alveolar bone by finite element analysis. J Dent (Tehran) **15**(1), 10–19 (2018)
13. Maietta, S., Gloria, A., Improta, G., Richetta, M., De Santis, R., Martorelli, M.: A further analysis on Ti6Al4V lattice structures manufactured by selective laser melting. J. Healthc. Eng. **2019**, 3212594 (2019)
14. Deshpande, V.S., Fleck, N.A., Ashby, M.F.: Effective properties of the octet-truss lattice material. J. Mech. Phys. Solids **49**(8), 1747–1769 (2001)
15. Elsayed, M.S.A., Pasini, D.: Multiscale structural design of columns made of regular octet-truss lattice material. Int. J. Solids Struct. **47**, 1764–1774 (2010)
16. Mareishi, S.: Design optimization of dental implants using additively manufactured lattice materials (2018). https://curve.carleton.ca/system. Accessed 13 Feb 2022
17. Vlah, D., Žavbi, R., Vukašinović, N.: Evaluation of topology optimization and generative design tools as support for conceptual design. Proce. Design Soc.: Design Conf. **1**, 451–460 (2020)
18. Querin, O.M., Victoria, M., Alonso, C., Loyola, R.A., Montrull, P.M.: Topology design methods for structural optimization. Butterworth-Heinemann (2017)
19. Bendsøe, M.P.: Optimal shape design as a material distribution problem. Struct. Optim. **1**, 193–202 (1989)
20. Bendsøe, M.P., Kikuchi, N.: Generating optimal topologies in structural design using a homogenization method. Comput. Methods Appl. Mech. Eng. **71**, 197–224 (1988)
21. Ausiello, P., et al.: Optimal design of surface functionally graded dental implants with improved properties. In: Lecture Notes in Mechanical Engineering, pp. 294–305 (2023). https://doi.org/10.1007/978-3-031-15928-2_26
22. Russo, T., et al.: Modification of PMMA cements for cranioplasty with bioactive glass and copper doped tricalcium phosphate particles. Polymers **12**(1), 37 (2019)
23. Rongo, R., et al.: Effects of intraoral aging on surface properties of coated nickel-titanium archwires. Angle Orthod. **84**(4), 665–672 (2014)
24. Reitmaier, S., Shirazi-Adl, A., Bashkuev, M., Wilke, H.-J., Gloria, A., Schmidt, H.: In vitro and in silico investigations of disc nucleus replacement. J. R. Soc. Interface. **9**(73), 1869–1879 (2012)
25. Guarino, V., Gloria, A., Raucci, M.G., Ambrosio, L.: Hydrogel-based platforms for the regeneration of osteochondral tissue and intervertebral disc. Polymers **4**(3), 1590–1612 (2012)
26. Goranov, V., et al.: 3D patterning of cells in magnetic scaffolds for tissue engineering. Sci. Rep. **10**(1), 2289 (2020)
27. Guariento, L., Buonamici, F., Marzola, A., Volpe, Y., Governi, L.: Graded gyroid structures for load bearing orthopedic implants. In: 2020 IEEE 10th International Conference Nanomaterials: Applications & Properties (NAP) (2020)
28. Lin, D., Li, Q., Li, W., Zhou, S., Swain, M.V.: Design optimization of functionally graded dental implant for bone remodeling. Compos. B Eng. **40**(7), 668–675 (2009)
29. Marzola, A., Buonamici, F., Furferi, R., Governi, L., Genitori, L., Mussa, F.: Additive manufacturing and reverse engineering in cranioplasty: a personalized approach to minimize skin flap complications. Appl. Sci. **11**(11), 4926 (2021)
30. Czyżewski, W., et al.: Low-cost cranioplasty—a systematic review of 3D printing in medicine. Materials **15**(14), 4731 (2022)

Additively Manufactured Lattice-Based Structures for Aeronautical Applications

D. Tumino(✉), G. Mantegna, C. R. Vindigni, C. Orlando, and A. Alaimo

Kore University of Enna, Cittadella Universitaria, 94100 Enna, Italy
davide.tumino@unikore.it

Abstract. Additive Manufacturing (AM) technologies are widely spreading into multiple engineering sectors thanks to their flexibility to create complex geometries with virtual no material waste. AM technologies capabilities can be fully exploited when working with periodic lattices, creating topology-optimized structures through different cell types with different dimensions and volume fractions. Several factors (i.e., process parameters, quality and type of raw materials) can modify the mechanical properties of printed components and can be exploited to selectively create functionally graded materials or conventional laminated hybrid materials structures.

This paper analyses and compares the mechanical properties of different additively manufactured lattice BCC structures through experimental and numerical means. At first, the manufacturing procedure followed by experimental tests is presented. The retrieved mechanical properties are then used as a benchmark for the numerical Finite Element Analyses and compared with analytical models available in the literature. The numerical simulation campaign includes the comparison of a full 3D model and a 1D/2D beam/shell formulation model. The research findings demonstrate a good correlation between the experimental tests and the numerical simulation results, indicating the potential for the proposed methodologies to be broadly implemented within various domains of structures and materials.

Keywords: Additive Manufacturing · Design for Manufacturing · Periodicity · 3D lattice · FEM

1 Introduction

Additive Manufacturing (AM) technologies are widely spreading thanks to their flexibility to create complex geometries with virtual no material waste with significant benefits for the aerospace, medical devices, and automotive industries, among others. Indeed, an increasing demand for reduced manufacturing costs and lead time, a shorter product design and development process, and the ability to create highly customizable products both in shape and mechanical properties, made the AM market one of the most flourishing in the past 30 years [1]. More recently, these technologies have combined the use of different materials in the so-called Multi-Material Additive Manufacturing (MM-AM), enhancing the design freedom and functionality by varying material compositions within the layers [2].

M. Carfagni et al. (Eds.): ADM 2023, LNME, pp. 84–92, 2024.
https://doi.org/10.1007/978-3-031-52075-4_11

AM technologies capabilities can be fully exploited when working with periodic lattices structures. Repeating a unit cell in a 3D patterned arrangement makes it possible to create topologies in the space to create ordered topology-optimized structures. The selection of the lattice type and parameters (such as cell size, strut thickness, and orientation) plays an essential role in determining the mechanical performance of the final product and with AM technologies is easy to use different configurations to achieve functionally-graded materials [3–5].

Due to their simplicity in construction, the Body-Centered Cubic (BCC) and the Face-Centered Cubic (FCC) are among the most utilized unit cell types [6]. Multiple studies are present in the scientific literature which seek to forecast and assess the behavior of cellular structures through analytical, numerical, and experimental methods. In [7] the authors present an analytical method to retrieve the mechanical properties of BCC lattice structures using the Timoshenko beam theory to characterize different cell parts with different elastic constants under compression loading. In a later work, [8], the equivalent shear modulus of the BCC lattice structure in different configurations is retrieved through an equivalent homogenized method. In [9] a stiffening effect due to strut intersection at the nodes is considered reducing the length of the flexible portions of the struts. A similar approach, based on the strut diameter is used in [10], while the effect of larger strut diameters is studied in [11]. Tumino et. al. in [12] optimize the beam stiff length as a function of the strut diameter-cell size ratio for both BCC and FCC cells, while in [13] the authors study the effect of waviness in the BCC struts.

This paper aims to characterize the mechanical behavior of additively manufactured lattice BCC structures through experimental tests and numerical simulations. Specifically, numerical tests with a 3D and 1D model on the single BCC cell are used to forecast the behavior of BCC structures in compression and in bending. Experimental tests are also performed to validate the numerical results obtained. This study, financially supported by the M.U.R. under the AGREED project, serves as the initial stage of a comparative analysis of various structural lattice cell topologies for the arms and landing gear of a high performance drone.

2 Experimental Tests

For this study different lattice BCC structures are manufactured via Fused Deposition Modelling (FDM) methodology employing Polylactic Acid (PLA) as the base material. The mechanical characteristics of the bulk material, which have been determined in previous experimental tests, are $E = 3132$ MPa, $\sigma_{yield} = 20$ MPa with an average density of $\rho = 1275 kg/m^3$. All the specimens have been printed with a Flashforge Dreamer, with several print configurations being evaluated and optimized to enhance both mechanical properties and surface finish. Ultimately, a nozzle print speed of 50 mm/s and a temperature of the extruder of 200 °C were selected.

2.1 Compression Tests

A BCC structure formed by a 4x4x4 unit cell array, resulting in a total dimension of 40x40x40 mm, was first manufactured for the compression test; a BCC unit cell with edge size $l = 10$ mm and strut diameter $d = 2$ mm was used as periodic element of the structure. For the sake of reproducibility three coupons were printed and tested using an MTS electro-mechanic machine with 50 kN load capacity at a crosshead rate of 5 mm/min. The compressive response of three specimens is illustrated in Fig. 1, which depicts the characteristic regions that typify compression phases of a lattice structure, as also reported in other studies [9, 10]; these areas are delimited by dashed vertical lines in the figure. At first a linear elastic regime characterizes the left area of the diagram, followed by the gradual collapse of the cells resulting in a full plastic behavior. Finally, a sharp increase of the stresses indicates the densification phase.

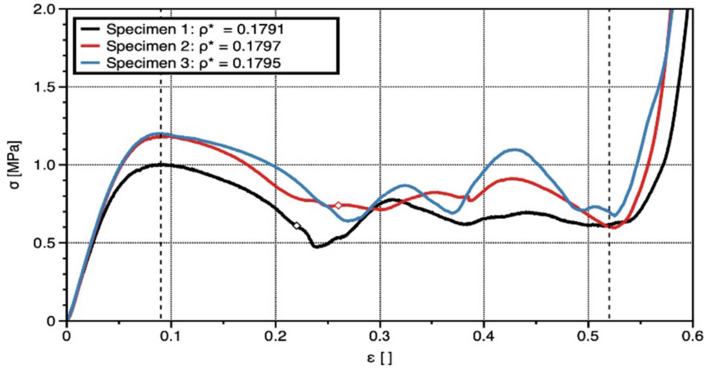

Fig. 1. Compression Stress-Strain diagram, BCC 4x4x4 lattice structure.

The two points highlighted in Fig. 1 indicate where the first and second specimens started to experience shear deformation bands due to the local buckling of a cell strut that is randomly weakened by manufacturing defects. Contrary, the third specimen showed a layer-by-layer failure as shown in Fig. 2.c.

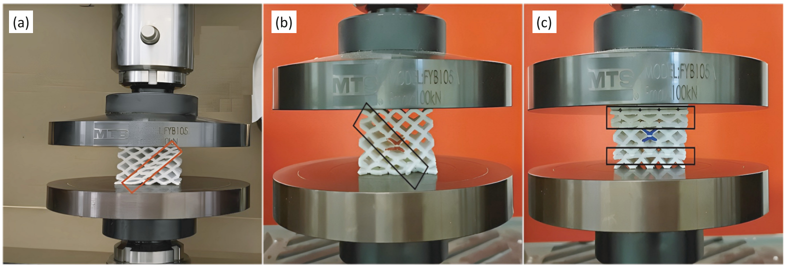

Fig. 2. Deformation patterns details in compression loading of BCC lattice structures.

An apparent elastic modulus $E = 22.57$ MPa with a yield strength $\sigma_y = 0.8$ MPa is retrieved for the BCC lattice structure under exam. The mechanical properties retrieved for single specimens are reported in Table 1.

Table 1. Experimental compression test results

Weight [g]	Relative density	Young Modulus [MPa]	Yield strength [MPa]	Maximum strength [MPa]
14.617	0.1791	21.06	0.76	1.01
14.67	0.1797	23.56	0.83	1.17
14.65	0.1795	23.11	0.80	1.20
14.65	**0.18**	**22.58**	**0.80**	**1.13**

2.2 Three-Point Bending Test

A lattice sandwich structure formed by a core made with BCC cells in a 22x3x1array within two skins with a thickness of 1 mm was 3D printed for the Three-Point Bending Test (TPBT), as shown in Fig. 3.a. Different support span lengths, specifically 200, 180, 160, 140 and 120 mm, were employed for the experimental tests. For the sake of reproducibility, two coupons were printed and tested under all supports combinations, utilizing an MTS electro-mechanic machine with a 1 kN load capacity at a crosshead rate of 2.5 mm/min.

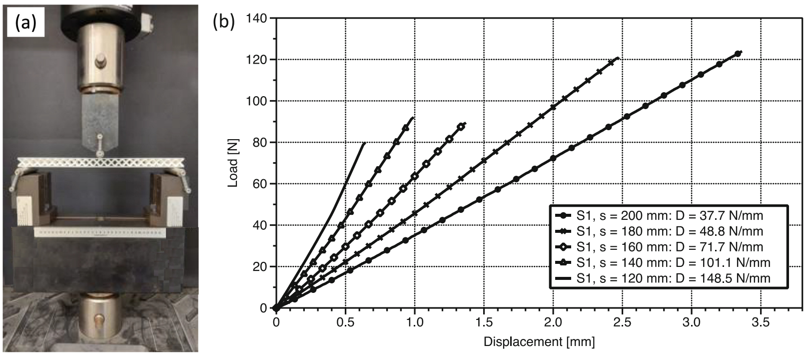

Fig. 3. TPBT Experimental test. (a) Experimental setup, 200 mm span, (b) Load-Displacement diagram.

Table 2 reports the bending rigidities of the two tested sandwiches, measured as $D = Load/Deflection$, and their average values.

3 Numerical Analyses

The mechanical properties of the BCC structures are carried out through Finite Element Analyses performed in the commercial software Ansys 2022.

Table 2. Experimental three-point bending test results

Span [mm]	200	180	160	140	120
D Sandwich 1 [N/mm]	37.7	48.8	71.7	101.1	148.5
D Sandwich 2 [N/mm]	37.7	49.7	68.7	96.9	141.4
Average	**37.7**	**49.2**	**70.2**	**99.0**	**145.0**

3.1 Unit BCC Cell Properties – Compression and Shear Tests

In this study compression and shear tests are used to characterize the mechanical properties of the single unit BCC and thus to determine the properties of the overall lattice structures. Various Finite Element (FE) models are employed, including a full 3D and a 1D beam models. The 1D beam model must consider a stiffening effect near the structural interconnections. This phenomenon, as reported in previous works [9, 12], can be numerically modeled by dividing the beam into a stiff and a flexible part. In an earlier study [12] the compression stiff beam length was numerically determined and optimized as a function of the cell diameter-to-length ration d/L. Figure 4 shows the 3D and 1D BCC cell models.

Cell size, L [mm]	10.0
Strut diameter, d[mm]	2.0
Stiff beam length, h_{comp} [mm] [13]	0.93
Stiff beam length, h_{shear} [mm]	0.35

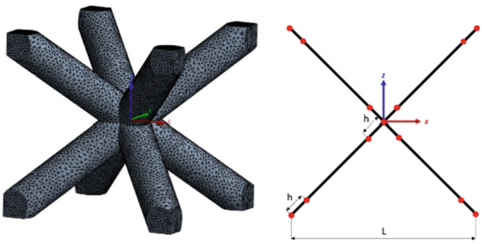

Fig. 4. 3D and 1D BCC cell dimensions.

In the 3D model, the periodicity of the BCC structure is enforced through special periodicity boundary conditions imposed at each node of the BCC lateral faces via constraint equations. Specifically, an ad-hoc Ansys Parametric Design Language (APDL) routine is employed to impose double periodicity along the x and y directions. Each node on the left face $n_{i|x=-L/2}$ is paired with the node on the opposite face that shares the same y and z coordinates $n_{i|x=+L/2}$. The displacements of the two nodes are thus coupled through the following constraint equations:

$$\begin{cases} u_x\left(n_{i|x=-L/2}\right) - u_x\left(n_{i|x=+L/2}\right) = u_x\left(n_{p_{|x=-L/2}}\right) - u_x\left(n_{p_{|x=+L/2}}\right) \\ u_y\left(n_{i|x=-L/2}\right) - u_y\left(n_{i|x=+L/2}\right) = u_y\left(n_{p_{|x=-L/2}}\right) - u_y\left(n_{p_{|x=+L/2}}\right) \\ u_z\left(n_{i|x=-L/2}\right) - u_z\left(n_{i|x=+L/2}\right) = u_z\left(n_{p_{|x=-L/2}}\right) - u_z\left(n_{p_{|x=+L/2}}\right) \end{cases} \quad (1)$$

where $n_{p_{|x=\pm L/2}}$ are two pilot nodes properly chosen in the two faces. The selection of these nodes aims to achieve maximum symmetry of their positions with respect to the center of the cell, thereby ensuring periodicity of the cell even under rotations around its center. In a similar way, from Eq. 1 it is possible to impose the periodicity along the y-direction paring the nodes at $y = \pm L/2$.

To ensure that each node in the BCC structure has a corresponding node in the opposite face that shares the same coordinates, only one eighth of the BCC cell is initially created and meshed and then mirrored to ensure the nodes correspondence on the BCC cell faces.

Since the 1D model has a single node at the end of the struts and no lateral faces, the periodic conditions are implemented coupling the nodes at the end of the struts through remote points. To the best authors' knowledge, previous investigations on 1D beam BCC lattice structures using a stiff beam approach solely considered compression loading. However, this stiff beam length, beside the strut diameter-cell size ratio d/L, must also considers the type of loading on the cell. More specifically, the stiff beam length law reported in [12] holds true for compression loading, when the cell struts are mainly subjected to bending stress. However, in pure shear loading, the cell struts are subjected in both bending and axial stresses. Therefore, a new stiff beam length must be used to account for the mixed loading combination.

Besides the double periodicity conditions imposed along the x and y directions, the boundary conditions for the 3D model consider an imposed displacement on the upper surface ($z = +L/2$) along the z-direction for the compression test. In contrast, the shear test considers an imposed displacement along the x direction. Simultaneously, the bottom surface ($z = -L/2$) has the respective displacement constrained. The boundary and periodicity conditions imposed for the 1D model are shown in Fig. 5.

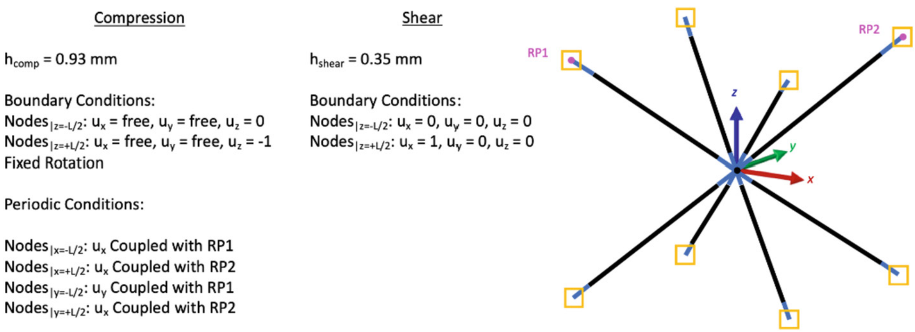

Fig. 5. 1D model, compression and shear boundary and periodicity conditions.

An equivalent elastic modulus $E_{3D} = 23.5$ MPa, A Poisson's ration $\nu_{3D} = 0.47$ and a shear modulus $G_{3D} = 82.4$ MPa were retrieved from the 3D model, while the 1D model results in an elastic modulus $E_{1D} = 22.6$ MPa, a Poisson's ratio $\nu_{1D} = 0.46$ and a shear modulus $G_{1D} = 82.7$ MPa. The 1D model accurately replicates the 3D model results while significantly reducing the computational costs due to a lower number of elements (190 vs 47200) and the absence of constraint equations pairing each node on the lateral faces. The directional displacement map along the z and x directions for the 3D and 1D models are shown in Fig. 6.

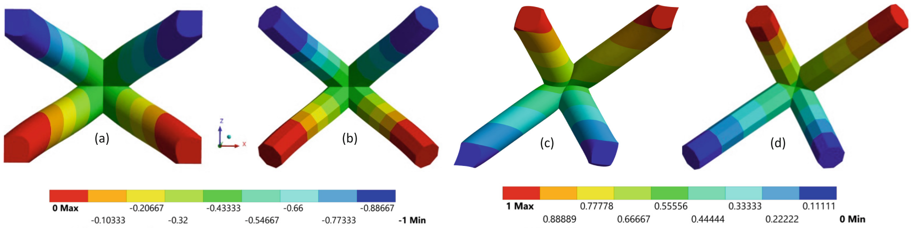

Fig. 6. Directional displacements maps 3D and 1D models: (a) and (b) along z during compression; (c) and (d) along x during shear.

The equivalent elastic modulus obtained from both the 3D and 1D models exhibits high accuracy with the elastic modulus derived from the experimental tests on the 4x4x4 array BCC structure in Table 1, thus validating the approach used to characterize the structure from the periodic unit cell.

3.2 Flexure Test

The numerical model of the TPBT considers only half specimen for both the 3D and 1D/2D analyses. All numerical analyses are conducted at variable span lengths as done in the experimental tests. Moreover, the 1D/2D considers both the stiff beam length of 0.93mm and 0.35mm. A directional displacement map along the z-direction of the 1D model with the compression stiff beam length is depicted in Fig. 7.

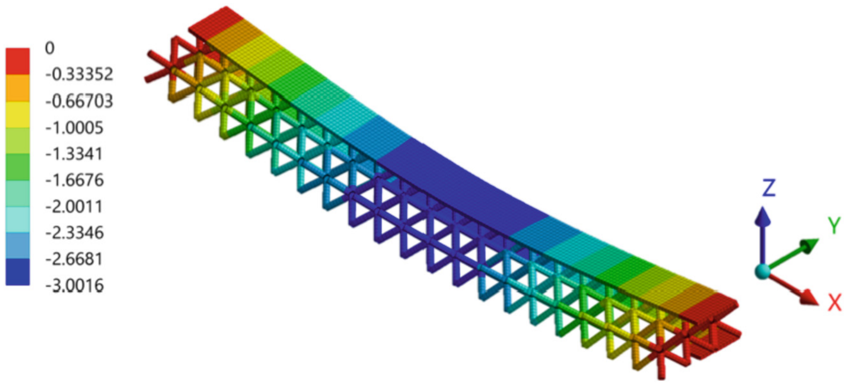

Fig. 7. Three Point Bending Test, Span = 200 mm, l_{stiff} = 0.93mm. Directional displacement in z-direction. Top and bottom skins partially sectioned for results visibility.

Figure 8 reports the normalized bending rigidities with respect to the 3D value at the different span lengths; the 3D value at each span length is reported above its corresponding bar. The 3D model overestimates the experimental rigidity values at all considered span lengths. This discrepancy could potentially be attributed to imperfections during the printing or in the utilized material. Moreover, both the stiff beam lengths considered for the 1D/2D beam/shell models underestimate the stiffness expected with the 3D model. Nevertheless, a better approximation with the experimental rigidity values is observed. As the span length varies, the difference between the 1D model with a stiff beam length of 0.93 mm and the 3D model is quite constant and smaller than 2% of the 3D value of rigidity. However, when a stiff beam length of 0.35 mm is used, this difference increases as the span decreases, starting from a minimum value of −3.6% of the 3D value of rigidity at 20 cell length span up to a maximum value of −6.3% at 12 cell length span. This could be explained due to the presence of the skins that redistribute the loadings on the core of the sandwich structure, stressing the struts predominantly in bending thus underestimating the stiffness of the whole structure.

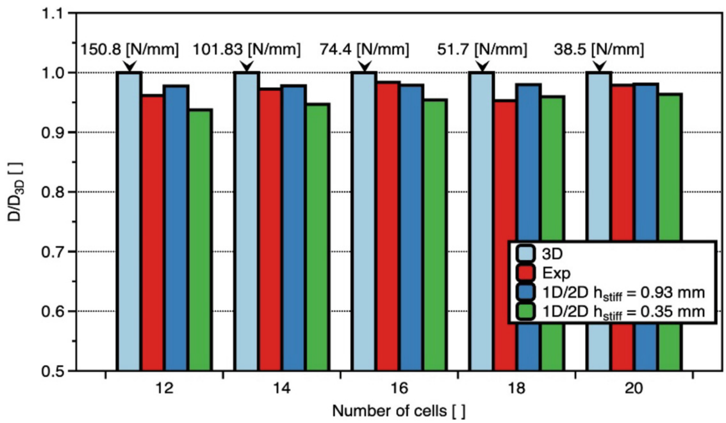

Fig. 8. Normalized bending rigidity with respect to the 3D value at different span length.

4 Conclusions

This study presents a comprehensive analysis and comparison of the mechanical properties of additively manufactured lattice structures. The research demonstrates the feasibility and effectiveness of using numerical simulations to accurately predict the behavior of these complex structures. A full 3D and a simplified 1D beam models are used to characterize the mechanical properties of a BCC cell and to predict the behavior of two lattice structures.

The experimental results well approximate the 3D model analyses on both compression and flexural tests, thus validating the procedure used. The 1D models consider a variable stiff beam length as a function of the main loading on the struts of the structure. Both the compression test on a BCC 3D array structure and the flexural test on a sandwich structure mainly stress the structure at bending. For this reason, the optimized stiff beam length under a compression loading returns more accurate results. On the other hand, the stiff beam length optimized with a shear loading are slightly less accurate for the considered loading conditions.

Future works aims to study different loading conditions such as a pure shear and in a mixed loading.

Acknowledgements. The study was financially supported by Ministero dell'Università e della Ricerca (M.U.R.) for the project "AGREED" – Agriculture, Green & Digital (ARS01_00254).

References

1. Thompson, M.K., et al.: Design for additive manufacturing: trends, opportunities, considerations, and constraints. CIRP Ann. Manuf. Technol. **65**, 737–760 (2016). https://doi.org/10.1016/j.cirp.2016.05.004
2. Bandyopadhyay, A., Heer, B.: Additive manufacturing of multi-material structures (2018)
3. Wang, Y., Zhang, L., Daynes, S., Zhang, H., Feih, S., Wang, M.Y.: Design of graded lattice structure with optimized mesostructures for additive manufacturing. Mater Des. 142, (2018). https://doi.org/10.1016/j.matdes.2018.01.011
4. Tao, W., Leu, M.C.: Design of lattice structure for additive manufacturing. In: 2016 International Symposium on Flexible Automation (ISFA), pp. 325–332. IEEE (2016)
5. Panesar, A., Abdi, M., Hickman, D., Ashcroft, I.: Strategies for functionally graded lattice structures derived using topology optimisation for additive manufacturing. Addit. Manuf. **19**, 81–94 (2018). https://doi.org/10.1016/j.addma.2017.11.008
6. Bai, L., Yi, C., Chen, X., Sun, Y., Zhang, J.: Effective design of the graded strut of BCC lattice structure for improving mechanical properties. Materials 12 (2019). https://doi.org/10.3390/ma12132192
7. Yang, Y., Shan, M., Zhao, L., Qi, D., Zhang, J.: Multiple strut-deformation patterns based analytical elastic modulus of sandwich BCC lattices. Mater Des. 181 (2019). https://doi.org/10.1016/j.matdes.2019.107916
8. Zhang, W., Zhao, J., Tan, Y., Gao, Y., Wang, J., Geng, X.: Study on the shear modulus based equivalent homogenization methods of multi-layer BCC lattice sandwich. Materials 15 (2022). https://doi.org/10.3390/ma15041341
9. Gümrük, R., Mines, R.A.W.: Compressive behaviour of stainless steel micro-lattice structures. Int. J. Mech. Sci. 68 (2013). https://doi.org/10.1016/j.ijmecsci.2013.01.006
10. Smith, M., Guan, Z., Cantwell, W.J.: Finite element modelling of the compressive response of lattice structures manufactured using the selective laser melting technique. Int. J. Mech. Sci. 67 (2013). https://doi.org/10.1016/j.ijmecsci.2012.12.004
11. Guo, H., Takezawa, A., Honda, M., Kawamura, C., Kitamura, M.: Finite element simulation of the compressive response of additively manufactured lattice structures with large diameters. Comput Mater Sci. 175 (2020). https://doi.org/10.1016/j.commatsci.2020.109610
12. Tumino, D., Alaimo, A., Orlando, C., Valvano, S., Vindigni, C.R.: Lattice core FEM simulation with a modified-beam approach. Lecture Notes in Mechanical Engineering, pp. 946–954 (2023). https://doi.org/10.1007/978-3-031-15928-2_83
13. Tumino, D., Alaimo, A., Orlando, C., Valvano, S.: A preliminary study on the effect of strut waviness on the mechanical properties of BCC lattice unit cells. In: Lecture Notes in Mechanical Engineering (2022)

Concurrent Product and Process Design of an Additively Manufactured Engine Piston

Enrico Dalpadulo(✉), Fabio Pini, and Francesco Leali

"Enzo Ferrari" Department of Engineering, University of Modena e Reggio Emilia, via Vivarelli 10/1, 41125 Modena, Italy
{enrico.dalpadulo,fabio.pini,francesco.leali}@unimore.it

Abstract. Additive Manufacturing (AM) Powder Bed Fusion (PBF) metal processes enable significant design freedom, addressing design complexity in high-end sectors. To build performant products, several Design for Additive Manufacturing guidelines must be considered. Nevertheless, it is still noticeable a lack of reliability for AM processes, which is a key factor to guarantee both the expected enhanced product requirements and the manufacturability. Even though few rules and best practices to mitigate defects are provided either by standards or equipment suppliers, they are still missing approaches to predict build failures and process flaws, and therefore achieve faultless build processes. This work suggests a concurrent product and process design approach, in which Computer Aided Engineering tools are involved in both product and process design to identify the components' shapes that match the expected performance and a feasible PBF build layout. An automotive component is the use case, whose design based on topology optimization and product validation is enriched by integrating the associated process simulation. The build process is modeled by (a) the additive manufacturing simulation to identify flaws and resources usage, and (b) the thermo-mechanical finite element -based simulation to predict residual stress and distortions. The approach based on CAD platforms integrates product and process design to reduce design iterations, trial-error practices, and build failures.

Keywords: Laser Powder Bed Fusion · Design for Additive Manufacturing · Product-process design · Process simulation · Finite Element Analysis

1 Introduction

In the last decade, Additive Manufacturing (AM) technologies are gaining interest both in academic research and industrial settings, since scientific papers, patents, and market growth are constantly increasing. AM enables the construction of highly specific, customized, and complex products, that are often impossible to produce with traditional manufacturing technologies. Powder Bed Fusion (PBF) metal processes allow to build either functional prototypes or end-use parts, exploiting the high design freedom to enhance products performance in high-end sectors [1], such as lightweight structures, heat exchangers, customized tools, and medical and dental parts. Besides the widely

M. Carfagni et al. (Eds.): ADM 2023, LNME, pp. 93–100, 2024.
https://doi.org/10.1007/978-3-031-52075-4_12

acknowledged potentials, the main drawbacks rely on the one hand costs and robustness of metal processes, on the other hand on the need for specific AM knowledge. While the breakeven point of production volumes is shifting due to the reduction of machines and materials costs, process reliability has still to be improved in order to produce flawless parts [1]. In particular, it is fundamental to mitigate process defects and failures to effectively achieve the requirements of high-performance designs. Moreover, it is still needed to address specific AM knowledge to develop proper approaches, allowing to streamline the design of complex products and the associated AM processes. The Design for Additive Manufacturing (DfAM) framework is the set of rules, guidelines, and workflows to support AM and spread actual industrial applications. Design and manufacturing have been for a while identified as the two key AM areas [2]. Enhanced product performance can be obtained by making use of such specific knowledge. Currently, most research and applications are focused on Computer Aided Engineering (CAE) techniques (e.g., topology optimization, latticing, generative design) and the development of related tools and methods to finalize optimized 3D part geometries [3]. Nevertheless, recent literature reviews assert that also process design, or rather industrialization, is a fundamental matter of research [4, 5]. The print-right first time is a challenging goal both to improve product quality and reduce production and materials scraps. Indeed, the holistic approaches have been identified as a key challenge for the spread of AM systems [2, 4, 5]. From this perspective, the aim of this work is to perform the concurrent product and process design for AM products, supported by proper implementation of CAE simulations. An Internal Combustion Engine (ICE) piston has been re-designed achieving the optimal targets of both design and manufacturing.

The next section provides the methods and tools involved to integrate CAE simulation along the workflow. Section 3 provides the analysis of the case study, resuming the key aspects of product design. Section 4 describes the results concerning the use of simulation to perform the integrated process design for practical applications. The final discussion highlights the prime advantages of the approach and the forecasts for further developments.

2 Methods and Tools

The AM-based design of components aims to rethink products layouts to exploit the design freedom. For the purpose of this work, the case of topology optimized components to be produced by Laser-based PBF (L-PBF) is considered.

2.1 Simulation for Metal AM Processes

Making use of CAE tools, optimal material distribution within a given domain is numerically computed, according to a set of objectives and constraints. Since the solution strongly depends on the constraints, local optima are provided (which is the basis for Generative Design approaches), and it is difficult to compare and select different design variants. Once the design interpretation occurs, CAE tools can be used to predict part behavior, and, generally, many iterations between re-design and simulation occur to meet the design targets. Afterwards, the industrialization phase is required to prepare the build process using Computer Aided Manufacturing (CAM) tools. Production of metal AM parts is hindered by a lack of process consistency and significant variation in physical properties [6]. Sources of defects and flaws are porosity, balling, geometric and dimensional deviation, and residual stress, causing even either material cracking or build failure [7, 8]. Build preparation highly affects defects onset [7, 9], but currently, short guidelines are provided by standards or AM equipment suppliers, and there is still a lack of predictive approaches. In most cases, the build preparation is strongly affected by the users' experience, and there is no shortage of trial-error procedures, that affect the lead time, the resources, and the costs of AM systems. Although the use of CAE tools for product design is consolidated [10], many AM process simulation physics and scales do exist but are missing implementation suitable for industrial practice [9, 11]. Proper predictive approaches for the identification of risks could bring the best manufacturing quality [1]. The balance between computational cost and results reliability is fundamental, especially at product scale [9, 11], and many simplified multi-scaling models are being developed [12].

2.2 Concurrent Product-Process Design

Literature asserts that holistic approaches are needed, and the use of process simulation to improve metal AM systems quality is challenging [4, 5]. In this work, we consider the integration between product and process design, and the enrichment of the general approaches by implementing CAE process simulation (Fig. 1). In order to do that, a CAD platform has been selected, to keep the associativity between CAD product structures, and CAE and CAM tasks. More, the data consistency along the workflow allows to introduce trade-offs to compare different design variants and build layouts [13], which is a challenging aspect of DfAM approaches [5]. The selected tool for product-process design is the Dassault Systèmes 3DExperience platform. As well as product design makes use of consolidated CAE simulation (e.g., finite element analyses) to perform design refinement, process simulations are integrated in the process design phase for the industrialization refinement. Indeed, it is essential to integrate design and simulation of the build process [10]. The build process is both modeled by (a) the additive manufacturing simulation to identify flaws and resources usage, and (b) the thermo-mechanical finite element -based simulation to predict residual stress and distortions. The first makes use of slicing and scanning path data and allows to check for localized issues (e.g., low-melting, roughness, etc.) and perform build time, material, and cost estimation. The second consists of weakly coupled thermal and mechanical analyses. It is based on a multi-scaling approach (lumped laser paths and lumped layers) to keep an accurate simulation of thermo-mechanical conditions within short runtimes. It is also based on a multi-step approach not only to reproduce the build process but also to consider the required post-processing operations.

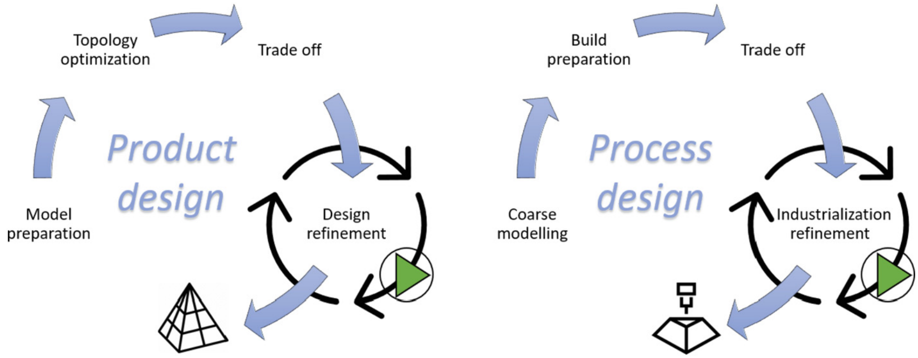

Fig. 1. Concurrent product-process design based on CAE simulation.

3 Case Study

The use case is an ICE piston of a racing motorcycle. The aim is to test engine additively manufactured components, exploiting topology optimization to reduce mass, since engine inertial loads have to be minimized. Literature provides some interesting piston design approaches, and even demonstrates industrial feasibility and endurance capability of such innovative solutions [14], such as for the Mahle and Porsche case. The Original Equipment Manufacturer (OEM) part is an Al2618 forged piston, which weighs 138 g. Its behavior has been analyzed considering worst-case working conditions of maximum combustion pressure and revolution speed, and the model preparation is performed. The simulation setup has been retrieved to set topology optimization and product validation, by applying the AlSi10Mg alloy suitable for L-PBF production. Different design variants have been developed, working on optimization constraints (mesh size, min/max element dimension, symmetry, iso-values, etc.) and compared by a product design trade-off based on structural indicators. Therefore, the re-design has been obtained using a double-level optimization, combining firstly automated tools to generate conceptual results, and finally manual design refinement based on CAE simulations. Details of the design approach can be found in [15]. Re-design of the engine piston achieves structural targets of 29 g mass saving with 15% mean stress reduction and 10% safety factor improvement [15]. Afterwards, the industrialization phase has been integrated, by setting up a SLM 280 HL PBF machine, preparing the machine characterization in the virtual environment and the relating simulations approaches, whose results are reported in the next chapter.

4 Results

Process design concerns tasks ranging from coarse modelling to industrialization refinement. Coarse modelling is achieved by applying proper oversizes to the functional features that require subsequent machining post-processing, thus obtaining the CAD crude model. Build preparation requires the virtual machine definition, including data on the build volume and the scanning, recoating, and inert gas systems. For aluminum alloy processing, parameters such as beam diameter, beam power, scanning speed, scanning strategies, and layer thickness are specified. The build preparation step is completed by introducing the AM part and defining the orientation and the supports strategies. Figure 2a depicts different support strategies (tree-based, wired-based, and volume-based) applied within the initial orientation. Conversely, Fig. 2b shows different orientation strategies, computed to minimize the area of the product requiring supports, the build height, and the cross-sectional changes along the build direction.

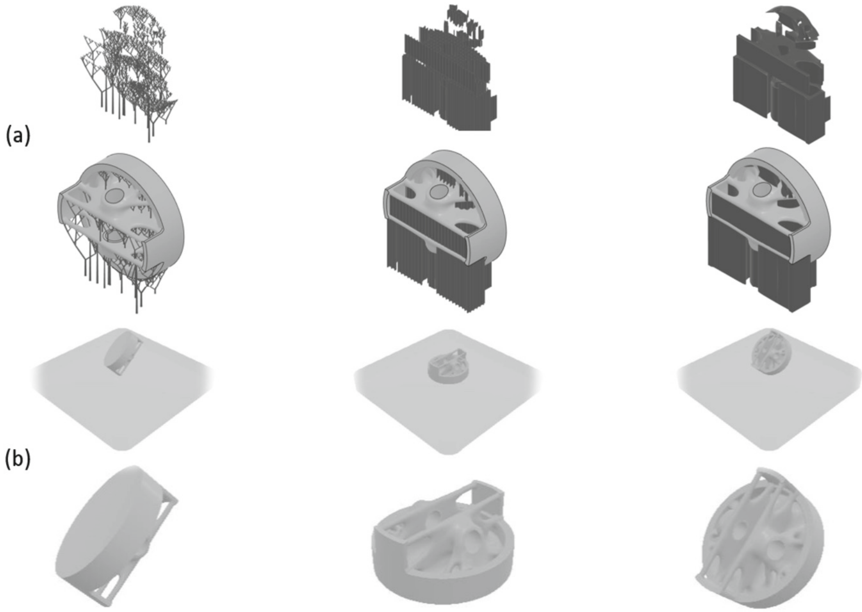

Fig. 2. Build cycle layout key tasks of supports generation (a) and part orientation (b).

The additive manufacturing simulation for given AlSi10Mg process parameters returns data related to the amount of the used material, build time, and energy usage for the build cycle, as well as areas of possible defects. The key subsequent task is the thermo-mechanical finite element -based simulation. In order to evaluate the AM system from the broadest perspective, a multi-step approach is implemented [16], aiming to model not just the build phase, but also the post-processing phases (Fig. 3).

The simulation setup aims to contain computational cost while keeping a decent accuracy, according to previous works and experimental studies [16]. Geometries are discretized by 1 mm tetrahedrons for the piston, 1 mm 2D quadrilaterals for the supports, 5 mm hexahedrons for the build platform, and proper tie connections. Using 1st order elements, the model returns about 100k nodes and 200k elements. Characterized AlSi10Mg material is assigned. The build platform is tied to the machine. The build step relies on a pattern-based thermo-mechanical simulation. For the thermal analysis, appropriate temperature boundary conditions are applied and heat flux loads of lumped laser paths are introduced. Chamber and build platform temperature is set to 423 K and

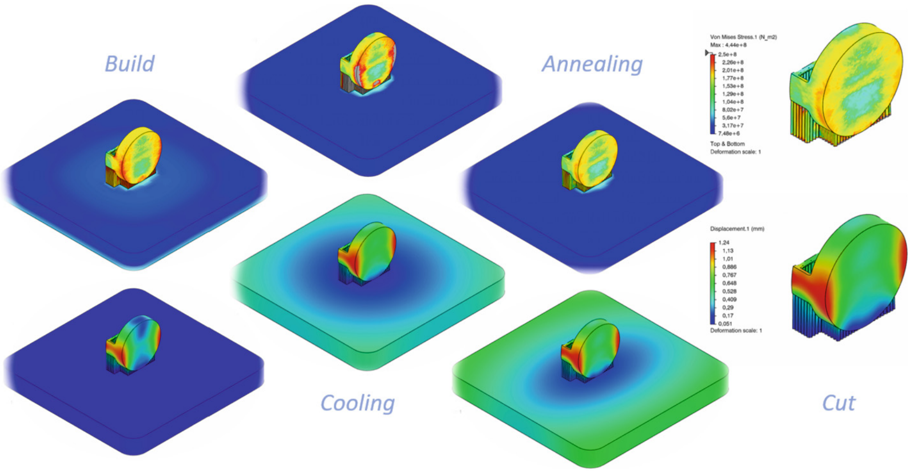

Fig. 3. CAE simulation approach including (right to left): Build; Cooling; Annealing; Cut.

heat transfer modes parameters are specified. The build phase total timestep is 15k s and time is discretized by time increments of 500 s. Cooling provides room boundary conditions for 10k s and steps up to 1000 s. Annealing requires a constraint switch and a post-processing thermal cycle based on a smooth temperature ramp curve for 22k s and steps up to 3600 s. The cut and supports removal rely on the constraints switch and provide the results of the part after post-processing. The simulations run on Abaqus code and take approximately 1 h on a typical desktop.

The initial layout provides residual stress close to the yield stress and deformations higher than 1 mm (Fig. 3). A process design trade-off can be performed by assessing industrialization indicators such as build time and material usage of the process and residual stress and distortions after post-processing. The implementation of the approach integrating the CAE simulation allows to define a build cycle that mitigates possible defects and process flaws (Fig. 4).

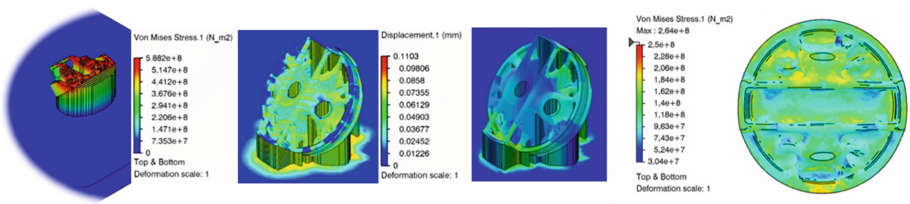

Fig. 4. Results of the final build cycle layout.

5 Discussion

The AM ICE piston has been developed from a holistic perspective, performing the concurrent product and process design. Figure 5 resumes the tasks of the design approach, including: model preparation; topology optimization; product trade-off; design refinement; coarse modelling; build preparation; process trade-off; and industrialization refinement. Making use of integrated tools and appropriate modeling approaches to contain computational cost, CAE simulation can be effectively used both for design and manufacturing. It is possible to exploit virtual engineering, to analyze the product and build cycle behavior, and perform engineering decisions and tradeoff studies from simulation data. Regarding the product, the design can be improved and refined to obtain high-performance models. Concerning the process, it is possible to obtain relevant information, so that product quality can be improved, and resources cost can be reduced. A multi-scaling and multi-step thermo-mechanical model can be used to predict process and post-process behavior so that defects can be mitigated and build failures can be averted. The industrialization based on process simulations provides a build cycle layout to carry out a reliable L-PBF production. Further developments could bring to the reduction of manual operations and the automation of refinement tasks by integrating multi-objective optimization tools, to streamline DfAM approaches even more.

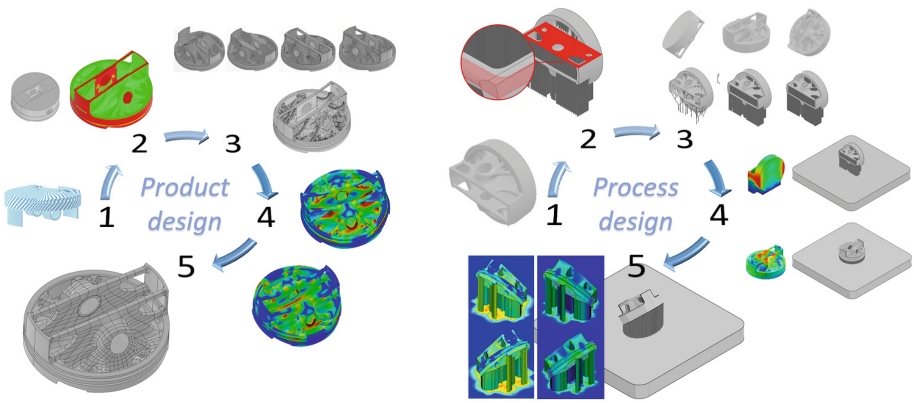

Fig. 5. The concurrent product-process simulation based on CAE simulation.

References

1. Blakey-Milner, B., et al.: Metal additive manufacturing in aerospace: a review. Mater. Des. **209**, 110008 (2021)
2. Kumke, M., Watschke, H., Vietor, T.: A new methodological framework for design for additive manufacturing. Virtual Phys. Prototyp. **11**, 3–19 (2016)
3. Fuchs, D., Bartz, R., Kuschmitz, S., et al.: Necessary advances in computer-aided design to leverage on additive manufacturing design freedom. Int. J. Interact. Des. Manuf. **16**, 1633–1651 (2022)

4. Wiberg, A., Persson, J., Ölvander, J.: Design for additive manufacturing – a review of available design methods and software. Rapid Prototyping J. **25**(6), 1080–1094 (2019)
5. Vaneker, T., Bernard, A., Moroni, G., Gibson, I., et al.: Design for additive manufacturing: framework and methodology. CIRP Ann. **69**(2), 578–599 (2020)
6. Taheri, H., Shoaib, M.R.B.M., Koester, L.W., Bigelow, T.A., Collins, P.C., Bond, L.J.: Powder based additive manufacturing A review of types of defects, generation mechanisms, detection, property evaluation and metrology. Int. J. Addit. Subtract. Mater. Manuf. **1**(2), 172–209 (2017)
7. Grasso, M., Colosimo, B.: Process defects and In-situ monitoring methods in metal powder bed fusion: a review. Meas. Sci. Technol. **28**, 1–25 (2017)
8. Zhang, J., Song, B., Wei, Q., Bourell, D., Shi, Y.: A review of selective laser melting of aluminum alloys: processing, microstructure, property and developing trends. J. Mater. Sci. Technol. **35**(2), 270–284 (2019)
9. Francois, M.M., Sun, A., King, W.E., et al.: Modeling of additive manufacturing processes for metals: challenges and opportunities. Curr. Opin. Solid State Mater. Sci. **21**(4), 198–206 (2017)
10. Schoinochoritis, B., Chantzis, D., Salonitis, K.: Simulation of metallic powder bed additive manufacturing processes with the finite element method: a critical review. Proc. Inst. Mech. Eng. Part B J. Eng. Manuf. **231**(1), 96–117 (2016)
11. Luo, Z., Zhao, Y.: A survey of finite element analysis of temperature and thermal stress fields in powder bed fusion additive manufacturing. Addit. Manuf. **21**, 318–332 (2018)
12. Bayat, M., Dong, W., Thorborg, J., To, A.C., Hattel, J.H.: A review of multi-scale and multi-physics simulations of metal additive manufacturing processes with focus on modeling strategies. Addit. Manuf. **47**, 102278 (2021)
13. Dalpadulo, E., Petruccioli, A., Pini, F., Leali, F.: Synergic product and process design for additive fabrication of lightweight vehicles. In: Proceedings of SAE CO_2 Reduction for Transportation Systems Conference 2022. SAE Technical Papers (2022)
14. Abele, D., Ickinger, F., Schall, V., Klampfl, M.: Additive manufacturing of high-performance powertrain components. MTZ Worldw **82**, 14–19 (2021)
15. Dalpadulo, E., Pini, F., Leali, F.: Optimization of an engine piston through CAD platforms and additive manufacturing based systematic product redesign. In: Rizzi, C., Campana, F., Bici, M., Gherardini, F., Ingrassia, T., Cicconi, P. (eds.) ADM 2021. LNME, pp. 486–493. Springer, Cham (2022). https://doi.org/10.1007/978-3-030-91234-5_49
16. Dalpadulo, E., Pini, F., Leali, F.: Components residual stress and deformation reduction: an integrated process design for additive manufacturing. In: Proceedings of ASME 2021 International Mechanical Engineering Congress and Exposition, NY, Virtual. ASME (2021)

Surface Roughness Prediction in Fused Deposition Modeling: An Engineered Model

Chiara de Crescenzo[1](✉), Maria Richetta[1], Ida Papallo[2], Pierpaolo Fucile[3], Massimo Martorelli[2], Antonio Gloria[2], and Antonio Lanzotti[2]

[1] Department of Industrial Engineering, University of Rome Tor Vergata, Rome, Italy
ch.decrescenzo@gmail.com
[2] Department of Industrial Engineering, Fraunhofer JL IDEAS, University of Naples Federico II, Naples, Italy
[3] Department of Advanced Biomedical Sciences, University of Naples Federico II, Naples, Italy

Abstract. Additive manufacturing (AM) allows to create complex shapes and to improve the performance of critical components in different fields. The characteristics of the as-built parts can be an obstacle in terms of satisfaction of the parts' quality requirements. Concerning the manufacturing process, the relationship among the process parameters, microstructure and mechanical properties is crucial in different areas and involves innovative and traditional fabrication techniques. Fused Deposition Modeling (FDM) is widely employed to fabricate devices with tailored and enhanced properties.

In this context, the process parameters clearly influence the quality of devices fabricated from different polymer-based materials, according to the specific AM technology. As reported in the literature, many theoretical models for the prediction of the surface quality focus on the concept of roughness. Furthermore, several parameters have also been proposed to assess the surface quality.

Benefiting from advances in design strategies and methodologies of analysis, the aim of the current research was to provide further insight into the development of models for surface roughness prediction in FDM.

The relationship among the layer height, printing speed, flow rate and extrusion width was considered and implemented in the model. Preliminary experimental analyses were also performed.

Keywords: Additive Manufacturing · Surface Roughness · Prediction Model

1 Introduction

Additive Manufacturing (AM) technologies are widely considered for the fabrication of 3D physical devices from digital 3D models through material deposition in a layer-by-layer fashion according to specific lay-down patterns [1–3].

If compared to the traditional computer numerical control manufacturing technologies, AM can allow for the rapid fabrication of devices with complex shapes (e.g., parting lines, draft angle, additional setup tools) [1, 3].

As a consequence of AM processes, the surface of the fabricated device shows a characteristic texture, which can be considered a surface manufacturing defect.

Such texture is clearly related to the employed process parameters (e.g., surface orientation with respect to the build direction), whose appropriate selection leads to a minimisation of surface defects [3].

M. Carfagni et al. (Eds.): ADM 2023, LNME, pp. 101–108, 2024.
https://doi.org/10.1007/978-3-031-52075-4_13

For this reason, many efforts have been devoted to the minimization of surface defects, thus improving the quality of the fabricated parts and reducing the costs.

In this scenario, a special focus was on the development of theoretical models for the prediction of the texture size for the surfaces of the manufactured device, also considering the overall range of potential surface orientations [3].

Fused Deposition Modeling (FDM) represents one of the most popular AM technologies to fabricate devices with tailored and enhanced properties. FDM is characterized by an easy use, without needing additional supervision, it is cheaper in comparison to other technologies, and also uses environmentally safe materials [1–3].

FDM is generally based on layer-by-layer deposition of a continuous thermoplastic filament injected/extruded through a heated nozzle and deposited on a build platform [3, 4].

However, the dimensional accuracy and the quality of the obtained devices are often not adequate for many engineering applications [1, 4–7]. As reported in the literature, many theoretical models have been developed for the prediction of the surface quality, especially focusing on the concept of roughness. In addition, different parameters have also been proposed to properly assess the surface quality [3].

As the cross-sectional shape of the deposited filaments is close to an elliptic curve, in a previous model the computation of the surface roughness involved a specific formulation, where the filament profile was assumed as an elliptic curve [1]. The ellipse proposed in such model can be considered the most similar to the real shape [1].

Furthermore, the surface profile was approximated by a train of ellipses overlapping each other in the vertical direction between two following layers (see Fig. 1) [3].

The cross-sectional shape, layer thickness/height and surface angle clearly affect the surface profile, which has been employed to properly model the surface roughness. Specifically, a model was developed for the computation of the surface roughness according to the surface angle variation. The angle between the deposition direction and the normal versor at the surface obviously influences the surface quality [1]. Ahn et al. [1] focused the attention on the evaluation of the surface roughness average (R_a), as defined in ISO 4287 (1997) [4]. On the other hand, Di Angelo et al. [3] proposed another parameter (i.e., P_a - ISO 4287) as an index to assess the surface quality, also developing a novel model for predicting P_a in the case of surfaces of parts manufactured by FDM. In particular, Di Angelo et al. [3] extended the model of Ahn et al. [1] to assess P_a in the overall range of the deposition angle. The results were in good agreement with those from theoretical models and from experimental findings reported in the literature.

Accordingly, benefiting from previous results and technical considerations [1, 3], the aim of the current research was to provide a further implementation of the model of Ahn et al. [1] for surface roughness prediction in Fused Deposition Modeling introducing for the first time technical and operation parameters, such as flow rate, printing speed and layer height, which are generally considered by designers and 3D printer users. The proposed model was also verified by comparing the obtained theoretical results with preliminary experimental data.

2 Basic Principles

The model of Ahn et al. [1] as well as further technical considerations from Di Angelo et al. [3] represented the starting point, providing basic principles for the development of a novel approach for formulating the surface roughness of FDM parts.

Briefly, according to the previous models [1, 3], an ellipse was considered for the definition of the cross-sectional shape of the filament and each layer overlaps the previous layer. The expression of cross-section profile of the filament on the n-th layer is reported below:

$$\frac{x^2}{a^2} + \frac{y^2}{b^2} = 1 \quad (1)$$

with a and b indicating the half-lengths of the long axis and short axis of the ellipse, respectively. Consequently, the width (w) and height (h) of the ellipse were $2a$ and $2b$, respectively. In addition, the actual interval of the layer thickness ($t = h - c$) was defined on the basis of the value of the overlap interval (c).

Based on the definition of the surface angle (θ) at one point of the surface of the FDM part as the angle between the normal vector of the spot and the build orientation (i.e., the direction of the fabrication process) (see Fig. 1), in the case of a manufacturing process at θ angle the expression of the elliptic curve of the next layer (n+1) was suitably implemented:

$$\frac{(x - k_1)^2}{a^2} + \frac{(y - k_2)^2}{b^2} = 1 \quad (2)$$

with k_1 and k_2 being the translated lengths of the n-th filament in agreement with the x axis and y axis directions, respectively, as defined in a previous work [1].

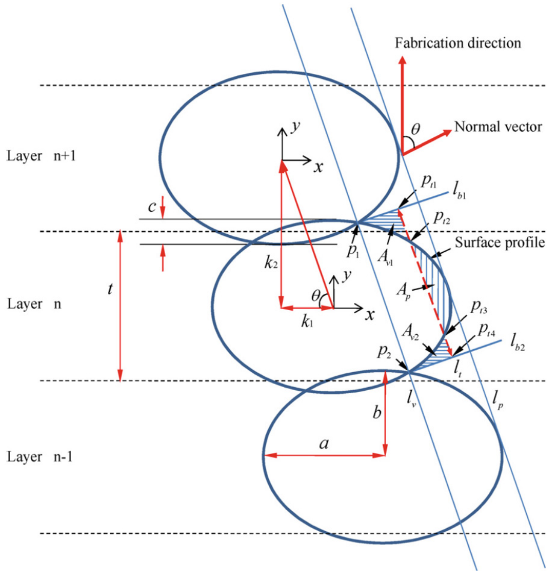

Fig. 1. A schematic representation adopted by Ahn et al. [1] for modeling the surface profile of the FDM part.

The determination of the area employed for the computation of the surface roughness was well defined starting from the two reported p_1 and p_2 intersection points between two adjacent layers located on the surface, as well as from further intersections and lines [1]. The parameter employed for the evaluation of the surface roughness considered in the model of Ahn et al. [1] was the surface roughness average (R_a) [1].

Di Angelo et al. [3] stressed the importance of P_a as an index for an appropriate estimation of the surface quality and developed a model for predicting such index in the case of FDM parts. However, in the current research the basic idea was to consider R_a, which is widely employed in the industrial field, while introducing in the previous formulation model technical and operation parameters, which are commonly considered using a 3D printer.

As the role of technical and operation parameters (i.e., process parameters), which clearly determine the surface quality, was not considered in the previous models, a dependency relationship among layer height (*LH*), printing speed (*v*), flow rate (*Q*) and extrusion width (*EW*) was introduced in the current study.

In general, such relationship employed for the printing process is expressed as follows:

$$Q = v \cdot LH \cdot EW \quad (3)$$

However, taking into account the elliptical shape of the filament cross-section, the following expression was implemented in the model of Ahn et al. [1]:

$$Q = v\pi ab \quad (4)$$

with *a* and *b* being the semi-axes of the ellipse.

Consequently, the main semi-axis (*a*) of the ellipse can be reported as a function of the other process parameters as follows:

$$a = \frac{Q}{v\pi b} \quad (5)$$

Thus, the main semi-axis *a* varies with varying *Q* value (since printing speed and layer height are kept constant); as a result, the shape of the ellipse clearly changes (see Fig. 2).

Fig. 2. An example of the effect of flow rate (*Q*) variation on *a* and, hence, on the shape of the ellipse at fixed values of *b* and *v*: $Q = 10\ mm^3/s$ (left) and $Q = 20\ mm^3/s$ (right).

Once implemented the previous model through the introduction of Eq. 4, it was possible to predict the surface quality by means of R_a index, before printing the 3D object, only by knowing in advance the values of some process parameters (i.e., flow rate, printing speed and layer height).

3 Design, Fabrication and Analysis of 3D Models

The SolidWorks®2017 (Dassault Systemes, Paris, France) computer-aided design (CAD) system was employed to develop 3D geometric models of test specimens, according to the aim of the work. The specimens were manufactured by Fused Deposition Modeling, using a commercially available 3D printer (Prusa i3 MK3) and PLA filament. The test specimens were manufactured varying some building conditions. Specifically, the specimens were printed at a fixed layer height (0.25 mm), considering different values of the surface angle θ (i.e., the angle between the normal vector of the spot and the direction of the fabrication process) ($\pi/4$ and $\pi/3$) and flow rate (10 and 20 mm^3/s).

Just to summarise, Tables 1 and 2 report the process parameters and their changes along with the fixed parameters.

Table 1. List of held factors.

Factor	Type	Value
PT (°C)	Held-constant	210
LH (mm)	Held-constant	0.25
Bed Temperature (°C)	Held-constant	60
Printing Speed (mm/s)	Held-constant	60
Infill Density (%)	Held-constant	100

Table 2. Levels selected for the control factors.

Control Factor	Levels	
	1	2
θ (rad)	π/4	π/3
Q (mm^3/s)	10	20

Flow rate and θ angle were varied to assess their influence on the surface roughness measured by R_a. For each combination of Q and θ, three specimens were additive manufactured to assess the surface roughness by means of experimental tests (see Fig. 3).

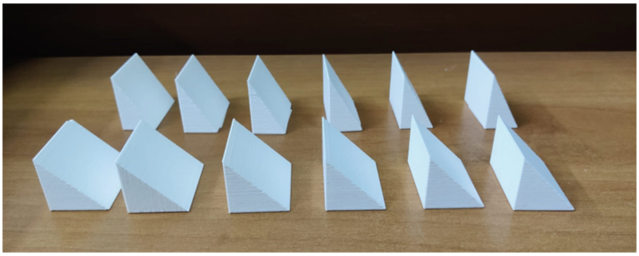

Fig. 3. An image of specimens for experimental tests manufactured by FDM at a fixed layer height (0.25 mm), considering different values of surface angle θ ($\pi/4$ and $\pi/3$) and flow rate (10 and 20 mm^3/s).

An appropriate support with dedicated cavities was also designed (see Fig. 4) and fabricated by FDM for the correct placement of the test specimens, in order to perform the experimental measurements of surface roughness.

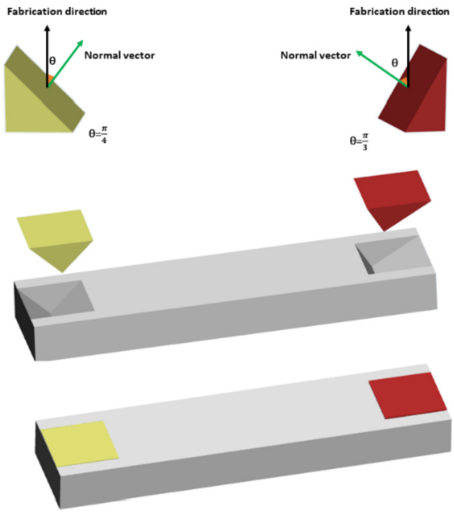

Fig. 4. 3D geometric models of the support with suitable cavities designed for the correct placement of the specimens with different values of θ, in order to perform experimental tests.

The experimental measurements were performed using a surface roughness Tester TR 200. During the test the probe/sensor moved linearly along the measured length and, hence, according to the profile on the surface. The experimental values of R_a were compared with the theoretical ones obtained from the model (Table 3).

Table 3. Results: theoretical (Th.) and experimental (Ex.) values of R_a.

Typology	θ (rad)	Q (mm^3/s)	Th. R_a (μm)	Ex. R_a (μm)
1	π/4	10	24.2	27.9 ± 2.0
2	π/3	10	20.2	23.1 ± 1.8
3	π/4	20	32.3	35.8 ± 3.1
4	π/3	20	34.4	37.1 ± 3.3

However, further experimental analyses were also performed by means of the surface roughness Tester TR 200 in a different configuration oriented at θ angle (i.e., at the level of the surface slope) without using the designed support for the specimens. The obtained experimental findings (data not reported) were consistent with those obtained using the designed support for the specimens as reported in Fig. 4.

4 Conclusions and Future Trends

Within the limitations of the current study, the model predictions would seem to show a good agreement with the experimental data in terms of R_a values. The interesting feature of the proposed implementation results in an a priori estimation of the surface quality of the FDM part through the R_a values, before printing (i.e., without manufacturing) the part, by simply knowing in advance some process parameters (i.e., flow rate, printing speed, layer height), which are very common for designers and 3D printer users. Even if a previous study [3] suggested that the use of R_a index may misrepresent the real extent of the surface defectiveness, also stressing the importance of choosing another index (i.e., P_a) to assess the surface quality, the current research would represent only a further step towards the implementation of a theoretical model, with the aim to improve the knowledge in the field. Further implementations would clearly involve potential extensions according to eventual critical regions for the model, as well as different shapes for the filament cross-section and the use of P_a index.

References

1. Ahn, D., Kweon, J.-H., Kwon, S., Song, J., Lee, S.: Representation of surface roughness in fused deposition modeling. J. Mater. Process. Technol. **209**, 5593–5600 (2009)
2. Ahn, D., Kim, H., Lee, S.: Surface roughness prediction using measured data and interpolation in layered manufacturing. J. Mater. Process. Technol. **209**, 664–671 (2009)
3. Di Angelo, L., Di Stefano, P., Marzola, A.: Surface quality prediction in FDM additive manufacturing. Int. J. Adv. Manuf. Technol. **93**, 3655–3662 (2017)
4. Boschetto, A., Giordano, V., Veniali, F.: 3D roughness profile model in fused deposition modeling. Rapid Prototyping J. **19**(4), 240–252 (2013)
5. Barari, A., Kishawy, H.A., Kaji, F., Elbestawi, M.A.: On the surface quality of additive manufactured parts. Int. J. Adv. Manuf. Technol. **89**, 1969–1974 (2016)

6. Ramli, F.R., et al.: Dimensional accuracy and surface roughness of part features manufactured by open source 3D printer. ARPN J. Eng. Appl. Sci. **13**, 139–1144 (2018)
7. Molero, E., Fernández, J.J., Rodríguez-Alabanda, O., Guerrero-Vaca, G., Romero, P.E.: Use of Data mining techniques for the prediction of surface roughness of printed parts in polylactic acid (PLA) by fused deposition modeling (FDM): a practical application in frame glasses manufacturing. Polymers **12**(4), 840 (2020)

Machine Learning Trends in Design for Additive Manufacturing

Michele Trovato[1](✉), Luca Belluomo[2], Michele Bici[2], Francesca Campana[2], and Paolo Cicconi[1]

[1] Dipartimento di Ingegneria Industriale, Elettronica e Meccanica, Università degli Studi ROMA TRE, 00146 Rome, Italy
michele.trovato@uniroma3.it

[2] Dipartimento di Ingegneria Meccanica e Aerospaziale, Sapienza Università di Roma, 00184 Rome, Italy

Abstract. Additive Manufacturing is becoming a widespread manufacturing system in several industrial fields such as automotive, aerospace, biomedical, etc. Design for Additive Manufacturing represents the branch of research that considers the technological constraints from the early stages of design, arriving at a geometrical model to be exported in G-code. The limitations of additive manufacturing are related to the complexity of the process, the high costs, the processing time, and the difficulties of ensuring adequate geometric and dimensional tolerances. A data-driven approach can be a solution to improve the Design for Additive Manufacturing. Artificial Intelligence and Machine Learning methods are employed in the literature to shorten the time for assessing the optimal combination of parameters and supporting decision-making. The current state of the art shows three macro-areas to apply Machine Learning methods in Design for Additive Manufacturing. These applications concern Geometrical Design Level, Process Configuration Level, and Process Monitoring Level. This paper aims to identify and classify the Machine Learning methods and algorithms most used in Design for Additive Manufacturing practices, analyzing parameters, results, processes, and materials involved.

Keywords: Design for Additive Manufacturing · Additive Manufacturing · Artificial Intelligence · Machine Learning

1 Introduction

In the last decade, the technological progress has led to a revolution in the factory concept, enhancing digital innovations in a context called Industry 4.0. Some of the main innovations are cyber-physical systems, new systems in distribution and procurement, the development of new products and services systems, the adaptation to human needs, and corporate social responsibility. All these innovations are possible thanks to the development of nine new technologies such as Internet of Things, Autonomous robots, Big Data and Analytics, Virtual and Augmented Reality, (Multiphysics) Simulations, Horizontal and Vertical System Integration, Cyber Security, Cloud and Additive Manufacturing [1].

M. Carfagni et al. (Eds.): ADM 2023, LNME, pp. 109–117, 2024.
https://doi.org/10.1007/978-3-031-52075-4_14

Additive Manufacturing (AM) is considered one of the main achievements of Industry 4.0. This process is considered fully digitalized due to the direct connection between geometrical modeling and manufacturing [2]. AM is defined by ISO/ASTM 52900:2022 as the process of adding material to produce parts from 3D CAD models, usually layer upon layer; the AM process is opposed to traditional processes such as subtractive and formative manufacturing [3]. Nowadays, AM, also known as 3D printing, has become a method for making parts, especially for the ability to realize complex geometries that are difficult to be fabricated with other technologies.

While AM was only used for rapid prototyping in the past, today this technology is also used for small-medium batch production. The success of AM is related to the capabilities to achieve complex and free-form shapes, design hierarchical structures from microscale to macroscale, to the possibility of using advanced materials, and improve part functionality [4]. In this context, Design for Additive Manufacturing (DfAM) represents the branch of research that considers all the known issues of this production process, from the early stages of design to the quality check of the realized part.

Following the above-mentioned standard, seven categories of production processes have been identified to realize an object from a 3D CAD model; these AM processes are Binder jetting (BJT), Directed energy deposition (DED), Material extrusion (MEX), Material jetting (MJT), Powder bed fusion (PBF), Sheet lamination (SHL), Vat photopolymerization (VPP). The materials involved in these processes are plastics, composites, ceramics, and metal alloys such as steel, aluminum, titanium-aluminum, copper, etc. The PBF process for metal parts is generally a Laser PBF (L-PBF), also called Selective Laser Melting (SLM).

In additive processes, it is difficult to guarantee geometric and dimensional tolerances due to the process resolution and thermal gradients. Moreover, it is also difficult to predict the fatigue response for metal additive manufactured parts [5]. The employment of DfAM tools and methods can reduce the risks of failure and defects on the 3D-printed parts, considering the specific AM process and the related constraints such as the printing volume, overhang angle, minimum thickness, maximum hole diameter, etc.

The high costs and the uncertainty of the results, due to the high number of parameters involved and the variation of the quality of the parts, have reduced the introduction of AM in the industry, especially for metal 3D printing. Designers can leverage Machine Learning (ML) to facilitate and accelerate parameter selection. An ML system can be employed in multi-objective problems with a high number of parameters related to geometry, process, material properties, and output. ML algorithms are able to identify the relationships between parameters and mechanical performance such as fatigue strength, density, residual stress, surface finishing, etc. [6]. In general, ML tools and methods are widely applied in Industry 4.0 and 5.0 where a great amount of data is produced from control systems, inspections, and sensors [7, 8]. These data-driven techniques can resolve relevant industrial issues and drastically reduce lead time in design and control.

This paper aims to introduce designers to ML methods in the context of DfAM. This work is intended to help designers to identify the most effective ML methods to reach their goals. The document describes the main types of ML in Sect. 2, and the application and methods in Sect. 3. Finally, Sect. 4 ends with conclusions.

2 Background Research on Machine Learning

ML is a branch of artificial intelligence that systematically applies algorithms to synthesize the underlying relationships among data and information to find solutions to unsolved problems [9]. The goal is to predict future events or scenarios that are unknown to the computer [10]. ML can be divided into three macro-categories as Supervised Learning, Unsupervised Learning, and Reinforced Learning.

Supervised Learning (SL) is the most well-established and known category of ML methods [11]. SL algorithms are trained with a training dataset of known input and output pairs. The most famous supervised ML algorithms are Decision Trees, Naive Bayes, and Support Vector Machines (SVM). Unsupervised Learning (UL) studies how systems can learn to represent input patterns in a way that reflects the statistical structure of the overall collection of input patterns. Semi-supervised ML is an intermediate category, known as a combination of SL and UL methods [12]. Reinforced Learning (RL) proposes a solution to the problem of learning from interaction to achieve a specific goal. RL methods are usually applied in autonomous robot and control system applications [13].

An important and increasingly relevant sub-category is Artificial Neural Networks (ANNs), or simply Neural Networks (NN), inspired by the working biological mechanisms of the human brain [14]. The ANNs can model complex nonlinear relationships and perform parallel processing and currently this method has reached a good fault tolerance [15].

3 Applications and Methods

Nowadays, the use of ML is increasingly spreading to optimize the many parameters acting in AM. The applications of ML methods mainly regard three levels: Geometrical Design Level, Process Configuration Level, and Process Monitoring Level (also called *"in situ"* monitoring). The following figure (Fig. 6) describes these three levels and their specifications.

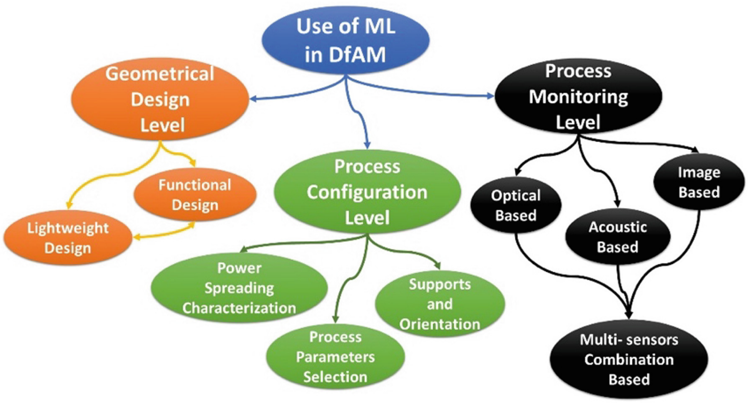

Fig. 6. ML application in AM.

3.1 Geometrical Design Level

The first level, the Geometrical Design, aims to optimize the geometry to maximize the functionality of the parts. The most relevant objective is to achieve a lightweight design. Given the boundary conditions, the aim is to realize parts as light as possible while still guaranteeing a suitable safety factor. The main tools at this level are Generative Design (GD), Topological Optimization (TO), shape optimization, lattice structures, and optimal material design. The ML algorithms are used here to elaborate customized micro and meso-structures to meet the specifications of the project [1]. The ML algorithms support the definition of the complex and free-form geometries which can be printed by AM technologies. However, ML algorithms are not only used in additive design, but they are also applied in other test cases where geometrical optimization is required [16, 17].

As example of TO, Langelaar [18] studied a fully self-supporting optimized part using a laser-wise filtering procedure to eliminate the unprintable geometries from the design space. Kallioras et al. [19] developed a GD framework that integrates ML into the generative design practice, combining TO and Long Short-Term Memory Networks. TO and GD can generate hundreds of possible solutions; therefore, the decision-making phase can be difficult and not well supported by the selected ML algorithms. As a solution, criteria can be applied when optimizing an AM part. Zhu et al. [20] studied a prescriptive deviation modeling method, coupled with ML techniques, to identify the solution with the minimum deviation, compared with the CAD geometry. Their ML approach consists of Bayesian inference to estimate geometric deviation patterns by statistical learning from multiple shapes data.

Lattice structures concern another practice in DfAM to achieve a better material distribution. This practice allows lightweight design to be achieved with reduced deviations. Després et al. [21] used a NN approach to support the generation of optimized micro-lattice structures for AM applications. They used Genetic Algorithms to design new micro-structures and FEM tools to evaluate the relative mechanical properties. The results of the FEM simulations feed the supervised ML implemented inside the NN. A similar approach was described by Alejandrino et al. [22]. They also studied a NN approach to generate optimized patters in lattice structure design.

The most of ML studies related to this level concern SL methods to achieve a better material distribution, using a NN approach.

3.2 Process Configuration Level

The second level, the Process Configuration, regards the optimization of the selection of the process parameters. In the case of Metal AM, it is also included the optimization of the powder spreading characterization. This phase is important for SLM processes due to the high number and complexity of the parameters involved [23]. The process parameters depend on the type of AM technique chosen and the specific 3D printer. For example, the main parameters for SLM processes are laser power, layer thickness, powder size and distribution, scanning schemes, etc. The uniformity of powder spreading plays a relevant role in the quality of the final part [24]. Improper powder spreading may introduce defects or lead to failures due to warping or swelling [25]. In general, the process parameters affect the mechanical properties of the component such as the surface roughness, porosity, density, fatigue strength [26].

Process Configuration also concerns the choice of the part's optimal orientation and the support structures' definition. The part orientation affects the quantity and the extension of the overhang surfaces. The supports allow surfaces with critical overhang angles to be printed while dissipating heat during the process [27]. The supports are necessary for metal printing processes to reduce deformation and residual stress due to the high thermal gradients. Moreover, the supports must be easily removable and lightweight to reduce the scraps. Therefore, the part orientation and supports also influence the costs and printing time. The geometrical parameters related to part orientation and supports can be optimized with ML.

In the literature, different cases of regression methods are used to study the values of the process parameters for AM. As an example, in [24] the ML approach, based on a Back Propagation Neural Network (BP-NN) with one hidden level, is analyzed to optimize the spreading parameters. Simulations are used in the training phase. The main objectives in this work regard the part porosity and roughness in metal AM.

The prediction of the part porosity was also studied by Tapia et al. for SLM processes [28]. Firstly, they developed a Gaussian regression model to correlate the porosity to the process parameters. Then, they implemented a Bayesian inference framework to estimate the statistical model parameters. Finally, a Kriging method is used to predict the porosity of the printed part. A Gaussian regression model was also used by Ren et al. [29] to optimize with ML the laser power while mantling constant the melt-pool size. They used two input parameters, such as power laser and thermal history, while keeping other process parameters fixed.

A regression and classification approach was proposed by Kappes et al. [30] to correlate the process parameters with the final microstructure of the part. The analyzed parameters are related to part orientation, percentage of recycled powder, heat treatment, laser power, laser speed, laser spot, and contour overlap. This study is based on a Random Forest Network (which is an SL method) to predict and avoid the lack of fusion defects in L-PBF.

Regarding the prediction of the part density in AM, Gor et al. [31] studied ML techniques such as ANN, K-nearest neighbor, support vector machine, and linear regression for objects printed in 316L stainless steel. The parameters analyzed here are related to the laser system, build chamber, hatch spacing, layer thickness, and scanning speed.

The combination of porosity, defects, roughness, and density, affects the fatigue response. The high cycle fatigue life of printed materials has been studied by Zhang et al. [32]. A variation of this mechanical property can be caused by the choice of processing and post-processing strategies. They used a neuro-fuzzy-based ML method to predict the high cycle fatigue life of stainless steel 316L parts.

All these studies confirm that SL methods are the most used algorithms for the prediction of the parameters involved in AM processes. The literature shows different types of regression methods with successful results.

3.3 Process Monitoring Level

The third level, the Process Monitoring phase or In Situ Monitoring, concerns the real-time control of the printing process. Several factors, internal or external, can compromise the result of the AM process. The AM process suffers from various processing-related defects such as cracks, delamination, distortion, rough surface, lack of fusion, porosity, foreign inclusions, and process instability (keyhole, balling). These defects usually originate from the layer-wise material deposition process [33]. Errors in the printing phase can compromise the result and the subsequent validation of a component. Consequently, process monitoring and a possible correction of the parameters during printing can significantly reduce the final printing time and cost. Traditionally, anomaly detection during the fabrication process greatly depends on the experience of the operators, and so can be prone to inaccuracy, inconsistency, and delays. Process monitoring systems for detecting defects are highly needed to evaluate the printing condition and product quality efficiently and accurately [34].

In the literature there are several methods to control the printing process, the principal ML approaches used are the Image-based approach, the Acoustic emission, the Optical emission, and the Sensor signal-based approach.

The Image-based approach uses images from cameras to analyze the layer-wise surface after building every single layer to detect defects and lacks. The Acoustic emissions approach is based on the energies of the narrow frequency bands using spectral convolutional neural networks. The Optical emission concerns the analysis of spectroscopy emissions during the process. This method has long been used to better understand physical mechanisms [35]. The signals are mainly plume and spatter signatures and melt pool profiles and intensity [33]. The Sensor signal-based approach is the fourth method for process monitoring and it is a combination of acoustic, optical, infrared, and multi-sensor signals [25]. All these methods are used for training ML algorithms used at the Process Monitoring level.

Image-based monitoring with ML often regards SL algorithms for classification ad recognition problems. A Deep Convolutional Neural Network is used in [36] for the recognition of defects in SLM the process by image processing. An SVM approach is used in [37] for the classification of the quality level using a high-speed camera. On the other hand, an UL method is used in [38] where images from Near-Infrared (NIR) cameras and a Deep Belief Network are used for in situ process monitoring and melted state recognition during the SLM process.

Regarding Acoustic Emission methods, the ML techniques used to analyze and interpret the dataset are still SL and UL. Mohammadi et al. [39] propose an approach with different ML techniques. First, a hierarchical K-means clustering is employed for labeling the data, followed by a supervised deep learning neural network to match acoustic signal with defect type. A Principal Component Analysis (PCA) was used to reduce the dimensionality of the dataset. Then, a Gaussian Mixture Model (GMM) is employed to enable fast defect detection suitable for online monitoring. Finally, a Variational Auto-Encoder (VAE) approach is used to obtain a general feature of the signal that could be an input for the classifier. Another ML algorithm, the Spectral

Convolutional NN, is used in [40] to differentiate the acoustic features of dissimilar quality using a sensitive acoustic emission sensor. All these works are related to SLM processes.

4 Conclusion

This article aims to help the designer to approach the use of ML in DfAM, providing an introductory overview of what ML is and how it is currently used in parameter optimization. To summarize, the use of ML in DfAM is a powerful tool to support the designer in the definition of additive projects considering geometries, process parameters, and monitoring phase. The geometry of the 3D parts can be optimized by ML algorithms implemented in generative and topological optimization tools to achieve lightweight and functional components. ML algorithms can also support the configuration of the best combination of the process parameters to obtain suitable mechanical properties. The literature also shows the possibility to use ML for powder characterization and distribution. Moreover, ML can be used to define the part orientation and select suitable supports for the printing phase. Finally, ML tools can be involved in monitoring the 3D printing process to prevent errors that can compromise the result.

The parameters can be classified into many categories, such as design, manufacturing, and monitoring parameters. The parameters that could be the most relevant for the success of the metal 3D printing are related to part orientation and support definition in the context of design parameters. Analyzing the manufacturing parameters, the most relevant could be laser power, laser speed, layer thickness, and scanning schemes. Finally, considering the monitoring phase, one of the main parameters is the melt pool geometry.

The main obstacles for an industry that wants to introduce AM processes in the production line are cost reduction, developing a knowledge base to support the DfAM phase, and enabling batch production. The quality of the AM-produced parts depends on the correct execution of the printing processes, and many factors influence the results such as the optimization of the part geometry to implement lightweight and functionality; the choice of suitable process parameters correlated to the obtained mechanical properties; the selection of the proper combination between orientation and supports to reduce deformation and residual stress due to the high thermal gradients; and the monitoring of the printing phase to avoid fatal errors and compromise the print. ML tools can support companies to achieve these results. Several approaches are described in the literature and discussed in this paper. As a future development, this study will be completed by comparing data-driven methods and simulation analysis in DfAM.

Acknowledgments. Project ECS 0000024 Rome Technopole, Concession Decree No. 1051 of 23 June 2022 adopted by the Italian Ministry of University and Research, CUP B83C22002820006, Rome Technopole.

References

1. Kumar, S., et al.: Machine learning techniques in additive manufacturing: a state of the art review on design, processes and production control. J. Intell. Manuf. **34**(1), 1–35 (2022)

2. Moshiri, M., Charles, A., Elkaseer, A., Scholz, S., Mohanty, S., Tosello, G.: An Industry 4.0 framework for tooling production using metal additive manufacturing-based first-time-right smart manufacturing system. Procedia CIRP **93**, 32–37 (2020)
3. Standard ISO/ASTM 52900:2022
4. Jiang, J., Xiong, Y., Rosen, D.: Machine learning integrated design for additive manufacturing. J. Intell. Manuf. **33**(4), 1073–1086 (2022)
5. Nicoletto, G.: Efficient determination of influence factors in fatigue of additive manufactured metals. Procedia Struct. Integrity **8**, 184–191 (2018)
6. Hertlein, N., Deshpande, S., Venugopal, V., Kumar, M., Anand, S.: Prediction of selective laser melting part quality using hybrid Bayesian network. Addit. Manuf. **32**, 101089 (2020)
7. Dalmarco, G., Ramalho, F.R., Barros, A.C., Soares, A.L.: Providing industry 4.0 technologies: the case of a production technology cluster. J. High Technol. Manage. Res. **30**(2), 100355 (2019)
8. Javaid, M., Haleem, A., Singh, R.P., Rab, S., Suman, R.: Significance of sensors for industry 4.0: roles, capabilities, and applications. Sens. Int. **2**, 100110 (2021)
9. Arthur, S.L.: Some studies in machine learning using the game of checkers. IBM J. Res. Dev. **44**(1.2), 210–229 (1959)
10. Awad, M., Khanna, R.: Machine Learning - Efficient Learning Machines: Theories, Concepts, and Applications for Engineers and System Designers. Apress (2015)
11. Cunningham, P., Cord, M., Delany, S.J.: Supervised Learning, Machine Learning Techniques for Multimedia, Chapter 2 (2008)
12. Mahesh, B.: Machine learning algorithms - a review. Int. J. Sci. Res. **7**, 426 (2018)
13. Sutton, R.S., Barto, A.G.: Reinforcement Learning: An Introduction. MIT Press, London (2018)
14. Gupta, N.: Artificial neural network. Network Complex Syst. **3**(1) (2013)
15. Zou, J., Han, Y., So, S.: Overview of artificial neural networks. Methods Protocols Methods Mol. Biol. **15**(458), 15–23 (2008)
16. Hsiaoa, S.W., Tsai, H.C.: Applying a hybrid approach based on fuzzy neural network and genetic algorithm to product form design. Int. J. Ind. Ergon. **35**, 411–428 (2005)
17. Jang, S., Yoo, S., Kang, N.: Generative design by reinforcement learning: enhancing the diversity of topology optimization designs. Comput. Aided Des. **146**, 103225 (2022)
18. Langelaar, M.: Topology optimization of 3D self-supporting structures for additive manufacturing. Addit. Manuf. **12**, 60–70 (2016)
19. Kallioras, N.A., Lagaros, N.D.: MLGen: generative design framework based on machine learning and topology optimization. Appl. Sci. **11**, 12044 (2021)
20. Zhu, Z., Answer, N., Huang, Q., Mathieu, L.: Machine learning in tolerancing for additive manufacturing. CIRP Ann. **64**(1), 157–160 (2018)
21. Després, N., Cyr, E., Setoodeh, P., Mohammadi, M.: Deep learning and design for additive manufacturing: a framework for microlattice architecture. JOM **72**, 2408–2418 (2020)
22. Alejandrino, J.D., et al.: A machine learning approach of lattice infill pattern for increasing material efficiency in additive manufacturing processes. Int. J. Mech. Eng. Robot. Res. **9**(9), 1253–1263 (2020)
23. Song, B., Dong, S., Zhang, B., Liao, H., Coddet, C.: Effects of processing parameters on microstructure and mechanical property of selective laser melted Ti6Al4V. Mater. Des. **35**, 120–125 (2012)
24. Zhang, W., Mehta, A., Desai, P.S., Higgs III, C.F.: Machine learning enabled powder spreading process map for metal additive manufacturing (AM). In: Proceedings of the 28th Annual International Solid Freeform Fabrication Symposium – An Additive Manufacturing Conference, pp. 1235–1249 (2017)
25. Xiong, Y., Tang, Y., Zhou, Q., Ma, Y., Rosen, D.W.: Intelligent additive manufacturing and design: state of the art and future perspectives. Addit. Manuf. **59**(Part A), 103139 (2022)

26. Babu, S.S., Mourad, A.I., Harib, K.H., Vijayavenkataraman, S.: Recent developments in the application of machine-learning towards accelerated predictive multiscale design and additive manufacturing. Virtual Phys. Prototyping **18**(1), e2141653 (2023)
27. Cloots, M., Spierings, A.B., Wegener, K.: Assessing New Support Minimizing Strategies for the Additive Manufacturing Technology SLM (2013)
28. Tapia, G., Elwany, A.H., Sang, H.: Prediction of porosity in metal-based additive manufacturing using spatial Gaussian process models. Addit. Manuf. **12**(Part B), 282–290 (2016)
29. Ren, Y., Wang, Q.: Gaussian-process based modeling and optimal control of melt-pool geometry in laser powder bed fusion. Intell. Manuf. **33**, 2239–2256 (2022)
30. Kappes, B., Moorthy, S., Drake, D., Geerlings, H., Stebner, A.: Machine learning to optimize additive manufacturing parameters for laser powder bed fusion of Inconel 718. In: Proceedings of the 9th International Symposium on Superalloy 718 and Derivatives: Energy, Aerospace, and Industrial Applications, pp. 595–610 (2018)
31. Gor, M., et al.: Density prediction in powder bed fusion additive manufacturing: machine learning-based techniques. Appl. Sci. **12**, 7271 (2022)
32. Zhang, M., et al.: High cycle fatigue life prediction of laser additive manufactured stainless steel: a machine learning approach. Int. J. Fatigue **128**, 105194 (2019)
33. Wang, C., Tan, X.P., Tor, S.B., Lim, C.S.: Machine learning in additive manufacturing: State-of-the-art and perspectives. Addit. Manuf. **36**, 101538 (2020)
34. Zeqing, J., Zhizhou, Z., Kahraman, D., Grace, X.G.: Machine learning for advanced additive manufacturing. Matter **3**(5), 1541–1556 (2020)
35. Qin, J., et al.: Research and application of machine learning for additive manufacturing. Addit. Manuf. **52**, 102691 (2022)
36. Caggiano, A., Zhang, J., Alfieri, V., Caiazzo, F., Gao, R., Teti, R.: Machine learning-based image processing for on-line defect recognition in additive manufacturing. CIRP Ann. Manuf. Technol. **68**, 451–454 (2019)
37. Zhang, Y., Hong, G.S., Ye, D., Zhu, K., Fuh, J.Y.H.: Extraction and evaluation of melt pool, plume and spatter information for powder-bed fusion AM process monitoring. Mater. Des. **156**, 458–469 (2018)
38. Ye, D., Ying Hsi Fuh, J., Zhang, Y., Hong, G.S., Zhu, K.: In situ monitoring of selective laser melting using plume and spatter signatures by deep belief networks. ISA Trans. **81**, 96–104 (2018)
39. Mohammadi, M.G., Mahmoud, D., Elbestawi, M.: On the application of machine learning for defect detection in L-PBF additive manufacturing. Opt. Laser Technol. **143**, 107338 (2021)
40. Shevchik, S.A., Kenel, C., Leinenbach, C., Wasmer, K.: Acoustic emission for in situ quality monitoring in additive manufacturing using spectral convolutional neural networks. Addit. Manuf. **21**, 598–604 (2018)

Engineering Methods in Medicine

A Fully Automated Procedure for the Creation of Digital Patient-Specific Surgical Guides for Ear Reconstruction

Elisa Mussi[1], Michaela Servi[1](✉), and Flavio Facchini[2]

[1] Department of Industrial Engineering, University of Florence, Florence, Italy
michaela.servi@unifi.it
[2] Meyer Children's Hospital IRCCS, Florence, Italy

Abstract. Autologous ear reconstruction is a surgical procedure aimed at total or partial reconstruction of the ear of patients with microtia, which is a malformation or absence of the anatomical element. This procedure involves harvesting cartilage material from the patient at the costal level, cut and sculpt the tissue to create the skeleton of the ear, which is then inserted into a subcutaneous pocket in the malformed region. The sculping procedure takes inspiration from the geometry of the patient's contralateral healthy ear and can be very complex given the particularity of the elements to be reconstructed. Taking advantage of Reverse Engineering and Additive Manufacturing technologies, the authors, in collaboration with hospital staff, proposed patient-specific three-dimensional cutting guides that can facilitate the surgeon in sculpting the ear structure. In this work, a fully automated procedure for creating the printable digital model of such guides is proposed: at first is performed the segmentation of ear elements, which represent the starting data for the automated CAD modelling of the surgical guides. The automatic CAD modelling procedure was tested and validated by medical personnel.

Keywords: Ear Reconstruction · Surgical Guide · CAD Modelling · Reverse Engineering

1 Introduction

In recent years, the use of custom-made medical devices (MD) is becoming a gold standard of care for the correction of congenital and non-congenital malformations. The rapid spread of this paradigm can be attributed to the extensive use in medicine of reverse engineering (RE) and additive manufacturing (AM) technologies [1]. In fact, these technologies offer great flexibility in geometry acquisition and manufacturing operations by enabling the production of MDs with high complexity and tunability on patient-specific anatomy. The typical workflow which leads to the fabrication of custom MDs starts with the digital acquisition of the patient's affected anatomy using diagnostic imaging techniques (i.e. Computed Tomography or Magnetic Resonance Imaging) or 3D scanners [2, 3]. The acquired data, in the form of images or point clouds, is appropriately processed and transformed into meshes. Subsequently, this data is used in CAD modelling

M. Carfagni et al. (Eds.): ADM 2023, LNME, pp. 121–128, 2024.
https://doi.org/10.1007/978-3-031-52075-4_15

programs to design custom MDs that are fabricated using AM techniques. 3D printing is thus rapidly becoming a leading manufacturing technique in the health and medical industry for a wide range of applications, including dentistry [4], tissue engineering and regenerative medicine [5], medical devices [6], anatomical models [7], and drug formulation [8]. In recent years, authors have applied this paradigm in the context of the treatment of microtia, a congenital defect characterized by malformation or complete absence of the outer ear. The correction of this defect involves a surgical procedure in which a portion of costal cartilage is taken from the patient, and it is appropriately cut and sculpted to create the missing anatomy (framework, visible in Fig. 1a) consisting of the auricular elements of the healthy anatomy (see Fig. 1b).

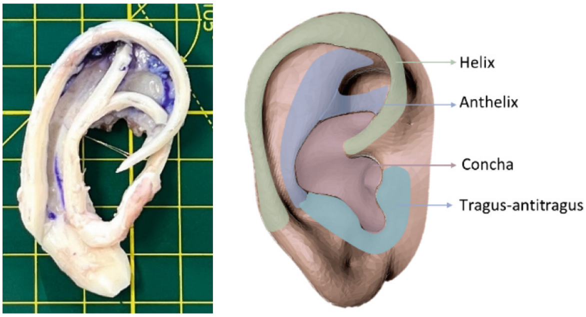

(a) (b)

Fig. 1. a) Example of framework, b) indication of ear elements.

To effectively assist the physician in the reconstruction, the authors in collaboration with physicians have designed 3D models of surgical guides that can be customized to each patient's anatomy. The modelling workflow involves acquisition with commercial [9] or ad-hoc [10] optical scanners of the patient's contralateral healthy ear. The anatomical data thus obtained, after appropriate mirroring, is used for CAD modelling of the surgical guides. After the definition of a standard design applicable to each new anatomy, the authors' research focus shifted toward automating the CAD modelling process. In this paper, the authors propose a fully automated procedure that from the digital model of the ear (in mesh format) provides printable models of the surgical guides. This was achieved using tools such as automatic segmentation of the ear elements from the depthmap image of the ear and the tools offered by the Rhinoceros environment (McNeel North America, Seattle, WA, USA) [11] with the Grasshopper plug-in (www.grasshopper3d.com) [12].

2 Materials and Methods

The correct shape of the surgical guides for the ear reconstruction was identified through an iterative process of design and physical simulation in which clinicians tested prototype guides by simulating the entire surgical procedure using silicone replicas of rib cartilage [13].

The simulations showed that the use of guides that faithfully traced the anatomical elements of the ear [14] (see Fig. 2) made it impractical to create the auricular framework due to the complexity of the geometry. As a result of this process, the shape of the surgical guides is defined as a simplification of the geometry of each anatomical element.

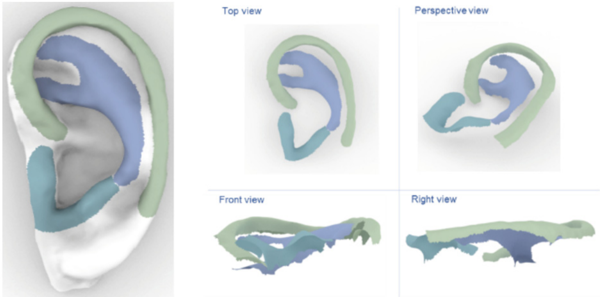

Fig. 2. Example of surgical guides highly adherent to the anatomy.

As can be seen in Fig. 3, there are three surgical guides for auricular reconstruction (for the helix, anthelix, and tragus-antitragus region), and each surgical guide has (1) simplified contours exempt from micrometric details and undercuts that are impossible for the surgeon to reproduce manually in the operating room, and (2) a planar base useful for their support on the cartilaginous material and notching.

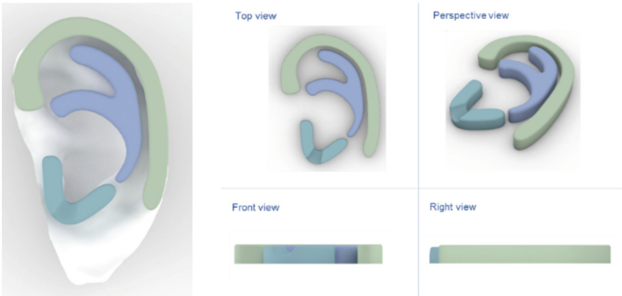

Fig. 3. Example of the proposed surgical guides.

The simplification of surgical guides thus devised can be modelled on a single plane. The reference plane for modelling was identified as the ear development plane, defined in [15] and visible in Fig. 4, which is the plane that establishes the viewpoint from which the auricular elements can best seen.

In order to create a fully automatic process for modelling such custom MDs, the workflow proposed in this paper is structured into two macroblocks (Fig. 5): 1) automatic segmentation of the ear elements, 2) automatic CAD modelling with routines that can be invoked for each new case.

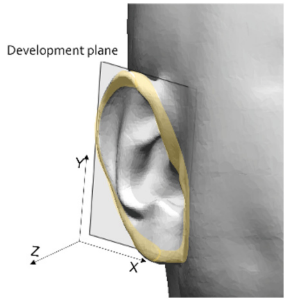

Fig. 4. Indication of the ear development plane.

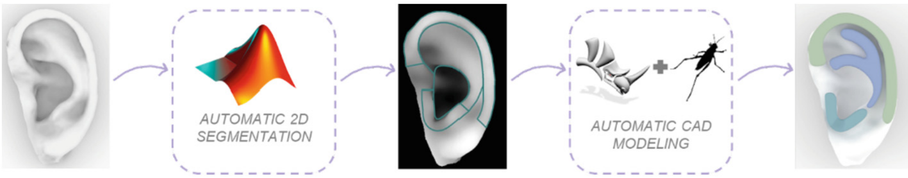

Fig. 5. Workflow of the proposed automatic modelling procedure.

Automatic ear segmentation exploits the algorithm presented by the authors in [15]. In brief, the algorithm, developed in the MATLAB environment, through a series of thresholding and output management operations performs 2D segmentation of the depthmap image obtained by fixing the viewpoint with the normal exiting from the ear development plane, as defined above. The steps of the algorithm are shown in Fig. 6 and a sample of results in Fig. 7.

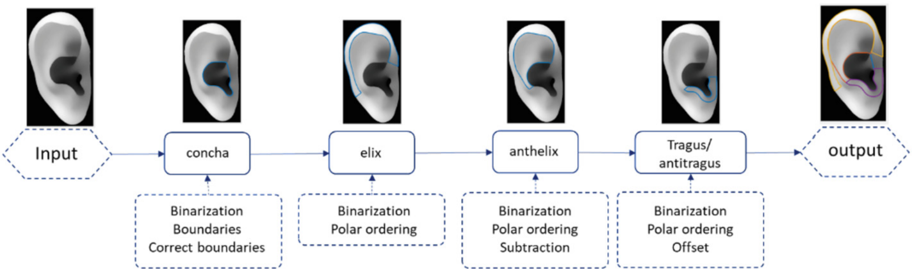

Fig. 6. Operations performed by the segmentation algorithm.

It is observed that the segmentation of the anthelix slightly deviates from the anatomy as it includes the triangular fossa. This will need to be properly considered and handled for the modelling surgical guides.

The segmentation algorithm saves a.txt file for each anatomical element containing the coordinates of the points of the curves that isolate these elements after being appropriately sampled. The.txt files are the input to the CAD modelling algorithm that makes the surgical guides.

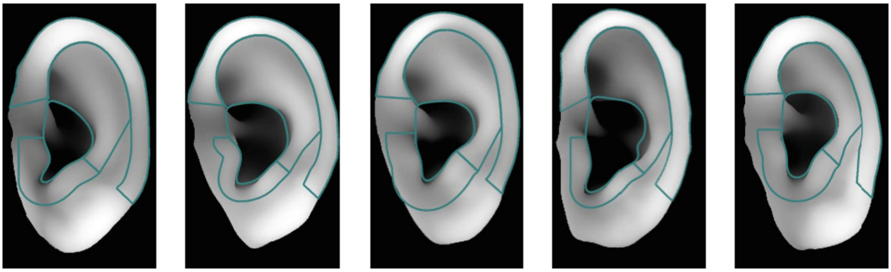

Fig. 7. Some results of automatic segmentation of the ear elements.

The systematic CAD procedure was automated in the Rhinoceros environment using the Grasshopper plug-in. Grasshopper makes it possible to automate Rhinoceros operations by providing operational blocks: each block receives input, performs an operation, and returns output results. The graphical interface allows the inputs provided to the developed procedure to be modified quickly and efficiently, making it perfect for the development of custom MDs in which the input changes for each patient.

Figure 8 shows the automatic routines created for modelling the guides of the different elements, and Table 1 shows more in detail the modelling steps.

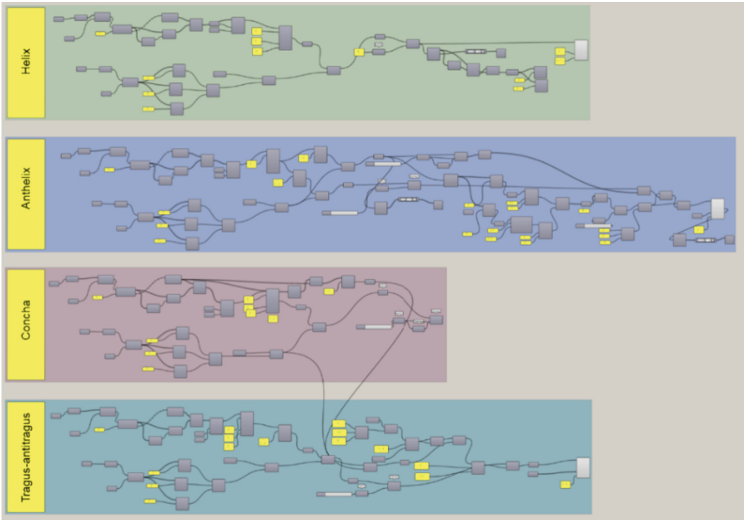

Fig. 8. Automatic modelling procedure implemented with Grasshopper.

Table 1. Proposed automatic modelling of surgical guides.

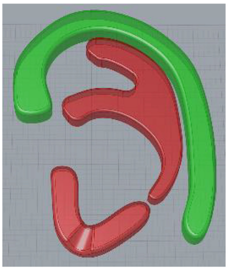	*Helix*: The .txt file relative to the segmentation of the element is read, a curve is created to which a smoothing operation is applied, the curve is extruded by 4 mm, and the edge with max z value is filleted by a value of 0.7 mm.
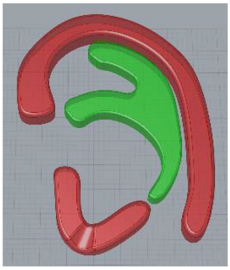 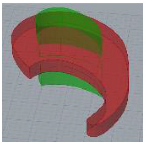 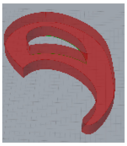 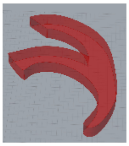 (a) (b) (c)	*Anthelix*: The .txt file related to the segmentation of the element is read, a curve is created to which a smoothing operation is applied, two offset operations are performed on the curve with value of -1 and -6 mm respectively The curve obtained with offset -1 is extruded by 3 mm to obtain the shape of the anthelix. The curve obtained with offset -6 is extruded in both directions by 7 mm and subtracted from that previously obtained (shapes in figure (a) on the left). The two lateral segments of the hole thus obtained (green in figure (b) on the left) are extended and used to create two cutting surfaces. The resulting shape ((c) on the left) is filleted on all edges perpendicular to the XY plane by 2 mm and all edges with max z value by 0.5 mm.
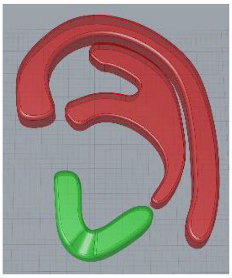  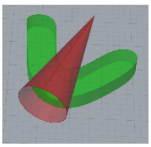 (a) (b)	*Tragus-antitragus*: The .txt file related to the segmentation of the element is read, a curve is created to which a smoothing operation is applied, and the curve is extruded by 3 mm. To create the bevel central to the shape, the lowest point of the concha (red in image (b) on the left, corresponding to the intertragic notch) is used to create a cone inclined at a 40-degree angle with respect to the XY plane (figure (b) on the left). The cone is subtracted from the extrusion obtained above, and the element is filleted at each edge by 0.6 mm except the one with min z value.

In the described procedure, the fillets values were chosen empirically to avoid the generation of errors in the procedure while realizing curves compliant with the physician's requirements.

3 Discussion and Conclusions

The workflow in Fig. 5. Was tested for modelling surgical guides of 50 ears retrieved from the database created by the authors in [15]. Regarding the segmentation step, the algorithm was already tested in terms of robustness and adaptability to different anatomies, and the segmentation result was validated by clinicians [15]. This result is exploited by the automatic algorithm proposed in this paper to make surgical guides suitable for autologous auricular reconstruction. The automatic algorithm was developed with the Grasshopper plug-in in the Rhinoceros environment. The procedure resulted in the correct generation of the tested 50 cases (Fig. 9 reports 10 examples).

Fig. 9. Ten examples of the results of automatic modelling of surgical guides.

Analyzing the proposed procedure, it can be observed that the modelling of the helix involves the direct extrusion of the curve obtained from the segmentation without any modification of the geometry. As for the anthelix, the contours derived from segmentation are not suitable for direct extrusion of the surgical guide due to the fact that it is characterized by a typical y-shape. Therefore, the procedure takes advantage of the original segmentation shape to obtain the desired shape of the guide through operations such as curve offsets and solid subtractions thus ensuring a y-shape consistent with the specific anatomy. Also for the tragus-antitragus, it was necessary to perform operations on the shape derived from segmentation in order to obtain a surgical guide that meets clinical requirements. Specifically, the saddle proper to this region is obtained by subtraction of a cone whose position is defined, inspired by the actual anatomy, by the point of the concha corresponding to the intertragic notch. The inclination and size of the cone were defined empirically by analyzing the 3D ear models of the dataset. The 3D digital models of the 50 surgical guides were validated by 3 surgeons specialized in the area with a bind questionnaire. The results show that the proposed procedure provides an improvement over previously proposed methods as it totally replaces manual modeling, introducing significant time savings: manual modeling can take up to 120 min, while the developed procedure is instantaneous. The modelled guides can be produced by additive manufacturing techniques using biocompatible and sterilizable materials for intraoperative use.

References

1. Javaid, M., Haleem, A.: Additive manufacturing applications in medical cases: a literature based review. Alexandria J. Med. **54**, 411–422 (2018)
2. Kulczyk, T., Rychlik, M., Lorkiewicz-Muszynska, D., Abreu-Gbowacka, M., Czajka-Jakubowska, A., Przystanska, A.: Computed Tomography versus Optical Scanning: A Comparison of Different Methods of 3D Data Acquisition for Tooth Replication (2019)
3. Paoli, A., Neri, P., Razionale, A.V., Tamburrino, F., Barone, S.: Sensor architectures and technologies for upper limb 3D surface reconstruction: a review. Sensors **20**(22), 6584 (2020)
4. Dawood, A., Marti, B.M., Sauret-Jackson, V., Darwood, A.: 3D printing in dentistry. Br. Dent. J. **219**, 521–529 (2015)
5. Richards, D.J., Tan, Y., Jia, J., Yao, H., Mei, Y.: 3D Printing for Tissue Engineering
6. Wang, Z., Yang, Y.: Application of 3D Printing in Implantable Medical Devices. Biomed Res. Int. 2021, (2021)
7. Bü Cking, T.M., Hill, E.R., Robertson, J.L., Maneas, E., Plumb, A.A., Nikitichev, D.I.: From medical imaging data to 3D printed anatomical models (2017)
8. Beg, S., et al.: 3D printing for drug delivery and biomedical applications. Drug Discov. Today **25**, 1668–1681 (2020)
9. Professional 3D Scanners | Artec 3D | Best 3D Scanning Solutions, https://www.artec3d.com. (Accessed April 2023)
10. Servi, M., Mussi, E., Profili, A., Volpe, Y.: An Ad-hoc Solution for Ear Anatomy Acquisition in Pediatric Setting. Comput. Aided. Des. Appl. **20**, 50–61 (2023)
11. McNeel, R.: Rhinoceros. NURBS modleing for Windows: http://www.rhino3d.com/jewelry.htm. (Accessed April 2023)
12. McNeel, R.: Grasshopper - algorithmic modeling for Rhino, http://www.grasshopper3d.com/. (Accessed April 2023)
13. Berens, A.M., Newman, S., Bhrany, A.D., Murakami, C., Sie, K.C.Y., Zopf, D.A.: Computer-Aided Design and 3D Printing to Produce a Costal Cartilage Model for Simulation of Auricular Reconstruction. Clin. Tech. Technol. Otolaryngol. Neck Surg. **155**, 356–359 (2016)
14. Flores, R.L., et al.: The technique for 3D printing patient-specific models for auricular reconstruction. J. Cranio-Maxillofacial Surg. **45**, 937–943 (2017)
15. Mussi, E., Servi, M., Facchini, F., Furferi, R., Governi, L., Volpe, Y.: A novel ear elements segmentation algorithm on depth map images. Comput. Biol. Med. **129**, 104157 (2021)

Manufacturing of Multilayer Replicas of Human Costal Cartilage for Realistic Medical Planning

Michaela Servi[1](✉), Elisa Mussi[1], Monica Carfagni[1], Kathleen McGreevy[2], and Flavio Facchini[2]

[1] Department of Industrial Engineering, University of Florence, Florence, Italy
michaela.servi@unifi.it
[2] Meyer Children's Hospital IRCSS, Florence, Italy

Abstract. Autologous ear reconstruction is a surgical procedure which aims to restore the anatomy of the outer ear whenever there are malformations due to congenital defects (microtia) or as a result of trauma and burns. Reconstruction involves the cutting, carving, and modeling of a portion of costal cartilage harvested from the patient. The aesthetic results of the surgery are highly dependent on the manual skill of the surgeon, which therefore needs a wide range of surgical experience. Appropriate simulation and training tools are essential to acquire adequate familiarity with the procedure without compromising the patient's aesthetic appearance. In such a context, the present work aims to create replicas of the costal cartilage that allow a realistic simulation of the surgery, thus taking into account important characteristics of the cartilage tissue such as the behavior to cut and suture, hardness, etc. The problem is approached with well-established Additive Manufacturing and Reverse Engineering techniques, which are increasingly being used in the medical field, addressing both the problem of identifying the most suitable materials and the possibility of providing medical personnel with simple interactive procedures for the fabrication of multilayer replicas, without the need to turn to expert CAD modelers.

Keywords: Medical simulation · CAD modeling · Costal cartilage mold · Ear reconstruction

1 Introduction

Physical and virtual simulation have been increasingly used in healthcare to reduce errors, increase accuracy, and improve manual skills by allowing physicians to repeat clinical procedures without injuring the patient [1]. Modern rapid prototyping techniques, like Reverse Engineering (RE) and Additive Manufacturing (AM), offer reduced cost, speed, and extreme freedom in terms of treatable geometries, which have been combined with simulation and planning to facilitate the creation of physical simulators that accurately follow patient-specific anatomies and enable high-fidelity simulation [2–4]. Autologous ear reconstruction (AER) surgery is no exception in benefiting from the use of physical simulation and rapid prototyping tools. This surgery is performed on

M. Carfagni et al. (Eds.): ADM 2023, LNME, pp. 129–137, 2024.
https://doi.org/10.1007/978-3-031-52075-4_16

patients affected by a pathology called microtia which entails the partial or complete absence of the outer ear [5]. In short, the method entails modeling the costal cartilage removed from the patient, building a three-dimensional framework that mirrors the shape of the patient's contralateral healthy ear, and then reconstructing the damaged or absent anatomy of the ear. AER surgery is an extremely difficult process for plastic surgeons because of the complicated shape that must be recreated, and the results are heavily reliant on the "artistic skills" of the surgeon [6].

Long and effective training is the prevailing response presented in the literature [7] to make this surgery more accessible to surgeons and, at the same time, to improve outcomes. With this in mind, through close collaboration with plastic surgeons at Meyer Children's Hospital of Florence, previous work has focused on the development of preoperative simulation tools and intraoperative tools to improve AER outcomes and to fabricate costal cartilage replicas with the characteristics of human cartilage, such as haptic return and flexibility. By manipulating these replicas, the surgeon can observe the spatial relationship of the sites of interest, allowing familiarization with anatomy in the operating room and creation of mental maps. Additive manufacturing techniques are often used in the manufacturing of accurate simulators. Material availability, in fact, allows direct printing of anatomical parts, such as bone tissue [8]. The manufacture of anatomical models based on soft tissue, however, involves molds and casting techniques due to high cost and limited material choices of soft materials for 3D printing [9]. Therefore, costal cartilage replicas are also produced with these techniques. This work also introduces the necessity to include the material's heterogeneity, a property that makes the outer layer more compact and less friable than the inner layer. In this light, the current study focuses on the creation of replicas of the costal cartilage that can imitate the normal properties of human cartilage, such as flexibility, heterogeneity, and tactile return.

2 Materials and Methods

To achieve the ambitious goal of providing surgeons with costal cartilage replicas that allow an accurate and realistic simulation of AER surgery, this work focused on two objectives: 1) to identify the best materials to replicate the costal cartilage when operations such as suturing and sculpting are performed 2) to establish a systematic, interactive CAD process that can automatically model the costal cartilage replica that will be used to create a multilayer heterogeneous replica. These two objectives are addressed in the following subsections.

2.1 Material Choice for Costal Cartilage Replica

The first goal was to identify the best material for realistic and effective cartilage reproduction. It must be taken into account that besides geometric accuracy, the rib cartilage replica must respect the mechanical properties of human cartilage, such as flexibility, elasticity, and hardness, must consist of two layers (one inner and one outer). In addition, it should be considered that the material must be sutured with nylon threads to enable the assembly of the ear's elements. To this end, in the first instance, the authors conducted a thorough analysis of the state of the art to define the mechanical properties of human costal cartilage [10, 11].

The lack of dedicated work and the wide variability of the identified values led the authors to engage in a different process for defining the best suitable material: rather than seeking to reproduce specific values defined in the literature, an attempt was made to identify the material that best qualitatively simulates the characteristics of costal cartilage by having the medical staff evaluate material samples. In accordance with state-of-the-art indications and authors' previous work, the following materials were considered for the first phase of qualitative testing to make the samples: 1) silicone Dragon Skin 10, 2) mixture of silicone Dragon Skin 10 and cornstarch in proportions of 2:1, 3) mixture of silicone Dragon Skin 10 and cornstarch in proportions of 3:2, 4) silicone Smooth-Sil 940, 5) mixture of silicone Smooth-Sil 940 and cornstarch in proportions of 2:1 and 6) mixture of silicone Smooth-Sil 940 and cornstarch in proportions of 3:2. The chosen silicones have different hardness characteristics so that different mixtures can be tested and the choice of mixing cornstarch stems from the literature review, which showed that cornstarch is often mixed with silicone compounds to achieve better cutting and suturing qualities [12]. The characteristics on which it was decided to conduct the qualitative analysis were: Texture, Friability, Cutting, Bending, Suturing. For each characteristic, five physicians, specialized in AER surgery, assigned a value from 1 to 5 (where 5 represents the best replication of the cartilage characteristic). Qualitative results showed that the mixture of Smooth-Sil 940 silicone and cornstarch in a 3:2 proportion has the best qualities to mimic external layer of cartilage tissue, while Dragon Skin 10 & cornstarch (3:2) proportion has the best qualities to mimic internal layer of cartilage tissue. To enable the multilayer model to accurately simulate the properties of costal cartilage, in collaboration with surgeons, the ratings given to the different items were analyzed taking into account the required properties of compactness of the outer layer and friability of the inner layer. Therefore, it was decided to use Smooth-Sil 940 and cornstarch mixture in a 3:2 proportion for the inner layer and Dragon Skin 10 and cornstarch in a 3:2 proportion for the outer layer, since it was found to be preferable with regard to Texture and Bending properties.

2.2 Multilayer Costal Cartilage Replica

As mentioned in the introductory section, the multilayer replicas are made through molding and casting techniques; however, experienced modelers frequently need to pay extra care while creating CAD models that are acceptable for casting costal cartilage so that they don't have draft issues. In fact, in the process of mold modelling, attention must be paid to the division of the mold into two half-shells so that the poured model can be easily removed, and this can slow down the time by which the final models are provided to the surgeons for simulation.

Table 1. Results of the qualitative analysis questionnaire, averaged over the five ratings.

	Texture	*Friability*	*Cutting*	*Bending*	*Suturing*	*Average ratings*
Dragon Skin 10	1.8	2.4	1.4	1.4	2.8	1.9
Dragon Skin 10 & cornstarch (2:1)	2.4	3	2.8	2.4	2.7	2.6
Dragon Skin 10 & cornstarch (3:2)	4.1	3.2	3.1	3.9	2.6	3.4
Smooth-Sil 940	2.6	2.6	2.6	2.2	3.6	2.7
Smooth-Sil 940 & cornstarch (2:1)	3.3	3.5	3.6	3.3	3.5	3.4
Smooth-Sil 940 & cornstarch (3:2)	4.1	4.5	4.2	3.7	3.8	4.1

To this end, a systematic CAD procedure for mold modelling was developed, with the idea of streamlining the fabrication process and using this procedure to make two molds for each cartilage model required: one mold for the inner layer of the replica and one for the outer layer, both made with the same procedure, with the only difference being that the geometry of the cartilages is offset inward by 3 mm before making the mold for the inner layer. This strategy allows to use the same procedure twice without any modification. In this context the offset value of 3 mm was requested by the medical staff. The steps of the systematic procedure are listed in Table 2., and they essentially consist of 1) creating a parallelepiped from which the cartilages' geometry is subtracted, and 2) splitting this parallelepiped into two halves so that the physical model can be extracted once the casted material has solidified. Since the geometry of the cartilages is very irregular, identifying such a dividing surface is the most difficult step of the process. From this perspective, it is necessary to find a surface that fits the shape of the cartilages while also making it simpler to manufacture. The method is accomplished out using built-in Siemens NX functionalities.

The stated process was automated using the NX programming API and implemented in a software interface developed in C++ to enable the medical personnel to produce the patient-specific molds without involving CAD expertise. The application, developed using the Qt framework, enables management of user interaction with CAD modeling processes.

A form for entering patient information, a tab for accessing the mold modeling process, and a 3D navigator constitute the interface in Fig. 1.

Table 2. CAD procedure for designing patient-specific mold of the costal cartilage.

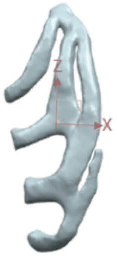	The orientation of the model is the first step in the CAD process: the primary axis of inertia are aligned with the Z-X plane and the origin of the global reference system is relocated to coincide with the model's center of gravity.
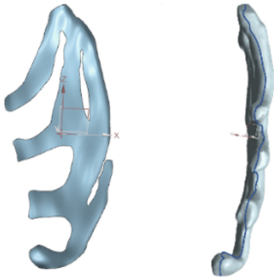	Using the NX function "Fit Surface" directly on the STL file, the initial model's best-fit surface is assessed. The surface is then retrieved by performing a Boolean operation between this surface and the STL model. It is necessary to simplify the extracted surface since it is too complex to be extended and utilized directly as a parting surface for splitting the mold. Because of this, the curve that marks the boundary of such a surface is extracted using Siemens NX's "Extracted geometry" procedure and then processed as shown below.
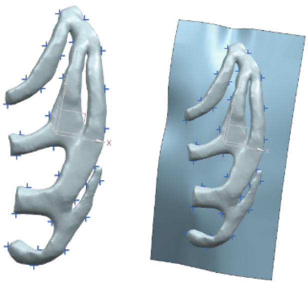	A set of 30 evenly spaced points are used to sample the curve that was extracted in the previous stage. The number of points was established as a compromise between the expense of computation and the precision of the outcome. The profiled parting surface is made using the points in the following step. Each edge of the estimated surface is extended by 15 mm to ensure that the subsequent split process goes smoothly. This dimension was chosen as a precaution to ensure that the solid is divided accurately by the surface in the subsequent step.
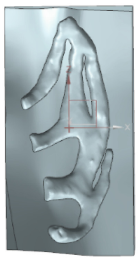	To produce an accurate mold, the solid bounding box of the cartilage model is calculated using the NX function "Bounding Body" and an offset of 5 mm in each direction. The costal cartilage model is subtracted from the solid and split into two parts by using the previously created parting surface
	On top of the upper shell of the mold, a single through-all hole with a radius of 7 mm is drilled in accordance with the rib cartilages. The material will be injected through this opening. As an additional air vent, a hole with a 2 mm radius will be employed. An automatic control has been implemented to identify where the holes should be placed. The program locates the cartilage model's maximum Y value point and places the initial injection hole there. The air vent hole is situated at the model's Z-value minimum point.

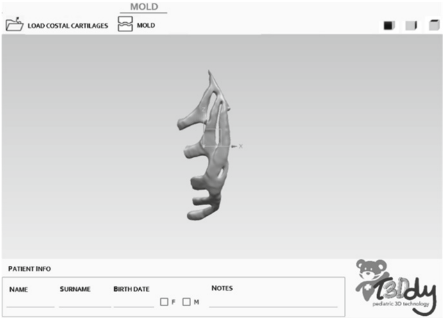

Fig. 1. UI for loading the cartilage anatomy and calling mold modelling.

The idea behind the implementation was to provide the surgeon with an intuitive process to manage the creation of the molds, simplifying as much as possible the modelling phase. Once the CAD model of the molds are available FDM (Fused Deposition Modelling) technology can be used employing low-cost 3D printers (such as the Makerbot Replicator+ [13] 3D printer) and low-cost materials (such as PLA [14], polylactic acid). As for the casting phase of the material, particular attention should be paid to the casting phase of the outer layer.

At this stage, in order to keep the inner layer in the correct position during casting, the most straightforward and simple solution identified was to fabricate small silicone spacers with the same mixture as the outer layer, of a thickness of 3 mm (Fig. 1a). To make these spacers, it is sufficient to create a small open parallelepiped-shaped mold with a height of 3 mm and depth of 3 mm (the length may vary depending on the size of the cartilage model) to accommodate the silicone mixture, and then, after curing time cut the material to obtain the spacers. The spacers must then be laid on the mold for the outer layer before placing the model of the inner layer. The distribution of the spacers should be done in such a way as to allow the silicone to reach the entire mold and not occlude regions during the casting of the outer layer. It will be sufficient to place the spacers at the bottom of the mold to keep the model in the correct position. The distribution of these spacers inside the mold ensures that the inner layer maintains the correct position and does not create problems in the final replica, since the spacers material is the same material used for casting the outer layer (Fig. 2a). Below are shown the CAD model of the mold for the outer layer (Fig. 2b) and an example of the usage of this mold to accommodate the inner layer and the spacers before pouring the outer layer (Fig. 2c).

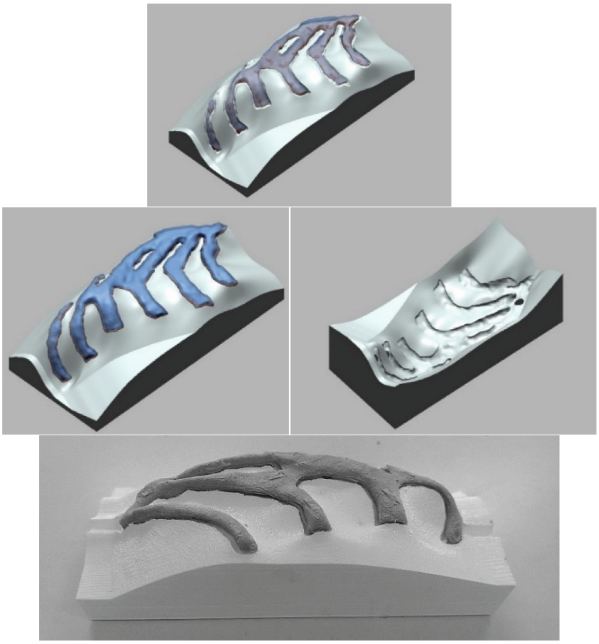

(a)

(b)

(c)

Fig. 2. a) CAD model of the mold for the outer layer with the inner layer supported held in place by spacers; b) CAD model of the result of the double phase casting procedure; c) FDM printed model of the outer layer with inner layer placed on the spacers.

3 Discussions and Conclusions

To date, the most common treatment for patients affected by microtia is reconstruction of the outer ear with autologous cartilage tissue. This technique, while definitely advantageous in terms of eliminating the risk of rejection, is highly dependent on the manual skills of the surgeon in making the auricular framework. It thus seems clear that there is a need to provide the possibility of practicing cutting curving and suturing operations to carefully plan the surgery in order to achieve aesthetically acceptable results and reduce surgical time.

In this context, the fabrication of costal cartilage replicas that behave like human cartilage in the realization of the auricular framework is a key element for a realistic simulation of the surgery and can be a determining factor in operation success. RE and AM technologies can be efficiently used to make patient-specific molds for casting silicone-based mixtures for cartilage reproduction. In this work, the choice of materials was based on the portioning of two ingredients, silicone and cornstarch. In fact, this combination makes it possible to obtain a compound that is as flexible and strong as silicone, yet at the same time responds correctly to carving and has friability characteristics. After qualitatively testing the materials, five physicians assigned a rating from 1 to 5 to each characteristic, and as a result the Smooth-Sil 940 & cornstarch mixture in 3:2 proportions was found to be the best. The second objective of the work was to define a systematic, interactive CAD procedure capable of semi-automatically modelling the mold replica of the costal cartilage to be used to make a heterogeneous multilayer replica. To this end, the systematic CAD procedure created was combined with user-friendly control software and used to produce two molds, each dedicated to one layer. The procedure was tested with a study conducted in collaboration with Meyer Children's Hospital on 10 patients with microtia. Informed consent was obtained from each patient, or his or her legal guardian, to use the data for scientific purposes. The diagnostic exams were also anonymized before this study. To test the robustness of the software for modeling different anatomies, the automatic routine (was performed for each rib cartilage, making the two molds, the one for the inner core and the one for the outer layer. All mold models were generated correctly without any complications in all cases examined. With regard to the synthetic material to be cast, the requirements imposed by the medical staff concerned the possibility of having a replica in which the outer layer, about 3 mm in size, more compact than the inner layer, more friable. Based on these requirements, the two materials were chosen on the basis of the results shown in Table 1.: the Smooth Sil 940 & cornstarch material in a 3:2 proportion was the best overall and was chosen for the inner layer of the cartilage replica, while the Dragon skin 10 & cornstarch material (3:2) was used for the outer layer, the second most highly valued material that, however, exhibits higher Texture and Bending qualities than the mixture with Smooth Sil 940. Figure 3 shows an example of multilayer replica.

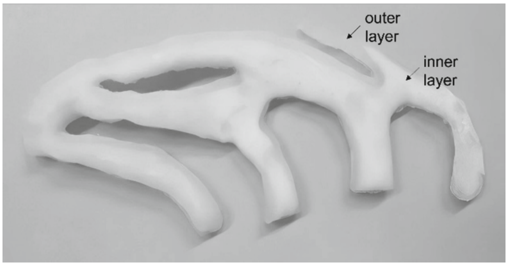

Fig. 3. Example of a multilayer costal cartilage replica realized with the proposed procedure.

This method for fabricating the multilayer model, compared, for example, with the use of a sacrificial core, has benefits in terms of reliability and repeatability. In fact, the use of soluble materials, besides incurring additional costs, could encounter problems in the removal of the core material, related to the peculiarity and non-regularity of the geometry. On the other hand, the method incurs some limitations, given, for example, by the difficulty of pouring material that, due to the proportion of cornstarch, becomes less fluid. One possible solution would include the use of additives, such as thinner, to make the mixture easily pourable without excessively altering the properties analyzed above. Future studies will explore more deeply this possibility. Moreover, the time required to fabricate the replica can also be considered a limitation, which includes mold 3D printing and the two casting steps that must be done sequentially, for which the time required for catalyzation is 24 h for Smooth Sil 940 and 15 h for Dragon skin 10.

In conclusion, this work has allowed a major step forward toward making realistic replicas of costal cartilage to provide the surgeon with effective tools for AER surgery planning, taking advantage of the semi-automated patient-specific mold-making system. Future developments involve firstly the thorough evaluation of this multilayer model and its use for the realization of an auricular framework in preoperative simulation, and then will address the automation of cartilage segmentation from the patient's chest tomographic sequence, so that this part of the process can also be performed automatically.

References

1. Mussi, E., et al.: Current practice in preoperative virtual and physical simulation in neurosurgery. Bioengineering **7**, 7 (2020)
2. Naddeo, F., Naddeo, A., Cappetti, N., Cataldo, E., Militio, R.: Novel procedure for designing and 3D printing a customized surgical template for arthrodesis surgery on the sacrum. Symmetry **10**(8), 334 (2018)
3. Naddeo, F., Cataldo, E., Naddeo, A., Cappetti, N., Narciso, N.: An automatic and patient-specific algorithm to design the optimal insertion direction of pedicle screws for spine surgery templates. Med. Biol. Eng. Comput. **55**, 1549–1562 (2017)
4. Petzold, R., Zeilhofer, H.F., Kalender, W.A.: Rapid prototyping technology in medicine—basics and applications. Comput. Med. Imaging Graph. **23**, 277–284 (1999)
5. Nagata, S.: A new method of total reconstruction of the auricle for microtia. Plast. Reconstr. Surg. **92**, 187–201 (1993)
6. Facchini, F., Morabito, A., Buonamici, F., Mussi, E., Servi, M., Volpe, Y.: Autologous ear reconstruction: towards a semiautomatic CAD-based procedure for 3D printable surgical guides. CAD Solutions, LLC, 1–5 (2020)
7. Firmin, F., Marchac, A.: A novel algorithm for autologous ear reconstruction. Semin. Plast. Surg. **25**, 257–264 (2011)
8. Bose, S., Vahabzadeh, S., Bandyopadhyay, A.: Bone tissue engineering using 3D printing. Mater. Today **16**, 496–504 (2013)
9. J750 Digital anatomy 3D printer for lifelike medical models, Stratasys. https://www.stratasys.com/3d-printers/j750-digital-anatomy
10. Pappa, A.K., Soleimani, S., Caballero, M., Halevi, A.E., van Aalst, J.A.: A pilot study comparing mechanical properties of tissue-engineered cartilages and various endogenous cartilages. Clin. Biomech. **50**, 105–109 (2017)
11. Lau, A., Oyen, M.L., Kent, R.W., Murakami, D., Torigaki, T.: Indentation stiffness of aging human costal cartilage. Acta Biomater. **4**, 97–103 (2008)
12. Gurjão Da Silva, A.P., Rios Rodriguez, J.E.: The alternative model of silicone for experimental simulation of suture of living tissue in the teaching of surgical technique. Acta cirurgica Bras. **34** (2019)
13. Replicator+ desktop 3D printer, MakerBot. https://www.makerbot.com/3d-printers/replicator/. Accessed Apr 2023
14. MakerBot PLA: rigid and glossy parts for quick and easy prototyping, MakerBot. https://www.makerbot.com/3d-printers/materials/method-pla/. Accessed April 2023

3D Printing Methods in Medicine: The Case of an Aortic Section

Giulia Alessandri(✉), Gian Maria Santi, Leonardo Frizziero, and Alfredo Liverani

University of Bologna, 40136 Bologna, Italy
{giulia.alessandri5,gianmaria.santi2,leonardo.frizziero,
alfredo.liverani}@unibo.it

Abstract. The paper focuses on the application of 3D printing technology in the medical field, particularly in cardiac surgery. Unlike traditional imaging techniques such as CT, MRI, and ultrasound, 3D printing offers a more detailed understanding and analysis of clinical cases. By using 3D printing, it becomes possible to study a patient's specific cardiac anatomy, manipulate objects before surgery, and accurately determine the surgical site. This reduces both the time required for the operation and the patient's recovery period.

This study presents a methodology for creating 3D-printed models of aortic arch sections affected by aortic dissection. The aim is to produce anatomical models with varying levels of quality and accuracy. The research goal is to assess the differences in 3D printing materials and technologies for creating complex anatomical models like the aorta. The process involves segmenting medical images obtained from Computed Tomographic Angiography (CTA) and then 3D printing digital models using different materials (such as PLA, TPU, and resin) and technologies (like FDM and SLA). The resulting 3D printed models are low-cost and demonstrate good accuracy in reproducing human anatomy.

Keywords: Engineering method · CAD · 3D Printing · Cardiac surgery

1 Introduction

This paper presents a novel research endeavor focused on the application of 3D printing technology in the field of medicine and healthcare, specifically in cardiac surgery. The study aims to leverage the capabilities of 3D printing to improve patient outcomes and revolutionize surgical procedures. By creating patient-specific 3D printed models derived from medical image data, the paper addresses the limitations of traditional preoperative planning based on two-dimensional images, particularly in complex cases like aortic diseases.

Aortic diseases encompass various conditions such as aneurysms, acute aortic syndromes, and congenital abnormalities, which necessitate meticulous planning based on radiological images like CTA or MRA. The integration of 3D printing has significantly enhanced preoperative planning by providing tangible anatomical models [1, 2]. These models facilitate better evaluation of clinical cases, support medical education, and aid in

M. Carfagni et al. (Eds.): ADM 2023, LNME, pp. 138–145, 2024.
https://doi.org/10.1007/978-3-031-52075-4_17

patient care [3–5]. Previous studies have evaluated the accuracy of 3D printing in assessing and preparing for surgery in complex congenital heart disease cases [6]. Additionally, virtual simulation serves as a guiding tool for assessing the final surgical configuration [7–9].

This paper acknowledges the potential of new technologies in understanding complex cardiac pathologies, particularly aortic dissection, through accurate replication of anatomical structures and pathologies [10]. The authors share their experience in creating low-cost, highly accurate 3D-printed models of an aortic dissection case. The objective is to conduct experiments and comparative analyses to thoroughly examine the printability, functional properties, and aesthetics of PLA, TPU, and clear resin materials. By printing aortic arch sections, evaluating printing process ease and effectiveness, and analyzing surface quality, the researchers aim to identify material strengths and weaknesses in terms of printability, flexibility, transparency, and compatibility with various applications. The study compares different technologies suitable for medical applications and complex cardiac diseases. In this case, a simple 3D representation is inadequate, and the abundance of printers and materials complicates the decision-making process. The paper provides an overview of printing possibilities and defines the best application for each.

2 Method

The methodology for creating a 3D anatomical model involves several steps. Firstly, imaging data from CTA or MRA are obtained and used for digital representation of the patient's anatomy through segmentation, separating relevant structures (Fig. 1a). Segmentation software like Materialise Mimics and 3D Slicer enable the creation of 3D anatomical models from medical images, allowing precise planning, surgical simulations, and patient education. Materialise Mimics provides advanced segmentation capabilities, while 3D Slicer is an open-source program for medical image analysis and

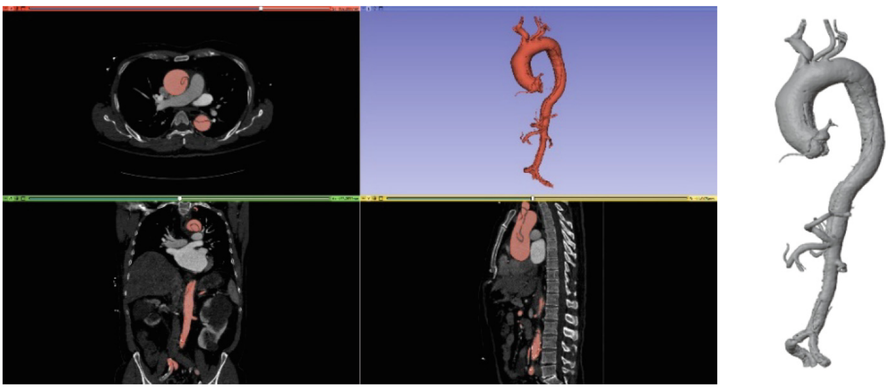

a) b)

Fig. 1. Reconstruction of a 3D anatomical model: a) segmentation of a CTA image, b) digital representation of the patient's anatomy.

visualization, chosen for research purposes. The segmented data is then used to create a 3D model, refined and modified with software such as MeshLab and Blender to accurately represent the patient's anatomy (Fig. 1b).

After segmenting the 3D model, the next step is to prepare it for 3D printing. This process involves outlining the blood vessel for internal visualization and analysis of the cardiac malformation. The analysis of CTA images determined the intimal flap's average thickness, separating the true lumen from the false lumen, to be 1.8 mm (Fig. 2). This value was chosen as the wall thickness for the entire aortic blood vessel in this analysis.

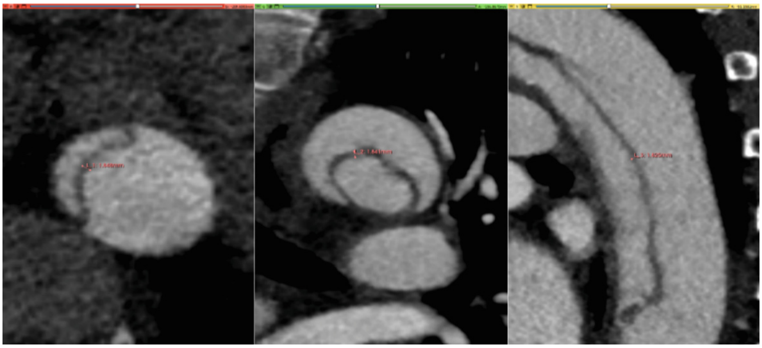

Fig. 2. The average thickness of the intimal flap.

Different 3D printed models of aortic dissection were created, converting the 3D model to STL format for compatibility with 3D printers. The choice of printing material depends on the model's purpose. Polylactic acid (PLA) or flexible thermoplastic polyurethane (TPU) can be used to visualize and study the anatomy, while clear TPU or clear resin are ideal for detailed visualization and endovascular device simulations. The selected materials were White FiloAlfa® PLA, Clear Recreus® Filaflex 82A (FDM printing), and Clear Anycubic® Water-Wash Resin (SLS printing). White PLA provides a simple aesthetic representation, Clear TPU offers flexibility and transparency for studying internal walls, and Clear Resin is suitable for specific technologies and desired outcomes. The 3D model is printed layer by layer using Ultimaker Cura software. Printing parameters are determined by referring to the filament supplier's datasheets, considering recommended temperature settings and print speeds. The optimal printing parameters are identified through careful review and experimentation, especially setting uncommon materials. It was important to balance temperature and printing speed especially for TPU and resin (Table 1 and Table 2). Support structures are removed after printing, and the final 3D-printed aortic section undergoes post-processing to ensure a defect-free result.

Table 1. 3D printing parameters for the FDM printer.

Material	FiloAlfa® PLA	Recreus® Filaflex 82A
Printing Temperature	200 °C	240 °C
Heated Bed Temperature	60 °C	60 °C
Nozzle Diameter	0.4 mm	0.4 mm
Layer Height	0.2 mm	0.2 mm
Printing Speed	60 mm/s	20 mm/s
Support	Yes	Yes
Color	White	Clear

Table 2. 3D printing parameters for the SLA printer.

Material		Anycubic® Water-Wash Resin+
Bottom layers	Number of Layers	3
	Exposure Time	25 s
	Lift Distance	4–7 mm
	Lift Speed	60–180 mm/m
	Retract Speed	180–40 mm/m
Normal Layers	Layer Thickness	50 μm
	Light-off Delay	2 s
	Exposure Time	3 s
	Lift Distance	4–7 mm
	Lift Speed	60–180 mm/m
	Retract Speed	180–40 mm/m
Color		Clear

3 Results

The objective of this study was to assess the advantages and potential future applications of 3D-printed models created using different materials and technologies. These models were specifically designed to represent a cross-sectional view of an aortic dissection, aiming to aid surgeons in analyzing challenging aspects of the aortic tract that are not easily visualized using traditional two-dimensional medical images. To ensure successful 3D printing, the complexity resulting from the arch's shape was simplified by dividing the model into sections. Additionally, anatomical features, including the tactile perception provided by wall thickness, were carefully considered to ensure the physical prototypes achieved good accuracy.

The 3D printed models, utilizing FiloAlfa® PLA material (Fig. 3), provided an accurate physical preview of the surgical field, taking into account the dimensions of the anatomical structures. They served as dimensional representations of the examined area, facilitating the surgeon's comprehension of the region of interest. Conversely, the models created using the clear Recreus® Filaflex 82A (Fig. 4) and the clear Anycubic® Water-Wash Resin (Fig. 5) materials were valuable for predicting the optimal access points for endoprosthesis insertion. The transparent TPU model offered tactile feedback, enhancing the flexibility of the aortic tract and providing a greater sense of realism. Meanwhile, the resin model achieved an impressive level of detail in terms of surface quality.

Fig. 3. 3D printed models through the FDM technology in FiloAlfa® PLA.

Fig. 4. 3D printed models through the FDM technology in Recreus Filaflex 82A Clear.

Among the tested materials, PLA was easy to print, requiring only temperature adjustments. It produced a formal model of the cardiac anatomy. On the other hand, TPU required specific guidelines, including printer configuration and filament moisture control. Handling TPU, as an elastic material, was more complicated than PLA. The resulting object was a satisfactory combination of printing parameters. Transparent resin often needs post-processing to remove excess material. A water-washable resin was used in this study, resulting in a smoother texture. Caution is needed due to the fragility, especially in thin sections.

Fig. 5. 3D printed model through the SLA technology in Anycubic Water-Wash Resin+ Clear.

Regarding material storage and handling, the uncured resin should be stored in a cool, dark place at room temperature, protected from light and high temperatures. The recommended operating temperature is 18–35 °C, and pre-heating the resin before use ensures optimal printing effects. After cleaning, timely removal from water immersion preserves the resin's properties. Post-curing, including controlling the light source, is critical for optimal material performance. Sun exposure should be limited to approximately one hour. It is advisable to print in a dark room or use a cover due to the resin's photosensitivity.

In the operating room, where strict hygiene measures are followed, it is beneficial for surgeons to handle 3D-printed models made from environmentally compatible, stable, and hygienic materials. These materials can undergo sterilization processes, involving high temperatures, chemicals, or radiation, to ensure cleanliness. The commonly used sterilization temperature is 134 °C, with a minimum exposure time of approximately one hour for devices. Therefore, chemically stable materials that withstand these temperatures are essential. PLA filament has a melting point of 135 °C, TPU filament has a melting point of 220 °C, and the resin has an autoignition temperature of 252 °C. Although theoretically capable of withstanding sterilization, potential deformation and decomposition require further investigation.

Through the use of various materials and meticulous considerations during the printing process, these models provided valuable insights for aortic dissection analysis. They offered an accurate physical preview of the surgical field, predicted optimal access for procedures, and closely resembled real-life counterparts. The combination of PLA, TPU, and resin enabled a comprehensive understanding of cardiac anatomy, ensuring high accuracy in reproducing anatomical features and pathologies. These models played a crucial role in producing physical prototypes resembling real objects, promoting better understanding and enhancing tangibility. Furthermore, they demonstrated high accuracy in reproducing both anatomy and pathology while remaining cost-effective.

4 Conclusion

The study used 3D printing to create patient-specific anatomical models with different materials and technologies, assessing their advantages and applications. 3D printing significantly improved cardiac surgery by producing patient-specific models for planning, training, and simulations [11–13]. These models enhance surgical preparation, accuracy, and confidence [14, 15], improving safety, communication, and replicating patient-specific properties [16]. Customized implants, like cardiac valves or aortic stents, can be 3D printed, tailored to the patient's anatomy and withstanding high sterilization temperatures [17]. Additionally, 3D printing allows personalized implants for each patient's anatomy, increasing successful outcomes and reducing complications. It aids in manufacturing surgical tools, enhancing precision and reducing operative time. Soft materials in 3D printing enable training in complex surgical procedures using realistic 3D models and fluid pumps to simulate blood flow. This approach improves surgeons' skills and patient outcomes. These 3D-printed models replicate physiological conditions, serving as valuable tools for surgical education.

Our experience with 3D-printed models has been positive, representing the first step in improving the representation and simulation of complex cardiac pathologies. Advancements include integrating bioprinting technology, conducting mechanical and fluid dynamic testing, and enhancing cardiac tissue reproduction. In conclusion, 3D printing in cardiology and other medical fields offers a methodology applicable to various disciplines. 3D-printed models have the potential to improve patient outcomes with accurate and personalized treatment options.

References

1. Hopfner, C., et al.: Design and 3D printing of variant pediatric heart models for training based on a single patient scan. 3D Print Med. **7**, 1–11 (2021)
2. Segaran, N., et al.: Application of 3D printing in preoperative planning. J. Clin. Med. **10**, 917 (2021)
3. Stana, J., Grab, M., Kargl, R., Tsilimparis, N.: 3D printing in the planning and teaching of endovascular procedures. Die. Radiol. **62**, 28–33 (2022)
4. Borracci, R.A., Ferreira, L.M., Alvarez Gallesio, J.M., Tenorio Núñez, O.M., David, M., Eyheremendy, E.P.: Three-dimensional virtual and printed models for planning adult cardiovascular surgery. Acta Cardiol. **76**, 534–543 (2021)
5. Sun, Z., Wong, Y.H., Yeong, C.H.: Patient-specific 3D-printed low-cost models in medical education and clinical practice. Micromachines **14**, 464 (2023)
6. Yang, D.H., Park, S.H., Kim, N., et al.: Incremental value of 3D printing in the preoperative planning of complex congenital heart disease surgery. JACC Cardiovasc. Imaging **14**, 1265–1270 (2021)
7. Abjigitova, D., Sadeghi, A.H., Peek, J.J., Bekkers, J.A., Bogers, A.J.J.C., Mahtab, E.A.F.: Virtual reality in the preoperative planning of adult aortic surgery: a feasibility study. J. Cardiovasc. Dev. Dis. **9**, 31 (2022)
8. Szugye, N.A., Zafar, F., Villa, C., Lorts, A., Morales, D.L.S., Moore, R.A.: 3D holographic virtual surgical planning for a single right ventricle Fontan patient needing Heartmate III placement. ASAIO J. **67**, E211–E215 (2021)

9. Grab, M., et al.: New perspectives in patient education for cardiac surgery using 3D-printing and virtual reality. Front. Cardiovasc. Med. (2023). https://doi.org/10.3389/FCVM.2023.1092007
10. Sun, Z.: Clinical applications of patient-specific 3D printed models in cardiovascular disease: current status and future directions. Biomol **2020**(10), 1577 (2020)
11. Hoashi, T., et al.: Utility of a super-flexible three-dimensional printed heart model in congenital heart surgery. Interact. Cardiovasc. Thorac. Surg. **27**, 749–755 (2018)
12. de Oliveira, M.A.B., Dos Santos, C.A., Brandi, A.C., Botelho, P.H.H., Braile, D.M.: Three-dimensional printing: is it useful for Cardiac Surgery? Braz. J. Cardiovasc. Surg. **35**, 549 (2020)
13. Benke, K., Barabás, J.I., Daróczi, L., et al.: Routine aortic valve replacement followed by a myriad of complications: role of 3D printing in a difficult cardiac surgical case. J. Thorac. Dis. **9**, E1021–E1024 (2017)
14. Wang, C., et al.: 3D printing in adult cardiovascular surgery and interventions: a systematic review. J. Thorac. Dis. **12**, 3227 (2020)
15. Vukicevic, M., Mosadegh, B., Min, J.K., Little, S.H.: Cardiac 3D printing and its future directions. JACC Cardiovasc. Imaging **10**, 171 (2017)
16. Gharleghi, R., et al.: 3D Printing for cardiovascular applications: from end-to-end processes to emerging developments. Ann. Biomed. Eng. **49**, 1598–1618 (2021)
17. Frizziero, L., Santi, G.M., Leon-Cardenas, C., et al.: Heat sterilization effects on polymeric, FDM-optimized orthopedic cutting guide for surgical procedures. J. Funct. Biomater. **12**, 63 (2021)

Preliminary Study of a 3D-Printed High-Fidelity Simulator for the Training on the EBUS TBNA Procedure

Marta Mencarelli(✉), Luca Puggelli, Rocco Furferi, and Antonio Marzola

Department of Industrial Engineering, University of Florence, via di Santa Marta, 3, 50139 Florence, Italy

{marta.mencarelli,luca.puggelli,rocco.furferi,
antonio.marzola}@unifi.it

Abstract. Lung cancer is the second neoplasia for incidence and the leading cause of death from neoplasia in the world. A consolidated practice for lung cancer early diagnosis and staging is EBUS TBNA (EndoBronchial UltraSound-guided TransBronchial Needle Aspiration).

Despite being a low-risk procedure, its success highly depends on the medical staff's skills, who therefore require appropriate training.

With the future aim of developing a novel realistic EBUS TBNA simulator that also allows tissue sampling, in this paper, the authors propose a simplified representation of the mediastinum to define a suitable layout.

As far as the authors know, the physical commercially-available simulators have poor echogenic properties, do not allow tissue sampling, and can be quite expensive.

The project was carried out within Custom3D, a joint laboratory between Careggi Hospital of Florence and the Department of Industrial Engineering of the University of Florence, under the request of the interventional pneumology ward. The model was validated by an expert medical doctor who assessed its anatomical accuracy and the suitability of its mechanical and acoustic properties.

Moreover, the possibility of performing lymph node needle aspiration is an added value that promises to bring the EBUS TBNA simulation to a new level of realism.

Keywords: simulation · EBUS TBNA · mannequin · echogenic

1 Introduction

According to the cancer statistics of 2022, lung cancer is the second neoplasia in order of incidence in men (15%) and the third in women (6%) and locates among the leading causes of death from neoplasia in the world [1]. In Italy, the five-year survival rates for men and women respectively correspond to 16% and 23% [1]. The status of the lymph nodes of the mediastinum (the area of the chest that locates between the lungs) is a major factor for staging, assigning treatment, and evaluating treatment efficacy in patients with

M. Carfagni et al. (Eds.): ADM 2023, LNME, pp. 146–153, 2024.
https://doi.org/10.1007/978-3-031-52075-4_18

lung cancer. The clinical challenge has always been represented by the early diagnosis to identify the tumor at its early stages and therefore offer the patient a better prognosis [2].

Metastatic involvement of mediastinal lymph nodes rules out the surgery, and thorough mediastinal investigation is therefore the crucial point of the diagnostic workup. EndoBronchial UltraSound-guided TransBronchial Needle Aspiration (EBUS TBNA) is the elective method of choice for tissue confirmation of mediastinal lymph node metastasis because of its non-invasiveness, especially if compared to other lung cancer staging procedures [3]. Endobronchial ultrasound (EBUS) is a bronchoscopy technique that utilizes ultrasound imaging to visualize structures around the airway wall, including lymph nodes, blood vessels, lung parenchyma, and mass lesions [4]. It is nowadays considered an advanced procedure for diagnosing neoplastic, infective, and inflammatory pulmonary diseases during which bronchial lymph nodes or tumoral tissue are sampled using an echo-guided probe equipped with a needle, while the patient is under sedation. From the results of the biopsy, oncological markers can be usually determined without subjecting the patient to further invasive and more expensive screening procedures [5].

The needle is inserted in the trachea using a flexible bronchoscope. The target lymph node is identified using an ultrasound (US) probe located at the end of the bronchoscope. The bronchial US allows precise identification of the suspicious tissue that needs to be analyzed. The linear EBUS-TBNA bronchoscope with the biopsy needle extended and a schematic diagram beside an ultrasound image illustrating EBUS-guided lymph node biopsy are shown in Fig. 1.

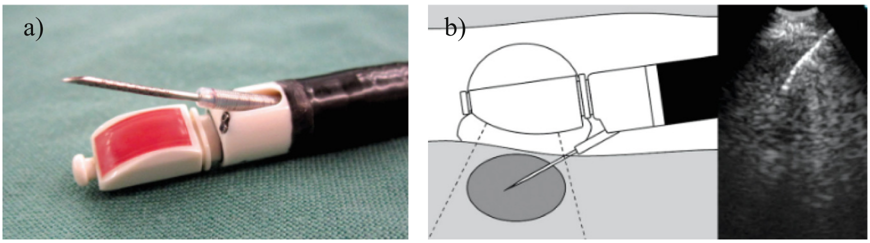

Fig. 1. a) Linear EBUS – TBNA bronchoscope with the needle in the extended configuration, and b) schematic representation of the EBUS-guided biopsy of a lymph node. Image from: https://mforum.com.au/.

To successfully perform EBUS TBNA without compromising the patient's safety or breaking the bronchoscope, a fair amount of dexterity is required. Training is, therefore, crucial to acquire the manual skills to successfully perform the procedure and is also considered one of the most important factors influencing its diagnostic [6].

Given the importance of training the medical staff on the procedure, the Department of Industrial Engineering of the University of Florence started a collaboration with the Careggi Hospital of Florence (Italy) within a joint laboratory named Custom3D, with the aim of developing a novel high-fidelity physical mannequin with which to simulate the entire procedure, including a real needle aspiration. The present paper describes a preliminary feasibility study aiming at the development of such a mannequin, with particular reference to the criteria for selecting potential materials with suitable acoustic properties.

In particular, a prototype representing a simplified portion of the mediastinum is developed to validate the layout and the chosen materials based on scientific and technical literature. The specimen reproduces a mediastinal portion that includes a tracheal section and a customizable combination of lymph nodes. All the structures are immersed in a gelatinous structure to both be held in position and return realistic haptic feedback of the needle penetration.

2 Materials and Methods

After dialoguing with the staff of the interventional pneumology ward of Careggi Hospital, it was decided to start the evaluation of the mediastinal structures to be reproduced from the trachea and the lymph nodes. To simplify the model, only the back portion of the trachea, and two lymph nodes of different materials and dimensions have been included. To hold those structures' position during needle penetration they were planned to be immersed in a gelatinous structure.

Besides high realism and adequate haptic feedback, the developed model was required to rely on realistic acoustic properties and to allow the complete simulation of the TBNA procedure. In particular, those two requirements implied respectively the necessity of identifying suitable echogenic materials and realizing empty lymph nodes' structures to fill with an overtime-stable colored liquid suitable for needle aspiration. Lymph node support systems were designed to allow the possibility of positioning them at a variable distance from the tracheal wall to properly reproduce the mediastinal lymph nodes' arrangement (see Fig. 2).

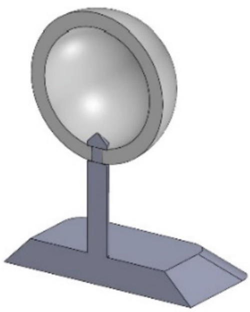

Fig. 2. CAD model of the hollow sphere representing the lymph node assembled on its support system – section view.

The presence of the lymph node support system's tip does not compromise the image, given the fact that during US identification of the target structures the US parameters are adjusted so that the image shows the middle section of the lymph node. Structures located behind are not included in the field of view. Due to the reduced dimensions of the support tip, it was also concluded that its presence should not cause disturbance to the needle insertion.

2.1 Specimen's Layout

A 70 × 30 × 25-mm box was designed forecasting the presence of two housings for as many lymph nodes' support systems and a fastening system for the layer reproducing a portion of the trachea. At this early stage of the study, the blood vessel has been consciously neglected to avoid the introduction of too many variables to be evaluated. The three-dimensional digital model of the specimen is shown in Fig. 3. Specimen's structure without the covering cap.

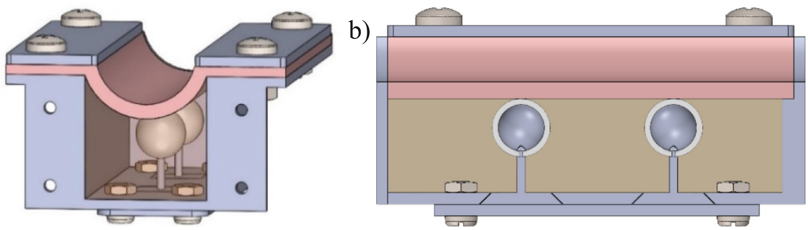

Fig. 3. Specimen's structure without the covering cap (a) and sectional view (b).

The box and the sealing plates were 3D-printed in PLA (PolyLactic Acid) using the FDM (Fused Deposition Modelling) technique. The tracheal layer and the lymph nodes' shell were planned to be realized using US-responding materials. As a support filler, a gelatinous structure was selected since its acoustic properties have been widely assessed as well as its haptic response [3, 7–9]. Gelatin is commonly used to reproduce soft biological tissues since it excellently mimics their scattering properties and US velocity [2, 5, 7]. The fact that such a material is subject to dehydration and maintains its properties for a limited period [7] was not considered a limit at this stage of development, but rather an aspect to be investigated and characterized.

2.2 Tracheal Portion

The tracheal portion was planned to be realized using a silicon-based material. Silicone is durable and stable over time, but it does not match soft tissue's acoustic properties [10] and therefore the addition of doping agents is needed [9].

The silicone rubber selected to be used as a base was DragonSkin 30® (from Smooth-On Inc, Pennsylvania) [11], a slow-curing liquid silicone with a 30 Shore A hardness.

According to the results reported by Santarelli et al. [12] who carried out a study dealing with the best combination of material and wall thickness to reproduce a pediatric trachea, a 1.75 mm wall thickness manufactured using silicone of Shore 40 A hardness results as the most accurate combination in terms of geometry and haptic response. Being the presented study focused on adult anatomy and characterized by slightly different requirements in terms of haptic feedback to the needle puncturing, the authors realized a 3-mm-thick layer to be manufactured by using a doped softer silicone.

The 3-mm-thick semi-cylindric layer was designed with two lugs with two holes each, to allow screws mounting (see Fig. 4) to ease the specimen's assembly. In this phase, the focus was on the material rather than on the geometry accuracy as can be deduced from the absence of the tracheal rings in the model and from the overall simplicity of the part.

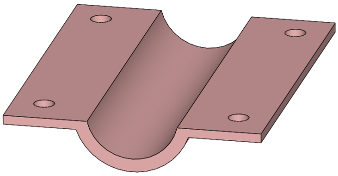

Fig. 4. CAD model of the 3-mm-thick silicon layer designed to simulate a tracheal portion and at the same time allow its fastening to the specimen's other structures.

Once the layer's shape was defined, the mold for the silicone casting was designed and 3D-printed using the FDM technique (see Fig. 5).

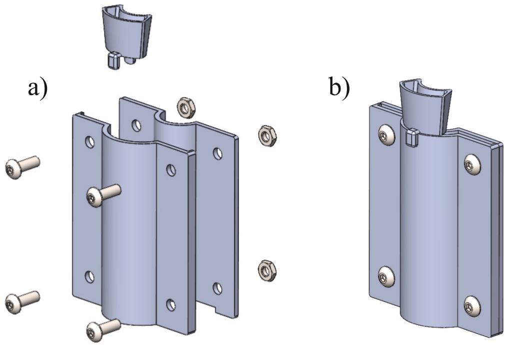

Fig. 5. CAD model of the mold, exploded view (a), and closed configuration (b).

2.3 Lymph Nodes

Lymph nodes were designed as hollow spheres to allow liquid filling. Two different materials were tested. One lymph node to be included in the model was realized by casting using the same doped silicone used for the tracheal layer. In this case, the spherical shape is obtained by assembling and gluing two silicone semi-spherical shells. Of course, a mold was designed and 3D-printed using the FDM technique. The other lymph node was directly 3D-printed in Elastic 50A using Formlabs Form 3B+ [13] 3D printer, based on the SLA (StereoLitogrAphy) technique. The use of direct 3D printing allowed the realization of single-piece hollow spheres. Elastic 50 A is a clear resin with a 50 Shore A hardness suitable for the realization of parts that can withstand deformations without damage and without compromising their capability of returning to their original shapes. As widely known, once printed, all the parts realized by SLA need a wash and curing post-processing.

In both cases, spheres of more than one size were realized to test their feasibility, being the final aim of the project the realization of a high-fidelity simulator with various lymph nodes dimensions. Three sizes characterized by an external diameter of 20, 16, and 10 mm were designed. The wall thicknesses of the spheres corresponded respectively to 1, 0,8, and 0,5 mm. The doped silicon semi-spheres (before and after assembly) and the Elastic 50A sphere are depicted in Fig. 6.

2.4 Assembly

Once ready, the lymph nodes were attached to the support, filled with a colored liquid (water and tempera), and inserted in the box. The colored filling was planned under the specific request of the medical staff to have unambiguous feedback on the success of the simulated procedure. Then, the silicone layer simulating the tracheal wall was placed in position and secured with plates and screws.

After the assembly of the structure, 90% water gelatin was cast in the box and let cool at a temperature of 4 °C for three hours.

(a) (b) (c)

Fig. 6. a) Semi-spheres realized by doped silicon casting in 3D-printed PLA molds, b) hollow doped silicon spheres obtained by combining two halves using doped silicone as a glue, and c) Elastic 50 A hollow spheres realized by direct 3D-printing using SLA technique.

3 Results

The medical staff of Careggi's interventional pneumology ward tested the specimen during a short EBUS simulation session (see Fig. 7).

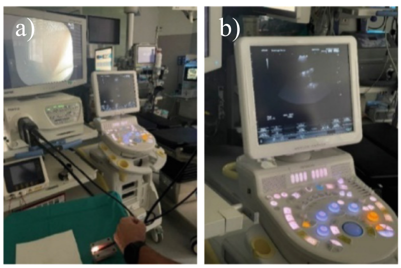

Fig. 7. Simulation setup (a) and US interface (b) used to evaluate the specimen.

The obtained results can be summarized as follows:

- The formula used to give the silicone acoustic properties similar to the human soft tissue is promisingly working. According to the doctors, the US image was clear and the haptic feedback both during navigation and needle puncturing was adequate.
- To definitely validate the tracheal material, navigation should be made possible by realizing a complete hollow cylindric structure. Moreover, tracheal rings should be inserted since they contribute to the thickness of the tracheal wall.
- The gelatin was not sufficiently mixed. Microgranules were still visible in the US image that, consequently, resulted compromised. This had a negative impact on the evaluation of the lymph node material, which was accordingly postponed to a later time. However, after a preliminary evaluation, according to the doctors, the gelatin seems to be a suitable structural medium to stable the parts and give adequate haptic feedback during needle penetration.
- The structure of the specimen was not sufficiently stable and complicated the test. A future version should be more robust.

From preliminary studies it has emerged that the silicone spheres tend to deflate after a short time (~24 h) if left in the open air. The process, whose reasons are still under investigation and may be due to some of the additives used to dope the silicone, may be slowed by the presence of the gelatinous structure. After the simulation, the specimen was monitored for a period of 10 days to assess the longevity of the materials used. The specimen was stored at a temperature of 4 °C and checked every 24 h. In particular, the authors wanted to determine the behavior of the filled spheres once covered in gelatin and of the gelatin itself.

After 7 days of monitoring the conclusions that could be drawn were the following:

- The deflation process on the doped silicon spheres after their filling with water and tempera is slowed when they are immersed in gelatin.
- The gelatin has a service life of not more than 7 days due to the shrinkage caused by dehydration. No mold has appeared during the monitoring period. The latter can be therefore not considered a life-limiting agent.

4 Conclusions

Among the limits of the study that the authors are already planning to overcome with a second version, there is the too-marked simplicity of the tracheal model and the not correct realization of the gelatin, the latter due to human error. Authors believe that by developing a precise standard for the realization of the gelatin, its quality can be made less operator-dependent. A potential limitation to this layout is represented by the realization time. The silicone at the base of the developed formula takes 16 h to vulcanize. This can represent a limit, if not for the trachea, surely for the lymph nodes, since a three-step process is required to obtain the hollow spheres. All the steps require both the usage of doped silicone to avoid the compromise of the echogenic properties of the structures and a high level of manual skill and precision. To obtain the empty spheres, three working days are therefore required.

Since it was assessed the tendency for the filled spheres to deflate after a short time, they need to be immediately covered in gelatin after their filling with water and tempera.

Gelatin has to rest at a 4 °C temperature for at least three hours to remain stable even at room temperature and therefore allow the use of the specimen for the simulation.

On the other hand, the specimen has a limited life due to the lymph nodes' shrinkage and the gelatin's dehydration.

All these time boundaries complicate the productive process especially if numerous specimens are required. However, with adequate time management, this limit too can be overcome.

Finally, further investigations concerning the acoustic properties of the materials chosen based on literature will be carried out in the near future.

In conclusion, the proposed specimen represents a good starting point from which to start developing a new advanced version. The obtained results, even if not complete, are interesting, especially regarding the suitability of the developed doping formula to make the silicone respond to US.

References

1. AIOM, et al.: I numeri del cancro 2022. www.medinews.it
2. Mountain, C.F.: Regional lymph node classification for lung cancer staging. Chest **111**(6), 1718–1723 (1997)
3. Sorger, H.: A novel platform for electromagnetic navigated ultrasound bronchoscopy (EBUS). Int. J. Comput. Assist. Radiol. Surg. **11**(8), 1431–1443 (2016)
4. Ling, I.: Endobronchial ultrasound. (2021). https://mforum.com.au/endobronchial-ultrasound/. Accessed 17 Feb 2023
5. Wahidi, M.: Technical aspects of endobronchial ultrasound-guided transbronchial needle aspiration: CHEST guideline and expert panel report. Chest **149**(3), 816–835 (2016)
6. Ishiwata, T.: A novel biosimulator based on ex vivo porcine lungs for training in peripheral tissue sampling using endobronchial ultrasonography with a guide sheath. J. Thorac. Dis. **11**(10), 4152–4158 (2019)
7. Hunt, A.: Low cost anatomically realistic renal biopsy phantoms for interventional radiology trainees. Eur. J. Radiol. **82**(4), 594–600 (2013)
8. Pacioni, A.: Patient-specific ultrasound liver phantom: materials and fabrication method. Int. J. Comput. Assist. Radiol. Surg. **10**(7), 1065–1075 (2015)
9. Maggi, L.E.: Development of silicone-based materials for ultrasound biological phantoms. In: 2009 IEEE International Ultrasonics Symposium, Rome, pp. 1962–1965 (2009)
10. Furferi, R., et al.: 3D printing-based pediatric trainer for ultrasound-guided peripheral venous access. In: Henriques, J., Neves, N., de Carvalho, P. (eds.) XV Mediterranean Conference on Medical and Biological Engineering and Computing – MEDICON 2019. MEDICON 2019. IFMBE Proceedings, vol. 76. Springer, Cham (2020)
11. Smooth-On. https://www.smooth-on.com/products/dragon-skin-30/
12. Santarelli, C., et al.: Preliminary study of a high-fidelity simulator for the management of paediatric tracheal pathologies. In: Rizzi, C., Campana, F., Bici, M., Gherardini, F., Ingrassia, T., Cicconi, P. (eds.) Design Tools and Methods in Industrial Engineering II. ADM 2021. Lecture Notes in Mechanical Engineering. Springer, Cham (2021)
13. Formlabs. https://dental.formlabs.com/it/products/form-3b/. Accessed 17 Feb 2023

Design and Development of Patient-Specific Medical Devices for Maxillofacial Surgery Through 3D Modeling, Topology Optimization, and Additive Manufacturing

Claudio Favi[1(✉)], Enrica Riva[1], Giovanni Fortese[1], and Andrea Varazzani[2]

[1] Department of Engineering and Architecture, Università di Parma, Parco area delle Scienze 181/A, 43124 Parma, Italy
claudio.favi@unipr.it

[2] Department of Maxillofacial Surgery and Facial Plastic Surgery, Lyon Sud Hospital, Hospices Civils de Lyon, Pierre-Bénite, Université Claude Bernard Lyon 1, Lyon, France

Abstract. Additive manufacturing presents unique opportunities for developing patient-specific medical devices and tools in orthognathic surgery. Devices used in maxillofacial surgery present several constraints which refer to the specific characteristics of the patient and the stress conditions that are in place during the surgery. This paper describes an integrated workflow used for the identification, design, optimization, and production of patient-specific devices while promoting synergy among specialists of vastly different backgrounds. Medical specialist interprets Computed Tomography scans with three-dimensional reconstruction of the patient and, supported by a CAD specialist design the required tools to restore the patient functionality. Preliminary tooling designs are checked for strength and stiffness by a structural engineer considering the mechanical properties of the perspective AM materials and passed in digital form to the AM technologist who will be responsible of the 3D printing. The medical specialist uses the devices through physical prototypes to assess effectiveness and usability. The integrated workflow allows to increase accuracy while reducing surgical time and costs.

Keywords: additive manufacturing · topology optimization · orthognathic surgery · reverse engineering

1 Introduction

Additive Manufacturing (AM) and the use of 3D printers has become a daily practice for maxillofacial surgeons [1–3]. AM allows several possibilities in this field including the production of custom-made medical devices (e.g., cutting guides for oncological resections, positioning guide for orthognathic surgery), anatomical models (e.g., cranium prototypes), and various types of surgical simulators [4]. Thanks to the decreasing cost of this technology as well as the spread of machines and equipment, AM has got easy access in many hospitals. AM is usually coupled with the rise of 3D imaging systems

M. Carfagni et al. (Eds.): ADM 2023, LNME, pp. 154–162, 2024.
https://doi.org/10.1007/978-3-031-52075-4_19

that allow the manipulation of data acquired by Computed Tomography (CT) scans or similar equipment [5]. Using a sequence of computerized mathematical algorithms, these data are converted into 3D images of a patient's craniofacial skeleton as well as soft tissues [6]. Advances in 3D imaging technology have resulted in a series of tools designed to provide software systems able to simulate surgery activities, to make a preoperative planning and the manufacture specific devices [7]. These tools are far away from being a full CAD system with limited possibilities in terms of design freedom or customized solutions [8]. Moreover, the engineering process related to the development of customized devices for surgical applications requires the adoption of other design tools such as CAE, and the involvement of other experts in addition to the surgeon [9]. As a result, limitations were observed in the development of patient-specific medical devices in maxillofacial surgeons: (i) limited possibility to create alternative geometries and shapes for new devices based on the surgeon's needs, (ii) difficulty in device testing (mechanical performance) following surgery stress conditions and constraints, and (iii) challenging interactions between different expertise and competencies. The goal of this paper is to give a preliminary and tentative approach to bridge the gap between the needs of maxillofacial surgeons and the skills of materials/mechanical engineers in the development of patient-specific medical devices. The paper provides a first insight regarding the creation of a proper workflow where the outcomes of a certain process, delivered using specific tools/equipment and elaborated by a specialized skill, become the input for other processes where other tools/equipment are involved and different skills are required. The method is based on five steps, and it describes who and where each process is performed, the equipment and tools used, and the outcome of each step. The method allows bringing joining experience and exploiting knowledge of surgeons and engineers making possible the design and fabrication of devices that simplify surgical interventions with the undeniable advantage for the patient, for the surgeon who will be facilitated in the task, and, finally, for the economic bottom line. The development of a novel device was done for a sample of 5 patients with dentofacial deformities who required orthognathic surgery to improve dental occlusion and facial aesthetics. The new device is presented in this work as a case study following the proposed approach and creating a working team involving different expertise at Parma University (from medicine and engineering departments). The overall approach can be replicated in other surgical practices such as oncology, cardiology, traumatology, and bone reconstructions. Finally, one of the main achievements of this research will be the possibility for surgeons to make use of AM for in-house customized device manufacturing, decreasing the overall time from 3D imaging acquisition to surgery, and avoiding the use of external services provided by specialized companies.

2 Materials and Methods

The workflow adopted for the development of the patient-specific medical devices employed in maxillofacial surgery consists of five steps: (i) 3D acquisition of patient bones; (ii) hybrid 3D CAD modelling, (iii) material characterization, (iv) topological optimization, and (v) 3D printing (see Fig. 1). Acquiring the patient's images is the first step in the proposed workflow and is achieved by performing a CT scan (DICOM images). DICOM images work with stacked 2D images that must be segmented to a data format (STL) allowing a 3D representation. The segmentation process to convert a medical imaging CT scan (DICOM file format) to a STL model file is performed at the hospital site with a dedicated tool (i.e., Blueskyplan - https://www.blueskyplan.com/). The software tool automatically sets the threshold for binarization and slicing allowing the medical specialist to perform this task with very limited accuracy errors. After the 3D conversion, file analysis is necessary to pursue three objectives: (i) to analyze the patient's dentofacial deformity, (ii) to simulate the skeletal movements that will be performed in the operating room, and (iii) to evaluate the result obtained. The medical specialist oversees this process, and a dedicated software is used for this purpose (i.e., IPS Case Designer). The expected outcomes of this phase are the following: (i) the STL files of the skeletal portions of the skull once the surgical planning has been performed, (ii) the STL file of standard devices (i.e. the wafer) that are usually employed in this kind of operations [10–12], and (iii) the surgical constraints defined by the medical specialist. Constraints are assessed based on medical specialist experience, considering the type of surgery and the device to develop (e.g., dimensions, forces, visual access).

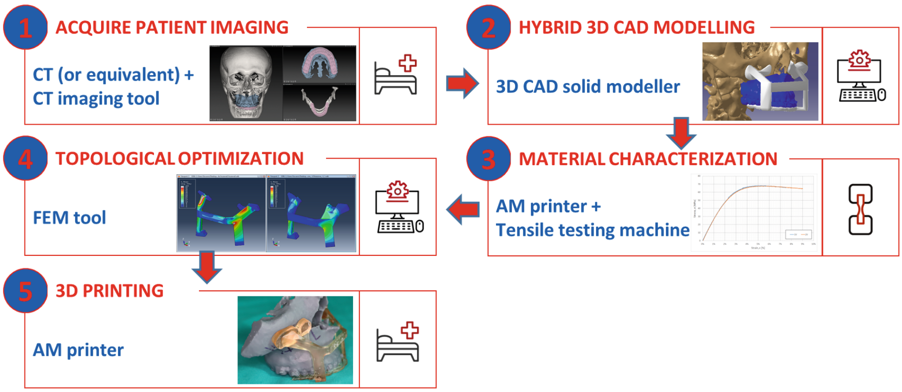

Fig. 1. Methodology workflow.

Hybrid 3D CAD modelling is the second step in the proposed workflow. This activity can be done remotely by a CAD specialist starting from the digital outcomes of the previous step (mesh files). In this case is mandatory to have a hybrid CAD modeler (i.e., CATIA) since both surfaces and solids are necessary to develop the customized device. Indeed, starting from the mesh surface, a closed surface is carried out (which fits with the specific geometry of the patient under analysis) and subsequently transformed into a solid model. Interactions between a CAD specialist and a medical specialist is always necessary to understand the needs of the surgeons during the intervention. Material characterization is the third step in the proposed workflow. This activity needs to be performed by a mechanical engineer or a material specialist by using typical equipment available in a material testing laboratory (e.g., tensile testing machine and/or other testing machines). Usually, a set of limited materials is available (due to conformity and certification in surgical application), and their characterization is mandatory when the employed material is manufactured with the same AM equipment and process parameters, although it can be used for different purposes and devices. This activity leads to the definition of material curve characteristics and the performance in terms of strength, stiffness, elongation, and elastic modulus. Topological optimization is the fourth step in the proposed workflow. This activity makes use of the previous documents such as the material curve characteristic, the CAD file (solid model) of the patient-specific device, and the surgical constraints (forces) to create a compliant FEM model of the system under investigation into a FEM tool. A mechanical engineer is in charge of this process, with the objective to optimize the device geometry by both increasing the mechanical performance and reducing employed material, focusing on: (i) reduction of stresses at every point of the device, at least down below the yield stress of the material (determined from the previous step); (ii) removal of material in low stressed zones and (iii) reduction of expected displacements, to guarantee the device to be sufficiently rigid to define a unique positioning in the space, if required. 3D printing is the final step, and a prototype of the patient-specific device is developed within the hospital facilities where the AM machine is placed.

3 Case Studies

A prospective study was carried out in a group of 5 patients with dentofacial deformities which required orthognathic surgery. All the 5 patients volunteered agreed to the use of their data acquired by CT. It is worth noting that the surgical treatments were done using conventional clinical practice (as described in [1]), which consists in adopting two surgical wafers (intermediate and final) designed by dedicated software for the pre-treatment plan (IPSCaseDesigner® from KLS Martin) and produced by certified manufacturer. The two surgical wafers are used during the surgical process to help reposition osteotomized bony structures with relative references (i.e., jaw and maxilla). The conventional practice shows a few drawbacks: (i) accuracy of the positioning of the upper jaw, especially regarding the anterior height of the face, since this is decided during the operation according to the surgeon's sensitivity and using a movable reference point (lower jaw), (ii) required surgical time, since the replacement of the intermediate wafer with the final wafer in order to perform the lower jaw displacement is necessary during surgery. From the statistical analysis of post-intervention follow-ups, the lack of accuracy can lead to a mismatch of up to 3 mm between the planned and the real reposition of the osteotomized bony structures. Moreover, the adoption of two wafers leads to a long surgical time. These drawbacks can be solved by the development of a patient-specific device that uses skull bone positioning by a fixed space reference (i.e., the portion of skull bone around the infraorbital foramen). The new approach and devices were tested by different approaches including the 3D-printed dummy reproduction of the patient's cranium bones. Concerning the first step (3D acquisition of patient images), patient CTs were performed, and STL models derived from DICOM files were used by a medical specialist to simulate the surgical plan, including osteotomies, repositioning of osteotomized bony structures, control interferences between osteotomized bony structures, as well as to assess the postoperative results. Two digital outcomes originated by this analysis that were transferred to the second step: (i) the STL file of the cranium and the osteotomized maxilla after the surgical planning, and (ii) the STL file of the final wafer. Additional constrains were also reported by the medical specialist such as the position of the anchor plates (i.e., the portion of skull bone around the infraorbital foramen), the overall dimensions of the device to allow surgical operations, and the forces applied to the device during the surgery. In the second step, a CAD specialist imported the two files into a 3D CAD tool for hybrid modelling. Due to the characteristics of the files (i.e., mesh) and the importance of accuracy in surface reconstruction, a hybrid modelling tool is necessary to firstly acquire the surface of the cranium for device positioning/anchoring and, consequently, to develop the solid model of the surgical device. Indeed, after the mesh extrapolation referring to a portion of the cranium for device anchoring, a surface reconstruction was necessary. Starting from the developed surface, a solid model was developed in accordance with the geometrical constraints reported by the surgeon. For orthognathic surgery the proposed devices shall leave to the surgeon the possibility to have access from front and lateral parts and the idea was to create a C-shape device (see Fig. 2). The C-shape device connects the two anchoring plates (attached to the cranium and fixed during the surgery process) to the base of the wafer (reference for maxilla positioning after osteotomies) with two symmetrical brackets. The output of this phase is the 3D CAD model, both the solid one (.stp format) that becomes the input for the topological optimization phase, and the mesh (STL format) that is used by the surgeon to simulate the surgical process.

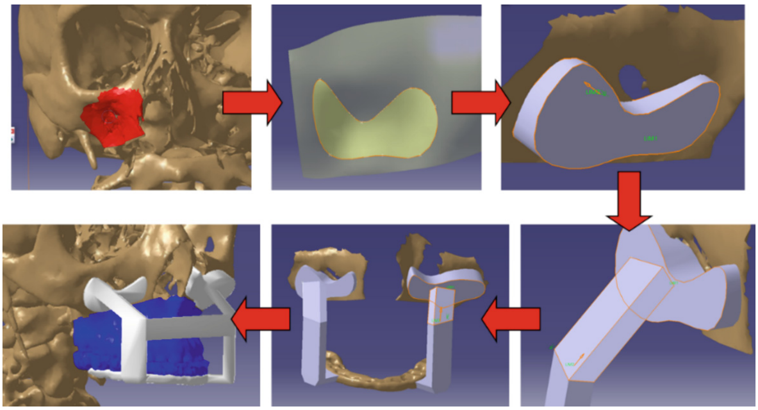

Fig. 2. CAD hybrid modelling for the development of C-shape device.

During the third step mechanical characterization of the material used for the device was carried out. It is worth noting that the material used was compliant with medical application standards and certified to produce medical devices (EN ISO 10993-5; EN ISO 10993-10; ISO 10993-11; ISO 10993-3; EN ISO 13485; EN ISO 14971). For the sake of confidentiality, the commercial name and the mechanical properties of the materials cannot be reported. Dogbones tensile specimens were developed using the same material and the same AM printer (a stereolithography 3D printer), and tensile tests were performed using static tensile testing machine (MTS810), allowing to obtain necessary mechanical parameters. In the fourth step, topological optimization was performed with the aim to reduce stress concentration areas increasing the robustness of the device itself. The following boundary conditions were considered to perform a FEM analysis, in compliance with the constraints provided by the medical specialist within the first step: 5 kg in Y-direction and 1.5 kg in X and Z directions (red areas, see Fig. 3A), while the anchoring plates were considered fixed (green areas, Fig. 3A). In Fig. 3B, Von Mises stress (in MPa) contours before and after topological optimization are shown, highlighting general stress reduction all over the device. It is worth noting that the topological optimization was done by inserting fillets where missing while increasing fillets' radii when the value was too small with the aim to reduce the stress concentration factor (notch effect). Another design change deals with the increment of dimensions for the most critical sections and the inclusion of structural ribs while keeping the design requirements provided by the surgeons.

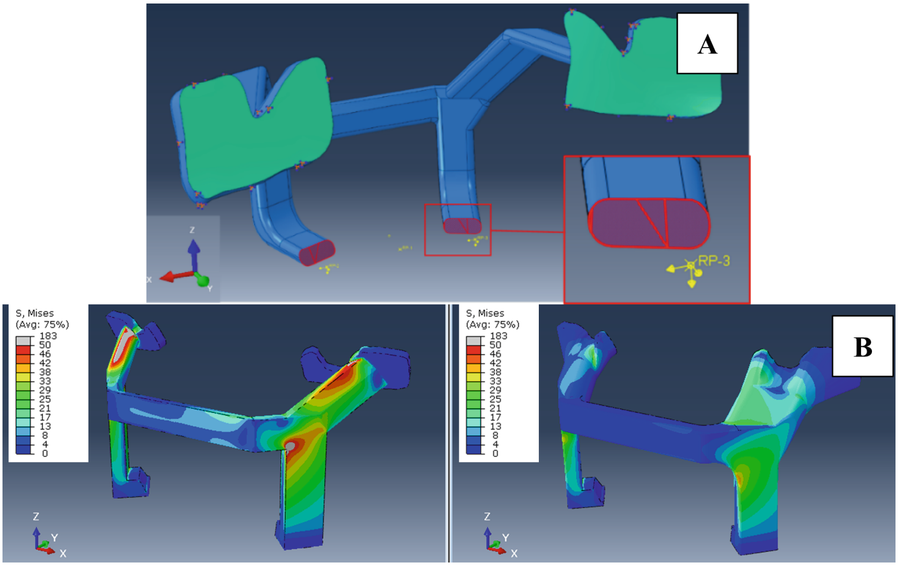

Fig. 3. Boundary conditions (A) and FEM results (Von Mises stress in MPa) before (left) and after (right) topological optimization (B).

The last step concerned the prototype manufacturing using AM printer (Form 3B from Formlabs) and the material characterized in the previous phase. The developed devices were fixed to the cranium prototypes with threaded elements (screws) and removed after the surgery simulation (as reported in Fig. 4).

4 Results and Conclusions

In this present paper, a preliminary approach to bridge the gap between maxillofacial surgeons and mechanical/materials engineering, with the aim to develop optimized devices for orthognathic surgery, has been proposed.

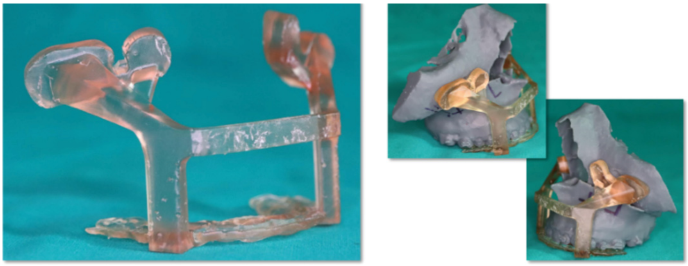

Fig. 4. Prototype of patient-specific device for orthognathic surgery.

The approach consists of five steps encompassing CT imaging, hybrid 3D CAD modelling, material characterization, topological optimization, and 3D printing of device prototypes. The material employed was tensile tested, to determine its mechanical properties by considering the same machinery and process parameters employed for AM printing of the device. Moreover, topological optimization has been performed with the aim to reduce both stresses below the material yield limit and displacements, to ensure a rigid and unique positioning device. At the present time, since the Parma hospital was not yet able to produce certified medical devices (IIa class device in accordance with EU 2017/745 standard), two different methods were employed to test the effectiveness and accuracy of the developed devices:

1. A software-based test using IPS Case Designer. The tool allows to import of the STL files, so the specific device has been overlapped with the patient's bones file with the purpose of visually assessing the accuracy of the fit of the anchoring plates to the skull in the area surrounding the infraorbital nerve.
2. A prototype simulation test with the use of a real bone prototype (more specifically the upper jaw and the portion of the skull up to the orbits and zygomatic bodies) and the patient-specific device (using 3D printed prototypes). The device was positioned to the cranium assessing visually whether the device fell precisely in the area around the infraorbital hole or whether gaps remained. Again, the anchoring plates of the device adhered perfectly and passively to the surface of the model, without having to apply any force.

Concerning accuracy, the proposed device allows a better position of the osteotomized bony structure with a fixed reference (the zone of the skull up to the orbits and zygomatic bodies which are not osteotomized). However, the in-vivo comparison with conventional practice (the use of the two wafers) was not possible since the devices could not be used during the surgery without a certification. By testing the device with the prototype simulation test, the maximum gap measured between the virtual environment and the prototype for the 5 case studies was less than 0.5 mm (one order of magnitude less than conventional practice). Concerning the time, following the surgical experience, the adoption of this device can allow gaining at least 30 min in a surgical intervention which lasts 150 min with a time saving of approx. 20%. This result is mainly due to two reasons: (i) no need to use an intermediate wafer, and (ii) when the device is used, the osteotomized bony structure is self-sustained and it is possible to fix (with screws), at the same time, each side of the device. Statistical analysis of the obtained results will be performed with a larger number of in-vivo evaluations and dedicated surgery practice campaigns (control groups), with the aim to validate the proposed device and its benefits. The present approach can be replicated in other surgical interventions such as oncology, cardiology, traumatology, and bone reconstructions, with the aim to drastically reduce time- and cost-demand for surgery devices, avoiding any external service by exploiting whole-in-house production and development. Additionally, the implementation of a collaborative software platform will lead to real-time access and collaboration streamlining device development and minimizing potential risks. On the other hand, data access and protection (privacy) need to be managed in a proper way especially when the involved actors are not belonging to the same organization.

References

1. Farré-Guasch, E., Wolff, J., Helder, M.N., Schulten, E.A.J.M., Forouzanfar, T., Klein-Nulend, J.: Application of additive manufacturing in oral and maxillofacial surgery. J. Oral Maxillofac. Surg. **73**(12), 2408–2418 (2015)
2. Ghai, S., Sharma, Y., Jain, N., Satpathy, M., Pillai, A.K.: Use of 3-D printing technologies in craniomaxillofacial surgery: a review. Oral Maxillofac. Surg. **22**(3), 249–259 (2018)
3. Lin, H.-H., Lonic, D., Lo, L.-J.: 3D printing in orthognathic surgery - a literature review. J. Formos. Med. Assoc. **117**(7), 547–558 (2018)
4. Matias, M., Zenha, H., Costa, H.: Three-dimensional printing: custom-made implants for craniomaxillofacial reconstructive surgery. Craniomaxillofacial Trauma Reconstruct. **10**(2) (2017)
5. Buonamici, F., Furferi, R., Governi, L., et al.: A practical methodology for computer-aided design of custom 3D printable casts for wrist fractures. Vis. Comput. **36**, 375–390 (2020)
6. Aboul-Hosn Centenero, S., Hernández-Alfaro, F.: 3D planning in orthognathic surgery: CAD/CAM surgical splints and prediction of the soft and hard tissues results - our experience in 16 cases. J. Craniomaxillofac. Surg. **40**(2), 162–168 (2012)
7. Calvo-Haro, J.A., Pascau, J., Mediavilla-Santos, L., et al.: Conceptual evolution of 3D printing in orthopedic surgery and traumatology: from “do it yourself” to “point of care manufacturing.” BMC Musculoskelet. Disord. **22**, 360 (2021)
8. Scolozzi, P.: Computer-aided design and computer-aided modeling (CAD/CAM) generated surgical splints, cutting guides and custom-made implants: Which indications in orthognathic surgery? Rev. Stomatol. Chir. Maxillofac. Chir. Orale. **116**, 343–349 (2015)
9. Chin, S.J., Wilde, F., Neuhaus, M., Schramm, A., Gellrich, N.C., Rana, M.: Accuracy of virtual surgical planning of orthognathic surgery with aid of CAD/CAM fabricated surgical splint-a novel 3D analyzing algorithm. J. Craniomaxillofac. Surg. **45**, 1962–1970 (2017)
10. Zinser, M.J., Sailer, H.F., Ritter, L., Braumann, B., Maegele, M., Zöller, J.E.: A paradigm shift in orthognathic surgery? A comparison of navigation, computer-aided designed/computer-aided manufactured splints, and “classic” intermaxillary splints to surgical transfer of virtual orthognathic planning. J. Oral Maxillofac. Surg. **71**(12), 2151 (2013)

11. Zinser, M.J., Mischkowski, R.A., Sailer, H.F., Zöller, J.E.: Computer-assisted orthognathic surgery: feasibility study using multiple CAD/CAM surgical splints. Oral. Surg. Oral. Med. Oral. Pathol. Oral. Radiol. **113**(5), 673–687 (2012)
12. Pascal, E., Majoufre, C., Bondaz, M., Courtemanche, A., Berger, M., Bouletreau, P.: Current status of surgical planning and transfer methods in orthognathic surgery. J. Stomatol. Oral. Maxillofac. Surg. **119**(3), 245–248 (2018)

Guidelines for Finite Element Modeling of Cell Adhesion Process

Lorenzo Santoro(✉), Luciano Lamberti, Lorenzo Vaiani, Antonio Emmanuele Uva, and Antonio Boccaccio

Department of Mechanics, Mathematics and Management, Polytechnic University of Bari, Via Orabona 4, 70126 Bari, Italy
lorenzo.santoro@poliba.it

Abstract. Cell adhesion is a phenomenon characterizing cell-environment interactions and affects cellular behavior. Cell-substrate adhesion is ensured by focal adhesions (FAs), which are multilayer protein complexes. External mechanical stimulus perceived by FAs is rapidly transmitted first to cytoskeleton load-bearing structures and finally to the nucleus thanks to an interlinked cellular architecture, thus inducing transcription mechanisms and changes in cell functionality. Prestress of cytoskeletal filaments allows mechanical information to be transferred along these stiffer transportation channels with respect to neighboring cell regions, thus avoiding the energy dissipation typical of soft matter. Peculiar items concerning adhesion mechanisms, i.e., stiffness inhomogeneity in cell architecture, and auto-supporting tension-based cell structure, can be effectively handled thanks to modeling strategies provided by finite element method (FEM), which represents a valid tool for simulating cell adhesion. With the aim of replicating experimental results and predicting cell behavior, useful guidelines for simulating cellular adhesion will be outlined in the proposed work.

Keywords: Cell Adhesion · Mechanotransduction · Finite Element Method

1 Introduction to Adhesion Phenomenon and Cellular Mechanotransduction

Cellular adhesion represents a prominent phenomenon which characterizes cell-environment interactions, in particular cell-substrate contact, thus determining key cellular functionalities such as motility and affecting cell life cycle stages like growth, development, and differentiation [1, 2]. Cell adheres to substrate through mature multilayer protein adhesion complexes, i.e., focal adhesions (FAs), which develop from smaller nascent adhesions localized at the GTPase Rac-promoted lamellipodia [3, 4]. Integrins represent the transmembrane components of FAs and are responsible for the cell-matrix binding through the establishment of a high-affinity connection with substrate ligands. The FA intracellular components ensure the link between integrins and cytoskeletal stress fibers, thus allowing cytoskeleton-membrane connection (Fig. 1). Recent studies [5, 6] highlight that cytoskeletal structure interacts with nuclear envelope through the

M. Carfagni et al. (Eds.): ADM 2023, LNME, pp. 163–175, 2024.
https://doi.org/10.1007/978-3-031-52075-4_20

linker of nucleoskeleton and cytoskeleton (LINC) complexes, which are composed of proteins, i.e., nesprin and SUN protein isoforms, that span the nuclear membrane and connect intranuclear architecture to load-bearing cytoskeletal filaments (Fig. 2).

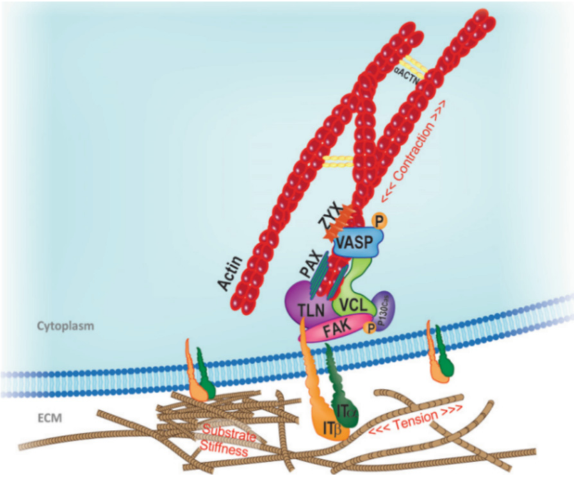

Fig. 1. Schematic representation of focal adhesion (FA). Heterodimeric proteins spanning through the cellular membrane, namely integrins (IT), allow to establish the connection with extracellular matrix (ECM). Integrin cytoplasmatic portion interacts with FA intracellular components (talin, vinculin, paxillin, zyxin, focal adhesion kinase, adaptor protein p130Cas, and vasodilator-stimulated phosphoprotein), which ensure the linking with cytoskeletal bundles of filaments. TLN, talin; VCL, vinculin; PAX, paxillin; ZYX, zyxin; FAK, focal adhesion kinase; VASP, vasodilator-stimulated phosphoprotein. Image reproduced with permission of Ref. [8].

The interlinked configuration involving FAs, cytoskeletal filaments, and nucleus allows FAs to perceive external mechanical stimulus and direct it towards cytoskeleton load-bearing structures, thus transferring mechanical cue to the nucleus as stress wave at a velocity 15 times bigger than chemical diffusion and about 28 times higher than motor-based transportation [5, 7]. In this way cell is able to rapidly transport mechanical information to several intracellular sites simultaneously, thus activating downstream biochemical events.

Forces transmitted to nucleus induce chromatin reorganization, nuclear pores opening, activation of genetic programming, and transcription processes which result in cell adaptation to external stimulus and changing of cell behavior and functionality [8]. The effective transferring of mechanical information towards the nuclear region through cytoskeletal filaments requires the prestress of these transportation channels in order to give rise to stiffer transmission pathways with respect to neighboring cytoskeletal regions, thus avoiding the rapid mechanical energy dissipation which occurs in completely soft materials. Stiffness inhomogeneity in cell architecture and auto-supporting tension-based cell structure, which dynamically evolves through cytoskeletal filaments polymerization and depolymerization, are intrinsic aspects of cellular behavior [9].

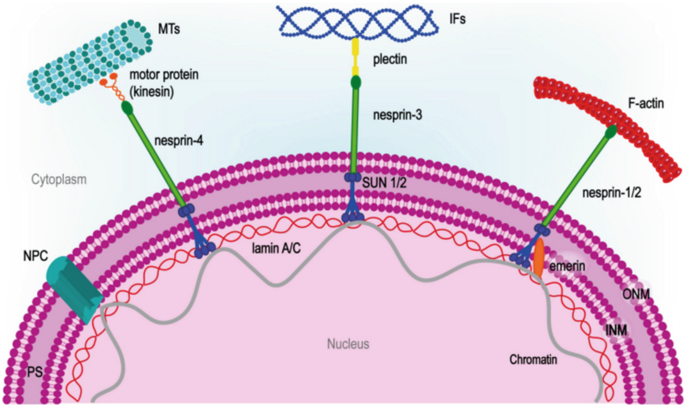

Fig. 2. Schematic representation of LINC complexes connecting cytoskeleton to nucleoskeleton. SUN proteins, spanning the inner nuclear membrane (INM), are linked to nuclear lamina through lamin A and emerin protein. As a result of the interaction of SUN proteins and lamin A with chromatin, mechanical stimulus transferring affects genetic activation and chromatin reorganization. In the perinuclear space (PS) SUN proteins link with nesprin isoforms, which in turn extend outside the outer nuclear membrane (ONM) and are connected to cytoskeletal F-actin, to intermediate filaments (IFs) through plectin, and to microtubules (MTs) through kinesin-1. Nesprin isoforms: nesprin-1/2, nesprin-3, nesprin-4; NPC, nuclear pore complex. Image reproduced with permission of Ref. [8].

Therefore, it is necessary to take into account all these items when a high-fidelity simulation of cellular adhesion mechanisms is required. Finite element method (FEM) is a powerful tool for replicating cellular adhesion phenomena as it provides several instruments to researchers for facing pivotal adhesion issues such as stiffness inhomogeneity, prestress state, and dynamic rearrangement of load-bearing elements. By using modeling strategies like cellular domain partitioning techniques, assignment of differentiated material properties evolving during the analysis, multistep loading procedures, and stress-strain predefined fields, it is possible to implement effective finite element computational frameworks. The present work aims to outline guidelines concerning the wise use of modeling strategies for simulating cell adhesion phenomena in order to replicate experimental results and predict cellular behavior.

2 Physical Models of Cell Adhesion Mechanical Behavior

A key aspect for analyzing the cellular response to external environment interactions is the development of cell physical models capable of describing the cellular behavior under determined assumptions. Once such physical models have been identified by researcher based on the cell type, then they can be implemented in the simulation environment which requires the input of the geometries, material properties, constitutive relations, and boundary conditions derived from the chosen model. The resulting computational framework can then be used to replicate cell response and validate experimental results. Enhancing the simulation complexity level, by taking into account further items of the physical phenomenon in the numerical computation, it is possible to obtain high-fidelity numerical framework which is able to predict cellular behavior with a high degree of result reliability.

The main approaches used to describe cell behavior during adhesion phenomena involve concepts derived from continuum mechanics and fluids mechanics. Cell is considered as a physical entity composed of an interior part, i.e., nucleus, cytoplasm, and cytoskeleton, which is modeled based on cell type by considering viscous fluid theory, elastic or viscoelastic theory, or tension-based architectures characterized by a network of filaments and struts. The interior portion of the cell is enveloped by an elastic membrane or elastic cortex. The choice of the most appropriate constitutive behavior for the intracellular domain and its relative assignment to portions of the cell interior depends on cellular morphology and characteristics. Cells with a well-structured and developed cytoskeleton are differently modeled than those whose mechanical behavior is predominantly affected by the cortex since intracellular components are less structured. For example, white blood and red blood cells present structural dissimilarities with respect to epithelial and endothelial cells, which show a prominent cytoskeleton [10].

With the aim of studying the spreading of chick fibroblasts on glass microplates, Thoumine et al. [11] described the interior part of the cell as a fluid having high viscosity η surrounded by an elastic contractile cortex which bears an isotropic bidimensional tension τ. Authors pointed out that this cellular representation is derived from that proposed for white blood cells, i.e., leukocytes. Moreover, they stated that, similarly to leukocytes, fibroblast during spreading can draw to a reserve of additional surface area arranged in the form of folded plasma membrane. Cortical tension τ is supposed to vary linearly with cell surface expansion through an area expansion modulus K. By developing a theoretical analysis of experimental data, the authors were able to estimate K (order of magnitude 10^{-2} N/m), cortical tension τ, and apparent viscosity η varying from 2×10^4 to 5×10^4 Pa•s. The values of τ, K, and η obtained for fibroblasts are higher with respect to those found for leukocytes due to the different functionalities performed by these two types of cells: unlike leukocytes, which are characterized by a softer structure to move in capillaries, fibroblasts have to sustain connective tissue and carry loads.

Starting from findings of Ref. [11], Frisch et al. [12] applied the wetting theory to define the time evolution of chick fibroblast contact radius during cell spreading on glutaraldehyde-coated glass coverslips. As reported in Ref. [12], cell was represented as a drop of high-viscosity fluid enveloped by an elastic cortex subjected to cortical tension τ (Fig. 3). The proposed approach is characterized by three parameters: the viscosity η of the fluid constituting the core of the cell, the cortical tension τ, and the cell-substrate spreading power w_a, i.e., the energy of adhesion per unit of area. Following the assumptions reported in Ref. [11], the theoretical model assumes that cell morphology during spreading is similar to spherical caps whose shape can be defined by a contact radius R and a contact angle θ. The cell-substrate contact region, which results from the interaction between cellular morphologies resembling spherical caps and the substrate planar conformation, can be assumed as a circular area. Therefore, the contact radius R is derived by evaluating the diameter of the circular contact region resulting from the adhesion process between cell and substrate. The contact angle θ

is defined by the plane tangent to coverslips top surface and the plane tangent to cell external surface passing through the point that in the wetting theory is considered to be the three-phase contact point, that is, the point where the cell free contour meets the substrate (see Fig. 3b). The model proposed by Frisch et al. does not take into consideration the localized variations in cell surface curvature and the local changes in cell contour during spreading. Therefore, the two morphological factors, i.e., the contact radius R and the contact angle θ, are functional to describe the evolution over time of the overall cell morphology at macroscopic level. The experimental measurements of R and θ resulted from the analysis of digital images which were extracted from video acquired by recording the process of cell spreading on the substrate. The monitoring of adhesion process time evolution was executed under bright-field illumination conditions by using the following equipment:

– an inverted microscope (Zeiss, Oberkochen, Germany) provided with a 40×/75 objective and a 1.6× Optovar lens;
– a CCD camera (Cohu Inc., San Diego, CA, USA);
– a memory support for video recording (Sanyo, Japan).

Images extracted from video and digitalized through a Macintosh computer (Apple, CA) show cell morphologies corresponding to several time instants. By rotating the glass substrate on which cell adhesion occurs by 90°, the side view of the cell, that is, the view reported in Fig. 3, can be captured by the CCD camera. Then, digitalized images representing the side view of the cell are processed by the image analysis software NIH Image v1.60, which enables to measure the diameter length of the interaction area and the contact angle θ. Alternatively, an estimate of the contact radius can be also derived from the top view of the cell by projecting the surface area of the cell onto the substrate: the square root of the projected area divided by π returns the contact radius R. The cell retains its original volume during the adhesion process and its shape during spreading derives from the equilibrium between w_a and τ. Under the hypotheses of neglecting cortex surface elasticity and considering τ, η, w_a as constant parameters, the approach developed by Frisch et al. is capable of finding out theoretical curves that approximate the experimental time evolution of contact radius well.

Successful validation of this theoretical approach through experimental data sets the stage for a possible use of the proposed physical model for implementing a finite element framework that could also simulate the stress-strain field induced in the cell, thus providing a more complete analysis of cell behavior during adhesion.

When cells characterized by a more developed cytoskeletal structure than that of blood cells are dealt with, it is useful to model the interior part of the cell by applying continuum mechanics elasticity theory to take into account elasticity effects within the cell. In the finite element (FE) model proposed by Kamm et al. [10] to compute the stress-strain field induced in airway epithelial cells in response to mechanical stimuli, a partitioning of the intracellular region into two solid domains, i.e., nucleus and cytoskeleton, has been carried out. Both nucleus and cytoskeleton were considered as incompressible isotropic linear elastic materials, whose Young's modulus is 1000 Pa and 100 Pa respectively, enveloped by a thin stiffer membrane.

In order to account for nonlinear material behavior, cells can also be modeled as homogeneous hyperelastic media through several strain energy function. Ohayon et al.

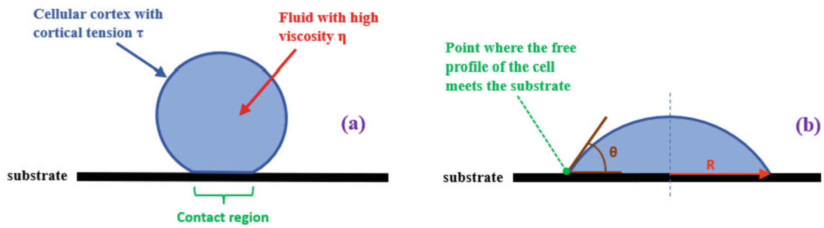

Fig. 3. Representation of the cell as high-viscosity core (light blue) surrounded by a cortex (dark blue) subjected to tension τ. The adhesion between cell and substrate results in a circular contact area. As the schematic representation in figure reports the cell side view, the contact area is identified by the line corresponding to the cell-substrate interaction region. Cell morphology during spreading is defined by contact radius R and contact angle θ. The contact radius R derives from dividing by two the length of the line, i.e., the contact diameter, which defines the interaction between cell and substrate. The contact angle θ corresponds to the angle defined by the plane tangent to the substrate top surface and the plane tangent to cell free surface passing through the point where the cell free surface meets the substrate, i.e., the three-phase contact point defined by the wetting theory. Schematic cell configurations in: **(a)** the early stages of adhesion, i.e., after a few minutes; **(b)** the last stages, i.e., after hours. The cell schematization in **(b)** shows: (i) the contact radius R drawn in orange color, (ii) the contact angle θ and the corresponding planes in dark brown, and (iii) the point where the cell free contour meets the substrate in dark green, i.e., the three-phase contact point defined by the wetting theory.

[13] developed a FE analysis to study the nonlinear behavior of adherent epithelial cells probed by magnetic bead twisting. The incompressible two-parameters Yeoh strain-energy function W was adopted to describe cell hyperelastic response:

$$W = \alpha_1 (I_1 - 3) + \alpha_2 (I_1 - 3)^2 \tag{1}$$

where α_1 and α_2 are material constants related to initial linear elastic behavior and to nonlinear response, respectively. I_1 is the right Cauchy–Green deformation tensor first invariant. The FE model implemented by Jean et al. [14] to simulate endothelial cells adhesion on rigid substrate adopted a neo-Hookean strain-energy function associated with an incompressible behavior:

$$W = C_{10}\left(\lambda_1^2 + \lambda_2^2 + \lambda_3^2 - 3\right) \tag{2}$$

where C_{10} is a constant related to Young's modulus and λ_1, λ_2, λ_3 are the principal stretches. The same material model was also used by Ref. [15]. Zeng et al. [16] simulated stem cell-extracellular matrix adhesion by developing a Lagrangian Meshfree Galerkin method hybridized with a continuum mechanics contact algorithm derived from FE method. In the proposed approach, the cell nucleus and the extracellular matrix were modeled as hyperelastic materials through a modified Mooney–Rivlin formulation characterized by the following strain-energy function:

$$W = C_1\left(I_1 - 3I_3^{1/3}\right) + C_2\left(I_2 - 3I_3^{2/3}\right) + \frac{1}{2}\lambda(\ln I_3)^2 \tag{3}$$

where C_1, C_2, λ are material constants and I_1, I_2, I_3 are the invariants of the right Cauchy–Green deformation tensor. Since stem cell do not have yet a well-structured cytoskeletal architecture, authors assumed that the remaining cellular domain surrounding nucleus is composed mainly of liquid having a low content of filaments. On the basis of this assumption, the cellular region outside nucleus was modeled as a bulk nematic liquid crystal material.

FE implementation of further hyperelastic constitutive relationships was conducted in Ref. [17] and an enhanced hyperelastic formulation which considers also material viscous behavior was presented by Ficarella et al. [18] concerning the study of the equine immature zona pellucida.

Cells that have a well-structured cytoskeleton are characterized by an intracellular network consisting of microfilaments, microtubules, and intermediate filaments embedded in the cytosol, which provides cell stability. In order to take into account the effects of cytoskeletal architecture on cell behavior, Ingber [9] developed the "cellular tensegrity model" that represents the cell as an auto-sustaining prestressed lattice structure which is based on equilibrium between the tensional forces borne by microfilaments (i.e., cables) and the compressive forces carried by microtubules (i.e., struts). Moreover, Ingber stated that the prestress state, which stabilizes the interlinked structure consisting of cables and struts, is induced by actomyosin contractility and focal adhesions-substrate interaction. This cell physical model can be implemented in a FE framework to simulate cells whose behavior is affected by cytoskeleton.

3 Examples of Finite Element Modeling Application to Adhesion Phenomena

The work proposed by McGarry and Prendergast [19] combines the tensegrity approach with continuum one to simulate cell adhesion process. Six idealized cell geometries representing consecutive stages of cellular spreading were modeled by integrating the interlinked cytoskeletal architecture provided by tensegrity (i.e., six struts and twenty-four cables) with other cell components treated as continuum elastic regions (i.e., nucleus, cytoplasm, and membrane). The connection among struts and cables resulted in twelve common nodes (i.e., receptor nodes) whose spatial disposition is rearranged during spreading according to the six configurations in order to redefine the cytoskeleton network morphology (Fig. 4). All six configurations were prestressed by applying an initial strain to microfilaments, and two loading conditions were considered to investigate cell mechanical response (i.e., horizontal force applied to two membrane nodes (letter A in Fig. 4), and vertical forces applied to a neighboring of membrane receptor node (letter B)). Author findings showed a nonlinear strain hardening behavior due to the initial prestress, and differences in compliance along the membrane surface. Moreover, material properties of cytoskeletal network and cytoplasm affected cellular stiffness more than those of nucleus and membrane.

Further FE models accounting for the effects of cytoskeletal filament bundles and focal adhesions on cell behavior were developed in Refs. [14, 20, 21].

FE modeling has also been successfully adopted to study adhesion on nanopatterned substrates in order to investigate surface bactericidal effects [22]. Therefore, a practical implication of FE analysis applied to adhesion phenomena consists in developing and optimizing nanopatterned substrates able to prevent harmful cells proliferation, such as

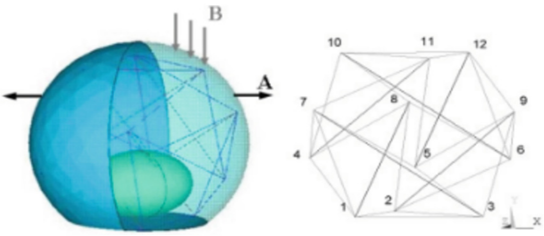

Fig. 4. FE model of cell consisting of membrane (blue), cytoplasm (light blue), nucleus (light green), and cytoskeleton network. Tensegrity network composed by struts (dark lines) and cables (light line) is also represented together with the two loading conditions indicated by letter A and B. Image reproduced with permission of Ref. [19].

bacteria, whose activity leads to infections, diseases, and failure of medical implants. The applications of such studies range over several fields, i.e., from food to medical sector, and aim also to address an important issue represented by the bacterial resistance. By using FE simulation, it is possible to identify the most effective substrate surface conformation capable of killing a specific species of adherent bacteria through the mechanical interaction between surface nanofeatures and bacteria wall. Substrates able to kill bacteria species by mechanical interaction with surface nanostructures allow to limit the use of chemical substances and antimicrobial agents, which contribute to increase the bacterial resistance over time. Moreover, FEM can also be applied to analyze adhesion phenomena in blood vessels (i.e., cancer cell-white blood cell interaction with microvessel morphology variations) [23]. Cancer cells departing from their original sites can move towards other body regions by passing through blood vessel walls and traveling across the circulatory system. During their motion in blood vessels, cancer cells can collide with other cells present in the bloodstream. FE analysis allows researchers to simulate cancer cell movement and the involved adhesion phenomena, thus evaluating the effect of blood vessel morphology on those parameters which characterize the motion of the cancer cell and its interaction with white blood cells (i.e., cancer cell velocity, and shear stress at the interaction region between cancer and white blood cell). Therefore, FE simulations can provide a valuable help in studying tumor cell behavior with the aim of preventing cancer metastasis. Another practical implication of adhesion phenomena FE analysis is proposed by the work of Kamgoué et al. [15] which has estimated correcting functions for the cell apparent Young's modulus measured experimentally by micromanipulation techniques. The correcting functions are able to return the cell intrinsic elastic modulus by taking into account the effect of characteristic parameters (i.e., bead embedding angle, bead radius, and under bead cell thickness) related to the type of probed cell and the experimental technique used for testing. This study allows to explain the discrepancy in cell stiffness shown by experimental data published in literature even when they refer to the same type of cell and the same micromanipulation technique, thus providing a useful tool for enhancing cell mechanical characterization and correctly comparing cell material properties. Finally, the mechanical properties detailed characterization of the ZP membrane in the immature, mature, and fertilized state reported in Refs. [17, 18] assumes a significant applicative relevance as it reveals crucial aspects of the material response to fertilization process. The enhanced knowledge of ZP membrane behavior represents a major step forward in optimizing fertilization procedures as it contributes to develop more efficient protocols.

4 Discussion and Conclusions

FE modeling is a powerful tool for analyzing cellular adhesion phenomena as it is able to replicate the morphology, constitutive behavior, and boundary conditions of the considered cell type. Several model simplification levels can be adopted to save computing time, and researchers can take advantage of model symmetries to reduce computational efforts (i.e., axisymmetry [14, 17], a quarter cell [20, 22]). Cell domain partitioning can be executed to assign constitutive relationships to the major cellular components (i.e., nucleus, cytoplasm, cytoskeleton, membrane). The continuum approach characterized by an isotropic linear elastic modeling allows to describe with good approximation the behavior of cells with a structured internal architecture, i.e., epithelial cells, avoiding nonlinear parameters definition [10]. The 2D isotropic linear elastic model adopted by Kamm et al. [10] has resulted effective in describing airway epithelial cells response to external stimulus resulting from magnetic tweezers. The validity of this modelling strategy is confirmed by the experimental study conducted by Laurent et al. [24], which points out that cells subjected to tweezers micromanipulation exhibit a linear elastic response, while a different cellular response presenting nonlinear behavior is induced by magnetic twisting cytometry. A homogeneous continuum model adopting the neo-Hookean strain-energy function has been implemented in the analysis developed by Kamgoué et al. [15] to define the influence of geometrical parameters, i.e., bead embedding angle, bead radius, and cell heigh, on the cell elastic properties when the cellular material is probed by optical and magnetic tweezers. The 3D model developed in Ref. [15] exploits the symmetry plane passing through the bead center to preserve computational resources. The more complex model architecture compared to that proposed by Kamm et al., i.e., 3D vs 2D, has allowed to accurately estimate the value of cell elastic response correcting functions for several testing configurations. However, Kamgoué et al. highlight that the geometric nonlinearity does not affect the cell response to external stimuli which is characterized by a linear behavior. In particular, repeating numerical simulations by adopting the linear elastic constitutive relationship instead of the neo-Hookean one, the resulting displacement-force curve maintains its linear trend, thus confirming that the linear elastic constitutive model used by Kamm et al. represents a good approximation of cell behavior in response to tweezers micromanipulation. This assumption is no longer valid when adhering epithelial cells are tested by magnetic twisting cytometry (MTC). This micromanipulation technique involves higher bead rotations (in the range 21°–35°) with respect to tweezers micromanipulation, thus inducing large deformation in the cell. This results in a cell strain hardening behavior characterized by an increase in cell stiffness, which differs from the linear cellular response shown in Refs. [10, 15]. Ohayon et al. [13] have successfully replicated the nonlinear experimental rotation-torque curve exhibited during MTC tests by implementing a 3D model which adopts the two-parameters Yeoh strain-energy function, whose material constant α_2 allows to take into consideration the nonlinear effects due to large deformation. The rotation-torque curve derived from numerical simulations using both the Neo-Hookean and the linear elastic constitutive behavior assumes a linear trend which is unable to match the nonlinear experimental curve. On the basis of this evidence, the authors have concluded that the neo-Hookean and linear elastic models are more suitable to analyze micromanipulation techniques involving lower bead deviation angles than those reported for MTC as they induce small deformation in the cell material. Both the numerical frameworks proposed by Ohayon et al. [13] and Kamgoué et al. [15] exploit the same symmetry plane to reduce computational efforts. In general, nucleus Young's modulus is assumed to be about 4 to 10 times greater than cytoplasm-cytoskeleton one, and cell material is assumed to be incompressible or quasi-incompressible [10, 13–15]. The models reported in Refs. [10, 13–15] neglect dissipative and viscous effects within the cellular material as these studies rely on the assumption that material response occurs under quasi-static operating conditions. More accurate constitutive models considering nonlinear elasticity and viscous effects are implemented through hyperelastic strain-energy functions with enhanced formulation [17, 18]. By integrating FE analysis with nonlinear optimization, Boccaccio et al. [17] have been able to find the mechanical properties heterogeneous distribution across the thickness of the bovine zona pellucida (ZP) membrane isolated from fertilized oocytes. An axisymmetric continuum FE framework accounting for large deformation and material nonlinearity was implemented to replicate the force-indentation curve derived experimentally from atomic force microscopy (AFM) nanoindentation tests. Three hyperelastic constitutive relationships, i.e., neo-Hookean (NH), Mooney–Rivilin (MR), and Arruda–Boyce (AB) eight-chain, were compared, and the most accurate matching between experimental and numerical results was obtained by adopting the AB constitutive law in the FE model. The biomechanical hardening exhibited by ZP membrane owing to fertilization is related to the rearrangement of interlinked glycoprotein filaments architecture which shows an increase in the cross-linking junctions density. On the basis of this hardening mechanism, authors state that the AB constitutive relationship, initially developed for describing polymeric networks mechanical behavior, results intrinsically effective in simulating the nonlinear mechanical response of ZP membrane reticulated structure. Ficarella et al. [18] have studied the time-dependency of the response of adherent equine ZP membrane subjected to AFM nanoindentation tests characterized by indentation rates ranging from 0.5 to 10 μm/s, thus overcoming the quasi-static testing condition assumption commonly adopted in AFM experiment simulations. In order to simulate viscous effects induced by indentation rate on the ZP membrane, Ficarella et al. modeled the viscous component of the material behavior by relaxing the hyperelastic material constants given in input to the FE solver through the two-term Prony series expansion. By comparing four hyperelastic constitutive relationships (i.e., MR, NH, AB, and 3rd-order Ogden's law), the implemented axisymmetric continuum FE framework has confirmed that the AB constitutive behavior represents the most appropriate model to describe the ZP membrane response, even when time-dependent viscous effects are taken into consideration. Tensegrity approach describing the cell as a prestressed interlinked network consisting of struts and cables is able to simulate nonlinear strain hardening cellular behavior [19]. By combining tensegrity theory with elastic continuum mechanics, McGarry and Prendergast [19] have developed a numerical framework having a high level of completeness which is capable of evaluating each cellular component contribution (i.e., nucleus, cytoplasm, cytoskeleton, and membrane) to the structural response exhibited by cells during spreading. Furthermore, integrating the cytoskeleton representation provided by tensegrity network with a classical 3D elastic continuum model allows the authors to investigate the effect of (i) actin filaments and microtubules rearrangement, and (ii) prestress state on cell mechanical behavior. The framework has been able to capture the influence of an increasing prestress state on (i) the nonlinear increase in cell stiffness, and (ii) the nonlinear strain hardening mechanism undergone by the cell during deformation. These two aspects, together with the compliance variation along cell surface exhibited when loads are applied at distance from receptors' sites, have confirmed the prominent effect of the cytoskeletal components on cell response. By varying the elastic properties assigned to nucleus, cytoplasm, microfilaments, microtubules, and membrane, the authors have also been able to establish a ranking defining the effect significance of cellular components on cell resistance to deformation. Microtubules followed by microfilaments and cytoplasm have resulted to predominantly affect cell rigidity with respect to the little contribution to cellular stiffness given by nucleus and membrane. Modeling approaches adopting a simplified framework for describing cytoskeletal architecture with respect to that of McGarry and Prendergast have also been proposed [14, 20, 21]. The simplified approaches for the cytoskeleton structure modeling reported in Refs. [14, 20, 21] do not consider the presence of microtubules, which instead represent a cell component that significatively affects the cellular structural response. The major role played by microtubules in cell mechanical behavior has also been highlighted by the work of McGarry and Prendergast: deactivating link elements corresponding to microtubules during simulations results in a drop in cell stiffness. Therefore, the absence of microtubules in simplified models leads to a less accurate simulation of cell response to external stimuli. A further simplification used in Refs. [14, 20, 21] consists in schematizing stress fibers arrangement not as a totally interconnected network of filaments interacting with other through common junction sites like in the tensegrity approach, but by disposing in the basal, apical, and side region of the cell a limited number of fibers (i.e., from 5 to 15) attached to the adhesion sites and the cell surface, which are either partially able to mutually interact [20, 21] or totally isolated [14]. As stated by McGarry and Prendergast [19], cell structural response is mainly guided by cytoskeletal architecture. Therefore, the adopted simplification in cytoskeletal network schematization results in a reduced FE framework capability of returning outcomes as accurate as those provided by models similar to the one reported in Ref. [19]. The change in tensegrity network nodes position deriving from cell deformation underlies another advantage characterizing models which embed tensegrity architecture in cell structure, that is, the FE framework ability to simulate (i) the rearrangement of filaments and microtubules during spreading, and (ii) the alteration in length and orientation exhibited by cytoskeletal filaments owing to actin polymerization and depolymerization process. Moreover, FE modeling allows different physical approaches describing cell structure to be combined, thus resulting in a high-fidelity computational framework. In conclusion, FEM capability to replicate experimental results and predict cell behavior can open up future perspectives about the deep understanding of mechanotransduction process that characterizes cellular response to external stimuli.

References

1. Guilak, F., Cohen, D., Estes, B., Gimble, J., Liedtke, W., Chen, C.: Control of stem cell fate by physical interactions with the extracellular matrix. Cell Stem Cell **5**(1), 17–26 (2009)
2. Engler, A., Sen, S., Sweeney, H., Discher, D.: Matrix elasticity directs stem cell lineage specification. Cell **126**(4), 677–689 (2006)
3. Hoffmann, M., Schwarz, U.: A kinetic model for RNA-interference of focal adhesions. BMC Syst. Biol. **7**(2), 1–18 (2013)
4. Milan, J., Lavenus, S., Pilet, P., Louarn, G., Wendling, S., et al.: Computational model combined with in vitro experiments to analyse mechanotransduction during mesenchymal stem cell adhesion. Eur. Cells Mater. J. **25**, 97–113 (2013)
5. Maurer, M., Lammerding, J.: The driving force: nuclear mechanotransduction in cellular function, fate, and disease. Annu. Rev. Biomed. Eng. **21**, 443–468 (2019)
6. Davidson, P., Cadot, B.: Actin on and around the nucleus. Trends Cell Biol. **31**(3), 211–223 (2021)
7. Wang, N., Tytell, J., Ingber, D.: Mechanotransduction at a distance: mechanically coupling the extracellular matrix with the nucleus. Nat. Rev. Mol. Cell Biol. **10**(1), 75–82 (2009)
8. Martino, F., Perestrelo, A., Vinarský, V., Pagliari, S., Forte, G.: Cellular mechanotransduction: from tension to function. Front. Physiol. **9**, 824, 1–21 (2018)
9. Ingber, D.: Tensegrity I. Cell structure and hierarchical systems biology. J. Cell Sci. **116**(7), 1157–1173 (2003)
10. Kamm, R.D., McVittie, A., Bathe, M.: On the role of continuum models in mechanobiology. In: Casey, J., Bao, G. (eds.) Proceedings of the ASME 2000 International Mechanical Engineering Congress and Exposition. Mechanics in Biology, vol. 242, pp. 1–11. ASME, Orlando (2000)
11. Thoumine, O., Cardoso, O., Meister, J.-J.: Changes in the mechanical properties of fibroblasts during spreading: a micromanipulation study. Eur. Biophys. J. **28**(3), 222–234 (1999)
12. Frisch, T., Thoumine, O.: Predicting the kinetics of cell spreading. J. Biomech. **35**(8), 1137–1141 (2002)
13. Ohayon, J., Tracqui, P., Fodil, R., et al.: Analysis of nonlinear responses of adherent epithelial cells probed by magnetic bead twisting: a finite element model based on a homogenization approach. J. Biomech. Eng. **126**(6), 685–698 (2004)
14. Jean, R.P., Chen, C.S., Spector, A.A.: Finite-element analysis of the adhesion-cytoskeleton-nucleus mechanotransduction pathway during endothelial cell rounding: axisymmetric model. J. Biomech. Eng. **127**(4), 594–600 (2005)
15. Kamgoué, A., Ohayon, J., Tracqui, P.: Estimation of cell Young's modulus of adherent cells probed by optical and magnetic tweezers: influence of cell thickness and bead immersion. J. Biomech. Eng. **129**(4), 523–530 (2007)
16. Zeng, X., Li, S.: Multiscale modeling and simulation of soft adhesion and contact of stem cells. J. Mech. Behav. Biomed. Mater. **4**(2), 180–189 (2011)
17. Boccaccio, A., Frassanito, M.C., Lamberti, L., et al.: Nanoscale characterization of the biomechanical hardening of bovine zona pellucida. J. R. Soc. Interface **9**(76), 2871–2882 (2012)
18. Ficarella, E., Minooei, M., Santoro, L., et al.: Visco-hyperelastic characterization of the equine immature zona pellucida. Materials **14**(5), 1223, 1–15 (2021)
19. McGarry, J.G., Prendergast, P.J.: A three-dimensional finite element model of an adherent eukaryotic cell. Eur. Cell. Mater. **7**, 27–33 (2004)
20. Migliorini, E., Cavalcanti-Adam, E.A., Uva, A.E., Fiorentino, M., et al.: Nanoindentation of mesenchymal stem cells using atomic force microscopy: effect of adhesive cell-substrate structures. Nanotechnology **32**(21), 215706, 1–15 (2021)

21. Vaiani, L., Migliorini, E., et al.:Coarse-grained elastic network modelling: a fast and stable numerical tool to characterize mesenchymal stem cells subjected to AFM nanoindentation measurements. Mater. Sci. Eng. C **121**, 111860, 1–17 (2021)
22. Cui, Q., Liu, T., Li, X., et al.: Validation of the mechano-bactericidal mechanism of nanostructured surfaces with finite element simulation. Colloids Surf. B Biointerfaces **206**, 111929, 1–10 (2021)
23. Khorram, A., Vahidi, B., Ahmadian, B.: Computational analysis of adhesion between a cancer cell and a white blood cell in a bifurcated microvessel. Comput. Methods Prog. Biomed. **186**, 105195, 1–8 (2020).
24. Laurent, V.M., Hénon, S., Planus, E., et al.: Assessment of mechanical properties of adherent living cells by bead micromanipulation: comparison of magnetic twisting cytometry vs optical tweezers. J. Biomech. Eng. **124**(4), 408–421 (2002)

Metrological Protocol for Comparison of Digital and Analogic Articulators for Complete Dentures

Mattia Maltauro[1(✉)], Lorenzo Menarini[2], Roberto Meneghello[1], and Leonardo Ciocca[2]

[1] Department of Management and Engineering, University of Padova, Stradella San Nicola 3, 36100 Vicenza, Italy
mattia.maltauro@phd.unipd.it

[2] Department of Biomedical and Neuromotor Sciences, Alma Mater Studiorum University of Bologna, Via S. Vitale 59, 40125 Bologna, Italy

Abstract. This paper proposes a methodology to compare the trajectories from different articulators - both physical and digital - during lateral and protusive movements. In the case of digital articulators, the articulated models are digitally moved and exported in position; in the case of mechanical articulators, the models are locked into position and 3D scanned. The digital models in position, both digital and scanned, are aligned to a common reference system and a maxilla-based reference system is tracked. The trajectories are defined as interpolating splines through the maxilla-based reference system origins. A Gerber mechanical articulator and an "Artex CR adjustable" virtual articulator were compared. The repeatability of the mechanical trajectory is found to be less than 184 microns. The resting position of the two articulators is found significantly different meaning that a bias is introduced by the operator in the analogic protocol. The trajectories have significantly different shapes as expected coming from two different articulator models. The proposed methodology proved to be a valid means to compare different articulators.

Keywords: Complete Dentures · Articulators · Trajectory Reconstruction · 3D Scanners

1 Introduction

During the last years, CAD-CAM procedures have been introduced in many fields of dentistry, in particular, digital workflows are now used to produce also complete dentures with remarkable advantages: increased biomechanical properties, reduced working times and costs, and fewer appointments at the office [1–4].

Among other digital design tools, digital articulators were introduced aiming to provide an alternative to the current golden standard analogic (mechanical) articulators [5]. A widely used mechanical articulator for the design of complete dentures is the Gerber semi-adjustable articulator, for which a set of specific intermaxillary occlusal

M. Carfagni et al. (Eds.): ADM 2023, LNME, pp. 176–183, 2024.
https://doi.org/10.1007/978-3-031-52075-4_21

registrations, measured from the patient, can be set to approximate a correct occlusion [6].

The use of digital articulators is still not completely independent, and some analogic clinical steps are necessary in digital workflows and cannot be substituted by digital steps so far, for example, the initial impressions, the gothic arch tracing, or the use of a facebow [7]. Nonetheless, the digital protocol allows for fewer steps and, therefore, should concatenate fewer uncertainty sources leading to a better design. Moreover, nowadays, the use of the digital facebow is a promising option for the evolution of such measurements.

There are still not many insights regarding digital articulators in the literature. Some studies looked at the influence of different parameters on the behaviour of digital articulators, such as the vertical dimension [8], or the inclination of the sagittal condylar path [9]. Another study compare the maximum intercuspal between classically articulated casts and digitally articulated ones [10], and the effect of the different settings for the digital articulator was tested on the occlusal morphology of restoration done with CAD/CAM technologies [11]. These results, with some limited disagreements, confirm the virtual articulator as a reliable tool to design denture bases.

However, these studies consider cases of patients with natural teeth; with edentulous cases, it is not trivial to define reliable landmarks on which to base the comparison. Moreover, to the best of our knowledge, there are no studies that specifically investigated if the simulation of occlusion of the digital articulator is comparable to the one from the semi-individual mechanical articulators, specifically for edentulous cases.

To fill this gap, this study aims to provide a methodology to compare the different simulations of occlusion given by different articulators for completely edentulous cases. The comparison is based on the actual trajectory of the casted or digital model during three movements: left and right lateral, and protusive movement. The procedure can work both digital vs analogic, digital vs digital or analogic vs analogic articulators. In this contribution, the comparison between an analogic and a digital articulator is provided.

2 Materials and Methods

The overall workflow used for the study can be seen in Fig. 1. Starting from the same impression and intermaxillary occlusal registrations, obtained from a simulated completely edentulous patient, two parallel clinical workflows are followed, the digital one obtaining the digitally articulated STL models, and the analogic one obtaining the plaster model mounted and articulated in the Gerber articulator.

For both cases, the trajectory of the maxilla is recorded by mapping a reference system built on the maxilla from a second common reference system built on the mandible. The trajectories are then compared to assess whether the twos are the same or are significantly different.

Three different movements are analyzed: left and right lateral and protrusive movements.

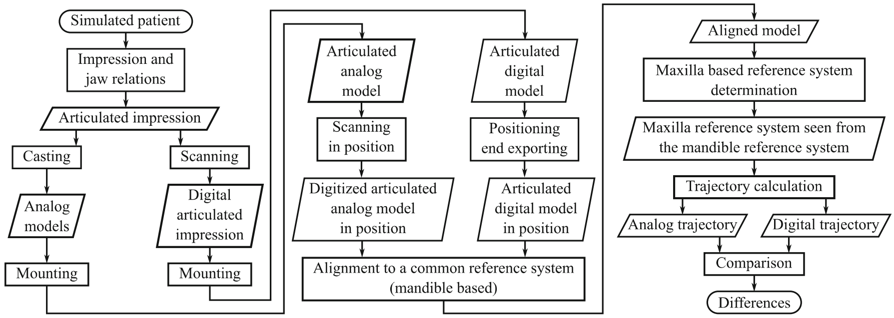

Fig. 1. Overall workflow of the study.

2.1 Clinical Protocol

A completely edentulous patient is simulated using two edentulous plaster models already mounted in a mechanical articulator, considered as the patient's oral cavity. The standard protocol to obtain the final impressions and the intermaxillary occlusal registrations for edentulous patients is followed. The intermaxillary occlusal registrations are set as the clinical average value for all settings, these values are used for both protocols. The final results are the articulated impressions, which were scanned using a E3 scanner obtaining a digital articulated impression used in the digital protocol, and then were cast with type IV plaster obtaining the physical model used in the Gerber articulator. The digital articulator "Artex CR Adjustable" in the Exocad software is used for the digital protocol. The digitally articulated impressions are imported. The software creates the two digital models already in position. The models, together with the digitally articulated impressions are aligned using the information contained in the intermaxillary occlusal registration following the standard clinical protocol. The plaster models are mounted into the Gerber articulator following the standard clinical procedure that involves the separation between the upper and lower impression and their recombination once the mandible model is fixed in position with the use of the face bow. Further details about the clinical protocol and the parameters available in analog and digital articulators can be found in [12].

2.2 Movement Mapping

To map the movement described by the maxilla in the articulator three incremental points were sampled per each movement plus the common resting position. Thus, each movement is characterized by a total of four points.

The digital articulator has no physical end to each movement: the operator can choose whatever displacement value for each movement and the maxilla is moved into position. Once in position, the two digital models can be exported into an STL file. The three incremental points were chosen to be 3mm apart from one another.

The Gerber articulator has a physical endpoint for each movement that is chosen as the last point to be sampled; two intermediate points were then sampled. Once locked in position the articulator was scanned as described in the following.

The scanning procedure is needed since a physical mechanical articulator is considered, Fig. 2. Since the two casted models are close to each other, it is impossible to acquire the actual oral cavity.

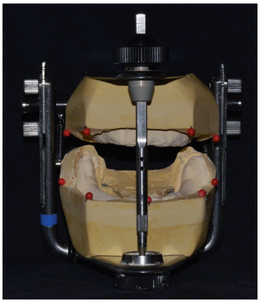

Fig. 2. Gerber articulator ready to be scanned.

To address this issue, a strategy commonly used with oral scanners is used: the two models are individually scanned, and then the articulated models are scanned obtaining mainly the external surface which is used to correctly align the individual scans. Five spherical landmarks were added to each model to increase the alignment accuracy.

To test the reproducibility of the workflow applied to the physical articulator, each position was scanned ten times, thus obtaining ten trajectories.

To compare the two articulators the same reference system was established on the mandibular model and the position of the articulated maxilla model was tracked through the position of three fixed points reconstructing the rigid body trajectory of the simulated occlusion. The three points define a cartesian reference system.

Starting from the digital models, two simplified bases were defined and three spherical markers were added, Fig. 3. The CAD reference system of the lower base was used as a common reference system for the comparison, therefore the scanned model or the exported model were first aligned to this base in GOM Inspect obtaining the aligned model that was exported.

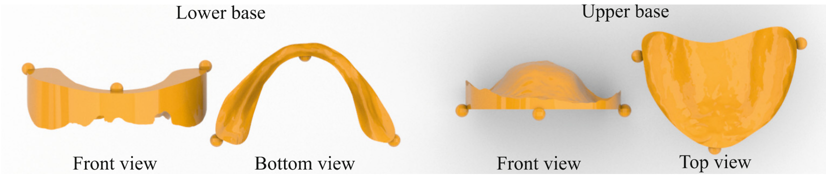

Fig. 3. Simplified bases with markers.

At this point, each newly exported model shares the same origin and orientation. This file is imported in GOM Inspect and the upper base is aligned to the mucosa. The locations of the three spheres are recorded and elaborated in Excel to define the maxilla-based reference system. The origin is defined as the centroid of the spheres, the x-y plane as the plane through the spheres, and the x-axis point towards the central sphere and z-axis pointing upwards.

This procedure was performed per each sampled point in the analogic and digital protocol. The trajectories are calculated in a mathematical graphical tool: GeoGebra. This tool was chosen since it allows real-time testing and modification of the procedure. The details of the maxilla-based reference systems were imported into the 3D space and the trajectories are defined as cubic interpolating splines through the origins. For the digital articulator, only one repetition was done since the exporting is by definition perfectly repeatable. At the same time, the scanning procedure of the mechanical articulator introduces variability due to the 3D Scan itself and due to the alignment. For this reason, the Gerber articulator was mapped ten times to determine the repeatability.

Among the ten trajectories derived from the mechanical articulator, the average trajectory had to be defined to define the repeatability. The intermediate points that were sampled cannot be considered repeatable because of the uncertainty in the looking of the articulator, but the length of the trajectory is theoretically the same. Therefore, congruent points along the trajectories were defined as points at the same percentual distance from the resting position, and points at 0%, 30%, 60%, 90%, and 100% of the trajectory length were sampled. The average trajectory was defined by averaging the position of these points. The dispersion of the mechanical articulator is defined by the distance of each trajectory to the average one, the distance is defined, point by point, in the plane normal to the average trajectories, Fig. 4.

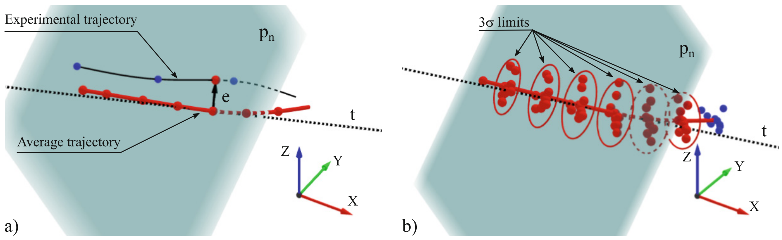

Fig. 4. Analog trajectories error definition (a) and dispersion (b).

The dispersion was sampled at steps of 15% of the average trajectory length excluding the resting position. Assuming a bivariate normal distribution with the same dispersion in each direction for the sampled trajectories, and therefore a Rayleigh distribution for the distances (radial component), the standard deviation of the bivariate distribution is defined by:

$$\sigma = \sqrt{\frac{2}{\pi}} \frac{\sum_{i=1}^{n} d_i}{n}$$

The dispersion of the resting position is divided into two contributions. For the lateral movement, the aforementioned formula is applied to the projection of the resting position point into the sagittal plane (lateral plane, x-z); for the protusive movement, the projection into the frontal plane (y-z) is considered instead.

2.3 Movement Comparison

The differences between the digital and analogic trajectories are defined by the distance between the average analogic trajectory - including its dispersion - and the digital one. Since the analogic trajectory ended up being shorter than the digital one, it was used as the baseline.

First, the baseline error, define as the distance between the resting positions is calculated and represents the initial bias between the two trajectories.

The digital trajectory is translated of the quantity defined as the baseline error to check for differences excluding the initial bias.

The distance between the two trajectories is calculated at steps of 15% of the analogic trajectory as the distance in the plane normal to the baseline trajectory.

3 Results and Discussion

Regarding the mechanical articulator, the ten trajectories that were sampled and the average trajectory, with its associated standard deviation, can be seen in Fig. 5a). The repeatability test, applied to the mechanical articulator, shows a maximum standard deviation of 184 microns for the left lateral movement, see Fig. 5b).

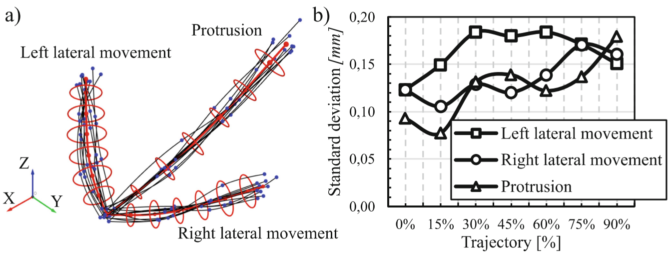

Fig. 5. Result of the ten trajectories sampled with the Gerber articulator (black lines), the average trajectories (red lines), and the standard deviation along the three movements.

The reparability of the rest position is 123 microns in the sagittal plane and 93 microns in the frontal plane. On average the repeatability decrease (higher standard deviation) the further from the resting position; indeed the locking in position adds a level of uncertainty to the procedure.

The comparison between the two articulators' trajectories can be seen in Fig. 6a). At first glance, the difference in length between the two trajectories can be noted. Nonetheless, this does not imply an actual difference because the shorter trajectory can still represent the first part of the longest one.

The first real difference that can be recorded is the initial bias between the two articulators, the resting positions are 1,373 mm apart. Considering the dispersion of the resting position for the mechanical articulator this difference is considered significant. This means the bias is not due to the measuring uncertainty but is based on an actual difference. The reason behind this deviation can be traced back to the analogic clinical protocol when the articulated impressions need to be separated for the alignment in the Gerber articulator. Maxillary and mandibular casts are then fixed again thanks to the gothic arch plates and the bite registration during the clinical protocol. This step may introduce a shift between the two impressions therefore it is the main candidate to explain the bias.

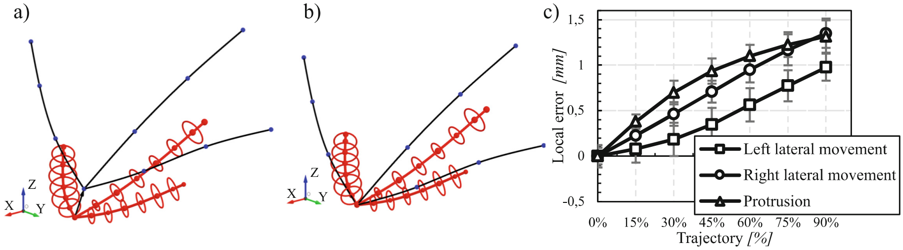

Fig. 6. Comparison between the analogic and digital trajectories.

To evaluate the actual differences between the two trajectories, excluding the bias, the digital trajectories are rigidly translated to share the same resting position with analogic ones, Fig. 6b). Comparing the two trajectories, taking into consideration the standard deviation associated with the analogic trajectory, it can be said that the trajectories are significantly different. The local error along the trajectories can be seen in Fig. 6c).

The local error increase as the distance from the resting position increase meaning that the two trajectories diverge. Looking at Fig. 6b) it can be seen that this divergence is not due to an alignment issue but it come from the trajectories having different shapes; for instance, the mechanical articulator has a shallow angle between the two lateral movement when compared to the digital one. The maximum recorded difference is 1.350 mm for the right lateral movement.

It must be noted that this study does not want to conclude that any of the tested articulators is better than the other. Differences were expected since the type of articulators is different. The same protocol may be used to check whether a digital articulator simulating a specific mechanical model and the actual physical counterpart coincide.

4 Conclusions

This paper aims to propose a methodology to compare the dynamic movements of different articulators used in dentistry. The methodology is designed having in mind to give the possibility to compare mechanical vs mechanical, mechanical vs digital, and digital vs digital articulators. To prove its usability the methodology was tested by comparing a mechanical articulator (Gerber) to a digital one (Artex CR Adjustable" in the Exocad). Therefore differences were expected.

As expected significant differences were found proving the overall methodology to be a valid means to compare different articulators. A far more interesting comparison for future works will be the study of corresponding digital and mechanical articulators to test whether the digital articulator can provide a precise replica of the, so far, standard clinical procedure based on mechanical articulators.

The late development of digital face bows capable of tracking the actual 3D jaw movement of the patient without any approximation (needed using an articulator both digital or mechanical based on a set of values) opens the possibility to compare the actual patient movements to the one approximated by the articulators.

Further studies will also be necessary to automate the procedure and test a clinically significant population to provide clinicians with useful data to improve dentures design.

References

1. Baba, N.Z., Goodacre, B.J., Goodacre, C.J., Müller, F., Wagner, S.: CAD/CAM complete denture systems and physical properties: a review of the literature. J. Prosthodont. **30**, 113–124 (2021). https://doi.org/10.1111/jopr.13243
2. Goodacre, B.J., Goodacre, C.J., Baba, N.Z., Kattadiyil, M.T.: Comparison of denture tooth movement between CAD-CAM and conventional fabrication techniques. J. Prosthet. Dent. **119**, 108–115 (2018). https://doi.org/10.1016/j.prosdent.2017.02.009
3. Srinivasan, M., Cantin, Y., Mehl, A., Gjengedal, H., Müller, F., Schimmel, M.: CAD/CAM milled removable complete dentures: an in vitro evaluation of trueness. Clin. Oral Invest. **21**, 2007–2019 (2017). https://doi.org/10.1007/s00784-016-1989-7
4. AlHelal, A., AlRumaih, H.S., Kattadiyil, M.T., Baba, N.Z., Goodacre, C.J.: Comparison of retention between maxillary milled and conventional denture bases: a clinical study. J. Prosthet. Dent. **117**, 233–238 (2017). https://doi.org/10.1016/j.prosdent.2016.08.007
5. Bisler, A., Bockholt, U., Kordass, B., Suchan, M., Voss, G.: The virtual articulator. Int. J. Comput. Dent. **5**, 101–106 (2002)
6. White, G.E.: The Gerber articulator and system of full denture construction. Dent. Tech. **26**, 12–20 (1973)
7. Úry, E., Fornai, C., Weber, G.W.: Accuracy of transferring analog dental casts to a virtual articulator. J. Prosthet. Dent. **123**, 305–313 (2020). https://doi.org/10.1016/j.prosdent.2018.12.019
8. Lee, H., Burkhardt, F., Fehmer, V., Sailer, I.: Accuracy of Vertical Dimension Augmentation Using Different Digital Methods Compared To A Clinical Situation-A Pilot Study. Int. J. Prosthodont. **33**, 380–385 (2020). https://doi.org/10.11607/ijp.6402
9. Hsu, M.R., Driscoll, C.F., Romberg, E., Masri, R.: Accuracy of dynamic virtual articulation: trueness and precision. J. Prosthodont. **28**, 436–443 (2019). https://doi.org/10.1111/jopr.13035
10. Arslan, Y., Bankoğlu Güngör, M., Karakoca Nemli, S., Kökdoğan Boyacı, B., Aydın, C.: Comparison of maximum intercuspal contacts of articulated casts and virtual casts requiring posterior fixed partial dentures. J. Prosthodont. **26**, 594–598 (2017). https://doi.org/10.1111/jopr.12439
11. Olthoff, L., Meijer, I., de Ruiter, W., Bosman, F., van der Zel, J.: Effect of virtual articulator settings on occlusal morphology of CAD/CAM restorations. Int. J. Comput. Dent. **10**, 171–185 (2007)
12. Goldstein, G., Goodacre, C.: Selecting a virtual articulator: an analysis of the factors available with mechanical articulators and their potential need for inclusion with virtual articulators. J. Prosthodont. **32**, 10–17 (2023). https://doi.org/10.1111/jopr.13517

A Methodology for the Dimensional and Mechanical Analysis of Surgical Guides

Federico Salerno(✉), Sandro Moos, Luca Ulrich, Andrea Novaresio, and Enrico Vezzetti

Department of Management and Production Engineering, Politecnico di Torino, C.so Duca degli Abruzzi, 24, 10129 Turin, Italy
{federico.salerno,sandro.moos,luca.ulrich,andrea.novaresio, enrico.vezzetti}@polito.it

Abstract. The use of CAD and 3D printing of surgical guides (SGs) for osteotomies is a widely developed practice in orthopaedic surgery, and particularly in maxillo-facial interventions, but validation studies rarely occur in literature. The present study defines a methodology to validate SGs dimensionally and mechanically through geometrical analysis, tensile testing, contact simulations, and abrasion testing. Distortions between the 3D printed SGs and the CAD model are quantified and an average deviation error for each production process step is obtained. Mechanical analysis identifies a way of applying the load on the SG to measure their equivalent linear stiffness (N/mm), maximum displacement (mm) and corresponding tolerable load (N) by varying some dimensional parameters. The stress state was assessed by finite element method (FEM) analysis, then the numerical results were compared with experimental ones using tensile tests: stiffness, maximum displacement and the corresponding loads were evaluated. The distribution of contact pressure on soft tissues was obtained numerically by FEM analysis. Finally, an ad hoc machine has been specially built to engrave discoidal specimens with typical operating room conditions. The methodology has been validated using 11 SG fibular and mandibular specimens and reporting the obtained results of each procedure step.

Keywords: Surgical guides · Cutting guides · Maxillo-facial surgery · CAD · FEM

1 Introduction

Orthopedic surgery often requires performing precise cuts in bone tissue, such as the removal of bone tissue tumors [14], bone flaps distraction [3], and repositioning [13]. In maxillo-facial surgery, the accuracy and precision of osteotomies are critical for proper execution of the surgery [8], as well as for the patient's aesthetics [5].

M. Carfagni et al. (Eds.): ADM 2023, LNME, pp. 184–193, 2024.
https://doi.org/10.1007/978-3-031-52075-4_22

Within Virtual surgical planning (VSP) a 3D anatomical model is built from the CT data using appropriate medical segmentation software. Surgical guides (SGs) are patient-specific tools that are fixed to patient's bone through special screws and are used to guide the cutting tool performing the osteotomies [4,17]. To guarantee a proper outcome the SGs must satisfy many requirements such as the dimensional discrepancies between the CAD model and the 3D printed SGs must be limited, the material must bear external forces, tightening torque [10,16] and abrasive cutting action [11]. Also SGs should evenly apply a pressure distribution over the underlying tissues to avoid damage.

This paper aims to address the design challenges by presenting an integrated methodology to validate SGs accordingly to various aspects of EU regulations. EU Regulation 2017/745, Annex I, Chapter II "Requirements regarding design and manufacture" requires tolerance and tensile analyses, EU Regulation 2017/745 Article 61 and Annex XIV requires contact pressure simulations, and EU Regulation 2017/745, Annex I, Chapter II requires abrasion testing.

SG geometrical analysis are not a novelty in the literature [6,15], especially regarding bio-compatible materials and their properties [7]. In this work the dimensional control is aimed to evaluate how tolerances evolve through the various production stages performing tests carried out numerically and experimentally.

The abrasion resistance of the SGs must be evaluated, because a piezoelectric vibrating blade is used to perform osteotomies [12]. In the literature there are several articles about abrasion tests (ASTM G65) on polymeric materials [9], but the methodology here presented evaluates the abrasion resistance of the SGs in the operating room working conditions.

2 Materials and Methods

Geometry: the effects of the various processes over the real geometry are estimated through a dimensional analysis, identifying the following four temporal instants: T1, CAD models of SGs; T2, SGs after 3D printing; T3, SGs after full polymerization by UV rays; T4, SGs after sterilization. T3 can be skipped for polymers that are not photosensitive.

Geometric tolerances and *datum* reference frames (DRFs) are identified on the CAD model accordingly to Fig. 1. The 3D printed part is scanned and the triangulated point cloud is aligned with the CAD model to assess deviations. T2, T3 and T4 triangulated point clouds are compared to the T1 CAD model in order to evaluate how the geometry evolves during production steps. The distance of all the points of the surface to be checked from the counterpart of the CAD model was evaluated to measure the profile tolerances. For each SG, the tolerances T_i in Fig. 1 are measured at T2, T3, and T4. Calling n the total number of T_i for each SG, the average tolerance AT for each instant is calculated as follows:

$$\mathrm{AT} = \frac{\sum_{i=1}^{n} \mathrm{T}_i}{n} \tag{1}$$

For the sake of clarity, an overall average tolerance (OAT) value is calculated by considering the T2, T3, and T4 time points, in order to obtain a comprehensive measure of the tolerance caused by each production step. Calling m the total number of SG, OAT value is calculated as follows:

$$\mathrm{OAT} = \frac{\sum_{j=1}^{m} \mathrm{AT}_j}{m} \tag{2}$$

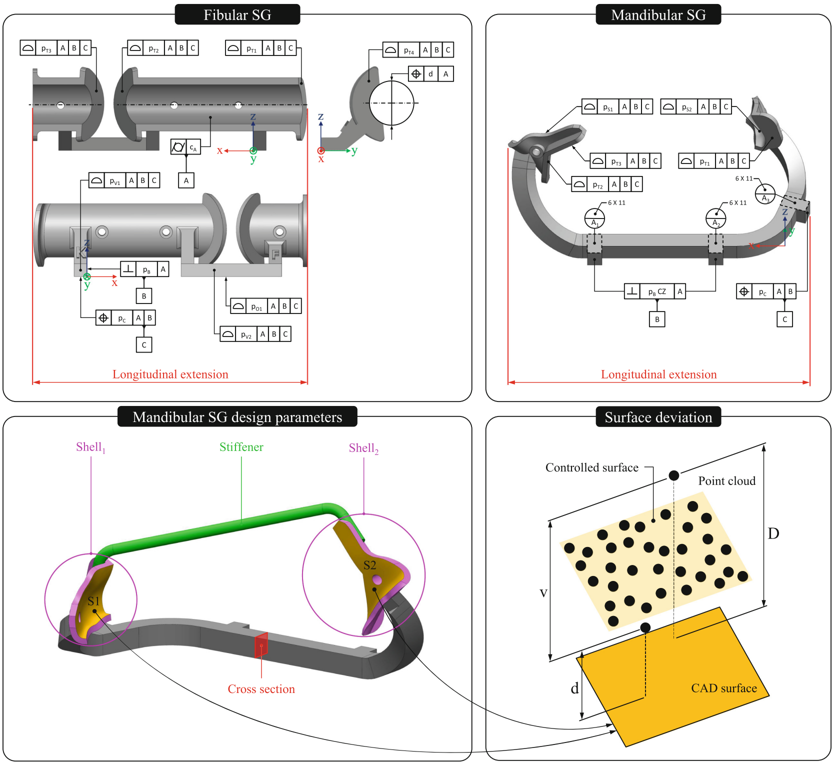

Fig. 1. DRFs, geometric tolerances T_i to be inspected and surface deviations. Fibular SG on the top-left and mandibular SG on the top-right. On the bottom-left, design parameters of mandibular SG are shown and on the bottom right, a scheme of surface deviations dev_{S1} and dev_{S2} is provided, where D is the maximum signed distance, d is the minimum signed one, while v is the maximum variation of distance between points of scanned surface and CAD counterpart

Furthermore, deviations in shell-bone adhesion surface, denoted as dev_{S1} and dev_{S2}, are compared among three different design variants applied to mandibular SGs: 1) without an additional stiffener connecting the two shells, 2) with a stiffener, and 3) with the stiffener removed after T4. Additionally, the first variant includes three different cross-section values, namely 6×6 mm, 7×7 mm, and 8×8 mm. To measure the deviations, the distance of all the points of the surface to be checked from the counterpart of the CAD model are evaluated. Calling D the maximum distance, d the minimum one, and m the mean of the distances, surface deviations are calculated as follows (Fig. 1 right):

$$dev_{S1}, dev_{S2} = m \pm \frac{v}{2}, \text{ where: } v = \begin{cases} D & \text{if } D, d \geq 0 \\ D - d & \text{if } D \geq 0 \text{and } d \leq 0 \\ d & \text{if } D, d \leq 0 \end{cases} \tag{3}$$

Stress field: given the complex geometry of the SGs it is necessary a FEM simulation to calculate the material tensile field when subjected to external forces under operative conditions. A virtual tensile test is simulated and the results are compared to a real physical test for the validation. The FEM simulation precisely reproduces the tensile test setup: each end of the SG is connected to the respective clamp of the traction machine through a chain of 4 elements. The first is a 3D printed PLA interface element that replicates the SG support surface, the second is a connecting bolt to rigidly connect the SGs with the interface, the third is a steel plate that connects the clamp to the interface, while the fourth is a steel pin thanks to which the interface is hinged to the plate. Specifically, the bolts are modeled as "beam elements" and an axial preload of 300 N is applied to simulate the bolt effect. The steel plate is clenched in the vise of the testing machine. The layout, the traction axis and the mechanical constraints are identified as in Fig. 2.

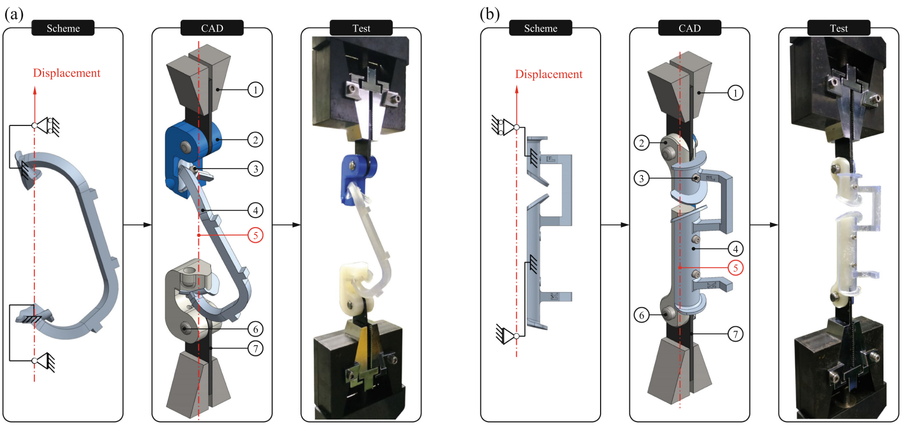

Fig. 2. Mechanical resistance test for mandibular (a) and fibular (b) SGs. (1) clamps, (2) interface, (3) threaded connection, (4) SG, (5) traction virtual axis, (6) steel pin and (7) steel plate.

The deformation rate of the virtual simulation is equal to that one of the real test. Von Mises stress field and force reactions at vise constraints are evaluated.

Finally, the engineering stress-strain curves of the virtual and physical simulation are compared to validate the FEM model.

Contact Pressure on Soft Tissue: For safety reasons, clinicians typically strive to preserve a thin layer of soft tissue surrounding the bone, where the SGs will be attached. This practice helps prevent bone tissue necrosis. The geometry is characterized as a set of three overlapped layers where the topmost is the surgical guide shell, the underlying layer is soft tissue and the lowest layer is bone tissue, with the geometry that conforms to the patient anatomy.

Soft tissue is characterized as a linear isotropic elastic material, according to Aloy at al. (2017) [1], with Young's modulus equal to 12 MPa, while bone is defined as linear isotropic elastic material with a Young modulus of 2.1 GPa and a breaking load of 14 MPa, according to Zerdzicki et al. (2021) [18]. Contact constraints between layers are inserted: bonded contacts are used to simulate the interaction between the bone and soft tissues. The contact interaction between SGs and soft tissue allows reciprocal sliding and distancing, setting 0.1 as friction coefficient. To simulate continuity with the surrounding material while reducing computational complexity, a superficial stiffness distribution (Ansys elastic foundation stiffness (EFS)) is set around both the soft and bone tissue with the following parameters: $EFS_{\text{Soft tissue}} = 0.04\,\text{N/mm}^3$ and $EFS_{\text{Bone tissue}} = 7.71\,\text{N/mm}^3$. Finally a preload of 50 N is applied to each threaded connection. The pressure map in the contact regions between SGs and soft tissue is then calculated.

Abrasion: the proposed method involves the construction of an *ad hoc* machine (Fig. 3). The machine consists of a wooden base with two vertical steel cylindrical guides, a slider mounted on these guides, and a stepper motor NEMA 17 42-34 affixed to the base, capable of Y-axis movement via a rail. The motor shaft accommodates Discoidal Clear V1 biomed samples. Custom components were developed with Solidworks CAD and 3D printed on a Prusa i3 MK3s using PLA. To lower sliding friction, linear bearings are utilized. An Aesculap GBL30R surgical piezoelectric handpiece, equipped with a blade, is attached to the slider. A vertical metal plate, connected to the guides by a crossbar, enhances the structure's stiffness. The handpiece and blade, along with the slider and bearings, form a movable assembly. A dynamometer and an adjustable mass counterweight are connected to this assembly via two rotating pulleys and a wire. The load on the sample, labeled as P, can be increased by reducing the mass of the counterweight. When the counterweight mass balances the moving assembly, $P = 0\,\text{g}$. The dynamometer allows direct reading of the counterweight value. Positioned at a 15° angle to the Z axis, the handpiece and blade favor material abrasion while mitigating the stick-slip effect.

The test procedure involves the following steps: 1) specimen initial mass measurement, m_i; 2) P calibration by adjusting the counterweight mass; 3) motor activation at constant rotation speed $n = 30\,\text{rpm}$ and simultaneous handpiece activation to make the blade vibrate; 4) handpiece and motor are stopped after a predefined number of revolutions; 5) specimen is removed and its final mass m_f is measured. The tests were repeated four times, increasing P, on two specimens

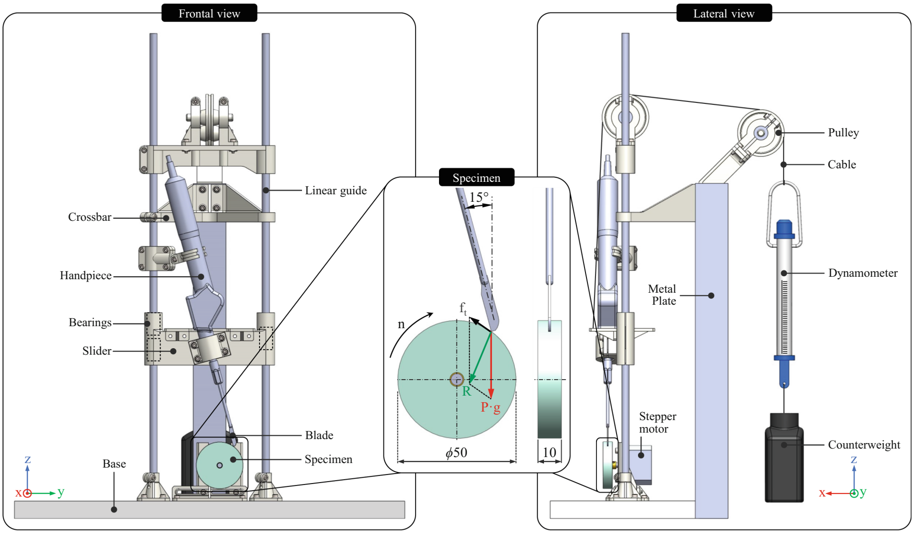

Fig. 3. Abrasion testing machine: a frontal view (left) and a later one (right); the central detail shows the blade tilt, forces between blade and specimen and the dimensions of the latter.

each, measuring the mass reduction. The abrasion coefficient a is defined by Eq. (4), while the material removal rate (MRR) by Eq. (5), where t is the abrasion time ($t = 12\,\text{s}$):

$$a = \frac{m_i - m_f}{m_i} \cdot 100 \qquad (4) \qquad\qquad \text{MRR} = \frac{m_i - m_f}{t} \qquad (5)$$

3 Results and Discussion

A review of literature and commercial sources lead to six materials, biocompatible, compliant to the EN ISO Standards 10993 and 18562 for class IIa applications. The one selected for the present tests is Formlabs BioMed Clear printed using Formlabs 3B+ SLA printer.

The dimensional analysis comprised 11 SG specimens, 5 fibular and 6 mandibular. The sterilization process lasted 20 min at 134 °C and 30 min at 121 °C.

In the left graph of Fig. 4, bars represent AT values, while the longitudinal extensions are represented by blue markers for both fibular and mandibular SGs. OAT in T2, T3 and T4 is 0.70 mm, 0.67 mm and 0.96 mm, respectively. By performing a one-tailed Student's t-test and assuming a significance level of 0.05, p-values are calculated. There is a significant difference between T3 and T4 ($p = 0.0007$), but not between T2 and T3 ($p = 0.3041$). Furthermore, for both fibular and surgical SG, there is a significant correlation between longitudinal extension and average tolerance in T4 ($p = 0.0023$ for fibular and $p < 0.0001$ for surgical SG). Deviations dev_{S2} of mandibular SG has a peak with 7×7 mm cross section: $m = 3.89$ mm and $v = 14.16$ mm. Conversely, by inserting and removing the bridge dev_{S2} is equal to 0.27 mm and 3.32 mm for m and v, respectively (Fig. 4 right). Results show that removing the support bridge after sterilization is preferable to increase the cross-sectional area of the handle section and, consequently, enhance the dimensional stability.

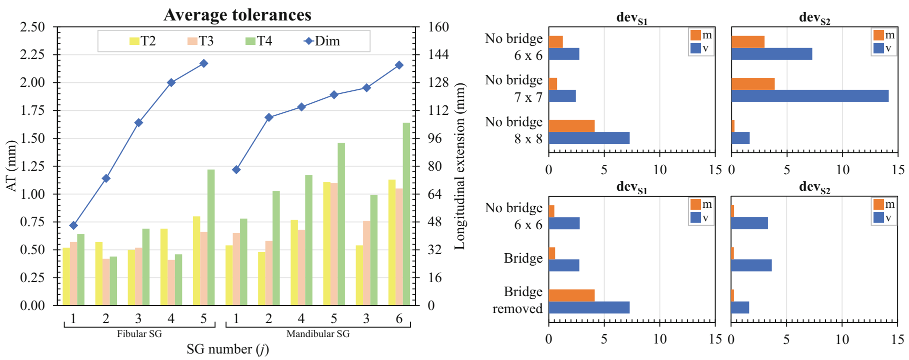

Fig. 4. Left: average tolerances AV and longitudinal extension (mm) for fibular and mandibular SGs at T2, T3 and T4 instants; Right: m and v values of surface deviations dev_{S1} and dev_{S2} by varying design parameters.

The mechanical evaluation was performed on mandibular SG variants with a cross sections of 6×6 mm, 7×7 mm, 8×8 mm and one fibular SG.

As for the simulations, a FEM analysis using the software ANSYS Workbench was performed. A total of 16 specimens were tested: 5 for SG 6×6 mm, 3 for SG 7×7 mm, 3 for SG 8×8 mm and 5 for fibular SG. The tensile test, force-displacement curves for both experimental and numerical tests are shown in Fig. 5.

As we could expect a proportional correlation within mean experimental stiffness values and cross section size was found. The curves match appropriately before the ultimate tensile strength (UTS) declared by the supplier (52 MPa), so it is possible to validate FEM analysis under that load limit. Moreover, graphs of Fig. 5 show that the material is able to sustain higher loads. With respect to contact pressure field on soft tissues, mandibular SG has a peak pressure of 0.47 MPa which falls between the two holes (Fig. 6 top-left). On the other hand, in the fibular SG, the maximum pressure amounts to 0.156 MPa (Fig. 6 bottom-left). These results can be considered safe for the patient according to the literature [2]. Figure 6 show $a - P$ and $\mathrm{MRR} - P$ correlations: a varies between 0.023 % and 0.033 % by adjusting P from 225 g to 325 g. The corresponding MRR for the latter load values are 0.032 g/min and 0.045 g/min, respectively.

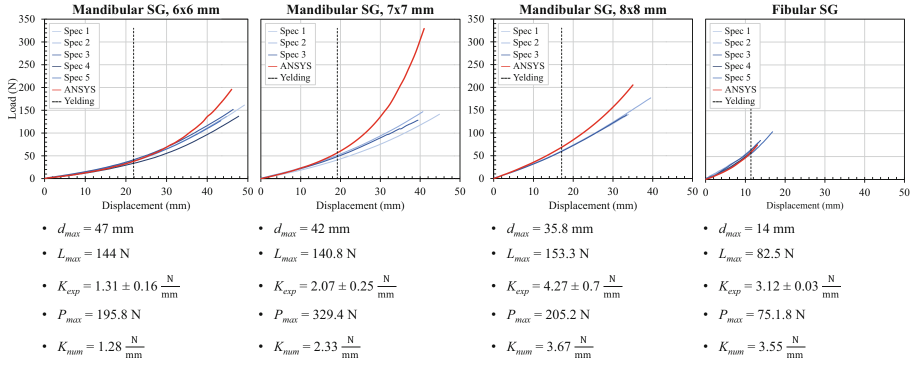

Fig. 5. Experimental (blue) and numerical (red) force-displacement curves obtained from both tensile test and ANSYS Workbench simulations. d_{max}: elongation at break L_{max}: numerical load corresponding to the elongation at fracture K_{exp}: experimental linear stiffness P_{max}: experimental load corresponding to the elongation at fracture K_{num}: numerical linear stiffness .

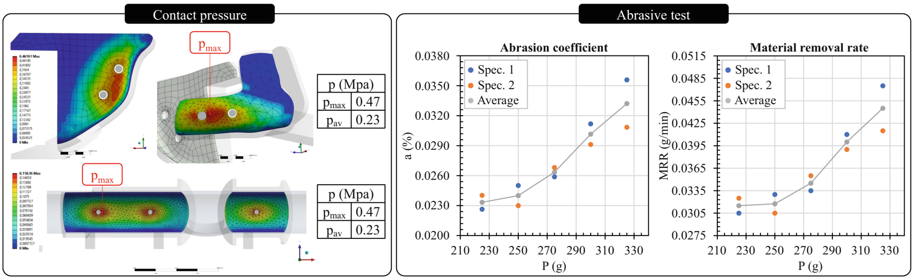

Fig. 6. Contact pressure and abrasion test results. (left): pressure distribution on contact surface caused by SG fixation on the patient, on the top mandibular SG and on the bottom fibular SG; (right): $a - P$ and MRR $- P$ correlations, where a is the abrasion coefficient, MRR is the removal material rate and P is the load on the sample.

4 Conclusions and Future Works

In conclusion, we proposed a methodology for the quality control of CAD-modeled and SLA 3D-printed surgical guides for maxillo-facial surgery. Through tolerance analysis, tensile testing, contact simulations, and abrasion testing, we evaluated both the geometric and mechanical properties of SGs. Our study found that sterilization was the main source of dimensional distortion and that changing design parameters could improve both the dimensional stability and the stiffness of SGs. Furthermore, we found that the maximum pressure on mandibular and fibular SGs during tensile testing was safe for patients. Finally, our abrasion testing methodology aimed to predict the abrasion resistance of SGs using the same instrument as in the operating room. Although our work has some limitations, it provides a valuable contribution to the quality control of SGs and highlights the need for further research in characterizing the plastic behavior of surgical guide polymers. The future work should be focused on addressing the following limitations: more specimens for each type of SG should be tested in order to carry out statistical evaluations; further resources should be allocated to characterize the resin through a campaign of tensile tests on unified samples; our study assumed that soft and bone tissues were isotropic and elastic materials without considering nonlinear behavior.

References

1. Aloy, M.A., et al.: Estimation of the mechanical properties of the eye through the study of its vibrational modes. PLoS ONE **12**(9), e0183892 (2017). https://doi.org/10.1371/journal.pone.0183892, publisher: Public Library of Science
2. Annaidh, A.N., Bruyere, K., Destrade, M., Gilchrist, M.D., Ottenio, M.: Characterising the anisotropic mechanical properties of excised human skin. J. Mech. Behav. Biomed. Mater. **5**(1), 139–148 (2012). https://doi.org/10.1016/j.jmbbm.2011.08.016. arXiv:1302.3022 [cond-mat, physics:physics, q-bio]
3. Gülses, A., Sencimen, M., Ayna, M., Gierloff, M., Açil, Y.: Distraction histogenesis of the maxillofacial region. Oral Maxillofac. Surg. **19**(3), 221–228 (2015). https://doi.org/10.1007/s10006-015-0495-4
4. Guariento, L., Buonamici, F., Marzola, A., Furferi, R., Volpe, Y.: A semi-automatic CAD procedure to design custom-made surgical cutting guides. Comput.-Aided Des. Appl. **19**, 733–740 (2021). https://doi.org/10.14733/cadaps.2022.733-740
5. Li, B., Zhang, L., Sun, H., Yuan, J., Shen, S.G., Wang, X.: A novel method of computer aided orthognathic surgery using individual CAD/CAM templates: a combination of osteotomy and repositioning guides. Br. J. Oral Maxillofac. Surg. **51**(8), e239–e244 (2013). https://doi.org/10.1016/j.bjoms.2013.03.007
6. Marei, H.F., Alshaia, A., Alarifi, S., Almasoud, N., Abdelhady, A.: Effect of steam heat sterilization on the accuracy of 3D printed surgical guides. Implant Dent. **28**(4), 372–377 (2019). https://doi.org/10.1097/ID.0000000000000908
7. Mullaveettil, F.N., Dauksevicius, R., Wakjira, Y.: Strength and elastic properties of 3D printed PVDF-based parts for lightweight biomedical applications. J. Mech. Behav. Biomed. Mater. **120**, 104603 (2021). https://doi.org/10.1016/j.jmbbm.2021.104603
8. Oka, K., et al.: Accuracy of corrective osteotomy using a custom-designed device based on a novel computer simulation system. J. Orthop. Sci. **16**(1), 85–92 (2011). https://doi.org/10.1007/s00776-010-0020-4
9. Pejaković, V., Jisa, R., Franek, F.: Abrasion resistance of selected commercially available polymer materials. Journal.fi, June 2014
10. Pop, S.I., Dudescu, M., Mihali, S.G., Păcurar, M., Bratu, D.C.: Effects of disinfection and steam sterilization on the mechanical properties of 3D SLA- and DLP-printed surgical guides for orthodontic implant placement. Polymers **14**(10), 2107 (2022). https://doi.org/10.3390/polym14102107, number: 10 Publisher: Multidisciplinary Digital Publishing Institute
11. Ray, S., Rout, A., Sahoo, A.: A comparative analysis of the abrasion wear characteristics of industrial wastes filled glass/polyester composites based on the design of experiment and neural network. Polym. Compos. **42**(1), 424–438 (2021). https://doi.org/10.1002/pc.25836

12. Robiony, M., Polini, F., Costa, F., Vercellotti, T., Politi, M.: Piezoelectric bone cutting in multipiece maxillary osteotomies. J. Oral Maxillofac. Surg. **62**(6), 759–761 (2004). https://doi.org/10.1016/j.joms.2004.01.010
13. Samaha, C.J., Tannous, H.J., Salman, D., Ghafari, J.G., Amatoury, J.: Role of surgical hyoid bone repositioning in modifying upper airway collapsibility. Frontiers in Physiology 13 (2022)
14. Schulze, M., et al.: Complex bone tumors of the trunk-the role of 3D printing and navigation in tumor orthopedics: a case series and review of the literature. J. Personalized Med. **11**(6), 517 (2021). https://doi.org/10.3390/jpm11060517
15. Stumpel, L.J.: Deformation of stereolithographically produced surgical guides: an observational case series report: deformation of stereolithographically produced surgical guides. Clin. Implant Dent. Relat. Res. **14**(3), 442–453 (2012). https://doi.org/10.1111/j.1708-8208.2010.00268.x
16. Tilton, M., Lewis, G.S., Bok Wee, H., Armstrong, A., Hast, M.W., Manogharan, G.: Additive manufacturing of fracture fixation implants: Design, material characterization, biomechanical modeling and experimentation. Addit. Manuf. **33**, 101137 (2020). https://doi.org/10.1016/j.addma.2020.101137
17. Ulrich, L., et al.: A procedure for cutting guides design in maxillofacial surgery: a case-study. In: Cavas-Martínez, F., Eynard, B., Fernández Cañavate, F.J., Fernández-Pacheco, D.G., Morer, P., Nigrelli, V. (eds.) Advances on Mechanics, Design Engineering and Manufacturing II. LNME, pp. 301–310. Springer, Cham (2019). https://doi.org/10.1007/978-3-030-12346-8_30
18. Zerdzicki, K., Lemski, P., Klosowski, P., Skorek, A., Trzebiatowski, M.Z., Koberda, M.: Tensile modulus of human orbital wall bones cut in sagittal and coronal planes. PLOS ONE **16**(11), e0259363 (2021). https://doi.org/10.1371/journal.pone.0259363, publisher: Public Library of Science

Short Overview on Trans-Septal Puncture Phantoms Materials and Manufacturing Technologies

Tommaso Stomaci(✉) and Francesco Buonamici

Department of Industrial Engineering, University of Florence, via di Santa Marta 3, 50139 Florence, Italy
{tommaso.stomaci,francesco.buonamici}@unifi.it

Abstract. The growing cooperation between physicians and engineers have been producing increasingly sophisticated anatomical phantoms for the training and planning of Structural Heart Surgery. Trans-Septal Puncture (TP) is a percutaneous, non-invasive cardio chirurgical procedure used to access the heart Left Atrium from the Right Atrium through the Fossa Ovalis (FO), a region of the Inter Atrial Septum with reduced thickness. TP is technically challenging and requires dedicated teaching and a skillful operator; as a result, application of phantoms to TP training have been gaining increasing interest. The aim of the present work is to investigate the current state of the art in TP simulators. The Scopus and PubMed databases were analyzed and the bibliography of the most impacting articles was reviewed. The results can be summarized as follows: i) mold casting and additive manufacturing (AM) are the only technologies documented for phantoms creation; ii) silicone rubbers and Polyvinyl Alcohol Cryogel are the most used materials for mold casting while Polyjet polymers are the most used material for AM; iii) quantitative data on force and haptic feedback from IAS and FO simulacra is scarcely documented; iv) procedure image guidance can be simulated during the training.

Keywords: Trans-Septal Puncture · Additive Manufacturing · Material Characterization · Silicone Casting · Medical Phantoms

1 Introduction

Trans-Septal Puncture (TP) is a non-invasive, percutaneous procedure consisting in the introduction a catheter in the heart Left Atrium (LA) through the Fossa Ovalis (FO), an anatomical region of the Inter Atrial Septum (IAS) with reduced thickness. The steps of the procedure are depicted in Fig. 1. The catheter, made of a dilatator and a sheath, is inserted in the femoral vein at the groin and advanced though the patient's venous circulation system to the Right Atrium (RA). Real time guidance of the catheter path is assured through Fluoroscopy, Intra Cardiac Echography (ICE) or Trans-Esophageal Echography (TEE). Image guidance and surgeon haptic feedback are used to locate the FO in the IAS. Once the FO is located, a delicate push, named tenting, is performed, then a needle is advanced through the catheter, piercing the FO. Finally the dilatator

M. Carfagni et al. (Eds.): ADM 2023, LNME, pp. 194–202, 2024.
https://doi.org/10.1007/978-3-031-52075-4_23

and the sheath are advanced through the puncture, completing the procedure [1–3]. TP is performed in various Structural Heart Surgery (SHS) interventions (Fig. 2): Transcatheter Mitral Valve Repair (TMVR), Left Atrium Appendage Occlusion (LAAO) and Transcatheter Aortic Valve Replacement (TAVR) [4–6] are applicative examples of this technique. All of the aforementioned interventions require different puncture locations on the FO to guarantee the needed positioning of the catheter in the LA [5, 7]. TP training for new operators is performed on actual patients under mentor's control and shows a steep learning curve [8]; hence the risk of causing dangerous clinical complications such as cardiac perforation or pericardial effusion is not neglectable [9]. In the latest years, the growing cooperation between engineers and physicians, opened new possibilities in teaching, counselling, training and planning of surgical procedures through the use of Additive Manufacturing (AM) and 3D models reconstructed from patients diagnostic images [10–13]. In particular the rehearsal on anatomically accurate, tissue-mimicking phantoms have been emerging as a teaching and training opportunity especially in the Structural Heart Surgery (SHS) field interventions [14–16] and TP. The aim of this article is to review the current state of the art of TP simulators and training devices.

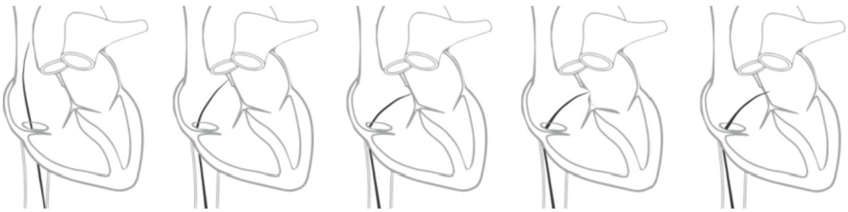

Fig. 1. TP Traditional Technique [2].

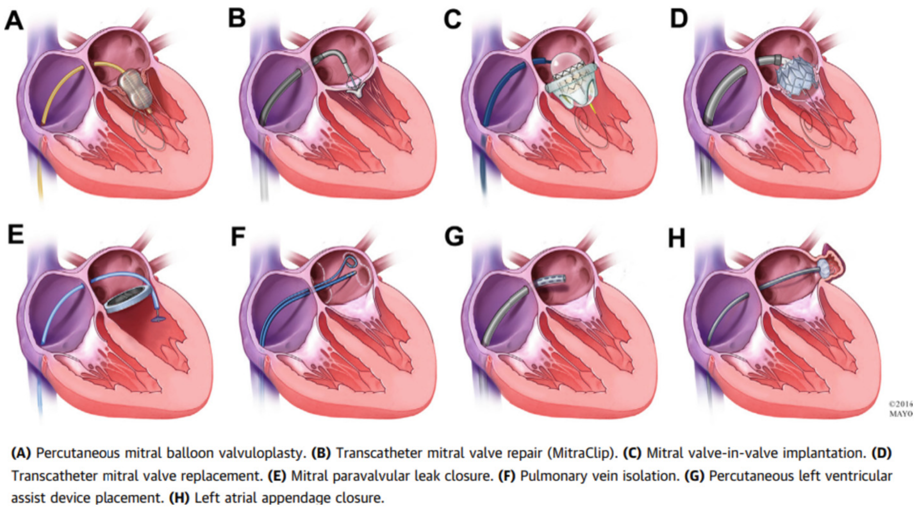

Fig. 2. Transcatheter Intracardiac Interventions involving TP [5].

2 Methods

The review was conducted by searching the Scopus and PubMed databases up to the end of January 2023 using the keywords "trans-septal puncture", "cardiovascular disease", "Fossa ovalis", "Atrium", "3D printing", "additive manufacturing", "casting", "molding", "phantom", "training", and "tissue-mimicking". Boolean operators "AND" and "OR" were used to combine the different keywords to restrict the research field. Different spellings for "Trans-septal" and "molding"/"moulding" were used sequentially to avoid loss of results. Only articles in English were considered.

The inclusion criteria for the articles were: i) description of TP phantoms realization or description of performed TP on cardiac models used for other SHS procedures and ii) characterization of synthetic materials for TP phantoms manufacturing. Articles describing cardiovascular procedures in which simulation of the TP was not reported were excluded from the literature review.

3 Results

The literature research returned 75 different articles. An initial abstract screening was followed by a deep reading of relevant articles. The screening phases brought the total to 8 articles whose content was considered valuable for the present work. The publications span from 2017 to 2021, showing the growing interest in the subject in the latest years. The selected works [17–24] are resumed in Table 1.

Table 1. Reviewed Articles Details

First Author	Publication Year	Source
Lang J. et al	2017	Progress in Biomedical Optics and Imaging
Morais P. et al	2017	Medical Physics
Bezek L. et al	2020	Journal of the Mechanical Behavior of Biomedical Materials
Zimmerman J.M. et al	2020	Catheterization and Cardiovascular Interventions
James R.C	2020	Journal of Invasive Cardiology
Wang S. et al	2020	3D Printing and Additive Manufacturing
Thompson N.A et al	2021	Proceedings of the 2021 Design of Medical Devices Conference
Zimmermann J.M. et al	2021	Cardiovascular Engineering and Technology

Technical data on simulator manufacturing extracted from each of the relevant articles are presented in Table 2. The main imaging technology used for the atrial geometry reconstruction is the Computed Tomography (CT), which was used in 5 articles; in addition, fusion of Magnetic Resonance Imaging (MRI) and CT is reported in 2 cases. Stand-alone MRI is reported in 1 article. Image resolution and voxel size are reported only for 3 articles [17–19].

Of the reviewed papers, 2 reconstructed the LA and the RA anatomies [17, 18]; Inferior Vena Cava, RA and FO were considered in 3 articles [20–22] and 4 chambers heart models were created in 2 articles [19, 23]. In a further work [24] the authors recreated functional specimen of the FO and a 4 chamber model of the heart after material characterization.

The literature review highlights that Silicone Casting (5/8 articles) is the main technological process used for the manufacturing of TP simulation phantoms. The casting moulds are usually created with AM manufacturing technologies starting from a CT image. The direct use of AM for IAS and FO phantoms is reported in 3 out of 8 articles, with Stratasys Polyjet Material Jetting (MJ) being the printing process of choice for both cases (Fig. 3). Fused Deposition Moulding (FDM) is reported as an alternative process. Lastly, the use of Selective Laser Sintering (SLS) with a powder bed machine is reported in 1 article to create the rigid simulacrum of the atrii.

The most used materials for casting are silicone with Shore hardness of 00–30 [18] or 00–50 and Polyvinyl Alcohol (PVA) [20] cryogel or hydrogel; a combination of Polyethylene glycol and TangoPlus is the material used for the Polyjet prints [19, 24]. Poro-Lay flexible filament is reported as the material used for the FDM prints [19]. Lastly, an example of general purpose office tape is documented to represent the FO in an atrium model realized with unspecified sintered rigid polymeric materials [23]. Direct mechanical test of the phantoms materials and comparison with the FO literature Young modulus and puncture force values is presented only in 1 of the 8 reviewed articles [24].

Surgeon feedback was used as qualitative assessment for the simulation experience, considering experience immersion [23] and haptic feedback of the FO in two articles [21, 22]. Dimensional assessment through medical imaging was performed in 3 different articles [17–19]. Evaluation of the simulacra under Ultrasound imaging is performed in 2 articles [17, 19]. Moreover, in [19] the authors furtherly evaluated their phantom under 2D X rays, Cone Beam CT and MRI. Fluoroscopy was simulated in 3 out of 8 different articles [20–22]. TEE was simulated in 2 different articles [21, 22]. Intra Cardiac Echography (ICE) was simulated in 1 article [20]. A Virtual Reality environment was used in 1 article to recreate TP operative conditions [23]. None of the reviewed articles presented a simulation of the blood pressure pulse.

4 Discussion

Literature analysis shows that the most used diagnostic imaging technique for the creation of TP simulators is CT, followed by MRI. Different matrix and voxel size are reported, suggesting that no literature-based evidence on the optimal parameters for image acquisition exists. Phantom creation relies heavily on AM technologies, both for direct creation of the heart models or for the tooling of silicone molds. In particular MJ

Table 2. Reviewed Articles Technical Data

First Author	Imaging Source	Manufacturing Technology	Phantom Materials	Image Guidance Simulation	Simulator and Phantom Validations
Lang J. et al	CT; Voxel size: 0.5 × 0.5 × 0.625 mm	Casting	Smooth-On Ecoflex 0–30; PVA-Cryogel	No	Dimensional Check using CT
Morais P. et al	CT; Isotropic voxel size: 0.4 mm; Matrix size: 512 × 512 × 96; Slice thickness: 1 mm	Casting	Silicone HB FLEX 5513 A + B Mowiol PVA-Cryogel	No	Dimensional Check using CT; US Transparency Check
Bezek L. et al	CT	AM (MJ)	CF and TangoPlus	No	Tension/Compression Tests; Puncture Test
Zimmerman J.M. et al	MRI + CT Fused Images	Casting	Silicone and PVA Hydrogel combination	Fluoroscopy and TEE	Qualitative Physician Haptic Evaluation
James R.C	MRI	AM (SLS)	Atrii: unspecified rigid plastic FO: General Purpose Office Tape,	VR and Fluoroscopy	-
Wang S. et al	CT; Isotropic voxel size: 1 mm; Matrix size: 512 × 549 × 519	AM (MJ and FDM)	Poro-Lay(FDM) TangoPlus(MJ)	No	Multi-Modal Imaging 2D US, 2D X-ray, CT and MRI-
Thompson N.A et al	CT	Casting	Atrii: EcoFlex 00–50: FO: Unspecified flexible materials	ICE	FO Tenting under puncture test
Zimmermann J.M. et al	MRI + CT Fused Images	Casting	Silicone Rubber and Rigid PLA	Fluoroscopy and TEE	Qualitative Physician Haptic Evaluation

technology seems to be the most promising technology for this application, due to the possible simultaneous usage of different materials which allows tailored stiffness in the print. No cost evaluation of the different technologies for the creation of the atrii or of the

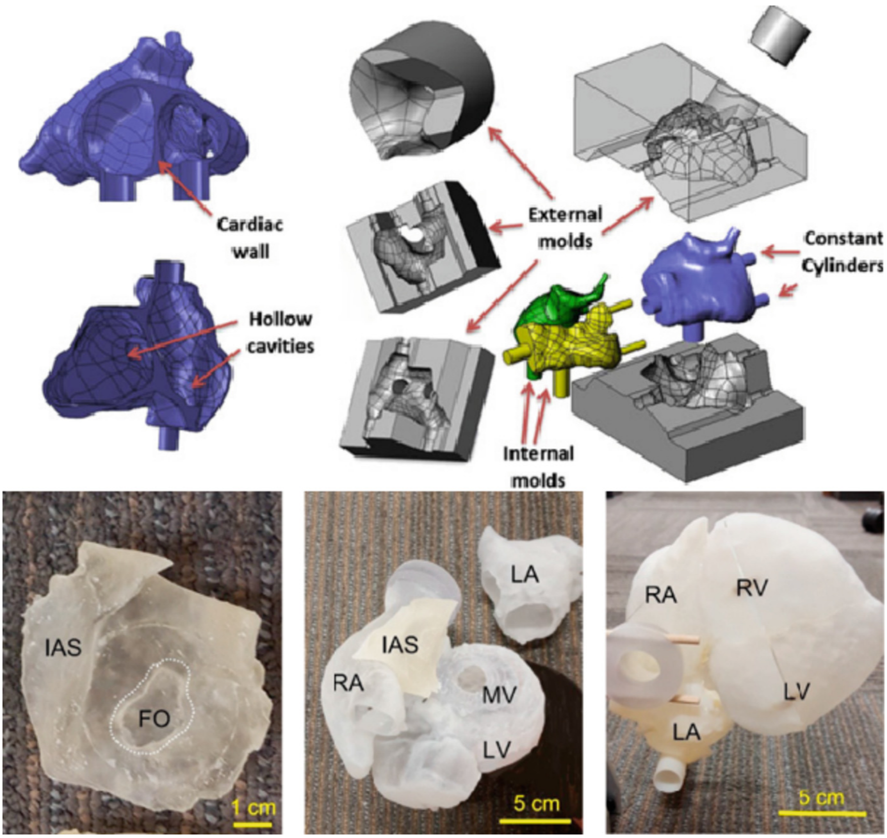

Fig. 3. Atrii Silicone Moulding and 3D Printed model [17, 24]

replaceable septum is reported in any of the reviewed works. The mechanical evaluation of materials for IAS and FO representation is scarcely documented in literature, since most papers rely on qualitative feedback from surgeons or simply use highly flexible materials to simulate tenting. Although no univocal consent on the most performing material for the FO models is reached, a quantitative investigation on MJ specimens [24] presents results considered representative of the real tissue properties [25, 26]. Definition of metrics for the quantification of haptic feedback in the FO location and tenting phases seems hence a still ongoing topic.

The reviewed literature reports examples of evaluation of the 3D printed phantom materials versus multiple diagnostic imaging techniques. In particular 1 article [19] assesses the better performances of FDM-printed Poro-Lay with respect to Polyjet TangoPlus under US imaging and similar performances in CT, X rays and MRI.

The literature review highlights that methods to reproduce image guidance in TP simulators have been developed. ICE, TEE and fluoroscopy are simulated similarly, combining time-of-flight cameras and led illumination [20] or stereo cameras and UV light and lasers [21, 22] for image acquisition. The acquired images are then post processed using dedicated templates to resemble the desired image format. Fluoroscopy is then simulated without the need to use X rays and hence radiation.

Although soft heart phantoms integrating a hydraulic circuit to represent blood circulation are already described [27] no example of application of similar technologies has been found in the reviewed literature to replicate the blood pulse.

5 Conclusions

Use of realistic phantoms and simulators in the Trans-Septal Puncture teaching and training is documented in specialized literature. Starting from standard patient diagnostic imaging, Additive Manufacturing is the key technological process for phantom manufacturing, either for direct fabrication or for molding creation for silicone casting. However, a direct comparison of the different manufacturing technologies, embracing technical and economic aspects, lacks in the current state of the art. Realism of the simulation experience is obtained using tissue-mimicking materials for the FO and IAS and through simulation of image guidance technologies (ICE, TEE or Fluoroscopy). However no systematic quantitative analysis on the haptic feedback of the simulators nor a profound quantitative comparison of the used materials to the cardiac tissue exists, demonstrating an ongoing and challenging direction for future investigations. Moreover, no comparison between the different methods image guidance simulation was found, showing that an answer on the pros and cons of each one is lacking.

References

1. Russo, G., Taramasso, M., Maisano, F.: Knowledge of interatrial septum anatomy, appropriate equipment, and proper technique are key to successful transseptal puncture. Transseptal puncture: a step-by-step procedural guide. Cardiac Intervent. Today **13** (2019)
2. Morais, P., Vilaça, J.L., Ector, J., D'hooge, J.: Tavares JMRS. Novel solutions applied in transseptal puncture: a systematic review. J. Med. Devices Trans. ASME **11** (2017)
3. Sharma, S.P., Nalamasu, R., Gopinathannair, R., Vasamreddy, C., Lakkireddy, D.: Transseptal puncture: devices, techniques, and considerations for specific interventions. Curr. Cardiol. Rep. **21**, 1–7 (2019)
4. Almendarez, M., Alvarez-Velasco, R., Pascual, I., Alperi, A., Moris, C., Avanzas, P.: Transseptal puncture: review of anatomy, techniques, complications and challenges, a critical view. Int. J. Cardiol. (2022)
5. Alkhouli, M., Rihal, C.S., Holmes, D.R.: Transseptal techniques for emerging structural heart interventions. JACC Cardiovasc. Interv. **9**, 2465–2480 (2016)
6. Babaliaros, V.C., Green, J.T., Lerakis, S., Lloyd, M., Block, P.C.: Emerging applications for transseptal left heart catheterization. Old techniques for new procedures. J. Am. Coll. Cardiol. **51**, 2116–2122 (2008)
7. Radinovic, A., Mazzone, P., Landoni, G., Agricola, E., Regazzoli, D., Bella, P.: Different transseptal puncture for different procedures: optimization of left atrial catheterization guided by transesophageal echocardiography. Ann. Card. Anaesth. **19** (2016)
8. Quinn, R.W., Vesely, M.R., Dawood, M., Benitez, M., Holmes, S.D., Gammie, J.S.: Transseptal puncture learning curve for transcatheter edge-to-edge mitral valve repair. Innov. Technol. Techniq. Cardiothorac. Vascul. Surg. **16** (2021)

9. Salghetti, F., Sieira, J., Chierchia, G.B., Curnis, A., de Asmundis, C.: Recognizing and reacting to complications of trans-septal puncture. Exp. Rev. Cardiovasc. Ther. **15**, 905–912 (2017)
10. Wang, D.D., Qian, Z., Vukicevic, M., Engelhardt, S., Kheradvar, A., Zhang, C., et al.: 3D printing, computational modeling, and artificial intelligence for structural heart disease. JACC Cardiovasc. Imaging **14**, 41–60 (2021)
11. Yoo, S.-J., Thabit, O., Kim, E.K., Ide, H., Yim, D., Dragulescu, A., et al.: 3D printing in medicine of congenital heart diseases. 3D Print Med. **2** (2016)
12. Ripley, B., Kelil, T., Cheezum, M.K., Goncalves, A., di Carli, M.F., Rybicki, F.J., et al.: 3D printing based on cardiac CT assists anatomic visualization prior to transcatheter aortic valve replacement. J. Cardiovasc. Comput. Tomogr. **10**, 28–36 (2016)
13. Premyodhin, N., Mandair, D., Ferng, A.S., Leach, T.S., Palsma, R.P., Albanna, M.Z., et al.: 3D printed mitral valve models: affordable simulation for robotic mitral valve repair. Interact. Cardiovasc. Thorac. Surg. **26**, 71–76 (2018)
14. Valverde, I.: Three-dimensional printed cardiac models: applications in the field of medical education, cardiovascular surgery, and structural heart interventions. Rev. Españ. Cardiol. (English Edn.). **70**, 282–291 (2017)
15. Oliveira-Santos, M. de, Oliveira-Santos, E., Gonçalves, L., Silva Marques, J.: Cardiovascular three-dimensional printing in non-congenital percutaneous interventions. Heart Lung Circ. **28**, 1525–1534 (2019)
16. Bartel, T., Rivard, A., Jimenez, A., Mestres, C.A., Müller, S.: Medical three-dimensional printing opens up new opportunities in cardiology and cardiac surgery. Eur. Heart J. **39**, 1246–1254 (2018)
17. Morais, P., Tavares, J.M.R.S., Queirós, S., Veloso, F., D'Hooge, J., Vilaça, J.L.: Development of a patient-specific atrial phantom model for planning and training of inter-atrial interventions. Med. Phys. **44**, 5638–5649 (2017)
18. Laing, J., Moore, J., Bainbridge, D., Drangova, M., Peters, T.: Patient-specific atrium models for training and pre-procedure surgical planning. In: Medical Imaging 2017: Image-Guided Procedures, Robotic Interventions, and Modeling (2017)
19. Wang, S., Noh, Y., Brown, J., Roujol, S., Li, Y., Wang, S., et al.: Development and testing of an ultrasound-compatible cardiac phantom for interventional procedure simulation using direct three-dimensional printing. 3D Print Addit. Manuf. **7**, 269–278 (2020)
20. Thompson, N.A., Kocheril, A.G., Hsiao-Wecksler, E.T., Krishnan, G.: A soft robotic simulator for transseptal puncture training. In: 2021 Design of Medical Devices Conference. American Society of Mechanical Engineers (2021)
21. Zimmermann, J.M., Steffen, O.J., Vicentini, L., Schmid Daners, M., Taramasso, M., Maisano, F., et al.: Novel augmented physical simulator for the training of transcatheter cardiovascular interventions. Catheteriz. Cardiovasc. Intervent. **95**, 1202–1209 (2020)
22. Zimmermann, J.M., Arduini, M., Vicentini, L., Maisano, F., Meboldt, M.: Transcatheter mitral valve repair simulator equipped with eye tracking based performance assessment capabilities: a pilot study. Cardiovasc. Eng. Technol. **12** (2021)
23. James, R.C., Monsky, W.L., Jorgensen, N.W., Seslar, S.P.: Virtual-reality guided versus fluoroscopy-guided transseptal puncture in a cardiac phantom. J. Invasive Cardiol. **33** (2020)
24. Bezek, L.B., Cauchi, M.P., de Vita, R., Foerst, J.R., Williams, C.B.: 3D printing tissue-mimicking materials for realistic transseptal puncture models. J. Mech. Behav. Biomed. Mater. **110**, 103971 (2020)
25. Howard, S.A., Quallich, S.G., Benscoter, M.A., Holmgren, B.C., Rolfes, C.D., Iaizzo, P.A.: Tissue properties of the fossa ovalis as they relate to transseptal punctures: a translational approach. J. Interv. Cardiol. **28** (2015)

26. Riedle, H., Molz, P., Franke, J.: Determination of the mechanical properties of cardiac tissue for 3D printed surgical models. In: Proceedings of the 2018 IEEE EMBS Conference on Biomedical Engineering and Sciences (IECBES 2018) (2019)
27. Cohrs, N.H., Petrou, A., Loepfe, M., Yliruka, M., Schumacher, C.M., Kohll, A.X., et al.: A soft total artificial heart—first concept evaluation on a hybrid mock circulation. Artif Organs. **41**, 948–958 (2017)

A New Tool for Preoperative Planning of Reverse Total Shoulder Arthroplasty

Tommaso Ingrassia, Vincenzo Nigrelli, V. Ricotta, and M. Tantillo(✉)

Department of Engineering, University of Palermo, Viale Delle Scienze Ed. 8, 90128 Palermo, Italy
micol.tantillo@unipa.it

Abstract. The Reverse Total Shoulder Arthroplasty (RTSA) is a complex surgical procedure also due to the difficulty in correctly positioning all the components of the prosthesis. Malpositioning of the prosthesis, in fact, can lead to various complications such as scapular notching, early mobilization, instability and reducing of the range of movement (ROM). Preoperative planning with 3D imaging and patient specific instruments can be very useful tools to help surgeon in selecting the optimal position of implant components.

Aim of this work is to develop a procedure based on a fully parametric CAD system that simulates the shoulder joint to identify the optimal positioning of the humeral and glenoid components of the prosthesis. In particular, the proposed system allows to find the optimal cutting angles of the humerus head and the glenoid cavity so to best fit the patient's bone structure and the prosthesis components and, consequently, to improve the range of movement.

The system allows to create, in a semi-automatic way, CAD assembly models composed of the patient shoulder bones and different reverse shoulder prostheses. For each assembly different positions of the components of the prosthesis can be evaluated and various scenarios of movements can be simulated. In this way it is possible to identify the optimal positioning of the prosthesis for each patient in the preoperative stage.

The proposed procedure has been tested with two types of prosthesis and two patients. Obtained results demonstrated that an optimal positioning of prosthesis an improve ROM up to 27%.

Keywords: Reverse engineering · CAD · Reverse total shoulder arthroplasty · Preoperative planning

1 Introduction

Reverse Total Shoulder Arthroplasty (RTSA) is one of the most common procedures used to treat patients with rotator cuff injuries, complex proximal humerus fractures or primary shoulder prosthesis failures. [1–4, 8–11].

The Reverse Shoulder Prosthesis (RSP) is a replacement device that inverts the typical kinematics of the joint, activating shoulder and arm movement through the function

M. Carfagni et al. (Eds.): ADM 2023, LNME, pp. 203–214, 2024.
https://doi.org/10.1007/978-3-031-52075-4_24

of the deltoid muscle alone. The reverse shoulder prosthesis, indeed, enables the compensation of the muscle-tendon deficit by leveraging the expansive superficial muscles, such as the deltoid, to facilitate the abduction of the arm and for arm.

A reverse shoulder prosthesis comprises two primary elements: the humeral component, consisting of a stem, tray, and polyethylene cup (insert), and the glenoid component, comprising a baseplate and glenosphere. Paul Grammont's introduction of this prosthetic type, with its innovative design, brought significant advancements to conventional shoulder arthroplasty.

The reverse shoulder prosthesis (RSP) emphasised several fundamental principles: (1) establishing a fixed centre of rotation positioned medially and distally to the glenoid surface, (2) ensuring stability of the prosthesis, (3) incorporating a convex weight-bearing component supported by a concave element, and (4) aligning the center of the glenosphere either at or within the glenoid neck. [4, 17, 21].

Despite the biomechanical advantages of medialization, the RTSA procedure remains technically challenging and complications such as scapular notching, premature loosening, instability, and poor function are possible, often associated with malposition.

The evolution of the RSA design is due to the increasing knowledge of implant biomechanics mainly, modern implants offer more modularity to compensate for some of the drawbacks above mentioned (Fig. 1).

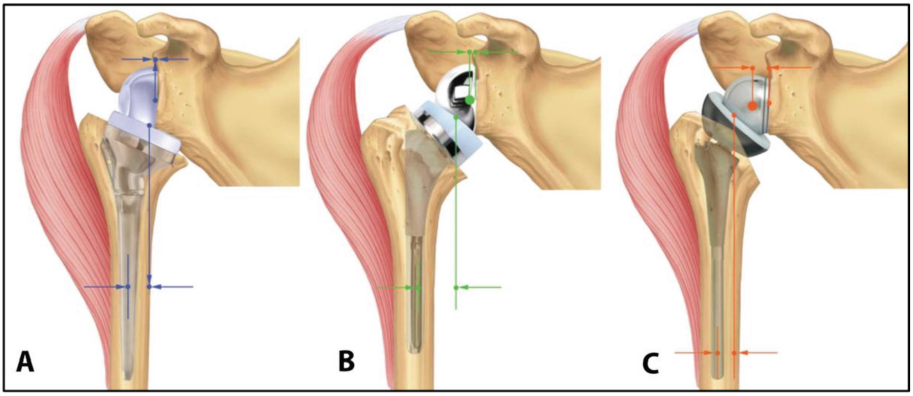

Fig. 1. Reverse shoulder prosthesis: Paul Grammont's original model (A), model with lateralized humeral component (B), model with lateralized glenoid component (C).

The positioning and fixation of the glenoid components is a key factor in the outcome and duration of shoulder arthroplasty. [7, 14–16, 20] In fact, malpositioning of RSP has a negative impact on shoulder stability, range of movement (ROM), impingement and glenoid implant duration. [1–5].

Prosthesis component positioning can be challenging due to an extreme variability in scapular anatomy related to patient, glenoid and humeral bone loss, and surgical technique to be used.

Surgical planning for patients undergoing reverse shoulder arthroplasty can be improved using virtual simulations which help to better understand the complexity of the scapular anatomy and manage the bone loss caused by the various pathologies.

Computer-assisted planning therefore offers an opportunity to improve the accuracy of reproducing the surgical plan for reverse shoulder replacement; indeed, its use has been suggested to improve the performance of implantation [3, 6, 16, 19, 20, 24].

The main aim of this study is to develop a procedure based on a parametric CAD system that simulates the shoulder joint to identify the optimal positioning of the humeral and glenoid components of the prosthesis. In particular, the proposed system allows finding the optimal cutting angles of the humerus head and the glenoid cavity so to best fit the patient's bone structure and the prosthesis components and to improve the ROM. The 3D parametric model has been implemented in two case studies related to two typologies of reverse prosthesis design. Anyway, the main feature of the system is the high flexibility, and it can be applied to a huge range of patients.

2 Materials and Methods

2.1 Shoulder Reconstruction

In this work the bone structure of two patients (subject 1 and subject 2) has been studied. The shoulder joint's CAD model was generated utilizing DICOM images from a computerized tomography (CT) scan. The 3D model was reconstructed through semi-automatic segmentation procedures employing the InVesalius medical imaging software, which is a commercially available open-source tool.

2.2 Prosthesis Reconstruction

The two Tornier-Wright Medical products studied in this work are the AEQUALIS ASCEND FLEX and the AEQUALIS REVERSED II. (Fig. 2).

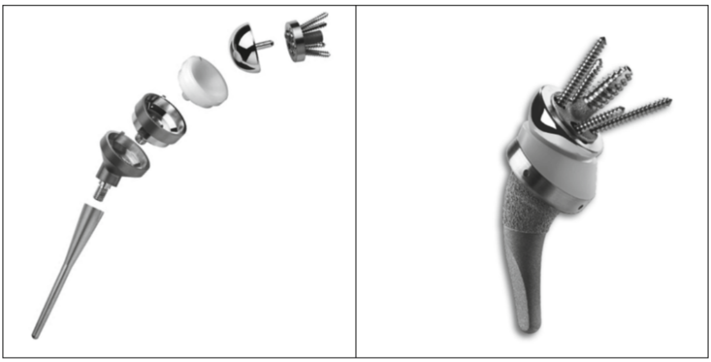

Fig. 2. Aequalis Reverse II (top); Aequalis Ascend Felx (down).

The Aequalis Reversed II reproduces the model designed by Grammont's and is composed of two parts: the humeral one, constituted by a stem, a metaphysis, a spacer, and a polyethylene insert, forming a humeral inclination of 155°; and the glenoid component, constituted by a baseplate and a 36 mm diameter glenosphere, a baseplate with central post.

The Aequalis Ascend Flex prosthesis is an innovative design characterized by a short and curved stem and, due to the asymmetric shape of the humeral insert, reproduces angles the neck-diaphyseal like angle of the healthy humerus. [2, 3, 12, 23].

The Aequalis Reverse Flex, consisting of a 145° neck-diaphyseal angle humeral component and a 36 mm diameter glenosphere with eccentric pin, has been selected for the study.

The shapes of the prosthetic components were captured using a 3D laser scanner based on triangulation, provided by Hexagon Metrology. Following the 3D acquisition, the point clouds underwent post-processing and were subsequently transformed into solid CAD models.

2.3 Cutting Plane Scenario

The proposed model permits to select a range of cutting angle variable from 135° to 155° of the humeral head. Precise positioning of the glenoid implant is crucial for ensuring the duration of RSP and postoperative function in total shoulder arthroplasty [7–10]. Incorrect positioning can contribute to scapular notching and compromise range of motion and joint stability A method has been developed to evaluate the effects of different angular parameter options of the glenoid component so that the shear plane that allows maximum ROM can be assessed. The parameters have been chosen according to different anatomical planes. Angle parameters to form angles of 0°, 5° and 10° with the frontal plane, creating shear planes that tilt the glenoid surface inferiorly.

With respect to the transverse plane, the following parameters have been chosen:

– angle values of 5° and 10°, creating shear planes tilting the glenoid surface towards the acromion.
– angle values of 2° and 3°, which generate shear planes of glenoid surface inclination in the direction of the coracoid process. The model evaluates up to fifteen different shear configurations of the glenoid cavity. (Table 1).

Table 1. Glenoid cutting planes

Angle for creation of cutting planes on the glenoid cavity			
Cutting Plane	Glenoid inferior tilt	Glenoid tilt to acromion	Glenoid tilt to coracoid process
A	0°	0°	0°
B	0°	0°	2°
C	0°	0°	3°
D	0°	5°	0°
E	0°	10°	0°
F	5°	0°	0°
G	5°	10°	0°
H	5°	5°	0°
I	5°	0°	2°
J	5°	0°	3°
K	10°	0°	0°
L	10°	0°	2°
M	10°	0°	3°
N	10°	10°	0°
O	10°	5°	0°

2.4 Virtual Assembly

To conduct a virtual biomechanical analysis of the shoulder joint, all bone and prosthesis models were assembled using a 3D parametric CAD software, adhering to the surgical guidelines outlined by Tornier [22] for total reverse shoulder arthroplasty (Fig. 3).

The entire model has been parametrized, enabling easy and quick adjustments of component positioning during motion simulations. Additionally, it is worth noting that the utilization of parametric CAD models facilitates an interactive procedure. Real-time updates of the results can be achieved by modifying variables within the model [13, 18].

2.5 Parametric Model

The characteristics of the configurations of the cutting planes have been suitably parameterized to automate the procedure and to manage variation of parameters easily.

The virtual collision analyses were performed within a digital environment, specifically the Solid Edge Motion Environment. Three different movements have been analysed for each cutting configuration:

– Abduction in the frontal plane.
– External and internal rotation of the humerus with the elbow at 90°.

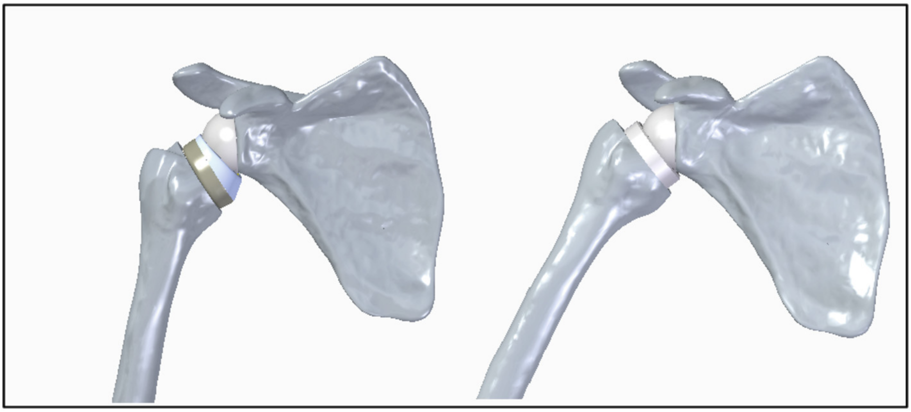

Fig. 3. 3D Assembly of RSA: Aequalis Ascend Flex (left); Aequalis Reverse II (right).

The extreme positions of the arm have been identified when a collision occurred between two components of the glenohumeral joint (Fig. 4). Superior impingement was characterized by virtual contact between bones or the implant and the acromion, which is the superior glenoid. On the other hand, inferior impingement was defined as virtual bone-to-bone contact on the scapular surface [3]. The peculiarity of this system is that, once the values for subject 1 have been determined, it is sufficient to update the programme by inserting the characteristics of other subjects, in our case subject 2, repeating only the analysis phases.

The system has been developed following a structured sequence of phases to be carried out for each patient.

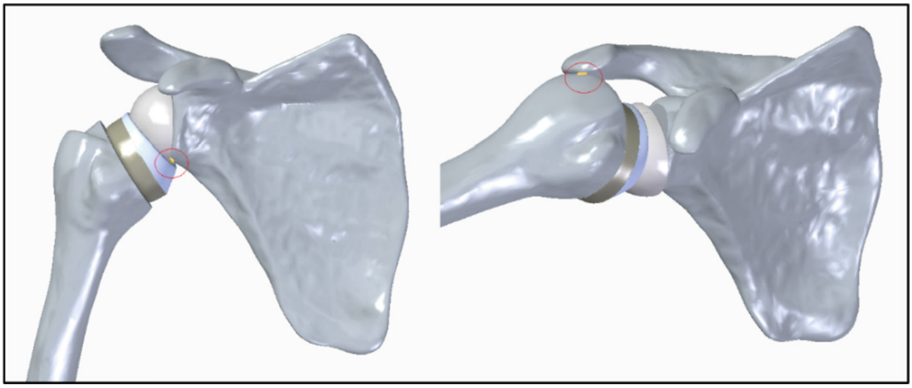

Fig. 4. The extreme position when the components of the glenohumeral joint collide.

3 Results

Fifteen different configurations of the cutting planes of the glenosphere have been studied by calculating the angular value of the ROM related to abduction, external and internal rotation movements.

In all analyses, the maximum angle has been determined on the transversal plane, for the internal and external rotation, and in the frontal plane, for the abduction.

The values obtained from the motion simulation are shown in the tables. Table 2 shows the angle values obtained for the abduction movement, while Tables 3 and 4 show the values for internal and external rotation for subjects 1 and 2 with Aequalis Ascend Flex. Tables 5, 6 and 7 show the values obtained for the Aequalis Reversed II prosthesis. Figures 5 and 6 show the frontal plane abduction ROM plots.

Table 2. Angle values obtained from simulation of abduction ROM with the Aequalis Ascend Flex prosthesis.

Maximum angle values measured for each cutting plane		
Cutting plane	Subject 1	Subject 2
A	60,07°	87,22°
B	58,83°	83,34°
C	58,28°	83,35°
D	62,77°	84,42°
E	73,12°	82,76°
F	63,35°	79,42°
G	64,06°	69,62°
H	64,74°	78,91°
I	62,78°	83,54°
J	61,46°	83,57°
K	65,58°	75,93°
L	72,34°	81,19°
M	70,22°	80,03°
N	64,74°	72,08°
O	70,37°	73,25°

The virtual simulations show an increase in the maximum achievable angle value with an increment of about 21% for the Aequalis Ascend Flex and approximately 27% for the Aequalis Reversed II in subject 1.

The choice of the optimal cutting plane is a compromise between maximum ROM in adduction and rotation. In fact, for subject 1 with the Aequalis Ascend Flex prosthesis, the optimal positioning is the L plane, as it achieves an increase in both abduction and rotation (external and internal) compared to the standard surgical positioning (A plane). For the same subject with the Aequalis Reverse II prosthesis, the O configuration is the optimal positioning.

For subject 2 with Aequalis Ascend Flex, abduction is not significantly affected by the different cutting planes. This is due to the different anatomy of the subject.

In contrast, internal and external rotation can be improved by selecting a cutting plane that produces an inferior glenoid tilt. Furthermore, an increase in the value of the maximum angle of about 13% has been observed in subject 2 with Aequalis Reversed II. The best position for the latter is one that produces an inferior glenoid tilt of the of 10°, thus obtaining an increase in both abduction and rotation.

Table 3. Angle values obtained from simulating external and internal rotation for subject 1 and the Aqeualis Ascend Flex prosthesis.

Maximum angle values measured for best abduction cutting plane		
Cutting plane	ER [°]	IR [°]
A	13,08	49,49
E	4,16	68,3
O	35,52	>90
L	33,65	>90
M	33,55	>90

Table 4. Angle values obtained from simulating external and internal rotation for subject 2 and the Aqeualis Ascend Flex prosthesis.

Maximum angle values measured for best abduction cutting plane		
Cutting plane	ER [°]	IR [°]
A	33,32	78,18
D	35,48	73,75
J	33,23	>90
I	32,35	>90
C	30,13	77,75

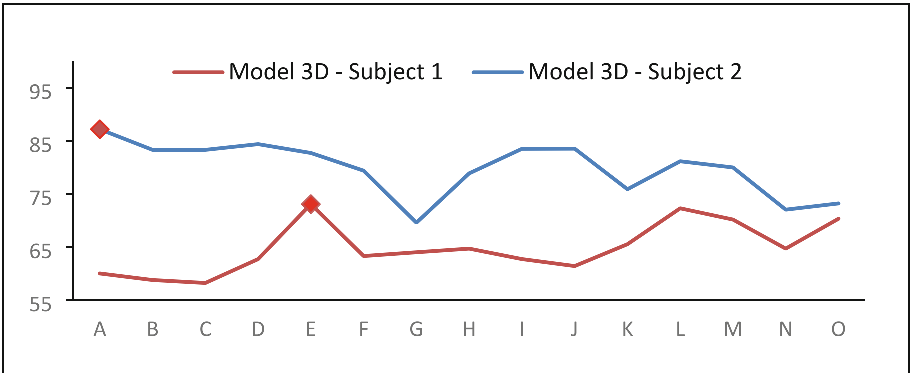

Fig. 5. Plot of abduction ROM versus glenoid cutting plane.

Table 5. Angle values obtained from simulation of abduction ROM with the Aequalis Reversed II

Maximum angle values measured for each cutting plane		
Cutting plane	Subject 1	Subject 2
A	53,04°	67,39°
B	55,72°	69,26°
C	66,59°	68,38°
D	62,25°	67,39°
E	62,38°	67,82°
F	63,47°	67,31°
G	54,57°	66,89°
H	57,70°	64,86°
I	63,48°	67,33°
J	62,10°	66,89°
K	66,90°	76,25°
L	67,46°	73,17°
M	61,48°	73,17°
N	64,96°	62,94°
O	67,58°	68,76°

Table 6. Angle values obtained from simulating external and internal rotation for subject 1 and the Aqeualis Reversed II prosthesis.

Maximum angle values measured for best abduction cutting plane		
Cutting plane	ER [°]	IR [°]
A	11,77	13,69
O	32,8	80,46
L	31,79	70,48
K	36,28	68,24
C	3,24	11,07

Table 7. Angle values obtained from simulating external and internal rotation for subject 2 and the Aequalis Reversed II prosthesis.

Maximum angle values measured for best abduction cutting plane		
Cutting plane	ER [°]	IR [°]
A	9,42	50,73
K	37,49	> 90
L	34,14	> 90
M	28,41	> 90
B	6,62	63,9

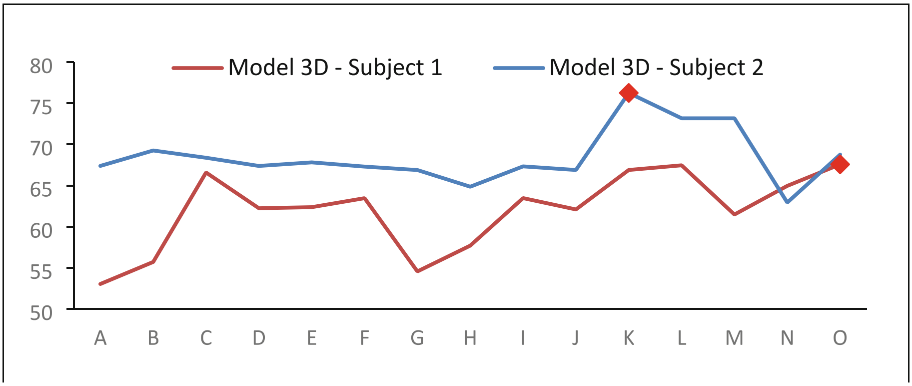

Fig. 6. Plot of abduction ROM versus glenoid cutting plane

4 Conclusion

In this work, a 3D parametric model has been developed for preoperative planning of RTSA. The positioning of the glenoid component has been investigated to understand how the cutting plane of the glenoid surfaces can affect the ROM of the shoulder, finding the optimal configuration in terms of ROM.

A classical reverse engineering approach has been used to digitalize the prosthesis components. 3-dimensional CAD models of the bones have been reconstructed by means of CT images. Two different prostheses have been studied for two different patients and are analysed the abduction, the internal and the external rotation. The positioning of the glenoid component has been determined with several cutting plane of the glenoid surface. Each configuration has been analysed to determine the optimal cutting plain in which to fix the prosthesis.

The results obtained have demonstrated that the different position of the glenoid component can affect the performance of a reverse shoulder implant and depend on the anatomy of the patient. The choice of the optimal cutting plane is a compromise between the best ROM in both abduction and rotation. The proposed framework has the potential to assess the ideal placement of the glenoid component prior to shoulder surgery, based on the specific structure and shape of the patient's shoulder bones.

References

1. Yoon, J.P., et al.: Patient-specific guides using 3-dimensional reconstruction provide accuracy and reproducibility in reverse total shoulder arthroplasty. Clin. Shoulder Elbow **22**(1), 16–23 (2019)
2. Ingrassia, T., et al.: A new method to evaluate the influence of the glenosphere positioning on stability and range of motion of a reverse shoulder prosthesis. Injury **50**, S12–S17 (2019)
3. Ingrassia, T., Nalbone, L., Nigrelli, V., Ricotta, V., Pisciotta, D.: Biomechanical analysis of the humeral tray positioning in reverse shoulder arthroplasty design. Int. J. Interact. Des. Manuf. **12**(2), 651–661 (2018)
4. Sabharwal, S., Bale, S.: The biomechanics of reverse shoulder arthroplasty. J. Arthroscopy Joint Surg. **8**(1), 7–12 (2021)
5. Glenday, J., Kontaxis, A., Roche, S., Sivarasu, S.: Effect of humeral tray placement on impingement-free range of motion and muscle moment arms in reverse shoulder arthroplasty. Clin. Biomech. **62**, 136–43 (2019)
6. Ricotta, V., Campbell, R.I., Ingrassia, T., Nigrelli, V.: A new design approach for customised medical devices realized by additive manufacturing. Int. J. Interact. Des. Manuf. **14**, 1171–1178 (2020). https://doi.org/10.1007/s12008-020-00705-5
7. Marcoin, A., et al.: The precision of patient-specific instrumentation guides for the positioning of the glenoid component in total reverse shoulder arthroplasty: an in vivo scanographic study. Inter. Orthopaedics (SICOT). **44**, 1761–1766 (2020)
8. Levy, J.C., Everding, N.G., Frankle, M.A., Keppler, L.J.: Accuracy of patient-specific guid-ed glenoid baseplate positioning for reverse shoulder arthroplasty. J. Shoulder Elbow Surg. **23**, 1563–1567 (2014)
9. Verborgt, O., Hachem, A.I., Eid, K., Vuylsteke, K., Ferrand, M., Hardy, P.: Accuracy of patient-specific guided implantation of the glenoid component in reversed shoulder arthroplasty. Orthop. Traumatol. Surg. Res. **104**, 767–772 (2018)

10. Zhang, M., Junaid, S., Gregory, T., Hansen, U., Cheng, C.-K.: Effect of baseplate position-ing on fixation of reverse total shoulder arthroplasty. Clin. Biomech. **62**, 15–22 (2019)
11. Burns, D.M., Newhook, S.C.P., Richards, R.R., Whyne, C.M.: Glenoid implant positioning: a new approach using structured light. Seminars Arthroplasty: JSES **30**, 132–138 (2020)
12. Schmalzl, J., Piepenbrink, M., Buchner, J., Picht, S., Gerhardt, C., Lehmann, L.-J.: Higher primary stability of tuberosity fixation in reverse fracture arthroplasty with 135° than with 155° humeral inclination. J. Shoulder Elbow Surg. **30**, 1257–1265 (2021)
13. Ingrassia, T., Nigrelli, V., Pecorella, D., Bragonzoni, L., Ricotta, V.: Influence of the screw positioning on the stability of locking plate for proximal tibial fractures: a numerical approach. Appl. Sci. **10**, 4941 (2020). https://doi.org/10.3390/app10144941
14. Arenas-Miquelez, A., Murphy, R.J., Rosa, A., Caironi, D., Zumstein, M.A.: Impact of humeral and glenoid component variations on range of motion in reverse geometry total shoul-der arthroplasty: a standardized computer model study. J. Shoulder and Elbow Surg. **30**, 763–771 (2021)
15. Patel, M., Martin, J.R., Campbell, D.H., Fernandes, R.R., Amini, M.H.: Inferior tilt of the glenoid leads to medialization and increases impingement on the scapular neck in reverse shoulder arthroplasty. J. Shoulder Elbow Surg. **30**, 1273–1281 (2021)
16. Minoo Patel, D.C., Knox, D.: Effect of suturing the femoral portion of a four-strand graft during an ACL reconstruction Ackland, Prosthesis Design and Placement in Reverse Total Shoulder Arthroplasty. J. Orthopaedic Surg. Res. **10**(1) (2015)
17. Ricotta, V., Campbell, R.I., Ingrassia, T., Nigrelli, V.: Additively manufactured textiles and parametric modelling by generative algorithms in orthopaedic applications. RPJ. **26**, 827–834 (2020). https://doi.org/10.1108/RPJ-05-2019-0140
18. Piles, L., Reig, M.J., Seguí, V.J., Pla, R.: Reverse shoulder arthroplasty: methodology improvement through personalized modelling techniques and FDM technology. Proc. Manufact. **41**, 755–762 (2019)
19. Rugg, C.M., Coughlan, M.J., Lansdown, D.A.: Reverse total shoulder arthroplasty: biomechanics and indications. Curr. Rev. Musculoskelet. Med. **12**, 542–553 (2019)
20. Sheth, U., Saltzman, M.: Reverse Total shoulder arthroplasty: implant design considerations. Curr. Rev. Musculoskelet. Med. **12**, 554–561 (2019)
21. http://www.tornier.com/epaule/ascendflex-pyro/data/AN/pdf/US/Aequalis_AscendFlex_ST.pdf
22. Ingrassia, T., Nalbone, L., Nigrelli, V., Pisciotta, D., Ricotta, V.: Influence of the metaphysis positioning in a new reverse shoulder prosthesis. In: Eynard, B., Nigrelli, V., Oliveri, S.M., Peris-Fajarnes, G., Rizzuti, S. (eds.) Advances on Mechanics, Design Engineering and Manufacturing, pp. 469–478. Springer International Publishing, Cham (2017). https://doi.org/10.1007/978-3-319-45781-9_47
23. Camarda, L., Pitarresi, G., Moscadini, S., Marannano, G., Sanfilippo, A., D'Arienzo, M.: Effect of suturing the femoral portion of a four-strand graft during an ACL recon-struction. Knee Surg. Sports Traumatol. Arthrosc. **22**(5), 1040–1046 (2014). https://doi.org/10.1007/s00167-013-2449-4
24. Mirulla, A.I.: Biomechanical analysis of two types of osseointegrated transfemoral prosthesis. Appli. Sci. (Switzerland) **10**, 1–16 (2020)

Statistical Shape Modelling as a Tool for Medical Reverse Engineering

Vincenza Sciortino[1](✉), Tommaso Ingrassia[1], Donatella Cerniglia[1], and Salvatore Pasta[1,2]

[1] University of Palermo, 90128 Palermo, Italy
vincenza.sciortino01@unipa.it
[2] Department of Research, IRCCS-ISMETT, 90100 Palermo, Italy

Abstract. Manipulating patient data acquired by Computer tomography (CT), e.g., anatomical shape and geometry, as well as studying the biomedical devices used in patient care, is certainly of remarkable importance. Here, Medical Reverse Engineering (MRE) and Rapid Prototyping (RP) play a key role in the 3D models reconstruction of patient anatomy, that can be exploit to make patient-specific, custom-made devices. The inherent variability of the human anatomy can be a problem, which is why the concept of custom-made devices is mentioned. In this field, MRE exploits the computational tools provided by Statistical Shape Modelling (SSM) and Principal Component Analysis (PCA) to achieve computer modelling of 3D data from real models. The PCA is a statistical tool for reducing the number of variables in a population, while the SSM enables the development of an infinite digital population of a given anatomy. This paper aims to show the potential of SSM in the field of the MRE. The study will focus on the pathological lumbar spine. Here, SSM provides new pathological geometries of the lumbar spine, which can be extrapolated and used to produce customized biomedical devices for that given pathological deformation, as well as to perform Finite Element (FE) simulations. Therefore, utilising SSM can bring an addi- tional edge to MRE, due to the infinite population of CAD models of patient anatomy, which can be useful in the medical industry, as already pointed out.

Keywords: Medical Reverse Engineering · Statistical Shape Modelling · Patient-specific · Lumbar spine

1 Introduction

Nowadays, technological and scientific evolution has evolved sufficiently to enable a great development in the medical research by exploiting engineering tools to improve the instruments available to clinicians and surgeons for patient care. These tools are Medical Reverse Engineering (MRE) and Rapid Prototyping (RP), which have several applications, e. g., medical diagnosis, therapeutic and rehabilitative [1–3]. Specifically, RP and MRE refer to all the technologies used to fabricate 3D objects in one step, starting from CAD model following a precise lead [4, 5]. The patient undergoes Computer Tomography (CT) imaging, through which the patient's anatomy is captured layer.

M. Carfagni et al. (Eds.): ADM 2023, LNME, pp. 215–223, 2024.
https://doi.org/10.1007/978-3-031-52075-4_25

by layer. The next step is the segmentation and reconstruction of the images through medical software, to recreate the 3D model of the patient's anatomy. Starting from the 3D model, it is possible to proceed in several ways [6].

The first focus is the biomechanical investigation of the anatomical part examined, with the virtual environment using finite element modelling (FEM), which is a useful tool for the study of physiological and pathological conditions, e.g., for the simulation of surgery and the implantation of medical devices [7, 8]. In pathological cases, patient care involve surgery requiring the implantation of well-designed medical devices and prostheses. Human beings are unique in their anatomy. The implementation of medical devices is generally done on a large scale, so designing medical devices having different geometries but adaptable to different patient anatomies. However, as the patient's anat omy is unique, the implementation of a patient-specific device would be a critical goal to achieve. This is where RP comes in. Here, the main goal is the fabrication of patient-specific custom-made devices according to the anatomical, geometrical, and pathological characteristics specific of the patients. The CAD model creation is the most complex design part of rapid product development. The most widely used technologies for RP involve layer-based Additive Manufacturing, e. g., Laser Selective Sintering and Fused Deposition Modelling [9–15].

The aim of this paper is to bring a new tool in the MRE and RP tools that could be extremely useful if implemented, i.e., Statistical Shape Modelling (SSM), through which our group has created an atlas of the pathological lumbar spine. [16]. SSM might be a breakthrough in MRE since, by creating the 3D digital population of the anatomical area, an infinite number of CAD models are available that could be used for different purposes, from the biomechanical analysis of the pathological lumbar spine, surgical planning and implantation of devices and creating a custom-made patient specific device.

2 Methodology

Based on a careful literature study, we proceed with the development of the spinal lumbar atlas, the main steps shown in Fig. 1 were followed.

2.1 CT Image Acquisition and Reconstruction

A population of 24 patients were included in this study and underwent to CT scans through which we obtain a large number of images showing the patient's anatomy in the three anatomical planes. The CT scans were examined using the software Mimics v21 (Materialise, Leuven, Belgium). 3D reconstructions were made of the vertebral bodies, as well as the intervertebral discs, following the segmentation process, which is done by establishing masks that target specific regions of the CT images, based on a grey scale range of the Hounsfield Unit (HU). Finally, smoothing, wrapping, and reducing operations followed the 3D reconstruction to improve the quality obtained.

2.2 Geometrical Measurements

The next step involved geometrical measurements of the patients' anatomies. Figure 2 shows the methodology used for vertebral bodies and the intervertebral disc [17–20].

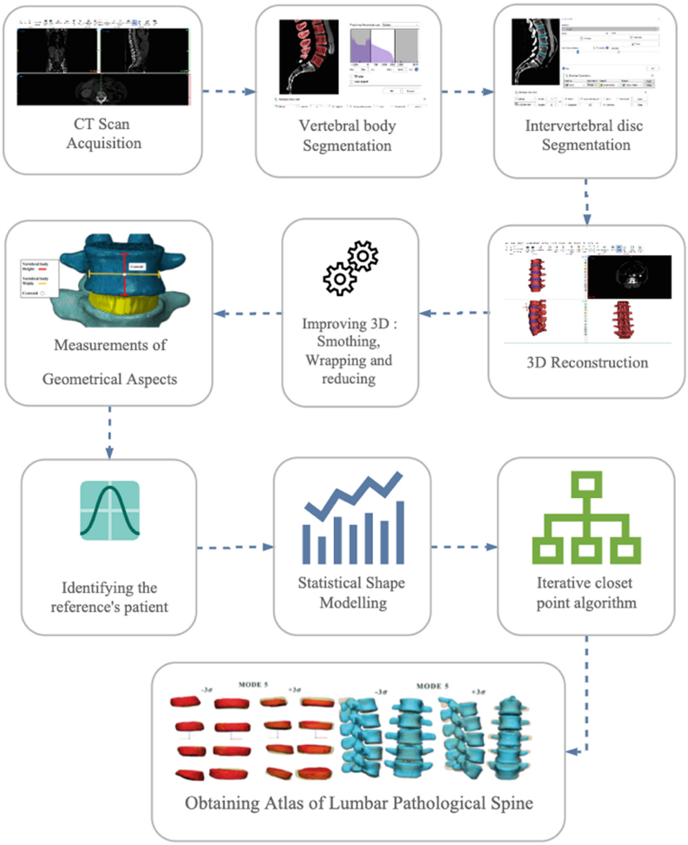

Fig. 1. Workflow for creating the Atlas of Lumbar pathological spine.

We used the measure and analyse tools from Mimics. Measurements of the height and width at the centroid's were taken from the coronal plane (Fig. 2A). Measurements of the lordosis degree were taken through Cobb's method (Fig. 2B), we proceed by drawing two straight lines in the sagittal plane. One line tangent to the plane of the upper L1 vertebra plate and the other tangent to the lower L5 vertebra plate. The angle formed by the two lines will be the lordosis degree. The same methodology was used for the scoliosis degree in the coronal plane, but drawing as straight lines those tangents to the upper and lower vertebrae that are more inclined. Measurements of the superior and lower layer area were taken, obtaining also the corresponding perimeters (Fig. 2C).

2.3 Statistical Shape Modelling (SSM) of the Lumbar Spine

The SSM model was built using a script developed in the MATLAB mathematical language (R2020, Math-Works Inc., USA) as previously described by our group [16, 21]. Figure 3 shows the SSM model for vertebral body and intervertebral disc. Figure 4 shows the instance probability profile of the model created, with a gaussian trend.

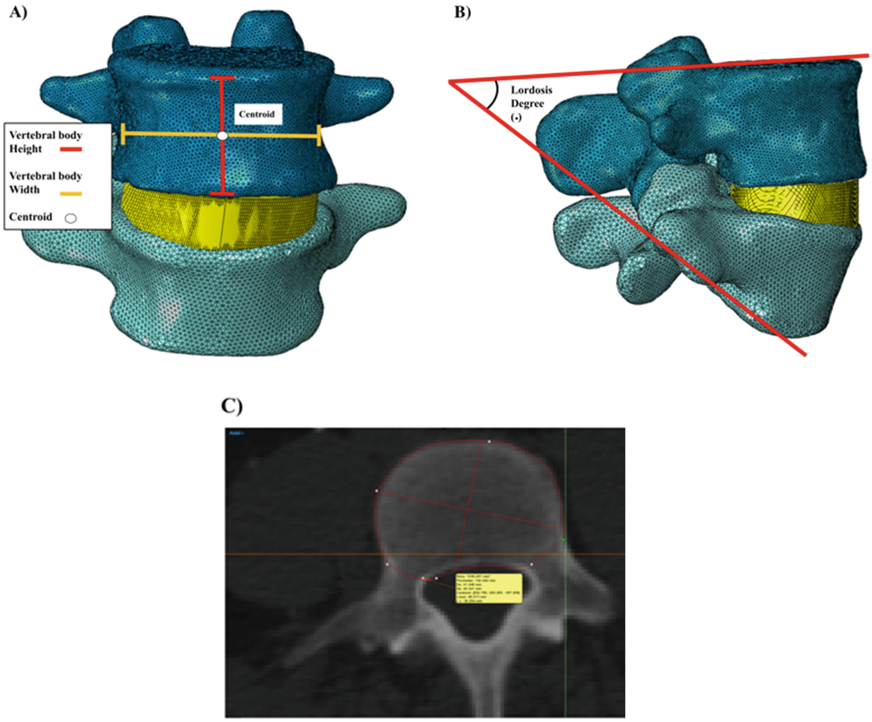

Fig. 2. **A)** Height-Width measures. **B)** Lordosis Degree measures. **C)** Surface measures.

The first step was to identify the reference patient, representative of the population's average anatomy. An iterative closest-point algorithm was used for the alignments of each sampled point of the lumbar area, exploiting the Principal Component Analysis, i.e., a statistical tool used to reduce the variables in a population and enclose them in specific variables, i.e., Shape Modes. The shape modes represent a specific variation in anatomical features. The contribution made by each shape mode is visualised by de forming the model according to the standards deviation values ($\pm 3\sigma$) [22–25].

3 SSM in the Medical Reverse Engineering

The atlas enabled to extrapolate several shape modes and provide a visual and numerical description of the complex lumbar spine shape. The SSM created proves the potential of the shape analysis and provides an infinite digital 3D population of the pathological lumbar spine. The infinite 3D pathological digital population is generated by deforming the average lumbar model according to standard deviations, so obtaining an infinite pathological CAD model. Following the atlas implementation, the further steps might be manifold. Figure 5 shows the workflow continuing from Fig. 1.

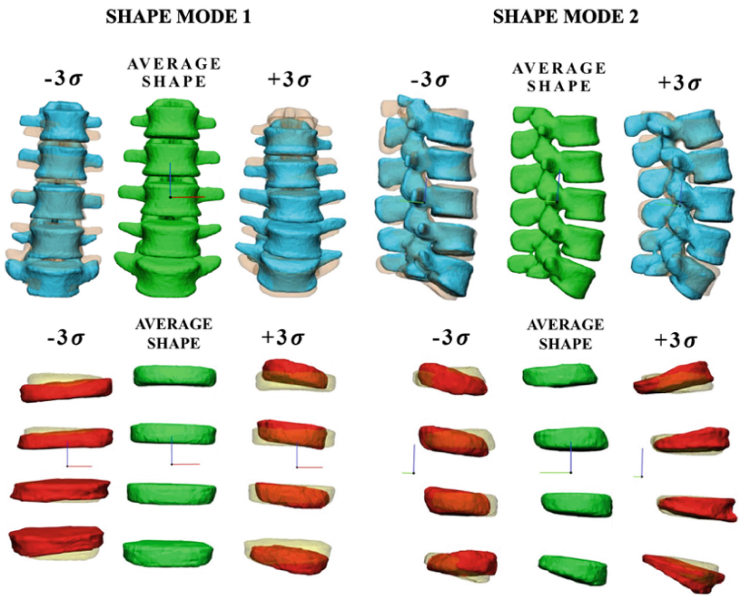

Fig. 3. Shape mode 1 and Shape mode 2 overlapped the average shape for vertebral bodies and intervertebral discs.

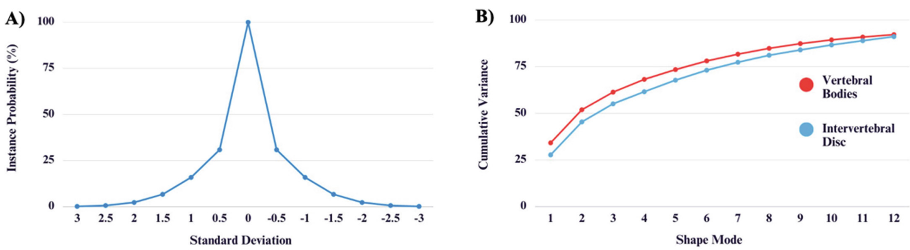

Fig. 4. Instance probability profile.

The atlas could be followed by MRE data processing and CAD geometric modelling, i.e., prostheses or medical devices to implant in a patient, created thought additive manufacturing techniques. Applications and biomedical research could involve the implementation of FEM model, with biomechanical or surgical simulations [26].

The patient population involved pathological patients with herniated discs and scoliosis. The medical solutions for these diseases are still uncertain. When a patient suffers from herniated disc, a discectomy surgery might be performed, in which the intervertebral disc is removed and then replaced with a disc prosthesis (cage), the sizes of which must be selected. This choice often involves uncertain decisions, owing to the patient's anatomy. On the other hand, scoliosis surgery is very challenging, it involves spinal fusion for all segments affected by scoliosis and a derotation in the sagittal plane of the spine. Spinal fusion involves the insertion of pedicle screws and metal rods to stabilize

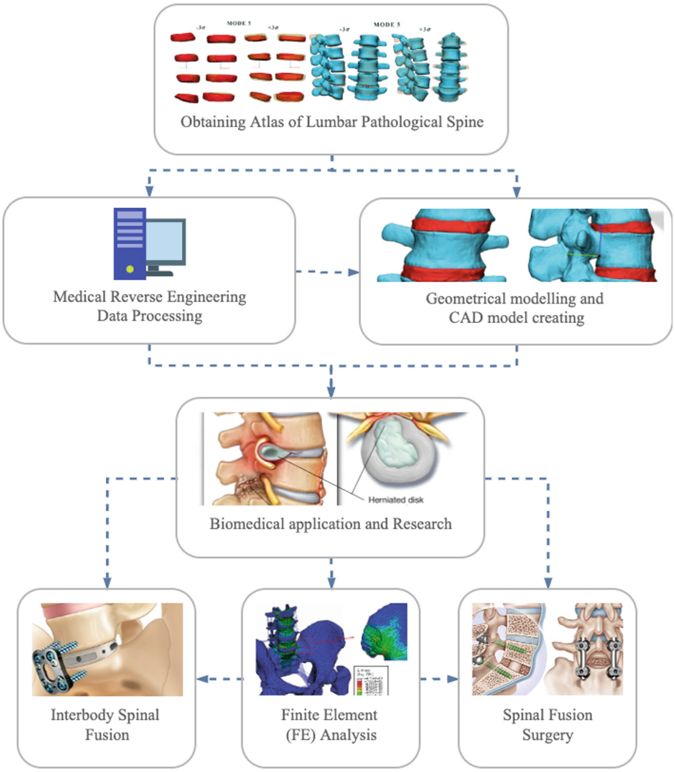

Fig. 5. Workflow by using SSM in the MRE.

the spine; this leads to significant changes in its biomechanics and flexibility. These surgical solutions although they succeed and can ensure a better living condition for the patient, they can be improved. Hence, SSM could be involved in stalemate situations. A given cage could be considered and the surgery simulated for a preliminary study, using the infinite 3D population. The results gained from the FEM simulation could help to understand how a prosthesis of a certain size may or may not be better if is a certain degree of low back pain, rather than a certain scoliosis degree, or a certain vertebrae's' height or width. These aspects cannot always be considered during the design stages. So, this could allow to observing how a specific geometric feature could affect or render ineffective a prosthesis that for another anatomical condition would be perfect. This would enable a patient-specific approach.

The infinite population can simulate any anatomical situation, with no limitation studies. The same could be done for scoliosis surgeries, so figuring out how a geometric features might affect the surgery and improve it, and perhaps implementing a different surgical plan. On the other hand, RP technologies might be used to make a custom made prosthesis, which requires 3D printing technologies for its fabrication. Therefore, as the device design needs several steps, since it has to be customised, all geometric features that can influence the design must be included. The SSM model appears extremely useful because it provides infinite CAD models, varying the specific geometric features one wants to study for this new prosthesis that needs to be designed.

4 Conclusion

MRE aims to exploit traditional reverse engineering techniques to reconstruct 3D models of patients' anatomy and implanted medical devices, with the goal of supporting biomedical engineering research and development [27, 28]. This article aimed to introduce a new tool, SSM, that could be utilized by MRE. The realization of the SSM model of the lumbar spine starts from the 3D reconstructions of the pathological anatomies, creating an infinite population of patients. This infinite population is extremely useful, as it provides new CAD model that can be used in stalling situations caused by indecision about which prosthesis and its sizes to choose to implant. It is possible to easily build a model from the atlas which considers all the different geometrical features in the patient's anatomy, thus ensuring the possibility of collecting data and information, and then deciding what is the best solution. The model has several limitations, the main one concerns the small number of patients included in the population. Future developments involve the extension of the model through a larger number of patients, thereby generalising and compacting the model as much as possible by including all possible anatomical configurations. Future developments, also, will aim to use the atlas, firstly to conduct biomechanical analyses of spinal biomechanical response, so as to understand how a given variation in a geometric feature, such as disc height, depending on the herniation level, or depending on the lordosis or scoliosis degree, affects the normal mechanics of the spine. Further steps could include FEM simulations concerning prosthetic implant and surgical procedures, so as to enable understanding of how the success of prosthetic implants may depend on certain relevant morphological aspects of the patient's anatomy, and what might be solutions to improve the flexibility of the spine, which is always disrupted following such surgeries, being truly complex as a whole.

References

1. Gibson, I. (ed.) Advanced manufacturing technology for medical applications: reverse engineering, software conversion and rapid prototyping. John Wiley & Sons (2006)
2. Le, C., et al.: Medical reverse engineering applications and methods, pp. 186–196 (2010)
3. Racasan, R., Popescu, D., Neamtu, C., Dragomir, M. Integrating the concept of reverse engineering in medical applications. In: 2010 International Conference on Automation, Quality and Testing, Robotics (AQTR), vol. 2, pp. 1–5. IEEE (2010)
4. Mirulla, A.I., Bragonzoni, L., Zaffagnini, S., Bontempi, M., Nigrelli, V., Ingrassia, T.: Virtual simulation of an osseointegrated trans-humeral prosthesis: a falling scenario. Injury **49**(4), 784–791 (2018)
5. Ingrassia, T., Nalbone, L., Nigrelli, V., Pisciotta, D., Ricotta, V.: Influence of the metaphysis positioning in a new reverse shoulder prosthesis. In: Advances on Mechanics, Design Engineering and Manufacturing: Proceedings of the International Joint Conference on Mechanics, Design Engineering & Advanced Manufacturing (JCM 2016), 14–16 September, 2016, Catania, Italy, pp. 469–478. Springer International Publishing (2017). https://doi.org/10.1007/978-3-319-45781-9_47
6. Prakash, K.S., Nancharaih, T., Rao, V.S.: Additive manufacturing techniques in manufacturing-an overview. Mater. Today: Proc. **5**(2), 3873–3882 (2018)
7. Cerniglia, D., Ingrassia, T., D'Acquisto, L., Saporito, M., Tumino, D.: Contact between the components of a knee prosthesis: numerical and experimental study. Frattura ed Integrità Strutturale **6**(22), 56–68 (2012)

8. Mirulla, A.I., Bragonzoni, L., Zaffagnini, S., Ingrassia, T., Zinno, R., Innocenti, B.: Assessment of paradoxical anterior translation in a CR total knee prosthesis coupling dynamic RSA and FE techniques. J. Experim. Orthop. **8**(1), 1–7 (2021)
9. Salmi, M.: Additive manufacturing processes in medical applications. Materials **14**(1), 191 (2021)
10. Javaid, M., Haleem, A.: Additive manufacturing applications in orthopaedics: a review. J. Clin. Orthop. Trauma **9**(3), 202–206 (2018)
11. Mouloodi, S., Rahmanpanah, H., Burvill, C., Davies, H.M.: Accuracy quantification of the reverse engineering and high-order finite element analysis of equine MC3 forelimb. J. Equine Vet. **78**, 94–106 (2019)
12. Chougule, V.N., Mulay, A.V., Ahuja, B.B.: Development of patient specific implants for Minimum Invasive Spine Surgeries (MISS) from non-invasive imaging techniques by reverse engineering and additive manufacturing techniques. Proc. Eng. **97**, 212–219 (2014)
13. Majstorovic, V., Trajanovic, M., Vitkovic, N., Stojkovic, M.: Reverse engineering of human bones by using method of anatomical features. CIRP Ann. **62**(1), 167–170 (2013)
14. Ovsepyan, A.L., et al.: Biomechanical analysis of the cervical spine segment as a method for studying the functional and dynamic anatomy of the human neck. Annals Anatomy-Anatomischer Anzeiger **240**, 151856 (2022)
15. Chougule, V.N., Mulay, A., Ahuja, B.B.: Clinical case study: spine modeling for minimum invasive spine surgeries (MISS) using rapid prototyping. Bone (CT) **226**, 3071 (2018)
16. Sciortino, V., Pasta, S., Ingrassia, T., Cerniglia, D.: A population-based 3D atlas of the pathological lumbar spine segment. Bioengineering **9**(8), 408 (2022)
17. Divya, V., Anburajan, M. Finite element analysis of human lumbar spine. In: 2011 3rd International Conference on Electronics Computer Technology, vol. 3, pp. 350–354. IEEE (April 2011)
18. Chernukha, K.V., Daffner, R.H., Reigel, D.H.: Lumbar lordosis measurement: a new method: versus: cobb technique. Spine **23**(1), 74–79 (1998)
19. Fernand, R., Fox, D.E.: Evaluation of lumbar lordosis a prospective and retrospective study. Spine **10**(9), 799–803 (1985)
20. Morrissy, R.T., Goldsmith, G.S., Hall, E.C., Kehl, D., Cowie, G.H.: Measurement of the Cobb angle on radiographs of patients who have scoliosis evaluation of intrinsic error. JBJS **72**(3), 320–327 (1990)
21. Cutugno, S., Ingrassia, T., Nigrelli, V., Pasta, S.: On the left ventricular remodeling of patients with stenotic aortic valve: a statistical shape analysis. Bioengineering **8**(5), 66 (2021)
22. Catalano, C., Agnese, V., Gentile, G., Raffa, G.M., Pilato, M., Pasta, S.: Atlas-based evaluation of hemodynamic in ascending thoracic aortic aneurysms. Appl. Sci. **12**(1), 394 (2022)
23. Nandi, D., Ashour, A.S., Samanta, S., Chakraborty, S., Salem, M.A., Dey, N.: Principal component analysis in medical image processing: a study. Inter. J. Image Mining **1**(1), 65–86 (2015)
24. Boisvert, J., Cheriet, F., Pennec, X., Labelle, H., Ayache, N.: Principal deformations modes of articulated models for the analysis of 3D spine deformities. Elect. Lett. Comput. Vis. Image Anal. **7**(4), 13–31 (2008)
25. Campbell, J.Q., Petrella, A.J.: Automated finite element modelling of the lumbar spine: using a statistical shape model to generate a virtual population of models. J. Biomech. **49**(13), 2593–2599 (2016)
26. Sciortino, V., Pasta, S., Ingrassia, T., Cerniglia, D.: On the finite element modeling of the lumbar spine: a schematic review. Appl. Sci. **13**(2), 958 (2023)

27. Sun, L., Tian, H., Wu, D., Du, Z.: Three-dimensional geometric modelling of the spine based on reverse engineering technology. In: 2010 3rd International Conference on Biomedical Engineering and Informatics, vol. 3, pp. 1292–1295. IEEE (October 2010)
28. Kozłowska, E., Zubrzycki, J.: Using methods of the reverse engineering to carry personalised preoperative stabilisers out on the example of vertebrae of human spine. In: ITM Web of Conferences, vol. 15, p. 02007. EDP Sciences (2017)

Towards Kinematic Assessment of Trendelenburg Gait After Total Hip Arthroplasty Using Mocap Systems

Anna Ghidotti[1](✉), Andrea Cattaneo[1], Andrea Vitali[1], Daniele Regazzoni[1], Caterina Rizzi[1], and Gennaro Fiorentino[2]

[1] Department of Management, Information and Production Engineering, University of Bergamo, via Pasubio 7/b, Dalmine, 24044 Bergamo, Italy
anna.ghidotti@unibg.it

[2] Humanitas Gavazzeni, via Mauro Gavazzeni, 21, Bergamo 24125, Italy

Abstract. Total hip arthroplasty (THA) is a surgical procedure advised to treat end-stage osteoarthritis. There are several surgical approaches involving different biomechanical effects, potentially affecting the outcome. A possible consequence of THA is the Trendelenburg gait, which consists of a pelvis drop and trunk lean during walking due to a unilateral weakness of the hip abductors. Gait analysis can be useful in assessing the disorder. The purpose of the present research is twofold: i) to assess the Trendelenburg disease in patients undergoing THA through gait analysis; ii) to investigate the relationship between the disorder and surgical approaches. Patients' gaits were recorded 7 days after THA surgery, using two Microsoft Kinect V2 sensors and virtual skeletons were reconstructed by iPi Soft software. A customized tool was developed to automatically identify walking phases and recognize characteristics compatible with the Trendelenburg gait. In addition to pelvic drop and trunk lean in the frontal plane, kinematic measurements are proposed for a more complete assessment of the Trendelenburg gait. These variables are found to be effective in highlighting the differences between surgical approaches.

Keywords: Trendelenburg Gait · Motion Capture · Total Hip Arthroplasty · Gait Analysis · Recovery of Function

1 Introduction

Total hip arthroplasty (THA) is the recommended surgical treatment for end-stage osteoarthritis (OA). Hip OA is a common chronic disease responsible for pain and disability in the older population [1]. When conservative therapies to manage symptoms are not helping anymore the painful patient, surgery is performed to reduce pain and improve physical function and health-related quality of life [2].

The most commonly used approaches for THA are posterior, lateral and anterior [3]. The posterior approach sacrifices external rotator muscles that play an important role as hip stabilizers and there is a risk of damaging the sciatic nerve, but it has the advantage

M. Carfagni et al. (Eds.): ADM 2023, LNME, pp. 224–232, 2024.
https://doi.org/10.1007/978-3-031-52075-4_26

of not interfering with the adductor mechanism. The direct lateral approach preserves external rotators but sacrifices part of the abductor muscles, such as gluteus medius and minimus and its associated risks are superior gluteal nerve injury and heterotopic ossification [4]. Direct anterior approach is a minimally invasive muscle-sparing approach since it does not require muscle incision. However, obese or very muscular people may not be good candidates for this procedure [5]. Furthermore, there is a risk of sensitive lateral femoral cutaneous nerve injury and the procedure implies a long learning curve. Nowadays, there is a continuing interest in these different surgical approaches, but the most effective one is still a matter of controversy [4]. The comparison takes into account several factors, such as operating time, blood loss, length of stay and post-operative recovery. Furthermore, walking abnormalities such as the Trendelenburg gait can be observed after THA [6]. It is caused by weakness of the abductors of the lower limbs, the gluteus medius and gluteus minimus. As the pelvis cannot be kept level by the lesioned abductors, the pelvis drops to the healthy side. In response, the trunk tilts towards the lesioned side in an attempt to maintain balance [7]. To evaluate the condition, the patient is asked to stand on the affected leg for up to 30 s. When the leg supports the body on the affected side, a positive Trendelenburg sign can be recognized by an ipsilateral pelvic elevation. This sign is more evident during the gait [8, 9]. A complete assessment should include both static and dynamic examination [10]. Hence, gait analysis can be incorporated to quantify and evaluate the impairments altering gait in patients after THA. For the gait test, patients are asked to walk for a short distance to assess the positive sign.

In this context, the purpose of the present research is twofold. The first goal is to quantitatively assess the Trendelenburg disease in patients undergoing THA by means of gait analysis. A specific tool is developed to conduct the analysis through motion capture systems. The second aim is to investigate the relationship between the disorder and the chosen surgical approaches.

2 Method

The procedure can be divided into phases: (i) Patient enrollment; (ii) Gait acquisition; (iii) Software package development; (iv) Statistical analysis.

Fifteen patients undergoing THA surgery were included (Table 1). Institutional review board (IRB) approval for the study was obtained at Humanitas Gavazzeni (Bergamo, Italy), and an IRB-approved informed consent form was signed by all enrolled patients.

The surgeons chose the surgical approach (posterior, lateral, and anterior) based on their experience and the patient's condition. Patients with previous lower limb joint replacement and neurological diseases were excluded from the study.

Each subject carried out a gait recording session 7 days after the surgery. The patient was asked to walk at his/her preferred speed for 6 m, with can support if necessary. Two full gait cycles were considered; thus, four steps per patient entered the analysis. Walking was recorded by means of two Microsoft Kinect version 2 sensors, placed opposite to each other and diagonally with respect to the walking path, as described in a previous work [11] and shown in Fig. 1. This technology uses a time-of-flight depth sensor to

Table 1. Mean and standard deviation of patients' characteristics, grouped by approach. No statistically significant difference in age and height among groups is reported, through ANOVA.

	Posterior	Lateral	Anterior	p-value
Age [years]	66.8 (11.2)	67.0 (8.8)	70.0 (8.3)	0.8396
Height [cm]	163.8 (9.6)	171.0 (11.4)	169.2 (4.7)	0.4456
Gender (F/M)	2 / 3	2 / 3	3 / 2	---
Affected side (R/L)	3 / 2	1 / 4	3 / 2	---

measure the distance between objects in its field of view. This enables it to create a 3D map of the environment and track the movement of the patients within that space. A virtual skeleton of the patients was reconstructed from the acquisition, through iPi Soft software.

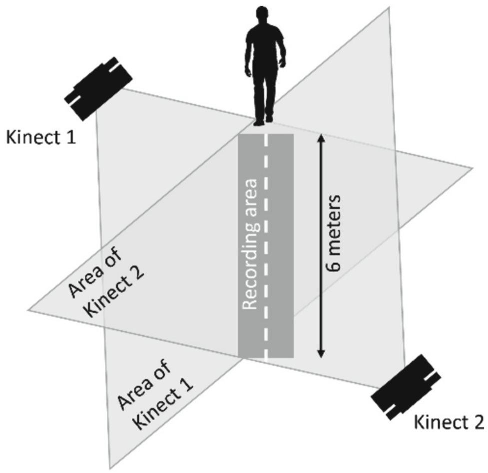

Fig. 1. Diagram of acquisition setup with two Microsoft Kinect sensors.

The analysis of pelvis and trunk kinematics throughout the gait cycle was conducted using a custom software developed with Python and the numpy library. The software workflow followed a systematic approach. Initially, the raw virtual avatar of each patient, acquired as a bvh file from iPi Soft, was imported and parsed within the software. Subsequently, through analysis of the foot joint dynamics, the software automatically detected the foot-floor contact events, allowing for the automatic segmentation of the gait into swing and stance phases. Then, it extracted the kinematics of the pelvis and trunk in the coronal plane, considering parameters such as mean angle, maximum angle, range of motion (ROM), peak angular velocity, and peak angular acceleration. The convention adopted in this software was to denote a descent toward the swinging limb with a positive sign and a descent in the opposite direction with a negative sign. Individual steps were identified as positive for the Trendelenburg sign if they satisfied the criteria proposed by Westhoff et al. [12]: a pelvic tilt greater than 4° relative to the swinging limb and a trunk tilt exceeding 5° relative to the pelvis. The collected information was exported in Excel format for further analysis.

To investigate the relationship between the presence of Trendelenburg gait and the surgical approach performed, a statistical analysis was conducted. Pearson's chi-squared test of independence was then applied, with a significance level set at $p\text{-value} < 0.05$. The gait kinematics between the different surgical approaches were then examined. For each patient, the kinematic parameters were averaged over the four recorded steps to obtain independent samples; since Bartlett's test did not confirm the assumption of homogeneity of variance, the non-parametric Kruskal-Wallis test was chosen as a suitable alternative. Post-hoc analysis was then performed using Conover's test, with adjustments made using the Holm-Bonferroni method to account for multiple comparisons.

3 Results

For each patient, two full gait cycles were considered, thus a total of 60 swing phases have been analyzed. 37 steps were found to be positive for Trendelenburg, according to the pelvic drop criterion ($> 4°$). Furthermore, 24 steps were identified as Trendelenburg positive, according to the lateral trunk tilt criterion ($> 5°$). Figure 2 shows the distribution of the maximum frontal plane angle of the swing phase.

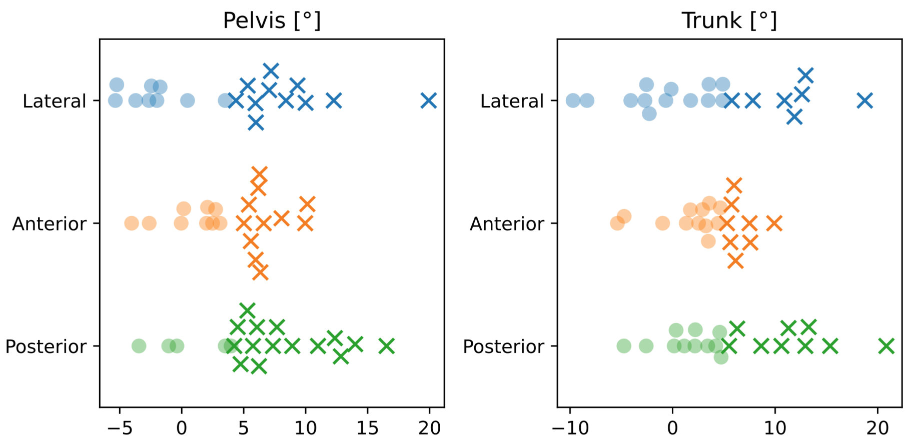

Fig. 2. Swarmplot of the maximum frontal plane angle detected during the swing phase. Values considered normal are shown as circles, while crosses indicate abnormalities. Thresholds are $\geq$ 4° for pelvic tilt and $\geq$ 5° for trunk tilt, according to the criteria of Westhoff et al. [12]. Positive signs indicate a lateral tilt towards the standing limb.

In total, two thirds of the examined swing phases were found to be positive for the pelvic drop and/or the lateral trunk tilt criterium. There was no statistically significant difference in the prevalence of Trendelenburg among the surgical approaches according to Pearson's chi-squared test of independence (p-value = 0.3012).

Then, the analysis was expanded to include information on pelvic and trunk kinematics. In addition to the maximum angles of pelvis drop and trunk lean, the average angles, ROM, velocity and acceleration of the joints were considered (Table 2). The Kruskal-Wallis test showed a statistically significant difference among the surgical approaches. Patients who underwent surgery via the posterior approach had greater ROM, peak angular velocity, and peak angular acceleration in both the trunk and pelvis, suggesting greater instability during gait. Post hoc analysis (Table 3) revealed several differences between the posterior approach and both the lateral and anterior approaches, while no significant differences were found between the lateral and anterior approaches.

Table 2. Kinematics of the pelvis and trunk in the frontal plane during the swing phase. Mean values are calculated, grouped by surgical approach. The standard deviation is depicted in parentheses. Statistical significant differences are bolded (p-value < 0.05, Kruskall-Wallis test). Abbreviation: ROM range of motion.

		Posterior	Lateral	Anterior	p-value
Pelvis	Average angle [°]	3.2 (3.7)	2.1 (7.2)	2.9 (3.3)	0.9509
	Maximum angle [°]	6.5 (5.0)	3.8 (6.5)	4.1 (3.7)	0.5418
	ROM [°]	8.0 (4.3)	4.2 (2.2)	2.9 (1.2)	**0.0029**
	Peak velocity [°/s]	-26.5 (32.9)	-2.6 (18.4)	7.9 (12.0)	**0.0347**
	Peak acceleration [°/s^2]	-321.9 (253.2)	-55.2 (146.7)	-123.8 (121.4)	**0.0230**
Trunk	Average angle [°]	3.4 (4.5)	2.2 (7.9)	2.9 (3.6)	0.9291
	Maximum angle [°]	6.0 (6.3)	3.4 (7.4)	3.5 (3.7)	0.6474
	ROM [°]	6.8 (5.1)	3.1 (1.8)	2.1 (0.8)	**0.0413**
	Peak velocity [°/s]	-35.7 (38.1)	-2.6 (19.3)	5.6 (13.7)	**0.0263**
	Peak acceleration [°/s^2]	-406.7 (323.8)	-127.2 (141.0)	-113.4 (129.5)	**0.0498**

Table 3. P-values of the post hoc analysis of significant differences found across approaches. Results are obtained using Conover's test, adjusted with the Holm-Bonferroni method. Statistical significant differences are bolded (p-value < 0.05). Abbreviation: ROM range of motion.

		Posterior vs Lateral	Posterior vs Anterior	Lateral vs Anterior
Pelvis	ROM [°]	**0.0462**	**0.0007**	0.0771
	Peak velocity [°/s]	0.2854	**0.0247**	0.2854
	Peak acceleration [°/s^2]	**0.0176**	0.0836	0.4001
Trunk	ROM [°]	0.2508	**0.0318**	0.2541
	Peak velocity [°/s]	0.0912	**0.0211**	0.4187
	Peak acceleration [°/s^2]	0.0975	0.0594	0.6830

4 Discussion

Gait analysis using motion capture systems is often used in clinical practice to determine appropriate treatments, evaluate the effectiveness of interventions and identify gait disorders, such as Trendelenburg gait [13]. Zügner et al. [14] highlighted the importance of using objective measurement instruments to assess THA outcomes and muscular complications, such as gluteus medius insufficiency. They observed two main parameters in the affected patients: lateral trunk flexion or lateral pelvic tilt or a combination of the two. Hamacher et al. [15] developed a system for assessing pelvic and trunk movements in the frontal plane in healthy subjects and patients with various gait disorders. In particular, they looked at ROM and the absolute mean inclination of the pelvis and trunk in the frontal plane, finding that reducing the pathological inclination of the trunk during gait may reduce degenerative changes in the spine. Correcting the gait pattern may be a direct way to reduce stress on the THA implants, thereby increasing longevity [16]. Chen et al. [17] developed a computer vision system based on artificial intelligence to discriminate different gait patterns associated with falls. They used Microsoft Kinect to detect normal gait, pelvic-obliquity-gait, and knee-hyperextension-gait walking. Even Thaler et al. [18] measured maximum and minimum pelvic obliquity to determine long-term functional outcome of THA. Bolink et al. analyzed the frontal plane angles of the pelvis during gait, since they can be useful indicators of functional impairment in hip OA patients and track improvements after THA [19]. Zeni et al. [20] suggested that increased pelvic drop may be indicative of residual hip weakness after THA.

In the present research, both pelvic drop and trunk lean dynamics were considered for Trendelenburg pattern recognition [12]. The developed software application permits to automatically compute pelvic drop and trunk lean to recognize the disorder, starting from the virtual skeleton. Average and maximum values of these variables were computed in degrees on the frontal plane, as suggested by the literature. ROM was considered for both trunk and pelvis joints. Furthermore, pelvic and trunk kinematics, such as peak velocity and peak acceleration were considered to study variability and stability during gait. Measures derived from the accelerations of the pelvis and the trunk are sensitive to reflect balance problems and gait instability [21]. These parameters have been used in literature to study stability in patients' gait with neurological disease, after stroke [22] or in ageing population [21] to evaluate the risk of falls. To the best of the authors' knowledge, this is the first attempt to measure them in the evaluation of Trendelenburg gait after THA.

Analysis of kinematic gait characteristics reveals differences among the approaches. Some studies highlighted a relationship between the surgical approach and the Trendelenburg gait due to abductor insufficiency following THA [23]. However, there is yet no clear link between the surgical approach and the risk of developing the disease. A recent systematic review by Patel et al. [24] suggested that there are higher chances of developing positive Trendelenburg sign in patients operated with lateral approach. Another review by Huang et al. [6] concluded that a lower rate of Trendelenburg gait was found in patients undergoing the anterior approach surgery compared to the lateral approach. However, Zeni et al. [20] found no differences between the two surgical approaches. As a result of the present study, several differences were identified between the posterior approach and the lateral and anterior approaches, while no significant differences were identified between the lateral and anterior approaches, in terms of pelvic and trunk kinematics. Although encouraging, these results should be interpreted with caution due to the limited size of the panel.

5 Conclusions

This work proposes a methodology to assess the Trendelenburg gait in individuals undergoing THA. To this end, a dedicated software package based on a markerless motion capture system has been developed. In addition to pelvic drop and trunk tilt, kinematic measurements are proposed for a more complete assessment of the Trendelenburg pattern. Hence, dynamic and kinematic measurements, such as ROM, peak velocity and peak acceleration could be considered as significant for the disorder evaluation. Analysis of these variables highlighted a possible correlation between the gait pattern and the surgical approach, that should be further investigated. The proposed procedure could help in identifying the best rehabilitation strategy based on the walking traits of the patient.

Acknowledgments. The authors acknowledge Fondazione Humanitas per la Ricerca for the financial support by grant 5x1000. Furthermore, the authors are grateful to Filippo Colombo Zeffinetti for his valuable assistance in data collection.

References

1. Bahl, J.S., Nelson, M.J., Taylor, M., Solomon, L.B., Arnold, J.B., Thewlis, D.: Biomechanical changes and recovery of gait function after total hip arthroplasty for osteoarthritis: a systematic review and meta-analysis. Osteoarthritis Cartilage **26**, 847–863 (2018)
2. Bertaux, A., et al.: Gait analysis dataset of healthy volunteers and patients before and 6 months after total hip arthroplasty. Sci Data **9** (2022)
3. Petis, S., Howard, J., Lanting, B., Jones, I., Birmingham, T., Vasarhelyi, E.: Comparing the anterior, posterior and lateral approach: gait analysis in total hip arthroplasty. Can. J. Surg. **61**, 50–57 (2018)

4. Meermans, G., Konan, S., Das, R., Volpin, A., Haddad, F.S.: The direct anterior approach in total hip arthroplasty: a systematic review of the literature. Bone Joint J. **99**-B, 732–40 (2017)
5. Ippolito, G., et al.: Direct anterior approach for total hip arthroplasty: Hip biomechanics and muscle activation during three walking tasks. Clin. Biomech. (Bristol, Avon) **89** (2021)
6. Tao, H.X., Guang, L.D., Jia, B., Xing, X.Y.: Comparisons between direct anterior approach and lateral approach for primary total hip arthroplasty in postoperative orthopaedic complications: a systematic review and meta-analysis. Orthop. Surg. 13, 1707–1720 (2021)
7. Yildirim, A., Ayanoglu, T., Ozer, M., Esen, E., Kanatli, U., Bolukbasi, S.: The evaluation of two different surgical approaches in total hip arthroplasty according to the patient satisfaction, plantar pressure distribution and trendelenburg sign. Med. Sci. (Turkey) **8**, 1–6 (2019)
8. Hattam, P., Smeatham, A.: Handbook of Special Tests in Musculoskeletal Examination: An evidence-based guide for clinicians (2020)
9. Ferreira, L.C.V., Rabelo, A.G., Vieira, M.F., Pereira, A.A., Andrade, A.d.O.: Gait variability and symmetry assessment with inertial sensors for quantitative discrimination of Trendelenburg sign in total hip arthroplasty patients: a pilot study based on convenience sampling. Res. Biomed. Eng. **34**, 65–72 (2018)
10. Zügner, R., Tranberg, R., Lisovskaja, V., Kärrholm, J.: Different reliability of instrumented gait analysis between patients with unilateral hip osteoarthritis, unilateral hip prosthesis and healthy controls. BMC Musculoskelet. Disord. **19** (2018)
11. Regazzoni, D., Vitali, A., Zefinetti, F.C., Rizzi. C.: Gait analysis in the assessment of patients undergoing a total hip replacement. In: ASME International Mechanical Engineering Congress and Exposition, Proceedings (IMECE), vol. 14, pp. 1–7 (2020)
12. Westhoff, B., Petermann, A., Hirsch, M.A., Willers, R., Krauspe, R.: Computerized gait analysis in Legg Calvé Perthes disease–analysis of the frontal plane. Gait Posture **24**, 196–202 (2006)
13. Boudarham, J., Roche, N., Pradon, D., Bonnyaud, C., Bensmail, D., Zory, R.: Variations in kinematics during clinical gait analysis in stroke patients. PLoS One **8** (2013)
14. Zügner, R., Hjelmberg, N., Rolfson, O., Strömberg, C., Saari, T.: Gluteus maximus transfer following total hip arthroplasty does not improve abductor moment: a case-control Gait analysis study of 15 patients with Gluteus medius disruption. J. Clin. Med. **11** (2022)
15. Hamacher, D., Bertram, D., Fölsch, C., Schega, L.: Evaluation of a visual feedback system in gait retraining: A pilot study. Gait Posture **36**, 182–186 (2012)
16. Foucher, K.C., Hurwitz, D.E., Wimmer, M.A:. Relative importance of gait vs. joint positioning on hip contact forces after total hip replacement. J. Orthop. Res. **27**, 1576–1582 (2009)
17. Chen, B., et al.: Computer vision and machine learning-based gait pattern recognition for flat fall prediction. Sensors **22**, 7960 (2022)
18. Thaler, M., Lechner, R., Putzer, D., Mayr, E., Huber, D.C., Liebensteiner, M.C., et al.: Two-year gait analysis controls of the minimally invasive total hip arthroplasty by the direct anterior approach. Clin. Biomech. **58**, 34–38 (2018)
19. Bolink, S.A.A.N., et al.: Frontal plane pelvic motion during gait captures hip osteoarthritis related disability. Hip Int. **25**, 413–419 (2015)
20. Zeni, J., Madara, K., Witmer, H., Gerhardt, R., Rubano, J.: The effect of surgical approach on gait mechanics after total hip arthroplasty. J. Electromyogr. Kinesiol. **38**, 28–33 (2018)
21. Zhang, Y., Zhou, X., Pijnappels, M., Bruijn, S.M.: Differences in gait stability and acceleration characteristics between healthy young and older females. Front. Rehabil. Sci. **2**, 69 (2021)
22. Van Criekinge, T., Saeys, W., Hallemans, A., Velghe, S., Viskens, P.J., Vereeck, L., et al.: Trunk biomechanics during hemiplegic gait after stroke: a systematic review. Gait Posture **54**, 133–143 (2017)

23. Petis, S., Howard, J.L., Lanting, B.L., Vasarhelyi, E.M.: Surgical approach in primary total hip arthroplasty: anatomy, technique and clinical outcomes. Can. J. Surg. **58**, 128–139 (2015)
24. Patel, N., Golwala, P., Patel, N., Golwala, P.: Approaches for total hip arthroplasty: a systematic review. Cureus **15** (2023)

Study of Stress Distribution in Press-Fit Transfemoral Implants: Standard Versus Patient-Specific Design

Tommaso Ingrassia, Giuseppe Marannano, Agostino Igor Mirulla, Vincenzo Nigrelli, and Andrea Valenti(✉)

Department of Engineering, University of Palermo, Viale delle Scienze Ed. 8, Palermo 90128, Italy
andrea.valenti@unipa.it

Abstract. Osseointegrated implant is a promising solution for limb amputations, but its widespread use is limited by risks such as bone resorption, infections, and strict patient requirements. Typically, the bone and prosthesis are coupled using a press-fit condition, providing short-term stability, or primary stability (PS), which leads to bone in-growth and long-term stability, or secondary stability (SS). However, the greater stiffness of the implant compared to the bone is a concern for SS. Currently, osseointegrated implants are commercially available only in fixed configurations, with a limited use of customization. This study aims to compare the contact effectiveness of three press-fitted intramedullary stems for femoral amputations, developed using three designs (straight, standard curvature, and patient-specific curvature). Moreover, a novel implant design methodology is reported, such is an easy way to develop a patient-specific design. The von Mises stress distribution at the bone-implant interface was analyzed. The study uses CAD models of a femur acquired through CT scans. A FEA was conducted to evaluate the elastic behavior of the bone when the implant is press-fitted with an interference of 0.1 mm. The outcomes show how the patient-specific implant result in a more physiological distribution of the load in the bone. This study could be used as a starting point for further studies on primary and secondary stabilities.

Keywords: Finite Element Model · Patient-Specific Design · Transfemoral Implant · Osseointegration · 3D Modelling

1 Introduction

Despite the promising improvement in patients' quality of life the risk of bone resorption, infections and the strict requirements asked to the patients, are limiting the diffusion of the osseointegrated implant to treat limb amputations [1, 2].

Nowadays the coupling between bone and prosthesis can be guaranteed by means of a press-fit condition that ensures the short-term stability, also called primary stability (PS). The effectiveness of the PS provides the optimal condition in which bone in-growth take places and the long-term stability, also called secondary stability (SS), occurs [3, 4].

M. Carfagni et al. (Eds.): ADM 2023, LNME, pp. 233–241, 2024.
https://doi.org/10.1007/978-3-031-52075-4_27

A major reason of concern for the SS is related with the effect of the grater stiffness of the implant compared to the one of the bones. The reduction in the stiffness of the implants, compared to the bones, is generally considered a key factor in obtaining long term stability. To achieve this long-term stability different strategies, allowed from additive manufacturing technique, like functionally graded materials and lattice structures are under investigation right now [5, 6]. Moreover, current osseointegrated implants for limb amputation commercially available are designed in a standard configuration, with fixed length and curvature, and different diameters. Customized designs are developed only for very short residual limb [3, 7].

Now days the reverse engineering is a widely spread approach such as the parametric modeling, applied in prosthesis and orthoses design and able to allow the realization of patient-specific prostheses that can potentially replicate the original morphology [8–10]. This, and the idea that a patient-specific stem could realize a physiological load transfer trough the bone-implant interface, have inspired this study that aims to compare the contact effectiveness of three different press-fitted intramedullary stems, developed for femoral amputations by following three designs (straight, standard curvature and patient-specific curvature), analysing the von Mises stress distribution at the bone-implant interface.

The results obtained during this work will be considered as starting point to develop further studies to investigating primary and secondary stabilities.

2 Material and Method

2.1 CAD Model

The CAD models of femur have been acquired through the segmentation of the CT scan using Mimics (Materialise NV - Leuven, Belgium). A threshold of the Hounsfield unit between 660 HU and 1500 HU was used to highlight the cortical bone and then obtain a 3D representation of the femur (Fig. 1).

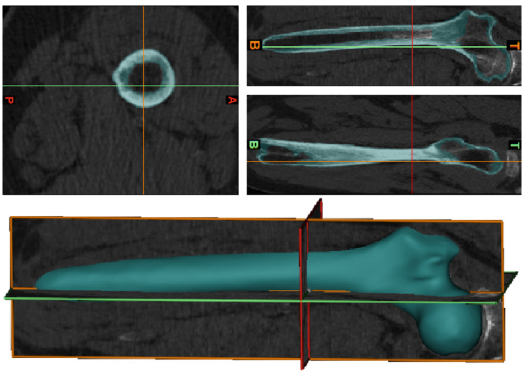

Fig. 1. The result of the segmentation procedure

Three copy of the bone's 3D model, exported to the CAD software Solidworks (Dassault Systèmes, Vélizy-Villacoublay, France), was treated by simulating the surgical procedure for the implantation of the prosthesis [11]. As described in the literature all the bones were reamed, to replicate the shape of the implant [7]. For the two specimen which represent the commercial implants the following steps was applied:

- Finding of the anatomical axis and the sagittal plane of the femur;
- Removal of the calcifications, usually encountered in long-term amputations, of the distal part Fig. 2(b);
- Identification of the straight line and the arc, with 2 m radius [12];
- Simulation of the reaming procedure of the medullary canal by performing a circular cut with a diameter of 19 mm.

For the patient-specific implant the longitudinal profile of the bone cavity was exploited to design the implant by following the below procedure:

- Identifying 18 transvers section, 10 mm spaced, and calculating their centroid coordinate, Fig. 2(c),
- Connecting the centroids with a spline, Fig. 2(d),
- Projecting the spline on the femur sagittal plane, Fig. 2(e),
- Executing a 19 mm circular cut along the projected spline.

From this procedure three medullary canal results, different from each other not only for the trajectory of the cut by even for the random vacancy that results in the contact surface, but that also reflect the reality better than a perfect match [4, 13].

Now, a circular profile of 19.1 mm was sweep extruded along the splines, for each implants design. At this point the portion of implant over 140 mm was cut, to obtain an implant profile independent from the length of the spline. Then, an abutment, on the distal part of the implant was modelled, representing the transcutaneous portion of the implant. Moreover, to decrease the computational cost of the simulation, the head of the femur where cut, neglecting the portion of bone over 170 mm from the cut plane. Now the assembly of the three specimens can be done, obtaining the bone-implant system that will now be exported, as Parasolid file, to a commercial FE solver. All the geometric parameter used are typical for this kind of applications [12–14].

2.2 FE Analysis

The CAD model of the bone-implant assembly was imported Abaqus/Explicit version 2019 (Dassault Systèmes, Vélizy-Villacoublay, France) to assess the elastic behaviour of the bone when the implant is press-fitted into the bone with a radial interference of 0.1 mm. All the simulations were conducted on a machine equipped with an Intel i7–7700, an Nvidia GTX 1070 and a RAM of 16 GB.

The implant was simulated as made of titanium grade 5 [7, 15], and the bone was considered orthotropic [15, 16], as reported in table 1.

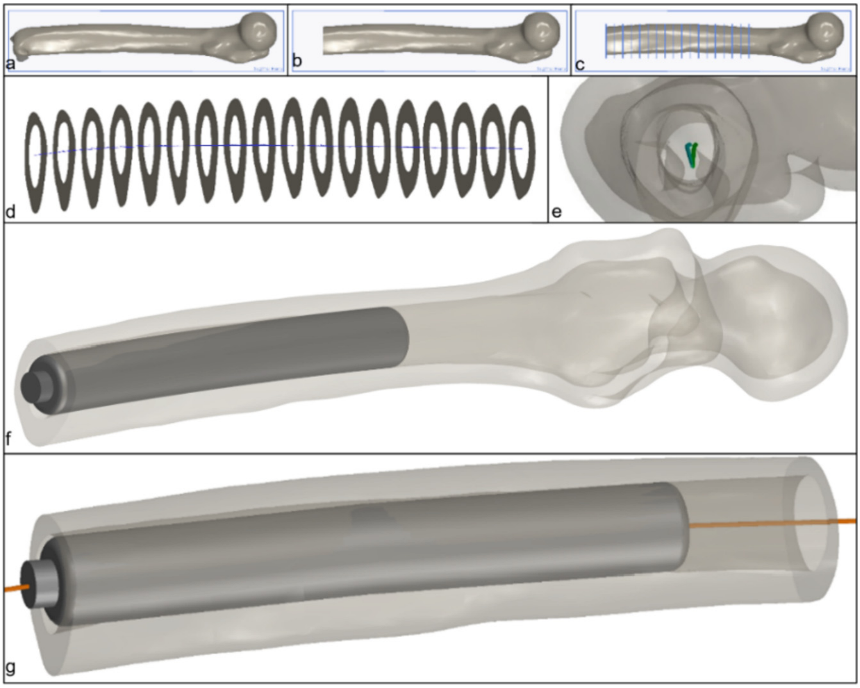

Fig. 2. The preparation of the bone: the original shape (a), after the removing of the ossification (b), the definition of the section used to identify the centroid (c), the sections considered with the spline that represent the longitudinal profile of the medullary canal (d), a detail that show the difference between the longitudinal profile of the medullary canal (blue) and his projection (green) on the sagittal plane (e), the complete assembly of the bone-implant system (f), the final assembly of the curved profile with a representation of the arc (orange) used to develop the implant, were the head of the femur was removed, (g).

The mesh was made by 10-nodes tetrahedral elements with an average element length of 3 mm, value selected after a sensitivity analysis ended when the von Mises equivalent stress changes is less than 5%.

As boundary condition, an encastre on the proximal part of the femur was applied [17, 18]. Moreover, the external part of the implant was embedded to avoid unrealistic longitudinal movements due to the spring back of the bone.

Table 1. Materials properties

	E_x [GPa]	E_y [GPa]	E_z [GPa]	G_{xy} [GPa]	Gyz [GPa]	Gxz [GPa]	νxy [GPa]	νyz [GPa]	νxz [GPa]
Cortical Bone	12	13.4	20	4.53	6.23	5.61	0.376	0.235	0.222
Ti6Al4V	110						0.3		

The bone-implant interface was simulated using surface-to-surface contact elements with a large sliding formulation.

To simulate the press-fit the interference fit options was allowed. As suggested from Abaqus's user manual, the tangential behavior of the contact surface was considered frictionless, while for the normal behavior a penalty formulation, with a normal thickness of 600N/mm, was considered [18–21]. All the parameters are reported in Table 2.

Table 2. Parameters used for the contact surface

Normal behaviour	Tangential behaviour	Normal Stiffness	Contact element	Interference Ø
"Hard" penalty	Frictionless	600 N/mm	Surface to surface	0,1 mm

3 Results

After performing the simulations, the maps of von Mises stress were extrapolated at the bone-implant contact surface for all analysed implants (Fig. 3).

The results obtained showed that both the straight and curved implants have inhomogeneous contact surfaces, highlighting a wide unloaded area on the lateral side of the bone, more extensive in the straight implant than in curved one.

Otherwise, the patient-specific implant showed a more homogeneous stress distribution at the bone-implant interface, with few unloaded zones located on the distal part and the lateral side at the diaphysis level, as it can be seen in Fig. 3.

Focusing the attention on the values, the highest maximum stress (70.8 MPa) has been calculated in the curved implant, while the highest average stress (29.6 MPa) has been found in the patient-specific implant.

To gain a more precise understanding of the situation, we also calculated the contact area and average von Mises stress, all of which are reported in Table 3.

Table 3. Analysis results

Implant	Contact surface [mm^2]	Average von Mises stress [MPa]	Maximum von Mises stress [MPa]
Straight	6326	21.9	67.3
Curved	6333	24.2	70.8
Patient-Specific	6622	29.6	65.3

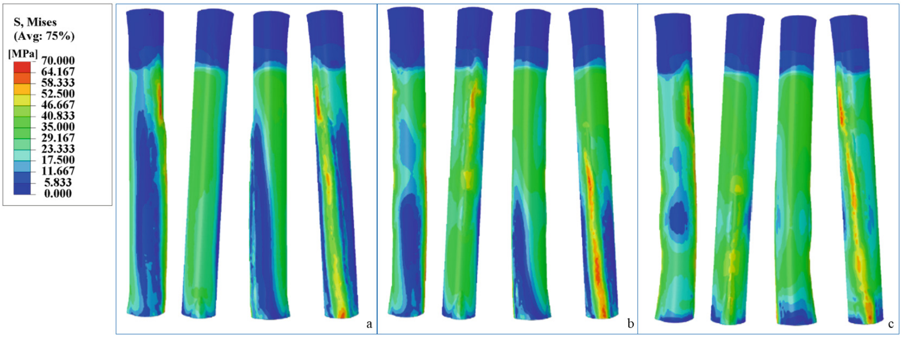

Fig. 3. The von Mises equivalent stress heatmaps for the straight (a), curved (b) and patient specific (c) implants.

4 Discussion

The main findings of this study, obtained by analyzing the von Mises stress distribution, showed that a more homogeneous contact distribution in a press-fit condition at the bone-implant interface could be obtained with a patient-specific implant compared to the straight and curved ones. Moreover, the methodology applied to obtain the novel implant represent a simple and easy way to develop patient specific osseointegrated prosthesis.

The results obtained in this study suggest that a patient-specific approach offer the possibility to equally distribute the loading due to the press-fit condition on the entire contact surface and could potentially confer better stability to the implant. In a long-term point of view, a customized implant could also allow a better bone remodelling process avoiding critical events such as bone resorption and fracture.

Since no similar studies are reported in literature, making an effective analysis of our results could be difficult. However, Thomson et al. [22] reported bone resorption at the distal level and in the diaphysis, for 2 years following implantation of a commercial transfemoral prosthesis with a press-fit system, as highlighted by the results reported in this work. The same kind of results are reported from Prochor et al. [14], where a bone resorption was recorded in the same region where a lack of load was found in the present study.

Moreover, the FE model reported in this study used input data referred to different anatomical districts [13, 19, 21, 23–25] or to different boundary conditions [14, 18, 26–29]. However, this study represented a preliminary analysis with a comparative purpose, analysing the press-fit condition and not investigating long-term behaviour that could be more useful for a predictive response.

Future study should be focused on the assessing of the mechanical behaviour of intramedullary implants under external cyclical loads, such as those applied during the rehabilitation protocol that could significantly influence the long-term bone remodelling phenomenon.

5 Conclusions

In this study a comparative FE analysis of three press-fitted implant designs, two standard and a patient-specific one, was conducted to assess the stress distribution at the bone-implant interface due to the geometrical interference. The outcomes showed that the implants result in different stress distributions across the bone-implant interfaces. Specifically, the results showed that a patient-specific implant, modelled following a planar projection of the real shape of the medullary canal, provided a homogeneous stress distribution at the bone-implant contact area. Moreover, despite the proposed FE model has not been validated by experimental tests, this study provided a methodological designing approach and may help the development of future patient-specific implants, potentially increasing the cohort of patients that could benefit of an osseointegrated implant.

References

1. Hebert, J.S., Rehani, M., Stiegelmar, R.: Osseointegration for lower-limb amputation: a systematic review of clinical outcomes (2017). https://doi.org/10.2106/JBJS.RVW.17.00037
2. Hagberg, K., Ghassemi Jahani, S-A., Kulbacka-Ortiz, K., Thomsen, P., Malchau, H., Reinholdt, C.: A 15-year follow-up of transfemoral amputees with bone-anchored transcutaneous prostheses mechanical complications and patient-reported outcomes. Bone Joint J. (2020)
3. Thesleff, A., Brånemark, R., Håkansson, B., Ortiz-Catalan, M.: Biomechanical Characterisation of Bone-anchored Implant Systems for Amputation Limb Prostheses: A Systematic Review (2018). https://doi.org/10.1007/s10439-017-1976-4
4. Gao, X., Fraulob, M., Haïat, G.: Biomechanical behaviour of bone-implant interface: a review biomechanical behaviours of the bone-implant interface: a review. J. R. Soc. Interface **16** (2019). https://doi.org/10.1098/rsif.2019.0259
5. Mirulla, A.I., et al.: Analysis of different geometrical features to achieve close-to-bone stiffness material properties in medical device: a feasibility numerical study. Comput Methods Programs Biomed. **221** (2022). https://doi.org/10.1016/j.cmpb.2022.106875
6. Bai, L., et al.: Additive manufacturing of customized metallic orthopedic implants: Materials, structures, and surface modifications (2019). https://doi.org/10.3390/met9091004
7. Hoellwarth, J.S., Tetsworth, K., Rozbruch, S.R., Handal, M.B., Coughlan, A., Al Muderis, M.: Osseointegration for amputees: Current implants, techniques, and future directions. JBJS Rev. **8** (2020). https://doi.org/10.2106/JBJS.RVW.19.00043
8. Ricotta, V., Campbell, R.I., Ingrassia, T., Nigrelli, V.: A new design approach for customised medical devices realized by additive manufacturing. Inter. J. Interact. Design Manufact. **14**, 1171–1178 (2020). https://doi.org/10.1007/s12008-020-00705-5
9. Ricotta, V., Campbell, R.I., Ingrassia, T., Nigrelli, V.: Additively manufactured textiles and parametric modelling by generative algorithms in ortho-paedic applications. Rapid Prototyp J. **26**, 827–834 (2020). https://doi.org/10.1108/RPJ-05-2019-0140
10. Cappello, F., Ingrassia, T., Mancuso, A., Nigrelli, V.: Methodical redesign of a semitrailer (2005)
11. Ingrassia, T., Nalbone, L., Nigrelli, V., Pisciotta, D., Ricotta, V.: Influence of the metaphysis positioning in a new reverse shoulder prosthesis. Presented at the (2017). https://doi.org/10.1007/978-3-319-45781-9_47

12. Atallah, R., van de Meent, H., Verhamme, L., Frölke, J.P., Leijendekkers, R.A.: Safety, prosthesis wearing time and health-related quality of life of lower extremity bone-anchored prostheses using a press-fit titanium osseoin-tegration implant: a prospective one-year follow-up cohort study. PLoS One. **15** (2020). https://doi.org/10.1371/journal.pone.0230027
13. Solitro, G.F., Whitlock, K., Amirouche, F., Santis, C.: Measures of micromotion in cementless femoral stems-review of current methodologies. Bio-materials and Biomechanics in Bioengineering **3**, 85–104 (2016). https://doi.org/10.12989/bme.2016.3.2.085
14. Prochor, P., Sajewicz, E.: The influence of geometry of implants for direct skeletal attachment of limb prosthesis on rehabilitation program and stress-shielding Intensity. Biomed. Res. Int. **2019** (2019). https://doi.org/10.1155/2019/6067952
15. Russell, R.D., Huo, M.H., Rodrigues, D.C., Kosmopoulos, V.: Stem geometry changes initial femoral fixation stability of a revised press-fit hip prosthesis: a finite element study. Technol. Health Care **24**, 865–872 (2016). https://doi.org/10.3233/THC-161235
16. Ingrassia, T., Nigrelli, V., Pecorella, D., Bragonzoni, L., Ricotta, V.: Influence of the screw positioning on the stability of locking plate for proximal tibial fractures: a numerical approach. Appli. Sci. (Switzerland) **10** (2020). https://doi.org/10.3390/app10144941
17. Mirulla, A.I., et al.: Biomechanical analysis of two types of osseointegrated transfemoral prosthesis. Appli; Sci. (Switzerland). **10**, 1–16 (2020). https://doi.org/10.3390/app10228263
18. Prochor, P.: Finite element analysis of stresses generated in cortical bone during implantation of a novel limb prosthesis osseointegrated fixation system. Biocybern Biomed Eng. **37**, 255–262 (2017). https://doi.org/10.1016/j.bbe.2016.12.001
19. Bernakiewicz, M., Viceconti, M.: The role of parameter identification in finite element contact analyses with reference to orthopaedic biomechanics appli-cations. J. Biomech. **35**, 61–67 (2002). https://doi.org/10.1016/S0021-9290(01)00163-4
20. Dassault Systèmes Simulia Corp.: ABAQUS/Standard User's Manual, Version (2021)
21. Viceconti, M., Muccini, R., Bernakiewicz, M., Baleani, M., Cristofolini, L.: Large-sliding contact elements accurately predict levels of bone-implant micromotion relevant to osseointegration. J. Biomech. **33**, 1611–1618 (2000). https://doi.org/10.1016/s0021-9290(00)00140-8
22. Thomson, S., Thomson, A., Tetsworth, K., Lu, W., Zreiqat, H., Al Muderis, M.: Radiographic evaluation of bone remodeling around osseointegration implants among transfemoral amputees. J. Orthop. Trauma **33**, 303–308 (2019). https://doi.org/10.1097/BOT.0000000000001488
23. Viceconti, M., Pancanti, A., Dotti, M., Traina, F., Cristofolini, L.: Effect of the initial implant fitting on the predicted secondary stability of a cementless stem. Med. Biol. Eng. Comput. **42**, 222–229 (2004). https://doi.org/10.1007/BF02344635
24. Conlisk, N., Howie, C.R., Pankaj, P.: Quantification of interfacial motions following primary and revision total knee arthroplasty: a verification study versus experimental data. J. Orthop. Res. **36**, 387–396 (2018). https://doi.org/10.1002/jor.23653
25. Ingrassia, T., et al.: A new method to evaluate the influence of the glenosphere positioning on stability and range of motion of a reverse shoulder prosthesis. Injury **50**, S12–S17 (2019). https://doi.org/10.1016/j.injury.2019.01.039
26. Camarda, L., Pitarresi, G., Moscadini, S., Marannano, G., Sanfilippo, A., D'Arienzo, M.: Effect of suturing the femoral portion of a four-strand graft during an ACL reconstruction. Knee Surgery, Sports Traumatology, Arthroscopy **22**, 1040–1046 (2014). https://doi.org/10.1007/s00167-013-2449-4
27. Lu, S., Vien, B.S., Russ, M., Fitzgerald, M., Chiu, W.K.: Novel osseointegration implant optimization - Australasian congress on applied mechanics. In: ACAM10: 10th Australasian Congress on Applied Mechanics, pp. 66–78 (2021). https://doi.org/10.3316/informit.321580783381592

28. Tomaszewski, P.K., Verdonschot, N., Bulstra, S.K., Verkerke, G.J.: A comparative finite-element analysis of bone failure and load transfer of osseointe-grated prostheses fixations. Ann. Biomed. Eng. **38**, 2418–2427 (2010). https://doi.org/10.1007/s10439-010-9966-9
29. Tomaszewski, P.K., van Diest, M., Bulstra, S.K., Verdonschot, N., Verkerke, G.J.: Numerical analysis of an osseointegrated prosthesis fixation with reduced bone failure risk and periprosthetic bone loss. J. Biomech. **45**, 1875–1880 (2012). https://doi.org/10.1016/j.jbiomech.2012.05.032

CNN-based Pose Estimation to Assist Medical Imaging

Andrea Cattaneo[1](✉), Alessia Zanni[2], and Daniele Regazzoni[1]

[1] Department of Management, Information and Production Engineering, University of Bergamo, Via Pasubio 7/B, 24044 Dalmine, Italy
andrea.cattaneo@unibg.it
[2] D/Vision Lab Srl, Dalmine, Italy

Abstract. The correct execution of scanning protocols is crucial to ensure the quality of radiographic examinations. Recent advances in machine learning methods have opened up new possibilities for medical imaging. However, the potential of pose estimation models in this field is still largely unexplored. This study aims to address this gap by investigating the performance and an application of pose estimation in the context of X-ray image acquisition. To this goal, a pose estimation model was selected from a pool of state-of-the-art models. It was then trained on a dataset of 213 images of humans undergoing X-ray imaging. Despite the limited size of the dataset, the model achieved an AP of 0.902 and a near real-time inference speed of 7 FPS on CPU. The detection of landmarks through pose estimation enables the automatic assessment of pose adherence to prescribed imaging protocols. This automation can reduce human errors and alleviate the mental workload on radiologists. The results of this study highlight the potential of convolutional neural network-based pose estimation models to assist radiologists in performing X-ray imaging tasks effectively.

Keywords: Pose Estimation · Deep Learning · Radiography · Optical Imaging · Convolutional Neural Networks

1 Introduction

Errors and discrepancies in radiology are a well-known and persistent challenge for healthcare professionals [1]. In daily practice, they are estimated to occur in 3–5% of cases, while in trauma and emergency settings they can reach up to 30% [2]. Scanning protocols, a set of guidelines and instructions that dictate how an imaging procedure should be performed, play a key role in ensuring the quality of the outcome [3]. They include information on the type of imaging technique to be used, patient positioning, exposure settings, and the specific body parts or regions to be aligned with the center of the beam. Adherence to a radiographic protocol is essential to ensure consistent and accurate imaging results and to minimize patient radiation exposure [3].

In recent years, pose estimation methods based on convolutional neural networks (CNNs) have emerged as powerful tools for accurately detecting the positions of body

M. Carfagni et al. (Eds.): ADM 2023, LNME, pp. 242–249, 2024.
https://doi.org/10.1007/978-3-031-52075-4_28

landmarks from two-dimensional images. These algorithms have achieved significant breakthroughs in a wide range of domains, including clinical applications such as gait analysis, fall detection, and physical therapy [4]. However, their potential for enhancing medical imaging remains largely unexplored. Moreover, the practical implementation of these methods in real-time scenarios often requires state-of-the-art hardware, which is currently not readily available in radiology settings.

The main objective of this study is to propose a novel CNN-based solution that leverages pose estimation techniques to provide valuable real-time assistance to radiologists during the image acquisition process. To achieve this goal, an evaluation of freely available pose estimation models was performed and the most suitable model was selected based on rigorous criteria. The selected model was then trained on a dataset of images of people positioned on an X-ray table. The performance of the model was quantitatively evaluated to assess its ability to accurately detect body landmarks. Finally, the detected patient landmarks were leveraged to ensure optimal positioning and to guide the radiologist in setting up the image acquisition procedure.

2 Methods

2.1 Dataset

The dataset comprises 213 two-dimensional photographs captured by a webcam mounted on the X-ray generator. These images depict individuals positioned on the table of an X-ray machine in various poses relevant to the acquisition of different body parts. The photographs solely focus on the part of the body targeted by the X-ray beam, resulting in a higher level of complexity for automatic keypoints detection. The samples were manually annotated in the COCO format [5]. All volunteers provided their consent to use the images for research purposes.

2.2 Model Selection

The challenge of this work demands a model capable of performing single-person pose estimation. A summary of the models available for this purpose is reported in Table 1.

In order to select the most appropriate model, the following criteria were defined:

1. The model has to be compatible with COCO keypoints, the annotation format used for the given dataset (models removed: [7, 8, 12, 16, 19]).
2. The license should allow commercial use to encourage industrial applications (models removed: [6, 10, 15]).
3. The model should provide clear instructions on how to perform training on custom datasets (models removed: [14, 20]).
4. Detection performance should be aligned to the state-of-the-art (models removed: [11, 18]).
5. The model has to be able to achieve an inference speed of 2 FPS on the CPU, which allows it to run on the PCs paired with the X-ray machine, which often do not have a GPU (model excluded: [9]).

Models that meet all the criteria are MMPose and RNS. Of these two, MMPose was chosen due to the completeness and clarity of the model documentation.

Table 1. Summary of the state-of-the-art models for single-person pose estimation.

Model	Framework	License
AlphaPose [6]	PyTorch	Research use only
BB-Pose [7]	Tensorflow	MIT
DeeperCut [8]	Caffe	N/A
Detectron2 [9]	PyTorch	Apache 2.0
Human Pose Regression with Residual Log-likelihood Estimation [10]	PyTorch	N/A
Lightweight OpenPose [11]	PyTorch	Apache 2.0
MediaPipe [12]	Tensorflow	Apache 2.0
MMPose [13]	PyTorch	Apache 2.0
MoveNet [14]	Tensorflow	Apache 2.0
MSPN [15]	PyTorch	N/A
OpenPose [16]	N/A	Research use only
RSN [17]	PyTorch	MIT
Simple Baselines for Human Pose Estimation and Tracking [18]	PyTorch	MIT
Unipose [19]	PyTorch	Research use only
ViTPose [20]	PyTorch	Apache 2.0

Table 2. Performance of the models over the test set.

Model	AP	AP.50	AP.75	AR	AR.50	AR.75
Off-the-shelf	0.749	0.918	0.754	0.837	0.957	0.837
Custom-trained	0.902	0.960	0.938	0.926	0.977	0.953

2.3 Model Training

The available samples were split into a test set of 20% and a training set of 80%, which was further divided into k = 8 equal parts using the k-fold cross-validation method. The model was trained iteratively on k-1 portions while using the excluded one for validation, until each part was excluded once.

Evaluation metrics of COCO were used to measure the performance of the model. The Object Keypoint Similarity (OKS) metric is based on the distance between the predicted and ground truth points, which is then normalized by the scale. The scale is defined for each ground truth object as the square root of the object segment area measured in pixels. Then, the average precision (AP) and average recall (AR) are computed establishing a threshold and comparing it to the OKS value.

To address the constraint posed by the limited size of the dataset, data augmentation was employed. This technique aims to expand the semantic coverage of a dataset by applying various transformations to the existing images. However, it is crucial to carefully select the appropriate augmentation techniques that are most suitable for the specific scenario. In this study, random flip, random shift of the bounding box center, random scale, and rotation were applied. These transformations were applied randomly at each epoch to allow the network to see slightly different training examples in each forward and backward pass through the training set. This allows the model to achieve better generalization and avoid overfitting [21].

3 Results

3.1 Model Performance

During cross-validated training, AP showed consistent growth with increasing batch sizes until reaching a plateau (Fig. 1). Notably, using a batch size of 16 on the GPU took 99 min to complete 200 epochs, with convergence occurring around 80 epochs. Conversely, a batch size of 32 resulted in a training duration of 138 min, and convergence was observed around epoch 100. Both scenarios yielded an AP between 0.95 and 0.97 at the plateau. Considering computational time and achieved average precision, 80 epochs and a batch size of 16 were chosen.

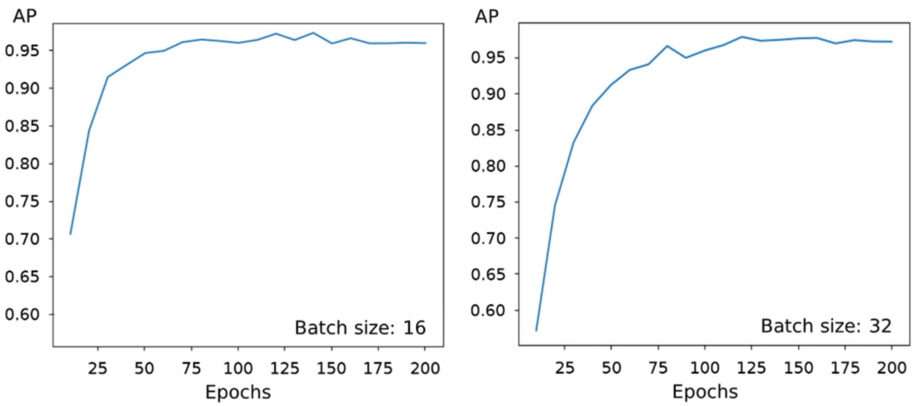

Fig. 1. Curve of AP during model training with k-fold cross-validation.

After selecting the hyperparameters, the model was trained on the entire training dataset and the performance was measured on the test set. Compared to the baseline performance obtained by running the off-the-shelf model, after custom training there is an improvement in both accuracy (AP + 20.4%) and recall (AR + 13.9%). In particular, the strict metrics showed the greater improvement (AP.75 + 24.4%; AR.75 + 13.9%). Furthermore, the inference speed of the custom trained model is 7 FPS on CPU.

A qualitative analysis of the keypoints of the model misclassifications highlights two main categories of errors. First, in cases where the images contain only one limb, the model often has difficulty distinguishing the side of the body, resulting in both left and right keypoints being placed in the same location. A second category of errors occurs when the landmark is slightly out of frame, but the adjacent joints are visible. In such cases, the model tends to place the landmark at the edge of the image.

3.2 Patient Pose Check

The patient landmark obtained from the pose estimation model allows for the evaluation of the optimality of the patient's pose according to the prescribed protocol (Fig. 2). This assessment can be performed using two approaches. The first approach is based on the absolute position of the keypoints with respect to the prescribed optimal pose for the individual (Fig. 2a-b). This ensures both the achievement of an optimal pose and the alignment of the body part of interest with the center beam. The second approach involves the computation of body angles to verify their alignment with the prescribed values (Fig. 2c-d). With the model's capability to perform near real-time inference, visual feedback can be provided to assist radiologists. In general, the focus is on obtaining the 3D pose of the individual. Considering that, during scanning, the patient's limbs lie flat on the X-ray detector, which is orthogonal to the camera, any errors related to projecting 3D points onto a 2D plane can be considered negligible. Thus, a reliable representation of the actual values is achieved.

4 Discussion

This work investigates the potential of two-dimensional single-person pose estimation based on deep learning to support X-ray image acquisition. A model was selected from a state-of-the-art pool and trained to detect the keypoints of patients placed on an X-ray table, achieving valuable performance. With an inference speed of 7 FPS on CPU, the trained model offers cost-effective benefits for industrial use, as it can be run on computers already paired with the X-ray machine.

The context of X-ray scanning is favorable for pose estimation algorithms for several reasons. The uniform and fixed background (i.e., the X-ray table), the single person being imaged, and the consistent lighting conditions provide a conducive environment for achieving high performance in pose estimation algorithms. Despite the limited number of samples and the challenging nature of partial human shape portrayal in the images, the model achieved an AP of 0.90, which is higher than the generally achieved AP of around 0.80 on heterogeneous datasets such as COCO [22].

CNN-based pose estimation can contribute to enhancing medical imaging in various aspects. Firstly, it enables the automated assessment of patient pose adherence to prescribed imaging protocols by accurately identifying anatomical landmarks. This guidance system effectively assists radiologists in achieving optimal image quality and consistency. Real-time feedback empowers radiologists to promptly make adjustments when there are deviations from the desired protocol, thereby improving the accuracy and reproducibility of imaging outcomes. Furthermore, by reducing the reliance on manual assessments, pose estimation not only saves time but also minimizes potential human errors. This streamlined imaging workflow allows radiologists to focus their attention on other critical tasks, leading to increased overall efficiency in healthcare settings.

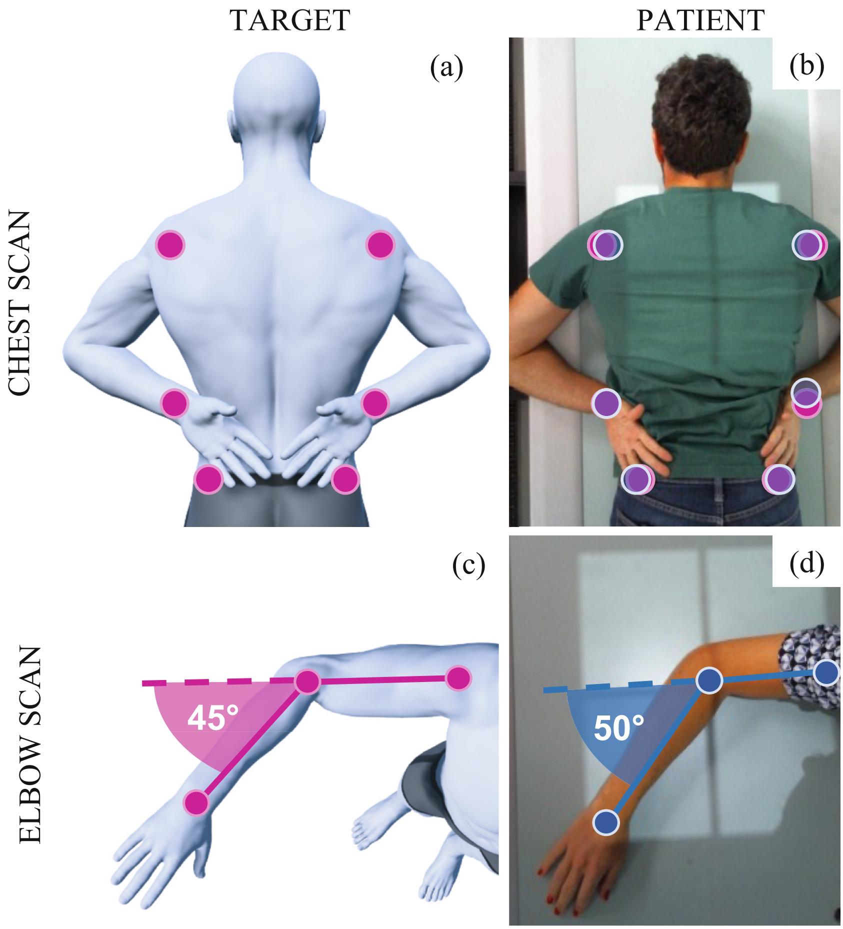

Fig. 2. Illustration of CNN-based pose estimation supporting radiologists for X-ray image acquisition. The model detects patient landmarks enabling automatic assessment of optimal landmarks alignment (a)(b) and joint angles (c)(d).

Additionally, recent research suggests that advancements in machine learning (ML) algorithms for medical imaging can enhance image quality by accommodating various patient profiles, pulse sequences, imaging planes, and multiple parameters. This capability addresses the variability and inconsistency observed in musculoskeletal care protocols [23]. In this context, pose estimation methods that accurately detect patient landmarks and body part dimensions can play a crucial role in enabling the adoption of a flexible X-ray acquisition protocol while effectively limiting radiation exposure [24].

Despite the limited size of the dataset, the custom trained model showed promising results. However, its predictive ability is expected to improve significantly with a larger dataset. One approach to tackle this challenge is by utilizing synthetic data generation techniques. By combining synthetic data with real data during training, the model can better handle variations in body characteristics and limb positions, improving its performance and generalizability. This approach can enable the model to effectively detect and distinguish overlapping limbs.

5 Conclusions

CNN-based pose estimation shows high potential for assisting radiologists in image acquisition. This technology provides the ability to automatically check patient pose compliance with the scanning protocol and optimal landmark placement. Although this work was conducted on X-ray machines, this technology could be extended to other scanning techniques such as CT and MRI. Furthermore, the ability to automatically identify the patient's landmarks can support the adoption of scanning techniques personalized to individual characteristics.

References

1. Brady, A.P.: Error and discrepancy in radiology: inevitable or avoidable? Insights Imaging **8**(1), 171–182 (2016). https://doi.org/10.1007/s13244-016-0534-1
2. Alessandrino, F., Bono, C.M., Potter, C.A., Harris, M.B., Sodickson, A.D., Khurana, B.: Spectrum of diagnostic errors in cervical spine trauma imaging and their clinical significance. Emerg. Radiol. **26**, 409–416 (2019). https://doi.org/10.1007/S10140-019-01685-0
3. Pinto, A., et al.: Errors in imaging patients in the emergency setting. British J. Radiol. **89**(1061), 20150914 (2016). https://doi.org/10.1259/bjr.20150914
4. Martini, E., et al.: Enabling gait analysis in the telemedicine practice through portable and accurate 3d human pose estimation. Comput. Methods Programs Biomed. **225**, 107016 (2022). https://doi.org/10.1016/J.CMPB.2022.107016
5. COCO - WholeBody data format, https://github.com/jin-s13/COCO-WholeBody/blob/master/data_format.md, Accessed 22 Mar 2023
6. Fang, H.S., et al.: AlphaPose: whole-body regional multi-person pose estimation and tracking in real-time. IEEE Trans Pattern Anal Mach Intell. (2022). https://doi.org/10.48550/arxiv.2211.03375
7. Bulat, A., Kossaifi, J., Tzimiropoulos, G., Pantic, M.: Toward fast and accurate human pose estimation via soft-gated skip connections. In: Proceedings - 2020 15th IEEE International Conference on Automatic Face and Gesture Recognition, FG 2020. 8–15 (2020). https://doi.org/10.48550/arxiv.2002.11098
8. Insafutdinov, E., Pishchulin, L., Andres, B., Andriluka, M., Schiele, B.: DeeperCut: A Deeper, Stronger, and Faster Multi-Person Pose Estimation Model. Lecture Notes in Computer Science (including subseries Lecture Notes in Artificial Intelligence and Lecture Notes in Bioinformatics). 9910 LNCS, 34–50 (2016). https://doi.org/10.48550/arxiv.1605.03170
9. Wu, Y., Kirillov, A., Massa, F., Lo, W.-Y., Girshick, R.: Detectron2, https://github.com/facebookresearch/detectron2, (2019)
10. Li, J., et al.: Human pose regression with residual log-likelihood estimation. In: Proceedings of the IEEE International Conference on Computer Vision. 11005–11014 (2021). https://doi.org/10.48550/arxiv.2107.11291

11. Osokin, D.: Real-time 2D Multi-Person Pose Estimation on CPU: Lightweight OpenPose. (2018). https://doi.org/10.48550/arxiv.1811.12004
12. Lugaresi, C., et al.: MediaPipe: A Framework for Building Perception Pipelines. (2019). https://doi.org/10.48550/arxiv.1906.08172
13. MMPose Contributors: OpenMMLab Pose Estimation Toolbox and Benchmark, https://github.com/open-mmlab/mmpose
14. Tensorflow: MoveNet: Ultra fast and accurate pose detection model, https://www.tensorflow.org/hub/tutorials/movenet
15. Chen, Y., Wang, Z., Peng, Y., Zhang, Z., Yu, G., Sun, J.: Cascaded Pyramid Network for Multi-person Pose Estimation. In: 2018 IEEE/CVF Conference on Computer Vision and Pattern Recognition (CVPR), pp. 7103–7112. IEEE Computer Society, Los Alamitos, CA, USA (2018). https://doi.org/10.1109/CVPR.2018.00742
16. Cao, Z., Hidalgo, G., Simon, T., Wei, S.E., Sheikh, Y.: OpenPose: realtime multi-person 2d pose estimation using part affinity fields. IEEE Trans Pattern Anal Mach Intell. 43, 172–186 (2018). https://doi.org/10.48550/arxiv.1812.08008
17. Cai, Y., et al.: Learning Delicate Local Representations for Multi-Person Pose Estimation. Lecture Notes in Computer Science (including subseries Lecture Notes in Artificial Intelligence and Lecture Notes in Bioinformatics). 12348 LNCS, 455–472 (2020). https://doi.org/10.48550/arxiv.2003.04030
18. Xiao, B., Wu, H., Wei, Y.: Simple Baselines for Human Pose Estimation and Tracking. Lecture Notes in Computer Science (including subseries Lecture Notes in Artificial Intelligence and Lecture Notes in Bioinformatics). 11210 LNCS, 472–487 (2018). https://doi.org/10.48550/arxiv.1804.06208
19. Artacho, B., Savakis, A.: UniPose: Unified Human Pose Estimation in Single Images and Videos. (2020). https://doi.org/10.48550/arxiv.2001.08095
20. Xu, Y., Zhang, J., Zhang, Q., Tao, D.: ViTPose: simple vision transformer baselines for human pose estimation. (2022). https://doi.org/10.48550/arxiv.2204.12484
21. Shorten, C., Khoshgoftaar, T.M.: A survey on image data augmentation for deep learning. J Big Data. **6**, 1–48 (2019). https://doi.org/10.1186/S40537-019-0197-0/FIGURES/33
22. COCO test-dev Benchmark (Pose Estimation) | Papers With Code, https://paperswithcode.com/sota/pose-estimation-on-coco-test-dev, Accessed 24 Mar 2023
23. Shin, Y.R., Kim, S., Lee, Y.H.: AI musculoskeletal clinical applications: how can AI increase my day-to-day efficiency? Skeletal Radiol. **51**, 293–304 (2022). https://doi.org/10.1007/S00256-021-03876-8
24. Martínez, A., García-Santos, A., Ballesteros, N., Desco, M., Abella, M.: XAP-Lab: a software tool for designing flexible X-ray acquisition protocols. Comput. Methods Programs Biomed. **177**, 243–252 (2019). https://doi.org/10.1016/j.cmpb.2019.05.013

Environmental Sustainability of a Televisit Process: Definition of Parameters and Preliminary Results

Anna Savoldelli(✉), Daniele Landi, and Caterina Rizzi

Department of Management, Information and Production Engineering, University of Bergamo, Via Pasubio, Dalmine (Bergamo), Italy
anna.savoldelli@unibg.it

Abstract. Healthcare sector has a significant impact on the environment. While telemedicine techniques could be a solution to increase its sustainability, the methods for a quantitative evaluation are poorly applied and often generate a partial assessment. Therefore, the main aim of the present research is the definition of a methodology for a preliminary quantification of the environmental impact generated by the process to perform a televisit. The methodology has been structured in 4 phases: process identification, impacts detection, data elaboration and results analysis. A real case study was performed including follow-up televisits for cardiopathic patients. After having defined the setting of the study, a list of tasks was prepared. For each task physical wastes, devices energy consumption, telecommunications and transportation were investigated. Equivalent CO_2 (CO_2 eq) was calculated involving sources from studies in literature and official websites. Although televisit reduces the impacts caused by patient travel, the use of telecommunications during supporting activities caused a significant amount of CO_2 eq. Therefore, a complete assessment has to include the entire process of televisit. Despite the average input data, the methodology offers a base that could be improved with other impact indicators.

Keywords: Environmental Sustainability · Telemedicine · Assessment Tool · Process Modeling · Sustainable Development

1 Introduction

The use of telemedicine techniques has become increasingly widespread; therefore, the effects generated by the implementation of these new practices are an interesting topic for many studies. The investigation of telemedicine long-term sustainability requires a comprehensive assessment, related not only to its clinical efficiency but also to the impacts generated by its use. Some researches highlight telemedicine as a tool for directing the healthcare sector toward the concept of sustainable development [1]. As declared by Gulis G. et al. [2], sustainable development goals are strictly correlated to environmental impact assessment. The healthcare sector is responsible for a strong impact on the environment, caused by high gas emissions and a large production of waste [3,

M. Carfagni et al. (Eds.): ADM 2023, LNME, pp. 250–258, 2024.
https://doi.org/10.1007/978-3-031-52075-4_29

4]. While telemedicine has the potential to limit this negative effect [5–7], also digital activities cannot be considered completely green. For this reason, it is crucial to objectively and systematically measure the impacts generated by the introduction of digital care, to improve their use and pursue the concept of sustainable development. The methodologies adopted by several studies in the literature are mainly related to avoided travels and involve questionnaires, case studies, and database information [8, 9]. However, as declared by Lokmic-Tomkins et al. [9], a standardized method is still lacking. Furthermore, issues of telecommunications usage are still poorly included in the evaluation.

According to the defined context, the present study proposes a methodology to identify and quantify the environmental impacts related to a televisit process. Hence, the main objective concerns the definition of parameters to systematize a comprehensive evaluation, including wastes, telecommunications and travels. Secondly, the research aims to perform a preliminary analysis of generated or avoided CO_2 eq caused by the televisit process, applying the approach to a real case study.

2 Methodology

The proposed methodology is subdivided in four main steps, as represented in Fig. 1: i) process identification, ii) impacts detection, iii) data elaboration, iv) results analysis. These phases are derived from the life cycle assessment approach, to define an objective and systematic framework.

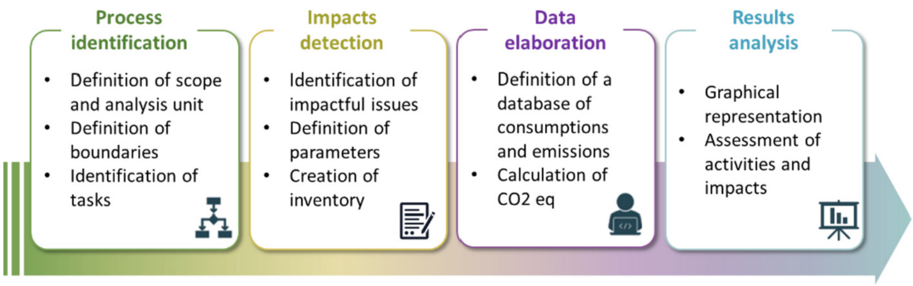

Fig. 1. Main steps of the proposed methodology.

During the first phase, the conditions required to set up and carry out the analysis are defined. Once determined the purpose of the study, the introduction of a reference unit and system boundaries allow to focus calculations only on relevant aspects. Through the analysis of the real care process, an objective framework is created, based on the activities actually performed during daily practices. For a more comprehensive evaluation, all direct and indirect activities of televisit are considered. As result, the whole process is resumed in a list of tasks performed by medical personnel and patient, required to deliver a remote visit.

In the second phase, tasks are analyzed according to the following categories: paper material, devices for televisit, devices for other purposes, hospital rooms, internet connection, web applications and data transmission. The study includes both the impacts generated by performing televisit and the ones avoided thanks to the use of digital tools. Activities carried out in both modes are omitted, because they don't have a quantitative impact on results. Each category is further explored by means of 4 parameters (Fig. 2), for a more detailed investigation. In this analysis, a fifth parameter, related to devices life cycle, is overlooked. Therefore, exploring each impact category and its related sub-parameters, a detailed and systematized inventory can be defined for the whole process.

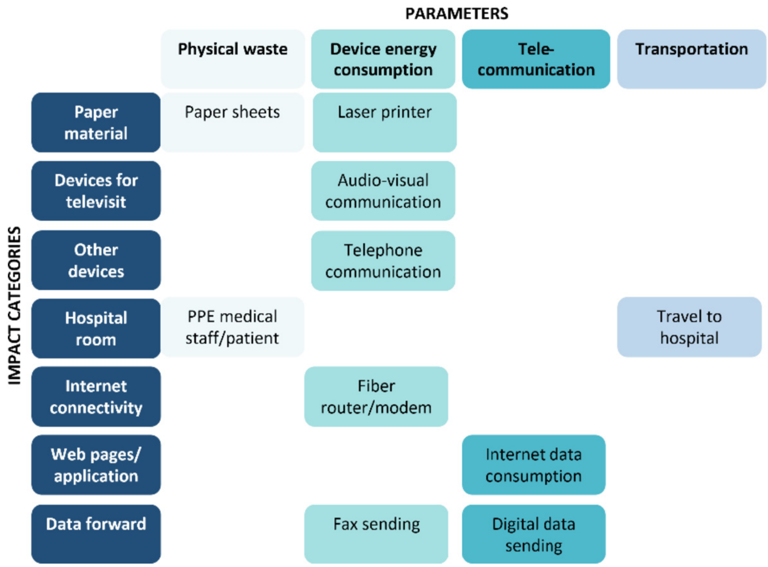

Fig. 2. Definition of parameters required for the analysis.

In the third step, a preliminary quantification of environmental impacts is performed by calculating the CO_2 eq related to each task. For the present research, secondary data from scientific studies or official websites are considered acceptable. In the case of electrical devices, watt consumption can be converted to CO_2 eq by calculating the kilowatt-hours and multiplying them by the conversion factor for electricity consumption. The estimated emissions are collected according to the previous inventory.

Finally, in the last phase, the preliminary results are collected by means of graphical representation, for an easier detection of CO_2 eq generated by each task. Moreover, the measurement of the CO_2 eq of parameters throughout the entire process allows the identification of the main sources of environmental impact.

3 Application to a Case Study

The proposed methodology has been applied to a real case at a large Italian hospital in the province of Bergamo (Italy). The process concerns the care of chronic heart failure (HF) patients and it investigates the follow-up medical examinations, which do not require further investigation with medical devices at the moment of the visit.

3.1 Process Identification

The scope of the research includes the quantification of impacts generated and avoided by performing follow-up televisits in the HF clinic. The delivery of one televisit for a single patient has been considered in the analysis. A direct comparison between a televisit and a face-to-face visit is allowed thanks to the similarity in the duration and performed activities. While the impact of wastes such as personal protective equipment (PPE) and paper have been considered during their life cycle from cradle to gate, information and communication technologies have been evaluated only during their usage. Indeed, the same digital instrumentation would be available in hospitals also without the implementation of televisits.

The methodology proposed in a previous study [10] has been applied to map the process. IDEF0 technique has allowed the acquisition of information from the healthcare staff and the detection of the involved instrumentation. The whole process has been schematized in 4 macro activities, as represented in Fig. 3.

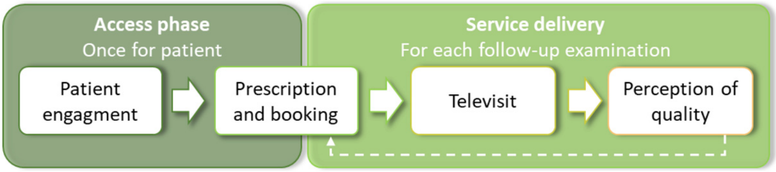

Fig. 3. Macro activities of televisit process

The process includes both the activities carried out during the televisit and the ones required to engage the patient and test the quality of the service. Specifically, a first access phase has been done only one time for each patient, while the other phase has been repeated for each televisit. Therefore, a list of tasks has been collected for each macro activity, for a total of 18 activities.

3.2 Impacts Identification

Information has been collected from the "mechanisms" arrows of IDEF0 diagrams, which indicate the tools and equipment required to perform the activity. Considered devices allowed the preparation of paper-based documents, the communication with patients during video calls and telephone calls, and a stable internet connection. Other medical devices have been neglected. Data consumption and digital data transmission have been included. In addition to paper material, wastes have concerned PPE used by healthcare personnel, patients, and caregivers during the visit. Room sanitation has not been taken into account. Lastly, in patients' travels, public transportation has been omitted, due to the preference for individual car movements.

Therefore, by applying the 4 parameters (Fig. 2), a set of critical issues have been identified in order to quantify their CO_2 eq and environmental impact. From the initial 18 tasks, 3 of them have been eliminated because they did not contain any differences between the digital and in-person visits.

3.3 Data Elaboration

A database has been created to quantify the items highlighted in the previous step. Table 1 shows data acquired through scientific papers, Italian and European websites, in order to define the amount of CO_2 eq generated by each task. For electronic devices, the consumption of watts has been investigated. Since the study has been carried out in Italy, 0.247 kgCO2eq/kWh [11] has been considered as a conversion factor to quantify the CO_2 eq. A reference unit has been specified in the table; these values have been multiplied by the effective usage during the process.

Table 1. Equivalent CO_2 database, for the calculation of tasks impact.

	Power [W]	Emissions [g CO2eq]	Unit
Devices energy consumption			
Professional laser printer	450	0.309	A4 sheet
Fax sending [13]	8,15	0.034	1 min
Desktop (hospital) [6, 12]	150	0.618	1 min
Camera [6, 12]	9,5	0.039	1 min
Sound system [6, 12]	4,1	0.017	1 min
Microphone [6, 12]	2,5	0.010	1 min
Cordless phone [12]	3	0.012	1 min
Laptop (patient) [6, 12]	40	0.165	1 min
Mobile phone (patient) [12]	5	0.021	1 min
Router fiber connectivity [14]	10	0.041	1 min
Physical wastes			
Paper sheet [15]		4.56	A4 sheet
Masks/sterile gloves/apron [5]		20/52/65	1 piece/pair
Telecommunications			
Email (text/text, attachment) [16, 17]		10/20	1 email

(*continued*)

Table 1. (*continued*)

	Power [W]	Emissions [g CO2eq]	Unit
Televisit (audio visual for 2 participants) [18]		400	1 min
Data transferring (upload/download) [19]		0.015	1 MB file
Google questionnaire [20]		1.16	1 page
Application use (internet use) [21]	100	4.117	1 min
Transportation			
Average petrol car [22]		0.1705	1km
Average diesel car [22]		0.1708	1km

Some assumptions have been made. An average of 6 A4 sheets printed per minute has been approximated for paper printing. Furthermore, each PPE has been used by a physician and a nurse for 4 visits, carried out in one afternoon; the patient is always accompanied by a caregiver, and both of them use a mask for each visit. The average distance of patients is 20 km; the conversion coefficient is an average between petrol and diesel cars. The impact of a televisit has been calculated by looking at the requirements of a Zoom video call [12] and approximating at 0.015 kWh/GB the value for the electrical energy intensity of transmitting data. Finally, an average value of emails has been estimated, considering a necessary writing time of 5 min.

By combining the acquired information and process analysis, the amounts of CO_2 eq produced and avoided for each task have been calculated. Finally, results have been collected and illustrated in Fig. 4.

3.4 Results Analysis

Although the implementation of televisits is considered a strategic choice to reduce the environmental impact of the healthcare sector, the proposed study shows that it is responsible for the generation of a certain amount of CO_2 eq. The following new approach, which includes the mapping of the real process as first step, allows to extend assessment approaches available in literature. Indeed, the addition of indirectly supporting activities, necessary to support a televisit, develops a more realistic evaluation. Specifically, as shown by the results in Fig. 4, the "patient engagement" and "prescription and booking" phases have a negative environmental impact, causing the emission of 102.43 g of CO_2 eq. In these cases, the saved CO_2 eq is only 10.03 g. Similarly, the "perception of quality" phase is responsible for 19.64 g CO_2 eq. In all these cases, the implementation of televisits has a negative effect on the environment. In contrast, during the actual visit, the generated CO_2 Eq. (46.2 g) is significantly less than the saved ones (150.9 g), thanks to the reduction of patients' travel to the hospital. Even if results are based on average

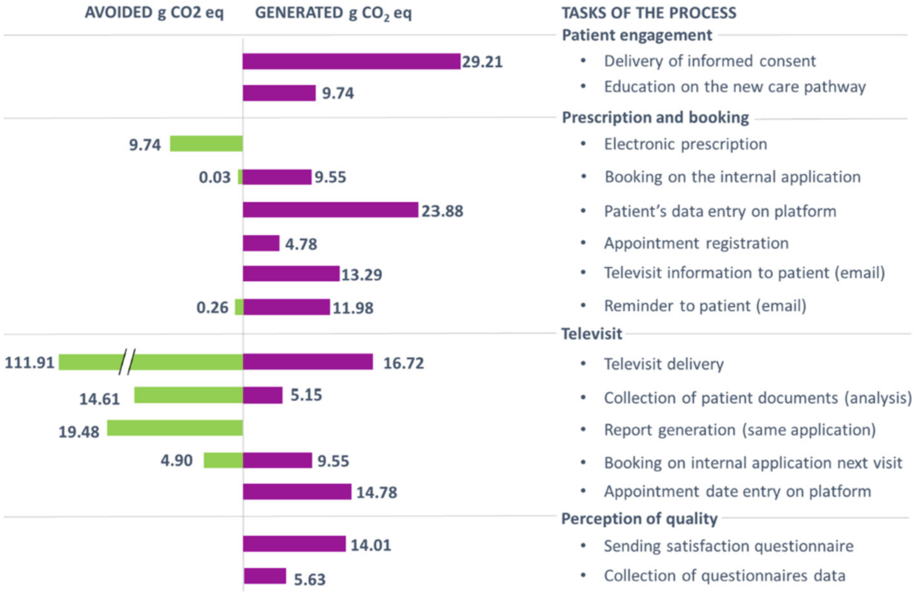

Fig. 4. Equivalent CO_2 generated and avoided during the entire process.

estimations, they demonstrate that in a more comprehensive evaluation, the achieved environmental benefits are limited by all indirect activities.

Generated CO_2 eq of each parameter (Fig. 5), shows that the release of televisits has significantly limited the negative impact of wastes, mainly related to paper sheets. At the same time, the impact of transportations has decreased. On the other hand, devices have been used for a longer period of time, causing increased consumption of electricity. Furthermore, telecommunications have a high negative impact, mainly related to audio-visual medical examinations.

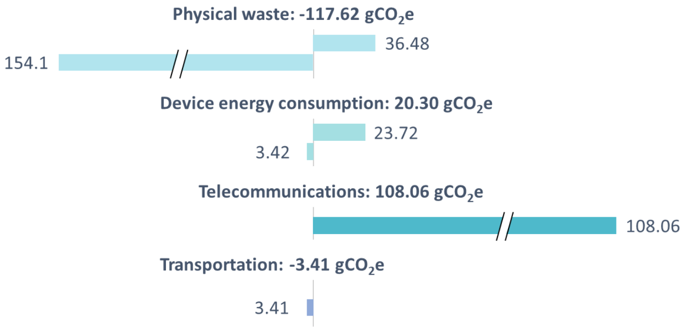

Fig. 5. Equivalent CO_2 generated and avoided for each parameter.

As a result, considering the release of a single televisit for one patient, the difference between a digital and in-person visit is not very relevant. However, since the most impactful issues are related to the patient access phase and they do not have to be repeated, the results would improve by considering a longer period and multiple visits for each individual patient.

4 Conclusion

In conclusion, the study presents a methodology for a systematic and reproducible assessment of the environmental impacts caused by the use of follow-up televisit. Being process-based, the approach allows for the investigation of actual tasks performed during clinical practice, including both direct and indirect activities. By following this approach, it is possible to identify the most significant sources of emissions and work to reduce them. The research is a primary tool for hospitals and other healthcare facilities to assess the environmental impact of telemedicine activities. However, the approach could be extended, including other environmental indicators and the use of software. Furthermore, to better understand the sustainability of telemedicine techniques, it will be necessary to expand the studies and include also social and economic aspects.

References

1. Bozoudis, V., Sebos, I., Tsakanikas, A.: Action plan for the mitigation of greenhouse gas emissions in the hospital-based health care of the Hellenic Army. Environ. Monit. Assess. **3** 194 (2022). https://doi.org/10.1007/s10661-022-09871-3
2. Gulis, G., Krishnankutty, N., Boess, E.R., Lyhne, I., Kørnøv, L.: Environmental impact assessment, human health and the sustainable development goals. Int. J. Public Health **67**, 2 (2022). https://doi.org/10.3389/ijph.2022.1604420
3. Rouvière, N., et al.: Ecoresponsible actions in operating rooms: a health ecological and economic evaluation. Int. J. Surg. **101**, 106637 (2022). https://doi.org/10.1016/j.ijsu.2022.106637
4. Maloney, B., et al.: The environmental footprint of single-use versus reusable cloFiths for clinical surface decontamination: a life cycle approach. J. Hosp. Infect. **130**, 7–19 (2022). https://doi.org/10.1016/j.jhin.2022.09.006
5. Bartlett, S., Keir, S.: Calculating the carbon footprint of a geriatric medicine clinic before and after COVID-19. Age Ageing **51**, 1–4 (2022). https://doi.org/10.1093/ageing/afab275
6. Holmner, Å., Ebi, K.L., Lazuardi, L., Nilsson, M.: Carbon footprint of telemedicine solutions - Unexplored opportunity for reducing carbon emissions in the health sector. PLoS ONE **9**, e105040 (2014). https://doi.org/10.1371/journal.pone.0105040
7. Agbafe, V., Berlin, N.L., Butler, C.E., Hawk, E., Offodile, A.C.: Prescriptions for mitigating climate change-related externalities in cancer care: a surgeon's perspective. J. Clin. Oncol. **40**, 1976–1979 (2022). https://doi.org/10.1200/JCO.21.02581
8. Anna Savoldelli, Daniele Landi, Caterina Rizzi,: Sustainability in Healthcare: Methods and Tools for the Assessment. In: Bernhard Pfeifer, Günter Schreier, Martin Baumgartner, Dieter Hayn, (ed.) DHealth 2023: Proceedings of the 17th Health Informatics Meets Digital Health Conference. IOS Press (2023). https://doi.org/10.3233/SHTI230037
9. Lokmic-Tomkins, Z., et al.: Assessing the carbon footprint of digital health interventions: a scoping review. J. Am. Med. Inform. Assoc. **29**, 2128–2139 (2022). https://doi.org/10.1093/jamia/ocac196

10. A. Savoldelli, D. Regazzoni, S. Ludi, and C. Rizzi, An Engineering Method to Evaluate Care Processes and Introduce Televisits, in: Lect. Notes Mech. Eng., Springer Science and Business Media Deutschland GmbH, 2023: pp. 181–191. https://doi.org/10.1007/978-3-031-15928-2_16
11. European Environment Information and Observation Network (Eionet), Greenhouse gas emission intensity of electricity generation in Europe, EEA Web Team. (2021). https://www.eea.europa.eu/ims/greenhouse-gas-emission-intensity-of-1
12. Blenkinsop, S., Foley, A., Schneider, N., Willis, J., Fowler, H.J., Sisodiya, S.M.: Carbon emission savings and short-term health care impacts from telemedicine: An evaluation in epilepsy. Epilepsia **62**, 2732–2740 (2021). https://doi.org/10.1111/epi.17046
13. ECO-FAX Support, (n.d.)
14. Fibre: the most energy-efficient solution to Europe's bandwidth needs, (2018)
15. Dias, A.C., Arroja, L.: Comparison of methodologies for estimating the carbon footprint-case study of office paper. J. Clean. Prod. **24**, 30–35 (2012). https://doi.org/10.1016/j.jclepro.2011.11.005
16. How bad are bananas?: the carbon footprint of everything. Choice Reviews Online **49**(04), 49-2023–49-2023 (2011). https://doi.org/10.5860/CHOICE.49-2023
17. S. Walkley, The Carbon Cost of an Email: Update! - The Carbon Literacy Project, (2022). https://carbonliteracy.com/the-carbon-cost-of-an-email/
18. Faber, G.: A framework to estimate emissions from virtual conferences. Int. J. Environ. Stud. **78**, 608–623 (2021). https://doi.org/10.1080/00207233.2020.1864190
19. ClimateCare, Infographic: The Carbon Footprint of the Internet, ClimateCare. (2021) 1–1. https://sphera.com/blog/the-carbon-footprint-of-the-internet/
20. Website Carbon Calculator, Website Carbon Calculator | How is your website impacting the planet?, Website Carbon Calc. (2021). https://www.websitecarbon.com/
21. Lawrence berkeley national lab, (2012) 2012
22. Footprinting and reporting | The Carbon Trust, (n.d.). https://www.carbontrust.com/what-we-do/strategy-delivery-and-reporting/footprinting-and-reporting

Human-Related and User-Centered Design

A Personalized Expert Guide for the Hybrid Museums of the Future

Elena Spadoni[1](✉), Riccardo Giussani[2], Marina Carulli[2], Nicolò Dozio[2], Francesco Ferrise[2], and Monica Bordegoni[2]

[1] Department of Design, Politecnico di Milano, Via Durando 10, 20158 Milan, Italy
elena.spadoni@polimi.it

[2] Department of Mechanical Engineering, Politecnico di Milano, Via La Masa 1, 20156 Milan, Italy
{riccardo.giussani,marina.carulli,nicolo.dozio, francesco.ferrise,monica.bordegoni}@polimi.it

Abstract. The increasing interest in technologies such as Metaverse, Augmented Reality (AR), and Artificial Intelligence (AI) opens up numerous possibilities that have the potential to shape our daily experiences in the future. We investigated how integrating today's popular chatbots and multisensory AR technologies can create personalized museum visiting experiences. The paper outlines the concept of a digital assistant-based application for museum visits. The visitor, equipped with AR technology, can ask questions about the exhibits and receive precise and contextually relevant answers from the digital assistant who can virtually appear as an avatar with accompanying multimedia AR information. In the paper, we describe the implementation of a prototype of the application.

Keywords: Augmented Reality · Metaverse · Chatbots · Museums

1 Introduction

Despite available interactive technologies, many museum exhibitions still follow traditional approaches, hindering visitor engagement. This paper explores the potential benefits and challenges of adopting interactive strategies for enhanced museum experiences. Artworks that visitors encounter may require explanation, which is typically provided in written or pre-recorded form. To access this content, visitors are asked to passively read or listen a predefined content. Therefore, we are used to listening to a text without being able to ask questions and satisfy our curiosity or deepen the topics explained in the text.

However, as frequent internet users, we have become accustomed to seeking direct answers to our queries. With the progress made in search engine technology, contemporary systems demonstrate enhanced capabilities in comprehending human language and delivering pertinent responses. The recent interest in Large Language Models (LLM) and their remarkable development, opens up several

M. Carfagni et al. (Eds.): ADM 2023, LNME, pp. 261–272, 2024.
https://doi.org/10.1007/978-3-031-52075-4_30

possibilities that would have been inconceivable just a few years ago. Even in areas such as culture where this method has not been applied, we can attempt to change our information consumption habits in a reverse manner. This study applies such innovative technology to the cultural heritage domain, in an attempt to revolutionize the way information is accessed. This study applies such innovative technology to the cultural heritage domain, in an attempt to revolutionize the way information is accessed in museums. In particular, these structures offer a chance to experiment with this new method of utilizing content. The concept involves posing questions related to the specific interests of each individual while observing a piece of art, rather than relying on a pre-determined text. This approach would result in a more immediate, engaging, and customized exploration of the artwork. Therefore, current technologies that allow natural language processing, text interpretation, and question-coherent answers may help museum curators make the experience more interactive or personalized.

Mobile devices, such as smartphones, are often considered a standard technology that visitors carry with them while exploring exhibitions. Smartphones are well-suited for becoming an augmented window into the real world due to their camera functionality. This is a common metaphor used when discussing Augmented Reality (AR). In fact, AR refers to technology that overlays digital information onto the physical world in real-time. One way to experience AR is through a smartphone camera, which can display digital information on top of the real world as seen through the camera lens. Therefore, smartphones are often used as a tool to experience AR. However, in addition to visual information, it is possible to create AR experiences that leverage other senses, such as sound or touch. For example, a piece of AR technology may use haptic feedback to provide a tactile sensation in response to a user's actions or movements, or it may use spatialized audio to create an immersive auditory environment [7].

By merging the AR metaphor with tools that help visitors understand language and utilize information, many exciting possibilities emerge. In fact, AR technology can help to provide a more immersive and engaging experience for visitors, and by enhancing this with language comprehension tools, it becomes easier for visitors to understand the content being presented.

In the near future, the possibilities for combining AR technology with language comprehension tools will be expanded by the introduction of wearable AR devices that offer higher performance than current market offerings, enabling users to interact with hybrid content in a more natural and seamless manner. The research outlined in this paper follows this approach by combining available and popular technologies, such as natural language transcription systems, Generative Pre-trained Transformers (GPT) algorithms, and AR technologies. We have devised a personalized museum guide enhanced by Artificial Intelligence (AI) in response to this, which we believe embodies the future of museum experiences. We outline the creation process of our initial prototype and the preliminary testing phase.

2 Related Works

Some museums opt to augment and complement the observation and comprehension of exhibits during the physical visit by integrating digital technologies alongside conventional approaches. Alternatively, they may employ such technologies prior to or after the exhibit to offer extra exploration or retrieval of content [10,13].

Numerous scholars have delved into the use of Virtual Reality (VR) technologies in museum exhibits. According to [11], the digital museum should not supplant the traditional museum. Instead, digital content should supplement the physical displays while taking into account the museum's function for the visitor. This aspect can be readily assessed through the use of Augmented Reality (AR) to complement physical artifacts displayed in museums and VR to recreate a virtual representation of the museum or its exhibits. Geroimenko [9] explores the potential of AR as a novel artistic medium, highlighting its advantages over other conventional media such as its lack of spatial limitations, low production and exhibition costs, and ease of creating interactive and multimedia content.

There is a wealth of literature that showcases how AR technologies can significantly enhance the museum visitor experience. For instance, Wei-quan et al. [12] created AR Muse, an iPad application that allows users to view AR-animated versions of six paintings by framing the original pieces. Their study showed that the use of AR led to longer viewing times of the artwork and better long-term identification. Similarly, Kei et al. developed Arart, an iPhone application that offers real-time animated versions of various paintings, including works by Van Gogh and Da Vinci [1]. Baradaran utilized AR to display an animation on the Mona Lisa painting, adding a political and patriotic message to the original artwork [6].

Several institutions have adopted VR technologies to enhance visitors' experiences. For example, the Tate Modern Museum in London incorporated "The Modigliani VR: The Ochre Atelier" experience into its Modigliani exhibition, providing historical information about the artist and his works [5]. Similarly, the Louvre's "Mona Lisa: Beyond the Glass" project offers a VR journey back in time to meet the real woman behind the painting [4]. The Salvator Dalì Museum also created an immersive VR experience called "Dreams of Dalí," which allows visitors to explore Dali's painting, "Archaeological Reminiscence of Millet's Angelus" [2]. Lastly, the Kremer Museum, launched in 2017, is a fully virtual museum that showcases Dutch and Flemish Old Master paintings from the Kremer Collection [3].

However, multisensory interactive and immersive technologies are commonly found in science and technology museums, which aim to enhance visitors' interactive experiences. In these museums, audience engagement is often encouraged through hands-on exploration. Dalsgaard, Dindler, and Eriksson noted that science and technology institutions facilitate active and participatory exploration of cultural heritage [8]. On the other hand, traditional technologies are typically preferred in art museums, where a contemplative paradigm prevails.

The objective of this paper is to introduce an innovative application called AI-enhanced Museum Guide, which merges AR and Artificial Intelligence (AI) technologies. The purpose of this application is to create a tailored and interactive guide that enhances visitors' museum experiences, making them more engaging and effective.

3 AI-Enhanced Museum Guide

The AI-enhanced museum guide consists of a chatbot capable of engaging with visitors in a natural way by offering clear verbal responses to their questions. The guide also includes additional multisensory content, such as overlaid images or audio tracks, which enrich the chatbot's verbal responses. Visitors can access the guide through either a smartphone screen or an AR Head Mounted Display, which allows for a more immersive experience. By combining AI technology with multisensory content, the museum guide can provide visitors with a more engaging and informative experience that is tailored to their interests and preferences.

The concept of the AI-enhanced museum guide is depicted in Fig. 1. When a visitor is standing in front of an artwork, the guide application uses image processing algorithms to identify it. Once it is recognized, an avatar appears in AR next to the artwork. The avatar serves as a virtual guide that provides a general description of the artwork and can answer any questions the visitor may have about the artwork. Starting from the points of interest, the visitor can ask targeted questions, both using voice or text commands. The avatar can respond audibly or through text displayed on the AR device, providing visitors with a choice of how they receive the information. Additionally, during the audio response, relevant visual details are superimposed in AR onto the painting, enhancing the visitor's understanding of the artwork.

This feature provides visitors with a more interactive and engaging experience, as they can receive personalized information about the artwork they are viewing in real-time, allowing them to engage with the artwork in a more meaningful way.

3.1 Artificial Intelligence for Museum Applications

The emergence of generative artificial intelligence has empowered researchers and developers to deploy tailored User eXperiences (UX) featuring immersive interactions systems (e.g., Q&A) based on real information. In this research, a state-of-the-art Generative Pre-trained Transformer (GPT) neural network, namely GPT-4 by OpenAI[1], is exploited to generate articulate and accurate responses to user queries. The GPT model uses deep learning techniques to generate human-like natural language text in response to a given prompt or input. It has been trained on a large amount of text data to understand and learn the structure and patterns of natural language, allowing it to generate coherent and contextually relevant responses. The GPT model has been widely used

[1] https://openai.com.

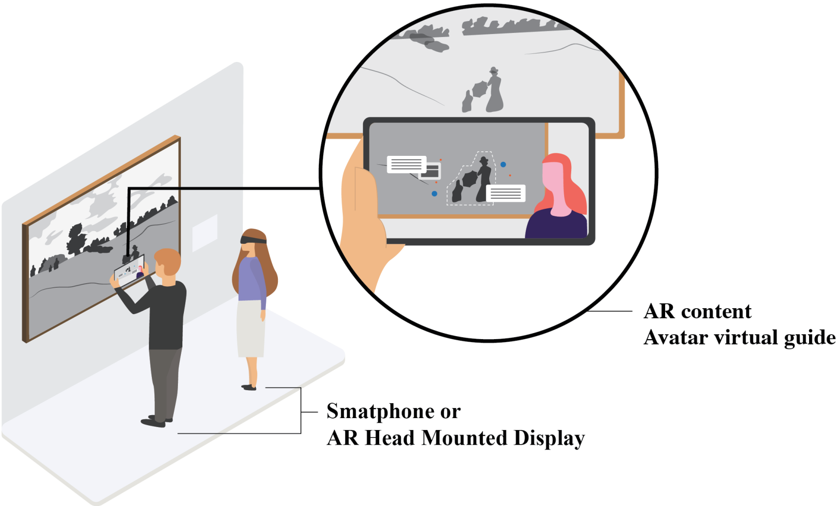

Fig. 1. Concept of the AI-enhanced museum guide

in various natural language processing (NLP) applications, such as chatbots, language translation, and text summarization. The OpenAI GPT APIs[2], have been recently introduced and are being used to efficiently handle user queries and generate precise and well-crafted responses. Moreover, the application has access to a dataset of text-based information which is provided and certified by the museum curator. Therefore, the information used to generate the answers must be inherently authentic.

3.2 AR Content

The application's content includes a collection of images of the paintings, written descriptions of the artwork, and detailed images that support the description of each painting. The set of images is used by the AR application's image processing algorithms to identify the artwork when viewed through the visitor's AR device. In the developed application the following paintings have been used: Poppy Field, The Japanese Footbridge, and Study of a Figure Outdoors: Woman with a Parasol by Claude Monet.

The descriptive text is used by the chatbot to formulate responses to visitors' questions. For example, this is a part of the text we have used for accompanying the Poppy Field painting: *"Poppy field was painted by Claude Monet in 1973, and it is now hosted at the Musee d'Orsay (Paris, France). The painting evokes the vibrant atmosphere of a walk through the fields on a summer day. Monet dilutes the contours and builds a colorful rhythm starting from the evocation of poppies, through brushstrokes whose huge format, in the foreground, shows the*

[2] https://platform.openai.com/overview.

relevance that the artist gives to the visual impression. In this landscape, the two couples formed by a mother and a son, in the foreground and in the background, are simply a pretext for constructing an oblique line that structures the picture. The young woman with the umbrella and the child in the foreground is definitely Camille, the artist's wife, and their son Jean".

Additional images are used to supplement the voice-based avatar's information with relevant visual details. For instance, in the case of the Poppy Field painting, the chatbot provides a general description that is complemented by the adoption of an AR image of the artist. Furthermore, certain portions of the painting are presented in a zoomed view using AR images, and specific details are highlighted by outlining them. Augmented texts that report the names of the figures are also utilized to supplement the audio information, as illustrated in Fig. 2.

Fig. 2. Example of AR Contents used for the Poppy Field painting

3.3 Application Architecture

The AI-enhanced museum guide application comprises a client, which is the kernel of the application, and four modules: the AR engine for the development of the AR application, the Microsoft Azure Speech Services for speech transcription and text synthesis, a Python server for processing the users' queries, and the

OpenAI's services for Natural Language Processing. The application architecture is depicted in Fig. 3.

The client has been developed using the Unity game engine[3], which is one of the standard development environments for VR and AR applications. Unity allows developers to exploit plug-and-play tools such as the Vuforia toolkit[4] which is used for the development of AR applications, and several APIs that are used to access online services. The Unity client is essential for facilitating communication between the Azure and Python servers by overseeing the transfer of data through HTTP requests. Similarly, the Python server communicates with the OpenAI servers using the HTTP protocol.

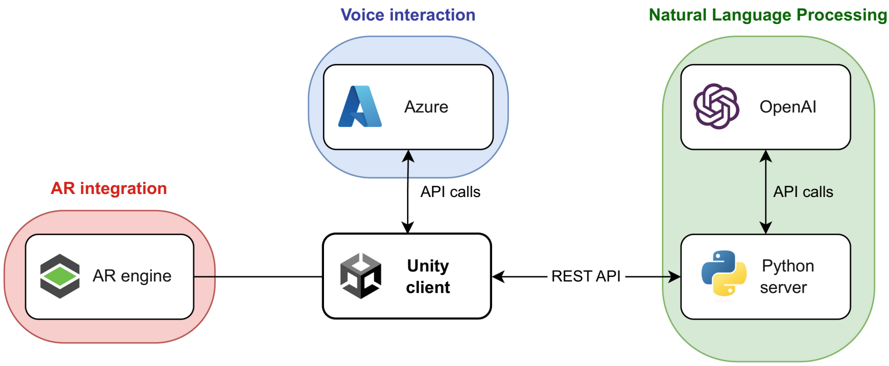

Fig. 3. System architecture: the Unity client enables the user interaction with the application, the AR engine manages AR content, the Python server processes the users' queries, the Microsoft Azure services manage the user-chatbot voice interaction, and OpenAI services process the natural language.

3.4 Modules

Unity Client

The Unity client is the central component of the applications, offering users a user-friendly and easy-to-navigate interface while serving as a connection point to external services. Users can choose their preferred topic through either a manual selection from a horizontal scroll menu that showcases a range of paintings, or by utilizing the smartphone's camera to frame the actual painting, triggering automatic selection of that particular artwork (Fig. 4a).

Once a topic is selected, an avatar appears in AR on one side of the painting. The avatar provides a general description of the painting, highlighting possible interesting aspects that the user can be curious to explore individually.The user

[3] https://unity.com.
[4] https://www.ptc.com/en/products/vuforia.

can then ask questions through either written or spoken prompts (Fig. 4b). The spoken prompts are transformed into text using the Voice Interaction Module. The text is then sent to the Natural Language Processing module. This module uses a GPT neural network to analyze the question and provide an answer, which is then sent back to the Unity client. The avatar reads the answer aloud using lip synchronization technology provided by the Oculus SDK[5], adding to the realism of the experience. Furthermore, the user experience is enriched through the presentation of multisensory AR elements that provide additional information to the user, notably through the use of visual and auditory cues such as overlayed images and environment sounds. AR details are activated through specific keywords in the chatbot's content. When a response includes a targeted keyword, an event is initiated, which leads to the presentation of the corresponding AR detail to the user.

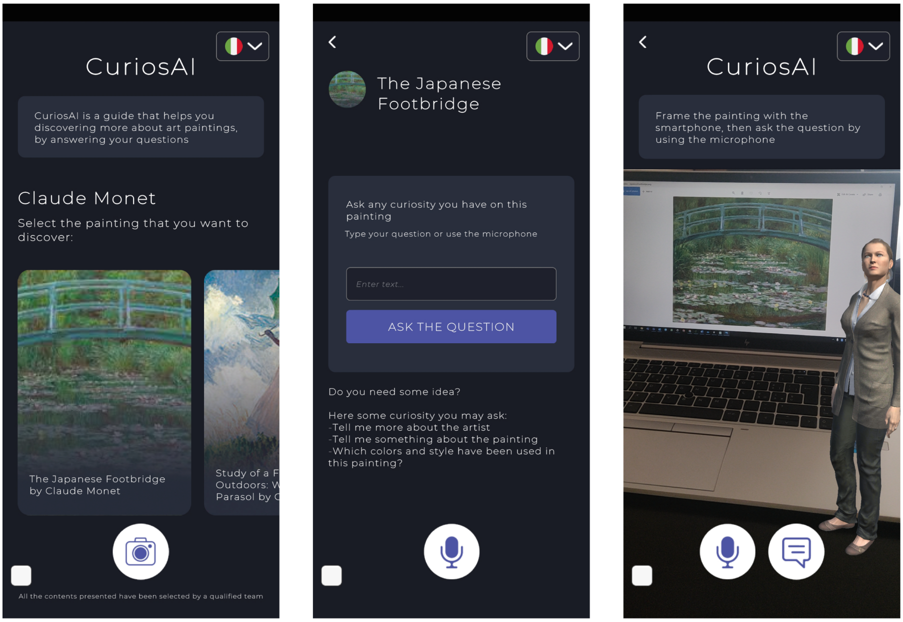

(a) (b) (c)

Fig. 4. The smartphone application that was developed includes: (a) a homepage featuring a horizontal scroll menu for selecting topics, as well as an icon for automatically detecting the topic using the camera; (b) a question page with a text input field for typing questions and an icon for using the microphone to ask questions; and (c) an Augmented Reality mode with automatic topic detection and a virtual avatar.

[5] https://developer.oculus.com/documentation/unity/unity-gs-overview/.

AR Engine

The AR engine has been implemented using Vuforia SDK that enables automatic image and 3D model detection and tracking. With this approach, the user can easily choose a topic by directing their smartphone camera towards it. The system accomplishes this by comparing the captured image to a pre-established collection of image targets or point clouds.

Voice Interaction

The chatbot utilizes Azure Speech Services to facilitate voice interaction between the user and the system. By utilizing the microphone on the smartphone, the user can ask a question which is then recorded as an audio clip and sent to Microsoft's servers for processing and transcription into a JSON message. This message is then used as a query for the OpenAI GPT model, which generates a written response. To convert the response into an audio clip, the Text-to-speech service employs a selected voice type. A visual representation of this process can be seen in Fig. 5.

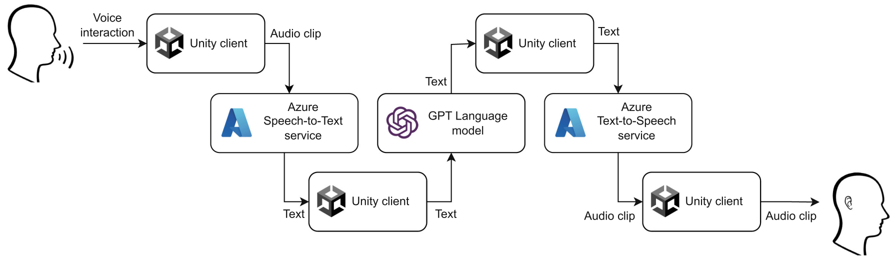

Fig. 5. The voice interaction workflow can be represented as follows: the Azure Speech-to-Text service transcribes the user's question, which is then submitted to the OpenAI GPT Language Model. The resulting answer is provided as text and sent to the Azure Text-to-Speech service to generate an audio clip.

Python Server

The Python server is in charge of handling user queries and generating responses through the use of the GPT model. The server is created as a Flask application and handles POST requests from the Unity client. It utilizes a Python indexing library (i.e., Llama Index[6]) to process the user's query, gather the required information from the dataset and send it to the language model to generate a response. The chatbot's information database, thoughtfully curated by the museum curator, serves as the foundation for a search index. When a query is submitted, the index is scanned for relevant data, which is then transmitted to the AI language model via an API call.

OpenAI GPT Model for Natural Language Processing

[6] https://gpt-index.readthedocs.io/en/latest/index.html.

In this research, the power of OpenAI GPT APIs is leveraged to deliver high-quality responses tailored to users' specific needs and requirements. The queries are gathered by the Unity client, processed by the Python server and sent to OpenAI servers by means of its official APIs. The GPT model, in turn, generates a coherent and precise response based on the context information that it is provided with. The question is received by the Python server and returned to the Unity client, where it can be either displayed or read to the user.

4 Use and Preliminary Evaluation of the AI-Enhanced Museum Guide

The AI-enhanced Museum Guide was tested with several different artworks and presented to experts in the field of Cultural Heritage to understand their opinion and possible implementations within a real museum experience. As an example, the user experience with a Claude Monet's painting, described below, has been presented. Once the painting is framed with the smartphone camera, an avatar appears alongside the painting. The user can now interact with the avatar asking some spoken questions, such as "Tell me about Poppy Field by Claude Monet". The AI-avatar replies: "Poppy Field is a masterpiece of Impressionist landscape painting by Claude Monet, painted in the area around Argenteuil, where Monet lived between 1871 and 1878. The painting depicts a woman and child (likely Monet's wife, Camille, and their son Jean) walking through a field of thick grass, with red poppies cloaking the bank that rises to the left. Another woman and child appear at the top of this bank. On the horizon, a ragged line of trees closes off the field, with a single red-roofed house at the center...". As the response is given, the user experience is enriched by the inclusion of both visual and auditory AR elements. For instance, when discussing Monet's spouse, the figures in the painting are highlighted. In a similar manner, when describing the scenery, the sound of chirping birds is played in the background. After consulting with the Cultural Heritage experts, we received valuable feedback. Our use of smartphone cameras and image recognition to identify artwork was deemed innovative, as it sets us apart from other museum apps that mainly rely on GPS information to locate users. This feature is considered valuable since it allows to create both indoor and outdoor cultural experiences. Additionally, our ability to tailor responses to the user's language level can enhance the user experience and improve the accessibility of museum tours. Moreover, it has been positively highlighted the power that the chatbot has in personalizing the experience in relation to different target users and levels of expertise. Indeed, the tone of voice and the contents delivered are adjusted by the application taking into consideration the users' questions complexity, and expertise on the topic. To further improve our system, the expert recommended conducting usability testing to ensure that our application performs as well as other tools available in the market, such as audio guides, labels, and guided tours.

5 Conclusion and Future Developments

The combination of the expanding prevalence of Artificial Intelligence-based systems and increasing interest in Augmented Reality technologies is driving multiple application fields to reconsider how information is utilized. This study presents an AI-enhanced museum guide that merges AI and AR technologies to enhance museum content usage and accessibility. The application was presented to experts in the Cultural Heritage sector and a preliminary assessment was made. The discussion showed that the application could be interesting to renew the interest of visitors and that the introduction of image recognition and Artificial Intelligence makes the system innovative and potentially more interactive than traditional methods. The feedback was positive and the results suggest numerous possibilities for enhancing cultural content accessibility and improving the overall museum experience. Despite the discussion provided encouraging results, it is crucial to conduct rigorous testing to evaluate the true effectiveness of the system. Future development should include comprehensive testing of the application in a controlled environment, thus enabling a comparative analysis of usability, user workload and learning outcomes between our approach and traditional methods. Moreover, it is important to provide users with clear guidelines on how to effectively interact with the chatbot. This can be achieved by incorporating elements such as a brief introduction to the artwork or providing sample questions on the screen. By offering these guidelines, users can enhance their engagement and maximize the benefits of the chatbot in the context of cultural heritage.

References

1. arart. https://www.designboom.com/technology/arart-augmented-reality-app-brings-paintings-to-life/. Accessed 7 Mar 2023
2. Dreams of dalí. https://thedali.org/dreams-of-dali-2/. Accessed 7 Mar 2023
3. The kremer museum. https://www.thekremercollection.com/the-kremer-museum/. Accessed 7 Mar 2023
4. The mona lisa in virtual reality in your own home. https://www.louvre.fr/en/what-s-on/life-at-the-museum/the-mona-lisa-in-virtual-reality-in-your-own-home. Accessed 7 Mar 2023
5. V.R. The Ochre Atelier. https://www.tate.org.uk/whats-on/tate-modern/modigliani/modiglianivr-ochre-atelier. Accessed 22 June 2022
6. Baradaran, A.: Frenchising mona lisa. https://amirbaradaran.com/2019/works-pages/fml.html. Accessed 7 Mar 2023
7. Carulli, M., Bordegoni, M.: Multisensory augmented reality experiences for cultural heritage exhibition. Lecture Notes in Mechanical Engineering, pp. 140–151 (2020). https://doi.org/10.1007/978-3-030-31154-4_13
8. Dalsgaard, P., Dindler, C., Eriksson, E.: Designing for participation in public knowledge institutions. In: Proceedings of the 5th Nordic Conference on Human-Computer Interaction: Building Bridges, NordiCHI 2008, pp. 93–102. Association for Computing Machinery, New York (2008). https://doi.org/10.1145/1463160.1463171, https://doi.org/10.1145/1463160.1463171

9. Geroimenko, V.: Augmented reality technology and art: The analysis and visualization of evolving conceptual models. In: 2012 16th International Conference on Information Visualisation, pp. 445–453 (2012). https://doi.org/10.1109/IV.2012.77
10. Kuflik, T., Wecker, A., Lanir, J., Stock, O.: An integrative framework for extending the boundaries of the museum visit experience: linking the pre, during and post visit phases. Inf. Technol. Tourism **15**, 17–47 (2014). https://doi.org/10.1007/s40558-014-0018-4
11. Li, Y.C., Liew, A.W.C., Su, W.P.: The digital museum: Challenges and solution. In: 2012 8th International Conference on Information Science and Digital Content Technology (ICIDT2012), vol. 3, pp. 646–649 (2012)
12. Lu, W., Nguyen, L.C., Chuah, T.L., Do, E.Y.L.: Effects of mobile ar-enabled interactions on retention and transfer for learning in art museum contexts. In: 2014 IEEE International Symposium on Mixed and Augmented Reality - Media, Art, Social Science, Humanities and Design (ISMAR-MASH'D), pp. 3–11 (2014). https://doi.org/10.1109/ISMAR-AMH.2014.6935432
13. Marty, P.: Museum websites and museum visitors: before and after the museum visit. Museum Manage. Curatorship (2007). https://doi.org/10.1080/09647770701757708

An Active Noise Control System for Reducing Siren Noise Inside the Ambulance

Massimo G. Buttarazzi(✉), Francesco Borchi, Alessandro Mambelli, Monica Carfagni, Lapo Governi, and Luca Puggelli

Department of Industrial Engineering, University of Florence, via S. Marta, 3, Florence, Italy
massimogeneroso.buttarazzi@unifi.it

Abstract. Siren noise constitutes a nuisance and could be harmful for ambulance personnel and patients. Several studies proposed simulated Active Noise Control (ANC) solutions to attenuate siren noise inside an ambulance. In this paper an implementation of a feedforward ANC system based on the classic FxLMS algorithm is presented, running it on a real-time hardware platform to test the efficacy of such solution in a laboratory environment. Algorithms are developed in MATLAB Simulink environment, and run on Speedgoat target hardware. The results of these experiments are presented, and while discussing our findings, the experienced limitations are described, and further work is suggested.

Keywords: Active Noise Control · FxLMS Algorithm · Feedforward ANC · Ambulance Siren Noise · Real-time Hardware Test

1 Introduction to Active Noise Control

Active Noise Control (ANC) is a technology that can be used to reduce unwanted sound in a given environment. Based on the superposition principle, ANC systems eliminate residual noise within a specific area called *zone-of-silence* (ZoS, or Z_s) by producing a secondary controlled noise with the same amplitude and opposite phase of the source noise, that creates the desired destructive interference with the primary noise at the right location. The basic working principle is depicted in Fig. 1.

Such systems employ acoustic sensors (speakers and microphones) and digital signal processors to generate the control signal. The control signal is usually shaped with the use of adaptive filters, since often the operational environment is non-stationary.

M. Carfagni et al. (Eds.): ADM 2023, LNME, pp. 273–282, 2024.
https://doi.org/10.1007/978-3-031-52075-4_31

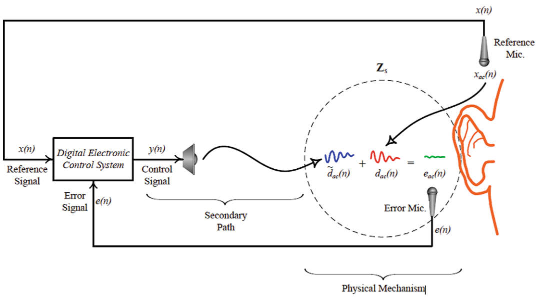

Fig. 1. Principle of noise cancellation, using a secondary noise source to generate a control signal $y(n)$ such as a desired destructive interference is obtained in Z_s, where noise $\tilde{d}_{ac}(n)$ is cancelled by antinoise $d_{ac}(n)$. Taken from [1].

A variety of ANC systems have been studied ([1,2]), based on different adaptive algorithms, depending on their application.

The first adaptive ANC system using the LMS algorithm was developed by B. Widrow in 1975 [3]. Dennis R. Morgan improved upon it [4] by adding an additional filter[1] to compensate for the effect of *secondary acoustic paths*[2] placed after the ANC adaptive filters, thus pioneering the so called *Filtered-x Least Mean Square Algorithm* (FxLMS), which is the one used in this study experiments too.

Several variations of the FxLMS algorithm can be found in [4]; for siren noise reduction, most systems seem based on variations of the LMS adaptive algorithm ([5] through [8]); In particular, a *Narrowband Feedforward ANC* structure (Fig. 2) seems to be the best solution to be applied because a reference signal $x(n)$ is available directly from the noise source, and the signal to be cancelled has a known limited-bandwidth spectrum, as described in detail in Sect. 1.1.

[1] In Fig. 2, please note $\hat{S}(z)$ is the aforementioned filter added by Dennis R. Morgan.

[2] The path the sounds travels between the secondary source, where the antinoise is produced, and the error microphone, where the cancellation has to be realised.

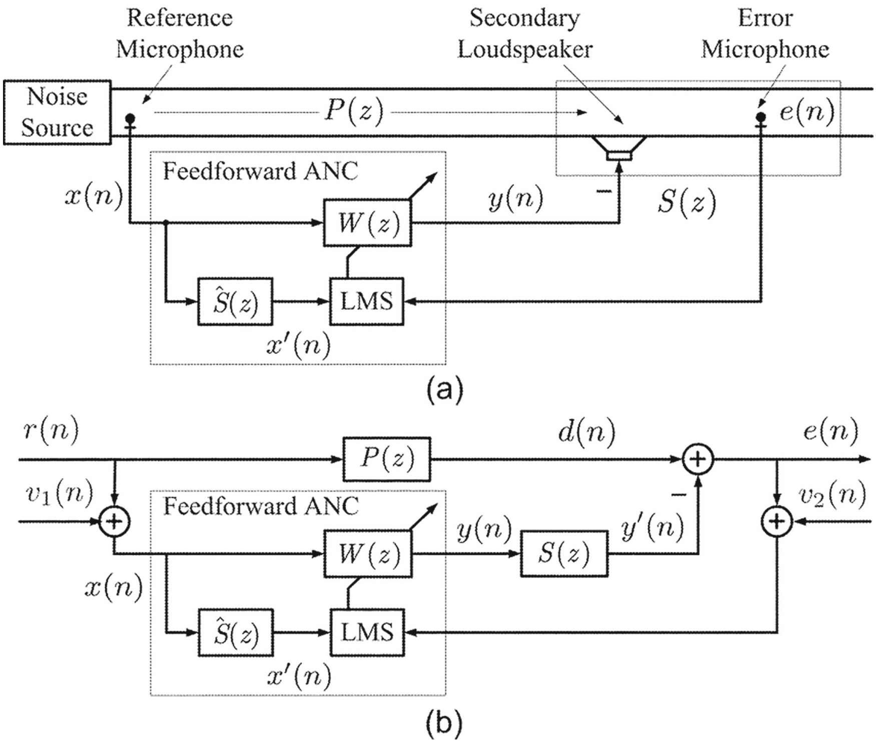

Fig. 2. FxLMS algorithm based single-channel feedforward ANC system. (a) Schematic and (b) block diagram. Figure taken from [9].

1.1 Characteristics of the Siren's Signal

The siren noise presents non-trivial characteristics, in the context of ANC, as it is non-stationary, although periodic, and presents several high-frequency components in its spectral content. Also the siren sound is fast-changing between two different *pitch sounds*, which introduces challenges in and on itself when those switches occur.

Following the Italian regulations on the matter, therefore the siren in this study produces two distinct sounds by emitting two different *pulse waves*, one with a lower pitch at the fundamental frequency of 390 Hz (Fig. 3a), and one with an higher pitch at 660 Hz (Fig. 3b). Figure 3 shows the siren signal reconstructed by measuring the actual output of a typical siren marketed in Italy.

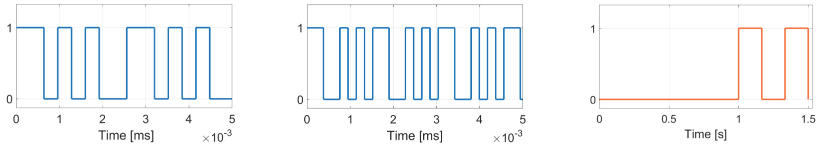

(a) Low pitch sound, 390Hz, T=2.56ms

(b) High pitch sound, 660Hz, T=1.52ms

(c) Siren pattern for switching pitches

Fig. 3. Siren's component pulse waves in the time domain.

These two pulse waves can each be generated with a series of 3 impulses, having periods of 2.56 ms and 1.52 ms respectively, with varying duty cycles and appropriate delays (the parameters for both pulse waves can be seen in table below). The siren then alternates between these pulse waves in a pattern described in Fig. 3c, where the low-level (or 0) is to be interpreted as the time when the siren is *playing* the low pitch sound, and high-level (or 1) when the high pitch is played instead. This pattern repeats periodically every 1.5 s. Finally, the spectrum of both those individual pulse waves is shown in Fig. 4.

Table 1. Parameters to generate the 390 Hz and 660 Hz pulse waves

	f=390 Hz:	pulse1,	pulse2,	pulse3	f=660 Hz:	pulse1,	pulse2,	pulse3
T [ms]		2.56	2.56	2.56		1.52	1.52	1.52
delay [ms]		0	0.96	1.6		0	0.76	1.14
d.c [%]		25	12.5	12.5		25	12.5	12.5

The most significant harmonics of the 390 Hz pulse wave are 780, 1170, 1560, and 1950 Hz. For the 660 Hz pulse wave we have 1320, 1980, 2640, and 3300 Hz.

2 Building Blocks to Reduce Real Siren Noise

The intention with this study was to test cancelling algorithms in a laboratory setting, using a real-time target hardware to produce the adaptive control signal.

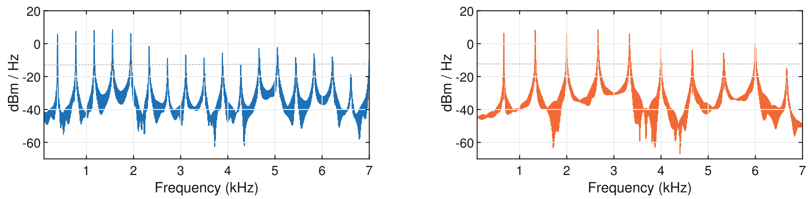

(a) 390Hz pulse wave (low pitch sound) spectrum

(b) 660Hz pulse wave (high pitch sound) spectrum

Fig. 4. Siren component signals in the frequency domain.

With a long-term goal of cancelling the siren inside a real ambulance, here the first steps towards the cancellation of a synthetic siren are presented; these are progressively achieving cancellation of: 1) Pure sinusoidal tones at increasing frequencies 2) Square waves at the same fundamental frequency as the siren pitches 3) Both pulse waves, components of the real siren as presented in Sect. 1.1, individually tested.

This objective was chosen as the steps above are considered preliminary to then move toward the real scenario where the system will be optimised to cancel the real fast-changing siren signal.

3 Setting up the Laboratory Experiment

For our experiments, all noises where internally generated by the target computer and emitted via loudspeaker. The components of the systems under test: Speedgoat Performance Real-Time Target Machine, running Simulink Real-Time, PreSonus DIGIMAX FS, mic. amplifier, Behringer ECM8000 condenser microphones, custom-built audio amplifier and speakers, and Haztec 8-82414 EuroSmart siren[3]

Cancellation was tested on two different setups: *single channel*, where one control speaker generates the antinoise to cancel the noise from the primary source, and *dual channel*, where two control speakers[4], are used (see Fig. 5).

A series of test were conducted using different noise sources, starting with simple sinusoidal tones at increasingly high frequency, then using square waves, and finally the siren's individual pulse waves, which were synthesised[5] to replicate the real siren sounds, and then emitted by a loudspeaker functioning as primary noise source, in place of the actual siren.

No reference microphone was placed in front of the primary source, but the noise signal was instead connected directly as an input into the target machine. Since this will be possible in the real ambulance scenario too, as the siren's electronic hardware can be accessed, this represents a promising *solution* for the future working system aboard the ambulance, saving on hardware, but moreover, highlighting that even though the sound is complex, we can have exact real-time information about the siren signal.

[3] Used to study the siren signal, which was then synthesized.

[4] Placed at the distance simulating the ambulance driver's headrest, with two error microphones placed in such a way to simulate the location of the driver's ears (the target area for our cancellation, *ZoS*).

[5] Internally generated by our target computer.

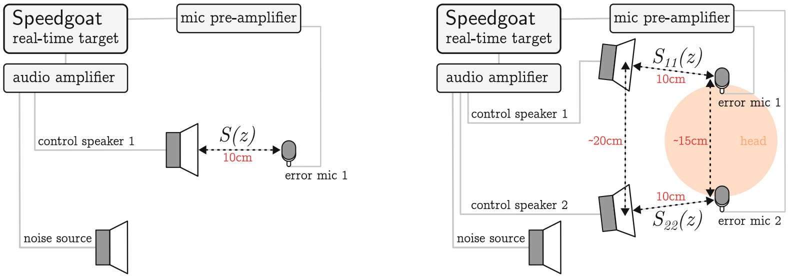

(a) 1-channel testing setup (b) 2-channel testing setup

Fig. 5. Please note that the only distance that once chosen should remain fixed is the distance between error mics and control speakers (the secondary paths $S(z)$, $S_{11}(z)$, and $S_{22}(z)$). In Fig. 5b the secondary paths between speakers and the mic not directly in front of it (i.e. between speaker 1 and error mic 2) are not taken into account as their effect are negligible. The primary noise source can be freely placed a few meters from the *ZoS*.

Once all sensors were set in place, the secondary acoustic paths were estimated; this process generates a set of coefficients that will be then used to initialise an FIR filter $\hat{S}(z)$[6] which approximates the transformation the sound undergoes by travelling through the air once emitted by the control speaker to the error microphone, $S(z)$.

4 Experimental Results

Here the outcomes of our tests are presented, showing the spectra of the signals detected by the error microphones with and without the ANC system generating the antinoise (*ANC ON* and *OFF* respectively) for all the combinations of noise source under test configuration. In **figure** 6 the 1-channel sine waves experiments are collected, in **figure** 7 the 1-channel square wave ones, and in **figure** 8 the 1-channel experiments with pulse waves. For the 2-channel configuration, only the results with sinusoidal tones are presented in **figure** 9, because no significant cancellation was obtained for the more complex signal with this setup.

In terms of individual frequencies, up to 3.6 kHz noise cancellation was obtained with pure sinusoidal tones, which is within range of the five more significant harmonics of both siren's pulse waves, hence the choice; consistent cancellation between 36–86 dB for all sine waves in the 1-channel setup (Figs. 6a to 6f), and similarly consistent cancellation between 31–70 dB for the 2-channel setup (Fig. 9) was measured, which is considered to be very good performance for the system in exam.

When cancelling square waves, the system performed well for the 390 Hz wave, cancelling the first three harmonics between 32–56 dB (Fig. 7a), but with

[6] As shown in Fig. 2 the additional filter is to be applied at the reference signal $x(n)$, coming directly from the siren in this case.

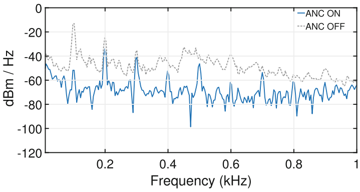

(a) 100Hz: -39dB of cancellation

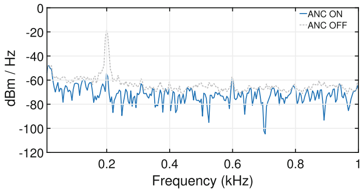

(b) 200Hz: -36dB

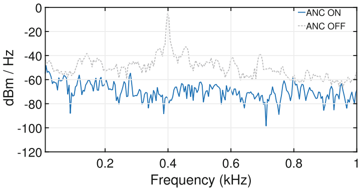

(c) 400Hz: -69dB

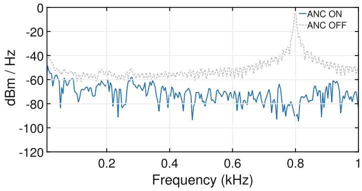

(d) 800Hz: -86dB

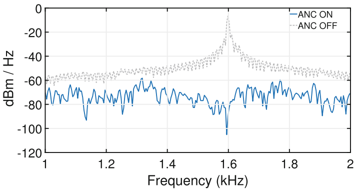

(e) 1600Hz: -84dB

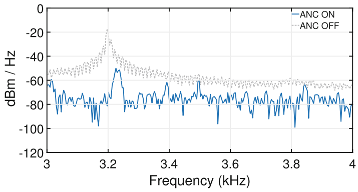

(f) 3200Hz: -64dB

Fig. 6. 1-channel configuration with sinusoidal tones, or sine waves.

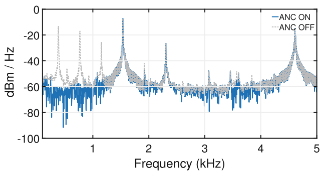

(a) 390Hz

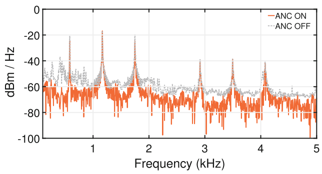

(b) 660Hz

Fig. 7. 1-channel square w. harmonic canc. [Hz],[dB]. a: 390,-56, 769,-43, 1158,-32 1532,0 1921,-4 2305,0 ; b: 660,-4 1166,0 1749,-5 2911,0 3494,0 4077,-1

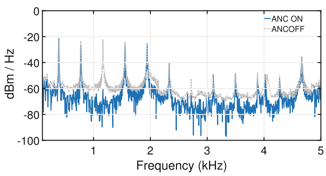

(a) 390Hz

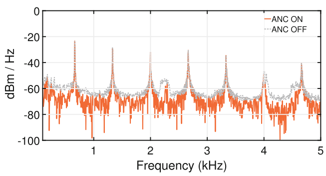

(b) 660Hz

Fig. 8. 1-channel pulse w. harmonic canc. [Hz],[dB]. a: 390,0 775,-3 1166,-38 1554,-2, 1941,0, 2333,0 ; b: 660,0 1330,0 2000,0 2665,0 3330,0 3995,-2

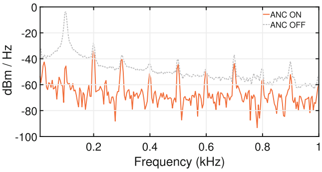

(a) 100Hz, left mic.: -42dB reduction

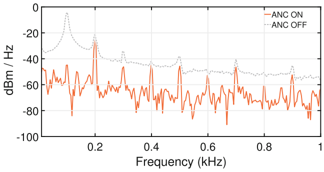

(b) 100Hz right mic.: -41dB reduction

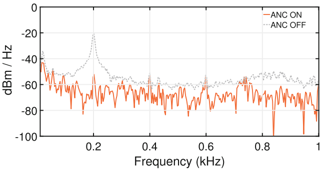

(c) 200Hz, L: -31dB

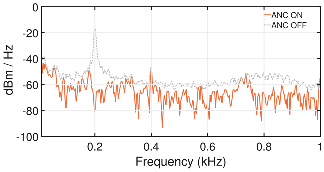

(d) 200Hz, R: -65dB

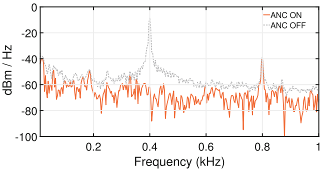

(e) 400Hz, L: -54dB

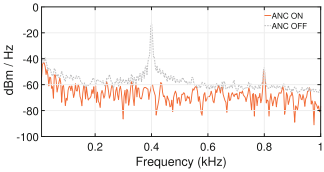

(f) 400Hz, R: -48dB

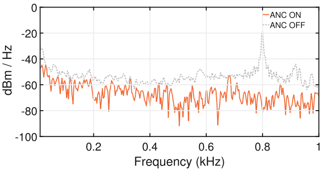

(g) 800Hz, left mic.: -62dB reduction

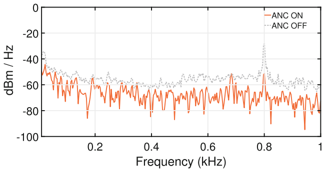

(h) 800Hz right mic.: -23dB reduction

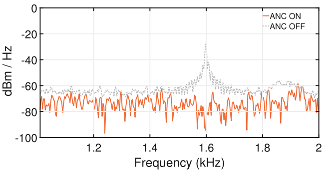

(i) 1600Hz, L: -67dB

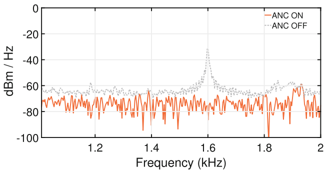

(j) 1600Hz, R: -44dB

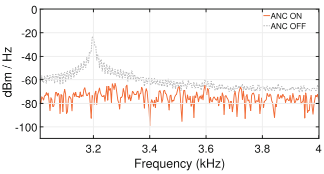

(k) 3200Hz, L: -70dB

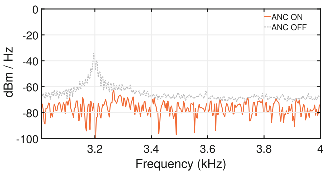

(l) 3200Hz, R: -46dB

Fig. 9. 2-channel configuration with sinusoidal tones, or sine waves

the 660 Hz square wave the cancellation performance was more modest, in the range of 4–5 dB (Fig. 7b), already showing signs of the limits of our system.

When the system was challenged with cancelling pulse waves, considering the first 6 harmonics, the 390 Hz pulse wave saw a cancellation between 3–38 dB (but most of it on the third harmonics only, see Fig. 8a), whereas the 660 Hz pulse wave saw almost no cancellation (Fig. 8b).

5 Conclusions

The use of the FxLMS algorithm is a well-established technique in active noise control applications, suited for reducing the sound of ambulance sirens. Such noise is proven challenging for the FxLMS algorithm. Therefore it seems that, overall, the feedforward ANC system based on the FxLMS algorithm variation presented here, is capable of cancelling signals that are *regularly changing with respect of time*, no matter how fast (within the ranges of our tests); but that same system cannot perform as well when signals behave in a less regular pattern in the time domain. Difficulties to latch onto the phase of the pulse and square waves is believed to be the cause of this system's declining performance. This could be mitigated by upgrading the DSP component, devising a faster performing target hardware, custom-built to operate with the signals in question.

Finally, the ANC system had difficulties updating the cancellation adaptive filter in the short time allowed by the fast-switching siren[7], but since we see promising results on the individual sounds of the siren, especially on the low-pitch one, and since we also believe that with the aforementioned hardware improvements we could obtain better performance for the high-pitch pulse wave as well, we believe it could be theoretically plausible to employ a set of individual ANC filters in parallel, each operating over a specific pulse wave/siren sound, and switch between them appropriately, to cancel the real siren, if the system would be able to correctly latch onto the phase of the siren's signal.

Acknowledgement. The publication was made by a researcher with a research contract co-funded by the European Union - PON Research and Innovation 2014-2020 in accordance with Article 24, paragraph 3a), of Law No. 240 of December 30, 2010, as amended and Ministerial Decree No. 1062 of August 10, 2021.

References

1. Ardekani, I.T., Abdulla, W.H.: FxLMS-based active noise control: a quick review. In: Proceedings of Asia-Pacific Signal and Information Processing Association Annual Summit and Conference, vol. 1, pp. 1–11. Xi'an, China (2011)
2. Buttarazzi, M.G., Bartalucci, C., Borchi, F., Carfagni, M., Paolucci, L.: Analysis of possible algorithms for active noise control of siren noise into an ambulance. In: Rizzi, C., Campana, F., Bici, M., Gherardini, F., Ingrassia, T., Cicconi, P. (eds.) Design Tools and Methods in Industrial Engineering II: Proceedings of the Second

[7] bringing the overall behaviour towards instability.

International Conference on Design Tools and Methods in Industrial Engineering, ADM 2021, September 9–10, 2021, Rome, Italy, pp. 630–640. Springer International Publishing, Cham (2022). https://doi.org/10.1007/978-3-030-91234-5_63
3. Widrow, B., Stearns, S.D.: Adaptive Signal Processing. Prentice-Hall Signal Processing Series, Upper Saddle River, New Jersey, USA (1985)
4. Kuo, S.M., Morgan, D.R.: Active Noise Control Systems Algorithms and DSP Implementations. Wiley, New York, USA (1996)
5. Singh, S., Sharma, M.K., Agrawal, S.: Ambulance siren noise reduction using psychoacoustic active noise control system with A-weighting filter. In: International Conference on Computing. Communication & Automation, pp. 990–993. Greater Noida, India (2015)
6. Pal, R., Sharma, M.K., Thangjam, S.: Ambulance Siren Noise Reduction Using Virtual Sensor based Feedforward ANC System. In: Proceedings 2nd International Conference on Advances in Computing and Communication Engineering, Dehradun, India (2015)
7. Gupta, P., Sharma, M.K., Thangjam, S.: Ambulance siren noise reduction using noise power scheduling based online secondary path modeling for ANC System. In: International Conference on Signal Processing. Computing and Control (ISPCC), pp. 63–67. Waknaghat, India (2015)
8. Sharma, M.K., Vig, R.: Ambulance Siren Noise Reduction using LMS and FXLMS Algorithms. Indian J. Sci. Technol. **9**(47), 1–6 (2016)
9. Akhtar, M.T., Abe, M., Kawamata, M.: Adaptive filtering with averaging-based algorithm for feedforward active noise control systems. In: IEEE Signal Processing Letters, vol. 11, no. 6, pp. 557–560 (2004)

Assistive Products for Accessible Tourism: Focus on Beach Wheelchairs

Barbara Motyl[1](✉), Ileana Bodini[2], Stefano Filippi[1], Alberto Girotto[2], Diego Paderno[2], Stefano Uberti[2], Valerio Villa[2], and Gabriele Baronio[2]

[1] DPIA - University of Udine, Udine, Italy
barbara.motyl@uniud.it
[2] DIMI - University of Brescia, Brescia, Italy

Abstract. The idea presented in this contribution stems from the authors' interest and previous experience in designing aids for individuals with disabilities in the field of Accessible Tourism - AT. Specifically, the focus has been directed towards devices utilized in the seaside sector, with an analysis conducted on beach wheelchairs. The study involved both a market analysis and an examination of the regulatory framework. Two main results were obtained. Firstly, the analysis of the regulatory framework revealed potential challenges in interpreting rules and regulations, particularly regarding design, safety, and testing requirements. Secondly, the market analysis demonstrated that all currently available devices necessitate users switching from their personal wheelchairs to beach wheelchairs. Considering these findings, a conceptual solution is proposed to adapt one's personal wheelchair for movement on sandy terrains. This solution entails a kit comprising beach wheels mounted on a lightweight frame, potentially incorporating a self-propelled device to replace the manual wheelchair's existing wheels. It is important to note that this solution is intended to supplement existing beach wheelchairs rather than replace them, thereby broadening the options available to individuals with mobility impairments.

Keywords: Accessible Tourism · Assistive products · Beach wheelchairs · Design methods · User-Centered Design

1 Introduction

The idea presented in this paper is the result of the authors' interest and previous experience in designing assistive devices for people with disabilities. While previous works focused on designing devices for sports and/or tourism activities in mountain environments [1, 2], this paper is more focused on the marine seaside environment. In addition, inclusiveness for people with disabilities is a growing concern, and many governmental and non-governmental associations are closely examining this issue. Data found in the latest 2019 ISTAT (Istituto Nazionale di Statistica) disability report [3] indicates that in Italy, there are 3.1 million people with disabilities, which accounts for 5.2% of the Italian population. Individuals with disabilities are defined as those who suffer from

M. Carfagni et al. (Eds.): ADM 2023, LNME, pp. 283–291, 2024.
https://doi.org/10.1007/978-3-031-52075-4_32

health problems or severe limitations that prevent them from engaging in normal activities. ISTAT data [3, p. 17] show that among people with severe limitations, only 19.2% express high satisfaction with their lives, which is much lower than the 44.5% reported for the rest of the population. The quality of life and well-being of people with disabilities are closely linked to their level of participation in social activities, sports, and cultural life in general. According to data from the 2019 ISTAT report [3, p. 16] regarding the participation of people with disabilities in social activities, only 9.3% of individuals with severe limitations frequently go to the cinema, theater, concerts, or visit museums during the year. In comparison, the percentage for the rest of the population is around 30.8%. When it comes to sports, the participation rate is even lower at only 9.1% for people with severe limitations, compared to 36.6% for the rest of the population. Furthermore, an additional 14.4% of individuals with limitations engage in some form of physical activity, although they do not participate in organized sports. Possible causes for this situation may include health issues, difficulties with inclusion, and limited accessibility of facilities. In addition, 62.5% of Italian museums, whether public or private, lack the necessary facilities to accommodate individuals with severe limitations [3, p.18, 4]. In terms of the European tourism sector, it is estimated that there are approximately 80 million people with disabilities, presenting a significant economic potential for accessible tourism, which amounts to around 352 billion euros in gross revenue [4]. For Italy specifically, ISTAT predicts a 70% increase in travelers with disabilities by 2035 [4]. However, this projection can only be realized if tourism and leisure experiences become increasingly accessible and inclusive. Accessible Tourism (AT) refers to tourist services and facilities that enable individuals with disabilities, the elderly, and those with special needs to participate in leisure activities and vacations [5–7]. The accessibility of a destination should encompass various aspects like accommodations, restaurants, transportation, infrastructure, entertainment, and cultural venues, ensuring no obstacles or barriers hinder access or enjoyment. Improving accessible tourism is both a social imperative and a business necessity, catering to a growing segment of the tourism market [8]. Also, Universal Design and Design for All principles promote the conception and design of tourism services and products that meet the needs of diverse users, including individuals with disabilities, without requiring special adaptations or aids.

The focus of this research revolved around AT in coastal areas, specifically the facilitation of individuals with disabilities or reduced mobility on beaches. The main objectives of this research were to examine the market for beach wheelchairs and analyze the relevant standards governing their design and implementation. This analysis aimed to gain a thorough understanding of the current situation and identify the most suitable strategies for designing and developing an alternative solution that effectively addresses the diverse needs of these individuals. The subsequent section presents the findings of the market analysis, along with a description of the existing regulatory standards applicable to this domain. On the other hand, section three introduces the concept of an alternative device in the form of a kit, specifically thought to offer wheelchair users easy access to beaches. Finally, the study concludes by summarizing key insights and outlining possible future advancements in this field.

2 Focus on Beach Wheelchairs

Seaside resorts have consistently ranked among the preferred tourist destinations, even for individuals with disabilities. In recent years, there has been a growing emphasis on creating accessible beaches that cater to the needs of all visitors by removing barriers and offering dedicated services and assistance [9]. One notable example is the provision of specialized wheelchairs known as "beach wheelchairs" which ensure full accessibility to the beach and the sea for individuals with mobility disabilities. They are an important accessibility feature for individuals with disabilities, as they provide the opportunity to enjoy the beach, engage in recreational activities, and experience the natural environment with greater ease. These wheelchairs are typically available for rental at beach destinations or can be provided by certain organizations or accessibility programs [10]. Extensive market and regulatory analyses have been conducted to assess the various aids and devices used and available in this domain.

2.1 Market Analysis

To conduct the market analysis, the research considered the UNI/PdR 92:2020 Beach Service - Guidelines for environmental sustainability, accessibility, quality, and safety services- as a starting point [11]. Specifically, these guidelines offer valuable insights into the types of water access aids that can be employed to facilitate water access for individuals with mobility disabilities. Within this document, several models of beach wheelchairs, mostly used in Europe, are mentioned, including J.O.B., Sand&sea, Tiralò, Ariel, and Hippocampe. These wheelchairs are designed to cater to diverse user needs. Figure 1 showcases these models, along with other popular or innovative options currently available in the market. Table 1 provides a summary of pertinent information regarding their characteristics and their designation as aids for individuals with disabilities, offering a comprehensive understanding of their features.

Fig. 1. Different models of beach wheelchairs: a) J.O.B., b) Solemare, c) Sand&sea, d) Ariel, e) Tiralò, f) Sofao, g) Hippocampe.

The depicted beach wheelchairs are primarily manual wheelchairs that require pushing or pulling for operation. The first row of Fig. 1 (from a to d) includes models that can be propelled by a caregiver positioned behind the chair, whereas the second row (from e to f) consists of models that need to be pulled. The Hippocampe model (Fig. 1g) is an example of a trekking chair that can be used in different scenarios. To gain a comprehensive understanding of how these products compare to other assistive aids available to individuals with disabilities, their classification was referenced using that proposed by the European Assistive Technology Information Network – EASTIN - association website (www.eastin.eu). This website aggregates data from various national databases that catalog assistive technology products based on ISO classification. More details on their classification can be found in Table 1.

Table 1. Characteristics and ISO classification of different beach wheelchair models.

Model	Manufacturer	Range of price	ISO classification
J.O.B	Neatech (Italy) https://www.neatech.it	< 1000 Euro	ISO 30.09.39
Solemare	OFFCARR (Italy) https://www.offcarr.com/homepage/	< 1000 Euro	ISO 30.09.39
Sand&Sea	OFFCARR (Italy) https://www.offcarr.com/homepage/	1000 Euro	ISO 30.09.39
Ariel	Gruppo Jolly Casa International	< 1000 Euro	ISO 30.09.39
Tiralò	ESAT l'Ensoleillade (France) https://tiralo.org/en	2000 Euro	ISO 12.22.18
Sofao	Ferriol Matrat (France) https://www.joeletteandco.com/it/bagno/sofao-al-mare/	> 2000 Euro	ISO 30.09.39 ISO 12.22.18
Hippocampe	Vipamat Europe (France) https://www.vipamat.it/	> 2000 Euro	ISO 12.22.18

The classification of the beach wheelchair models, as indicated in Table 1, raises an important point regarding their categorization according to ISO 9999:2022 "Assistive products - Classification and terminology" [12]. In most cases, these models are classified as assistive products for other sports (ISO 30.09.39). However, a few models (letters from e to g in Fig. 1) are classified as manual wheelchairs, falling under ISO classification code 12.22.18. This dual classification possibility prompts further investigation into the design process and regulatory framework that governs this kind of medical device. To gain a better understanding of the requirements and regulations associated with such devices, the authors deemed it necessary to delve into the relevant regulatory framework, as explained in the next section.

2.2 Regulatory Framework Analysis for Beach Wheelchairs

As mentioned earlier, the ISO 9999:2022 serves as the reference standard for cataloging assistive products for individuals with disabilities [12]. It provides classification and terminology guidelines for assistive products that are specifically designed or generally available to optimize functionality and reduce disability. It also includes assistive products that require the assistance of a caregiver for their operation. Within this standard, beach wheelchairs are mentioned under the code 30.09.33, which pertains to assistive products for swimming, water sports, and beach-related activities. The specific term "beach wheelchair" is associated with codes 12.22 and 12.23, which are part of the manual wheelchairs section. According to these suggestions, one would expect the reference standards for beach wheelchairs to align with those for manual wheelchairs. However, the data presented in Table 1, sourced from the EASTIN website, indicates that beach wheelchairs are primarily classified under the code 30.09.39 as "Auxiliary products for other sports". This suggests that they may follow a different certification process. Typically, manufacturers of manual wheelchairs refer to the EN 12183:2022 standard, which encompasses the requirements and test methods for manual wheelchairs [13]. This standard also makes references to EN 12182:2012 [14], which covers general requirements and test methods for assistive products for persons with disabilities, as well as the ISO 7176 series of standards that detail various test methods for wheelchairs [15]. However, manufacturers of beach wheelchairs solely refer to EN 12182:2012, omitting reference to the ISO 7176 series. From a regulatory perspective, beach wheelchairs are classified as class I medical devices under the Medical Device Regulation (EU) 2017/745 [16]. This classification necessitates that manufacturers self-certify compliance with the requirements to obtain the CE marking for the device. In the Italian national legislative framework, the "Nomenclatore Tariffario" [17] is the document issued and regularly updated by the Italian Ministry of Health which establishes the type and manner of provision for prostheses and aids covered by the National Health Service. Since beach wheelchairs are not explicitly mentioned in this document, a procedure is in place for their traceability through "functional homogeneity" to other listed and recognized types of aids within the National Health System. For instance, one manufacturer of beach wheelchair models listed in Table 1 and represented in Fig. 1b has designated its product as a "shower chair", which can be traced back to the ISO code 09.12.03 - Commode chairs [12]. As evident, the classification of beach wheelchairs is not definitively fixed, allowing manufacturers to consider the aid as belonging to different categories depending on the context. Table 2 provides a summary of the regulatory framework applicable to both manual wheelchairs and beach wheelchairs.

Table 2. The regulatory framework of the standards for manual and beach wheelchairs.

Standard	Manual wheelchairs	Beach wheelchairs
ISO 9999:2022	12.22.18 (Push wheelchairs)	12.22.18 (Push wheelchairs) or 30.09.39 (Assistive products for other sports)
Regulation (EU) 2017/745	Class I medical device	Class I medical device
EN 12182:2012	yes	yes
EN 12183:2022	yes	no
Nomenclatore tariff.(Italy)	Wheelchairs	Shower chairs/ Commode chairs

3 A New Concept: the "SailOnSand – SOS" kit

The idea of developing a new concept of a beach aid stems from some considerations of previous analyses. All devices presented in Table 1 focus on enabling people with disabilities to bathe in the sea requiring them to transfer from their personal wheelchair to the beach wheelchair. Moreover, as depicted in Fig. 1, these devices are simpler in design compared to everyday manual wheelchairs, lacking specific comfort features, and resembling more basic transport wheelchairs. In addition, through input gathered from individuals with disabilities who collaborate with our research group, it has been revealed that disabled individuals do not always visit the beach solely for swimming purposes. Often, they prefer to stroll along the shoreline, relax under an umbrella, and simply move around, potentially even independently, to engage in social activities, use restroom facilities, or visit refreshment points. Taking into consideration these factors and user needs, our working group has conceptualized a device that enables wheelchair users to navigate the beach. The device was carefully designed considering a number of key features, including adaptability to different wheelchair models (standardized sizes), ease of assembly and setup for both experienced and novice users, and modularity to accommodate different terrains and levels of user disability. In our search for similar products on the market, we came across the Sandapter kit (www.offroadsolutions.nl), listed in the EASTIN database, which allows for the replacement of the two rear wheels of a manual wheelchair with sand-specific wheels. However, this kit still requires assistance from another person to push the wheelchair and lift its front wheels. As we couldn't find a product with the desired characteristics, our focus shifted toward developing a new product concept.

Our proposed solution is a kit called "SailOnSand – SOS", as depicted in Fig. 2. The kit utilizes two support frames, one on each side, which can be easily installed on a wheelchair. These frames take advantage of the quick-attach interface available for rear wheel attachments on regular wheelchairs once the wheels are removed (Fig. 2a). The frames can be fitted with sand wheels and are placed on the two sides instead of the rear wheels, while the front wheels are securely placed on a platform using appropriate straps or belts (Fig. 2b). We have designed the kit in two versions: i) a manual push version that requires assistance from an assistant (Fig. 2b), and ii) a self-propelled version that allows the user to operate it independently (Fig. 2c). Throughout the entire design process,

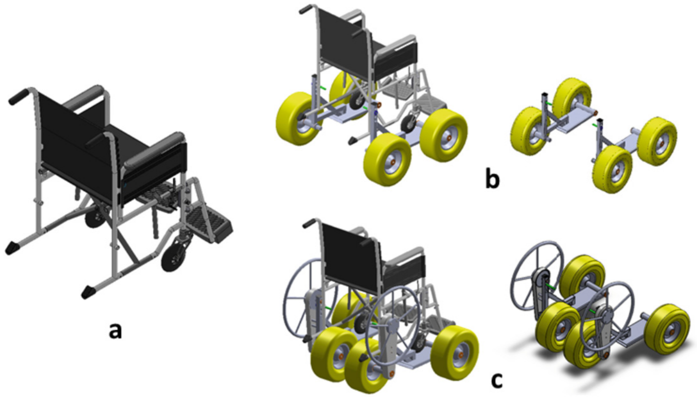

Fig. 2. The "SailOnSand - SOS" concept.

we will adhere to the principles of user-centered design, ensuring that the device not only meets the user's requirements but also aligns with their personal preferences. In line with the conducted analyses, special emphasis will be placed on the preparation of comprehensive technical documentation, ensuring compliance with regulations, and following the structure outlined in Fig. 3. As the kit is classified as a Class I medical device and categorized as an aid for other sports (ISO 30.09.39) [12], careful attention will be given to critical stages such as sizing, detailed component design, risk analysis, and the subsequent development of the technical documentation.

Fig. 3. Steps for the design and development of the SOS device and technical documentation.

The risk analysis process will involve identifying potential hazards associated with the use of the SailOnSand - SOS kit and evaluating their severity and likelihood. Mitigation measures will be implemented to minimize risks, ensuring the safety and effectiveness of the device. The technical documentation will encompass essential information about the design, materials, manufacturing processes, instructions for use, and any relevant testing and validation procedures conducted. By meticulously adhering to regulatory requirements and following a thorough risk analysis process, the research group aims to develop a technically robust and compliant product that meets the needs of individuals with disabilities, promoting accessibility and inclusivity at the beach.

4 Conclusions

This research project has yielded two main outcomes. Firstly, the analysis of the market and regulatory framework has revealed critical issues associated with these types of products. In terms of the regulatory framework, difficulties were identified in the clear interpretation of standards and regulations by manufacturers, particularly regarding design, safety, and testing requirements. The lack of unambiguous guidelines can lead to inconsistencies and challenges in ensuring compliance. Secondly, the research group has conceptualized a novel solution in the form of the SailOnSand (SOS) kit, which aims to adapt a traditional everyday wheelchair into a beach wheelchair. Unlike existing beach wheelchairs that require users to transfer from their personal device, the SOS kit offers a newer design approach. It consists of two lightweight frames with sandy wheels that can be easily mounted on a manual wheelchair. The kit also provides the option for a self-propelled configuration, enhancing independence for the user. Currently, the team is focused on the detailed design and dimensioning of the components. It is also planned to build a prototype of the device for testing in the coming months. This prototype will undergo evaluation to assess its functionality, usability, and compatibility with different terrains with both the group's designers and real users. By developing this innovative solution, the research group aims to expand the options available to individuals with mobility disabilities, improving their beach accessibility and overall quality of life.

References

1. Baronio, G., Copeta, A., Motyl, B., Uberti, S.: Gölem project: concept and design of a trekking/hiking wheelchair. Adv. Mech. Eng. **9**(11) (2017). https://doi.org/10.1177/1687814017730541
2. Baronio, G., Bodini, I., Motyl, B., Uberti, S.: Prototyping, testing, and redesign of a three-wheel trekking wheelchair for accessible tourism applications. Appl. Sci. **11**(20), 9641 (2021)
3. ISTAT: Conoscere il mondo della disabilità: persone, relazioni e istituzioni. https://www.istat.it/it/archivio/236301 Accessed 16 June 2023
4. Progetto SI PUÒ, https://www.apmarr.it/progetto-si-puo/disabilita-con-il-progetto-sipuo-le-linee-guida-per-il-turismo-e-tempo-libero-accessibile-e-inclusivo/, Accessed 16 June 2023
5. ENAT Homepage, https://www.accessibletourism.org, Accessed 16 June 2023
6. Henríquez, C.S., Cano, A.J.R., Galán, J.H., de la Fuente Robles, Y.M.: The past, present, and future of accessible tourism research: a bibliometric analysis using the Scopus database. J. Accessibility Design All **12**(1), 26–60 (2022)
7. AA.VV. Libro Bianco del turismo accessibile, https://projectforall.net/libro-bianco-turismo-accessibile/ Accessed 16 June 2023
8. Verdonck, M., Wiles, L., Broome, K.: Lived experience of using assistive technology for sandy beach based leisure for Australian people with mobility limitations. Disabil. Rehabil. Assist. Technol. 1–11 (2023). https://doi.org/10.1080/17483107.2023.2217859
9. Disabili.com, https://www.disabili.com/viaggi/speciali-viaggi-a-tempo-libero/guide-alle-vacanze-accessibili-ai-disabili, last accessed 2023/06/16
10. Collins, M. 2016. Beach wheelchairs: more available than ever. New Mobility, https://newmobility.com/beach-wheelchairs/ last accessed 2023/06/16
11. Legambiente and Ente Italiano di Normazione. (2020) Beach services - Guidelines for environmental sustainability, accessibility, quality and safety of services UNI/PdR 92:2020. https://www.senato.it/application/xmanager/projects/leg18/attachments/documento_evento_procedura_commissione/files/000/422/623/2022_02_15_Legambiente.pdf, last accessed 2023/06/16
12. International Organization for Standardization: Assistive products for persons with disability—Classification and terminology. ISO Standard No. **9999**, 2022 (2022)

13. European Committee for Standardization: Manual wheelchairs - Requirements and test methods. EN Standard No. **12183**, 2022 (2022)
14. European Committee for Standardization: Assistive products for persons with disability - General requirements and test methods. EN Standard No. **12182**, 2022 (2022)
15. International Organization for Standardization. (2014) Wheelchairs. ISO Standard No. 7176–1
16. Regulation (EU) 2017/745 of the European Parliament and of the Council of 5 April 2017 on medical devices, amending Directive 2001/83/EC, Regulation (EC) No 178/2002 and Regulation (EC) No 1223/2009 and repealing Council Directives 90/385/EEC and 93/42/EEC http://eur-lex.europa.eu/legal-content/EN/TXT/?uri=OJ:L:2017:117:TOC last accessed 2023/06/16
17. Nomenclatore Tariffario delle protesi (1999). https://www.salute.gov.it/imgs/C_17_pagineAree_1312_listaFile_itemName_0_file.pdf, last accessed 2023/06/16

A Cataloging Matrix-based Approach to Unify the Classification of Digital Games

Laura Cormio[1](✉), Thomas Agostinelli[1], Silvia Ceccacci[2], José Y. Villafan[1], and Maura Mengoni[1]

[1] Department of Industrial Engineering and Mathematical Sciences, Università Politecnica delle Marche, via Brecce Bianche, 12, 60131 Ancona, AN, Italy
l.cormio@pm.univpm.it

[2] Department of Education, Cultural Heritage and Tourism, Università Degli Studi di Macerata, Via Luigi Bertelli, 1, 62100 Macerata, MC, Italy

Abstract. The paper proposes a novel unified classification of digital games, i.e., video games and serious games, due to the recent interest of academia and industry for their use to achieve several educational purposes. The paper reviews existing cataloging systems and proposes a five-definition based matrix cataloging including a set of key digital game metadata, unifying existing knowledge and highlighting commonalities between cataloging systems. It offers a higher-level categorization of digital games that retain distinctions where necessary, thus unifying both categories of digital games. Such taxonomy enables the creation of a correlation matrix that will provide a theoretical basis necessary to specify guidelines for the concept design phase of digital games.

Keywords: Cataloging · Videogame · Serious games · Concept Design

1 Introduction

Digital games include both entertaining videogames and edutainment serious games. Its market has grown exponentially over the years, gaining an important role in everyday life, and fitting seamlessly into a variety of sectors [1]. In 2015 it was estimated that the total revenue of the global digital game market was between $81.5 billion and $93 billion [2]. This situation hinges on the fact that digital games are no longer just limited to the field of entertainment but have expanded to edutainment as well. Serious games particularly incorporate various aspects, such as wellness, education, and cultural heritage [1]. Some serious games examples include: (i) Le Village Aux Oiseaux, a therapeutic game whose goal is to train patients with Alzheimer's disease to slow down the cognitive decline due to the condition [3] and (ii) The Prepared Partner, an educational video game about labor and childbirth designed to prepare for parenthood [4, 5]. The growing development of the video game industry is directly proportional to the increase in the segments of the population that use it. The overall male target user is now only slightly outnumbering the female target user [2], compared with the past. Moreover, the same categories of users have expanded according to the sphere that the game embraces, including children,

M. Carfagni et al. (Eds.): ADM 2023, LNME, pp. 292–299, 2024.
https://doi.org/10.1007/978-3-031-52075-4_33

teachers, corporate workers, as well as patients in therapy or people with different types of disabilities. One of the challenging issues in game design is cataloging and classification, due to the large variety of software solutions, game's scopes, target users and hence the needed interaction modality and usability requirements. The term *classification* refers to a process that "[…] involves the orderly and systematic assignment of each entity to one and only one class […]" [6].

While *cataloging* is the process that provides "[…] users with timely access to information relevant to their needs. The task of identifying resources collected by libraries, results in rich metadata that can be used for many purposes" [7]. Therefore, classifying and cataloguing games has become a fundamental step to allow game designers to unravel the complexity of the current state-of-art, to identify the target users' needs and how to meet them, and hence to better guide their development.

Several authors attempted to classify them. In [8] a three-dimensional taxonomy is suggested: (i) type of computer software; (ii) the genre of the game; (iii) the mode of interaction. In [1] an in-depth multidimensional classification of serious games is proposed, focusing on the qualities that are crucial to their design, i.e., style of interaction offered to the player, activity, mode, environment, and area of application. Despite these attempts, there is still a lack of a classification that enables research to unify the various proposals identified in the literature. This paper aims to analyze these classifications by providing a unified cataloging, following a review methodology as proposed by [9]. A starting point to achieve a 'matrix cataloging' to bring out possible correlations among the collected data is here proposed. The data will be separated and organized using specific classification criteria, creating a unified digital games cataloging. In this way, applying the proposed cataloging to real use cases it will be possible to define correlation values that will form the theoretical basis necessary to specify a guideline for the preliminary conceptual design of digital games.

2 Literature Review

The review is conducted by adopting the light version of the guidelines proposed by Kitchenham et al. [9], adapted to the needs of the present research. This work aims to analyze previous video and serious games cataloging to propose a unified model that encompasses all of them to guide designers in tailoring the application they want to design to their specific needs. The first step of the guidelines is to formulate a research question that will guide the review. Our review tries to answer the following:

- **RQ**: How are video and serious games catalogued, and on which criteria?

After the formulation of the research question and having defined the database pool from which to extrapolate the papers (i.e., electronic databases such as Scopus, IEEEXplore and Web of Science, including scientific papers, review articles and conference proceedings) the research question aids in the formulation of a search string. Our search string is the following: ("recategorization" OR "cataloging" OR "cataloguing") AND ("videogames" OR "digital" OR "serious") AND ("games"). The survey is limited to English-only articles in the Computer Science and Engineering fields and resulted in 1135 records, which decreased to 911 after duplication removal. Filtering the records, including only works from 2010 to 2023, resulted in 695 papers. A preliminary selection based on title, keywords and abstract results in 31 titles, further reduced to 5 records after a rigorous selection based on inclusion criteria. The criteria are that a screened record is admitted to the review only if it proposes a video and/or serious game cataloging system. The first reviewed paper [10] proposes a cataloging system based on G/P/S (gameplay, purpose, scope) concept, gaming platform and UX for container terminal logistics serious games. Then, [11] proposes a simple genre-based cataloging system for entertainment videogames, while [12] proposes a comprehensive cataloging system for health rehabilitation serious games based on UX (feedback, adaptation), interaction, technology, and other domain-specific criteria. Finally, [1] proposes a cataloging system for serious games based on the style of interaction offered to the player, activity, mode, environment, and area of application, while [13] proposes a cognitive stimulation serious games' cataloging based on similar criteria to that of [12].

3 Data Analysis

The review results in five different cataloging systems, each with several metadata. A higher-level framework proposed by [8] is followed to achieve the objective of unifying such cataloging systems. The framework illustrated in [8] proposes to classify digital games by three definitions, namely:

- **D1**, "The game is seen as a computer program and all its related properties such as the admissible number of users, networking features and the like are considered"
- **D2**, "The game as a piece of artwork and media has a genre"
- **D3**, "Through intense interaction, players act and experience engagement such as building, fighting, or trading, e.g., Interaction determines the psychological/social impact".

The first step is to remove the domain-specific parameters (e.g., patient monitoring/assessment in [12]) from the cataloging systems obtained from the literature review. The following step is to identify the definition to which each parameter belongs. Some criteria are omitted from the three-definition classification: the target audience and the application area. This is because such classification is of general application and is not targeted towards serious games. As a matter of fact, videogames aim to entertain and amuse the player, while serious games present a practical purpose (e.g., training, education, well-being). Therefore, to include the left-out parameters too, the three-dimensional high-level classification system is extended to include two other definitions, namely:

- **D4**, a digital game is always oriented towards a specific audience and market. The Design phase must take the target into consideration to tailor the product to the user that is intended for
- **D5**, serious games always have a practical purpose that, in conjunction with the audience and market, guides the Design phase.

Once each parameter is categorized in one of the five high-level definitions (where parameters are contained in two or more cataloging system, these are joined together), the result is obtaining a model that unifies the five cataloging systems obtained from the review. Four of the five definitions enable the abstraction of four classification dimensions that can be useful for classifying digital games. Those dimensions are:

- **Genre,** is the dimension that specifies the genre of the digital game (e.g., RPG, strategic, puzzle) and suggests to both the user and the designer which kind of experience the game should deliver. It is derived from definition D2
- **Engagement,** is a quantitative dimension that specifies the intensity of the interaction between the player and the digital game. It can be affected by several factors (e.g., immersiveness, narrative, fidelity), and it's derived from definition D3
- **Target,** combines the targeted market (e.g., healthcare, education, culture & art) and the targeted audience (e.g., the general public, professionals, students). It is the dimension that characterizes a digital game based on who it is targeted. It is derived from definition D4
- **Purpose,** specifies the goal of the digital game, whether it is intended for entertainment only (videogames) or for more pragmatic goals such as serious games (e.g., marketing, training). It is derived from definition D5.

These dimensions, abstracted from the unified cataloging system proposed here, enable the classification of digital games. D1 is left out of the abstraction process because it is not strictly related to digital games but rather to the features that designate them as software (as the authors stated). Figure 1 shows how two digital games could be classified with this system. The three qualitative dimensions (Genre, Target, and Purpose) are depicted one for each axis of the Cartesian space: their arrangement on the axis is not ordinal and only serves as a visual representation of their differences in value. The quantitative parameter (Engagement) is defined by the dimension of the sphere representing the game.

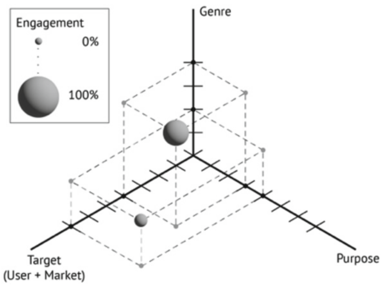

Fig. 1. A classification example of two digital games

4 Metadata for Cataloging

Although excluded from the process of abstraction of classification dimensions, the D1 definition in conjunction with the other four remains useful for defining the metadata that enables cataloging digital games. From D1, it is possible to derive the metadata useful to determine the software and hardware characteristics that characterize a digital game.

Our proposed cataloguing metadata derive from the cataloging systems resulted from literature review and are arranged according to the five definitions: D1, D2, D3, D4, and D5.

The first four definitions (D1-D4) are generalizable to all types of video games since they are based on game characteristics that are closely related to (i) the software, (ii) the artistic choices related to the video game's genre, (iii) the user's interaction experience with the game, and (iv) the end user.

The fifth dimension (D5) is distinctive to Serious games since it is centered on game qualities that vary depending on the specific objective of the game.

Each definition embraces several categories, subdivided into more detailed metadata relating to the core issue.

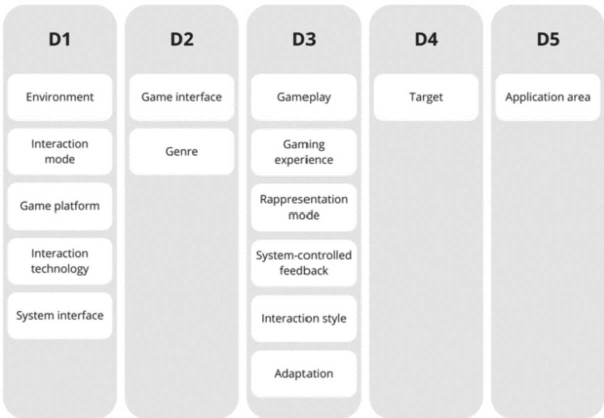

Fig. 2. The unified model with the five definitions

Figure 2 depicts the unified model with only the categories to produce a compact scheme presenting essential information. The next sub-paragraphs provide a comprehensive overview of each definition. Each sub-paragraph presents a list of categories and its metadata, with the corresponding author(s) that discussed each of them.

4.1 Definition 1

Definition 1 (D1) provides information on the different aspects of software-related games, including the environment, interaction modes, game platform, interaction technology, and system interface. The category "Environment" lists the different types of environments the gaming system supports, including (i) *Social presence*, (ii) *Mixed reality*, (iii) *Virtual environment*, (iv) *Location awareness*, and (v) *Online*. These metadata were discussed by [1, 13]. The second category is "Interaction Modes", which includes two metadata: (i) *Single-player* and (ii) *Multiplayer*. The paper [11] includes these metadata.

The third category, "Game Platform", includes two metadata, (i) *Hardware architecture* and (ii) *Deployment*, which were discussed by [10, 12, 13]. The fourth category is "Interaction Technology", which comprises several metadata such as (i) *Keyboard*, (ii) *Mouse*, (iii) *Voice/speech*, (iv) *Motion capture*, (v) *TUI*, (vi) *Touch/multitouch*, (vii) *Eye gaze tracking*, (viii) *Haptics*, (ix) *Facial expression recognition*, (x) *Biofeedback*, and (xi) *Gamepad*. The works [1, 12] addressed these metadata. The fifth category is "System Interface", which comprises four metadata: (i) *Visual*, (ii) *Auditory*, (iii) *Haptic*, and (iv) *Mixed*. These metadata were discussed by [12].

4.2 Definition 2

Definition 2 (D2) appears to provide information regarding the design of a game interface, with a focus on two essential components: "Game interface" and "Genre". Two metadata are given under the "Game interface" category: (i) *2D graphics* and (ii) *3D graphics*, with the authors [1, 13] associated with both. The second category is "Genre", which is discussed by the authors [11, 13]. It includes various metadata such as (i) *RPG (Role Playing Games)*, (ii) *Adventure*, (iii) *Puzzle*, (iv) *Action*, (v) *Strategy*, (vi) *Sports*, (vii) *Learning*, (viii) *Exercise*, and (ix) *Simulation.*

4.3 Definition 3

Definition 3 (D3) is that which contains the most items. In this case, the categories are "Gameplay", "Gaming experience", "Representation mode", "System-controlled feedback", "Interaction style", and "Adaptation"; each of them includes specific metadata. The category, "Gameplay", includes two possible metadata: (i) *Game-based* and (ii) *Play-based*. Both were discussed by [9]. The second category includes metadata related to the gaming experience, such as (i) *Challenge*, (ii) *Competence*, (iii) *Flow*, (iv) *Negative/positive effects*, and (v) *Tension.* All these metadata were examined by [10].

The third category, "Representation mode", includes metadata related to (i) *Visual*, (ii) *Auditory*, (iii) *Haptic representation*, and (iv) *Mixed modes*. Authors [1, 12] went through these metadata. The fourth category, "System-controlled feedback", has metadata related to feedback provided by the game (i) *During gameplay* and (ii) *After gameplay*. These metadata were discussed by [12]. The fifth category is "Interaction style". It includes metadata that describe the different ways players can interact with the game: (i) *Standard (traditional peripherals)*, (ii) *Active (alternative peripherals or body)*, and (iii) *Pervasive*. The author [12] discussed all of them. The last category is "Adaptation", which has three metadata: (i) *Off-game configuration*, (ii) *In-game adaptability*, and (iii) *None*. These categories define how the game can adapt to the player's preferences or abilities and were described by [10, 12, 13].

4.4 Definition 4

Definition 4 (D4) shows an essential aspect to consider when designing a digital game: the target. This category refers to the importance of tailoring the game to meet the needs and preferences of the target user during the design phase. It includes two metadata: (i) *Target Market* and (ii) *Audience*. These metadata were addressed by [10, 12, 13].

4.5 Definition 5

Definition 5 (D5) details Serious Game application areas, which are fundamental to the game design because each serious game is guided by a practical purpose that aligns with the audience and market. The only category, “Application Area,” includes several metadata: (i) *Education*, (ii) *Well-being*, (iii) *Training*, (iv) *Advertising*, (v) *Interpersonal communication*, (vi) *Healthcare*, (vii) *Storytelling*, (viii) *Informative*, and (ix) *Others*. These metadata have been explored by [1, 10].

5 Discussion and Conclusions

This paper proposes a unified cataloging system based on a matrix approach for digital games (video games and serious games), based on a five-dimension matrix comprising all the key digital games classification metadata (also known as “tags”) proposed in the literature. It aims to collect the existing knowledge and highlight commonalities between existing cataloging systems. Considered cataloging systems proposed a heavily domain-specific or low-level approach. In [13], a cataloging of cognitively stimulating serious games based on characteristics from the conventional cataloging of serious games has been suggested. This system is limited in scope since it is domain-specific, meaning it only applies to serious games focusing on cognitive stimulation and does not give a high-level categorization. A cataloging system based on the G/P/S (gameplay, purpose, scope) concept, gaming platform and UX is presented in the study [10]. The system proposed provides insights into existing studies on gamification in the container port logistics field. It considers both video games and serious games, and mainly focuses on game characteristics closely related to the user’s interaction experience, the end-user, and the specific goal of the game. However, it excludes other equally important aspects, such as software-related game features and artistic choices related to the video game genre. In [11], the focus is solely on cataloging video games meant for entertainment, while [12] puts forth a cataloging system for health rehabilitation games focusing on UX (feedback, adaptation), interaction, technology, and other criteria specific to the activity. Neither [11] nor [12] encompass all types of digital games, and [12] introduces a cataloging system that is tailored to a specific domain. Finally, [1] proposes a system based only on serious games. The novelty of this work is that the proposed model unifies kind of digital games although retaining distinctions where necessary (e.g., the fifth definition specific only to serious games). This result is achieved by interpreting the cataloging identified in the literature according to a higher-level framework, as illustrated by [8]. Moreover, the paper proposes a four-dimension classification system. Although it is only hinted at in the present paper, future works will assess whether the proposed cataloging and classification systems could work together: the cataloging system and its metadata are intended to classify digital games by following the classification system. Future works will test the proposed cataloging on various video and serious games to validate the model. By applying the proposed “matrix cataloging”, it will be possible to assess how the several metadata interact with each other, thus enabling the creation of a correlation matrix. This work could be considered a starting point to draft guidelines based on the correlation matrix that will help the game designers in the Concept Design phase, enabling them to better suit the product they are designing to the users they are targeting.

Starting from a general idea of the game that the designers should develop (e.g., a fantasy serious game intended to educate teenagers on the risk of smoking), the correlation matrix could suggest to them a list of optimal metadata that have a high correlation with the goal of the game. These metadata could be considered as suggested specifications that will guide the game's development (e.g., a high-engaging game developed in VR and with social networking features to capture the attention of teenagers). This work may be limited by the evaluation of only review studies rather than primary studies on video games and serious games, some key features of digital games may have been missed. Similarly, the review conducted in this study may have left out other taxonomies already proposed.

References

1. Laamarti, F., Eid, M., Saddik, A.E.: An overview of serious games. Int. J. Comput. Games Technol. **2014**, 11 (2014)
2. Ivory, J.D.: A brief history of video games. In: The Video Game Debate (pp. 1–21). Routledge (2015)
3. Mader, S., Natkin, S., Levieux, G.: How to analyse therapeutic games: the player/game/therapy model. In: International Conference on Entertainment Computing, pp. 193–206. Springer, Berlin, Heidelberg (2012)
4. Holloway, A., Kurniawan, S.: System design evolution of The Prepared Partner: How a labor and childbirth game came to term. Meaningful Play (October 2010)
5. Holloway, A., Kurniawan, S.: Human-centered design method for serious games: a bridge across disciplines. In: Proceedings from UCSC-SOE, pp. 10–36 (2010)
6. Jacob, E.K. (2004). Classification and categorization: a difference that makes a difference
7. Esse, U.C.: Current trends in cataloguing and the challenges of a cataloguer in the digital age. Inform. Impact: J. Inform. Knowl. Manage. **4**(2), 16–23 (2013)
8. Jantke, K.P., Gaudl, S.: Taxonomic contributions to digital games science. In: 2010 2nd International IEEE Consumer Electronics Society's Games Innovations Conference (pp. 1–8). IEEE (December 2010)
9. Kitchenham, B. A., Kitchenham B.: Guidelines for performing Systematic Literature Reviews in software engineering. EBSE Technical Report EBSE-2007–01. In: ICSE (pp. 1051–1052) (2007)
10. Nasution, N.K.G., Jin, X., Singgih, I.K.: Classifying games in container terminal logistics field: a systematic review. Entertain. Comput. **40**, 100465 (2022)
11. McMahon, N., Wyeth, P., Johnson, D.: Exploring the role of activity in genre. In: Proceedings of The 9th Australasian Conference on Interactive Entertainment: Matters of Life and Death (pp. 1–3) (Sept. 2013)
12. Rego, P.A., Moreira, P.M., Reis, L.P.: Proposal of an extended taxonomy of serious games for health rehabilitation. Games for Health Journal **7**(5), 302–309 (2018)
13. Zaki, N.A.A., Wook, T.S.M.T., Ahmad, K.: Analysis and classification of serious games for cognitive stimulation. In: 2015 International Conference on Electrical Engineering and Informatics (ICEEI) (pp. 612–617). IEEE (Aug 2015)

Industrial Design and Ergonomics

Virtual Reality in Design Methods: Case Study of an Automotive Design Product

Giulio Galiè(✉), Marco Freddi, Edoardo Pignatelli, Giampiero Donnici, and Leonardo Frizziero

Alma Mater Studiorum, Università di Bologna, Viale Risorgimento 2, 40136 Bologna, Italy
giulio.galie2@unibo.it

Abstract. The design of a product consists of several stages to be carried out in sequence until the result is achieved, some of them are performed trough the help of CAD software. This design step is very rigorous with as little margin for error as possible, and it often goes to make a clean break from other stages that precede it. On the other hand, virtual reality technology is certainly an element of interest within various design areas. One of the most promising uses of this type of technology is in the visualization and review of products in the design process. But in this paper we will see a next step compared to this just described, that is, the application of virtual reality within the design making itself. By delving into the design timeline, we will then go on to explore how this technology can provide support not limited to visualization alone, but extended to modeling, what possibilities can be offered by the realization of three-dimensional surfaces, modeled already at the correct scale, and how these aspects can be efficiently integrated within a methodology, assessing variations in timing and quality of work. We will also try to intercept any downsides to try to get a clear understanding of what possibilities could be offered soon by this technology and whether indeed these types of processes can replace current methods, established for years.

Keywords: Industrial Design · Virtual Reality · Design Methods

1 Introduction

1.1 Introduction of Design Processes

Many of the steps within the design process are carried out by computer. In fact, in the modern way of thinking about design there always comes the stage when one must go on to the construction of a virtual three-dimensional model. These models are often made with the help of rigorous software like CAD modelling.

As was mentioned earlier, this design step turns out to be very rigorous and precise with very little margin for error, and it often goes to make a clean break from other stages that precede it such as freehand sketches made at earlier stages of the project. We shall be able to observe how all these stages can be in some ways and in some steps unrelated to each other or subject to an evident leap in the approaches and technologies utilized

M. Carfagni et al. (Eds.): ADM 2023, LNME, pp. 303–310, 2024.
https://doi.org/10.1007/978-3-031-52075-4_34

by looking at the design schedule offered by a case study. Virtual reality technology has been providing an element of interest within various areas including product design for several years [1].

One of the most promising uses of this type of technology is in the visualization and consequently visual review of products designed using conventional software [2]. In fact, the possibility by means of a viewer to be able to have in front of one's eyes the model that is being drawn in a 1:1 scale guarantees in a quick way and with a good degree of precision to be able to understand in a very intuitive way the shapes of the object in relation to its dimensions and therefore to be able to evaluate its proportions in a very natural way [2], almost as if we had built a physical prototype of the product but with evident savings in terms of time and money used [3].

Instead, in this paper we will see a next step compared to this just described, that is, the application of virtual reality within the design itself and no longer only related to the review phase. We will then go on to explore how this technology can provide support not limited to visualization alone, but extended to modeling, what possibilities can be offered by the realization of three-dimensional surfaces, modeled already at the correct scale, and how these aspects can be efficiently integrated within a methodology.

This aspect will be important in assessing variations in timing and quality of work. We will also go on to investigate any disadvantages due to the application of this technology to get a clear under-standing of what possibilities will be offered in the near future by this type of technology and whether new procedures can really take the place of current, tested procedures.

1.2 Virtual Reality Overview

Virtual Reality (VR) is a technology that allows users to immerse themselves in a virtual environment, which can be created using computer-generated graphics, 3D modeling, and simulations [3, 4]. VR has numerous applications in design and engineering, providing new capabilities to designers and engineers that were not previously possible.

Some current application of virtual reality in design and engineering are [6, 7]:

1. Design reviews: Virtual reality allows designers to review their designs in a 3D immersive environment. This can help identify design flaws, aesthetic issues, and other design considerations that may not be immediately apparent in 2D representations.
2. Prototyping: Virtual reality can be used to prototype and test new products, structures, and systems in a simulated environment. This allows designers and engineers to test and refine their designs before producing physical prototypes.
3. Training and education: An example of this scenario could be the use of virtual reality in simulating the operation of complex machinery, allowing engineers to practice and learn in a safe and controlled environment.
4. Visualization: Virtual reality can be used to visualize complex data and designs. This can be particularly useful in fields such as architecture, where virtual reality can be used to visualize a building's layout and interior design.
5. Collaboration: Virtual reality can be used to facilitate collaboration between designers, engineers, and other stakeholders. By working together in a virtual environment, team members can make design decisions more efficiently and effectively.

2 Materials and Methods

To make the analysis of this technology more effective, it was chosen to apply it within a known design methodology. In the field of product design, to arrive at the final definition of a product concept certain key steps are followed, carried out sequentially, leading to an effective result-to. The main objectives of these methods are [8]:

1. Realize an effective product both from the performance point of view according to the constraints re-challenged and according to the competitiveness in the market.
2. Achieve high efficiency in the ratio of quality (real/perceived) and price.
3. Decrease the variability of the end result as the different designers/project teams vary, so that the end result is more robust and predictable, and new elements can be more efficiently integrated into the team.

The various design steps are united by some common steps, so we are going to describe one of the most significant methodologies and analyze its various steps. This method under consideration is called SDE (Stylistic Design Engineering). SDE is a field of engineering that focuses on the aesthetic and stylistic aspects of product design. It combines principles of engineering, design, and aesthetics to create products that are not only functional and practical but also visually appealing and user-friendly. SDE professionals work closely with other engineering and design teams to ensure that products are not only functional but also aesthetically pleasing [9].

The SDE method consists of the following steps to be followed in strict chronological order. 1- Research and brand analysis, 2- Style analysis, 3- Freehand sketching, 4- 2d drawing, 5- 3d modeling, 6- rendering and final review [9].

3 Discussion

As can be seen from the description on methodologies set out above, the phase of design on CAD software, turns out to be very different in typology from previous phases such as freehand sketching. In fact, while we note how in the initial phases the operations of both study and work leave a substantial space for creativity and for some aspects to the free interpretation of certain aspects by the designers, however much the design path remains framed within a well-defined methodology, the moment we move on to the use of CAD software, whether 2d type for the realization of blueprints on the basis of sketches, or three-dimensional modeling software, we can immediately notice that the approach to be used changes radically.

Indeed, in these applications, the approach becomes much more systematic, and in some respects rigid. The fact that these two types of approaches turn out to be so different from each other suggests that the levels and types of skills needed at the various stages of design may be very different depending on the various stages one is in. It thus proves difficult for the same people to go about operating equally effectively in all these various steps observed, consequently the control of individuals throughout the entire pro-design process diminishes. Allowing individual designers to be able to have control over as many stages as possible helps to achieve a good level of consistency in the project, both because it allows those who operated in the initial ideas to go in and actually verify the transposition of those concepts into the projected mathematical models, and because a single look during the various stages helps the project, once it reaches the final stages in maintaining a certainly greater overall consistency.

One of the greatest advantages expressed by virtual reality turns out to be that it brings the work of visualization and final revision of tridimensional models much closer to a freer and more creative environment such as that of freehand sketching [10, 11]. The great advantage expressed by this technology consists-re being able to visualize by anyone virtual model in 1:1 scale, differentially from what happens through a computer monitor [12]. In fact, being able to be inside a project and being able to observe it in real proportions respectively to one's own person and point of view, allows a much more effective revisions not only by those who are actually working on the realization of the 3d model, but also by external parties, such as may be, for example, other elements of the design team who worked in the initial stages of ideation, or elements outside the team, such as clients, customers, administrative staff [13, 14].

Considering this, it becomes clear how it can be an interesting advantage to be able to integrate this technology within the design not only for the visualization and review phase, but also directly within the modeling phase by allowing designers to go and draw and model directly within a three-dimensional environment, with the model in front of them at 1:1 scale.

4 Results

In order to find the most efficient way to insert virtual reality modeling technology within one of the design methods, as set forth above, we applied this technology within two types of work. In the first type, we used the standard SDE path for the complete realization of the project by inserting virtual reality in the final modeling phase. All modeling was done using CAD software, and when the model was nearly completed, the file was imported into VR visualization software to allow for review. The review of the model was not merely visual, but interactive. In fact, Gravity Sketch was chosen as the revision software. Such software allows drawing via special viewer controllers directly within the three-dimensional space. This work was applied to a dissertation in which the student found himself making a model of an automobile for the first time having never had design experience with it, thus having the typical initial difficulties in reference to even simple elements such as general proportions and between the various parts. A shared virtual room was therefore created, within which designers with experience in the field were given access, who were able to view the car almost as if it were a live model at 1:1 scale, walk around it, and draw on it, either simple sketch lines or elementary surfaces, to best enable the student to be able to understand how to go about modifying the curvatures of the various parts (Fig. 1). This car model was later reimported within CAD software, where the modifications suggested in the review phase were made.

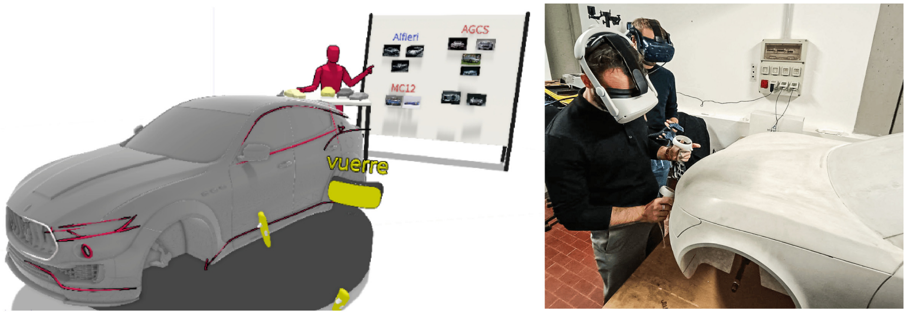

a b

Fig. 1. (a) The imported model within the virtual room is compared with reference images and revised to 1:1 scale, simulating a clay style maquette. (b) Real-life relief from a scale model of an automobile.

For the second type of work, on the other hand, it was chosen to realize the entire automobile completely within virtual reality. For the realization of the purpose, once again the software Gravity Sketch was chosen, the use of which was already being explored through the other work exhibited earlier. This program makes it possible to create virtual classrooms of various sizes in which, through the use of a visor, it is possible to walk and move around inside as if they were physical spaces. Within these spaces it is possible to use some tools for drawing, modeling, and testing. Inside this room it is possible to import 2d reference drawings, whether taken from previously realized paper sketches, or taken from images of reference or competitor cars. It is also possible to place within it point clouds of auto-mobiles obtained, for example, through 3d scanning technologies (Fig. 2).

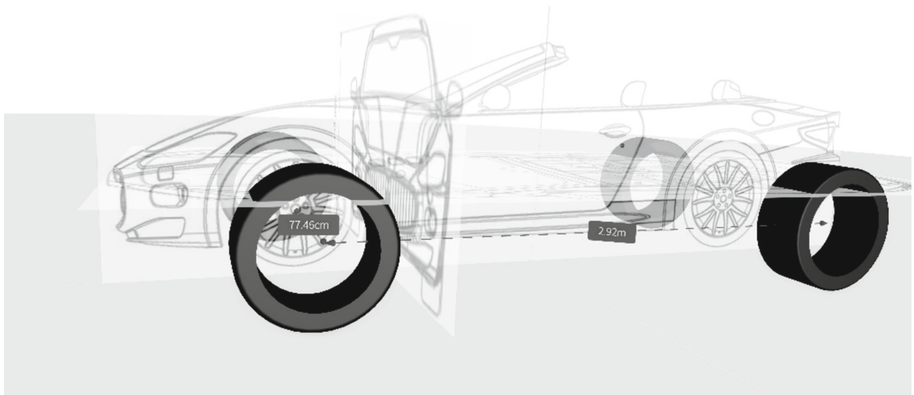

Fig. 2. Start of car setup based on imported blueprints of a reference vehicle belonging to the same segment, used as a measure.

The program provides different modeling tools, starting from the simplest lines with which to make three-dimensional sketches, up to surfaces of varying curvature and complexity, which can be made of both Nurbs and SubD types, allowing the model to be exported in different formats depending on the intended use for different applications, whether they be rendering or prototype making. The combination of all these elements allowed the styling design of a car to be realized entirely within the software and fully realized via viewer. An additional element of interest was to have imported within the room the car chassis that had already been previously modeled by CAD software based on actual specifications, and to have been able to use it as a dimensional and ergonomic constraint in the realization of the body (Fig. 3).

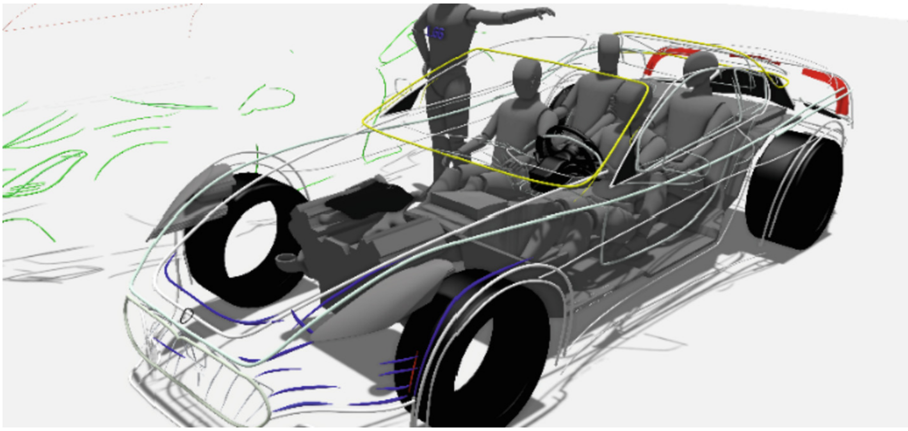

Fig. 3. Based on the entered mechanical constraints, the 3d style sketch is made.

The procedure used in making the model started from some imported reference images, which were used as the basis in making the three-dimensional sketches. Then surfaces were made that con-joined the sketch lines to arrive at the definition of a closed three-dimensional model. The fact that the model was already within the virtual space greatly speeded up verification and revision operations, even going so far as to include within, as in the last project, more-qualified personnel to evaluate shapes and dimensions, no longer needing the ancillary step of importing and exporting the model between different soft-ware. Corrections this time are made directly on top of the model and modified in real time, even by several people at the same time in different positions of the reading, thus going to simulate what is done in reality on top of a Clay model, where skilled craftsmen go to make precision changes to arrive at the desired appearance (Fig. 4).

Fig. 4. Final rendering of the car in different colors.

5 Conclusions

As it was then possible to observe, we managed to successfully create a styling proposal for an innovative car model completely within virtual reality, using this technology for all the various stages of the work, from the initial sketches to the creation of renderings to better evaluate proportional shapes of the car. The fact that all this work was done individually by a student who had never had experience modeling on surfaces adds an additional element of interest. In fact, thanks to the very gamification-oriented approach of virtual reality, the soft-ware made possible a very simplified user experience, which successfully allowed us to arrive at the desired result in a short time frame. As can also be seen from (Fig. 5), this working model can be successfully inserted within an already proven design methodology, replacing some phases, and integrating others, ensuring an overall beneficial result.

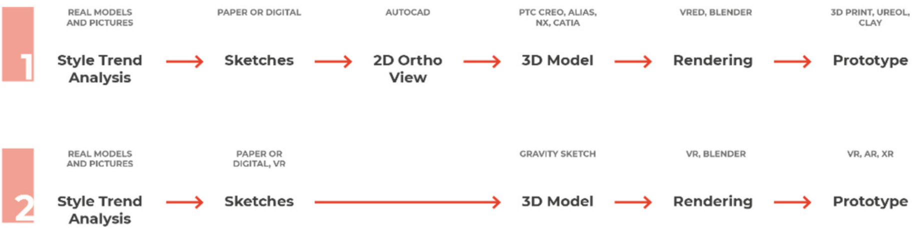

Fig. 5. SDE method (1) and the same model integrated with Virtual Reality (2).

References

1. Wolfartsberger, J.: Analyzing the potential of virtual reality for engineering design review. Autom. Constr. **104**, 27–37 (2019)

2. Horvat, N., Kunnen, S., Štorga, M., Nagarajah, A., Škec, S.: Immersive virtual reality applications for design reviews: systematic literature review and classification scheme for functionalities. Adv. Eng. Inform. **54**, 101760 (2022)
3. Elghaish, F., Matarneh, S., Talebi, S., Kagioglou, M., Hosseini, M.R., Abrishami, S.: Toward digitalization in the construction industry with immersive and drones technologies: a critical literature review. Smart Sustain. Built Environ. **10**(3), 345–363 (2020)
4. de Souza Cardoso, L.F., Mariano, F.C.M.Q., Zorzal, E.R.: A survey of industrial augmented reality. Comput. Ind. Eng. **139**, 106159 (2020)
5. Bottani, E., Vignali, G.: Augmented reality technology in the manufacturing industry: a review of the last decade. Lise Trans. **51**(3), 284–310 (2019)
6. Masood, T., Egger, J.: Adopting augmented reality in the age of industrial digitalization. Comput. Ind. **115**, 103112 (2020)
7. Mourtzis, D., Zogopoulos, V., Xanthi, F.: Augmented reality application to support the assembly of highly customized products and to adapt to production re-scheduling. Int. J. Adv. Manufact. Technol. **105**(9), 3899–3910 (2019)
8. Frizziero, L., et al.: Computer-aided surgical simulation through digital dynamic 3D skeletal segments for correcting torsional deformities of the lower limbs in children with cerebral palsy. Appl. Sci. **12**(15), 7918 (2022)
9. Frizziero, L., et al.: An innovative ford sedan with enhanced stylistic design engineering (SDE) via augmented reality and additive manufacturing. Designs **5**(3), 46 (2021)
10. Delgado, J.M.D., Oyedele, L., Demian, P., Beach, T.: A research agenda for augmented and virtual reality in architecture, engineering and construction. Adv. Eng. Inform. **45**, 101122 (2020)
11. Gattullo, M., Scurati, G.W., Fiorentino, M., Uva, A.E., Ferrise, F., Bordegoni, M.: Towards augmented reality manuals for industry 4.0: A methodology. Robot. Comput.-Integr. Manufact. **56**, 276–286 (2019)
12. Masood, T., Egger, J.: Augmented reality in support of Industry 4.0—Implementation challenges and success factors. Robot. Comput.-Integr. Manufact. **58**, 181–195 (2019)
13. Chen, Y., Cui, Z., Hao, L.: Virtual reality in lighting research: comparing physical and virtual lighting environments. Light. Res. Technol. **51**(6), 820–837 (2019)
14. Fiorentino, M., et al.: User study on virtual reality for design reviews in architecture. In: 2020 IEEE International Symposium on Mixed and Augmented Reality Adjunct (ISMAR-Adjunct), pp. 283–288. IEEE (2020)

Exploiting Immersive Virtual Reality for Investigating the Effects of Industrial Noise on Cognitive Performance and Perceived Workload

Alessandro Evangelista[1], Vito M. Manghisi[1(✉)], Vito De Giglio[1], Francesco Martellotta[2], Claudia Giliberti[3], Raffaele Mariconte[3], and Antonio Emmanuele Uva[1]

[1] Department of Mechanics, Mathematics, and Management, Polytechnic University of Bari, Bari, Italy
vitomodesto.manghisi@poliba.it

[2] Department of Civil Engineering Sciences, Architecture Polytechnic University of Bari, Bari, Italy

[3] Dip. Innovazioni Tecnologiche e Sicurezza degli Impianti, Prodotti ed Insediamenti Antropici Inail Rome, Rome, Italy

Abstract. The Industry 5.0 paradigm emphasizes the importance of the operator's well-being by seeing human-centricity as one of its cardinal principles. This enables a twofold benefit, improving the sustainability of the production process and enhancing performance.

Improving performance and increasing operators' safety is often related to cognitive load optimization. Confined spaces are working environments where elements of distraction, such as noise, can cause accidents with major, even fatal, consequences. Studies on the effects of noise on cognitive abilities present mixed results, and those concerning confined spaces are limited as they require an expensive experimental setup replicating the working scenario. Immersive Virtual Reality (IVR) technology enables overcoming this gap by replicating the experimental conditions in a synthetic environment. We exploited IVR to study noise's impact on cognitive performance in confined spaces. We compared the impact of a stationary continuous noise source with an intermittent non-periodic one by administering the Stroop Color and Word Test. We also assessed the perceived cognitive effort by administering the modified noise-induced task load index questionnaire. We also compared the effects on the operator's physiological activity through Heart Rate Variability (HRV) analysis. Results show that by keeping the equivalent noise level lower than 85 dB, noise has no statistically significant effects on cognitive performance and Heart Rate.

Keywords: Cognitive Performance · Noise Effects · Stroop Color and Word Test · Virtual Reality · Heart Rate Variability

M. Carfagni et al. (Eds.): ADM 2023, LNME, pp. 311–318, 2024.
https://doi.org/10.1007/978-3-031-52075-4_35

1 Introduction

The Industry 5.0 paradigm sees human-centricity as one of its cardinal principles. Guaranteeing the operator's well-being in the industrial environment becomes a key element that improves the sustainability of the production process and the operators' performance. The latter result can be achieved by optimizing the physical and cognitive load associated with the operators' tasks. Cognitive load optimization is critical not only for improving productivity but also safety. Indeed, there are working environments where elements of distraction can cause accidents with major, even fatal, consequences. One such distracting element is noise which represents a pervasive element. The effects of noise can be particularly harmful in confined spaces, as the presence of reverberation can amplify the levels of exposure and negatively affect cognitive abilities. [1]. Occupational safety regulations aim to eliminate noise sources whenever feasible. However, if it is not possible to eliminate the noise, the NIOSH standard mandates that workers wear personal protective equipment (PPE) for hearing protection when their exposure to noise reaches 85 dBA or higher, based on an 8-h Time Weighted Average.

The impact of noise on cognitive abilities such as concentration and short-term memory has been studied in the literature concerning many working environments [2]. A review study revealed that among 58 studies, 29 reported a negative effect, 7 reported a positive effect, and 22 reported no effect of noise on cognitive performance [3]. Experimental evidence has shown a deteriorative impact of speech noise, such as the background buzz of an office [4]. By simulating a 70-h activity period aboard the International Space Station, Smith et al. found no impact of such noise conditions on cognitive capabilities [5]. Halin conducted a study to assess the influence of various types of noise on students' reading ability. The findings revealed a detrimental impact of background noise in situations that required less cognitive effort. However, no significant effects were observed when the task presented a higher level of challenge [6].

Mixed results belong to different experimental setups. Jafari et al. [7] compared the workload associated with four noise levels and found statistically significantly increased workload only between 45 dBA and 95 dBA background noise. Dogget et al. reported significant noise effects on the recall task [8]. However, their experimental procedure provided stimuli using voice. Consequently, it is not possible to establish if such an effect was due to the noise superimposed to the vocal stimuli.

Studies concerning noise effects in confined environments are limited as they require an expensive experimental setup replicating the confined environment and removing risk components. IVR technology enables overcoming this gap by replicating the experimental conditions in a synthetic environment, thus lowering costs and removing risks [9]. Furthermore, IVR allows for precise control of experimental conditions. Recent studies provided encouraging findings by successfully using IVR to assess the effects of noise on cognitive performance, producing results comparable to a setup in a real-world setting [8, 10]. For instance, a recent study utilizing IVR to investigate the effects of continuous stationary noise on cognitive performance within confined environments corroborated the findings of Liebl et al. in [4]. The study revealed that various continuous noises, including stationary noise, produced similar error rates in recall tasks as those observed in a quiet environment [9]. Mixed results could also depend on the nature of disturbing sounds [11]. or instance, according to Schlittenlacher et al., it was postulated that the dynamic nature of speech (or irrelevant sound in general) gives rise to the phenomenon known as "irrelevant sound interference." This phenomenon has an impact on performance in memory tasks. [12].

Such a hypothesis suggests further investigating the effect of disturbing noises on cognitive capabilities by considering noise sources with different temporal variability and frequency content. In addition, previous studies exploiting IVR to evaluate di effects of noise in confined spaces limited the investigation from the perspectives of reaction time and short-term memory, neglecting other cognitive capabilities.

With this in mind, we designed and conducted an experimental study exploiting IVR to simulate a confined space with a Virtual Environment (VE) to compare the impact of continuous noise with that of intermittent non-periodic noise. In contrast to previous studies focused on confined spaces, our research delved into examining the impact on the ability to inhibit cognitive interference. This interference occurs when the processing of one specific stimulus feature hinders the simultaneous processing of another stimulus attribute, a phenomenon commonly known as the Stroop Effect [13].

We formulated the following research questions:

- RQ1: Is there any difference in the effects of noise on cognitive capabilities and perceived workload/annoyance between a continuous and stationary disturbance sound source and an intermittent non-periodic one?
- RQ2: Does Heart Rate Variability analysis allows to detect noise effect on cognitive capabilities?

2 Materials and Methods

2.1 Design of Experiment

To answer RQ1, we designed a 1 x 3 within-subjects experiment considering two independent variables: cognitive load and noise. The cognitive task consisted in the Stroop Word and Color Test (SWCT). The test required the participant to correctly recognize the color used to fill the characters of one out of six target words (stimuli) displayed randomly on a canvas in the VE. The target words corresponded to color names that differed from the color used to fill the characters. The participant had to select, among four buttons displayed on the bottom side of the canvas, the one matching the color used to fill the characters of the target word on the upper side Fig. 1. Three conditions were considered for noise: i) no noise (from now on NN-condition), ii) continuous stationary noise (from now on CN-condition), and iii) intermittent non-periodic noise (from now on IN-condition).

To answer RQ2, we recorded the Electrocardiogram (ECG) signal. We measured user performance, perceived cognitive load, noise annoyance, and HR as dependent variables.

Fig. 1. The canvas for the SWCT interface with the word whose character color defines the button to be selected by the participant.

2.2 Participants

The study consisted of 30 participants, including nine females, with ages ranging from 19 to 51 years (Mean: 25.5; SD: 5.8). The participants were recruited from the student and researcher population at the Polytechnic University of Bari. Prior to their involvement, all participants confirmed having normal hearing and normal vision. Among the participants, nine individuals required prescription lenses, which they were allowed to wear during the experiment to ensure optimal visual acuity.

2.3 Hardware

The IVR system used in the experiment was an HTC Vive Pro Eye Head Mounted Display. For acoustics analysis, a binaural dummy head B&K 4410D was connected to a 01dB Symphonie acquisition system (Fig. 2a). Physiological signal acquisition was performed using the Biosignalplux research kit (Fig. 2b). The setup had a 16-bit resolution and a sampling frequency of 1000 Hz.

Fig. 2. a) The B&K 4410D wearing the HTC Vive Pro Eye; b) The Biosignalplux research kit.

2.4 Virtual Environment and Acoustic Analysis

To simulate the noise in the virtual environment (VE), we generated a noise source based on recordings captured in an open environment with minimal reverberation. The original recordings were sampled at a rate of 48 kHz and had a resolution of 32 bits. We recorded the signal generated by an electric drill. The power spectrum of the anechoic signals is characterized by a notable drop in emitted power at frequencies below 1 kHz (Fig. 3).

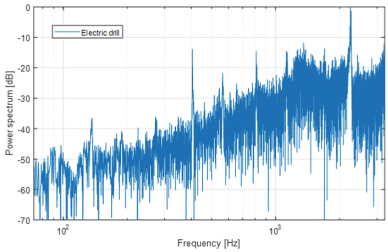

Fig. 3. The noise source frequency spectrum.

We used the Autodesk Inventor CAD software to model the experimental VE, a cylindrical steel silo. For modeling the noise source within the VE, we utilized CATT-Acoustic software (v.9.0a), which utilizes geometric acoustics to simulate sound propagation. Additionally, we modeled the noise environment by numerically solving the wave equation in the time domain. The acoustic level was calibrated using a binaural dummy head connected to the HTC Vive Pro Eye Head Mounted Display (HMD) and the 01dB Symphonie acquisition system (Fig. 2). We established a noise level that adhered to the maximum permitted by the NIOSH standard, assuming operators would be wearing hearing PPE. Consequently, the noise level in the experiment was equivalent to an approximately 85 dBA continuous sound level. The VR software-controlled trial (SWCT) was implemented using Unity, enabling the playback of various audio tracks.

2.5 Measures

For RQ1, we assessed reaction time by measuring the duration between the stimulus timestamp (visualizing the target word) and the user's button selection timestamp. In cases where a participant skipped a stimulus, we recorded a fixed value of 5000 ms, representing the time between consecutive stimuli. Additionally, we recorded errors by noting incorrect and missed button selections. To evaluate the perceived cognitive load, we administered the modified Noise-Induced Task Load index questionnaire (NOISE TLX). The NOISE TLX, developed by Lee et al., is an adaptation of the NASA TLX, with questions on physical demand, temporal demand, and frustration replaced by two questions assessing the perceived loudness and annoyance caused by noise [14].

Regarding RQ2, we recorded the participants' ECG signals during the SWCT. We used the OpenSignal software tool to evaluate the mean of the Instant HR, the square root of the mean squared differences of successive NN intervals RMSSD [15].

2.6 Experimental Procedure

The study was conducted in an isolated room. Participants were provided with an explanation of the study's objective, and after confirming their understanding and signing the consent form, demographic information was collected. ECG electrodes were then attached to the participant's chest for recording. Following this, each participant entered the VR test scene within the customized SWCT interface located inside the aforementioned silo (Fig. 1). Participants underwent a preliminary training session to familiarize themselves with the SWCT. The experiment involved completing the SWCT under three different noise conditions, administered in a counterbalanced order to mitigate any potential order effects. Test sessions were interspersed with five-minute rest periods, during which participants filled out the Noise-TLX questionnaire. Each SWCT session comprised 170 target words and lasted approximately 300 s.

3 Results

3.1 RQ1-Noise Effects on Users' Performance, Perceived Workload, and Noise Annoyance

As regards reaction times, we positively checked the normality and the equality of variance assumptions for the NN-, CN-, and the IN-conditions samples. There was no statistically significant difference between groups as determined by one-way ANOVA ($F(2,87) = 1.852$, $p = 0.163$).

As regards execution error, samples were not normally distributed. A Kruskal-Wallis H test showed no statistically significant difference in execution errors among noise conditions, $\chi 2(2) = 3.959$, $p = 0.138$, with mean rank execution errors of 53.17 for NN, 41.60 for CN, and 41.73 for IN.

For perceived workload and noise annoyance, we compared NOISE-TLX values of each subscale among the three conditions. A Kruskal-Wallis H test showed there was no statistically significant difference in the Mental demand, Performance, and Effort scales among the noise conditions, and there was a significant one in the Loudness and the Annoyance ones (Table 1).

Table 1. Kruskal-Wallis H tests for the NOISE TLX questionnaire samples. Scales evidencing a statistically significant difference among noise conditions are reported in bold

Subscale	NN-condition Mean Rank	CN-condition Mean Rank	IN-condition Mean Rank	χ2(2)	p-value
Mental demand	38.4	53.3	47.8	3.457	0.178
Performance	41.6	44.3	50.6	1.897	0.387
Effort	45.9	44.3	46.3	0.100	0.951
Loudness	**17.7**	**59.9**	**58.9**	**51.601**	**< 0.001**
Annoyance	**17.5**	**58.7**	**60.3**	**52.289**	**< 0.001**

Post hoc Mann-Whitney U test evidenced that perceived loudness and annoyance are statistically significantly higher in the CN and IN conditions than the NN one and that there is no statistically significant difference between the CN and IN conditions (Table 2).

Table 2. Mann-Whitney U test results. Scales evidencing a statistically significant difference among noise conditions are reported in bold.

Subscale	Compared noise Conditions	Mean Rank	U	p-value
Loudness	**NN-CN**	16.5–44.5	**30**	**< 0.001**
	NN-IN	16.7–44.3	**35**	**< 0.001**
	CN-IN	31.0–30.1	436.5	0.841
Annoyance	**NN-CN**	16.5–44.5	**30.5**	**< 0.001**
	NN-IN	16.5–44.5	**29.5**	**< 0.001**
	CN-IN	29.7–31.3	427	0.733

3.2 RQ2-Noise Effects on Physiological Signals

A Kruskal-Wallis H test showed no statistically significant difference for the mean instant HR and the RMSSD NN among the noise conditions (Table 3).

Table 3. Kruskal-Wallis H tests for HRV-derived indicators samples.

HRV indicators	NN-condition Mean Rank	CN-condition Mean Rank	IN-Condition Mean Rank	$\chi 2(2)$	p-value
Mean Instant HR (BPM)	52,95	42,67	40,88	3.734	0.155
RMSSD NN (ms)	44,60	43,25	48,65	0.695	0.706

4 Conclusions

Our results, along with previous ones, show that, independently of the frequency content and the temporal trend of the sound source, exposure to non-speech noise at a level lower than the exposure limits specified by safety regulations does not affect cognitive performance. The simulation, positively carried out through IVR technology, supports the use of hearing PPE to prevent physical harm and the deterioration of operator performance. In any case, although no effects of noise are evidenced, not even at the level of physiological parameters, operators perceive the disturbance, and thus the effects of exposure in the long term remain to be evaluated.

Acknowledgments. This work was part of the SPIRiT project founded by INAIL through the BRIC 2019 call for proposals (ID036).

References

1. Naghavi K.Z., Mortazavi, S.B., Asilian, M.H., Hajizadeh, E.: Exploring the contributory factors of confined space accidents using accident investigation reports and semistructured

interviews. Saf. Health Work **10**(3), 305–313 (2019). https://doi.org/10.1016/J.SHAW.2019.06.007
2. Schlittmeier, S.J., Marsh, J.E.: Review of research on the effects of noise on cognitive performance 2017–2021 LITERATURE SEARCH
3. Gawron, V.J.: Performance effects of noise intensity, psychological set, and task type and complexity. **24**(2), 225–243 (2016). https://doi.org/10.1177/001872088202400208
4. Banbury, S., Berry, D.C.: Disruption of office-related tasks by speech and office noise. Br. J. Psychol. **89**(3), 499–517 (1998). https://doi.org/10.1111/J.2044-8295.1998.TB02699.X
5. Smith, D.G., Baranski, J. V., Thompson, M.M., Abel, S.M.: Noise and Health. Noise Health, vol. 6, no. 21, p. 3 (2003). https://www.noiseandhealth.org/article.asp?issn=1463-1741;year=2003;volume=6;issue=21;spage=3;epage=16;aulast=Smith. Accessed 26 Feb 2023
6. Halin, N.: Distracted while reading? Changing to a hard-to-read font shields against the effects of environmental noise and speech on text memory. Front. Psychol. **7**, 1196 (2016). https://doi.org/10.3389/FPSYG.2016.01196/BIBTEX
7. Jafari, M.J., Khosrowabadi, R., Khodakarim, S., Mohammadian, F.: The effect of noise exposure on cognitive performance and brain activity patterns. Open Access. Maced. J. Med. Sci. **7**(17), 2924 (2019). https://doi.org/10.3889/OAMJMS.2019.742
8. Doggett, R., Sander, E.J., Birt, J., Ottley, M., Baumann, O.: Using virtual reality to evaluate the impact of room acoustics on cognitive performance and well-being. Front Virtual Real **2**, 20 (2021). https://doi.org/10.3389/FRVIR.2021.620503/BIBTEX
9. Manghisi, V.M., et al.: Investigating the effects on user performance and perceived workload of environmental noise in immersive virtual reality. In: 2022 IEEE International Workshop on Metrology for Extended Reality, Artificial Intelligence and Neural Engineering, MetroXRAINE 2022 - Proceedings, pp. 46–51 (2022). https://doi.org/10.1109/MetroXRAINE54828.2022.9967541
10. Muhammad, I., Vorländer, M., Schlittmeier, S.J., Vorl€ Ander, M.: Audio-video virtual reality environments in building acoustics: an exemplary study reproducing performance results and subjective ratings of a laboratory listening experiment. J. Acoust. Soc. Am. **146**(3), EL310 (2019). https://doi.org/10.1121/1.5126598
11. Liebl, A., Haller, J., Jödicke, B., Baumgartner, H., Schlittmeier, S., Hellbrück, J.: Combined effects of acoustic and visual distraction on cognitive performance and well-being. Appl. Ergon. **43**(2), 424–434 (2012). https://doi.org/10.1016/J.APERGO.2011.06.017
12. Schlittenlacher, J., Staab, K., Çelebi, Ö., Samel, A., Ellermeier, W.: Determinants of the irrelevant speech effect: changes in spectrum and envelope. J. Acoust. Soc. Am. **145**(6), 3625 (2019). https://doi.org/10.1121/1.5111749
13. Scarpina, F., Tagini, S.: The stroop color and word test. Front. Psychol. **8**, 557 (2017). https://doi.org/10.3389/FPSYG.2017.00557/BIBTEX
14. Lee, J., Francis, J.M., Wang, L.M.: How tonality and loudness of noise relate to annoyance and task performance. Noise Control Eng. J. **65**(2), 71–82 (2017). https://doi.org/10.3397/1/376427
15. Digiesi, S., Manghisi, V.M., Facchini, F., Klose, E.M., Foglia, M.M., Mummolo, C.: Heart rate variability based assessment of cognitive workload in smart operators. Manag. Prod. Eng. Rev. **11**, 56–64 (2020). https://doi.org/10.24425/mper.2020.134932

Semi-immersive Virtual Environment to Evaluate Working Conditions in Logistic Tasks Using NIOSH Method

Daniel Lanzoni(✉), Andrea Vitali, Daniele Regazzoni, and Caterina Rizzi

Department of Management, Information and Production Engineering, University of Bergamo, via Pasubio 7/b, 24044 Bergamo, Italy
daniel.lanzoni@unibg.it

Abstract. The logistics industry involves various processes in the warehouse work environment on a daily basis, such as handling, storage, and packing. Therefore, workers are often engaged in manual activities such as pushing, pulling and lifting loads. These types of movements are repetitive and, together with adverse physical factors of the environment, they affect employees' health condition. The aim of this study is to test a proactive evaluation approach exploiting the potential of a professional virtual wall to simulate specific tasks performed in a warehouse to find the better solution in terms of working condition and productivity. The proposed framework includes the following steps: at first, it is required to design the virtual environment by means of 3D modelling tools; afterwards, simulation tests are performed by objectively assessing the physical working condition of the operator; finally, the valuable information are provided to improve the design of the workstation, based on the operator's ergonomics. The framework is modular and can be scaled to complex industrial environments.

Keywords: Ergonomics · Logistics · Virtual Reality · Virtual Wall

1 Introduction

Industry 4.0, driven by cyber-physical systems, IoT, digital twin, and smart products, has revolutionized the industry. However, the focus on process efficiency has sometimes neglected the human impact [1]. With Industry 5.0, operator's well-being has become crucial [2]. In logistics, manual processes result in inefficiency, high costs, complex sorting, and worker fatigue [3]. These tasks can be physically demanding and there is compelling evidence linking the work environment to human health [4]. Certain factors have been identified as increasing the risk of musculoskeletal diseases for the operators or even directly causing occupational injuries [5]. According to Estember et al. [6], the greatest mistake toward musculoskeletal disorders (MSDs) is to ignore them and wait for people to get injured before intervening. The occurrence of the related risks previously described is so high that it prompted the European Union to issue a standard (Directive No. 90/269 [7]) aimed at conditioning, within acceptable levels, the use of

M. Carfagni et al. (Eds.): ADM 2023, LNME, pp. 319–327, 2024.
https://doi.org/10.1007/978-3-031-52075-4_36

manual force in load handling work operations (recently updated with Title VI of Legislative Decree 81/08) [8]. Employers must design workstations to enable safe and healthy manual handling of loads, considering individual risk factors, workplace characteristics, and activity demands [9]. Moreover, by adopting approaches that include human factors and ergonomics, positive outcomes can be achieved in terms of product/process quality and performance [10]. Ergonomic programs can be approached in two ways: proactively or reactively. The proactive approach is more economically favorable as it involves identifying and addressing potential ergonomic issues during the design and planning phases of the production system, when changes can be made at minimal costs [9, 11]. However, many companies only focus on ergonomic issues after injuries or illnesses have already occurred, i.e., following a reactive approach. A proactive approach implies the use of technologies such as Motion Capture (Mocap) and Virtual Reality (VR) to create immersive scenarios and investigate potential ergonomic issues during the design phase of the production systems [12]. Some studies [13, 14] reported the pros and cons of semi-immersive VR tools, such as the virtual walls, for simulating work environments, highlighting the ability to carry out complex and hazardous operations in a safe environment, as well as the simulation of manual tasks requiring the cooperation of multiple operators. Others exploited digital human modeling and simulation tools, such as Siemens Jack, IPS IMMA, and Santos, to optimize the workplace starting from an ergonomic analysis [15, 16]. However, these solutions cannot mimic a real work environment or the operator's capabilities and limitations because they are often based on empirical data collected from observations. Considering the mentioned limitations, this research work proposes a proactive approach providing real-time evaluation of ergonomic indexes by means of a Mocap system and a semi-immersive virtual wall to design logistics activities for a generic warehouse. Suggestions are reported to improve logistics and/or warehouse design so that the quality of the operator's work can be improved.

In the following sections, the ergonomic evaluation framework and the workflow of the proposed solution are described. Then, test and results are discussed as well as future developments.

2 Ergonomic Evaluation Framework

Assessing ergonomics of a workstation where manual handling of goods is performed requires an iterative approach. Design and check activities are run in a loop until the final outcome meets the desired requirements in terms of safety, comfort, productivity, or other evaluation parameters a company may want to define.

The design activity consists in creating:

- The environment where the tasks will take place including the operator, the workstation, the goods to be handled, eventual tools, and any other object that may be relevant for performing the tasks;
- The tasks to be performed: for manual handling the initial and final position of items to be moved are required, as well as the number of repetitions and the interaction modalities in terms of the kind of grip used (e.g., depending on to presence or absence of handles on the item).

Once cleared the design step, the way of checking the operator's tasks by performing a test campaign must be defined. To this aim, evaluation criteria can be selected among those regulated by international standards, having the best match with the designed scenario and tasks. Up to this step, the process is conceptually similar to conventional ergonomics analysis, making exceptions for the adoption of a virtual scenario and operator instead of the actual ones. What is changing the paradigm is the way in which the tasks are performed since a virtual approach permits a complete dematerialization of the process. This brings all the well-known benefits of a 3D simulation (i.e., ease of change of the configuration, sizes, weights), and the specific one characterizing this research work that relies in the capability of evaluating in real time the desired ergonomic indexes, providing feedbacks for the workstation design and task planning.

To virtualize the entire ergonomic evaluation several technical solutions are required. Some of them are well known within the research community and used by early industrial adopters, e.g., for the motion tracking of body movements. By the way, the whole framework includes innovative solutions, which have been developed, making it new respect to the state of the art in this field.

3 Proposed Solution

A set of specific technologies have been chosen to develop the software solution for properly design the environment. A workstation warehouse for storing ready-to-sell goods has been considered as case study and the ergonomic assessment has been based on the NIOSH index [22]. Figure 1 depicts the workflow of the proposed solution, where the output of the NIOSH index calculus determines the acceptance of the existing design or suggests improvements for a re-design. The virtual semi-immersive environment is the key step for achieving ergonomic evaluation.

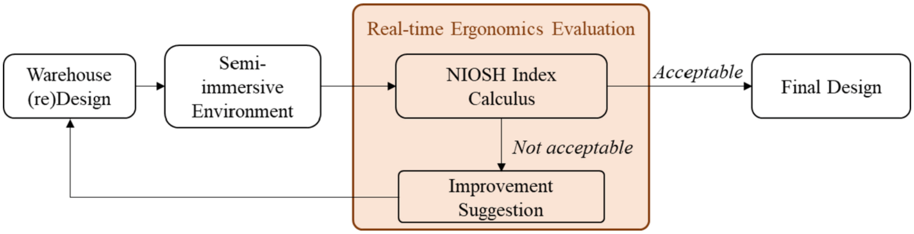

Fig. 1. Cycling workflow of the proposed solution.

3.1 Semi-immersive Environment

Each item in the virtual environment is modeled by using Solid Edge [17] or Blender [18]. Some of the 3D specific objects are also available in Unreal Engine (UE) marketplace [19] or on Turbosquid website [20]. Once all required items are defined, they are positioned in the 3D virtual environment designed using UE. In the specific case study the environment mimics a common workstation composed by a conveyor belt transporting goods, an operator supposed to handle them and a roll container for storage. Figure 2 depicts the initial configuration of the environment and shows the heights of the shelves and the distance respect to the conveyor belt.

To create the semi-immersive environment, a virtual wall has been chosen, which permits to obtain a visual depth sense and hands interaction.

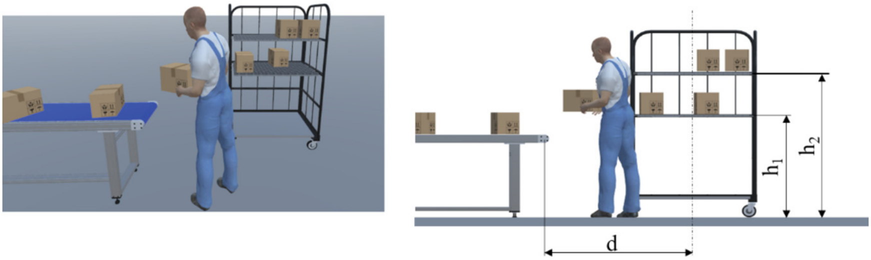

Configuration 1		
$h_1 = 105$	$h_2 = 150$	$d = 1000$

Fig. 2. Initial configuration with two shelves: on the left the perspective view with the position of products; on the right the orthographic view and shelves height [mm].

Interacting with the virtual wall does not affect the user's way of moving and permits computing ergonomics parameters, avoiding cybersickness. Two stereoscopic projectors and active glasses are used to create the 3D semi-immersive experience. Four Optitrack cameras track the active glasses to ensure the correct visualization of the scene on the wall according to the user's position and orientation. In addition, interaction with virtual objects can be obtained by placing markers on the back of each hand.

Finally, the Xsens Mocap system [21] is used to capture the operator's movements required to perform tasks evaluation (Fig. 3).

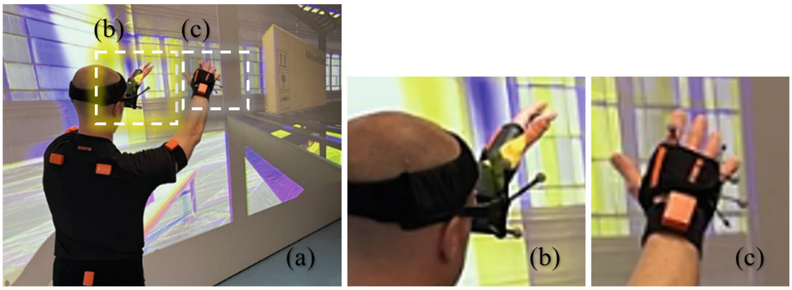

Fig. 3. Semi-immersive environment projected on the virtual wall (a), tracking markers for (b) head and (c) hands, and orange IMUs of the Xsens Mocap system.

3.2 Real-Time Ergonomics Evaluation

According to NIOSH, as described in the National Plan of Prevention 2014–2018 [8] and cited in the ISO TR 12295 [23], during the study of manual lifting activities it is possible to identify different types of lifting tasks: mono, variable and sequential task. To this aim, Waters et al. manual [22] proposes the NIOSH lifting equation and parameters to assess them: Frequency-Independent Recommended Weight Limit (FIRWL), Single-Task Recommended Weight Limit (STRWL), Frequency-Independent Lifting Index (FILI), Single-Task Lifting Index (STILI) and, the Composite Lifting Index (CLI). Furthermore, the quality of the hand-to-object coupling (e.g., handle, cut-out, or grip) is classified as good, fair or poor. The hand-to-object coupling classification is important because the nature of the gripping can affect the maximum force a worker can or must exert on the object and the vertical location of the hands during lifting. According to this classification, since the boxes used in the simulation do not have any handles or cut-outs, the coupling quality is classified as "fair".

After having defined the technical solutions to gather motion data and the way of elaborating them according to standard indexes, an ad hoc software module has been implemented. This automatically calculates in real time the NIOSH index and the parameters to assess the ergonomics of lifting tasks. The module requires the following input data: participant's gender and age to determine the maximum weight the user can lift, lifting frequency and duration, coupling quality, and weight of the object. Based on these, the module determines whether the ergonomics of the workstations is acceptable or must be improved. In the latter case, each parameter of the NIOSH index (e.g., horizontal/vertical displacement, task frequency, origin and destination of the lift) are analyzed and compared with predetermined thresholds. This allows providing suggestions to enhance the workstation design and improve the operator's working conditions. Each suggestion is related to one or more sub-tasks performed, e.g., proposing to change a specific feature of the workstation (e.g., a shelf height).

4 Test and Results Discussion

In this paragraph the tests performed are presented and the results obtained are discussed. The test concerns in picking and placing 3 boxes of the same size 30 cm x 40 cm x 30 cm and weighting 5 kg, thus 3 sub-tasks are defined. The operator is not provided with haptic feedback; therefore, it is important to know a priori the weight of the boxes. Each box is moved toward the operator on the conveyor belt, the operator reads the label on the box, lifts it and places it on the appropriate shelf of the roll container. The first configuration of the roll container has two shelves, as shown in Fig. 2.

Supposing that the operator may place 12 boxes per minute for 1 h, the resulting evaluation of the NIOSH and the sub-indexes are reported in Table 1.

According to these results, the initial configuration is not acceptable (the final value of the CLI is not valuable). Actually, the 'sub-task 1' has the FIRWL = 0. This is due to the fact that a second box must be positioned behind the first one the lowest shelf. Therefore, a third shelf in the lower part of the roll container is suggested to be added, for instance, as shown in the configuration depicted in Fig. 4.

Table 1. NIOSH results in the first configuration.

		FIRWL	STRWL	FILI	STILI	CLI
Conf. #1	Sub-task 1	0	0	---	---	**---**
	Sub-task 2	7,37	6,19	0,68	0,81	
	Sub-task 3	5,82	4,89	0,86	1,02	

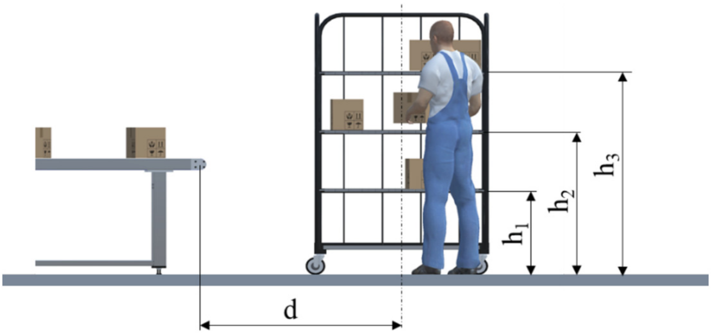

Fig. 4. Second configuration of the roll container with three shelves.

New tests are performed using the same approach and varying shelves heights until an acceptable result, after three trials, is reached. Table 2 reports the heights of the 3 shelves relative to each of the three trial tests. Table 3 lists the calculated indexes for each of them.

Table 2. Shelves height [mm] for the second configuration.

TEST 1			
$h_1 = 70$	$h_2 = 115$	$h_3 = 160$	$d = 1000$
TEST 2			
$h_1 = 60$	$h_2 = 100$	$h_3 = 140$	$d = 1000$
TEST 3			
$h_1 = 70$	$h_2 = 105$	$h_3 = 140$	$d = 2000$

In the first test the CLI value results 1.64, that is in the '*moderate*' range (compared with the NIOSH value table [22]). Focusing on each sub-index, the most critical value is related to the highest shelf. Therefore, a re-design of the roll container has been carried out, altering its position. In test 2 the CLI value did not decrease as expected. Therefore, keeping the height of the highest shelf unchanged, the lower shelves are moved back to a height similar to test 1. Furthermore, the report shows that during the placement of the boxes, the operator must significantly rotate the torso. Although the other several

Table 3. NIOSH results in the second configuration.

		FIRWL	STRWL	FILI	STILI	CLI
Test 1	Sub-task 1	7,97	6,70	0,63	0,75	**1,64**
	Sub-task 2	6,92	5,81	0,72	0,86	
	Sub-task 3	6,28	5,27	0,79	0,95	
Test 2	Sub-task 1	9,10	7,65	0,55	0,65	**1,72**
	Sub-task 2	6,69	5,62	0,75	0,89	
	Sub-task 3	5,59	4,70	0,89	1,06	
Test 3	Sub-task 1	11,61	9,75	0,43	0,51	**1,10**
	Sub-task 2	10,11	8,49	0,49	0,59	
	Sub-task 3	9,45	7,94	0,53	0,63	

alternative redesign suggestions, reducing the asymmetric angle should be given a high priority because a significant number of overexertion lifting injuries are associated with excessive lumbar rotation and flexion [22]. From the report, a solution can be to move the origin and destination further apart to force the worker to turn their feet and step, rather than twist the body. The analysis of test 3 resulted in a CLI just above the '*borderline'* range. Despite this, the FILI values are less than 1.0, which means that strength is not expected to be an issue for any of these tasks. Additionally, all of the STLI values are less than 1.0, which suggests that performing any of these tasks individually should not be physically demanding. However, when the combined physical demands of the tasks are considered, the final CLI values exceeds 1.0. This is likely due to the high frequency rate for the combined job. Therefore, a reduction in frequency could decrease the CLI to about 1.0.

The results reached so far confirm that the solution provides valuable information for improving manual handling tasks and workstation ergonomics. However, if the workstation becomes more complex, it could show a lower efficiency. While the redesign can be successfully performed based on the suggestions proposed, it is worthwhile to note that this applies when the variables to be controlled are limited. When variables such as the number of tasks, products, or shelves increase, a more advanced and precise software module is required.

5 Conclusion

This research work exploits VR and Mocap devices to simulate tasks in a virtual warehouse workstation and calculate in real time the NIOSH index to ergonomically evaluate the workstation design until a correct solution is achieved.

The simulation of a generic industrial task allows the analysis of the workplace's design before its implementation or the evaluation of an existing one in a controlled environment, such as a simulation room, where high performing Mocap system (e.g., marker-based systems) can be used. The application to a simple case study shows the high potential of the solution proposed. Actually, it provides the designers with immediate evaluation of a specific configuration and with straightforward suggestions to solve ergonomic issues by varying design parameters.

Future developments will include the possibility of using mixed reality to emulate the loads to be lifted during the simulation. Finally, it will be feasible to test the developed method in a real use case.

Acknowledgement. This research work has been funded by Regione Lombardia (Italy), regional law n° 9/2020, resolution n° 3776/2020. Also, we would like to thank the Joiint Lab (Intellimech) for the case study proposed.

References

1. Saeid, N.: Industry 5.0—a human-centric solution. Sustainability **11**(16), 4371 (2019)
2. Müller, J.: Enabling Technologies for Industry 5.0. Results of a workshop with Europe's technology leaders (2020)
3. Li, Y.: Investigation into ergonomics in logistics sorting equipment. In: 2019 IEEE International Conference on Computation, Communication and Engineering (ICCCE), pp. 167–169. IEEE (2019)
4. Rolander, B., et al.: Measurements and observations of movements at work for warehouse forklift truck operators. Int. J. Occup. Saf. Ergonomics **28**(3), 1840–1848 (2022)
5. Bhatia, V., Kalra, P., Randhawa, J.S.: Ergonomic interventions for manual material handling tasks in a warehouse. In: Ergonomics for Improved Productivity: Proceedings of HWWE 2017, pp. 205–212. Springer Singapore (2021). https://doi.org/10.1007/978-981-15-9054-2_23
6. Estember, R.D., Que, B.: The prevalence of musculoskeletal disorders among workers in outlets and warehouses of courier service industry. In: Proceedings of the 2020 2nd International Conference on Management Science and Industrial Engineering, pp. 296–303 (2020)
7. Directive 90/269/EEC - manual handling of loads. https://osha.europa.eu/en/legislation/directives/6. Accessed 19 Mar 2021
8. Piano Nazionale della Prevenzione 2014–2018: linee di indirizzo per l'applicazione del titolo VI del D. Lgs. 81/08 e per la valutazione e gestione del rischio connesso alla Movimentazione Manuale di Carichi (MMC)
9. Zhao, Y.S., et al.: Ergonomics risk assessment for manual material handling of warehouse activities involving high shelf and low shelf binning processes: application of marker-based motion capture. Sustainability **14**(10), 5767 (2022)
10. Loske, D., et al.: Logistics Work, ergonomics and social sustainability: empirical musculoskeletal system strain assessment in retail intralogistics. Logistics **5**(4), 89 (2021)
11. Radin, U., Radin, Z., et al. Development of framework integrating ergonomics in Lean's Muda, Muri, and Mura concepts. Prod. Plann. Control 1–9 (2023). https://doi.org/10.1080/09537287.2023.2189640
12. Silva, D., Gonçalves, A., Gomes, M., Vinicius, M., Ingrid, W.: Virtual reality and digital human modeling for ergonomic assessment in industrial product development: a patent and literature review. Appl. Sci. **12**(3), 1084 (2022)
13. Hasanzadeh, S., Garza, D.L., Jesus, M.: Productivity-safety model: debunking the myth of the productivity-safety divide through a mixed-reality residential roofing task. J. Constr. Eng. Manag. **146**(11), 04020124 (2020)

14. Nguyen, H., et al.: VR-based operating modes and metaphors for collaborative ergonomic design of industrial workstations. J. Multimodal User Interfaces **11**, 97–111 (2017)
15. Kumar, R., et al.: Ergonomic evaluation of workstation design using Taguchi experimental approach: a case of an automotive industry. Int. J. Interact. Des. Manufact. (IJIDeM) **15**, 481–498 (2021)
16. Hanson, L., et al.: Implementation of ergonomics evaluation methods in a multi-objective optimization framework. In: DHM2020: Proceedings of the 6th International Digital Human Modeling Symposium, August 31-September 2, 2020, p. 361. IOS Press (2020)
17. Solid Edge. https://solidedge.siemens.com/. Accessed March 2023
18. Blender. https://www.blender.org/. Accessed March 2023
19. Unreal Engine. https://www.unrealengine.com/. Accessed March 2023
20. Turbosquid. https://www.turbosquid.com/. Accessed March 2023
21. Xsens. https://www.movella.com/. Accessed March 2023
22. Waters, T.R., Putz-Anderson, V., Garg, A.: Applications manual for the revised NIOSH lifting equation (1994)
23. ISO TR 12295. https://www.iso.org/standard/51309.html

Design for Sustainability and EcoDesign

Prospective Life Cycle Assessment Based on Patent Analysis to Support Eco-design

Christian Spreafico(✉), Daniele Landi, and Davide Russo

University of Bergamo, Via Marconi 5, 24044 Dalmine, Bg, Italy
christian.spreafico@unibg.it

Abstract. Eco-design has increasingly become a necessity to safeguard the ecosystem. However, eco-assessment methodologies, e.g. the Life Cycle Assessment (LCA), fail to rigorously and reliably support the evaluation of future products, as well as emerging technologies, ideas and concepts in eco-design. This study lays some theoretical foundations for the development of a step-divided systematic method to support Prospective LCA based on a structured patent analysis. In order to answer the prescribed requirements, for each of them, some specific strategies of patents analysis have been collected and systematically organized. The aim of the proposed method is to compare technologies with a different level of maturity, contrary to the traditional LCA which overestimates the existing ones only because are more optimized. The proposed method was applied to a real case study about the production of titanium powder to perform the prospective LCA of the patented future developments of the components of this process. The results showed that, patent analysis, systematized through the proposed method, can be used to forecast the environmental impact of a future product. The scale-up of the performances can be esteemed, by ensuring at the same time the comparability and the reliability and the results, as prescribed by reference standards.

Keywords: Prospective LCA · patent analysis · product forecasting · eco-design

1 Introduction

In a rapidly changing manufacturing world, also driven by the new industry 5.0 paradigm, the introduction of new products is essential to keep a company competitive. Given the environmental problems of today's world, this task cannot ignore the aspects related to the eco-sustainability.

For this reason, eco-design has to be compared with reliable eco-assessment of the ideas and the concept. However, current approaches and methodologies, such as the Life Cycle Assessment (LCA), regulated by ISO 14040 and ISO 14044, not allow to evaluate new products. This is because the obtainable environmental impacts arise from manufacturing, use and end-of-life experience rather than on experimental data or design estimates. Furthermore, the same methodologies set stringent limitations to obtain quantitative assessment. They are related to consistency and reliability of the data and scale-up problems passing from lab-scale concept to industrial-scale production.

M. Carfagni et al. (Eds.): ADM 2023, LNME, pp. 331–338, 2024.
https://doi.org/10.1007/978-3-031-52075-4_37

To overcome the current problems relating to the eco-assessment of new products during the development stage, prospective LCA [1] was proposed. In extreme synthesis, this approach uses scientific and patent literature and simulations to build foreground inventory. However, a pragmatic approach to support industrial practice in this task is still missing, because all those proposals (see Sect. 2) mainly support the prediction of the background. While when they try to estimate the impacts of a future product or an idea, in a rigorous way, through the canons of the LCA. Furthermore, they do so only with a few sources and do not use a systematic search and selection procedure for supporting literature, such as patent literature.

In summary, the suggestion emerging from the prospective literature about LCA is to use patent analysis to support the prospective LCA. However, the contributes in the literature have done so only considering a few patents at a time and a structured methodology is still missing which integrates LCA and patent analysis [1, 2]. In synthesis, it has not yet been established how to search for patents and how to extract data from them to be included in the life cycle inventory, while respecting the consistency and reliability requirements of the LCA which are prescribed by the ISO 14040/44 standard.

This study lays some theoretical foundations for the development of a step-divided method to support prospective LCA based on a structured patent analysis. In order to answer the prescribed requirements, for each of them, some specific strategies of patents analysis have been collected and systematically organized. The proposed method can be used to evaluate the environmental impacts a priori of an idea emerging from eco-design as well as a prototype for which there is no primary data to measure.

In order to show and discuss the application of the proposed methodology a real case study about the prospective LCA of the future development of a system for producing titanium powder has been presented.

2 Literature Background

LCA consists of four main steps that, according to ISO 14040/44, are: (i) define the goal and scope of the study, or the identification of the technical system to be measured, the operative scenario, the motivation for performing the assessment and all the requirement for performing it; (ii) collect all the sources of impacts, i.e. system parts and lifecycle phases, trough the life cycle inventory (LCI), (iii) assess the impacts according to environmental indicators and (iv) interpret the results.

A LCA is prospective when an immature product (e.g. an emerging technology), or even a design idea, studied is in an early phase of development (e.g. small-scale production), but the technology is modelled at a future more-developed phase (e.g. large-scale production). Prospective LCA is useful for predicting whether an immature product will be sustainable if and when it will become a mature product. For this reason, it can be used in decision making during eco-design [3].

However, the ISO14040/44 standards are very strict on the use of sources in order to guarantee the reliability of LCA. Therefore, the few prospective LCA studies present in the scientific literature, to reconstruct future scenarios, have always referred to only a few selected sources [4].

But this constraint, although it gives reliability to the analysis, significantly limits the diffusion of the prospective LCA, and more generally, the environmental analyses of immature products, for two reasons. On the one hand, the lack of reliable sources that make forecasts on the development of certain elements (e.g. a component of the product, electricity mix) does not allow to model the latter in the future [5]. In addition, few forecast data on an element, even if extrapolated from selected sources, does not guarantee the truthfulness of the forecasts, for which it would instead be necessary to analyze as much data as possible [1]. In this way, different kind of uncertainties about future fields of applications, industrial scale, technological development.

To overcome these limitations relating to the prospective LCA, and at the same time satisfy the requirements of the reference regulations, to date the scientific community has reached the convergence on two general proposals that must be undertaken [2]: enlarging the database to carry out prospective LCA and defining unified foreground inventories, since the current ones are always customized. In this context, the patent analysis is suggested as a method to fulfill these objectives, specifying to analyze as much data as possible but without providing indications on how it should be structured to adequately support the prospective LCA.

3 Methodology

The proposed method consists of three patent analysis steps, each of which responds to one of the prospective LCA/traditional LCA requirements (see Table 1) and the following sections describe these aspects.

Table 1. STEPs of the proposed method.

Prospective LCA requirements	STEPs of the proposed method of patent analysis-based Prospective LCA
REQUIREMENT 1 - Comparability	STEP 1 - Product breakdown and patent search based on components
REQUIREMENT 2 - Data quality	STEP 2 - Patent selection and data extraction filtration
REQUIREMENT 3 - Scale-up	STEP 3 – Dynamic patent analysis

3.1 REQUIREMENT 1 - Comparability

If a concept and an existing product, where the first one is an improvement of the second, must be compared trough LCA, the same boundary conditions must be preserved. However, a concept can differ greatly from the reference product, both structurally and functionally. Therefore, it is very common that in the prospective LCA of a concept, three aspects may vary [4, 6]: aim of the study, functional unit, system boundaries. Therefore, if the variations in the environmental impacts of the evolution of a current product must be evaluated, it is not possible to extract data from patents that describe these evolutions at a too aggregated level.

This study therefore proposes to decompose the initial product (or in general a problem) into sub-components and research for future evolutions of these sub-components in the patents. The detail level that must be sought in the decomposition is established by the comparability of aim of the study, functionality and system boundaries between the sub-components of the initial product and those of future evolutions. More specifically, this means that the different components must process the same input and/or output flows of raw material, energy and information.

3.2 STEP 1 - Product Breakdown and Patent Search Based on Components

To support the product decomposition, the Energy Material Signal (EMS) model [7] was adopted in this study. In this model, a component is intrinsically associated with its function which is reported in a black-box. Its inputs and outputs are flows of mass, energy and information (signals). While the function is the transformation of these flows. In functional decomposition, the product is decomposed into components, through the decomposition of its overall function. In this case each component performs a given sub-function by processing certain sub-flows of energy, material and information, which are in turn portions of the initial flows (see Fig. 1).

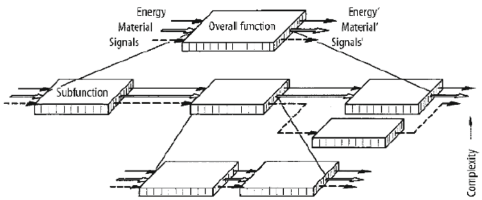

Fig. 1. Product breakdown through energy, material, signal (EMS) model functional decomposition [7].

In practice, this means using the EMS model to decompose the current product into components performing certain sub-functions. Then the patented evolutions of these components that perform the same sub-functions are found. These latter could be implemented in the current product in the next few years. The EMS model was chosen for two reasons. First of all, dividing the current product at the right level of detail allows for the identification of components to be compared with the patented evolutions of the same which process the same material flows. In this way, the aim of the study, the functional unit and the system boundaries of the LCA of the current product are not modified. In addition, the comparison of the environmental impacts of the current components and of the evolutions of the components can be carried out in accordance with ISO standards. Furthermore, the subdivision of the product, being carried out at the same time according to the functional logic, allows to determine the sub-functions which are used as patent search queries. In this way, the latter can be carried out according to the logic of function-oriented search, with all the advantages that it entails compared to traditional research, especially in technological forecasting, e.g. [8].

3.3 REQUIREMENT 2 – Data Quality

In extreme synthesis, the problems related to the data to carry out the prospective LCA and reconstruct the foreground concern their availability and quality. The data used in the LCI can be primary, i.e. collected directly by studying and analysing the technology under consideration, and secondary, i.e. collected from databases or other sources and typically include average data relating to certain categories of materials and consumption. The collection of primary data ensure reliability to LCA, however data are not always available to collect. Consequently, it is necessary to exploit secondary data as an alternative, which unlike the previous ones, tend to increase the uncertainty about the obtainable results. Starting from laboratory-level processes, many times the primary information is not always representative even at an industrial level and this may make it necessary to approximate them which leads to possible errors at the level of subsequent evaluations. The influence and uncertainty just expressed is linked to the construction of the LCI which, based on the data collected and being a fundamental element of the entire study, can impose a brake on the LCA given that it is a quantitative method and is based on the information used and collected in the inventory.

3.4 STEP 2 – Patent Selection and Data Extraction Filtration

To guarantee the quality of the data, various precautions can be taken in the patent selection and in the data extraction from the patents.

Time consistency can be ensured, by selecting only the most recent patents. In this way, considering the development time of the product, the data present in the most recent patents could be the most likely to be implemented in future evolutions of the product itself. Another useful filter in this sense is the legal status that divides alive patents from dead (lapsed) ones, where the latter are generally older or their development has been abandoned by companies.

The data reliability can be ensured on two levels. It is possible to select only the patents that have passed the exam, i.e. the granted ones, excluding patent applications, which may have been rejected because they contain untruthful data or inventions that cannot be industrialized. On the other hand, it is possible to select the data themselves, considering only those supported by documented experimental evidence.

3.5 REQUIREMENT 3 - Scale-Up

The scale-up of an innovative process refers to the passage from the LCI typically carried out at the laboratory or pilot plant level to industrial scale. This scalability, starting from the pilot plants, is less difficult because more data and information have already been collected. While in the laboratory process there are many differences respect to their subsequent evolutions, such as the level of complexity and the differences in the components, undermining the very credibility of the lab-scale LCA in decision making [6]. Then there is the uncertainty in the collection itself of the data collected in the laboratory: small errors in this phase can then have major repercussions for the scale-up.

3.6 STEP 3 – Dynamic Patent Analysis

[1] prescribes to consider as much patents as possible to support the prospective LCA in order to obtain significant relative average values on performances future product developments. However, this is useful to increase the reliability of the analysis, but not to provide information to support the scale-up analysis. In fact, the average levels out the data, without providing information on their changes over time, which is useful, for example, for predicting the future performance of a given product. In turn, this trend over time may be due to a given development direction which has been taken by the companies which claim such results in the patents, as the technological knowledge on the given product increases moving towards its industrialisation. The basic requirement of this type of analysis is the collection of homogeneous patents regarding the type of product described.

Starting from these considerations, the performance estimate of the future developments of a given product can result, for example, from the moving average of a given time trend. Or, the use of certain indices that measure innovation can allow the selection of only certain patents, which claim solutions with greater chances of being implemented, which are used for the calculation of the average value, e.g. [9]. In this way, to express the evolution of a technology towards environmental sustainability, the reductions of environmental impacts guaranteed by future developments can be related to time, e.g. priority date of the patents. The resulting curve is useful for to explore trends in addition to consider average values.

4 Case Study

This case study concerns the prospective LCA of the future developments of a system for the production of titanium powder, based on the Electrode Induction Gas Atomization (EIGA) reactor use. In general, the system transforms titanium ore, i.e. ilmenite, in pure titanium sponge, in the Kroll metallurgical process, then there is the remelting of the latter and the rolling which transform it into an electrode, which is melted in the EIGA, through induction assisted by a flow of argon. In the same reactor, the drops of molten titanium fall by gravity and solidify, creating the titanium powder.

The environmental impacts of the current product have been assessed through the LCA. The primary data was collected from a manufacturing company.

Then the proposed method has been applied to obtain the prospective LCA of the future developments of this product.

First, with the product breakdown (STEP 1), the components that perform different sub-functions were obtained. For example, the Kroll process increases the purity of the material, the vacuum arc remelting changes its shape, the smelting chamber inside the EIGA melts the electrode obtaining the drops of molten titanium. Then, the patent search queries were formulated including such functions as keywords, e.g. that referred to Orbit DB syntax: “((TI OR TITANIUM) 2D (KROL + OR SMELT +))/TI/AB/CLMS”. After launching these queries in the patent DB and analysing the obtained results, the patents relating to the various components were collected.

Then the patents were filtered on the basis of legal status (STEP 2), selecting only those granted and alive, and having the first priority year in the last 10 years. These criteria were introduced to ensure reliability to the analysis and time consistency.

All data extracted, relating to their performances (i.e. energy consumption) and their technical characteristics (e.g. construction materials) are justified by tests, the results of which are explicitly reported in the same patents.

The collected patents show different evolutions of the current product. There are interventions, for example, on the geometry of the crucible within the EIGA reactor. The advantage of these interventions derives mainly from energy efficiency, due to an improved transit dynamics of the molten titanium through the EIGA reactor. In this way, heat can be delivered to the titanium before atomization into droplets in a more homogeneous and optimized manner.

Finally, the environmental impacts of the patented components were calculated using LCA methodology and the results were mapped according to the first priority year of the patent from which they were extracted (STEP 3). In this regard, Fig. 2 shows the global warming potential (GWP) reduction that the patented evolutions of the EIGA reactor allow to obtain. For each patent, the minimum and maximum GWP reductions have been reported since these patents, as usual in patent practice, report performance ranges, not precise values. As can be seen from Fig. 2, a trend about GWP can be identified in addition to the arithmetic mean.

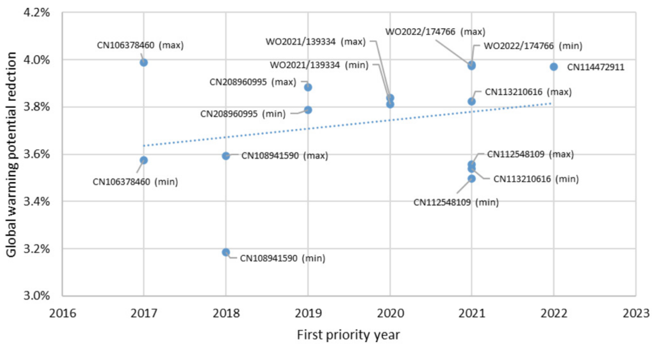

Fig. 2. Prospective GWP reduction using data from patent literature.

5 Conclusions

This work presented a novel method to support prospective LCA, consisting of a step-divided procedure of patent analysis to build the foreground inventory. Net of the limitations, i.e. the uncertain nature of the data in the patents and the essentially manual supervision, the main advantages of this work are:

- Fill a methodological gap on how to integrate patent search and LCA systematically and considering large amounts of data.

- Ensuring LCA requirements prescribed by ISO standards, i.e. comparability, allocation and data-quality.
- Suggesting an approach to hypothesize the scale-up of the data.

The main limitations of the proposed method mainly concern the times and costs of patent analysis, which increase in number as the number of components of the analyzed product and its complexity increase. Moreover, the execution of the functional decomposition and the experience of the person carrying it out are fundamental requisites for the correct application of the method.

Planned future developments of this work, partially addressed in [10], are: the automation of the method aimed both at reducing execution times and at correlating the forecasts with other factors relating the integration between the different evolutions of many components in complex products and with the evolution of the scenario operational, e.g. electricity mix.

References

1. Arvidsson, R., et al.: Environmental assessment of emerging technologies: recommendations for prospective LCA. J. Ind. Ecol. **22**(6), 1286–1294 (2018)
2. Adrianto, L.R., et al.: How can LCA include prospective elements to assess emerging technologies and system transitions? The 76th LCA discussion forum on life cycle assessment, 19 November 2020. Int. J. Life Cycle Assess. **26**(8), 1541–1544 (2021)
3. Barjoveanu, G., Teodosiu, C., Bucatariu, F., Mihai, M.: Prospective life cycle assessment for sustainable synthesis design of organic/inorganic composites for water treatment. J. Clean. Prod. **272**, 122672 (2020)
4. Thonemann, N., Schulte, A., Maga, D.: How to conduct prospective life cycle assessment for emerging technologies? A systematic review and methodological guidance. Sustainability **12**(3), 1192 (2020)
5. Vance, C., Sweeney, J., Murphy, F.: Space, time, and sustainability: the status and future of life cycle assessment frameworks for novel biorefinery systems. Renew. Sustain. Energy Rev. **159**, 112259 (2022)
6. Hetherington, A.C., Borrion, A.L., Griffiths, O.G., McManus, M.C.: Use of LCA as a development tool within early research: challenges and issues across different sectors. Int. J. Life Cycle Assess. **19**(1), 130–143 (2014)
7. Pahl, G., Beitz, W.: Engineering design: a systematic approach. Nasa Sti/Recon Tech. Rep. A **89**, 47350 (1988)
8. Spreafico, C., Spreafico, M.: Using text mining to retrieve information about circular economy. Comput. Ind. **132**, 103525 (2021)
9. Spreafico, C., Russo, D.: Investigating the evolution of the technologies for collecting microplastics. J. Environ. Manage. **326**, 116710 (2023)
10. Spreafico, C., Landi, D., Russo, D.: A new method of patent analysis to support prospective life cycle assessment of eco-design solutions. Sustain. Prod. Consumption **38**, 241–251 (2023)

Hydrofoil Technology: Current Applications and Future Developments for Sustainable Boating

Domenico Speranza[1], Stefano Papa[2], Claudio Pensa[3], and Romolo Di Bernardo[1](✉)

[1] University of Cassino and Southern Lazio, 03043 Cassino, Italy
romolo.dibernardo@unicas.it
[2] Università degli Studi Niccolò Cusano, 00166 Rome, Italy
[3] University of Naples Federico II, 80125 Naples, Italy

Abstract. Submerged lifting surfaces technology, born in the early 1900s, allows boats to lift the hull above the water and, in some cases, halves the resistance compared to dislocated and planning boats.

This paper illustrates the state-of-the-art on hydrofoil technology, highlighting the fundamental aspects of the study of submerged wings and focusing on the problems that this technology presents, evaluating the solutions currently used to optimize its work.

Key aspects of hydrofoil design are addressed, such as the choice of geometric configurations and two-dimensional profiles suitable for each type of mission. This results in addressing issues associated with cavitation and ventilation and emphasizing structural solutions that reduce these phenomena, thus improving hydrofoil efficiency.

The study analyses and discusses the problems of wing systems used in existing applications, with the aim of developing a sustainable transport technology compatible with ecological propulsions such as hydrogen and electric.

Keywords: hydrofoil · sustainable · hydrodynamics · green

1 Introduction

Hydrofoil technology was born in the early 1900s thanks to Eng. Enrico Forlanini, who installed load-bearing surfaces under the hull of the hydroplanes, very similar to aircraft wings, which allowed him to completely lift the hull out of the water. Research into hydrofoils, particularly in the mid-20th century, was primarily carried out in the military and only after some years, during the 60s, this technology was also used in the commercial ship [1], thus the first hydrofoils ferries with tandem geometry were built [2].

The lifting surfaces installed under the hull, have a key feature of reducing drag during navigation due to the small *Wetted Surface Area* (WSA) of the boat [3], according to estimates, hydrofoils can decrease resistances by fifty percent in comparison to a similar

M. Carfagni et al. (Eds.): ADM 2023, LNME, pp. 339–346, 2024.
https://doi.org/10.1007/978-3-031-52075-4_38

and comparable fast ship [4], leading to increased speeds, decreased power requirements, and a reduction in fuel consumption for motorboats. Although some applications of hydrofoil had already been used in racing sailing, the great diffusion of this technology began in 2013 thanks to America's Cup which for was regattated on foiling boats the first time in history. The great interest that has arisen, together with the technological development, has allowed the birth of new classes and new types of competitions; this is evident in the development of dinghies such as the *Moth* class [5] or in the case of daily cruiser motorboats. Furthermore, the use of software of numerical analysis (CFD, FEM, FSI) [6] and *Velocity Prediction Program* (VPP), which allows to simulate the behaviour of hydrofoils and the dynamics of the hydrofoil-hull system [7], have made it possible to speed up the design phases.

If the energy advantages caused using hydrofoil are evident, the design of this boat is challenging and together with the danger caused by the high speeds reached, means that these boats are used only in limited applications. Through the study of the state of the art, it was possible to investigate to evaluate what the main research areas are, identifying key aspects and design problems with the aim of directing research towards the use of this technology for a more sustainable boating which exploit the benefits of hydrofoils, reducing emissions without reaching the extreme performance of racing boats.

2 Introduction to Hydrofoil Sailing

Hydrofoils can mainly be divided into two categories in relation to the type of wing system (Fig. 1): The first, known as *piercing*, is characterized by a wing system designed with a *deadrise angle* $\delta > 0$ with respect to the horizontal, during navigation the tips of the wings come out from the water interacting with the free surface. The second category, called *fully submerged* hydrofoils, usually have $\delta = 0$ e and remain totally submerged during navigation [8].

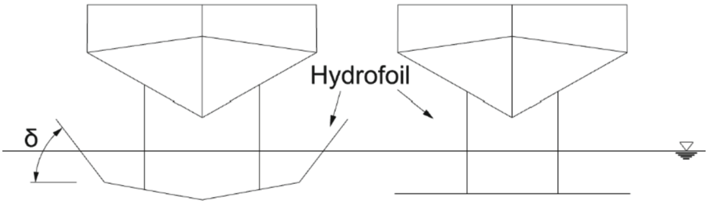

Fig. 1. Piercing hydrofoil vs fully submerged hydrofoil.

In an initial phase of motion these boats sail in a displacement mode (*hullborne sailing*), accelerating, the hydrodynamic forces of lift generated by the appendages enabled the hull to rise from the water's surface (*foilborne sailing*), eliminating shape and viscous drags and effectively reducing the impact of the waves [4] and making navigation more comfortable.

2.1 Types of Hydrofoil Boats

Hydrofoil technology can be used in various boat configurations, for example in the case of monohulls as for hydrofoil ferries [9], latest generation vessels or sailing classes such as the *AC75*. The most energy-consuming sailing phase for these types of boats is the take-off [10] as the wave resistance and viscous drags of the hull, partially submerged, add up to those generated by the hydrofoils. In some cases, the foils are also used to stabilize or partially lift the boat, reducing the WSA and improving fuel consumption. Also for multihulls, the use of submerged appendages, together with a different volume distribution compared to monohulls, allow, in sailing and motor boating, a reduction in drag is proven in several studies as in the case of and Suastika et Al. [11] on motor hydrofoil-assisted multihull.

2.2 Lift and Drag

The Lift of a hydrofoil is obtained as in the case of a classic wing [12]:

$$L = \frac{1}{2} C_L \cdot \rho \cdot v_\infty^2 \cdot A \tag{1}$$

Where, C_L is the Lift Coefficient, ρ is the density of the fluid $\left[\frac{\mathrm{kg}}{\mathrm{m}^3}\right]$, v_∞ is the relative speed of fluid-wing $\left[\frac{\mathrm{m}}{\mathrm{s}}\right]$ A is the wing surface in plan $\left[\mathrm{m}^2\right]$.

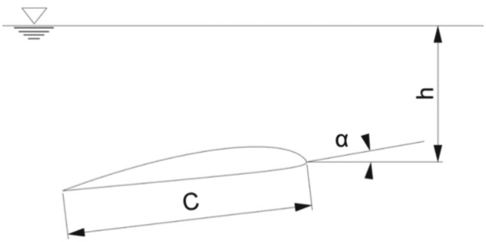

Fig. 2. Characteristic parameters of a submerged airfoil.

Furthermore, since we are in a multi-fluid environment and considering C as the chord, as verified by Parnold et Al. [13], C_L is almost constant if the submergence h is $h > 2C$. If the profile approaches the free surface and the wing is at $h = 0,911 \cdot C$, C_L, so the lift, increase by a few percentage points and if $h < C$ the C_L decreases drastically. Drag calculation turns out to be more complex as it is caused by various phenomena: in addition to the resistances generated by the profiles, it is necessary to consider induced resistances, sprays, viscosities, and interferences caused by the geometry of the wings and uprights [8].

3 Design Problems Identification

As previously stated, the purpose of this article is to identify the most active and most interesting areas to direct future research activities and for this reason, a deep bibliographic analysis was carried out. For our research, we utilized the Scopus database to identify articles related to hydrofoils published in journals during the past decade following the 2013 edition of the 34th America's Cup, which marked the advent of hydrofoil technology in the maritime domain. From 2013 to 2023, the publication of papers in this area increased by approximately 300%. By investigating the keywords, we were able to pinpoint the major research areas of interest in the sector as illustrated in Fig. 3. In this paper, for reasons of maximum length, only the most soundness are cited. Once the major areas of importance were identified, it was then possible also to delve deeper into the topics, including articles predating 2013, to expand the knowledge.

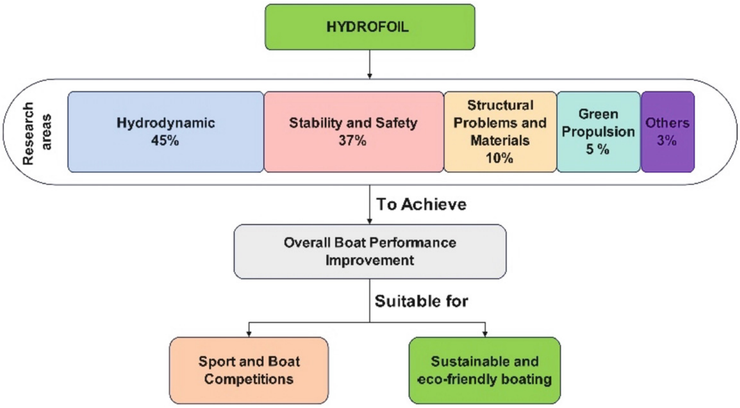

Fig. 3. Hydrofoil design, main design problems.

3.1 Hydrodynamic

From the results it can be stated that the most extensively addressed topic in the field of hydrofoils concerns the hydrodinamics of submerged wings. Although the characteristics of the profiles have been widely studied in aeronautics, the choice of the correct profile to use on a hydrofoil wing turns out to be a recurring topic since, in addition to the behaviour in terms of lift, drag and stall, it is also necessary to consider even to phenomena such as ventilation and cavitation. For these two reasons, the geometry of the airfoils used for hydrofoils and struts differs from aeronautical ones; if the speeds are higher than 40–45 knots ($Re \sim 10^7$), the use of profiles super-cavitating is necessary as they allow to delay the cavitation [14] and to avoid the sudden reduction in lift and increasing of drag. Moreover, for versatile foilborne navigation, Reynolds number calculated with the chord of hydrofoil can vary in a range between 10^4 and 10^7, resulting in a different hydrodynamic response of the wing which must necessarily have a system of mobile surfaces (flap) or a system to vary the overall incidence of the system.

If cavitation occurs when the pressure on the upper surface of the wing is so low that the water evaporates, the area affected by this problem is hit by the water and damaged due to the collapse of the steam bubbles, ventilation instead is linked to the interaction of the wings with the free surface and occurs in hydrofoil piercings or when

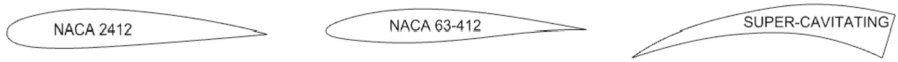

Fig. 4. Three different types of profiles: NACA 2412 (left), which is widely used to many aeronautical applications for low Re numbers; NACA 63–412 and Super-Cavitating (centre and right, respectively), two examples of profiles used to design hydrofoils.

fully-submerged wings get too close to the free surface. The low pressure causes the injection of air which, spreading along the entire span of the wing, drastically decreases lift, increasing drag and generating vibrations [15]. Ventilation is a characteristic of the piercing configuration of hydrofoils and is related to wing configurations with smaller δ (Fig. 1) and higher α (Fig. 2), additionally, profiles with sharp leading edges increase the likelihood of this phenomenon occurring [16]. The solutions proposed to stop this phenomenon are different, but one of the most common is the insertion of bulkheads or fences [17], which decrease the propagation of the air, increasing the WSA of the wing.

3.2 Stability and Safety

Another relevant topic concerns the analysis of boat stability and consequently both performance and safety. The behavior of a hydrofoil, especially if under sail, is particularly complex to evaluate because it is subject to a multiplicity of external forces, and this limits the use of these boats in restricted fields of application. To improve trim and safety, in numerous instances, a VPP is used to predict the dynamic response of the boat [18], which is subject, in addition to the hydroelastic behaviour of the wings, also to multifluid conditions. Considering that the lift is obtained from the relation (1) in which the surface A of the wing appears, a fundamental consideration can be made in terms of vertical stability: if the wing system is of the piercing configuration, also called *variable area foils*, the greater the speed, the greater the lift, the tips of the wings progressively come out from the water, self-balancing the system vertically and the foilborne flight will be stable. In fully submerged wing systems, with angle $\delta = 0$, increasing speed or because of external forces, such as wave motion, the wing can approach the surface of the water, varying its lift as expressed previously. Therefore, the fully submerged configuration is unstable and require a mechanical, or electronic control, which allows changing the lift of the wings making the boat stable, as in the case of the *wand* in the *Moth* class, to control the boat in free surface or waves and avoid capsizing [19]. Furthermore, the control of a large vessel, such as a ferry hydrofoil, turns out to be much simpler since the large inertia moments of the vessel make the system response to external forcing slower than in small vessels.

Hydrofoils can also be used to change the trim of the boat, partially lifting the hull with the aim of reducing the WSA and stability problems, as in the case studied by Shen et Al. in which a wing installed on the bow has allowed to improve performance and fuel consumption consequentially by always keeping part of the hull wet [20].

3.3 Structural Problems and Materials

A fundamental aspect also concerns the choice of materials, both for the wings and for the supporting structures. The latter two can be likened to beams which, interacting with the fluid, are subject to stresses and moments that change over time, The most used materials for their construction are composite fibres, while steel is also used in some applications. In the design phase, in addition to structural dimensioning, hydroelastic issues are being referred to, such as the deformation of the wings under load and the vibrations induced by flutter. This phenomenon, known also as *singing*, could appears on the steel wings in the form of a high-tone sound, which, in addition to damaging the structure, is uncomfortable for the people on board [21], as well as causing continuous maintenance. To avoid structural problems, the analysis using *Fluid Structure Interaction* (FSI), such as the one carried out by Maung et Al. [22] on carbon fibre wings, can play a fundamental role also in evaluating hydroelastic response, according to loads and fatigue, allowing also the study of environmentally friendly materials, such as particular metal alloys or natural composite fibres which can be disposed of more easily at the end of their life.

3.4 Green Propulsion

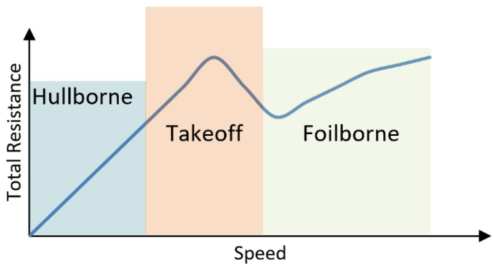

Fig. 5. Total resistance curve for a hydrofoil boat.

In addition to the hydrodynamic and overall optimization of the vessel, the development of environmentally sustainable propulsion systems can give a push towards greater adoption of these vessels. In terms of optimizing fuel consumption, the use of electric propulsion coupled with hydrofoils is particularly suitable [23] as it allows the motors to be installed directly on the wing structures, allowing greater freedom in optimizing the fluid dynamics of the system. On the other hand, however, despite the low resistance generated, the weight and the battery capacity, do not allow for ranges of navigation comparable to traditional thermal-powered motorboats. For this purpose and considering the total resistance curve indicated in Fig. 5 [10], the development of hybrid engines that allow the delivery of maximum power in take-off, thanks to an electric motor, would allow the internal combustion engine to be used only in foilborne navigation when the total resistance decreases and the engine speed is constant, thus increasing the general efficiency of the propulsion unit and the sailing range.

4 Discussion

Based on the analysis of bibliographic articles, it is evident that in recent years, a large part of the scientific community has been directing its attention towards the development of hydrofoil technology as a means of enhancing the performance of boats.

The main themes addressed by the articles (82%) concern the hydrodynamic study and stability analysis of boats, as revealed by the analysis of keywords. Therefore, despite these topics having been extensively covered in literature, they remain highly relevant and represent areas of research that are still open to innovative solutions.

Furthermore, it can be stated that the pursuit of increased performance and improved stability in most studies is aimed at achieving better results in narrow usage contexts, such as the sports sector, and for fast ferries. The remaining part of the articles analysed deals with issues relating to the study of materials (10%) and, still to a lesser extent (5%), the use of green propulsion. However, it should be considered that if the intention is to leverage hydrofoil technology to create commercial green boats suitable for crews made up of non-professionals, the search for extremely high performance may not be necessary. To achieve a hydrofoil-based craft that is environmentally sustainable, it is essential to address, in addition to safety concerns, the topics that have received little attention in literature. For instance, the use of eco-friendly materials should be considered to facilitate the disposal of the vessel at the end of its life cycle. Simultaneously, expanding knowledge on the different types of propulsion could also lead to the development of environmentally friendly boats. As previously mentioned, the development of hybrid propulsion units could identify an optimal point between navigation range and ecological propulsion. Furthermore, a hybrid propulsion could equally reduce battery disposal problems compared to a full electric boat.

Lastly, to optimize the performance of hydrofoil boats even at lower speeds, a study could be undertaken on morphing profiles [24], this could be an idea to reduce the drag generated by the mobile surfaces and improve the wing performances, even in a wider range of Reynolds numbers. However, any problems related to use in a marine environment must be adequately evaluated.

5 Conclusions

Despite being invented years ago, hydrofoil technology has only begun to gain popularity in the boating industry in recent years and it can be a valid opportunity to reduce consumption and improve boat performance.

The work carried out has made it possible to identify research topics for the development of boats that do not require extreme performance comparable to racing boats, but which can equally take advantage of the benefits of using hydrofoils, making pleasure and commercial boating increasingly eco-compatible and respectful of the environment.

References

1. Johnston R.J.: Hydrofoils. Chapter V, Naval Engineers Journal, Feb (1985)
2. Matveev, K.I., Matveev, I.I.: Tandem hydrofoil system. Ocean Eng. **28**, 253–261 (2000)

3. Giovannetti, L.M., Banks, J., Turnock, S.R., Boyd, S.: Fluid Structures Interaction of High-Performance Catamaran C-Foils Under Load. 5th High Performance Yacht Design Conference, March 10–12. Auckland, New Zealand (2015)
4. Miranda, S.: Architettura Navale. Elementi di dinamica della nave. Liguori, Napoli (2014)
5. Findlay, M.W., Turnock. S.: Investigation of the effects of hydrofoil set-up on the performance of an international moth dinghy using a dynamic VPP. In: International Conference Innovation in High Performance Sailing Yachts, pp. 43–56. Lorient, France (2008)
6. Ruggiero, V., Morace, F.: Methodology to study the comfort implementation for a new generation of hydrofoils. IJIDeM **13**, 99–110 (2018)
7. Speranza, D., Di Bernardo, R., Martorelli, M., Gloria, A., Pensa, C., Papa, S.: Basic design and virtual prototyping of a hydrofoil hybrid daysailer. In: Gerbino, S., Lanzotti, A., Martorelli, M., Mirálbes Buil, R., Rizzi, C., Roucoules, L. (eds), Advances on Mechanics, Design Engineering and Manufacturing IV JCM2022, pp. 122–134. Springer (2023). https://doi.org/10.1007/978-3-031-15928-2_11
8. Odd, M.F.: Hydrodynamics of High-Speed Marine Vehicles. Cambridge University, Cambridge (2005)
9. Giallanza, A., Marannano, G., Morace, F., Ruggiero, V.: Numerical and experimental analysis of a high innovative hydrofoil. IJIDeM **14**, 43–57 (2020)
10. Vellinga, R.: Hydrofoils: Design, Build. Fly. Peacock Hill Publishing, Washington (2009)
11. Suastika, K., Nadapdap, G.E., Aliffrananda, M.H., Hermawan, Y.A., Utama, I.K.A., Aryawan, W.D.: Resistance analysis of a hydrofoil supported watercraft (Hysuwac): a case study. CFD Lett. **14**(1), 87–98 (2022)
12. Larsson, L., Eliasson, R.E.: Principles of Yacht Design, 5th edn. Adlard Coles, London (2022)
13. Parnold, L., Sacher, M., Wackers, J., Augier, B., Bot, P.: Free-Surface Effects on Two-Dimensional Hydrofoils by RANS-VOF simulations. The SNAME 24th Chesapeake Sailing Yacht Symposium. Annapolis, USA (2022)
14. Brizzolara, S., Federici, A.: Super-Cavitating Profiles for Ultra High-Speed Hydrofoils: a Hybrid CFD Design Approach. IX HSMV May 25–27 2011. Naples, Italy (2011)
15. Brizzolara, S., Young, Y.L.: Physical and theoretical modeling of surface-piercing hydrofoils for a high-speed unmanned surface vessel. In: 31st International Conference on Ocean, Offshore and Arctic Engineering, 1–6 July 2012. Rio de Janeiro, Brazil (2012)
16. Vermeulen, J.C., Barr, R.A, Martin, M.: Hydrodynamics of Hydrofoil Craft Subcavitating Hydrofoil Systems (1964)
17. Basic, M., Šarić, B., Basic, J., Blagojević, B.: CFD Analysis of Surface-Piercing Hydrofoil Ventilation Inception. XXII Theory and practice of Shipbuilding, Trogir, Croatia (2016)
18. Eggert, F.: Flight Dynamics and stability of a hydrofoilng international moth with a dynamic velocity prediction program (DVPP). Universität Berlin, D.M.S.T (2018)
19. Kebbell, S., Binns J.: Development of a full-scale moth hydrofoil control system test rig. In: The 9th Conference on Computational Methods in Marine Engineering, 1328 (2022)
20. Shen, H., Xiao, Q., Zhou, J., Su, Y., Bi, X.: Design of hydrofoil for the resistance improvement of planning boat based on CFD technology. Ocean Eng. **225**, 111413 (2022)
21. Matveev, K.I.: Maintenance of hydrofoil systems. High Performance Marine Vehicles, Hamburg (2001)
22. Maung, P., Prusty, B.G., White, J.M., David, M., Phillips, A.W., St John, N.A.: Structural performance of a shape-adaptive composite hydrofoil using automated fibre placement. Eng. Struct. **183**, 351–365 (2019)
23. Giovannetti, L.M., Farousi, A., Ebbesson, F., Thollot, A., Shiri, A., Eslamdoost, A.: Fluid-structure interaction of a foiling craft. J. Mar. Sci. Eng. **10**(3), 372 (2022)
24. Takahashi, H., Yokozeki, T., Hirano, Y.: Development of variable camber wing with morphing leading and trailing sections using corrugated structures. J. Intell. Mater. Syst. Struct. **27**(20), 2827–2836 (2016)

Customization in Inventory Datasets: Effects on Life Cycle Assessment Results

Marta Rossi[1], Federica Cappelletti[2](✉), Luca Manuguerra[2], and Michele Germani[2]

[1] Università eCampus, Via Isimbardi, 10 - 22060 Novedrate, Italy
[2] Università Politecnica delle Marche, Via Brecce Bianche 12, 60131 Ancona, Italy
f.cappelletti@univpm.it

Abstract. The present paper aims to analyze the influence on Life Cycle Assessment results of the inventory datasets selected, considering their recentness and their customization operated by practitioners, also including the modeling of certain parameter temporal evolution (e.g., electricity grid mix). The source of uncertainty still needs to be treated in detail and quantitatively analyzed, especially regarding the practitioners' choices. These can significantly affect the final results, so evaluating their impacts and effects is needed. This paper would like to contribute to this sector, by investigating energy-using products. The product selected as the case study is a professional coffee machine, an energy-using product category, produced by an Italian manufacturing company in the Marche region. A Life Cycle Assessment analysis for one reference product is realized, based on ISO 14040/44 standards, using different inventory datasets, all suitable to model the product but characterized by different levels of customization. The quantification of the result range allows producing supporting guidelines for inventory data selection and arbitrary customization, but also correct results interpretation and external communication of product life cycle environmental profile. The comparison of different modeling scenarios shows that the customization of the electricity datasets determines a reduction of impact in the Climate Change indicator of about 31%, while the inclusion of the elec-tricity evolution over time determines a reduction of about 41% compared with the reference LCA results.

Keywords: Life Cycle Assessment · Sensitivity · Practitioners choice

1 Introduction

Life Cycle Assessment (LCA) represents the most consolidated method and tool to evaluate the environmental impact of a product during its lifecycle [1;2]. It is based on a standardized methodology [3;4] and supports eco-design activities and decision processes inside industrial contexts. Several types of uncertainty characterize LCA, limiting the reliability of its results [5] and introducing variability in scenario comparison [6]. Among them, the most analyzed in the last decades comprises random and systematic errors which can occur during the Life Cycle Inventory (LCI) phase and epistemic

M. Carfagni et al. (Eds.): ADM 2023, LNME, pp. 347–354, 2024.
https://doi.org/10.1007/978-3-031-52075-4_39

uncertainty due to lack of scientific knowledge [7]. Further uncertainties are related to the practitioners' choice during the modeling phase, e.g., subjective choice of datasets, allocation procedure and system boundaries definition [5]. Uncertainty analysis has been a subject of intensive study in LCA in recent years, and it has been recommended in technical standards to improve the reliability of LCA [8;9]. When an uncertainty analysis is carried out, the object is to evaluate the uncertainty of LCA results considering the uncertainty in input inventory parameters. Montecarlo is the widely used approach to include uncertainty analysis in the LCA study [10]. Sensitivity Analysis (SA) can be used in conjunction with uncertainty analysis to study the robustness of the results and their sensitivity to scenarios and models. Currently, there are two major types of methods: Local Sensitivity Analysis (LSA), which investigates the consequences on the output value of a small perturbation around a reference input and Global Sensitivity Analysis (GSA), which studies the effects of uncertain factors when these factors may vary over a significant range of uncertainty [11]. Methodological choices (e.g., functional unit, geographical scale, time scale) can be considered an uncertainty in the scenario, while the selection of impact assessment methods represents uncertainty in the model [10]. The present paper aims to analyze the effect on LCA results related to practitioner methodological choices while modeling energy-using products. In particular, the effects of modeling the temporal evolution of certain parameters (i.e., electricity grid mix), and the customization of secondary datasets, according to geographical and temporal scale, will be evaluated in the case of the professional coffee machine. With increased number of LCA applications, even for products without defined and published Product Category Rules (PCR), considering these aspects becomes a significant issue [2]. Out of the purpose, is the analysis of datataset intrinsic uncertainties (lognormal distribution), which are well documented in the EcoInvent database.

1.1 State of the Art

LCA has been widely applied as a decision support tool to identify important environmental factors in product systems and evaluate and compare diverse products' environmental profiles [13]. If standards contain guidance and rules to model products [4], they do not report any guidance on how to carry out uncertainty evaluation or sensitivity analysis to support declarations on the difference of impact between products. However, very often, sensitivity analysis is conducted to evaluate the effect of specific choices made on system boundaries [14], allocation approaches [15], parameter values [16] and characterization methods [17]. In the literature, several examples are available, covering different sectors and applications. Forcina et al. [18] used the sensitivity analysis to verify the environmental convenience of spent coffee ground reuse strategies based on the location of sites; Meneses et al. [19] evaluated the most influencing input in the environmental profile of red wine production; Zhao et al., [20] evaluate the most influencing parameters in composite structures.

On the contrary, uncertainty analysis is not commonly performed in LCAs [22; 23], although a great effort has been made to define, classify and identify sources of uncertainty and methodological aspects to express them. For example, a pedigree matrix approach was recommended to estimate data inaccuracy [23], while among statistical methods, the Monte Carlo simulation was the most commonly recommended [24], also implemented in several LCA tools. Regarding the focus on LCA in the field of energy-using components, the literature is broad on environmental impact studies. Refrigerators [25], cooker hoods [26], kettles and vacuum cleaners were analyzed through LCA [27] or taken as case studies to implement and validate eco-design approaches [28]. However, the source of uncertainty still needs to be treated in detail and quantitatively analyzed, especially regarding the practitioners' choices, for example, in building the lifecycle model, selecting processes from databases, defining allocation procedures, and system boundaries [29]. All these choices can significantly affect the final results, so evaluating their impacts and effects is needed. This paper would like to contribute to the sensitivity analysis in LCA of energy-using products. It answers the following research question: what are the effect of practitioner choices in LCA analysis of a energy-using products? For this reason, different alternative modeling scenarios for the most significant parameters were applied and related LCA results derived. The significance level of parameters is evaluated according to sensitivity analysis, applying the principles of LSA.

2 Approach

According to the LCA methodology phases, the following steps need to be performed during a product environmental assessment: goal and scope, LCI, impact assessment and interpretation. The authors propose two levels for the interpretation phase. The first one comprises the analysis of results and includes an LSA to identify the most significant parameters in terms of contribution to the product's life cycle environmental impact. The second, includes a deeper evaluation of significant parameters' modeling procedures. When a LCA is performed inside an industrial context, a management perspective is usually followed, e.g., LCA practitioners apply modeling procedures which usually consist of using secondary data to describe background systems and primary data to describe foreground ones. Raw material, use and end-of-life stages, which belong to the background system from the producer's perspective, are depicted as background systems and consequently usually modeled with secondary data. This represents a strong assumption that can directly affect the final environmental impact assessment results, especially for energy-using products, for which the use phase represents a significant parameter. In particular, the authors propose to reflect on the following aspects and their effects of results:

- Use of secondary data to model significant parameters;
- Use of not customized datasets to describe production processes and materials;
- Presence in the product of parameters subjected to temporal evolution, e.g., increasing renewable sources in the energy grid mix composition.

If the modeling choices of practitioners regard some of the previous points, an analysis of alternative scenarios and their effects on LCA results needs to be performed. This will allow an understanding of the real effect of simplifications made during the modeling phase (e.g., the use of secondary data or not customized datasets) and a better results characterization and the related optimization strategies. As an example, the case of the EU energy grid mix evolution over time is presented in Table 1.

Europe is facing relevant changes to reduce the environmental burden related to electricity production; consequently, it is crucial to consider its evolution in terms of

Table 1. Evolution of energy mix composition [30]

	Renewable					Not renewvable		
Year/Source		Wind	Solar	Bioenergy	Hydro	Gaseous fuels	Hard coal & Lignite	Oil
2020	36,5%	14,0%	5,0%	5,5%	12,0%	18,0%	21,5%	1,0%
2025	40,3%	16,0%	6,0%	6,8%	11,5%	18,5%	18,0%	0,8%
2030	44,0%	18,0%	7,0%	8,0%	11,0%	19,0%	14,5%	0,5%
2035	50,0%	21,5%	9,0%	8,5%	11,0%	20,0%	9,8%	0,3%
2040	56,0%	25,0%	11,0%	9,0%	11,0%	21,0%	5,0%	0,0%

sources over the next years. According to prevision planes [30], the author proposed to model the evolution of the energy grid mix composition in a simplified way in related dataset, considering a change every 5 years between 2020 and 2040 in the energy sources.

3 Case Study

The proposed approach was applied to a professional coffee machine, which belongs to the energy-using product category and is characterized by a long lifetime. For this machine, an attributional LCA was realized according to the standards [3;4].

3.1 Goal and Scope

The object of the analysis is to calculate the environmental impact of a professional coffee machine along its life cycle (including the material and manufacturing, the use and the EoL phase). In addition, consequences on LCA results related to the energy grid mix evolution will be evaluated according to the approach proposed in this paper. The defined functional unit is the production of bar drinks (12/hour coffee, 5/hour cappuccino, 4/hour tea) using professional machines in a life cycle of 7 years in Italy. The reference flow is represented by one professional coffee machine produced by an Italian company located in the center of Italy. The system boundary includes the raw material used to produce the coffee machine, the manufacturing processes (pre-processed for semi-finished material, manufacturing processes for the finished component and assembly phase), the use phase (i.e., the electricity consumption) and the EoL (recycling/landfilling according to materials type and detailed in the following). The impact category selected is Climate Change, expressed through the unit of kg of CO_2 equivalent calculated using the ReCiPe method [31]. The cut-off allocation approach was selected from the EcoInvent version 3.

3.2 Life Cycle Inventory

The product under analysis is a professional coffee machine with 2 dispensing units characterized by a total weight of about 80 kg. The company provided information regarding materials and manufacturing processes and they were modeled using secondary data (see Table 2). The use phase of the machine is described through the electricity consumption which correspond, for the total life cycle of 7 years, to 16972,5 kWh. The dataset used, modeled using a secondary dataset directly derived from the EcoInvent database, is one of the Italian low voltage electricity grid mix. EoL treatments foresee i) the recycling of ferro-metals, aluminum, and copper with a recycling efficiency of about 70%; ii) the recycling of brass and plastic material with a recycling efficiency of about 50%; iii) the sanitary landfill for the remaining fraction. Also in this case, secondary datasets were used.

Table 2. Material and related manufacturing process

Material type	Manufacturing process
Aluminum removed by milling	Milling, small parts; Metal working, average for aluminum; Turning, computer numerical controlled
Aluminium	Impact extrusion of aluminum; Laser machining; Metal working, average for product manufacturing
Brass	Brass removed by turning; Casting
Copper	Wire drawing
Nylon 6–6; Polyethylene; Polypropylene; Polyurethane; Polyvinylidenchloride; ABS	Injection molding
Steel, chromium steel	Chromium steel removed by turning; Deep drawing; Welding, gas; Wire drawing
Synthetic rubber; Tetrafluoroethylene	Extrusion, plastic pipes; Injection molding

3.3 Results

LCA results, expressed in terms of Climate Change, are presented in Table 3.

Table 3. Climate Change [kgCO2eq.] results and relative weight on the life cycle

Total	Material & Manufacturing	% of total	Use phase	% of total	EoL	% of total
1,16E + 04	8,39E + 02	7	1,08E + 04	93	−2,30E + 01	0,20

The use phase is the most impactful due to electricity consumption, while the EoL impact is negligible. In order to identify the consequences on the output value of a small perturbation around the reference input, a LSA (local Sensitity Analysis) is performed.

The LSA shows that a variation of ±10% in the input value of the energy consumption corresponds to a 9% variation in the total life cycle impact. Negligeble the variations on the output results, if the same perturbation (±10%) is applied to the other life cycle phases (Material & Manufacturing and EoL). The most significant parameter is therefore the annual energy consumption.

3.4 Definition of Alternative Scenarios

Two alternative scenarios regarding the electricity consumption parameters were modeled:

- Scenario1: Dataset customization according to the specific grid mix of the company provider by modeling in the EcoInvent database the specific grid mix of the company provider;
- Scenario 2: Dataset modification according to the evolution of the Italian grid mix in the next seven years, assuming a linear evolution in renewable sources (SC2), according to a simplified approach (linear) as presented in Sect. 2.

The results of these two scenarios were then compared with the baseline case (i.e., LCA initial results) and shown in Table 4.

Table 4. Scenarios comparison (Climate Change, kgCO2eq.)

	Baseline	Scenario 1	Scenario 2
Total impact	1,16E + 04	8,00E + 03	6,50E + 03

The comparison of different modeling scenarios shows that the customization of the electricity datasets determines a reduction of impact in the Climate Change indicator of about 31%, while the inclusion of the elec-tricity evolution over time determines a reduction of about 41% compared with the reference LCA results. This demonstrates the need for this type of produc to select the dataset used to describe the electricity datasets accurately. At the same way, in depth study should focus on the EoL phase. For energy using products and for the Climate Change impact category, this phase has a very low impact if compared to the entire product life cycle one (less than 0,5%). Variations of the recycling rate will not determine significant modification on the final results (as observed in the LSA); however, if alternative dismantling scenarios will be analysed (e.g., reusing or remanufacturing), they could determine higher effects on the final results, due to the recovery of some components functionalities and consequently benefits for the environment. Future works will focus on these aspects.

4 Conclusion

The uncertainty that characterizes LCA may limit its results' reliability. This paper contributes to the sensitivity analysis in LCA, applying the principles of LSA in a case of a professional coffee machine. The use of alternative modeling scenarios for the most significant parameter (energy in this case) counts a variation of impacts between 31% and 41% (Climate Change). Consequently, the importance of detailing the LCI data, at least for the most critical parameters, is proven. The use of secondary data that ensures faster analysis should be restricted to parameters that do not retain high percentage of environmental impacts and to factors that do not significantly change over time. On the contrary it is suggested for all these significant parameters, the use of primary data, their customization (e.g. in terms of geographical characterization) including the modeling of their temporal evolution (e.g., electricity grid mix).

References

1. Bjorklund, A.: Life cycle assessment as an analytical tool in strategic environmental assessment. Lessons learned from a case study on municipal energy planning in Sweden. Environ. Impact Assess. Rev. **32**(1), 82–87 (2011)
2. Igos, E., Benetto, E., Meyer, R., Baustert, P., Othoniel, B.: How to treat uncertainties in life cycle assessment studies? Int. J. Life Cycle Assess. 1–14 (2018)
3. ISO 14040 Environmental management. Life cycle assessment Principles and framework (2022)
4. ISO 14044 Environmental Management. Life Cycle Assessment Requirements and Guidelines (2022)
5. Scrucca, F., et al.: Uncertainty in LCA: an estimation of practitioner-related effects. J. of Clean. Prod. **268**, 122304 (2020)
6. Cherubini, E., Franco, D., Zanghelini, G.M., Soares, S.M.:Uncertainty in LCA case study due to allocation approaches and life cycle impact assessment methods. Int. J. Life Cycle Assess. **23**(3), 1–16 (2018)
7. Rosenbaum, R.K., Georgiadis, S., Fantke, P.: Uncertainty management and sensitivity analysis. LCA Theor. Pract. 271–321 (2018)
8. Haimes, Y.Y.: Risk Modeling, Assessment, and Management in John Wiley & Sons: New York (2011)
9. Bjorklund, A.E.: Survey of approaches to improve reliability in LCA. Int. J. Life Cycle Assess. **7**, 64–72 (2002)
10. Scrucca, F., et al.: Uncertainty in LCA: An estimation of practitioner-related effects. J. Cleaner Prod. **268**, 122304 (2020) https://doi.org/10.1016/j.jclepro.2020.122304.
11. Wei, W., Larrey-Lassalle, P., Faure, T., Dumoulin, N., Roux, P., Jean-Denis, M.: How to conduct a proper sensitivity analysis in life cycle assessment: taking into account correlations within LCI data and interactions within the LCA calculation model. Environ. Sci. Technol. **49**, 377−385 (2015)
12. The Danish Centre for Environmental Assessment. Getting the data right https://www.en.plan.aau.dk/getting-the-data-right/.UNSD (2021)
13. Guo, M., Murphy, R.J.: LCA data quality: Sensitivity and uncertainty analysis. Sci. Total Environ. **435–436**, 230–243 (2012)
14. Kim, S., Dale, B.E.: Regional variations in greenhouse gas emissions of biobased products in the United States—corn-based ethanol and soybean oil. Int. J. Life Cycle Assess. **14**, 540–546 (2009). https://doi.org/10.1007/s11367-009-0106-4
15. Gnansounou, E., Dauriat, A., Panichelli, L., Villegas, J.: Energy and greenhouse gas balances of biofuels: biases induced by LCA modelling choices. J. Sci. Ind. Res. **67**, 885–897 (2008)
16. Laser, M., Larson, E., Dale, B., Wang, M., Greene, N., Lynd, L.R.: Comparative analysis of efficiency, environmental impact, and process economics for mature biomass refining scenarios. Biofuels Bioprod. Biorefin. **3**, 247–270 (2009)

17. Dreyer, L., Niemann, A., Hauschild, M.: Comparison of three different LCIA methods: EDIP97, CML2001 and Eco-indicator 99. Int. J. Life Cycle Assess. **8**, 191–200 (2003)
18. Forcina, A., Petrillo, A., Travaglioni, M., Di Chiara, S., De Felice, F.: A comparative life cycle assessment of different spent coffee ground reuse strategies and a sensitivity analysis for verifying the environmental convenience based on the location of sites, J. Cleaner Prod. **385**, 135727 (2023). https://doi.org/10.1016/j.jclepro.2022.135727
19. Meneses, M., Torres, C.M., Castells, F.: Sensitivity analysis in a life cycle assessment of an aged red wine production from Catalonia. Spain Sci. Total Environ. **562**, 571–579 (2016). https://doi.org/10.1016/j.scitotenv.2016.04.083
20. Zhao, M., Dong, Y., Guo, H.: Comparative life cycle assessment of composite structures incorporating uncertainty and global sensitivity analysis. Eng. Struct. **242**, 112394 (2021). https://doi.org/10.1016/j.engstruct.2021.112394
21. Huijbregts, M.A.J.: Priority Assessment of Toxic Substances in the frame of LCA–Time horizon dependency in toxicity potentials calcuated with the multi-media fate, exposure and effects model USES-LCA. University of Amsterdam, Amsterdam, The netherlands, Institute for Biodiversity and Ecosystem Dynamics (2000)
22. Ross, S., Evans, D., Webber, M.: How LCA studies deal with uncertainty. Int. J. Life Cycle Assess. **7**, 47–52 (2002)
23. Huijbregts, M.A.J., Norris, G., Bretz, R., Ciroth, A., Maurice, B., von Bahr, B., et al.: Framework for modelling data uncertainty in life cycle inventories. Int. J. Life Cycle Assess. **6**, 127–132 (2001)
24. Hung, M.L., Ma, H.W.: Quantifying system uncertainty of life cycle assessment based on Monte Carlo simulation. Int. J. Life Cycle Assess. **14**, 19–27 (2009)
25. Rossi, M., Favi, C., Germani, M., Omicioli, M.: Comparative life cycle assessment of refrigeration systems for food cooling: eco-design actions towards machines with natural refrigerants. Int. J. Sustain. Eng. **14**(6), 1623–1646 (2021)
26. Castorani, V., Rossi, M., Germani, M., Mandolini, M., Vita, A.: Life cycle assessment of home smart objects: kitchen hood cases. Procedia CIRP **69**, 499–504 (2018)
27. Subramanian, K., Winco, K.C.Y.: Review of life cycle assessment on consumer electronic products: developments and the way ahead. Crit. Rev. Environ. Sci. Technol. **46**(18), 1441–1497 (2018)
28. Mandolini, M., Marconi, M., Rossi, M., Favi, C., Germani, M.: A standard data model for life cycle analysis of industrial products: a support for eco-design initiatives. Comput. Ind. **109**, 31–44 (2019). https://doi.org/10.1016/j.compind.2019.04.008
29. Scrucca, F., et al.: Uncertainty in LCA: An estimation of practitioner-related effects. J. Cleaner Prod. **268**, 122304 (2020) https://doi.org/10.1016/j.jclepro.2020.122304
30. CAN Europe/EEB technical summary of key elements, Building a Paris Agreement Compatible (PAC) energy scenario (2020). https://www.pac-scenarios.eu/fileadmin/user_upload/PAC_scenario_technical_summary_29jun20.pdf
31. Huijbregts, M.A.J., et al.: ReCiPe, A harmonised life cycle impact assessment method at midpoint and endpoint level Report I: Characterisation (2016)

An Analytical Tool to Support Decision-Making in the Design Phase

Federica Cappelletti(✉), Luca Manuguerra, and Michele Germani

Università Politecnica delle Marche, Via Brecce Bianche 12, 60131 Ancona, Italy
f.cappelletti@pm.univpm.it

Abstract. The high consumption of energy and materials during their life cycle makes buildings among the most significant contributors to environmental impacts. Choosing sustainable materials and their reuse is crucial to positively decreasing their environmental impact. The design phase is essential throughout the lifecycle, where designers and customers are called to make informed decisions. Those are easier as more quantitative data are available. The present work presents the extension of a tool previously developed intended to introduce the topic of environmental sustainability in the design phase. It allows quantitatively assessing the goodness of reusing construction materials in terms of environmental avoided impact. The primary potentiality is represented by the possibility of executing sustainability assessment already in the early stages of building design when design choices significantly contribute to the global environmental impact of solutions. An application related to choosing and evaluating the use of second-life materials whose End of Life management is highly complex is shown. The case study is associated with the reuse of composite materials for indoor furniture. The results show how important it may be to re-employ materials because, from one side, it prevents the need for additional virgin resources and avoids the complex management of End of Life phase.

Keywords: Environmental sustainability · Knowledge Based Engineering · Environmental impact · Eco-design · Life Cycle Assessment

1 Introduction

Buildings are characterized by high energy and materials consumption; therefore, they are known as one of the most significant emissions contributors. Diversified stakeholders have put effort and increasing attention to reducing emissions worldwide; in addition to that, sustainable design practices have been put into practice; these pervaded many sectors, from dwellings [1], public infrastructures [2] offices [3], and even worship buildings [4] both in brand new construction and refurbishment [5].

Besides the use phase, the extensive employment of valuable materials also considerably generates emissions. However, the never-fulfilled willingness to reach the best performance, also with a glance at the aesthetic perspective, can sometimes overcome the environmental perspective. The use of composite materials is growing with the global

M. Carfagni et al. (Eds.): ADM 2023, LNME, pp. 355–362, 2024.
https://doi.org/10.1007/978-3-031-52075-4_40

business sector for composite products reaching about £73 billion by 2020 [6]. Consequently, enterprises must face the big challenge of developing approaches and technologies to optimize the waste generated from their manufacturing operations and End of Life (EoL) [7]. Very few alternatives are available to the three main options for treating EoL wastes (landfill, incineration and recycling); however, it is essential that those are valorized and spread over many applications can make their feasibility profitable.

Design for X is a crucial strategy for mitigating the impact of buildings on the environment. Sustainable architecture has become a critical aspect of today's design construction industry, as it combines aesthetics, functionality, and environmental responsibility. It attempts to reduce its environmental impact through advanced systems, conscious use of resources, and efficient use of energy and water for operations [8].

The most effective and simple method for integrating sustainable concepts in construction projects has been recognized as the choice of sustainable building materials. The development of certification programs (compulsory or on a voluntary base), building rating systems [9, 10], and directives (such as the Energy Performance of Buildings Directive [11]) has taken place throughout time, however they frequently do not suggest brand-new procedures or materials.

Efrosini et Papadopoulos [12] firmly observe that the improvement of quality of living and going to market with systems and products cannot neglect sustainability. They foresee a continual increase in certificates and sustainability policies because they reduce energy and raw materials. Sustainable material selection is critical, as many products and materials are available. Moreover, material selection is affected by multiple technical, economic, environmental and socio-cultural factors [13]. Abdelaal et Brian [14] investigated the multiple stakeholders' knowledge, attitude, and practice of green building design and assessment. Different stakeholders, such as architects, engineers, sustainability consultants, contractors, and suppliers have distinct perception toward green building design and assessment process; the results of the study highlighted a positive attitude, even though outlines limits in these practices.

Guidelines for material selection [16], are now available in manuals [15]. Through specific approaches, databases support the screening, the evaluation of materials compliance and therefore the choice of eligible [17]. Nonetheless, the literature still claims a lack of scientific methods to select new and sustainable materials, able to provide a solid basis to designers and projects stakeholders; such methods should overcome the single focus of thermal and energy efficiency.

The evaluation of environmental impacts through life cycle assessment (LCA) should become part of the design [18]. Hollberg et al. [19] affirm that the number of buildings' LCA tools and the published literature has increased substantially in recent years. Most of them include some type of visualization. However, the lack of guidelines or harmonized way of presenting LCA results may affect decision-making in the design process of buildings.

Božiček [18] proposes a comparative method that supports designers in comparing and interpreting LCA results in the context of the Environmental Product Declaration (EPD). The method effectively simplifies the LCA results interpretation and enables straightforward decision-making; however, it is not yet a fully functional tool and is one-driver based (environmental impacts).

In this context, this work comes up with a framework intended to provide information about generic materials and detailed commercial solutions when materials are selected. The main goal is to provide useful tools intended for capitalizing on knowledge about environmental sustainability and supporting the decision-making process. The approach is developed for the very early stages of the design process, even before the CAD model is developed.

The present work overcomes the current state of the art because: i) the focus is on environmental sustainability and comparison of choices is simultaneous, based on materials properties and characteristics; ii) the approach aims at including also materials with optimized lifecycle, such as material recycled or re-manufactures in close loops. The capitalized knowledge is expected to be updated as the company experience increase, new suppliers or expertise are acquired. The tool is characterized by high usability and fast materials comparisons; this makes the tool valuable for very early project phases, such as the commission phase, when professional experts have contact with the customer.

The present work, through the definition of the approach and development of the tool, investigates solutions to extend the company's knowledge, collect it and therefore increase its effectiveness in supporting the decision process. The paper is structured as follows: Sect. 2 introduces the approach developed to support and stimulate the project's stakeholders. The approach aims at capitalizing on know-how, deriving from previous projects' experience and structured information available from suppliers and stakeholders. Simultaneously, it proposes alternative materials, with a more sustainable lifecycle, based on objective data; the approach is innovative in this sense. A tool is derived from it. Section 3 describes the approach's potential through two applications of the tool. The conclusion closes the work by summarizing the main outcomes and suggesting further integrations.

2 Approach

The proposed approach is developed to support and stimulate the choice of materials that bring, along with their use, lower environmental burden and/or have an improved lifecycle from the environmental perspective. Furthermore, the method helps companies and professional experts implement eco-design strategies and their collections in a structured repository. It presents five main steps (Fig. 1) and is integrated into the classical design phases.

- Pre-design phase; this phase defines the main objectives, such as the main project goal, the issues and wishes the project attempts to solve and fulfill and the results and targets to reach. The needed resources and the timing are set. In addition to that, designers and experts in the project are called to assess their competencies on the specific matter. This is crucial for the definition of knowledge level occurs during this phase: the type of support they need to solve the problems and answer to the previously defined objective. Specific material, adequately collected and organized, enables designers to acquire knowledge and become aware.
- In the concept design, the main requirements of the project are set. Then, thanks to the consultation of specific materials (e.g., previous environmental analysis realized on products), they can select design strategies and verify their validity iteratively.

– The functional design where the main materials are chosen and the product structure is defined.
– The detailed design, where shapes and more accurate detail are modelled. Here the design solutions are approved; if not, additional attempts have to be made.

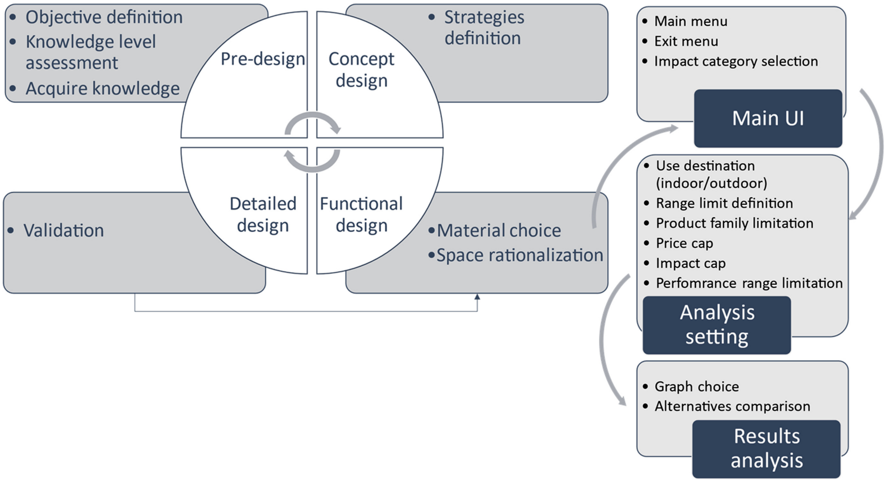

Fig. 1. Approach and tool structure

2.1 Tool

A structured and well-organized repository is the core of the approach presented in Fig. 1; the repository collects materials technical, aesthetical, and environmental information and supports the decision-making process from the very early stages of a project when details are not defined yet. The repository contains two main types of information: the first are more general, such as data retrieved from literature; the second is more specific, such as EPD developed by enterprises that contain data referring to their processes and flows. The main idea is to store quantitative environmental assessments retrieved by suppliers. The tool's output quantitatively evaluates and compares several alternatives for the building sector.

Starting from the base of the current tool, the database records are further updated by environmental specialists, as their experience and company's know-how increase [17]. The materials are then manually selected by the user and comparisons and calculations are automatically retrieved.

The tool can be used by different stakeholders of a project within the building sector because it provides graphs and intuitive charts, useful also to correlate product alternatives. The tool is structured into five main tabs: the main one allows the main analysis settings (such as the indicator to choose when plotting the results and whether only material or material and EoL phases are considered). The graphs can be generated; they automatically appear in two other tabs. Ultimately, one tab contains the principal repository; whenever information is retrieved, this can be added in the form of new items (that means that new alternative materials are inserted) or as an update of information (i.e., a new version of EPD for the same material). The attributes of the repository can be divided into three main groups. The first describes the material on a broad basis, and thus contains information about product name, family and class; the second covers the environmental aspect and the unitary environmental impacts for the material ([A1-A3]) and EoL phases are reported ([C2-D]), for four different indicators. In the third group, performance indicators are indicated (when applicable); some examples are recyclability, density, cost, breaking strength, thermal and sound insulation.

3 Application

In this section, one application of the tool is reported. The material to produce modern table covers must be chosen. The aesthetic boundaries aim at getting a natural effect. Figure 2 shows the first comparative graph obtained by using the tool.

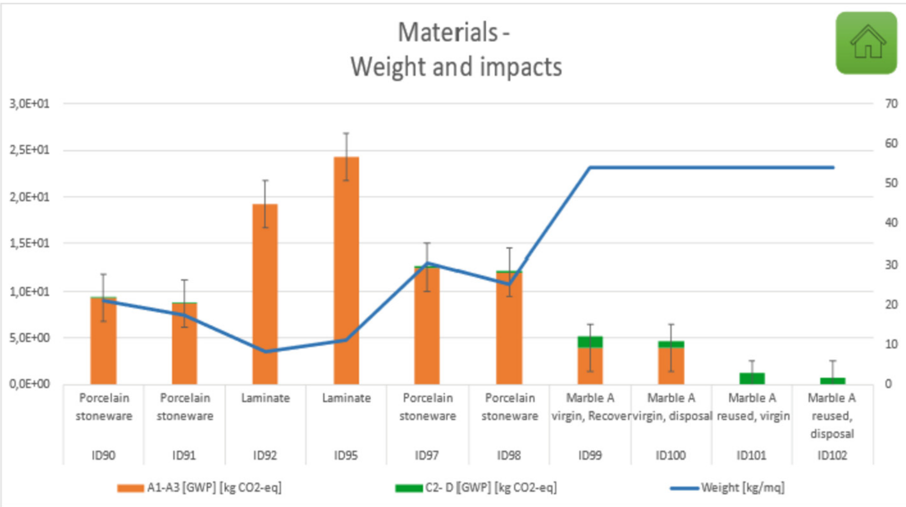

Fig. 2. Materials comparison: Material and EoL phases environmental impacts (Global Warming Potential) and weight.

Ten alternative materials are considered. Their environmental impacts are very inhomogeneous. The green and orange bars depict the environmental performance per surface unit (1 m^2), while the blue line follows the unitary weight (kg/m^2). Two laminates are very light, but their environmental impact is higher. The marble presents lower environmental impacts; moreover, ID 101 and ID 102 present null material related to the environmental impacts, as they come from a supplier who employs other manufacturing scraps as material. However, not all sizes may be available, and the choice may be limited to the available scraps. Figure 3 shows the graph that compares the material extraction phase and the cost for each material. The green angle on the bottom left stands for the lower environmental impact and cost, while the opposite, the red angle on the upper right depicts the less convenient alternatives.

Fig. 3. Materials comparison matrix: Material phase environmental impacts (Global Warming Potential) and costs.

4 Discussion

In the building context, the customer demand that joins aesthetic satisfaction and functionality led the sector to investigate very performing materials. Nevertheless, too often their outstanding characteristics are evaluated from several perspectives (i.e., aesthetic, robustness, durability, cost, availability) but their environmental burden is neglected or considered in a later stage. Consequently, invisible issues are raised when composite materials are considered, as they make the products highly performing, but often cannot be easily handled at their EoL [20].

Therefore, the tool aims at providing insights into the environmental impacts of materials, setting them at the same level of choice with other material features (i.e., recyclability and disassemblability, breaking strength [N], modulus of rupture [N/mm^2], weight [kg/m^2], thermal and sound insulation, surface and treatment, supplier).

Different users may benefit from the tool's output: from technical roles (i.e., designers and architects) to customers that pay high attention to environmental matters.

The tool is consistent with the current trend of BIM-oriented design. However, it is intended for the decision-making step, earlier than the detailed and accurate CAD documentation of all building components, as the design has the power to influence all downstream phases, affecting their probability to happen, their efficiency and success rate [21]. The tool is an alternative to traditional LCA software, which require much information about the analyzed functional unit. The database can be extended as the user and the context requires; therefore, the tool may be applied to other engineering sectors too. Many different sectors (i.e., agriculture, cloth industry) may require too many customizations of the materials' features.

5 Conclusion

The high consumption of energy and materials makes the building sector one of the most significant contributors to negative environmental impacts. By acting since the design phase, it is possible to mitigate the impact of buildings on the environment. The main goal is to provide useful tools intended for capitalizing on knowledge about environmental sustainability and supporting the decision-making process. The approach is developed for the very early stages of the design process, even before the CAD model is developed. The main functions are illustrated together with the main tool outputs. The knowledge capitalized by the tool allows for estimating the environmental impact of buildings from the early stages of design. However, the designer should continuously repeat this process to update the LCA results based on possible design changes.

The validation of the tool may be expected to focus on i) the identification of the required resources to implement the methodology and to use the tool; ii) the acceptability (evaluation of obstacles during the methodology implementation and tool use); iii) the implementation time (of implementing the methodology and to complete a project); iv) the validation of usefulness and strength of the methodology and tool and v) cost-effectiveness.

Future works will consist of testing the tool in a building design context, including also functionalities of the BIM model.

References

1. Akadiri, T.P.O.: Understanding barriers affecting the selection of sustainable materials in building projects. J. Build. Eng. **4**, 86–93 (2015)
2. Meneghelli, A.: Whole-building embodied carbon of a North American LEED-certified library: Sensitivity analysis of the environmental impact of buildings materials. Build. Environ. **134**, 230–241 (2018)
3. Mariede Klijn-Chevalerias, S.: The Dutch approach for assessing and reducing environmental impacts of building materials. Build. Environ. **111**, 147–159 (2017)
4. Azmi, N.A., Kandar, M.Z.: Factors contributing in the design of environmentally sustainable mosques. J. Build. Eng. **23**, 27–37 (2019)
5. Ali Tighnavard, B., Abdul Kadir, B.M., Adel, G.: Sustainable materials selection based on flood damage assessment for a building using LCA and LCC. J. Clean. Prod. **222**, 844–855 (2019)
6. Job, S., Leeke, G., Mativenga, P.T., Oniveux, G., Pickering, S., Shuaib, N.A.: Composites recycling. Where are we now? Composites UK report (2016)
7. Mativenga, P.T., Sultana, A.A.M., Agwa-Ejonb, J., Mbohwab, C.: Composites in a circular economy: a study of United Kingdom and South Africa. Procedia CIRP **61**, 691–696 (2017)
8. Wijesooriya, N., Brambilla, A.: Bridging biophilic design and environmentally sustainable design: a critical review. J Clean. Prod. **283**, 124591 (2021)

9. U. G. B. council 2019. LEED v4 for building design and construction
10. Bonna, H.R., El-Hakim A.S., El-Behairy, H.S.: Technical evaluation of BREEAM-international-NC-2016 for rating of sustainable new construction outside the UK (2019)
11. E.P.a.t.C.o.t. EU 20190 IRECTIVE 2010/31/EU OF The European Parliament and of the Council of 19 May 2010 on the energy performance of buildings
12. Efrosini, G., Papadopoulos, A.M.: Construction materials and green building certification. Key Eng. Mater. **666**, 89–96 (2016)
13. Aghazadeh, E., Yildirim, H.: Assessment the effective parameters influencing the sustainable materials selection in construction projects from the perspective of different stakeholders. Mater. Today: Proc. **43**, 2443–2454 (2021)
14. Abdelaal, F., Brian, G.H.W.: Knowledge, attitude and practice of green building design and assessment: New Zealand case. Build. Environ. **201**, 107960 (2021)
15. Boix Rodríguez, N., Rossi, M., Cappelletti, F., Favi, C.: Engineering eco-design of heat exchangers in domestic heating systems using life cycle assessment methodology. Int. J. Interact. Des. Manufact. (2023)
16. Davis, J.R.: Guide to Materials Selection, Engineered Materials Handbook Desk Edition (1995)
17. Rossi, M., Cappelletti, F., Germani, M.: Design for environmental sustainability: collect and use company information to design green products. Procedia CIRP **105**, 823–828 (2022)
18. Božiček, D., Kunič, R., Košir, M.: Interpreting environmental impacts in building design: application of a comparative assertion method in the context of the EPD scheme for building products. J. Clean. Prod. **279**, 123399 (2021)
19. Hollberg, A., et al.: Review of visualising LCA results in the design process of buildings. Build. Environ. **190**, 107530 (2021)
20. Cappelletti, F., Rossi, M., Ciccarelli, C., Germani, M.: Industrial scraps valorization: designing products to make detached value chains circular. In: Gerbino, S., Lanzotti, A., Martorelli, M., Mirálbes Buil, R., Rizzi, C., Roucoules, L. (eds.) Advances on Mechanics, Design Engineering and Manufacturing IV. JCM. Lecture Notes in Mechanical Engineering. Springer, Cham (2022). https://doi.org/10.1007/978-3-031-15928-2_4
21. Rossi, Marta, Cappelletti, Federica, Marconi, Marco, Germani, M.: A design for de-manufacturing methodology to improve the product end of life environmental sustainability. In: Rizzi, C., Campana, F., Bici, M., Gherardini, F., Ingrassia, T., Cicconi, P. (eds.) Design Tools and Methods in Industrial Engineering II. Lecture Notes in Mechanical Engineering, pp. 373–380. Springer, Cham (2022). https://doi.org/10.1007/978-3-030-91234-5_38

The Application of Circular Economy Principles Through Re-design, Scraps De-manufacturing, and Value Chains Merge

Federica Cappelletti[1(✉)], Luca Manuguerra[1], Marta Rossi[2], and Michele Germani[1]

[1] Università Politecnica delle Marche, Via Brecce Bianche 12, 60131 Ancona, Italy
f.cappelletti@pm.univpm.it
[2] Università eCampus, Via Isimbardi, 10, 22060 Novedrate, Italy

Abstract. Nowaday the industrial interest, as well as the academic one, on the development and implementation of circular approaches is growing. In parallel, the use of composite materials steeply increased in the last decades which are hardly disposable. The present work proposes an eco-design method that guides the reuse and remanufacturing of scraps. The core is the re-design of processes that introduce materials derived from scraps from other value chains. Two cases are investigated: the first concerns the production of panels for the wind sector. Using scraps from the wind blades' trimming almost eliminates the emissions derived from the panel production. Also, the material of a component of an espresso coffee machine has been replaced by scraps from kitchen sinks; this process requires resources only for shredding. The case study allows to highlight also the importance of sharing information and networking among the actors of the supply chains and the relative distance of cooperating organizations.

Keywords: Circular Economy · Design for de-manufacturing · Composite materials · Industrial Symbiosis · Remanufacturing

1 Introduction

Circular economy strategies require a wider perspective for industrial companies, to cosider the EoL phase of their product, e.g. recover materials of their dismantled products. Methodologies and tools for de-manufacturing and remanufacturing, applied during design can support this activity [1]: the anticipation of questions related to the EoL in the first phase of design can improve the environmental performance of products when they will be dismantled [2]. Circular Economy (CE) is strictly related to industrial symbiosis (IS); the first requires a whole system to change, the second has a high potential to lower CO2 emissions of industrial processes [3], even if more studies and applications are needed to evaluate further benefits (in terms of costs and social benefits) [4].

M. Carfagni et al. (Eds.): ADM 2023, LNME, pp. 363–370, 2024.
https://doi.org/10.1007/978-3-031-52075-4_41

This paper explores the context of composite materials, which use is recently grew steeply [5]; despite their large use, it is extremely difficult to recycle them. Circular strategies are then explored for this kind of material. To obtain the highest environmental benefits and minimum negative impacts from reuse [6], composite scraps must become secondary input materials; this prevent costs and environmental burden related to waste treatments, as well as those related to the production of virgin materials.

1.1 Design for De-manufacturing: The Turning Point in CE

Design choices impact on the dismaltling procedures [7]. The literature claims strategies to consider circularity in the design process [8]. The present work fills the gap of minimal offers available for possible design solutions, especially regarding application-oriented solutions, having a multiple life cycle approach [9]. Three key points of circularity are accomplished [10]: material recirculation, utilization and endurance. The present paper presents a method to support the identification of circular strategies, through the calculation of environmental impacts. Among the main innovations, the focus on composite materials. Secondarily, the evalution of benefits related to the re-use of scrap components/materials between companies of different sectors; moreover, they are close each other, but not adjoining. However, the method is suitable for non-composite materials too. Differently from the existing literature, the proposed approach aims to evaluate the benefits related to the use of scraps with different functions they were initially conceived for (Sect. 2). The case study (Sect. 3) applies the proposed method and identifies a cluster of Italian companies where apply circular strategies. The environmental benefits for the companies involved are quantitatively evaluated. Results highlight the need for strong cooperation between companies to take advantage of the products' hidden value and are further discussed Sect. 4, before the conclusion.

2 Materials and Method

The proposed approach, shown in Fig. 1, aims at supporting enterprises in identifying and evaluating circular strategies for IS with a structured process; it is structured in four main steps. First, the linear lifecycle is assessed, and so are the availability and type of scraps. This enables the second step, the process design, that considers materials, geometries, production processes. The present approach is particulary intended for composite materials; therefore, the re-design may be helpful to overcome the challenges projected by the scraps feature and the characteristics to be reached by the target component. The step 3 includes some technical evelautions for the identification of the best applications, e.g. production processes practicality, analysis of components' shape, and environmental assessment analysis. The (prototype) production allows the quantification of the resources employed and emissions produced through standardize methods, as LCA (Life cycle Assessment). Figure 1 shows the main steps suggested to have scraps from composite materials acquire new value and avoid unworthy EoL treatments.

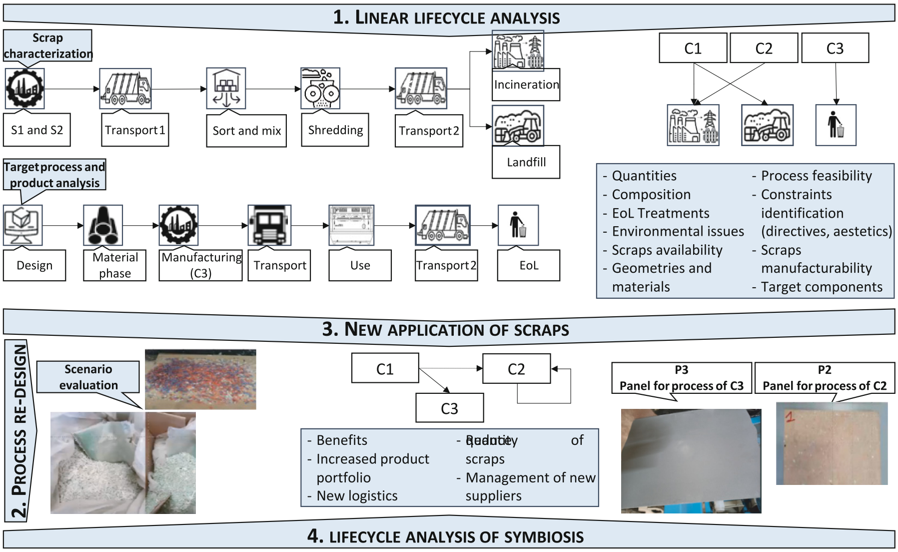

Fig. 1. Valorization of industrial composite materials waste. Light blue-filled boxes stand have general validity; no filled boxes show how the case study applied the approach. Scraps S1 and S2 are produced by Companies C1 and C2 respectively. The new processes involve C2 and C3 to produce P2 and P3 respectively. Network representation adapted from [11]

3 Results

3.1 Scraps Characterization

Three companies applied the proposed method from the Marche region in the center of Italy. Two of them (Company 1 and 2 - C1 and C2) made their scraps available to be worked and employed as secondary raw materials in different production processes. C2 turned out to be also a host for circular products, together with C3, which produces professional espresso coffee machines. C1 produces sinks for domestic kitchens. C2 designs and produces wind blades. The scraps (S1 and S2 from C1 and C2's processes respectively) are off-quality products that cannot be commercialized because they do not satisfy the customer quality standards and requirements or process scrap as dust or pieces from Computerized Numerical Control - CNC – machining, trimming scraps, consumables containers. Moreover, their dimensions are often unstable and unpredictable due to process inaccuracy. The environmental burdens are calculated through LCA methodology and tool, deriving from the extraction, production, and disposal of the annual quantity of scraps produced by the companies (Life Cycle Inventory (LCI) for C1 and C2 summarized in Table 1). Data about the annual quantity of produced scraps and their disposal treatments are collected. In Table 1 the current disposal scenario is reported, with details of the means of transportation used to move the scraps: the blades' scraps are shredded and compressed, partially incinerated and partially disposed in landfill. Regarding the sink scraps, they are incinerated after some preliminary treatments. Enterprises are unaware of what happens to their scraps (nor their product) once they are discarded: what

C2 and C3 expect from their scraps is different from what happens. The information was retrieved by interviewing the supplier the companies have contact with. The sorting and mixing phase refers to sorting the scraps collected by the supplier and the mix with scraps of the exact nature that come from other industrial realities.

Table 1. LCI scraps and Environmental impacts distribution

SCRAPS/COMPONENTS			Disposal	Transport
Category	%	Material		
Company1				
Sink scraps	87%	Mineral + PMMA [a]+ Additives	Incineration	Road, truck
Sink dust	13%	Mineral + PMMA [a]+ Additives	Incineration	Road, truck
Company 2				
Glass fiber scraps	32%	Glass fiber	Landfill (33%) Incineration (66%)	Road, truck
Plastic waste	66%	PVC [b] + Polyamide + Synthetic rubber + Buthacrylate + PET [c] + Epoxy Resin (85%)	Landfill (75%)	Road, truck
		Epoxy adhesive + Glass fiber + Epoxy Resin (13%)	Incineration (25%)	
		Glass fiber + Epoxy Resin + Carob fiber (2%)		
Coating dust	2%	Epoxy Resin + Insulating	Landfill	Road, truck

0-10%	11-20%	21-30%	31-40%	41-50%
51-60%	61-70%	71-80%	81-90%	91-100%

[a] PMMA= Polymethyl methacrylate [b] PVC= Polyvinylchloride [c] PET= Polyethylene Terephthalate

The colors of the cells in Table 1 quantify the percentage of life cycle phases impact in terms of the Global Warming Potential (GWP) indicator. The first most impacting is the material phase, then the EoL. Wind blades and sink scraps disposal is responsible for about 10% and 15% respectively. Regarding the pre-treatment and the transport to the treatment centers are negligible in terms of impacts. For C3 waste pre-treatment impact is lower than 1%. The analysis is realized using the LCA software SimaPro 8.0, EcoInvent v3.6 database, applying the Recipe MidPoint (H) method; and so was the linear lifecycle of the professional coffee machine assessment. In this case, the Functional Unit (FU) was the production, use and disposal of a professional espresso coffee machine, daily used in Italy for 5 years to produce on average of 36 coffees per hour. The use phase largely retains the impacts (more than 90% of the overall impacts). The Back Assembly is the second most impacting assembly.

3.2 Process Re-design

Wind Blades

The geometric features and the manufacturability constraints of the wind blade process scraps did not find any components of C1, C2 or C3. Therefore, alternative treatments have been investigated (Table 2). The scraps cannot undergo any chemical process, otherwise their properties change. However, mechanical treatments are allowed. The core material, the blade trim (that comes from the blade finishing process) and the blade root trim (what is left from the finishing of the base of the blade) were shredded so that they were used to obtain new panels as their dimension dropped. However, those are introduced in the wind blade production process with a new function: the panels are employed to make models or mold to be milled; subsequently, prototypes are obtained from them. The panels with secondary raw materials replace sheets of polyurethane polymer (i.e., Eulithe, Ureol) or MDF.

Table 2. Process re-design.

Part	As-is			To-be		
	Mat.	**Man.**	**EoL**	**Mat.**	**Man.**	**EoL**
P2	Eulithe, Ureol, MDF*	Mill	S2	S2	Shredding + cold cure + mill	S2
P3	Aluminum	Mill + coat	S1	S1	Shredding + cold cure + coat	S3

Figure 2 compares the environmental burden caused by traditional and innovative processes. Please note that the panels milling to produce the molds is neglected, as it is a common phase for both. Regarding the new panels, both the resources employed in shredding and curing are considered.

Back Cover

The back cover is a part that presents big dimensions, and its function is mostly aesthetic, as it consists of hiding (from the bartender and the coffee shop customer) and protecting (from dust and other undesired substances) internal components. S1 scraps, especially those of lower dimensions, deriving from the trim of the safety and drain holes and the sink profile, have been shredded and subsequently the back cover obtained from them, through cold cure. The main material composition and environmental impacts are compared in Table 2 and Fig. 2, respectively. All the investigated situations account for a reduction of CO2 emissions and line up as promising measures aimed both at combating climate change and achieving a successful application of the CE principles: what is produced from an industrial process is employed as raw material for a different product, attesting a reduction of natural resources exploiting.

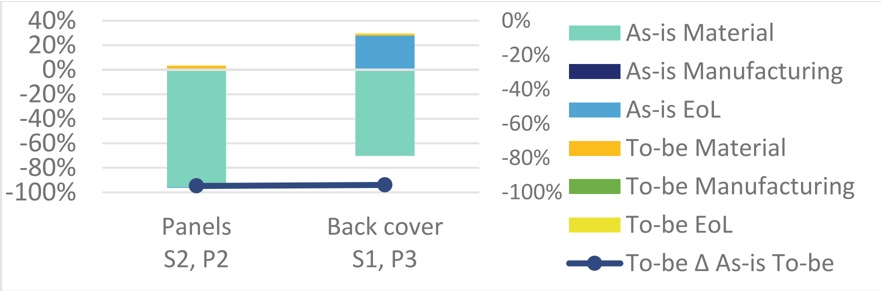

Fig. 2. Environmental impact comparison

4 Discussion

The present work proposed and applied an approach to join detached supply chains to give value to manufacturing scraps; therefore, the companies (C1 and C2) that produce the scraps unlikely phase cannibalization or low demand for remanufactured products, which is often a sore point that distresses enterprises and hampers circular initiatives, if not adequately exploited [12]. It lets enterprises overcome the main obstacles related to the lifecycle extension of composite materials. Furthermore, the use of scraps coming from sink is related to environmental benefits for the coffee machine production. As there was not any waste type suitable for the dimensions of the back cover (part dimensions), and any re-design could not offset this lack, an alternative process has been investigated. In the current state, the prototype has reached high finishing quality. However, the back cover's final appearance differs from the original one. This may hamper customer satisfaction, which expects to coat. Therefore, the back cover made of secondary raw material would be an alternative material for the customer, copper, satin or matte steel options.

The panel almost nullifies its environmental impacts; as it is employed in the process, it is one step toward the net-zero emission aimed by organizations. The benefits are due to avoided impacts related to the: i) extraction of the raw material; ii) EoL treatment and disposal of the scraps; iii) EoL treatment and disposal of P2 and P3. The choice of the target processes is a combination of factors: part and material features, functionalities, design constraints and environmental impacts. Once the waste exits the production plant perimeter, organizations lose any trace of their products and scraps. Direct interviews with downstream suppliers made the picture clear. Data, knowledge and information exchange could bring significant benefits to enterprises. More outstanding communication with actors in charge of dismantling processes improved the detail of modelling the EoL phase, outlining the actors and the steps, and what is done.

The introduction of economic assessment for the proposed de-manufacturing activities represents an improvement fo the present work and will be done in next activities. This would be the basis of the supply analysis. In fact, it may be hard to balance and optimize volumes and demand. While process waste might be slightly predictable (if intrinsic to the process), and thus known if the production volumes are known, the off-specification scrap availability is unpredictable and highly variable. Therefore, compensating strategies must be investigated.

S2 has a wide variety of scraps; some are available in a process and heterogeneous state and as virgin materials (i.e., fiberglass or PVC). The latter, rags of various dimensions (order between 1 E-2 to 7E-2 m), are discarded only because of their dimensions (they are too small for the whole blade) but may be reused in other processes since they are still virgin material. Alternative applications (i.e., processes that require smaller patches of fiberglass) can be further investigated.

5 Conclusion

The current approach is based on the milestone that designing for the CE involves giving new meaning to the EoL of products. The method presented in this work enables the valorization of composite materials, whose EoL management is currently highgly inefficient and unsustainable from the environmental perspective. Furthermore, the approach expects cooperation between multiple manufacturers active in different sectors so that they can apply cicular strategies.

The approach is relatively simple, well-known, and applied standardized methods and tools (i.e., LCA). The potential applicability is vast: the growing boom recorded for many industrial markets and applications in the composites industry provide multiple applications; moreover, the approach can also be applied to homogeneous waste materials. The novelty of the proposed method is in support the identification of employment of scraps to existing or new products instead of dismantlyign them. The first implementationof the proposed approach highlight interesting potentialities of establishing circular relationships among companies. In the first place, only components and scraps without special treatment were considered and studied to be employed as secondary raw materials. Chemical and thermochemical decomposition (i.e., pyrolysis, de-polymerization) were neglected, as they belong to the recycling action, which was aside from the focus of the study.

Two cases involved a re-design of production processes: the first concerns the production of panels for the wind sector (P2) (employed as consumables in the wind blades production process). The use of scraps from the wind blades' trimming (S2), after an intermediate step of shredding, almost eliminates the CO2 emission derived from the panel production. Also, the material of the back cover of an espresso coffee machine (P3) has been produced with shredded and cold-cured scraps of sinks (S1). Its production emissions are halved. The results show positive environmental effects. However, the application of the method outlines essential factors to consider while finding possible paths to establish successful IS: dismantler's involvement, information, networking, disassembly, simple shapes and short distances. Future works will focus on the economic evaluation of the proposed de-manufacturing actions and strategies supporting the materials' acquisition. The study might be extended to off-the-shelf components and investigate alternative applications for fiberglass patches and virgin material waste that are discarded only for their dimensions.

Aknowledgments. The activities are related to the project MARLIC "Marche Applied Research Laboratory for Innovative Composites", which is part of the project POR Marche Region FESR 2014–2020, Asse 1 – OS 2 – Intervento 2.1.1 e Asse 8 - OS20 – Azione 20.1 – Intervento 20.1.1.

References

1. Cappelletti, F., Rossi, M., Germani, M., Hanif, M.S.: A methodology to support companies in the first steps toward de-manufacturing. Proc. Des. Soc. **1**, 131–140 (2021). https://doi.org/10.1017/pds.2021.14
2. Cappelletti, F., Rossi, M., Germani, M.: How de-manufacturing supports circular economy linking design and EoL - a literature review. J. Manuf. Syst. **63**, 118–133 (2022). https://doi.org/10.1016/j.jmsy.2022.03.007
3. Sun, L., et al.: Energy-saving and carbon emission reduction effect of urban-industrial symbiosis implementation with feasibility analysis in the city. Technol. Forecast. Soc. Change **151**, 119853 (2020). https://doi.org/10.1016/j.techfore.2019.119853
4. Demartini, M., Tonelli, F., Govindan, K.: An investigation into modelling approaches for industrial symbiosis: a literature review and research agenda. Clean. Logist. Supply Chain **3**, 100020 (2022). https://doi.org/10.1016/j.clscn.2021.100020
5. Job, S., Leeke, G., Mativenga, P., Oliveux, G., Pickering, S., Shuaib, N.: Composites recycling. Where are we now? Composites UK (2016)
6. Mölsä, K.M., Horn, S., Dahlbo, H., Rissanen, M.: Linear, reuse or recycling? An environmental comparison of different life cycle options for cotton roller towels. J. Clean. Prod. **374**, 133976 (2022). https://doi.org/10.1016/j.jclepro.2022.133976
7. Perry, N., Pompidou, S., Mantaux, O., Gillet, A.: Composite fiber recovery: integration into a design for recycling approach, 281–296 (2014). https://doi.org/10.1007/978-1-4471-5544-7_14
8. Mangers, J., Amne Elahi, M., Plapper, P.: Digital twin of end-of-life process-chains for a circular economy adapted product design – a case study on PET bottles. J. Clean. Prod. **382**, 135287 (2023). https://doi.org/10.1016/j.jclepro.2022.135287
9. Aguiar, M.F., Jugend, D.: Circular product design maturity matrix: a guideline to evaluate new product development in light of the circular economy transition. J. Clean. Prod. **365**, 132732 (2022). https://doi.org/10.1016/j.jclepro.2022.132732
10. Boyer, R.H.W., et al.: Three-dimensional product circularity. J. Ind. Ecol. **25**(4), 824–833 (2021). https://doi.org/10.1111/jiec.13109
11. Fraccascia, L., Giannoccaro, I., Albino, V.: Rethinking resilience in industrial symbiosis: conceptualization and measurements. Ecol. Econ. **137**, 148–162 (2017). https://doi.org/10.1016/j.ecolecon.2017.02.026
12. Raza, S.A., Govindaluri, S.M.: Pricing strategies in a dual-channel green supply chain with cannibalization and risk aversion. Oper. Res. Perspect. **6**, 100118 (2019). https://doi.org/10.1016/j.orp.2019.100118

Engineering Education

Educational Test Bench for Full Field Vibration Measurements

Paolo Neri(✉), Alessandro Paoli, Armando Viviano Razionale, and Sandro Barone

University of Pisa, 56122 Pisa, Italy
paolo.neri@unipi.it

Abstract. Full-field methods can significantly improve measurement quality in experimental dynamic analysis, which is a critical issue in the industry. Optical methods based on digital image correlation (DIC) are widely used in this regard. This paper aims to present an experimental setup to perform full-field vibration measurements using off-the-shelf components costing tens or hundreds of euros rather than thousands. This allows for the construction of multiple measurement systems with a small investment, giving students hands-on experience. The system's inherent low cost, ease of assembly, and ease of use ensure that the student can handle the system from the design stage to the setup stage, and finally to the testing stage. A simple Matlab app was developed to set up and control the test, analyze data and display the results. The system's modularity allows it to further extend measurement capabilities over time, performing 2D measurements or more complex 3D measurements under single or multiple inputs. A prototype of the proposed system was assembled and tested on a planar specimen for 2D DIC measurements. The total cost of the equipment was less than 250 €. The setup was validated for geometrically complex torsional deformed shapes up to 660 Hz.

Keywords: Full Field Vibration Measurement · Digital Image Correlation · Educational Test Bench

1 Introduction

Optical methods based on industrial cameras and digital image correlation (DIC) are effective in improving measurement quality in experimental dynamic analysis. These methods have become increasingly popular in the industry due to their ability to provide high-resolution, full-field measurements that can accurately capture the deformation of a structure under dynamic loading. Full-field methods can identify local displacement values that may not be noticeable using traditional point-based measurement techniques. This can provide valuable insights into the performance of a structure and help in the development of more accurate models and simulations.

Depending on the specific measurement requirements, different hardware configurations can be used for DIC. For example, a single camera setup can be used for 2D measurements, while a stereo camera setup can provide 3D measurements. In addition,

M. Carfagni et al. (Eds.): ADM 2023, LNME, pp. 373–380, 2024.
https://doi.org/10.1007/978-3-031-52075-4_42

various types of illumination sources can be used to optimize image quality and contrast. High-speed camera setups can provide the highest acquisition frame rate in the dynamic analysis [1]. However, they are costly and result in low sensitivity measurements because of low sensor resolution. For this reason, there has been a growing interest in developing low-cost measurement setups that use conventional industrial cameras and alternative approaches methods to improve sensitivity and accuracy in vibration measurements. One approach is based on high-resolution low frame rate cameras and on the down-sampling strategy to use conventional cameras in dynamic analysis [2, 3]. Down-sampling refers to the process of reducing the sampling frequency of a signal to overcome the Nyquist-Shannon frequency limitation. The hardware cost of these systems is in the range of ten thousand euros, which is roughly one order of magnitude less than the cost of high-speed camera setups. As a result, a great number of research centers can use the technique for research and industrial purposes. Nonetheless, the cost for educational purposes remains prohibitively high, as at least one measurement system would be required for a couple of students to directly face the conventional measurement challenges. It is also worth noting that designing a measurement setup can be an integral part of the teaching experience since it presents a range of technical and practical challenges that require students to engage in critical thinking, problem-solving, and decision-making. In addition, it represents an interdisciplinary learning experience, requiring knowledge and skills from various subject areas (i.e., mechanical engineering, signal theory, image processing). Some attempts have been made in the scientific literature to describe the ideation and testing conditions of experimental architectures to pursue the active learning paradigm in the study of vibrating systems [4–7]. First- and second-order spring-damper systems were considered in [5, 7], while a setup to engage students with the experimental modal analysis of a physical system was conceived in [4]. A simple vibrating "build-at-home" system was instead ideated in [6] to provide a hands-on laboratory experience that could be remotely and safely undertaken by students during the COVID-19 pandemic. However, no evidence exists about the construction of an education low-cost test bench oriented to the vibration's measurement using optical full-field acquisition methodologies.

This paper presents an experimental setup to carry out full-field vibration measurements using off-the-shelf components that cost tens or hundreds of euros rather than thousands. Setting up a test bench for DIC measurements with a small investment cost allows for the construction of multiple systems, thus providing students with hands-on experience in using this technology for testing and experimentation. Because of the system's inherent low cost, ease of assembly, and ease of use, the student can handle the system from design to setup, and finally to testing.

2 Measurement Approach

To avoid the need for expensive high-speed cameras, the down-sampling approach is used in this research. In practice, through the down-sampling approach, high-frequency signals can still be acquired with low-frequency acquisition, if they contain only a single harmonic contribution of a known frequency. The aliasing phenomenon is used so that a high-frequency signal is detected as a fictitious low-frequency response. Indeed, provided that the vibration signal is purely sinusoidal (i.e., the component is excited with a single frequency sine wave) it is possible to demonstrate that the signal can be properly reconstructed even if the acquisition frequency (f_s) is much smaller than the vibration frequency (f_v), e.g. by using the following equation [8]:

$$f_s = \frac{f_v (n_s/n_p)}{1 + (n_s/n_p)k} \tag{1}$$

where n_s is the number of recorded frames, n_p is the number of fictitious full periods to be described (in the following, $n_p = 1$ will be used) and k is an arbitrary integer. From Eq. 1 it follows that, for a given vibration frequency, it is always possible to select a large value of k to find a value of f_s small enough to fulfill camera specifications. Even if this approach drastically relaxes the constraint on the sampling frequency, good quality acquisition still needs the exposure time to be sufficiently shorter than the vibration period, to avoid blur images. In this paper, a ratio of at least 10 between the vibration period and the exposure time was chosen, which proved to be sufficient to obtain reliable results.

3 Experimental Equipment

The educational test bench must be designed under one major constraint: the use of low-cost hardware is required to allow for the setup of a relatively large number of measurement systems at a low investment cost. Indeed, having only one system in the class would result in a limited experience for the students, requiring the teacher to perform most of the work while the rest of the class passively listens. On the other hand, one system available for every two students would allow the scholar to actively and directly face all of the experimental challenges, gradually gaining confidence and experience. Furthermore, the development of a low-cost setup reduces the risk of untrained students damaging expensive equipment, resulting in laboratory delays and a lack of self-confidence in the student during use.

The main steps to set up a DIC test bench for educational purposes are:

1. Hardware: the most critical aspect is the availability of the necessary equipment, such as a low-cost digital camera, a light source, an excitation device, and a stage to hold and excite the object under testing conditions.
2. Software: a DIC software package is required to analyze the images and extract displacement information. There are several DIC software packages available, some of which are free and open source.
3. Testing, analysis, and interpretation: images are captured while the object is under load. The DIC software is then used to process the images and extract the displacement information. The displacement information is then analyzed and interpreted to understand the mechanical behavior of the target object under test. This can involve plotting full-field displacement maps.

3.1 Hardware Setup

Excitation Device. The test bench is intended for desktop use, thus only small specimens can be tested, such as small beams or light components, and a low-power excitation source will be sufficient. Conventional modal shakers are unsuitable for this application because of their relatively high cost and the need for an external amplifier and signal generation board, which would drastically increase the system cost and reduce the ease of use. The market offers off-the-shelf, low-cost, extremely simple-to-use devices that can be controlled in frequency in the form of standard PC speakers, which are provided with an internal amplifier (standard bandwidth in the range of 20 kHz). Conventional speakers also have the advantage of being stereo devices, which means that two separate channels are usually available and multi-exciter setups can be easily created. On the other hand, PC speakers can introduce noise from a variety of sources, including poor quality of the audio board and amplifier, poor cable shielding, and poor moving parts quality. In the present paper, the speakers Tacens Anima AS1 USB speaker were selected, featuring an 8 W and 3.5 mm jack with a 2.0 channel configuration (cost lower than 6 euros). An M3 screw was glued in the center of the speaker, to allow a secure bolted connection of the specimen.

Illumination Source. High-frequency vibrations require short exposure time and, thus, high intensity and time-constant illumination. A simple and feasible solution is given by commercial home illumination devices such as LED spotlights. Low-cost and flicker-free spotlight are available on the market and can be directly powered through conventional 220 V electric sockets, such as the 7 W spotlight VRD 25_07 BI (Vivida International SRL, costing less than 8 Euros).

Digital Camera. The crucial component of the acquisition system, however, is given by the optical device, i.e. digital camera. A standard webcam would be a low-cost and simple solution. Nevertheless, all the low-cost digital camera devices on the market have unstable sampling frequencies, and they are based on rolling shutters, that may produce image artifacts when depicting fast-moving objects. To solve these issues, an industrial camera was adopted in this research. A DMK 41BU02 (The Imaging Source, 1.2 Mp) was selected, allowing for a reliable sampling rate and image quality, to validate the measurement approach. The cost of the camera was lower than 250 Euros. It is worth noting that ArduCam devices [9] represent a low-cost and promising alternative, offering global shutter cameras with interesting sampling rates for about 50 Euros. These devices will be considered in future developments.

Independent Vibration Sensor. Significant vibration amplitudes can be obtained only near specimen natural frequencies that are unknown in advance. An external vibration sensor could be used to measure the component response in a wide frequency range and detect the response peaks of interest. Microphones represent a low-cost solution capable of sensitively measuring vibrational response without requiring fancy electronics, since they provide a signal that is proportional to sound intensity and, thus, to vibration amplitude. Furthermore, all modern laptops include embedded microphones, meaning that the sensor is already available in the majority of acquisition environments. The standard available sampling frequency is approximately 8 kHz, limiting the acquisition capabilities to 4 kHz, which is sufficient for educational purposes. All the described equipment is shown in Fig. 1(a), while a front view of the tested specimen is shown in Fig. 1(b).

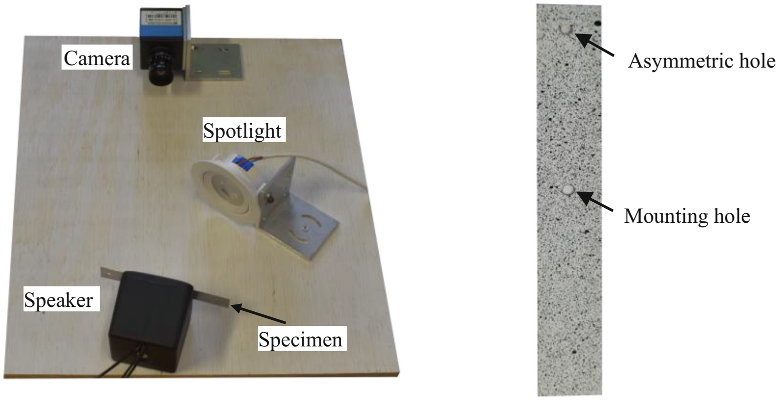

(a) (b)

Fig. 1. Experimental devices: (a) hardware setup and (b) specimen detailed view.

3.2 Software Architecture

Vibration acquisition requires the synchronization of various devices for structure excitation and image acquisition. Furthermore, the software could assist the test setup by experimenting with different loading conditions and suggesting possible acquisition parameters, such as those shown in Eq. 1. To this extent, a Matlab app was developed to control the USB camera, microphone, and speakers. The app's main controls allow the user to connect to the camera, start and stop the preview, and begin the actual acquisition (i.e., saving the required frames). Two signals were implemented in this research: purely sinusoidal and periodic sweep. The purely sinusoidal signal will be used to excite the selected mode shape during camera acquisition. The sweep excitation source, on the other hand, can be used during test setup: the structure is excited in the desired frequency range, while the microphone records the response. The recorded signal's Fast Fourier Transform can then be computed to detect any response peak in the measured frequency range, which can then be used to select the resonance frequencies. It is worth noting that any excitation signal can be designed and easily used during testing if needed (e.g. for bandpass excitation, as investigated in [10]). After the acquisition, DIC is performed by using the 2D algorithm cited in [2], which allows to define the measurement grid and to select the main DIC parameters, such as the subset size (which represents the dimension of the region of interest around a measurement point to be considered for the correlation process in the DIC algorithm).

4 Experimental Results and Interpretation

An experimental campaign was performed to assess the performance of the described system, and to assess its measurement capabilities despite the extremely low cost of the equipment. A rectangular aluminum plate was used as a testing specimen (20 × 130 × 0.5 mm). A first hole was drilled roughly in the middle of the specimen for speaker connection, and a second hole was drilled close to one edge to add additional asymmetry to the structure and investigate the reliability of the results, as shown in the following. The frequency range of 100–700 Hz was investigated and excited with the sweep function, showing several different peaks in the microphone signal. In particular, two peaks, found at 647 Hz and 660 Hz, were investigated. Given that the camera's minimum available exposure time is 2^{-13} s, the ratio between the period of the 660 Hz vibration and the minimum shutter time is approximately 12, which was deemed sufficient to obtain still images and allows to investigate the system's limit. Purely sinusoidal tests were performed for both frequencies, recording the plate response. The displacement maps obtained with the DIC algorithm are reported in Fig. 2. As can be seen, the full-field maps evidence a torsional deformed shape of the plate, providing low noise measurements. It is worth noting that, since only a single camera was used, a 2D measurement was obtained and displacements are measured in pixels. Figures 2(a) and (b) highlight an interesting property of the structure: if the test was performed in perfectly symmetric conditions (i.e. plate geometry and material, boundaries and load) a single mode shape would be found showing a symmetric deformation of the plate between the left and right portion (with respect to the central mounting point).

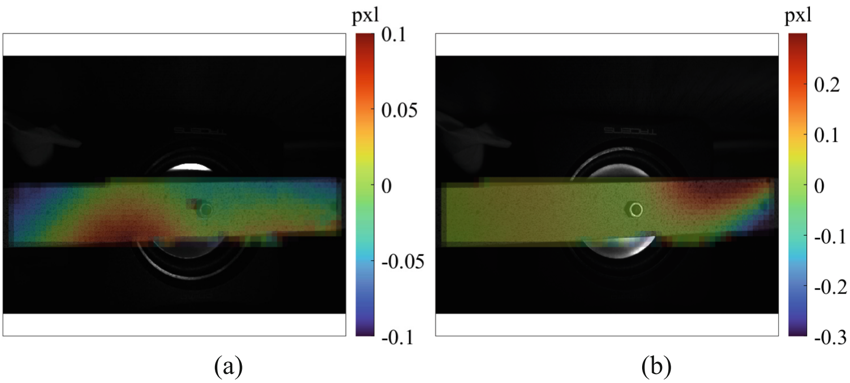

Fig. 2. Displacements along the horizontal direction at (a) 647 Hz and (b) 660 Hz.

Experiment results, on the other hand, show the presence of two distinct modes with slightly different frequencies and a similar mode shape, but having displacement localization on the two opposite edges of the plate. This phenomenon is common any time that the symmetry of a theoretically symmetric structure is broken in practice by some experimental condition. In this case, the deviation from symmetry is caused by a non-perfect placement of the central hole and the presence of a further hole close to the right edge of the plate. The deviation between theoretical and experimental response is a worthy finding derived from the really simple presented testing setup, and could help the students to gain sensitivity to experimental challenges. A further investigation is to be referred to the right edge of the plate, with particular reference to Fig. 2(b). The figure shows that the DIC results are good also in the plate region where the second hole was drilled. This could be counterintuitive, since the speckle pattern is not available in the hole region and, thus, DIC should fail. The computation of meaningful data in the presented results is due to the chosen subset size. The results in Fig. 2(b) were obtained by using a subset size of 21 pixels, which is larger than the image's hole dimensions. Thus, the obtained results show the displacements' mean value related to the region surrounding the hole. Figure 3(a) shows a detailed view of the results around the hole region, with a subset size of 21 pixels.

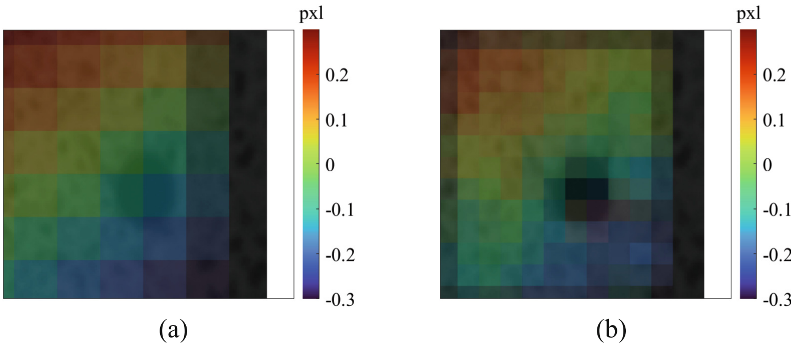

Fig. 3. Zoomed view of the hole region with a subset size of (a) 21 pixels and (b) 7 pixels.

This can be further investigated by using a smaller subset size in the DIC algorithm, such as 7 pixels. In this case, the hole is larger than the subset, so the DIC algorithm is unable to compute any displacement value in the hole region. This is illustrated in Fig. 3(b), which depicts a detailed view of the hole region with a subset size of 7 pixels. The comparison of the results can help students to understand the significance of this algorithm parameter: larger values of the subset size can provide higher correlation accuracy and, as a result, higher measurement sensitivity. Enlarging the subset, on the other hand, results in averaging the displacements of a larger region of the specimen, thus smoothing gradients, and reducing detail levels.

5 Conclusions

This paper describes a test bench for DIC vibration measurements that was created for educational purposes. The main constraint of the equipment is cost reduction, which allows for the development of a relatively large number of test benches with a small investment, providing hands-on experience even for a large number of students. By carefully selecting the hardware and signal processing techniques, it is possible to achieve high-frequency, high-sensitivity measurements that can provide valuable insights into the behavior of structures under dynamic loading. The experimental equipment is composed of a PC speaker, a global shutter digital camera, a LED spotlight and a microphone. The total cost of the setup was less than 250 Euros, which can be further reduced by adopting newly introduced low-cost global shutter digital cameras. The system was capable of measuring vibrations at high frequencies up to 660 Hz with sub-pixel sensitivity. The measurements also allowed to investigate the impact of the subset size, which is an important parameter in DIC algorithms. The modularity of the developed system would allow for simple future developments, such as the addition of a stereo camera setup (3D DIC), and the extension to multi-input excitation measurements. These assumptions ensure that the test bench can be expanded during the course, allowing for the investigation of many different aspects of the use of optical devices for vibration measurements. A thorough investigation of the feedback received by students in classes would be needed to assess the equipment's effectiveness for didactic purposes, which will be the subject of future developments.

References

1. Beberniss, T.J., Ehrhardt, D.A.: High-speed 3D digital image correlation vibration measurement: recent advancements and noted limitations. Mech. Syst. Signal Proc. **86**, 35–48 (2017)
2. Neri, P., Paoli, A., Razionale, A.V., Santus, C.: Low-speed cameras system for 3D-DIC vibration measurements in the kHz range. Mech. Syst. Signal Proc. **162**, 108040 (2022)
3. Fruehmann, R.K., Dulieu-Barton, J.M., Quinn, S., Tyler, J.P.: The use of a lock-in amplifier to apply digital image correlation to cyclically loaded components. Opt. Laser Eng. **68**, 149–159 (2015)
4. Di Carlo, S., Benedetti, L., Di Gialleonardo, E.: Teaching by active learning: a laboratory experience on fundamentals of vibrations. Int. J. Mech. Eng. Educ. **50**, 869–882 (2022)
5. Podrzaj, P., Regojevic, B., Kariz, Z.: An enhanced mechanical system for studying the basics of control system dynamics. IEEE Trans. Educ. **48**, 23–28 (2005)
6. Schajer, G.S.: A build-at-home student laboratory experiment in mechanical vibrations. Int. J. Mech. Eng. Educ. **50**, 240–252 (2022)
7. Liu, Y.C., Baker, F., He, W.P., Lai, W.: Development, assessment, and evaluation of laboratory experimentation for a mechanical vibrations and controls course. Int. J. Mech. Eng. Educ. **47**, 315–337 (2019)
8. Neri, P., Paoli, A., Razionale, A.V., Santus, C.: Time-domain image filtering for DIC vibration measurements. J. Phys. Conf. Ser. **2041**, 012008 (2021)
9. ArduCam. https://www.arducam.com/product-category/uvc-usb-camera-module/usb-uvc-global-shutter-cameras/. Accessed 20 Feb 2023
10. Neri, P.: Frequency-band down-sampled stereo-DIC: beyond the limitation of single frequency excitation. Mech. Syst. Signal Proc. **172**, 108980 (2022)

Holistic Scientific-Technical Communication: A Teaching Proposal

Edoardo Rovida and Roberto Viganò(✉)

Department of Mechanical Engineering, Politecnico di Milano, Milan, Italy
{edoardo.rovida,roberto.vigano}@polimi.it

Abstract. Technical-scientific communication is essential, particularly for engineers, because they work in interrelationships with others. Such communication is characterized by three fundamental aspects: graphical, written, and oral transmission. In addition, each communication includes a system of signs and rules, some defined by standards, others adopted in a specific context, allowing information transmission. Finally, essential requirements of any communication are completeness, immediacy, and non-ambiguity. In general, most information exchanges integrate these forms and requirements. Still, they must also consider many aspects that lead to thinking of technical communication as "holistic communication". Considering the importance of technical-scientific communication in the professional career of engineers, the teaching programs in Engineering schools have begun to include specific activities and experiences to improve the students' communications skills. Authors think it is necessary to consider these experiences holistically to allow the students to select the kinds of media concerning the information content and reflecting the audience's needs. This approach could be similar to the design for X approach and may be considered a "communication for X" approach.

Keywords: Technical communication · Engineering Education · Technical product documentation

1 Introduction

The communication consists of some fundamental elements:

- Initial behavior - that is the starting point of the communicative process.
- Terminal behavior - that is the arrival point of the communicative process.
- Structure of the contents - the set of concepts that needs to connect initial and terminal behavior.
- Communication unit - part of the communication devoted to transmitting a concept.
- Communication means - the medium used to transmit a set of concepts.

Communication engages people, so the use of the name "behavior" in this field is based on the consideration that a human being behaves concerning the acquired knowledge. For this, the terminal behavior could be observed as divided into three components:

M. Carfagni et al. (Eds.): ADM 2023, LNME, pp. 381–388, 2024.
https://doi.org/10.1007/978-3-031-52075-4_43

Informative, which is acquiring knowledge; Critical, which is the ability to reason on the knowledge gained; Practical, which is the ability to apply the knowledge.

To get the "terminal behavior", it is necessary to organize the communication in basic units that allow the transmission through rules (RUL) and examples (EG), where (RUL) can be related to the informative component and (EG) to the critical/practical components. In that manner, the structure of the communication can assume two different approaches to transmission:

- RULEG - Rules before examples - Deductive approach
- EGRUL - Examples before rules - Inductive approach

The effectiveness of the transmission of the communication requires a validation phase which is the verification of the "terminal behavior" obtained [1, 2]. In the logical schema of the communication (Fig. 1), the source aims to structure the communication as a transition from the "initial behavior" to the "terminal behavior", corresponding to the recipient's behavior after acquiring the transmitted knowledge. The transmission is the link between knowledge and a system of signs through a physical medium that influences communication because it requires coding and decoding the concepts. After perceiving the transmitted signs, the recipient acquires the contents, which may differ from those intended due to unavoidable communication disorders. For this, this transmission chain corresponds, in a symmetric manner, to the validation chain to verify the reached level of acquisition of the transmitted knowledge.

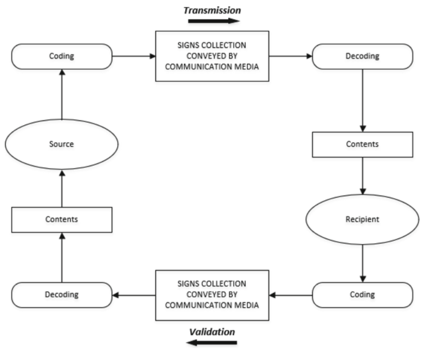

Fig. 1. Logical schema of the communication.

2 Technical Communication and Its Holistic Frame

Technical communication in design refers to the exchange of technical information between various stakeholders involved in the designing and manufacturing of things [3]. Effective technical communication is crucial for ensuring the design specifications and requirements are accurately understood, preventing miscommunication and rework, and improving overall project efficiency. In design, technical communication occurs through various media, including written documents, drawings, visual aids, and presentations.

Technical reports, design specifications, and product manuals are common written documents used to communicate technical information. Illustrations, such as engineering drawings and schematics, are also essential for conveying product design, assembly, and functionality information. Today, visual aids, such as 3D models, prototypes, and animations, can also be used to help stakeholders understand complex systems. Good technical writing skills are crucial for effective technical communication in design but also require collaboration abilities and teamwork. Design teams should regularly communicate and share information to ensure that all stakeholders are aligned and have a shared understanding of the design specifications and requirements. Team members should also be open to feedback and be willing to make changes based on suggestions and recommendations from other stakeholders. Technical writers should have a solid understanding of engineering concepts and industry standards and effectively communicate technical information clearly and concisely. They should also be familiar with technical illustration and drafting techniques and understand the tools and technologies used in the design, such as computer-aided design (CAD) software.

Technical communication in design can also be viewed from a more holistic perspective. This holistic approach would consider the impact of technical communication on the entire design process, including the design methodology, team dynamics, and project outcomes [4, 5]. From this perspective, technical communication is considered an integral part of the design process, not just a means of conveying technical information. How technical information is communicated can influence the design methodology, team dynamics, and project outcomes. For example, using visual aids such as 3D models and animations can help to facilitate a more collaborative design process, with team members able to understand better and contribute to the design. On the other hand, poor technical writing skills can lead to miscommunication and misunderstandings, resulting in errors, rework, and delays. The holistic approach to technical communication in design also recognizes the importance of considering the needs and perspectives of all stakeholders. Effective technical communication requires a deep understanding of the audience, including their technical expertise, level of knowledge, and requirements. Therefore, technical communicators should strive to provide information in a clear, concise, and accessible manner tailored to the audience's needs. Finally, the holistic approach recognizes the importance of continuous improvement in technical communication. This may include incorporating new technologies, such as augmented reality and virtual reality, to enhance the communication of technical information.

A holistic approach to teaching technical communication in engineering courses focuses on teaching the technical aspects of communication and developing the broader communication skills needed for effective and successful engineering practices. This approach considers the various forms of communication that engineers engage in, including writing, speaking, and visual representation. Such an approach would also emphasize the importance of considering the audience and purpose of the communication and the ethical and cultural aspects inherent in technical communication. In this way, students are equipped with not just the technical knowledge but also the communication skills necessary to effectively convey their ideas and collaborate with others in their field. Overall, a holistic approach to teaching technical communication in engineering courses can help produce well-rounded engineers who can effectively communicate and collaborate with others in their field, which is crucial for success in today's rapidly changing and globally connected engineering landscape. There are several ways to implement a holistic approach to teaching technical communication in engineering courses:

1. Incorporating a variety of communication genres: This can include teaching students how to write technical reports, give presentations, create visual aids, and engage in team communication.
2. Emphasizing audience awareness: This involves teaching students to consider their audience and tailor their communication accordingly. For example, they may need to communicate technical information to a non-technical audience or international colleagues with different cultural backgrounds.
3. Integrating ethics and culture: This involves teaching students to consider ethical and cultural issues when communicating, such as avoiding plagiarism and considering cultural differences when presenting the information.
4. Encouraging collaboration: Group projects, peer review, and team-based presentations can help students develop communication skills while allowing them to practice working with others.
5. Providing real-world context: Assignments and projects based on real-world problems or industry-relevant scenarios can help students understand the importance of effective communication in their future careers.
6. Incorporating technology: Technology, such as video conferencing and online collaboration tools, can help students develop virtual communication skills, which is becoming increasingly important in the modern engineering landscape.

By incorporating these strategies, engineering educators can help students develop communication skills that will be valuable in their professional lives.

3 Implementation

The industrial product includes a wide range of information that is mainly needed for its physical realization but follows its entire life cycle (Fig. 2) [6]. This information is constantly developing; it changes and evolves with technology and new production scenarios. Teaching the rules of writing and reading this information follows the same evolution, adapting to the new symbols of the normative that support the language. This is dictated by the need to provide the student with the tools to understand the information correctly. For this, the information that has to be conveyed could be divided and arranged differently to favor more effectiveness of the message transmitted. This subdivision could happen in the function of a specific topic or concerning a well-defined communication goal. This approach could be defined as a Communication for X (CfX) [8] in parallel to the most know concept of Design for X (DfX). As well as the DfX (Design for X) concept indicates the operations and criteria able to improve the behavior of the product in the "X" phase of its life cycle, where "X" could mean: "manufacturing", "assembly", "distribution", and so on, CfX concept might be adopted to express the communication associated to the "X" phase of the same cycle. The dashed links shown in Fig. 2 represent the communication required in every phase of the product life cycle. Therefore, such a figure can be a significative example of holistic communication and confirm that communication follows all phases of a product's life.

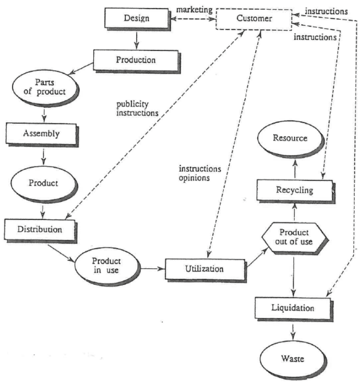

Fig. 2. Life cycle of the product.

Teaching the language, and particularly the signs, is necessary to allow them to convey information in a technical field. Still, the educational field also requires us to give the students the capacity to understand the technical reasons for the signs. So, rather than simply presenting a list of signs to which product features and quality requirements refer, focusing on the product's functionalities can help students better understand why certain features and quality standards are necessary. In this manner, students can see the bigger picture and understand how all the different features and requirements work together and how the various pieces fit together and contribute to the overall function of the product. Emphasizing the functionalities required of the product asks the students to develop a deeper understanding of the underlying principles and concepts that govern the product's design and give them a solid foundation in the field's fundamental principles. Independently by the specific sign language adopted, which could change in the future as they changed in the past, leaving unchanged the technical and quality functions required for the product. For example, the roughness sign changed over time, but the quality needs for the functional surface defined by the symbol remained the same from a physics and engineering point of view. To implement this approach in a holistic communication manner, it is possible to use various techniques and strategies to engage students:

- By using real-world examples of products that students are familiar with can help them better understand the functionalities required and how different features and requirements contribute to the overall function of the product.
- Encouraging students to engage in group discussions and work on hands-on projects actively, they will be actively involved in the learning process. A collaborative learning environment allows students to share their insights and learn from each other, which can help to deepen their understanding of the material.
- Providing visual representations of the product and its features, such as videos and animations, can help students better understand how everything works together.
- Rather than simply presenting a list of features and requirements, emphasize the problem-solving process that goes into designing and building a product. By showing students how engineers and designers approach problems and develop solutions, you

can help them to develop a deeper understanding of the underlying principles and concepts that govern the field.

So, as an example of the first implementation manner proposed, it is possible to involve students in discussing a simple can crusher tool by showing them an animation of the system during its use (Fig. 3), extracting the organs used for the crushing movement [7], and focusing them on the assembly surfaces engaged in the mechanism.

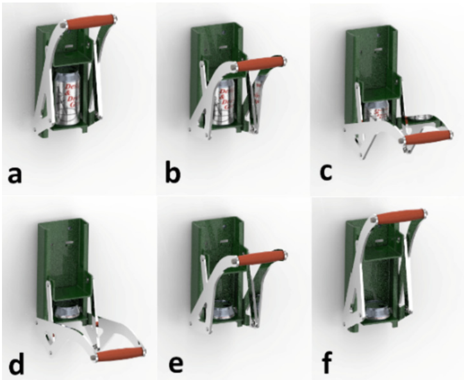

Fig. 3. Animation sequence of a can crusher.

In this part, the physical phenomenons involved can also take into consideration to under light the importance of the materials adopted and their performances. When the full functionalities of the tool are straightforward, it is possible to introduce the technical requirements and the quality aspects needed to guarantee its work. Finally, it is possible to engage students on the choice of the better communication system that could be adopted to transfer that information into a specific contest and introduce the set of signs required for that communication. So, 2D, 3D, assembly, and exploded drawings could be brought as examples for the production, and rendering, animation, and virtual visual tools as examples for marketing and maintenance.

Although the practical application of the CfX concept could require many words and ample space, a simple example be given here. Suppose the communication is focused on explaining the basic information needed to guarantee a good assembly between parts. In that case, the initial focus should be on the coupling needs, underlining the functional surfaces that interact in the assembling, what constraints they generate, and the required quality. Topics should include materials, manufacturing, and assembly techniques. The communication focus (X) could be declared as the information required to "identify the functional surfaces for a product". Only when the assembly properties framework is completed, it will be possible to face the question of how that information could be transmitted. This is influenced by the receiver and the contents that must be sent. So it is possible to send an assembly drawing (Fig. 4), where the functional surfaces and their quality must be identified using engineer knowledge and experience, transmit a 3d model (Fig. 5) where colors highlight the functional surfaces of any single part and engineering and quality knowledge is less required, or finally, define a detailed drawing

(Fig. 5) where standard signs describe the functional concept and the quality of the surface and where to the engineering knowledge must be associated a good known of the symbols.

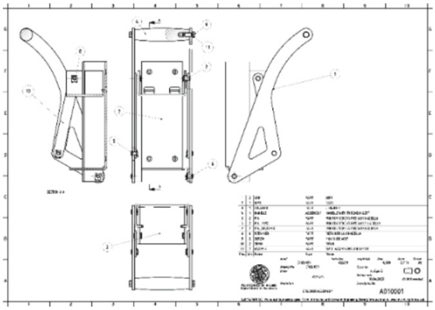

Fig. 4. Assembly drawing of the crusher.

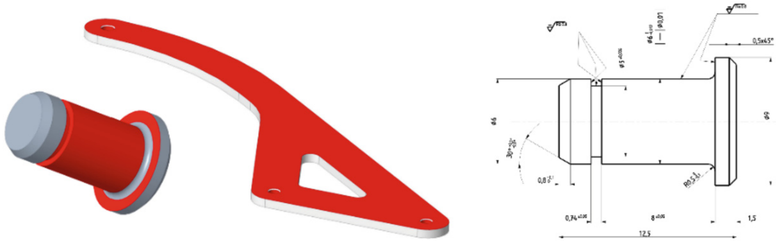

Fig. 5. Pin and arm 3D parts of the crusher with functional surfaces highlighted (left) and detailed drawing of the crusher pin (right).

The approach permits them to understand that different kinds of communication and tools can obtain the same goal and must be adopted concerning the contest where the communication happens. Furthermore, it also aims to teach that communication must be designed concerning the contest and the stakeholders involved [8]. CfX could also help characterize the properties of the communication in the different phases of the product's life cycle. For example, although the information about the product could be the same, the manufacturer's communication might differ for technicians operating in distribution or maintenance fields. Any different task has different requirements that should be reflected in different initial and terminal behaviors besides the structure of the contents. Teaching the product functionalities in an aseptic manner concerning the language that will be adopted to communicate them has another vital purpose. In fact, for example, standard signs adopted in drawings change over time according to the technic evolution, but their functional aim is not. Teaching students the most up-to-date signs is important because it will prepare them to work with the most current standards and technologies, but, at the same time, it's also essential for students to learn about the history of technical drawings and the evolution of symbols. A holistic approach to the communication of the product can give them a deeper understanding of the field and help them to interpret better older signs included in drawings and documents still in industrial use.

4 Conclusions

The conclusions can start from the consideration of the word "holistic": whose etymology means all, whole, global, and the word comes from the current philosophy of "holism" [9]. Holism is a philosophical concept that suggests that the whole is more significant than the sum of its parts. In other words, it is the idea that systems and phenomena should be viewed as a whole, not just as a collection of individual parts. This approach emphasizes the interconnectedness of things and the idea that everything is interdependent. Therefore, it is reductive to understand reality by considering its individual components. Observing that technical communication is in continuous evolution in both its general logic and tools, but particularly, in relation to technological developments and to the evolution of production scenarios, the teaching of communication is called to follow this evolution, not only explaining the symbols but also highlighting the engineering causes that determined them. For this, it is necessary to consider communication holistically, where the whole communication aspect must include chronological and historical elements. In addition, communication has to consider another important aspect, i.e., the target: the formalization of the initial and terminal behavior that are the communication's starting and arrival points. By considering such two factors, it is possible to make available the communication of a large number of recipients of very varied preparation.

Starting from these observations, a didactic plan should consider the aspects mentioned above, permitting the implementation of communication learning, which could also include some historical-critical considerations on the evolution of engineering.

References

1. Markle, S.M. Good frames and bad – a grammar of frame writing (1964)
2. Gavini, G.P. Manuel de formation aux techniques de l'enseignement programmé. Hommes et techniques (1969)
3. Lannon, J.M., Gurak, L.J. Technical communication, MLA update. Pearson (2017)
4. Smart, K.T.: Defining quality in technical communication: a holistic approach. Tech. Commun. **42**(3), 474–481 (1995)
5. Ingelsson, P., et al.: Taking a holistic perspective on technical communication and lean. Qual. Innov. Prosperity **19**(2), 103–122 (2015)
6. Asimov, M. Introduction to Design (1962)
7. Hansen, C.T., Andreasen, M.M.: Two Approaches to Synthesis Based on the Domain Theory. Springer, London (2002)
8. Rovida, E., Viganò, R. Communication for X (CfX): a contribution to the design for sustainability. In: Proceedings of the 7° International Conference on Technology and Quality for Sustained Development, pp. 615–618. AGIR Publishing House (2006)
9. Nicola, U. Atlante illustrato di filosofia Giunti (2003)

VR Lab: An Engaging Way for Learning Engineering and Material Science

Beatrice Aruanno(✉), Francesco Tamburrino, Paolo Neri, and Sandro Barone

Department of Civil and Industrial Engineering, University of Pisa, Pisa, Italy
beatrice.aruanno@ing.unipi.it

Abstract. In recent years, virtual reality technology has grown more widely available. This creates new opportunities and methods in the field of education, particularly for STEM (science, technology, engineering, and mathematics) disciplines. This study describes the design and the development of an immersive virtual reality laboratory (VR Lab) that aims to introduce novel activities and practical experiments in the field of industrial engineering and material science that can be highly beneficial for students. The laboratory enables students to experience and learn the macro and micro behavior of various engineering materials. The VR Lab is designed as an open-space room that is digitally divided into multiple learning stations, each of which is dedicated to a specific aspect of the subject. A virtual mechanical tensile test machine may operate with various materials and display the results by combining finite element analysis simulations and stress-strain curve. In another station, students can be transported inside atomic and molecular structures of various materials and can investigate how dislocations and slipping planes influence the mechanical behavior of metals or how the alignment of molecular chains affects the strength of polymers. Immersive VR Lab showed great potential for education. The developed virtual learning stations can be used to complement learning activities and physical experiments that are generally too risky, too expensive, or simply too time-consuming to be carried out in a real classroom, particularly in the STEM area.

Keywords: Virtual Reality · Engineering Education · VR Lab · Material Science Teaching · STEM

1 Introduction

In the past, virtual reality (VR) experiences were used in different fields including military training, flight simulator, and the entertainment industry. However, they were limited due to their technological features and price. In the last decade, the number of experiences has grown notably with the introduction of some consumer-oriented immersive VR headsets. Devices like the HTC VIVE, Meta Quest, and Sony PlayStation VR opened up new opportunities and markets [1]. Today, VR gained interest in numerous fields such as healthcare, industry, gaming, training, education, and cultural heritage [2–4].

Three methods are generally used to experience VR environments: desktop computers, Cave Automatic Virtual Environment (CAVE), and Head-Mounted Displays (HMD).

M. Carfagni et al. (Eds.): ADM 2023, LNME, pp. 389–396, 2024.
https://doi.org/10.1007/978-3-031-52075-4_44

Desktop VR allows users to interact with digital content using peripherals like a monitor, mouse, keyboard, or touch screen. A CAVE is a physical space where the walls, floor, and ceiling act as projection surfaces. Users in the CAVE equip stereoscopic glasses that are tracked to adjust the projected images and allow interaction with the visual content [5]. Recent HMDs are devices that incorporate small display optics placed in front of the eyes when it is worn on the user's head. They track the orientation of the head and, in some cases, also the position of the user [6].

One feature that distinguishes the different VR systems is the level of immersion. It can be described as the extent a user feels like part of the virtual environment and can shut out the outside world [7]. Accordingly, only the CAVE and HMD-based system can be defined as immersive virtual reality (IVR) technologies because lead to a higher sense of presence and immersion compared to desktop VR.

A century ago, Dewey [8] proposed the concept that students should learn by doing. This argument is likely to be realized today with IVR. Through the use of IVR scenarios in the classroom, students become more involved in their education and shift from a passive to an active state of learning. Hence, a student-centered strategy like this one strengthens the practical problem-solving skills that students need, particularly for STEM disciplines. The cognitive and pedagogical advantages of utilizing IVR in engineering education have been demonstrated by numerous investigations [9]. However, the design should maximize the students' learning experiences and be validated through testing with engineering students and educators for further improvement [10].

This aspect becomes even more evident with workshops, practical work, and laboratory activities, which play an important role in delivering essential knowledge. Physical activities, such as lab experiments, have numerous limitations for universities, including safety, equipment, space, and budget. The traditional learning approach in the STEM area is usually done through oral lectures in a classroom with the support of a board, projector, and computer. The adoption of IVR laboratories based on HMD technologies can arise students' interest and deepen their understanding of complex theories. Furthermore, the use of an IVR lab could give the possibility to distance-learning students or students with special needs to benefit from the laboratory experience as the students on campus [10].

Based on these concepts, this work presents an immersive VR Lab for engineering and material science education that aims to engage students in the discovery of the macro and micro behavior of various engineering materials.

2 The VR Lab

The VR Lab has been designed and developed starting from the need of engineering and material science educators to have a complementary tool that can be used in conjunction with the traditional learning approach. The possibility of actively engaging students in immersive experiences arouses interest in professors of the STEM disciplines.

The virtual laboratory aims to improve student's learning experience and comprehension of the mechanical behavior of different materials (principally metals and polymers) in different situations from the macro and micro points of view. For instance, students can experiment with different deformation behaviors and find the reasons behind the materials' performances by analyzing the molecular structure of the material. An advantage of the VR Lab is its modularity. It is subdivided into multiple learning stations, each focused on a specific aspect of the main topic. This is particularly important in IVR educational experiences. Studies realize that simplifying and focusing on virtual environments can limit students' distractions [11]. However, considering the vast amount of information and aspects that can be addressed in the field that combines engineering with material science, this modular approach allows further development and add-ons to the original laboratory without altering the previous parts.

2.1 The Design and Interaction of the Learning Stations

To design the virtual environment and manage the interaction between the VR Lab and the user, the software Unity has been used with the SteamVR plugin. The 3D models that are included in the environment have been realized with 3D CAD modeling software like Solidworks and Blender.

An important aspect that drove the design of the VR Lab was that the user could feel immersed in the VR environment and could freely move and interact with the virtual elements. A desktop VR solution could not have had the desired immersion level. On the other hand, a CAVE system requires a dedicated infrastructure and space that cannot be feasible for some institutions or at the students' homes. For these reasons, we decided to adopt the HMD-based technology, in particular the VIVE Focus 3 device, one of the last-generation wireless HMDs. According to the literature, some users can experience side effects like dizziness or headache while wearing HMDs [12]. The 5K resolution of the LCD panels and the visual refresh rate till 90 Hz aim to limit them. The ergonomic shape, the limited weight, and the long-lasting battery allow a comfortable wireless VR experience. Furthermore, the device allows the position and rotation tracking of the body, head, and hands of the user to improve the feeling of immersion and presence [13]. To interact with the virtual objects and machines the user has two motion-tracked handheld controllers. To debug and run the VR Lab the devices was connected to an MSI GE66 Raider laptop (Intel Core i7–10870 x64, RAM 32Gb, NVIDIA GeForce RTX3060) using VIVE Business Streaming. It allows connecting the VIVE Focus 3 to a PC, wirelessly or with a USB cable, and renders more complex applications with low latency.

The VIVE device is designed for room-scale setup. It means that the user can define a "play area" up to 10 m x 10 m in which can freely move and walk. The VR Lab has been designed to replicate these dimensions. If the area available in the real world is smaller, the user can use teleportation to reach every point in the VR Lab. Teleportation is a common locomotion technique in VR. The user specifies the destination by pointing at the desired area, usually by the tracked handheld controller. When confirmed the action, usually with a button press, the user is instantly moved to the destination. This technique has been widely adopted in VR because it generally does not cause motion sickness [14]. In the VR Lab, the user visualizes some deformable 3D model of default hands that follow the fingers' position and actions performed on the controllers. For example, when the user grabs something by pressing the grip button, the fingers close around the object. The VR Lab is subdivided into three different learning stations: a tensile test station for the macro behavior of multiple engineering materials, and two stations for the micro behavior of metals and polymers.

2.2 Tensile Test Station: Macro Behavior of Materials

The first learning station aims to teach how different materials behave in a mechanical tensile test. Figure 1 shows the main elements of the station. The application suggests the user teleport in front of the tensile machine (f). From this position, the user can grab one among the different specimens on the shelves (a) and place it between the two grippers (b). To start the test the user needs to press the green pushbutton (c). At this moment, the 3D model of the specimen deforms while the screen on the left displays the progress of an example stress-strain curve of the specific material (d). In the meantime, a video of the finite element analysis (FEA) shows the stress distribution on the specimen (e).

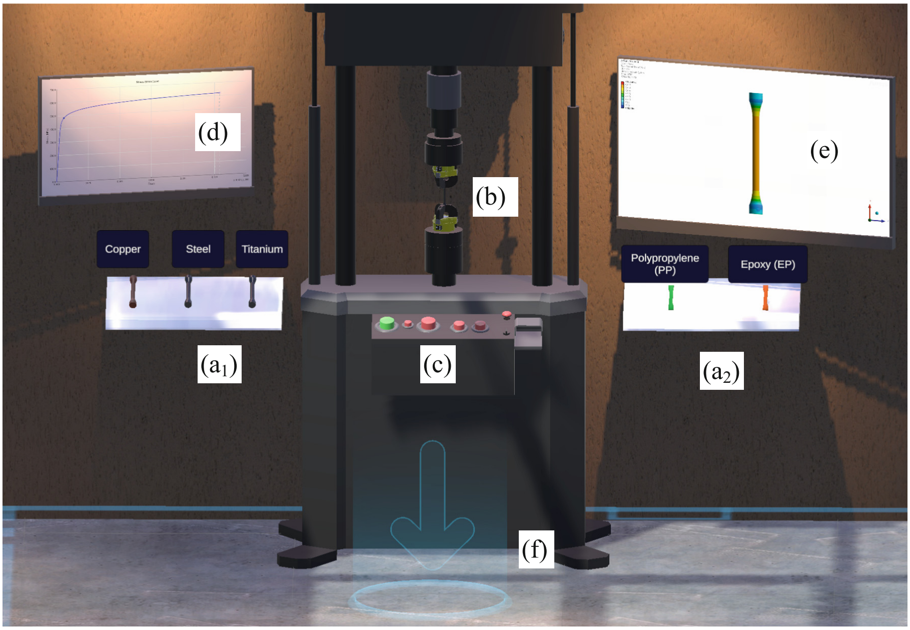

Fig. 1. The tensile test station.

Five different specimens are aligned: three metals (a_1: copper, steel, and titanium) and two polymers (a_2: polypropylene, and epoxy). The choice behind the three materials is to exemplify some of the major different mechanical behavior (3D model deformation, stress-strain curve, and stress distribution by numerical simulation) in a tensile test. Furthermore, each metal has a different atomic lattice structure and the two polymers are examples of thermoplastic and thermosets materials. These classes will be described more in depth in the dedicated learning stations. However, the proposed material library can be easily extended to numerous other materials.

The results of the numerical simulation visualized during the test (Fig. 1 (e)), is used to exploit the potentiality of the VR environment, augment information and provide an insight into the results, which would not be visible in an actual test. The geometry of the specimen is meshed with brick elements, and a bi-linear material model is used to represent both the elastic and the plastic behavior during the test. The properties can be adjusted to any different material. A static analysis is then performed, imposing a fixed displacement at one end of the specimen and a load to the other end, divided in sub-steps. An animation of the results throughout the sub-steps can be setup, showing several quantitative details such as displacements, stresses, strains (plastic and/or elastic). This allows the students to understand the distribution of different quantities and to evaluate the effect of the specimen shape, which guarantees a uniform stress distribution in the central region of the specimen. Additionally, different geometries can be implemented, to show the effect of notches or geometrical details (e.g. small holes) on the stress distribution, to study stress intensification phenomena.

2.3 The Micro Station for Metals

The development of the VR Lab has been conducted with the collaboration of educators of engineering and material science. According to them, one of the major difficulties in learning is to visualize three-dimensional space models, in particular, when it comes to microscopic dimensions. Regarding metals, students experience difficulties in imagining the atomic distributions, and all the engineering aspects related to this topic such as slipping planes, lattice structures, and elastic/plastic deformations. To assist them in this visual process we created a specific learning station for the atomic structure of metals, to show how they behave under different loading conditions (Fig. 2).

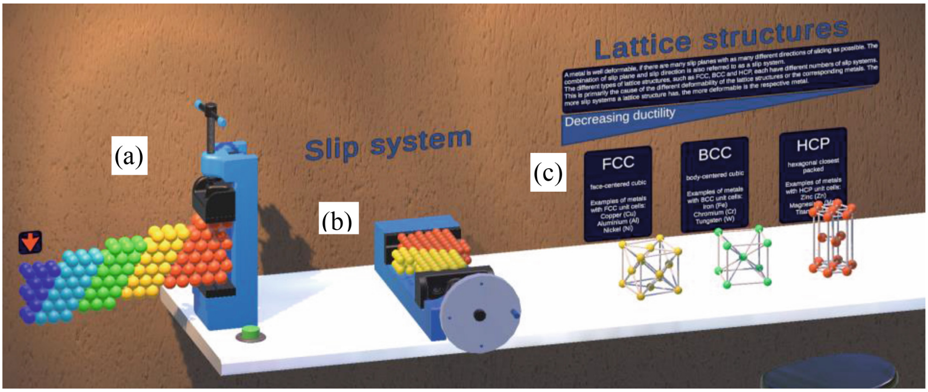

Fig. 2. The learning station for metals at the microscopic level.

It focuses on two different aspects. The first (c) presents the 3D models of the unit cells of the main lattice structures: face-centered cubic (FCC), body-centered cubic (BCC), and hexagonal closest packed (HCP). The user can grab and examine each virtual element. Next to the 3D models, there is a graphical board that reports some details about the relation between the lattice structure and the ductility of metals, plus some examples of materials constituted by each atomic structure. The examples include also the materials available in the tensile test learning station. This allows students to connect the macro with the micro behavior of these materials. The second aspect focuses on the gliding of atomic blocks that occur in the plastic deformation of metals. Starting from the concept of 'slip system' under different load conditions, a 3D virtual metal bar composed of out-of-scale atoms blocks grouped in different colors was modelled. Then, the user can activate the animation of a bending load using a pushbutton (a) or a bench vise to simulate compressive stress using a circular drive (b). This allows the student to visualize the principles behind the deformation behavior of metals and how dislocations are responsible for their ductility.

2.4 The Micro Station for Polymers

The third learning station is dedicated to the molecular structures of polymers (Fig. 3). Initially, the user can grab and examine the 3D models of the main structures of polymeric chains: linear, branched, crosslinked, and networked (b). A dedicated GUI reports the classification of the structures and includes details about how the physical properties of thermoplastic, thermoset polymers, and elastomers are affected by the different kinds of chains that constitute the materials.

The learning station also aims to assist students in learning the reasons behind the tensile deformation of amorphous polymers, also known as 'cold drawing' phenomenon. To exemplify this concept, the molecular structure of the polymer was modeled in the steady state and under a tensile load. In the second case, the molecular chains appear aligned along the force direction (a).

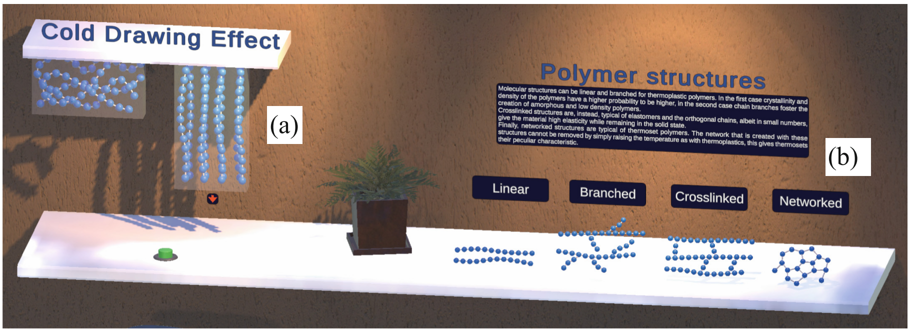

Fig. 3. The learning station for polymers at the microscopic level.

To simulate this behavior, the user can push a button next to the hanging 3D model of amorphous polymer and observe the deformation with the internal molecular chains that align towards the load direction. Near the 3D models, also in this part of the learning station a graphical panel was added to describe the cold drawing phenomena.

3 Discussion

The VR Lab was designed and implemented to exploit potentiality of VR in the field of learning STEM among university's students. The laboratory was created as a complementary tool for engineering and material science educators to improve students' learning experience, facilitate the comprehension of some abstract concepts, and let them experiment with augmented laboratory equipment that is impossible to replicate in the real world. The development of the immersive laboratory was assisted by educators in the fields of material science and engineering with suggestions and intermediate evaluations. In particular, three positive aspects of the immersive laboratory emerged. The first is the possibility to visualize and manipulate 3D models of molecular structures that are commonly difficult for students to recognize. The second aspect, partially related to the previous, regards the use of animations for concepts like slip planes for metals and the cold drawing effect for polymers. Observing these concepts in a three-dimensional space, exemplified with a schematic model, can provide a more immediate and straightforward representation of the phenomena than static images, as is usual in traditional learning approaches. The last point that emerged regards the opportunity to perform a laboratory experience in a controlled environment without the concerns of safety, space, and equipment of a real lab. The VR Lab requires only an HMD and could be used also by remote or distance-learning students who have no access to physical labs. On the other hand, it should be taken into account that immersive VR requires an expense for the HMDs and that can be experienced by one student at a time per device. However, educators did not consider these aspects as critical compared to the advantages. The experiences have been designed to be brief, and students in small classes or groups can use the laboratory sequentially with a couple of devices.

The VR Lab's modular approach will allow multiple add-ons in a future version of the lab. According to the educators involved in the development process, adding new materials and geometries at the tensile test station could be intriguing. Furthermore, they would allow students to modify also some test conditions (for example, room temperature or cracks/inclusions). This will allow for the inclusion of other engineering topics such as how crystallinity and degree of curing affect mechanical properties for polymers, as well as an examination of various fracture behaviors.

4 Conclusions

This work introduces an immersive VR Lab to help educators and students to learn about some material science and engineering principles. The collaboration with educators enabled us to focus on the important concepts and issues that students emphasize during traditional lectures, as well as how to exemplify challenging notions. Positive aspects include: a more straightforward concepts' representation using 3D models and animations, a more active learning approach, and the possibility to use an interactive VR Lab reducing the physical limitations derived from a real laboratory. Even though the laboratory aroused interest and seems promising, this work has some limitations. The next step will be an evaluation phase with university students and educators to assess the system's usability, as well as the effectiveness of the VR Lab in students' understanding of the contents. Initially, both usability and perceived workload will be assessed using standard questionnaires. Then, surveys aimed at highlighting the aspects to be improved and issues will be created and submitted to both students and educators to further develop the VR Lab. This way, in a future version of the VR Lab, it will be incorporated the suggestions derived from the users' remarks during the assessment and brainstorming.

References

1. Pirker, J., Dengel, A., Holly, M., Safikhani, S.: Virtual reality in computer science education: a systematic review. In: Proceedings of the 26th ACM Symposium on Virtual Reality Software and Technology, pp. 1–8 (2020)
2. Cipresso, P., Giglioli, I.A.C., Raya, M.A., Riva, G.: The past, present, and future of virtual and augmented reality research: a network and cluster analysis of the literature. Front. Psychol. **9**, 2086 (2018)
3. Aruanno, B., Barone, S., Tamburrino, F., Covarrubias Rodriguez, M.: Tintoretto unveiled: interactive virtual experience for artworks. In: Gerbino, S., Lanzotti, A., Martorelli, M., Mirálbes Buil, R., Rizzi, C., Roucoules, L. (eds.) Advances on Mechanics, Design Engineering and Manufacturing IV. JCM 2022. Lecture Notes in Mechanical Engineering. Springer, Cham, pp. 1352–1363 (2023). https://doi.org/10.1007/978-3-031-15928-2_118
4. Aruanno, B., Covarrubias, M.: Handy novel hand exoskeleton for personalized rehabilitation. Comput. Aided Des. Appl. **19**, 405–425 (2022)
5. Cruzneira, C., Sandin, D.J., Defanti, T.A., Kenyon, R.V., Hart, J.C.: The cave - audio-visual experience automatic virtual environment. Commun. ACM **35**, 64–72 (1992)
6. Jensen, L., Konradsen, F.: A review of the use of virtual reality head-mounted displays in education and training. Educ. Inf. Technol. **23**, 1515–1529 (2018)
7. Meyer, O.A., Omdahl, M.K., Makransky, G.: Investigating the effect of pre-training when learning through immersive virtual reality and video: a media and methods experiment. Comput. Educ. **140**, 103603 (2019)
8. Dewey, J.: Democracy in education. Elem. Sch. Teach. **4**, 193–204 (1903)
9. Pellas, N., Dengel, A., Christopoulos, A.: A scoping review of immersive virtual reality in STEM education. IEEE Trans. Learn. Technol. **13**, 748–761 (2020)
10. Soliman, M., Pesyridis, A., Dalaymani-Zad, D., Gronfula, M., Kourmpetis, M.J.A.S.: The application of virtual reality in engineering education. Appl. Sci. **11**, 2879 (2021)
11. Parong, J., Mayer, R.E.: Cognitive and affective processes for learning science in immersive virtual reality. J. Comput. Assisted Learn. **37**, 226–241 (2021)
12. Coban, M., Bolat, Y.I., Goksu, I.: The potential of immersive virtual reality to enhance learning: a meta-analysis. Educ. Res. Rev. **36**, 100452 (2022)
13. VIVE Focus 3. https://www.vive.com/us/product/vive-focus3/specs/. Accessed 20 Feb 2023
14. Prithul, A., Adhanom, I.B., Folmer, E.: Teleportation in virtual reality; a mini-review. Front. Virtual Reality **2**, 730792 (2021)

VR Technical Drawing Learning Activity for College Engineering Students: Design, Development and Evaluation

Jordan Henstrom, Raffaele De Amicis(✉), Christopher Sanchez, and Onan Demirel

Oregon State University, Corvallis Oregon, USA
{henstroj,raffaele.deamicis,christopher.sanchez, onan.demirel}@oregonstate.edu

Abstract. Virtual Reality (VR) research has shown promising benefits in several educational areas, particularly those necessitating interaction with spatial information - a key element in teaching engineering skills such as technical drawing. This paper presents a broad process for designing and developing VR-based instructional activities, ultimately producing a VR application that employs immersive visualization and interaction. An evaluation of the application's effectiveness revealed that engineering students using the VR application performed comparably to those using conventional methods, such as analog drawing, on course exercises. The study also explored cognitive load, comparing the VR group with a control group and a glass box animation group. While the glass box group showed an advantage over the VR group in cognitive load, no significant difference in aggregate scores between the VR and control groups was found. This is notable, given the increased interaction required by the VR exercise. These results provide initial evidence that traditional learning activities can be effectively translated into an immersive VR context and strengthen the case for VR as a viable medium for remote learning. However, it also points to the need for further research which improves the VR exercise and identifies the factors contributing to the management of cognitive load.

Keywords: virtual reality · technical drawing · engineering education

1 Introduction

Technical drawing is a critical skill that engineering students must learn to communicate effectively with other engineers and collaborators. It provides a standardized way to describe and represent 3D objects, which is essential for manufacturing, construction, and other engineering-related fields. Technical drawing is also an important foundation for more advanced design tools, such as computer-aided design (CAD) software, which is widely used in engineering today. By

M. Carfagni et al. (Eds.): ADM 2023, LNME, pp. 397–404, 2024.
https://doi.org/10.1007/978-3-031-52075-4_45

learning technical drawing, engineering students develop their ability to create accurate, detailed representations of designs, making it a fundamental ability that emerging engineers must develop [4]. Virtual Reality (VR) offers a novel approach to technical drawing instruction by allowing learners to visualize 3D objects in a more immersive and interactive way than traditional 2D drawings. Students can examine and manipulate objects from any angle and explore their features in real-time. The use of such dynamic visualizations to enhance instruction has been a focus on research surrounding spatial learning activities in the field engineering [3,7]. The research presented in this paper aims to apply VR-based instruction to the training of technical drawing. While research has reviewed the potential of AR and VR for technical drawing instruction [1,6,9,10], much of this previous research focused on testing or developing specific, course-independent, technical drawing exercises, rather than the full translation existing course content into a VR context. Several methods for designing and developing VR engineering applications exist [7,10,12]; however, more specific guidelines are needed concerning applications that model existing course exercises [2]. The contributions of the current paper are twofold. Firstly, it implements a process for translating existing course activities and assessments into immersive VR environments. By following this process, instructors can create VR applications that accurately reflect the learning objectives of the syllabus and can be integrated into existing course structures or deployed in remote learning environments. Secondly, this paper provides results from a user evaluation of an original VR-based activity, which extends the existing work on the use of such activities in science, technology, engineering and mathematics (STEM) education. These results shed light on the viability of using VR for technical drawing instruction through remote learning activities analogous to existing course exercises and the challenges associated with creating these activities. In contrast to previous research [1,6,9,10], the VR application proposed in this paper empowers students to carry out a constructivist process to practice orthographic drawings

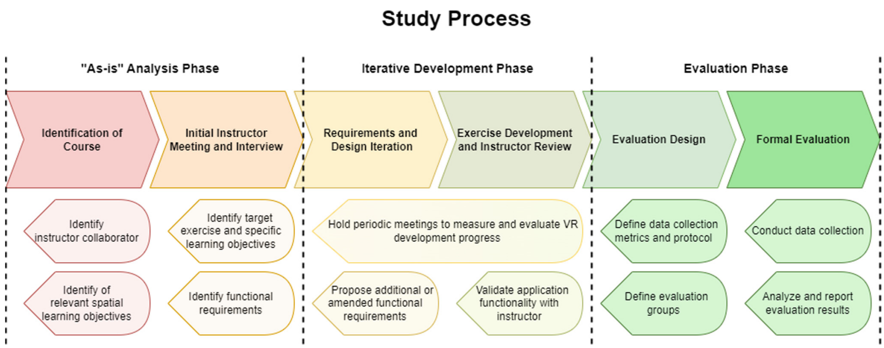

Fig. 1. Design, development, and evaluation phases. The process starts with an "as-is" analysis phase, followed by iterative development of the VR application, and ending with an evaluation of the resulting system

within an immersive VR context. By providing students with this opportunity, we have demonstrated VR's ability to conduct robust course learning activities. Section 2 describes the methodology followed for designing and developing the VR-based activity and formal evaluation. Section 3 reports and discusses the results of a user evaluation and Sect. 4 provides a conclusion and discussion of future research objectives.

2 Design, Development, and Evaluation Process

Choosing the appropriate design model is crucial to successful development, and research has highlighted the viability of iterative design methods that focus on improving a core set of functionalities throughout the software development lifecycle [2,12]. Research has also considered detailed design methods, targeted at virtual distance laboratories [7]. Our process focuses on the translation and evaluation of existing course content into an immersive VR environment and consists of three overarching phases: (1) "as-is" analysis, (2) iterative development, and (3) final evaluation (see Fig. 1). In the "as-is" analysis phase, a target learning activity is identified with the assistance of the course instructor and functional requirements based on the assessment's learning objectives are enumerated. The assignment identified in the current study involved practicing orthographic projections through analog drawings of two objects (see Fig. 2a and Fig. 2b). The functional requirements identified were (a) load and manipulate a 3D model, (b) draw lines from the model to projection planes, (c) draw lines on projection planes, and (d) denote hidden lines and features. After the "as-is" analysis was completed, the iterative prototyping process was carried out to create the application (see Sect. 2.1). At each iteration, the prototype was shared with research members and the course instructor to ensure the application did not deviate from the learning outcomes of the target assessment. Once a satisfactory prototype was completed, an evaluation was designed and carried out (see Sect. 2.2).

2.1 VR Interaction Design

The design of our system focused on providing simple and easily understood methods for loading and manipulating the 3d model, drawing projection lines,

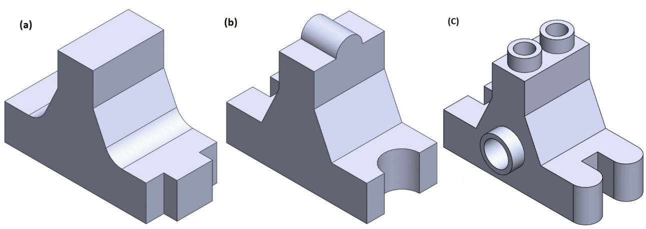

Fig. 2. **(a)** The simple object without hidden features **(b)** The complex object with hidden features **(c)** The evaluation object with holes

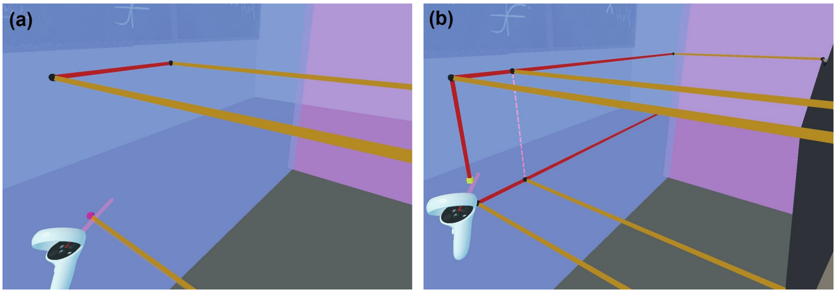

Fig. 3. Example construction done by students. (a) the drawing of projection lines, (b) the construction of drawings on a plane with dashed lines indicating hidden features

and constructing drawings along a projection plane. Automated systems for resizing and generating vertices on 3D models were used, allowing the modification of the learning activity to work with different models based on instructor needs. Furthermore, specific interaction techniques around how lines are drawn and visualized were necessary to ensure the process is similar to the analog drawing of orthographic projections with pen and paper. Lines can be drawn directly from the loaded 3-D object to three projection planes using a drag-and-release controller interaction, snapping the resulting line to the nearest 90-degree angle (see Fig. 3a). Lines on a plane describing the orthographic view can be similarly drawn using a drag-and-release controller interaction, or by selecting sequences of vertices and choosing an auto-draw menu command (see Fig. 3b). The drag-and-release interaction preserves the decision making process students engage in when constructing the drawings, requiring students to determine the correct plane when drawing projection lines and the correct placement of lines on projection planes. To further assist students with organizing their drawings, they can draw both solid or dashed lines to denote hidden features, or toggle the visibility of projected lines. The resulting system allows students to construct complete orthographic projections within the VR environment.[1]

2.2 Evaluation Design

The main purpose of the evaluation was to examine how the proposed VR-based learning activity performs relative to other methods of instruction that use analog methodology, including more traditional methods and glass box methods (described below). The performance of each module was examined via three different evaluation metrics including perceived usability (System Usability Scale) [5], assessment performance, and cognitive load (NASA Task Load Index) [8].

Participants. The current experiment was conducted with engineering students at enrolled in ENGR 248: Engineering Graphics and 3-D Modeling. Students that

[1] Supplemental video demonstration available at https://youtu.be/2o_z0QwxiuI.

were interested in participating first filled out a demographic questionnaire and an informed consent document where they were screened for eligibility based on four criteria: (a) they were a student in the class, (b) they were not prone to motion sickness, (c) they did not have an implanted medical device, and (d) they were not prone to seizures.

Experimental Groups. Participants completed the study following initial exposure to analog technical drawing through the course exercise described in Sect. 2. Upon arrival at their study appointment, participants were assigned to one of three experimental groups: control, glass box animation, and VR. The control group was provided with 2D depictions on paper of two 3-D objects: a simple object with no hidden features, and a complex object with hidden features (see Fig. 2a and Fig. 2b). They then constructed analog orthographic drawings using grid paper and a pencil. The glass box animation group was given the same materials as the control group, but were also given additional video animations that demonstrated the animated unfolding of the objects from three different perspectives. Participants then constructed analog orthographic drawings using grid paper and a pencil. Finally, the VR group was able to visualize the objects within an immersive VR environment. Within the environment, they constructed orthographic projection drawings using the interactions described in Sect. 2.1. A time limit of 10 min per drawing was enforced, and after each drawing participants completed the NASA TLX questionnaire. After completing both drawings, participants were then given 15 min to complete a third drawing (see Fig. 2c), however for this 3rd drawing they were asked to use grid paper and a pencil. Finally, after completing the activities, all groups completed an exit questionnaire that included the System Usability Scale (SUS) questionnaire. Observational data was also gathered through either students' scratch notes in the case of the control and glass box animation groups, or video recordings in the case of the VR group.

3 Results and Discussion

25 students filled out the initial recruitment questionnaire, of which 18 met exclusion criteria and scheduled times to participate. The 18 students were evenly split between the three treatment groups, resulting in 6 students in each group.

3.1 Technical Drawing Performance

The orthographic projection drawings of the 3D objects were scored based on existing evaluation guidelines used within the course that were adapted with the assistance of the course instructor. The guidelines quantify students' performance on a 75-point scale based on three criteria: overall completeness of the object represented as an orthographic projection (33%), the correct representation of the visible part features (27%), and the hidden features in the final orthographic projections (40%). Results from this scoring were compared across the three different training groups using a one-way analysis of variance (ANOVA) test. The test revealed no significant effect of the treatment group on performance score ($F(2,9) = 1.20, p = 0.34$). While the highest performance was observed in the glass box group ($\overline{X} = 52.5, \sigma = 5.75$), followed by the control group ($\overline{X} = 50.17, \sigma = 10.94$), and then the VR group ($\overline{X} = 45.67, \sigma = 8.71$); these group differences were not statistically reliable. Since each sub-category was not equally weighted, additional ANOVA tests were performed for each of the three sub-categories (completeness, visible features, and hidden features), but again no significant effect was observed ($F(2,9) < 2.6$). These results indicate that although the VR activity did *not* produce a significant positive performance advantage over the traditional or glass box alternatives, VR simulation was just as effective for learning these skills, and thus an equivalent medium for practicing orthographic drawing.

3.2 NASA Task Load Index

NASA TLX scores were analyzed using a 3 (treatment group) x 2 (object complexity) mixed ANOVA. Both the aggregate score from the NASA TLX, and scores representing different aspects of cognitive load, were analyzed. Where significant differences were identified, post-hoc tests were conducted. The test revealed that the treatment group had a significant effect on cognitive load ($F(2,18) = 5.59, p = 0.01, n^2 = 0.27$), with the glass box animation treatment group exhibiting an advantage over the VR group ($p = 0.01, d = 1.37$). However, no significant difference was identified between the control and VR groups. The VR exercise required more interaction from students than the other exercise versions to construct the technical drawings, and we would expect to see an increase in cognitive load unless other factors counteracted this. The fact that we did not see significant differences in overall scores between the VR and control groups indicates that the VR application may provide benefits that help compensate for the increased cognitive load from the high number of interactions. One contributing factor could be increased engagement and enjoyment from the immersive medium, however further research would be needed to confirm this. There was also no significant interaction between the treatment group and object complexity, suggesting that complexity did not affect cognitive load, nor did complexity influence load differently for any of the treatment groups. When considering specific facets of the NASA TLX score, the treatment group had a significant effect on mental demand ($F(2,18) = 4.69, p = 0.02, n^2 = 0.24$), physical demand ($F(2,18) = 6.77, p < 0.01, n^2 = 0.31$), and frustration ($F(2,18) = 6.23, p = 0.01, n^2 = 0.29$). For example, the paper-and-pencil group exhibited less frustration than the VR group ($p = 0.02, d = 1.15$). Similarly, the glass box animation treatment group showed lower levels than VR in mental demand ($p = 0.01, d = 1.23$), physical demand ($p < .01, d = 1.47$), and frustration ($p = 0.01, d = 1.33$). From these results, it seems that using the VR application for instructing technical drawing results in higher cognitive load in some facets compared to the paper-and-pencil and glass box animation versions. VR's higher physical demand may be explained by the fatigue from repeatedly drawing lines, and thus having to engage in gross motor movements to produce the drawings. This is in direct contrast to the traditional and glass box groups that only use hand drawing movements to complete the exercise. Consequentially, this highlights the importance for determining more effective methods to reduce the physical strain of VR users. Additionally, VR resulted in higher frustration than both the glass box animation and control groups indicating that students' expectations of the application were not met. One possible reason for this difference is students' unfamiliarity with the technology; students only had a short 10-minute tutorial to assist with learning the application, which in hindsight may have been insufficient. In addition to this, there were several usability concerns that were identified that may have lead to students' increased frustration.

3.3 Usability

A one-way ANOVA on SUS score found no significant overall effect of the treatment group, however, the SUS results still do indicate some concerning usability issues for all of the treatment groups. The control and VR groups both had an average SUS score of 61.25; usability is considered to be *below average* if SUS scores are < 68 [11]. This indicates that both the traditional and VR activities could benefit from usability improvements. However, the glass box animation group's SUS score of 76.25 implies that the glass box assessment presented usability advantages. The only distinction between the glass box and the paper-and-pencil control group was access to glass box visualizations. This suggests that these visualizations may have increased the usability of the activity. Students were also prompted to leave comments regarding their experience, and students from the VR group were more likely to provide written feedback than the other two groups, indicating a potentially higher level of engagement. These comments identified several usability concerns. For example, two participants pointed out the need for error correction with one stating they "wish[ed] there was a back button or a way to undo mistakes or erase lines". While the system provided an option to reset the model, these comments indicate a need for additional undoing functionality. Additionally, one participant remarked that they would have liked to "toggle between the tutorial and the object [they were] working on without having to start over" once again indicating the need for improvements to the tutorial, or additional help resources.

4 Conclusion

Our research has demonstrated the feasibility of translating existing course content into an immersive VR context while preserving learning outcomes. Results from our evaluation indicates that student performance and usability levels are similar between the VR and traditional exercise, despite students' lack of experience with the technology. Although our study is limited by a small sample size and identified issues in usability, it provides evidence that VR may serve as an equivalent medium for practicing technical drawing. Furthermore, the VR application's overall cognitive load was not significantly different from the control group, despite higher scores in some individual facets. However, the differences in cognitive load between the VR and glass box groups highlight that the VR exercise still requires improvement to fully leverage the advantages of the medium. Future research will seek to improve the usability of the activity, conduct more extensive evaluations using multiple drawings, and expand our data collection to investigate how the VR application effects student engagement. Additionally, we will consider how the benefits of VR can affect different students who vary in their experience with spatial tasks or visuospatial ability. This future research will help strengthen our understanding of VR's role for the remote instruction of engineering students.

References

1. Akkus, I., Arslan, P.: The effects of augmented reality in the technical drawing course on engineering students' spatial ability and academic achievement. J. Learn. Teach. Digital Age. **7**, 160–174 (2022)
2. Alnagrat, A., Ismail, R., Syed Idrus, S.Z.: The opportunities and challenges in virtual reality for virtual laboratories. Innov. Teach. Learn. J. **6**, 73–89 (2022)
3. Álvarez-Marín, A., Velázquez-Iturbide, J.Á., Castillo-Vergara, M.: Intention to use an interactive AR app for engineering education. In: 2020 IEEE International Symposium on Mixed and Augmented Reality Adjunct (ISMAR-Adjunct), pp. 70–73. IEEE (2020)
4. Białkiewicz, A.: Propaedeutics of teaching drawing to architects. Glob. J. Eng. Educ. **21**(2), 115–120 (2019)
5. Brooke, J.: SUS: a quick and dirty usability scale. Usability Eval. Ind. **189**, 189–194 (1995)
6. Cardoso, O.I.H., Unver, E., Aslan, R., Kus, A., Chotrov, D.: Application of VR and AR tools for technical drawing education. In: The 16th Annual International CAD Conference, pp. 363–366 (2019)
7. Gattullo, M., et al.: Design of a mixed reality application for stem distance education laboratories. Computers **11**(4), 50 (2022)
8. Hart, S.G., Staveland, L.E.: Development of NASA-TLX (task load index): results of empirical and theoretical research. In: Hancock, P.A., Meshkati, N. (eds.) Human Mental Workload, vol. 52, pp. 139–183. North-Holland (1988)
9. Huerta, O., Unver, E., Arslan, R., Kus, A., Allen, J.: An approach to improve technical drawing using VR and AR tools. Comput. Aided Des. App. **17**, 836–849 (2019)
10. Rubio, M.P., Vergara, D., Rodríguez, S.: Immersive virtual reality in technical drawing of engineering degrees. In: Gennari, R., et al. (eds.) MIS4TEL 2019. AISC, vol. 1007, pp. 71–79. Springer, Cham (2020). https://doi.org/10.1007/978-3-030-23990-9_9
11. Sauro, J.: A practical guide to the system usability scale: Background, benchmarks & best practices. Measuring Usability LLC (2011)
12. Vergara, D., Rubio, M.P., Lorenzo, M.: On the design of virtual reality learning environments in engineering. Multimod. Technol. Interact. **1**(2), 11 (2017)

A Study on Educators' Requirements for Integrating VR in Post-secondary Classes

Vaishnavi Rangarajan, Arash Shahbaz Badr, Christopher Sanchez, and Raffaele De Amicis(✉)

Oregon State University, Corvallis OR 97333, USA
{rangarav,shahbaar,christopher.sanchez,raffaele.deamicis}@oregonstate.edu

Abstract. The acceleration in affordable hardware has fueled a tremendous increase in the number of Virtual Reality (VR) applications in the learning domain. However, understanding the extent to which existing VR products satisfy instructors' expectations in teaching university-level classes is crucial to streamlining future design endeavors. We conducted a study with 16 university-level instructors to understand their outlook toward VR technology and selected off-the-shelf applications. Through qualitative analysis of semi-structured interviews and observations across multiple stages, we present trends in instructors' requirements. Additionally, we collected information about the instructors' expectations and preferences for teaching a VR-led course, along with a general assessment of the aptitude of the selected applications through their lens. The results identify the opportunities and challenges surrounding the adoption of VR technology in higher education and help define the needs for future software design as well as curriculum planning efforts.

Keywords: Engineering Education · Virtual Reality · e-Learning · Educational VR

1 Introduction

The expansion of online university education over the last decade has produced a wide body of knowledge on the subject of electronic-learning (e-learning), however, this has brought to light more limitations of the remote classroom than strengths [12,21]. While remote learning is superior to in-person instruction in terms of cost and accessibility, it often fails to provide students with practical hands-on experience, and the distance between students and instructors can impair communication, collaboration, and engagement, all of which are essential to the learning process [2,25,26]. In recent years, extended reality (XR) technologies have sought to augment digital classrooms by facilitating learning experiences in an immersive manner, aiming to compensate for some of the limitations of remote learning. Research on this augmentation so far has been conducted from a variety of angles. For example, evaluating the impact of synchronousness, return-on-investment, distance barriers, and facilitator modeling

M. Carfagni et al. (Eds.): ADM 2023, LNME, pp. 405–413, 2024.
https://doi.org/10.1007/978-3-031-52075-4_46

in the context of e-learning presence [18,20,22]. The primary goal of the current study is to facilitate the integration of VR into the curriculum by comprehending instructor's needs and expectations.

2 Related Work

Despite the growing popularity of VR technology, educational applications suffer from challenges, such as technological constraints, operational costs, and lack of content, that may impact the widespread adoption [17]. Buabeng-Andoh [4] highlighted multiple factors that impact the technology adoption for teaching; teachers' beliefs and attitudes towards technology, lack of support and training, and lack of appropriate educational tools are a few factors. These impeding factors are consistent with other studies in the literature [6,8,24]. Ashrafzadeh and Sayadian [3] listed several factors that may influence the technology integration: perception about technology usage, including the usefulness of the technology for classroom instruction, institutional support provided, and individual characteristics. Specifically, the authors emphasize the need for awareness of the technology, its benefits, and implementation scenarios to ease the educators' concerns. Research suggests that involving educators in the design and development efforts will lead to positive outcomes and changes in their attitudes towards technology [7,16,19]. Furthermore, considering educators as primary stakeholders may also help generate awareness of technological capabilities, which is an essential driver [1]. It may also enable pedagogically founded applications and effective integration of VR in the existing curriculum. Jensen and Konradsen [15] describe two barriers impacting the use of Head-mounted Display (HMD) in education: lack of content and hardware needs. The authors further underscore that most educational applications are not classroom-ready, are directed at self-learners and demand a certain degree of technical expertise for effective classroom usage. Furthermore, with the ever-growing development of VR applications in the educational space, it is pertinent to understand their effectiveness as an instructional tool rather than a mere engagement device. A further gap observed is that only a small number of studies evaluated applications and prototypes developed for HMDs. Many papers consider virtual environments made for web and desktop platforms, even when they call them immersive virtual environments. Radianti et al. [23] noted this ambiguity in the term immersive in literature. They highlight the lack of a comprehensive overview of existing VR applications for educational purposes and the need for educators to develop technical expertise and up-to-date familiarity with the market of suitable VR applications. The widening stream of devices and applications of uneven quality and uncertain utility reaching the market these days calls for a periodic assessment of the current state-of-the-art. Hence, it is essential to review the current off-the-shelf applications to assess their quality, effectiveness, affordability, and utility in educational settings to elicit requirements for future design endeavors.

3 Methodology

Participants: The participants in the study were 16 educators (9 women, 7 men), recruited from various colleges across Oregon State University (OSU) using a multimodal recruitment strategy. The recruitment survey included questions to exclude participants with susceptibility to VR-induced motion sickness and digital screens-related illnesses. Participants' current instructional methods were collected through a questionnaire dubbed Pre-exposure questionnaire. Table 1 summarizes the corresponding responses. Some participants mentioned additional methods such as live working on problems, use of whiteboard/docCAM/fill-in-the-blank notes, and in-farm practices.

Table 1. Summary of current instructional methods for in-person class delivery.

Method	Frequency				
	More than 90% of lectures	More than 60% of lectures	More than 30% of lectures	30% or less of lectures	Never
Real-time Demonstration	6	1	4	3	2
Prepared Instruction	7	3	1	5	0

Phases: An overview of the adopted methodology and the data collection tools is shown in Fig. 1a. The stages of this approach are described in the following.

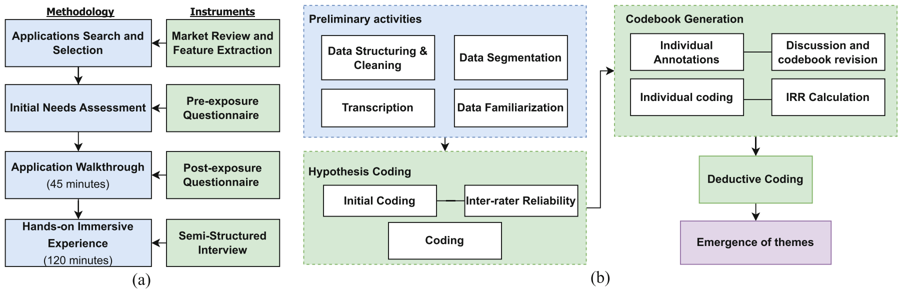

Fig. 1. Overview of the methodology: (a) data collection (b) qualitative analysis.

Applications Search and Selection: We performed a search for commercial collaborative VR applications for teaching activities. The applications were identified by conducting both a web search and searching through various app marketplaces. The search was conducted using keywords such as collaborative, learning, education, or edutainment. The inclusion criteria were the availability of shared collaborative spaces for learning activities. We further excluded apps that don't support the HMD selected for the study, don't have a free license option, or are limited to a certain subject (e.g., chemistry or anatomy). Following the search, we individually examined all the identified applications to investigate the features and information available. We created a feature table and generated user scenarios based on the features observed. Using this table, we selected three applications that offer features such as a generic learning space, classroom collaboration, and content presentation tools. One of the applications was used as a warm-up space to familiarize the participants with VR interactions. The other two were used for data collection.

Initial Needs Assessment: In this phase, we identified the initial user requirements and expectations for collaborative virtual environments through the lens of instructors utilizing the Pre-exposure questionnaire. The questionnaire comprises a mix of close-ended and open-ended questions, inquiring about participants' current methods of teaching, their experience using VR, their motivations and expectations from a VR classroom, and potential scenarios of integrating VR in their teaching.

Application Walkthrough: During this session, participants saw the applications in action and observed different usage scenarios demonstrated by the research team. To maintain consistency among participants, we created a video showcasing several use cases across the three selected apps. After watching the video, the participant was interviewed in a semi-structured discussion designed to clarify any questions about the VR technology and its suitability for their courses. Participants then filled out the Post-exposure questionnaire. The responses were compared to the Pre-exposure questionnaire to identify potential changes in their expectations or perspectives after the initial VR exposure.

Hands-on Immersive Experience: At the beginning of the immersive experience, participants explored a 'warm-up' application to familiarize themselves with VR interactions and the environment. Subsequently, participants began interacting with the two applications selected for the study and performed three tasks with each. The order of experiencing the apps was randomized across participants to avoid sequence effects. The tasks included drawing on a virtual whiteboard (2D drawing), drawing in 3D, loading and manipulating 3D models, opening PDF slides, administering quizzes, and playing videos. Additionally, suggestions for improving any features were collected. Once all the tasks for an app were completed, participants disconnected from VR and were debriefed, where they provided additional feedback. This process was repeated for both apps with a short break in between. At the end of the session, a final semi-structured interview was conducted to collect further comments or reflections.

4 Data Analysis

Qualitative data were collected at four points during the study: Application Walkthrough discussion and open-ended responses, think-aloud comments during the Hands-on Experience, verbal debriefing questions, and semi-structured interviews. Figure 1b depicts an overview of the activities conducted for processing and analyzing these data. The research team transcribed the video recordings of the Application Walkthrough and Hands-on Experience and segmented the data into stanzas [10]. We created rules and templates to maintain consistency during this procedure. Subsequently, a-priori codes, derived from the research objectives, were applied to code the data into three overarching categories: Needs, Satisfaction, and Challenges. Two researchers coded the data from three participants, which roughly covered 20% of the data, and calculated inter-rater reliability (IRR) based on Jaccard's index [14]. Throughout the coding, the researchers discussed their decisions and calculated the partial IRR for roughly every 5% of the data. The average IRR for this 20% of data was 83%. The remainder of the data was coded by the two researchers individually.

Next, a codebook was generated on another set of roughly 20% of the data. An IRR of 90.8% was achieved in this phase, and the researchers coded the rest of the data using the developed codebook. We then used affinity diagramming [11] to organize the coded stanzas into themes and sub-themes and labeled them.

An overview of the themes and subthemes that emerged under the Needs category can be seen in Fig. 2. The top three themes were 2D media (26.57%), 3D media (22.54%), and immersive and interactive experiences (21.83%).

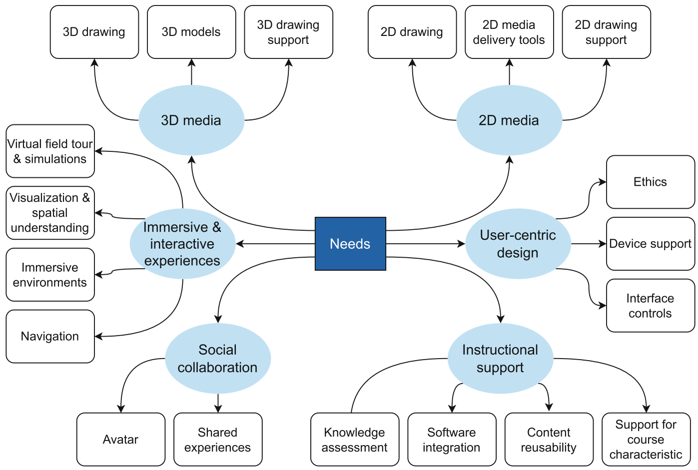

Fig. 2. Overview of the themes and sub-themes under the category of Needs.

Need for 2D Media Support: This category comprises a wide range of traditional media tools such as images, videos, slides, screen share, and web browser. Participants expect the VR environment to support their current instructional delivery methods but raised questions about the advantage of VR over existing methods of delivering 2D content. A frequent requirement was the support for multiple file formats and advanced features for presentation and control.

Need for 3D Media Support: Participants expressed that their need for 3D models extends beyond the limited, generic repository of 3D models available in the tested apps. A common response was that this functionality would only be relevant if there is an extensive library of models or an opportunity to import custom models. Furthermore, participants emphasized the need for 3D model interactions and repeatedly examined the visibility of their manipulations from a student's point of view. Questions about creating 3D models were also common. Participants also found the 3D drawing capabilities relevant and engaging. They discussed multiple uses, including annotations on virtual objects, 3D sketching, and teaching mathematical or abstract concepts (e.g., convex optimization).

Need for Immersive and Interactive Experience: Participants expressed great interest in virtual field tours and simulations, enabling taking students to places that otherwise are risky or not feasible to travel. Such needs align with the motivations for using VR technologies found in the literature [5,9]. A few examples of virtual field trip ideas proposed by the participants include: visiting manufacturing factories, dairy farms, data centers, construction and steel fabrication sites, and nuclear power plants. Immersive learning environments, both formal and informal, were of great interest to the participants. However, there were mixed opinions about the presence or absence of furniture in the class, indicating a need for the creation and customization of the space based on necessity. A few participants loved the minimalist details in the experienced environments. But others expressed that aspects of the same environment may not be comfortable for students, including the closely placed chairs, large-sized presentation boards, lack of personal space, and dull colors. The need for moving freely in the environment and being able to easily turn and look at students was also mentioned. A related sub-theme is the need for visualization and spatial understanding. Participants indicated an interest in using VR for visualizing abstract concepts, comparing or contrasting, and interacting with 3D artifacts for spatial comprehension.

Need for Social Collaboration: Shared learning spaces and tools to enable collaboration were recurring recommendations. This theme contains responses indicating the need for learner-learner and learner-instructor interaction tools. This includes verbal and non-verbal feedback (voice, chat, emojis), team break-out rooms, collaborative presentations, and planning or brainstorming tools (e.g., Kanban board). Ideas of social constructivism and experiential learning were manifested in educators' comments on providing students with spaces, where they learn by doing and communicate with their peers. When asked about preferences for avatars, most participants either didn't have a specific preference or mentioned that they would respect their students' choice of self-representation. Based on our observations and participants' comments, there is a potential concern that avatars' movement or appearance may unintentionally look disruptive. For instance, unwanted avatar movements when the HMD is taken off or is temporarily disconnected may distract others. Nonetheless, participants highlighted the importance of personalized representation for an inclusive learning space.

Need for User-Centric Design and Content Management Support: Participants expressed a variety of needs and preferences for teaching in VR, including:

– Customization and organization of content placement using virtual tablets that mimic real-life devices

- Easy switching between content presentation modes for managing the class
- Privacy, safety, and personal space to create a safe and inclusive experience
- Personalization that respects individual differences
- Access to external tools such as keyboards for text entry and note-taking capabilities within the VR environment
- Reusing course materials, for example through recordings and session saves, offering significant benefits especially for asynchronous or hybrid teaching.

Overall, participants had various course-structure requirements, such as support for large numbers of students, interoperability with existing content delivery methods, and time duration for VR experiences. Addressing these needs and preferences can facilitate a more engaging and effective virtual learning space.

5 Discussion and Conclusion

We observed a few trends in participants' responses: 1) ideas of combining multiple features for teaching activities, 2) comparing features with existing non-VR tools in terms of completeness and effectiveness, and 3) effort concerns related to performing similar activities in VR compared to existing tools. A majority of participants expressed some form of skepticism towards the use of VR for teaching. They were unsure of the applicability and suitability of certain features for their current instruction style and questioned the relative advantage of VR for 2D features compared to existing tools. Specifically, participants wondered about the startup time and effort invested in using VR for their class, given their busy schedule and tight course constraints. Although the initial experience was described as promising, concerns were expressed about the potential frustrations due to technical difficulties in using the technologies. Therefore, we believe future classroom-focused studies are required to understand long-term feasibility, course-specific requirements, and technology barriers. The pattern observed follows the Hooper and Rieber technology adoption model [13], with participants currently at the first stage: familiarization. We noted that participants expected longer interactions with VR to assess its relevance and aptitude for their instructional style and course demands. A future direction should be investigating the effects of self-paced familiarization to better understand educators' adoption of the technology. Finally, studies aiming to measure the effectiveness of domain-specific applications in classroom instruction are also warranted.

References

1. Alfalah, S.: Perceptions toward adopting virtual reality as a teaching aid in information technology. Educ. Inf. Technol. **23**(6) (2018)
2. Arnseth, H.C.: Activity theory and situated learning theory: contrasting views of educational practice. Pedagogy Cult. Soc. **16**(3), 289–302 (2008)
3. Ashrafzadeh, A., Sayadian, S.: University instructors' concerns and perceptions of technology integration. Comput. Hum. Behav. **49**, 62–73 (2015)

4. Buabeng-Andoh, C.: Factors influencing teachersâ adoption and integration of information and communication technology into teaching: a review of the literature. Int. J. Educ. Dev. Using ICT **8**(1) (2012)
5. Chen, C.J.: Theoretical bases for using virtual reality in education. Themes Sci. Technol. Educ. **2**(1–2), 71–90 (2010)
6. Chittaro, L., Ranon, R.: Web3d technologies in learning, education and training: motivations, issues, opportunities. Comput. Educ. **49**(1), 3–18 (2007)
7. Cviko, A., McKenney, S., Voogt, J.: Teacher roles in designing technology-rich learning activities for early literacy: a cross-case analysis. Comput. Educ. **72**, 68–79 (2014)
8. Ertmer, P.A., Ottenbreit-Leftwich, A.T., Sadik, O., Sendurur, E., Sendurur, P.: Teacher beliefs and technology integration practices: a critical relationship. Comput. Educ. **59**(2), 423–435 (2012)
9. Freina, L., Ott, M.: A literature review on immersive virtual reality in education: state of the art and perspectives. In: The International Scientific Conference Elearning and Software for Education, vol. 1, pp. 10–1007 (2015)
10. Gee, J.P.: An Introduction to Discourse Analysis: Theory and Method. Routledge, London (2004)
11. Haskins Lisle, A., Merenda, C., Gabbard, J.: Using affinity diagramming to generate a codebook: a case study on young military veterans and community reintegration. Qual. Res. **20**(4), 396–413 (2020)
12. Helms, J.L.: Comparing student performance in online and face-to-face delivery modalities. J. Asynchron. Learn. Netw.**18**(1) (2014)
13. Hooper, S., Rieber, L.P.: Teaching with technology. Teach. Theory Pract. **2013**, 154–170 (1995)
14. Jaccard, P.: The distribution of the flora in the alpine zone. New Phytologist (1912)
15. Jensen, L., Konradsen, F.: A review of the use of virtual reality head-mounted displays in education and training. Educ. Inf. Technol. (2018)
16. Jiang, J., Zhi, L., Xiong, Z.: Application of virtual reality technology in education and teaching. In: 2018 International Joint Conference on Information, Media and Engineering (ICIME), pp. 300–302. IEEE (2018)
17. Laurell, C., Sandström, C., Berthold, A., Larsson, D.: Exploring barriers to adoption of virtual reality through social media analytics and machine learning-an assessment of technology, network, price and trialability. J. Bus. Res. **100**, 469–474 (2019)
18. McClannon, T.W., Cheney, A.W., Bolt, L.L., Terry, K.P.: Predicting sense of presence and sense of community in immersive online learning environments. Online Learn. **22**(4), 141–159 (2018)
19. Patterson, T., Han, I.: Learning to teach with virtual reality: lessons from one elementary teacher. TechTrends **63**(4), 463–469 (2019)
20. Peterson, A., Beymer, P., Putnam, R.: Synchronous and asynchronous discussions: effects on cooperation, belonging, and affect. Online Learn. **22**(4), 7–25 (2018)
21. Phirangee, K.: Students' perceptions of learner-learner interactions that weaken a sense of community in an online learning environment. Online Learn. **20**(4), 13–33 (2016)
22. Preisman, K.A.: Teaching presence in online education: from the instructor's point of view. Online Learn. **18**(3) (2014)
23. Radianti, J., Majchrzak, T.A., Fromm, J., Wohlgenannt, I.: A systematic review of immersive virtual reality applications for higher education: Design elements, lessons learned, and research agenda. Comput. Educ. **147**, 103778 (2020)

24. Tondeur, J., Van Braak, J., Ertmer, P.A., Ottenbreit-Leftwich, A.: Understanding the relationship between teachers' pedagogical beliefs and technology use in education: a systematic review of qualitative evidence. Educ. Tech. Res. Dev. **65**(3), 555–575 (2017)
25. Wilson, J.M., Goodman, P.S., Cronin, M.A.: Group learning. Academy of management review **32**(4), 1041–1059 (2007)
26. Woods, T., Williams, G., McNeal, B.: Children's mathematical thinking in different classroom cultures. Journal for research in mathematics education **37**(3) (2006)

Virtual Reality Workshop for Massive Laboratory Learning Experience of Engineering Students

Federico Morosi(✉) and Gaetano Cascini

Mechanical Engineering Department of Politecnico di Milano, Milan, Italy
federico.morosi@polimi.it

Abstract. Virtual Reality (VR) technology has the potential to revolutionize engineering education by providing students with real-world simulation scenarios. This paper presents a user study to measure the effectiveness of VR applications in teaching technical representation and machine elements to first-year mechanical, energy, and aerospace engineering students. The VR application was designed to immerse the students in a virtual mechanical workshop where they could interact with a 3D model of a gearbox and access task instructions and technical drawings through an interactive whiteboard. A total of 448 students voluntarily participated in the one-hour lecture and were divided into groups of two to use the available 15 headsets. The study was assessed by analyzing the log files and their answers to a satisfaction and usability questionnaire. The results indicated that the VR application was an effective supplement to traditional instruction, as the students reported that it helped them better understand technical representation concepts and made the learning experience more enjoyable.

Keywords: Virtual Reality · Engineering education · Laboratory experience · User-centered evaluation

1 Introduction

Education is essential for preparing future engineers to solve complex real-world problems. However, the traditional methods of teaching engineering concepts using textbooks, lectures, and laboratory experiments have limitations in providing students with practical experience and a comprehensive understanding of the subject matter. Recently, traditional media also revealed limitations in attracting students' attention to lectures and, most of all, in promoting active learning mechanisms.

Students often struggle to visualize how theoretical concepts learned in the classroom apply in real-world scenarios, especially in situations where hands-on experience is hard to come by.

In recent years, Virtual Reality (VR) technologies have been increasingly used to enhance engineering education, providing students with a game-changing approach to learning. VR offers a simulation environment where students can explore, interact with others, and even manipulate complex engineering systems, providing a level of practical

M. Carfagni et al. (Eds.): ADM 2023, LNME, pp. 414–422, 2024.
https://doi.org/10.1007/978-3-031-52075-4_47

experience that is not easily achievable using traditional teaching methods. With VR, students can work with 3D models of real systems, allowing them to understand how individual components work together to form the larger systems they are studying.

VR has proven to be an effective tool for teaching engineering concepts by making learning more immersive, engaging, and fun [13]. It makes abstract theories and concepts more intuitive and perceptual, thereby enhancing students' comprehension of complex ideas. Spatial thinking abilities, for instance, are fundamental skills for engineers, but they can be challenging to teach with language alone. A three-dimensional simulated environment can support all the students, even those with poor spatial sense, in exploring the nature and the shapes of geometries [1] and in understanding the theory behind the learning concepts thanks to the "contextually enriched interactions" provided by the technology [2]. Moreover, VR-based education can provide students with cognitive, psychomotor, and affective benefits. Immersive experiences improve students' cognitive skills in remembering and understanding spatial and visual information and knowledge, leading to better learning outcomes than traditional classroom instruction [3]. Students can also develop psychomotor skills related to head movement, visual scanning, and body movements, which can be trained until the acquisition of the desired level of proficiency and then transferred to the real world [4]. Finally, affective skills such as interpersonal communication and emotional regulation can be improved towards the control of the emotional response to stressful or difficult situations [5] and higher self-confidence while moving to professional activities [6].

One of the key advantages of VR is that it provides an immersive and interactive environment to practice new skills and concepts in a simulated yet realistic setting [7]. This feature enables the exploration of complex systems and large-scale devices that can be challenging to teach due to financial and space constraints. The features provided by a virtually simulated scenario allow students to correct their mistakes, repeat procedures, and experience non-dangerous failures in a safe environment without risking injury or damage to equipment [12].

Moreover, VR technology can offer a more comprehensive and enriched learning experience through visualization and interactivity, which are crucial components of effective learning. For instance, virtual tutors can interact with students in real-time and help students solve basic engineering problems and conduct related experiments [9]. Furthermore, creating imaginative scenarios and simulations that help students understand complex topics in exciting ways can enhance the effectiveness of the learning process. This approach enables students to remember the content better, fostering a more engaging and enjoyable learning experience [11].

Another key benefit of using VR technology in engineering education is its flexibility [10]. Unlike physical laboratories, virtual laboratories can be easily adapted to suit the specific needs of students and can be updated quickly to reflect changes in the curriculum. This flexibility can significantly reduce the costs associated with experimental teaching, which can be prohibitively high due to the need for specialized equipment, safety precautions, and maintenance. Additionally, the safety of virtual laboratories reduces the risk of injury, and the virtual environment can be used to create hazardous scenarios that would be dangerous or impossible to recreate in a physical laboratory.

Despite the promising results reported in many studies, there are still several limitations to using VR technology in engineering education. One of the primary concerns is the lack of standardization in the evaluation processes and metrics used to assess the effectiveness of VR in engineering education. Therefore, further research is needed to establish standardized evaluation processes and metrics to evaluate the effectiveness of virtual reality in engineering education. Additionally, the absence of formal evaluation and small participant populations in reported studies may be detrimental to fully understanding the benefits and limitations of virtual reality in engineering education. Another limitation of VR technologies is the lack of realism in their 3D virtual environments. This weakness may distract students from the specified learning tasks, negatively impacting the immersive learning experience [8]. Additionally, the use of head-mounted displays (HMD) and VR devices can cause cybersickness, motion sickness, disorientation, nausea, pallor, sweating, and headaches.

2 Research Objective

This research aims to address some of the limitations previously described and associated with the adoption of VR technologies in engineering education. The study utilizes data collected from log files and a usability questionnaire to demonstrate the successful adoption of innovative technologies, such as VR headsets, for delivering didactic concepts to a large number of engineering students. The feedback received from this study may prove useful for other researchers who intend to undertake a similar didactic approach in the design and implementation of VR applications. For this reason, the paper first presents detailed information on the tasks and exercises implemented in the VR environment, the organization of the activity, and the profile of the students participating in the study. The results of the experimental activity are then presented in the final section, followed by a discussion of their significance in terms of future research directions. This research contributes to the understanding of the effectiveness of VR technologies in engineering education and provides insights into the potential of this technology for delivering didactic concepts to a broader audience.

3 Materials and Methods

In this study, a VR application was developed using Unity 3D, a powerful graphics engine that enables seamless integration with commercial VR devices and executed on the Oculus Quest 2. The VR experience was set within a highly realistic mechanical workshop, with the intention of immersing users in a familiar virtual environment and providing an accurate perception of the represented objects (Fig. 1). The experience features a working table containing objects that users can interact with, as well as a whiteboard that displays all the instructions and elements necessary to complete each task of the activity.

Fig. 1. The high-realistic virtual environment developed for the learning activities.

3.1 VR Application

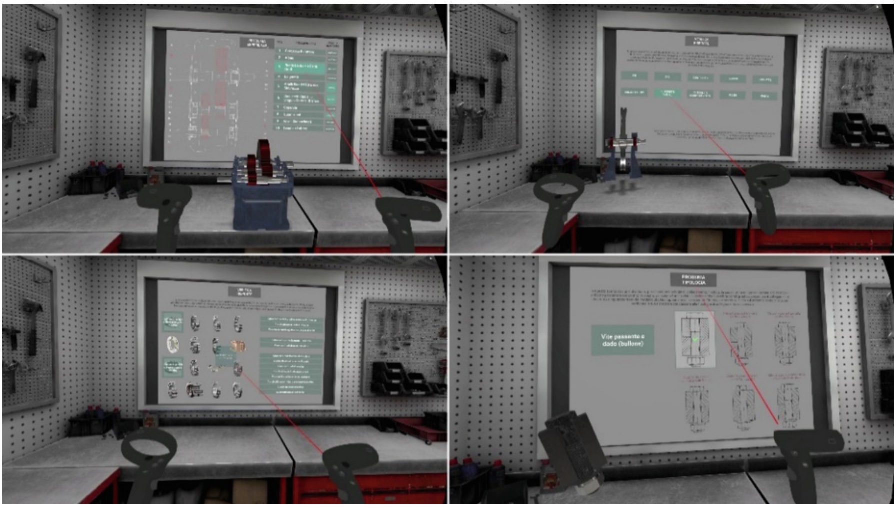

Fig. 2. Screenshot of 4 different levels of the VR experience (top-left: gearbox technical drawing and BOM; top-right: sectional view participation; bottom-left: bearings identification; bottom-right: technical representation of threaded connections).

The VR activity is composed of nine levels, which are structured to provide opportunities for exploration, learning, and verification of acquired skills. A two-stage mechanical gearbox is the primary focus of the initial phase, which involves disassembling a 3D model of the gearbox and observing all its mechanical components. The subsequent phase consists in identifying the components and their technical representation using a sectional view and a bill of materials. Students can use these tools to correlate the two different types of representation and better recognize the components (see Fig. 2).

The knowledge gained in the initial phases is then applied to disassembling the gearbox's output shaft, reordering a sequence of successive steps. This task leads to the first question of the experience, which can be verified using an interactive animation applied to the gearbox. The second part of the activity focuses on demonstraing general skills, such as selecting mechanical components that are not visible in a sectional view due to representation rules, recognizing different types of bearings, and selecting the appropriate technical representation for various threaded connections. Interactive videos are provided to complement these exercises and explain how to create a sectional view correctly and how threaded connections should be represented.

Each exercise provides the opportunity to view the different elements in 3D, enabling an immediate check of correct answers and, if necessary, an explanation of incorrect answers.

3.2 Participants

First-year mechanical, energy, and aerospace engineering undergraduate students at Politecnico di Milano attending a course entitled "Methods for Technical Representation" were involved in the testing activity. Among the 2180 students regularly enrolled in the 2022/2023 academic year, 448 voluntarily, aged between 18 and 21 years old (80% male and 20% female, 95% were in their first year of attending the course, while 5% were repeating the course for the second consecutive year) have decided to try the immersive experience. Among all participants, 69% had never used a Virtual Reality system. The remaining 31% of students stated that they used a virtual reality system for recreational purposes (81%), for academic purposes (2%), for both reasons (13%), or for tourism and cultural projects (3%) (Fig. 3).

3.3 Methods

The VR activity was conducted over a period of two weeks at the end of the semester to facilitate the effective delivery of the didactic content presented in Sect. 2.1. The classroom was equipped with 15 workstations, each comprising a desktop computer and an Oculus Quest 2 headset. Despite the provision for running 15 parallel experiences, the large number of participants required to split them into groups of two. Each pair of students performed the activity in its entirety. Streaming the VR experience on the computer screens and providing printouts of the contents on the whiteboard for each level enabled active collaboration among students, even for those not currently wearing the headset. Prior to the activity, all students received a customized user manual and instructional video to familiarize themselves with the proper use of the VR headset.

Participants were pre-assigned to specific workstations, time slots, and execution orders. Upon arrival, they received a brief orientation on the technology's functionalities and the activity's objectives. The activity began when each team had a student wearing a headset and the other sitting in front of their designated monitor. The activity lasted for 50 min, after which students could view their performance in terms of the percentage of success achieved in different tasks. They also completed an online survey to evaluate

Fig. 3. A student during the execution of the VR experience.

their experience. The decision not to adopt a standard questionnaire available in the literature was driven by the need to harmonize the results related to students' experiences with similar experiments carried out at Politecnico di Milano on other subjects. For this reason, the questionnaire was divided into two parts: the first part includes questions specifically aimed at assessing the experience and its characteristics, while the second part adopts a set of questions to enable the comparison of student feedback regarding the effectiveness and appreciation of the delivery mode of educational content across different courses and types of virtual laboratories.

4 Results

Results of the survey indicate that the majority of students (76%) did not encounter any particular difficulties when using the application. Only 7.5% experienced disconnection problems, and 5% found it difficult to navigate the virtual environment during their first use. A smaller minority reported issues included focusing the image in the headset, pressure on the head, loss of initial data, dead controller, voice communication, and app crashes.

66% of the participants did not experience discomfort when using the headset for a prolonged period. However, 9% experienced nausea, 16% experienced disorientation, and 9% reported headaches and eye strain, difficulties due to glasses and focus.

During the activity, 49% of participants did not encounter any particular difficulties, while 6% asked teachers/technicians for help to solve problems within the virtual environment. 11% had trouble communicating with their peers while wearing the headset. 31% would have preferred more time to complete the activity, and 9% encountered difficulties in performing the task.

The most appreciated aspects were the use of a first-person VR system and the ability to apply the concepts learned in class in practice. Students also appreciated the ability to independently compare objects and their sectional representation and to manipulate objects in virtual reality.

Responses to open-ended questions indicated that many students appreciated the concrete experience and found it useful to better understand the topics studied, the ability to observe and interact with mechanical objects seen in class, the ability to assemble and disassemble parts, the direct evidence of the table-object relationship, and collaboration with colleagues.

Finally, students suggested having more time to complete the activity, verifying that all theoretical topics were covered, and improving the physics at the beginning of the experience.

ASPECT TO EVALUATE	**RATE [%]**					**TOT**
	1	2	3	4	5	3 + 4 + 5
Adoption of a VR headset	0	0	10	31	59	100
Applying concepts delivered in class	0	2	13	27	58	98
Being immerse in realistic environment to understand mechanical objects	1	1	23	31	44	98
Performing activities to test practical and theoretical skills	0	3	21	27	49	97
The introduction and the orientation videos	7	7	28	27	31	86
Exercises aimed to prepare the execution of practical activities	8	6	26	26	34	86
Possibility to manipulate objects in a 3D and immersive virtual environment	2	1	9	18	70	97
Possibility to view the sectional view of objects together with their 3d models	1	2	13	24	60	97
Quiz to assess the level of understanding	2	2	17	35	44	96

5 Discussion

The results of the survey indicate that the use of VR technology in education has the potential to enhance student engagement and understanding of complex concepts. The majority of students did not encounter any significant issues when using the VR application, and the most appreciated aspects were the first-person perspective and the ability to apply theoretical concepts in practice. This suggests that VR technology can be an effective tool in promoting active learning and critical thinking in students.

However, some students did experience discomforts, such as nausea and disorientation, and reported issues with communication and time constraints. These issues should be addressed to improve the overall user experience and promote the widespread adoption of VR technology in education.

The open-ended responses also highlight the benefits of hands-on, experiential learning in improving student engagement and understanding. Overall, these results suggest that VR technology has the potential to change the way we teach and learn by overcoming some of the limitations of the traditional approach. Still, careful consideration should be given to user experience and the design of VR applications in education. Future research could explore the effectiveness of VR technology in promoting deeper learning and the transfer of knowledge to real-world contexts or final exams. A comprehensive evaluation of the achievement of expected learning outcomes will be conducted at the conclusion of the academic year, when all student examination grades for the course become available. The large number of participants will enable a comparative analysis of these results with those of previous years, facilitating a thorough assessment of potential variations. Additionally, the questionnaire will allow to assess and compare student ratings with those obtained in other courses that have implemented different VR-based experiences. This comparative analysis will furnish valuable insights into the characteristics of the VR application that can be further refined to enhance its effectiveness in promoting students' learning outcomes and engagement.

References

1. Cardoso, O.I.H., Unver, E., Aslan, R., Kus, A., Chotrov, D.: Application of VR and AR tools for technical drawing education. In: The 16th Annual International CAD Conference, pp. 363–366 (2019). https://doi.org/10.14733/cadconfP.2019.363-366
2. Chih-Fu, W., Ming-Chin, C.: Effectiveness of applying 2D static depictions and 3D animations to orthographic views learning in graphical course. Comput. Educ. **63**, 28–42 (2013). https://doi.org/10.1016/j.compedu.2012.11.012
3. Wadee, A.: Virtual reality systems enhance students' achievements in engineering education. Behav. Inf. Technol. **35**(11), 919–925 (2016). https://doi.org/10.1080/0144929X.2016.1212931
4. Kahlert, T., van de Camp, F., Stiefelhagen, R.: Learning to juggle in an interactive virtual reality environment. In: Stephanidis, C. (ed.) HCI International 2015 - Posters' Extended Abstracts. Communications in Computer and Information Science, vol. 528, pp. 196–201. Springer, Cham (2015). https://doi.org/10.1007/978-3-319-21380-4_35
5. Gutiérrez, J., Ferrer-García, M., Plasanjuanelo, J., Andrés-Pueyo, A., Talarn-Caparrós, A.: Virtual reality to train diagnostic skills in eating disorders. Comparison of two low cost systems. In: Annual Review of Cybertherapy and Telemedicine 2015: Virtual Reality in Healthcare: Medical Simulation and Experiential Interface (2016)
6. Nelson, M.E., Ahn, B.: Virtual reality activities for teaching engineering students professional development skills. In: 2018 IEEE Frontiers in Education Conference (FIE), San Jose, CA, USA, pp. 1–5 (2018). https://doi.org/10.1109/FIE.2018.8659258
7. Kumar, V.V., Carberry, D., Beenfeldt, C., Andersson, M.P., Mansouri, S.S., Gallucci, F.: Virtual reality in chemical and biochemical engineering education and training. Educ. Chem. Eng. **36**, 143–153 (2021). https://doi.org/10.1016/j.ece.2021.05.002

8. Kamińska, D., Sapiński, T., Aitken, N., Della Rocca, A., Barańska, M., Wietsma, R.: Virtual reality as a new trend in mechanical and electrical engineering education. Open Phys. **15**(1), 936–941 (2017). https://doi.org/10.1515/phys-2017-0114
9. Damasceno A., Martins A., Chagas M.L., Barros E., Maia P.H., Oliveira F.: STUART: an intelligent tutoring system for increasing scalability of distance education courses. In: 19th Brazilian Symposium on Human Factors in Computing Systems, pp. 1–10 (2020). https://doi.org/10.1145/3424953.3426640
10. Prieto, M.D., Sobrino, Á.F., Soto, L.R., Romero, D., Biosca, P.F., Martínez, L.R.: Active learning based laboratory towards engineering education 4.0. In: International Conference on Emerging Technologies and Factory Automation, pp. 776–783 (2019). https://doi.org/10.1109/ETFA.2019.8869509
11. Singh, G., Mantri, A., Sharma, O., Kaur, R.: Virtual reality learning environment for enhancing electronics engineering laboratory experience. Comput. Appl. Eng. Educ. **29**, 229–243 (2021). https://doi.org/10.1002/cae.22333
12. Halabi, O.: Immersive virtual reality to enforce teaching in engineering education. Multimed. Tools Appl. **79**, 2987–3004 (2020). https://doi.org/10.1007/s11042-019-08214-8
13. Cardoso, O.I., et al.: A design-based approach to enhancing technical drawing skills in design and engineering education using VR and AR tools. In: 14th International Joint Conference on Computer Vision, Imaging and Computer Graphics Theory and Applications, pp. 306–313 (2019). https://doi.org/10.5220/0007566003060313

Experimental Methods in Product Development

Directly Cooled Silicon Carbide Power Module: Pin-Fins Roughness Effect on Pressure Drop

Luca Donetti[1(✉)], Alessandro Sitta[2], Michele Calabretta[2], Marco Torrisi[2], Stefano Mauro[1], and Gaetano Sequenzia[1]

[1] Università degli Studi di Catania, Catania, Italy
luca.donetti@phd.unict.it
[2] STMicroelectronics, Catania, Italy

Abstract. The use of silicon carbide (SiC) in power semiconductor modules has led to higher power density, increased maximum junction temperature, high voltage application, and more compact devices, which require efficient cooling systems. This study was to investigate the influence of the surface roughness on the pressure drop of ACEPACK^{TM} DRIVE, a commercial SiC-based power module for traction inverter. This power module has a cylindrical pin-finned baseplate that is mounted on a dedicated cooling device (water jacket) in which coolant media flows. The analysis aimed to characterize the pressure drop between the inlet and exhaust sections of the water jacket, with the objective of optimising the coolant flow for an efficient module cooling, avoiding both excessive resistance and insufficient flow. Confocal laser scanning microscope was used to measure roughness on two different pin-fins with the same geometric characteristics but different surface roughness. Pressure drop measurements were taken at different coolant temperatures and flow rates using a hydraulic test bench. Results indicate that the pressure drop of the higher roughness configuration is 13-19% smaller than the first one, depending on the flow rate and coolant temperature. The suggested reason is that this decrease is caused by a reduction in pressure drops due to concentrated losses associated with fluid flow separation.

Keywords: Power modules · Pin-Fins · Roughness · Pressure drop · CLSM

1 Introduction

Power electronics systems have an increasingly central role in providing high-efficient power conversion for renewable energy systems, energy storage systems, electric and hybrid vehicles [2]. In the past, power electronic devices were based on silicon, but its physical properties are not suitable for modern high voltage applications. Silicon carbide (SiC) and gallium nitride (GaN) have become popular alternatives as they offer better physical properties [15], resulting in higher

M. Carfagni et al. (Eds.): ADM 2023, LNME, pp. 425–432, 2024.
https://doi.org/10.1007/978-3-031-52075-4_48

power density, increased maximum junction temperature, higher voltage applications, and more compact devices. These characteristics lead to higher heat fluxes to be dissipated through smaller surfaces, so the efficient dissipation of heat generated by power modules is crucial for their reliability and performance [5]. Different cooling systems, such as jet impingement cooling, spray cooling, and mini- or micro-channel cooling, can be used depending on the heat flows to be dissipated. Cooling systems can also be differentiated as direct or indirect. A direct cooling system is a method of cooling where the coolant directly comes in contact with the power module, whereas in indirectly cooled systems there is a thermal interface material (TIM), necessary to reduce thermal resistance, through which heat is dissipated from the power module to the coolant. Direct cooling system being preferred for high-power applications due to its better thermal performance and higher power density [10]. Heat sinks with mini- or micro-channels are often used for direct cooling. Inadequate cooling systems can lead to failure mechanisms such as lifting of bond wires, delamination of welds, or presence of cracks [13]. Therefore, optimising the cooling system is an important aspect of power module design, as efficient heat extraction is necessary. Optimising the pressure drop is significant to ensure that the coolant flows at an adequate rate to provide effective cooling to the module without causing excessive resistance or insufficient flow, reducing also the size of the cooling pump, whilst maintaining the same thermal performance. Multi-objective optimisations are often used to find the best trade-off between these aspects by optimising various parameters. Different studies have focused on analysing cooling system performance using pin-fins of different cross-sections [12] as well as varying pin-fins spacing [14]. Another parameter that may has a considerable influence both on pressure drop and thermal performance of the power module's cooling system is the surface roughness of pin-fins [6,7,12], especially given their small size. In fact, the shape and size of the roughness irregularities have an influence upon the overall fluid flow characteristics [8] because an increase in surface roughness leads to an earlier laminar-turbulent transition than in the smooth-walled case, as well as the observation of more vortical structures within the channels [11]. However, the authors just mentioned do not explicitly analyse the influence of roughness on pressure drop.

This study evaluated the pressure drop of direct-cooled power semiconductor module using an experimental approach. Two different design options were considered. Each configuration has the same geometric characteristics such as pin-fins diameter and height, longitudinal and transversal distance. Options are characterised by different surface roughness, which was measured using a confocal laser scanning microscope (CLSM) [9]. Pressure drop measurements were conducted using a hydraulic test bench at different coolant temperatures and flow rates.

2 Materials and Methods

This analysis was aimed to evaluate the influence of surface roughness on pressure drop of a commercial SiC-based power module, which is ACEPACK^{TM} DRIVE by STMicroelectronics. ACEPACK^{TM} DRIVE is a module with a compact, low-inductance design able to withstand the high power density demanded by hybrid and electric vehicle traction applications. The module, shown in Fig. 1a, based on silicon carbide 3rd generation Power MOSFETs, consists of a six-pack topology, with six switches located on three legs. Each switch has a nominal on-state drain-source resistance of 2.55 $m\Omega$, guaranteeing a blocking voltage of 1200 V. The presented module features active metal brazed substrates made of silicon nitride (Si_3N_4) and a direct cooling systems, using a copper baseplate with cylindrical pin-fins, shown in Fig. 1b. Two different design of the baseplate were evaluated. Each configuration has $h_{pin} = 6\ mm$, the same diameter, longitudinal and transversal distance. Figure 1b show also the dimensions of the baseplate.

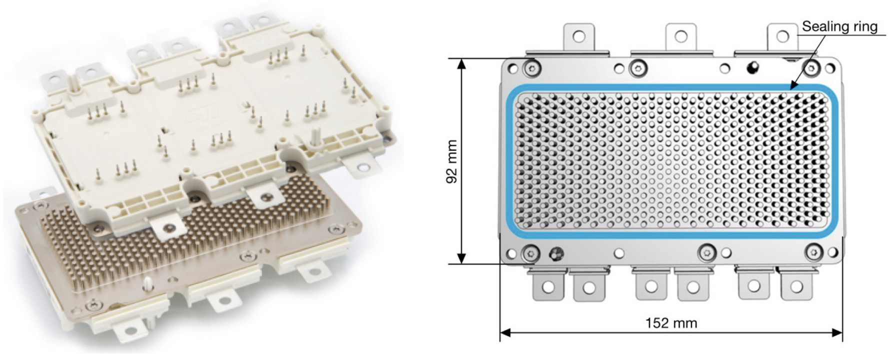

(a) (b)

Fig. 1. ACEPACK^{TM} DRIVE and its baseplate.
(Source: ACEPACK^{TM} DRIVE ADP360120W3 Datasheet and TN1412)

The equipment used to measure surface roughness of the cylindrical pin-fins is LEXT^{TM} OLS5100 Laser Microscope [1]. It is a CLSM and was used to measure the arithmetic mean height S_a in different point on the baseplate. However, additional information can be acquired through CLSM, such as maximum height, root mean square height, skewness and maximum peak height. The use of CLSM eliminates the chromatic aberration that result from using a convectional optical microscope and blurring, allowing to acquire an image with higher contrast and better lateral resolution. In addition, no sample preparation is required to perform the measurement. To scan the sample in the z-direction, CLSM captures multiple confocal images at different focus positions: a small point is created by converging a laser beam and a lens is used to scan the sample at this point.

The microscope then detects the light emitted from the sample and creates a 2D image. Confocal optics use a pinhole at an optically conjugate position to the focusing point, which blocks out light from areas different from the focus point. This ensures that only the light that is focused with the convergence of the laser beam passes through the confocal hole, resulting in bright spots and providing digital data, which will be processed using dedicated software. The wavelength of the optical microscope used in this study is $\lambda = 405\ nm$ and the light acquisition element is made of a two-channel photo-multiplier. This wavelength allows to capture fine patterns and defects that red laser-based microscope or white-light interferometers are unable to detect.

Specifically, roughness measurements were performed at three different points on the baseplate, as shown in Fig. 2. Note that the point B is outside the pin-fins area, so there will be no influence from this surface on the pressure drop, while the points A and C are inside this area. Then, the attention was focused on these points, while the point B is a reference point for assessing how the surface roughness changes after a possible power cycle due to the flow of the coolant.

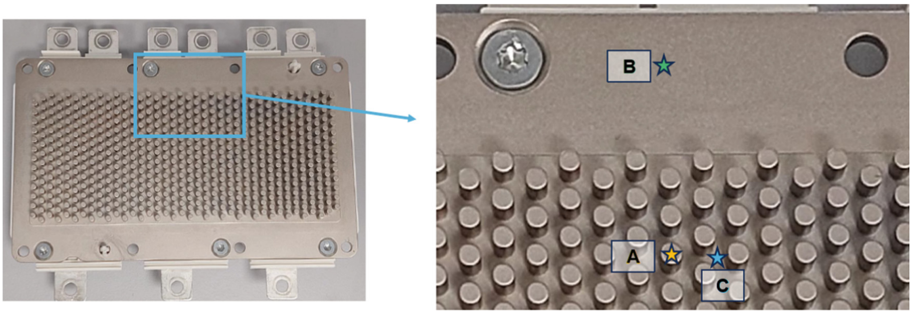

Fig. 2. Measurement points: A) pin-fins top side, B) external area pin-fins, C) between pin-fins on bottom side.

In order to perform the pressure measurements, the baseplate was mounted on a dedicated cooling device (water jacket). The connection of these two elements, which should comply with flatness and straightness tolerances to avoid any hydraulic leakage, results in the formation of the channels in which the coolant flows [3]. This system was connected to the Alpitronic power cycle test bench cooling system (PCTB), where up to 12 modules can be mounted in parallel to their respective cooling stations, as shown in the electrical and hydraulic scheme in Fig. 3a. The cooling system of the test bench consists of two circuits. The primary circuit cools the tempering unit and the switching unit, and it is connected to the building's cooling system. The secondary cooling circuit is a closed circuit operated with a mixture of water and ethylene glycol (50% − 50%), designed to cool the modules. Finally, the pressure drop between inlet and outlet sections of the water jacket was measured using the C98-SDT digital differential pressure manometer (Fig. 3b): this has an accuracy of 0.075%, with a measuring range from 1 to 400 mbar and an operating temperature of -40°C to +85°C.

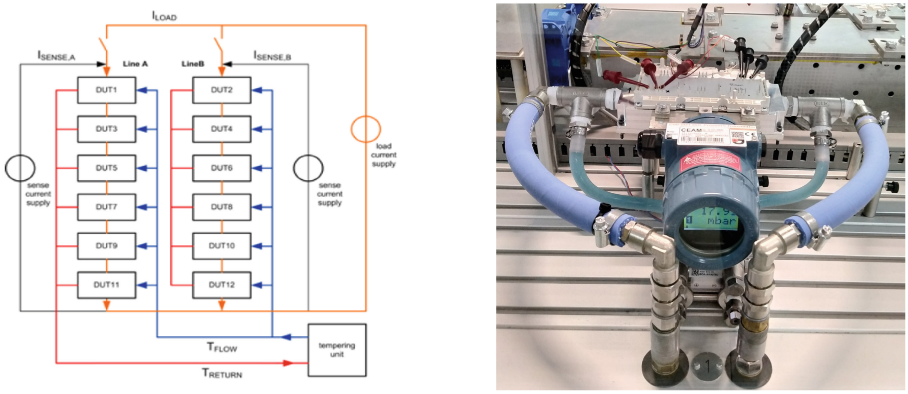

(a) (b)

Fig. 3. a) Electrical and hydraulic scheme of PCTB Alpitronic [4]; b) used experimental setup. (DUT_i = device under test i)

3 Results and Discussion

Roughness and pressure drop measurements were conducted in order to assess the performance differences of the two different design options discussed in Sec. 2. The arithmetic mean height S_a was chosen as parameter for the roughness characterisation because this variable is widespread in industrial practice, as it is well established with available literature, as well as widely used as a process specification. The obtained values by CLSM are shown in the Table 1; it can be seen that the 1st configuration has lower roughness values than the 2nd in the three measurement points, especially on pin-fins top side (point A).

Table 1. Surface roughness (in μm) in different points of the baseplate.

Design option	Point A	Point B	Point C
1st	0.956	1.139	0.956
2nd	6.578	1.803	1.813

As mentioned above, pressure drop measurements were performed by connecting the power module to the Alpitronic PCTB, in which the coolant was a water/glycol (50-50%) mixture. In particular, pressure measurements were carried out at different flow rates, from 2 and 12 l/min with an increase of 1 l/min each time, and at three different coolant temperatures T_f, which are 30, 50 and 75°C. In this way, the influence of pin surface roughness was investigated under varying motion conditions as well as under varying physical properties of the coolant. As expected, when the temperature of the coolant increase the pressure drop decrease for a given flow rate. In fact, the friction losses are proportional to density, so the pressure drop decreases due to the decrease in density. Pressure drop, at different flow rate is shown in Fig. 4a-c, for the analysed temperatures.

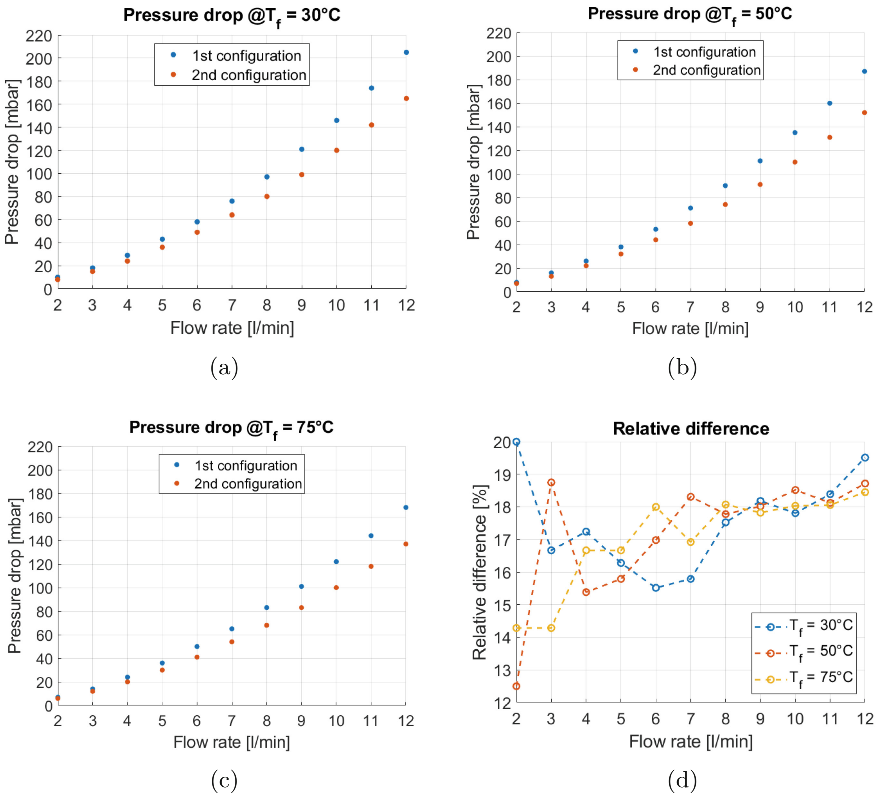

Fig. 4. Pressure drop varying coolant temperature: a) $T_f = 30°C$, b) $T_f = 50°C$, c) $T_f = 75°\ C$. d) Relative difference between two configurations.

From the curves it can be seen that the 2nd configuration, which is the higher roughness design option, presents a lower pressure drop in all cases considered. Assuming the relative difference RD between the 1st and 2nd configuration defined as $RD = (\Delta p_{1st} - \Delta p_{2nd})/\Delta p_{1st}$, represented in Fig. 4d, it can be seen that the second configuration has a lower pressure drop than the first. Note that the major differences in correspondence of the lowest flow rate values is due to the accuracy of the measurements. In fact, due to the lower value of pressure

drop, the measurement error is approximately 5%. Overall, difference ranges between 13 and 19%.
The reason for this observation lies in the fact that the pressure drop is mainly due to two factors: one linked to viscous friction, which is generated near the walls, and the other connected with the pressure drag. This represents a concentrated loss component associated with the detachment of the fluid flow downstream of each cylindrical pin, with dissipative vortex phenomena localised on each of them. Although it is true that first factor increases with surface roughness, it has been shown experimentally that, for Reynolds (Re) numbers greater than 300, in the case of heat sinks with pin-fins, the second factor is the prevalent one [16]. Considering that in the present work $670 < Re < 12300$ at inlet, the distributed pressure drop (viscous friction) increases in the case of baseplate with higher roughness. On the other side, a turbulent boundary layer is likely generated, which reduces the vortex wake and separation downstream of each pin-fin. This effect is enhanced by higher roughness, that lead to an overall pressure drop reduction of the power module cooling system.

4 Conclusions

In this work the influence of the surface roughness of a semiconductor power module's pin-fins on the pressure drop was evaluated. In particular, studies were performed on ACEPACK^{TM} DRIVE power module, which features a direct cooling system with cylindrical pin-fins. Two possible design options were analysed, having the same geometric characteristics but different roughness values. Surface roughness was measured in three points of the baseplate using a confocal laser scanning microscope; pressure measurements were varying the temperature and flow rate of the refrigerant fluid. Configuration with higher roughness has pressure drop values smaller between 13% and 19%. The proposed explanation is that the pressure drop decreases due to the reduction of concentrated losses associated with the separation of the fluid flow, i.e. there is less fluid separation for higher roughness value. The authors propose to develop a CFD (Computational Fluid Dynamics) model to analyse in detail the field of motion established, as function of different fluid and roughness conditions. Simulation can quantify the aforementioned components of pressure drop.

References

1. Specifications of lext^{TM} ols5100 laser microscope. user manual, OLYMPUS, https://www.olympus-ims.com/en/microscopes/laser-confocal/ols5100/#!cms[focus]=cmsContent14937
2. Afonso, J.L., et al.: A review on power electronics technologies for electric mobility. Energies **13**(23), 6343 (2020). https://doi.org/10.3390/en13236343
3. Calabretta, M., Sitta, A., Messina, A.A., Olivieri, S.M., Sequenzia, G.: Geometrical tolerances:"planarity" measurements on automotive power module during its assembly processes-flow. In: Advances on Mechanics, Design Engineering and

Manufacturing IV: Proceedings of the International Joint Conference on Mechanics, Design Engineering & Advanced Manufacturing, JCM 2022, June 1–3, 2022, Ischia, Italy. pp. 1138–1148. Springer (2022). https://doi.org/10.1007/978-3-031-15928-2_99
4. Calabretta, M., Sitta, A., Oliveri, S.M., Sequenzia, G.: Silicon carbide multi-chip power module for traction inverter applications: thermal characterization and modeling. IEEE Access **9**, 76307–76314 (2021). https://doi.org/10.1109/ACCESS.2021.3080505
5. Choi, U.M., Jørgensen, S., Blaabjerg, F.: Impact of cooling system capacity on lifetime of power module in adjustable speed drives. IEEE J. Emerging Selected Topics Power Elect. **7**(3), 1768–1776 (2019). https://doi.org/10.1109/JESTPE.2019.2912387
6. Croce, G., D'agaro, P., Nonino, C.: Three-dimensional roughness effect on microchannel heat transfer and pressure drop. Int. J. Heat Mass Transf. **50**(25–26), 5249–5259 (2007). https://doi.org/10.1016/j.ijheatmasstransfer.2007.06.021
7. Gamrat, G., Favre-Marinet, M., Le Person, S., Baviere, R., Ayela, F.: An experimental study and modelling of roughness effects on laminar flow in microchannels. J. Fluid Mech. **594**, 399–423 (2008). https://doi.org/10.1017/S0022112007009111
8. Kandlikar, S.G., Schmitt, D., Carrano, A.L., Taylor, J.B.: Characterization of surface roughness effects on pressure drop in single-phase flow in minichannels. Phys. Fluids **17**(10), 100606 (2005). https://doi.org/10.1063/1.1896985
9. Launhardt, M., Wörz, A., Loderer, A., Laumer, T., Drummer, D., Hausotte, T., Schmidt, M.: Detecting surface roughness on sls parts with various measuring techniques. Polym. Testing **53**, 217–226 (2016). https://doi.org/10.1016/j.polymertesting.2016.05.022
10. McPherson, B., McGee, B., Simco, D., Olejniczak, K., Passmore, B.: Direct liquid cooling of high performance silicon carbide (sic) power modules. In: 2017 IEEE International Workshop On Integrated Power Packaging (IWIPP), pp. 1–5. IEEE (2017). https://doi.org/10.1109/IWIPP.2017.7936760
11. Natrajan, V., Christensen, K.: The impact of surface roughness on flow through a rectangular microchannel from the laminar to turbulent regimes. Microfluid. Nanofluid. **9**(1), 95–121 (2010). https://doi.org/10.1007/s10404-009-0526-2
12. Sadaghiani, A.K., Koşar, A.: Numerical investigations on the effect of fin shape and surface roughness on hydrothermal characteristics of slip flows in microchannels with pin fins. Int. J. Therm. Sci. **124**, 375–386 (2018). https://doi.org/10.1016/j.ijthermalsci.2017.10.037
13. Smet, V., et al.: Ageing and failure modes of igbt modules in high-temperature power cycling. IEEE Trans. Industr. Electron. **58**(10), 4931–4941 (2011). https://doi.org/10.1109/TIE.2011.2114313
14. Vasilev, M., Abiev, R.S., Kumar, R.: Effect of circular pin-fins geometry and their arrangement on heat transfer performance for laminar flow in microchannel heat sink. Int. J. Therm. Sci. **170**, 107177 (2021). https://doi.org/10.1016/j.ijthermalsci.2021.107177
15. Yang, Y., Dorn-Gomba, L., Rodriguez, R., Mak, C., Emadi, A.: Automotive power module packaging: current status and future trends. IEEE Access **8**, 160126–160144 (2020). https://doi.org/10.1109/ACCESS.2020.3019775
16. Zhao, H., Liu, Z., Zhang, C., Guan, N., Zhao, H.: Pressure drop and friction factor of a rectangular channel with staggered mini pin fins of different shapes. Exp. Thermal Fluid Sci. **71**, 57–69 (2016). https://doi.org/10.1016/j.expthermflusci.2015.10.010

Experimental Reliability Assessment of ACEPACK SMIT Power Module

Davide Maria Amoroso[1,2](✉), Biagio Schifano[1], Michele Calabretta[2], Giuseppe Mauromicale[2], and Gaetano Sequenzia[1]

[1] University of Catania, Catania, Italy
[2] STMicroelectronics, Catania, Italy
davidemaria.amoroso@st.com

Abstract. This paper presents a method to study the reliability behavior of the ACEPACK^{TM} SMIT, which is a top side-cooled power module employing high-voltage silicon MOSFETs in a half bridge topology.

The experimental test involves power cycling: this is an accelerated stress test, which allows monitoring a temperature-sensitive electric parameter to study the thermal behavior of the package. The efficiency of heat exchange between the module and the cooling plate surfaces is strongly influenced by the thermal interface material (TIM) used between them. TIM is designed to fill gaps and voids between two surfaces, in order to to increase the effective contact area and improve thermal conductivity at the interface. In this work, the thermal performance of two different TIMs, a thermal grease and a phase change material, will be analyzed.

The aim of the paper is to provide an experimental approach for characterizing the reliability behavior of power modules, considering the thermal behavior when different TIMs are considered.

Keywords: Power Module · Reliability · Accelerated stress test · Thermal Interface Material · TIM

1 Introduction

Power electronic devices have become increasingly important in various industries due to their ability to efficiently convert and control electrical power [2]. The use of semiconductor technology has led to the development of devices such as IGBTs, MOSFETs, and diodes, which are widely used in electric traction applications, including locomotives, subways, and automobiles [1]. This technology plays a crucial role in addressing the current issue of energy consumption and improving the efficiency of industrial motors and generators [8]. Power modules, which are capable of storing high power densities, are particularly useful in the automotive sector and can be utilized in various types of vehicles [12].

M. Carfagni et al. (Eds.): ADM 2023, LNME, pp. 433–440, 2024.
https://doi.org/10.1007/978-3-031-52075-4_49

This study will focus on the stress generated on the power module under cyclic temperature action, which can have negative impacts on the device's performance and reliability. The reliability studies aim to estimate the life of the device and predict when it may fail according to different failure mechanisms by determining the acceleration factors between test and application conditions, thus forecasting device lifetime during its mission profile [4].

The thermal interface material (TIM) plays a critical role in the thermal management of electronics by facilitating efficient heat exchange between the electronic components and the heat sink or other cooling system. TIMs are typically placed between the electronic component and the heat sink to ensure optimal thermal contact and minimize the thermal resistance at the interface. There are various types of TIMs available, such as thermal greases, adhesives, tapes, phase-change materials, and gap fillers, each with its unique properties and benefits. The choice of TIM depends on several factors, including the application requirements, operating temperature range, thermal conductivity, viscosity, and ease of application. When managing the temperature of metallic housings, it's crucial to focus on the TIM. The performance of the TIM is directly related to the reliability of the components, and not having TIM can lead to significantly higher temperatures. In power electronic applications that generate a lot of heat and handle high currents, even small changes in the thickness and thermal conductivity of the TIM can have a significant impact [7].

The thermal resistance of the entire power module is a critical aspect for electronic package designers, as it enables them to design the package to function effectively throughout its useful life [13]. To estimate this, TIM reliability studies are conducted using accelerated stress tests. However, it is also possible to first characterize the TIM's material properties before performing these tests. Due et al. conducted various stress tests, including temperature and humidity stress test (THT/HAST), high temperature storage (HTS), thermal cycle (TC) and power cycle (PC), to evaluate the reliability of different TIM materials [3]. They focused on the methodologies and provided commentary on the obtained results.

2 Materials and Methods

2.1 Materials

The ACEPACK^{TM} SMIT (illustrated in Fig. 1) is a surface-mounted power module which employes an epoxy compound. It contains two silicon-based power MOSFETs, having a breakdown voltage equal to 650 V, in half-bridge configuration. The semiconductor chips are connected to a three-layer direct-bonded copper ceramic substrate, which includes copper, an alumina substrate for insulation, and copper. The performance of power semiconductor devices is dependent on the temperature of the silicon chip : hence, the electrical parameters are given at a specific temperature. To ensure that these devices perform safely, the heat transfer between the chip and its surrounding ambient must be managed to limit the junction temperature. The ACEPACK^{TM} SMIT Power Module is designed to be attached to a printed circuit board, and its top side should be connected to an external heatsink to extract the heat generated in the devices.

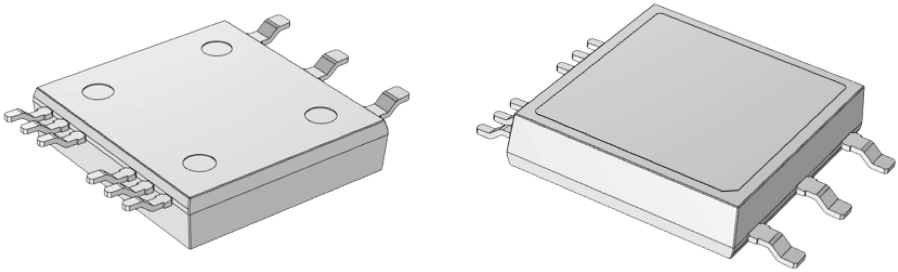

Fig. 1. ACEPACK^{TM} SMIT Power Module SMIT package overview.

Selecting an appropriate TIM is a critical aspect of assessing the reliability of a power module, as it must satisfy specific requirements based on the application. The key factors considered while choosing the ideal TIM include [10] thermal conductivity, which determines the TIM's ability to transfer heat across interfaces, and thereby, influences thermal performance to a great extent and thermal resistance, which indicates the level of difficulty heat encounters while passing through a material. Other characteristics are the phase change temperature that is the temperature at which a substance changes from a solid to a liquid, enabling it to fill gaps and remove any trapped air. The substance must have a high enough viscosity to prevent it from flowing too easily when exposed to high temperatures or pressures. The operating temperature range is determined by the typical temperatures experienced in a specific application. Mounting pressure from tightening can have a significant impact on the performance of the TIM. For this project, TIMs were chosen in order to enable a comparison. Two TIMs were selected: a thermal grease and a phase change material (PCM).

TIMs that consist of greases are widely used and have a thermal resistance that falls within the range of 10–100 $mm^2\ K\ W^{-1}$. Greases are made up of thermally conductive fillers that can be combined, for example, with organic silicone. When pressure is applied, greases can achieve a thin bond line thickness, and their low viscosity allows them to fill gaps easily. However, researchers have found that there is often a significant discrepancy between the data provided by grease manufacturers and the results of tests conducted by investigators. Additionally, controlling the thickness of greases can be challenging, and their low viscosity means that excess grease may flow out beyond the edges, creating a messy manufacturing environment. Furthermore, thermal recycling can cause greases to pump out and separate, which reduces their reliability as a TIM [14]. For what concern the thermal grease, the Kerafol KP99 from KERATHERM® was used.

On the other hand, a PCM has a component that changes phase, and a filler that improve its thermal conductivity. They have the ability to act as an energy buffer by absorbing heat during the phase change process and generating an additional path for heat dissipation. Unlike other TIMs, PCMs do not experience issues such as dry out or delamination and they are less likely to be affected by pump out. However, voids can occur with thermal cycles, and PCMs are unable to fill these voids once they have formed [14]. According on the considered application type, the latent energy, related to the phase change, can provide or absorb heat [9]. In this framework, the TCP 4000PM from HENKEL® was used.

2.2 Methods

To determine the dependability of the manufactured devices, the reliability testing based on AQG 324 was employed [5]. In the context of power modules, power cycling refers to the process of turning the device on and off repeatedly under controlled conditions to evaluate its reliability and performance [11].

Reliability tests for power cycles (PC) are performed to replicate the temperature changes caused by device self heating during its on state. Power Cycling tests are the most realistic, as they accurately capture the thermomechanical loading conditions during temperature/power cycles. This is because there are temperature gradients between the base component and the thermal attach. Thus, the stress field during the reliability test closely resembles real-life conditions. Overall, power cycling is an essential part of the testing and validation process for power modules and plays a critical role in ensuring their long-term reliability and performance.

The power cycle is divided into two categories based on the cycle timing [6]: this study simulated PCsec with a $t_{on} = 3.5\,s$. During the power cycle, parameters are monitored to determine the end of life (EoL) of a module. In PCsec, the EoL condition (from AQG 324) is determined by two parameters, V_{ds} and R_{th} (see Table 1). V_{ds} is the drain-source voltage of the MOSFET, while R_{th} is the thermal resistance, defined by the following equation:

$$R_{\mathrm{th,j-NTC}} = \frac{T_j - T_{NTC}}{P} \tag{1}$$

Table 1. EoL criteria.

Parameter	Drift from
Increase of forward voltage - Mosfet: V_{ds}	+5%
Increase of thermal resistance - R_{th}	+20%

The ACEPACK^{TM} SMIT Power Module was attached to a printed circuit board (Fig. 2). Its top side was linked to an external heatsink and positioned in the Alpitronic® power cycling test bench (PCTB). During each power cycle, various measurement data are collected by PCTB test bench, including drain-source voltage, thermal resistance, maximum and minimum junction temperatures, and other characteristic parameters. The Alpitronic® power cycling test bench is created for testing the lifespan of up to 12 half bridges concurrently. These half bridges are linked in a sequence on two test lines and exposed to a current load of 1200A maximum. Device under test (DUT) is connected to the current circuit load. The test bench incorporates a cooling system, which is important for testing some electronic components, and it can sustain a broad temperature range of 25 °C to 120 °C. In accordance with AQG-324, the power cycle was conducted with a t_{on} of 3.5 s and a t_{cycle} of 7.5 s, with a temperature jump of 100 °C and a maximum junction temperature (T_{jmax}) of 150 °C, a current of 50A and indirect cooling with a mixture of water and glycol.

The TIMs were applied manually, using a stencil. The TIM was placed between the between the cooling plate and the module. The Kerafol KP99 thermal grease did not require any preparation prior to the power cycle, while the PCM TCP 4000PM needed to undergo a drying process. The drying times were specified in the datasheet and depended on the temperature and thickness of the TIM.

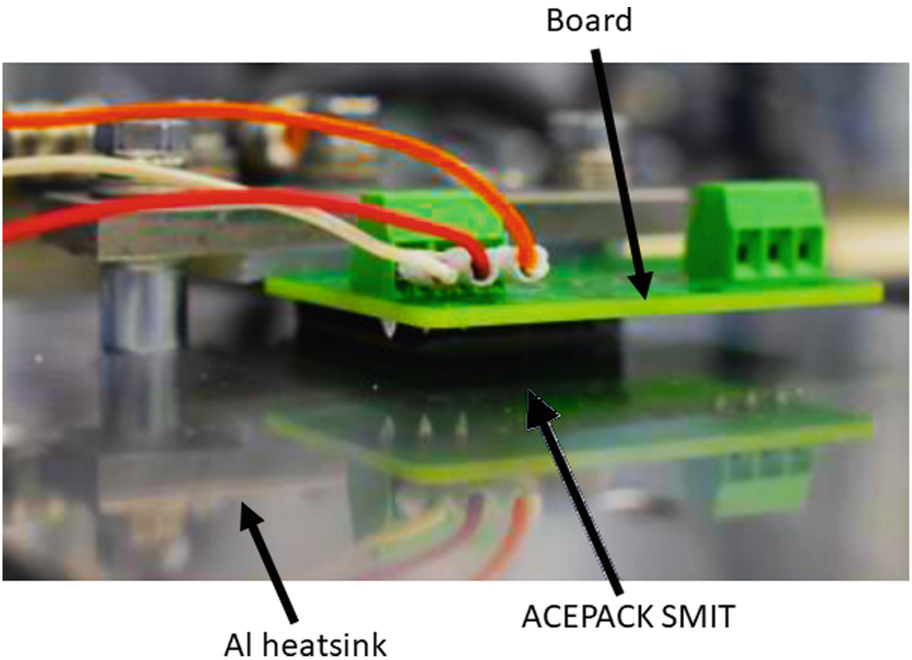

Fig. 2. Test setup ACEPACK^{TM} SMIT Power Module

3 Experimental Results

The power cycle assessment executed in this paper gives a reliability assessment of the ACEPACK^{TM} SMIT module by using the two TIMs introduced in the previous section. To ensure that the reliability results were not affected by the degradation of the thermal grease, it was renewed by taking it off and reapplying it (at roughly 0.1 normalized cycles) once the failure criteria (V_{DS} drift) were met. The EoL conditions were reset and the power cycle was initiated again. However, the PCM was never replaced during the test.

The normalized curves of V_{DS} and R_{th} for Kerafol and Henkel TIMs are plotted and analyzed in Fig. 3 and in Fig. 4, respectively.

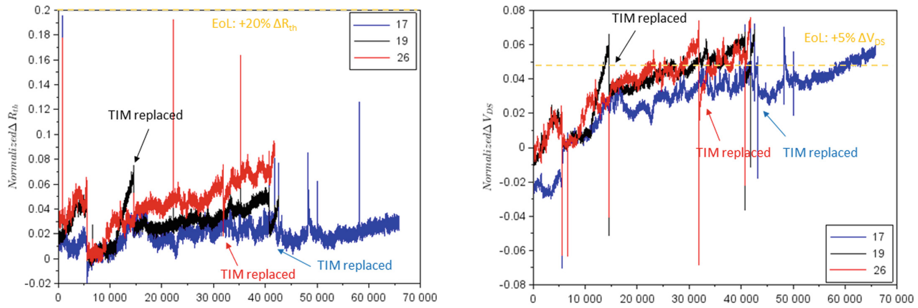

Fig. 3. Power cycle results: normalized V_{DS} and R_{th} for Kerafol sample.

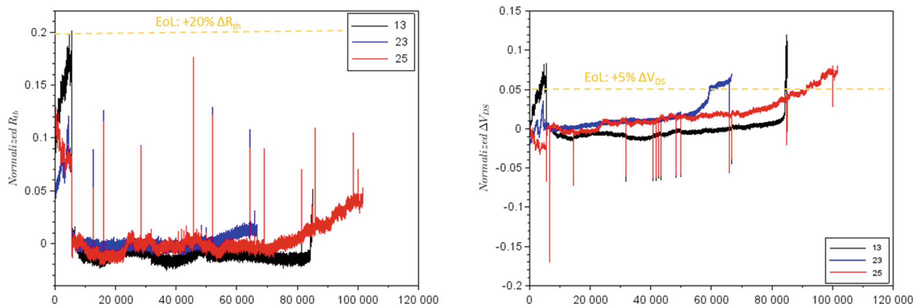

Fig. 4. Power cycle results: normalized V_{DS} and R_{th} for Henkel sample.

The modules that used thermal grease (KP99) demonstrated more decay during the power cycle, with the TIM being replaced once to reach the End of Life (EoL) standard. The graph then revealed a steadily increasing trend, eventually surpassing the 5% V_{DS}, which is the EoL criterion. In contrast, the behavior of the phase change material (TCP 4000PM) was quite different, with

the V_{DS} and R_{th} values staying at contained levels and drifting beyond the EoL values after a significantly longer period compared to thermal grease.
By examining the values of R_{th}, it can be observed that the thermal grease operates at temperatures higher than the PCM.

Finally, by comparing the number of cycles of samples with thermal grease and PCM, it can be observed that on average, the modules equipped with the PCM cycled about 40% more than the modules with thermal grease.

4 Conclusion

This study investigated the reliability behavior of ACEPACK^{TM} SMIT power module, considering two distinct thermal interface materials. The experimental analysis carried out during the study provided an opportunity to evaluate the performance of both materials under the same conditions. The test results showed the behaviours of PCM and thermal grease materials. More specifically, the PCM has exhibited superior performance as it was able to endure a significantly greater number of cycles before reaching the end of its lifespan compared to the other TIM.

Overall, the findings of this study can be useful for engineers and researchers working in the field of power electronics and thermal management, as they can provide insights into selecting appropriate thermal interface materials.

References

1. Anoldo, L., et al.: Thermal simulation of a 7kw interleaved module for fast automotive charger. In: 2021 IEEE International Conference on Environment and Electrical Engineering and 2021 IEEE Industrial and Commercial Power Systems Europe (EEEIC/I&CPS Europe), pp. 1–5. IEEE (2021)
2. Bose, B.K.: Power electronics: my life and vision for the future [my view]. IEEE Ind. Electron. Mag. **16**(2), 65–72 (2022)
3. Due, J., Robinson, A.J.: Reliability of thermal interface materials: a review. Appl. Therm. Eng. **50**(1), 455–463 (2013). https://doi.org/10.1016/j.applthermaleng.2012.06.013
4. Durand, C., Klingler, M., Coutellier, D., Naceur, H.: Power cycling reliability of power module: a survey. IEEE Trans. Device Mater. Reliab. **16**(1), 80–97 (2016). https://doi.org/10.1109/TDMR.2016.2516044
5. ECPE: AQG 324 qualification of power modules for use in power electronics converter units in motor vehicles (2019)
6. Heuck, N., et al.: Aging of new interconnect-technologies of power-modules during power-cycling. In: CIPS 2014; 8th International Conference on Integrated Power Electronics Systems, pp. 1–6. VDE (2014)
7. Kesarkar, T.M., Sardana, N.K.: How TIM impacts thermal performance of electronics: A thermal point of view study to understand impact of thermal interface material (TIM). In: 2019 International Conference on Electronics Packaging (ICEP), pp. 200–206. IEEE (2019). https://doi.org/10.23919/ICEP.2019.8733441

8. Lee, H., Smet, V., Tummala, R.: A review of sic power module packaging technologies: challenges, advances, and emerging issues. IEEE J. Emerg. Sel. Top. Power Electron. **8**(1), 239–255 (2019). https://doi.org/10.1109/JESTPE.2019.2951801
9. Ramaswamy, C., Shinde, S., Pompeo, F., Sablinski, W., Bradley, S.: Phase change materials as a viable thermal interface material for high-power electronic applications. In: The Ninth Intersociety Conference on Thermal and Thermomechanical Phenomena In Electronic Systems (IEEE Cat. No. 04CH37543). vol. 2, pp. 687–691. IEEE (2004). https://doi.org/10.1109/ITHERM.2004.1318354
10. Sarvar, F., Whalley, D.C., Conway, P.P.: Thermal interface materials-a review of the state of the art. In: 2006 1st Electronic Systemintegration Technology Conference. vol. 2, pp. 1292–1302. IEEE (2006). https://doi.org/10.1109/ESTC.2006.280178
11. Schiffmacher, A., Strahringer, D., Malasani, S., Wilde, J., Kempiak, C., Lindemann, A.: In situ degradation monitoring methods during lifetime testing of power electronic modules, pp. 895–903 (06 2021). https://doi.org/10.1109/ECTC32696.2021.00149
12. She, X., Huang, A.Q., Lucia, O., Ozpineci, B.: Review of silicon carbide power devices and their applications. IEEE Trans. Industr. Electron. **64**(10), 8193–8205 (2017). https://doi.org/10.1109/TIE.2017.2652401
13. Sitta, A., Renna, M., Messina, A.A., Sequenzia, G., D'Arrigo, G., Calabretta, M.: Thermal measurement and numerical analysis for automotive power modules. In: 2020 21st International Conference on Thermal, Mechanical and Multi-Physics Simulation and Experiments in Microelectronics and Microsystems (EuroSimE), pp. 1–3. IEEE (2020)
14. Zhao, J.W., Zhao, R., Huo, Y.K., Cheng, W.L.: Effects of surface roughness, temperature and pressure on interface thermal resistance of thermal interface materials. Int. J. Heat Mass Transf. **140**, 705–716 (2019). https://doi.org/10.1016/j.ijheatmasstransfer.2019.06.045

Design and Development of a Liquid Crystal Elastomers Infiltration Prototype

Andrea Profili[1](✉), Francesco Di Iorio[1], Søren Aasmul[2], and Lapo Governi[1]

[1] Department of Industrial Engineering, University of Florence, Florence, Italy
andrea.profili@unifi.it

[2] Medtronic Bakken Research Center, Maastricht, Netherlands

Abstract. Liquid crystal elastomers (LCEs) are deformable materials that can be programmed to respond to physical stimuli such as light, heat, and electricity. In order to achieve controllable macroscopic deformation in LCEs, it is important to design the orientation of the liquid crystal molecules. Capillary infiltration of LCEs between two coated laboratory glasses with microscopic grooves along one direction created by rubbing with a velvet-like cloth is a commonly used fabrication method. During infiltration, the desired orientation is influenced by the intermolecular shear force between the liquid crystal monomers and the material of the coated glasses, as well as the glasses surface rubbing direction. It is also important to ensure a constant thickness in the LCE. To address these issues, the authors propose a 3D printed prototype for LCE fabrication that can provide a repeatable procedure and uniform layer thickness. The paper describes the steps involved in the fabrication process, including rubbing, LCE infiltration, and photopolymerization. The results demonstrate that the implemented system can improve the reliability of LCE fabrication by ensuring consistent film thickness and alignment.

Keywords: Liquid Crystal Elastomer · Smart Material · 3D Print Design · Rubbing

1 Introduction

Liquid crystal elastomers (LCEs) are a class of polymers that possess unique properties, such as the ability to exhibit both liquid crystal and elastic behavior [1–4]. These properties enable LCEs to undergo reversible deformation in response to external physical stimuli, such as changes in temperature, exposure to light, and application of electric fields. For example, prior research has indicated the potential of utilizing liquid crystal elastomers (LCEs) in the field of tissue engineering to replicate structures such as intervertebral disks [5] or muscles [6]. Recent studies have shown that a carefully selected set of specially designed LCEs can exhibit similar mechanical properties to artificial cardiac muscles, both in terms of active and passive characteristics. These LCEs, when subjected to light stimulation, can generate maximum tensions comparable to those observed in fully calcium-activated striated muscles, reaching approximately

M. Carfagni et al. (Eds.): ADM 2023, LNME, pp. 441–448, 2024.
https://doi.org/10.1007/978-3-031-52075-4_50

400 mN mm^{-2} [7]. In broad terms, the methods used to synthesize liquid crystal elastomers (LCEs) can be classified into two main categories [1, 3]: two-step cross-linking and one-step cross-linking. The two-step cross-linking process involves the partial cross-linking of the polymer network, which allows for the mechanical orientation of the LCE. In contrast, the one-step cross-linking process involves the direct polymerization of low molecular weight monomers to produce LCEs. One-step cross-linking is particularly suitable to produce LCEs by infiltration between two surfaces, due to the low viscosity of the precursor materials. To achieve controlled macroscopic deformation of LCEs it is necessary to design the orientation of the liquid crystal molecules. Various methods have been developed to determine the alignment of mesogens; these can be broadly categorized into three types [1–4]: alignment by mechanical stress, alignment by external field, and alignment by surface effect. Surface-induced alignment is preferred for practical applications of LCE because it can achieve high-resolution spatial alignment of LC monomers. Surface-induced orientation can be achieved through methods such as local friction, photolithographic patterning, and optical alignment, among others. Alignment layer technology, which is commonly used in the liquid crystal display industry, can also be applied to LCEs. There are two mechanisms involved in achieving alignment. Firstly, intermolecular forces between the liquid crystal monomers and the alignment layer material induce the alignment of the liquid crystal molecules [1, 3, 4]; secondly, the orientation of mesogens is further improved by creating tunnels in the alignment layer. To create microchannels on the surface, a common method is to rub the alignment layer with a velvet cloth [7–9]. These microstructures aid in aligning the long axis of the liquid crystal molecules with the microchannels. After creating the sacrificial coating, the infiltration cell is built. Typically, spacers such as borosilicate microspheres are employed to attain the required thickness [7]. Afterward, the material is capillary infiltrated between the two alignment layers in an isotropic phase at the phase transition temperature (TNI) and then polymerized. It is clear that the creation of microgrooves (rubbing) and the construction of the infiltration cell are crucial steps in the correct fabrication of LCEs. In this paper, the authors propose a prototype for rubbing, positioning the lab slides at a predetermined distance, and maintaining it during the infiltration step.

2 Materials and Methods

Currently, the production process of LCEs involves several sequential steps as shown in Fig. 1. Firstly, the laboratory slides are coated with a sacrificial layer of polyvinyl alcohol (PVA). Next, the slides are rubbed in one direction using a velvet cloth. Afterward, the infiltration cell is constructed for the material to be infiltrated in an isotropic phase. The material is then photopolymerized and cured to form the film. Finally, the film is extracted to complete the process [7].

The PVA sacrificial layer on the glass slide surface is obtained using a spincoater. The slide is then rubbed by placing it on an aluminum plate and vacuum aspirated to maintain the correct position during the rubbing phase. Next, the infiltration cell is created using borosilicate microspheres as spacers between the two glass slides (a rectangular 25 × 50 mm for the bottom one and a circular Φ30 mm for the top one) to maintain the correct distance and then glued together (Fig. 2a). Material infiltration is achieved by capillarity

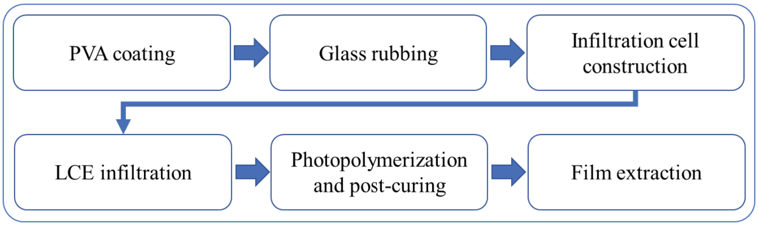

Fig. 1. Liquid crystal elastomers' production steps.

at the TNI temperature by placing the LCE mixture in the free interface between the glass slides (Fig. 2a–b). The mixture used in the study consisted of a monoacrylate monomer called C6BP and a diacrylate crosslinker known as RM257. Both of these components exhibited a nematic mesophase. Additionally, the mixture was doped with Disperse Red 1 Acrylate (DR1 Acrylate) to introduce photo responsiveness. To initiate the radical polymerization reaction, a UV-responsive photoinitiator called Irgacure 369 was utilized [7]. After infiltration, the system is cooled and brought to a temperature of 45 °C for photopolymerization, followed by a post-curing step at 60 °C (Fig. 2c). At the end of the process, the glasses are immersed in water to dissolve PVA and ease the subsequent film extraction (Fig. 2d).

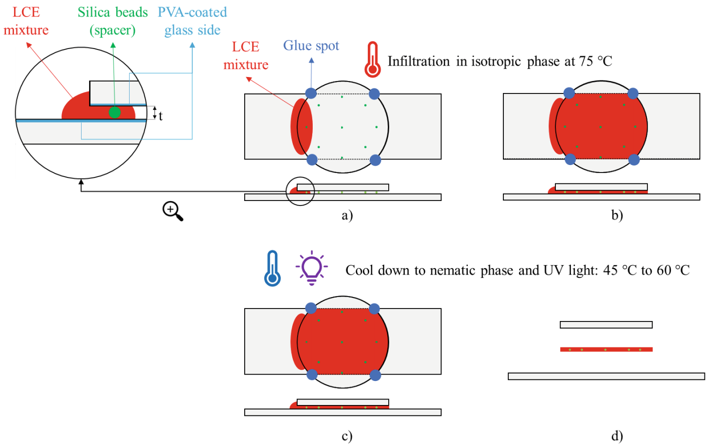

Fig. 2. Cell construction, infiltration and film extraction phases.

The described manufacturing process poses a number of challenges, especially during the rubbing and infiltration phases. For the first one, using a vacuum pump to secure the laboratory slide can lead to slippage or inconsistent rubbing direction between passes. Dealing with the infiltration phase, the use of borosilicate microspheres to separate the slides does not guarantee uniform distance between all points of the slide and may result in the beads remaining within the film at the end of production. Gluing the two slides together to maintain position is also problematic, as the material shrinks during drying of the cyanoacrylate, possibly resulting in thickness unevenness. Furthermore, it is crucial to handle the slides with extreme care and avoid crushing them to prevent contact with the PVA-coated surfaces.

To address these issues, two novel systems were developed, one for the initial rubbing phase and another for the infiltration cell construction. The vacuum pump was deemed unsuitable due to the aforementioned problems, as was the use of glue or microspheres for spacing during rubbing. Instead, a 3D-printed base was created which has a recessed slot on which to place the glass slide (dimension 25 × 75 mm), as shown in Fig. 3. The slot is half the depth of the slide, so that the PVA-coated part emerges. The upper slider has a clearance of 0.4 mm with the side surfaces of the base so that it can slide inwards while maintaining the rubbing direction unchanged for all passes. Two lateral grooves are provided so that the slide can be handled after rubbing without damaging the coating. The 3D printed parts were manufactured using PLA material with a 0.2 mm layer thickness, 25% gyroid infill, extrusion temperature of 210 °C, build plate temperature of 60 °C and nozzle extrusion diameter of 0.4 mm on a Prusa i3MK3S+.

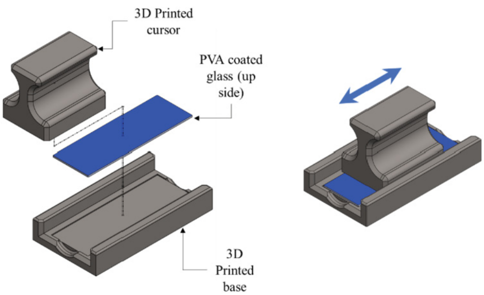

Fig. 3. CAD model of the new rubbing system.

To assemble the infiltration cell, calibrated metal strips were used as spacers and inserted laterally between the slides. The spacers were held in place by a series of magnets positioned in two aluminium supports. To streamline the assembly process, a 3D-printed structure (bottom and top support base) was created to securely hold the components. The same parameters were applied to print these components as were used to manufacture the rubbing system. The assembly process involves six steps, as shown in Fig. 4: a) The lower aluminium base (dimension 76 × 44 mm) is inserted into the 3D-printed support base (dimension 100 × 55 mm), with a maximum side clearance of 0.4 mm, allowing only vertical movement. b) The first slide is placed on the base with the PVA-coated side facing upwards, after having been previously rubbed off. c) The metal spacers are positioned externally and held in place by magnets on the metal base. d) The upper support is inserted to guide the positioning of the second slide. e) The second slide is placed with the PVA-coated side facing downwards. f) The upper metal part is inserted and attracted to the lower metal part by the magnets, bringing the two slides closer together and maintaining the distance defined by the spacers. It is important to highlight that the bases that held the glass slides were specifically fabricated from aluminum due to the expected heating conditions. Utilizing PLA for the entire system would not have been suitable due to PLA's susceptibility to thermal deformation and its lower thermal conductivity compared to metal materials.

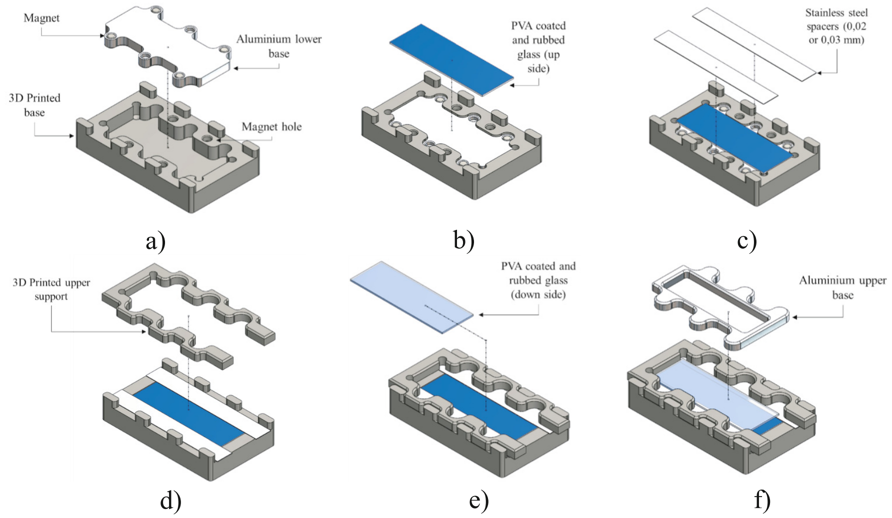

Fig. 4. Infiltration cell construction steps.

Finally, the infiltration cell structure can be removed and placed on the heating plate for infiltration and subsequent UV light photopolymerization. The CAD model of the infiltration cell and the manufactured parts are shown in Fig. 5.

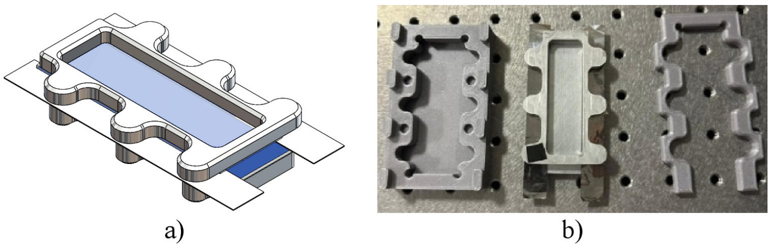

Fig. 5. Infiltration cell CAD model and real parts.

In Fig. 6, images of the infiltration phase of the material (a–b) and detail images (d–e) taken with the FLIR E60 infrared camera are shown and allow to assess the correctness of the infiltration system temperature. Additionally, images (c–f) were taken to document the initial phase of the photopolymerization process.

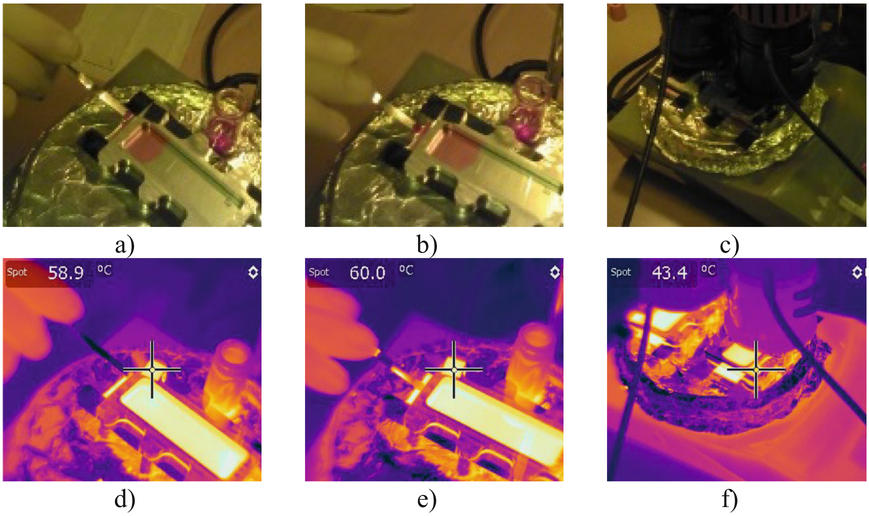

Fig. 6. Infiltration and photopolymerization phases.

3 Results

To evaluate the effectiveness of the system, LCEs films with different thicknesses were produced, the Figure displays two films created using two spacers with nominal thicknesses of 0.02 mm and 0.03 mm (in Fig. 7b the lighter shade represents the thinner film). The maximum allowable error in the average film thickness was set at 20% of the nominal size of the spacers utilized. The thickness of individual films was measured at nine different positions (P1 – P9), as shown in Fig. 7a, using a micrometer with a measurement sensitivity of 0.001 mm. The mean thickness of three films produced using the two different types of spacers was determined to be 0.023 mm (whit a standard deviation of 0.00069 mm) and 0.032 mm (whit a standard deviation of 0.00077 mm), respectively.

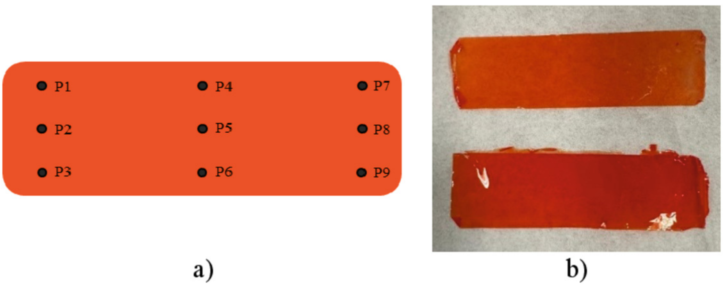

Fig. 7. LCEs Film measures points and LCEs Film production.

The implemented infiltration system produced films that measure approximately 20 × 65 mm, which is larger than the previous system's films that measured about 20 ×

30 mm. The absence of microspheres allows for the entire film to be used for downstream applications.

The proper alignment of the films was assessed using Polarised Light Microscopy (POM). The accuracy of the alignment can be observed in Figs. 8a and 8c for a light refraction angle of 0°, and Figs. 8b and 8d for an angle of 45°. When the material is properly aligned, no light can pass through at a 0° angle, while light can pass through at a 45° angle. The image shows a correctly aligned LCE film produced by the proposed system and an inaccurately aligned one.

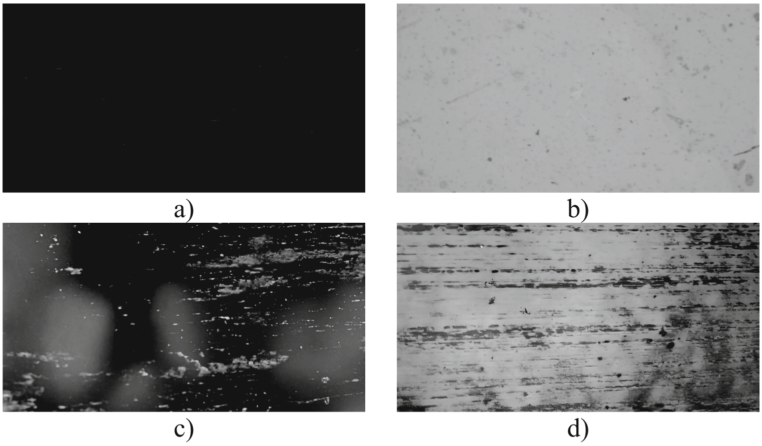

Fig. 8. Properly aligned (a–b) and non-aligned (c–d) LCEs.

4 Conclusions

The aim of this work was to develop a manual infiltration system for LCEs films. Specifically, the prototypes developed were manufactured by low-cost 3D printing technology (FDM) and CNC milling. The vacuum system was eliminated during the rubbing phase, resulting in a simpler and more effective solution. The use of magnets and calibrated strips used as spacers in the infiltration system guarantees that no microspheres are present in the film itself, allowing for the entire film to be utilized. Additionally, the length of the film is almost doubled. Currently, the main issue in film fabrication is the time required for the photopolymerization phase. It currently takes about 30 min to create a film. Future developments will certainly focus on optimizing this process, such as modifying the UV lamp intensity or adjusting its wavelength. Furthermore, by polymerizing multiple films simultaneously, it would be possible to significantly improve production times. In the future, the processes described above could be automated to make the film preparation process operator independent.

Acknowledgements. This work was financially supported by the European Union's Horizon 2020 research and innovation programme under grant agreement No 952166 (REPAIR).

References

1. Herbert, K.M., Fowler, H.E., McCracken, J.M., Schlafmann, K.R., Koch, J.A., White, T.J.: Synthesis and alignment of liquid crystalline elastomers. Nat. Rev. Mater. **7**, 23–38 (2022). https://doi.org/10.1038/s41578-021-00359-z
2. Ambulo, C.P., Tasmim, S., Wang, S., Abdelrahman, M.K., Zimmern, P.E., Ware, T.H.: Processing advances in liquid crystal elastomers provide a path to biomedical applications. J. Appl. Phys. **128**, 140901 (2020). https://doi.org/10.1063/5.0021143
3. Zhang, W., Nan, Y., Wu, Z., Shen, Y., Luo, D.: Photothermal-driven liquid crystal elastomers: materials, alignment and applications. Molecules **27**, 4330 (2022). https://doi.org/10.3390/molecules27144330
4. Kularatne, R.S., Kim, H., Boothby, J.M., Ware, T.H.: Liquid crystal elastomer actuators: synthesis, alignment, and applications. J. Polym. Sci. B Polym. Phys. **55**, 395–411 (2017). https://doi.org/10.1002/polb.24287
5. Hussain, M., Jull, E.I.L., Mandle, R.J., Raistrick, T., Hine, P.J., Gleeson, H.F.: Liquid crystal elastomers for biological applications. Nanomaterials **11**, 1–19 (2021). https://doi.org/10.3390/NANO11030813
6. Thomsen, D.L., et al.: Liquid crystal elastomers with mechanical properties of a muscle. Macromolecules **34**, 5868–5875 (2001). https://doi.org/10.1021/MA001639Q/ASSET/IMAGES/LARGE/MA001639QF00012.JPEG
7. Vitale, G., et al.: Photoresponsive polymer-based biomimetic contractile units as building block for artificial muscles. Macromol. Mater. Eng. **307**, 2200187 (2022). https://doi.org/10.1002/mame.202200187
8. Varghese, S., Crawford, G.P., Bastiaansen, C.W.M., De Boer, D.K.G., Broer, D.J.: Microrubbing technique to produce high pretilt multidomain liquid crystal alignment. Appl. Phys. Lett. **85**, 230–232 (2004). https://doi.org/10.1063/1.1773375
9. Yamahara, M., Nakamura, M., Koide, N., Sasaki, T.: Influence of rubbing conditions of polyimide alignment layer on optical anisotropy of immobilized liquid crystal film. Liq. Cryst. **34**, 381–387 (2007). https://doi.org/10.1080/02678290601097334

Geometrical Product Specification, Geometric and Functional Characterization of Products

A Tool for ISO GPS Diffusion and Knowledge Assessment in Industry and Academia

Mattia Maltauro[1](✉), Roberto Meneghello[1], and Gianmaria Concheri[2]

[1] Department of Management and Engineering, University of Padova, Stradella San Nicola 3, 36100 Vicenza, Italy
mattia.maltauro@phd.unipd.it

[2] Department of Civil, Environmental and Architectural Engineering, Laboratory of Design Methods and Tools in Industrial Engineering, University of Padova, Via Venezia 1, 35131 Padova, Italy

Abstract. This paper proposes a tool to analyze the diffusion and knowledge of the ISO GPS language in both industry and academia. A survey has been designed based on the maturity model concept to achieve this goal. Six Key Performance Indicators (KPI) arguments have been defined: general concept, datum systems, geometric tolerances, dimensional tolerances, modifiers and indications, and tolerance stack-up. Per each of these, three assessments are proposed, and a rating is given based both on self-assessment and unbiased check questions. The result is a survey that takes between 10 to 15 min to be filled out. The assessment is based on both knowledge and usage. The defined survey, through testing, proved to be a simple and usable tool to test the actual diffusion and knowledge of the ISO GPS language thanks to its shortness and the different levels of analysis it allows.

Keywords: ISO GPS · Maturity Model · Geometric Specification · Survey

1 Introduction

Technical product documentation, or TPD, is the comprehensive set of documents needed to describe all the significant characteristics of a product from a technical point of view (i.e., geometrical and functional, but also manufacturing, maintenance, etc.). The ISO-GPS language aims to give designers a common language to translate functional requirements into admissible geometrical and dimensional deviations (i.e., tolerances). If the functional requirements, as stated in the TPD, are not transmitted clearly and coherently, different unwanted scenarios may come up. On one side it is possible to experience a loss in performance in the final product. On the other side, an increase in scraps during manufacturing can occur, increasing the overall manufacturing cost.

Since its introduction in the mid-'90s, the ISO GPS language has proved itself as a great tool to decrease ambiguity compared to the previous linear dimensioning scheme [1]. Nonetheless, the experience gained by the authors in several industrial collaborations with Italian firms, either small and medium enterprises (SMEs) and belonging to multinational enterprises, has shown that the implementation of the overall ISO GPS

M. Carfagni et al. (Eds.): ADM 2023, LNME, pp. 451–459, 2024.
https://doi.org/10.1007/978-3-031-52075-4_51

system is lacking. The same evidence was collected in Germany, focusing in particular on SMEs [2, 3]. At the same time, it is recognized that only a comprehensive application of the overall ISO GPS system allows for obtaining the advantages postulated by the system itself and previously addressed [4].

For these reasons, it becomes important to map the current status of the knowledge and usage of the ISO GPS language in industry to highlight critical areas in the standard system and guide the transition towards a better implementation of the ISO GPS system.

In 2017 a survey to compare the usage of the ISO GPS system vs ASME Y14.5 was performed showing that the ASME standard is more used worldwide. In China, a survey has been used to test the status of delivery of ISO GPS, showing a significant gap between education and industry [5]. In Germany, a survey to test the awareness, use, and need of statistical tolerance analysis found that tolerance analysis is not systematically used in most of the companies that were interviewed, nonetheless the awareness of the importance of managing geometric deviations is high [6]. Always in Germany, after the evaluation of the implementation of a maturity model for the assessment of the current integration of the ISO GPS system in companies [2], a tool based on a survey to be used within companies to drive the systematic implementation of the ISO GPS system was developed by Schuldt and Gröger [3].

In literature, the surveys in the field of ISO GPS focused on three main areas: the education gap, the tolerance analysis, and the implementation of the ISO GPS system within companies. None of them was designed to assess the current implementation of the system over a geographic area and/or a specific industrial sector. To fill this gap, this contribution aims to propose a tool to assess the actual knowledge and usage of the ISO GPS language in industry and academia.

2 Design of the Maturity Model

The application of the maturity model for the assessment of ISO GPS implementation has proved to be a valid model for assessing the level of penetration of the system within a company [2, 3]. Maturity models are used to determine the actual and current performance in a specific field of application [7]. Thus, in this work, the maturity model is used to assess the knowledge and use of the ISO GPS language in industry and academia.

Maturity models can also be clustered into three different groups based on their structure: the quick test, the topic generator, and the individual transformation [8]. The quick test is based on a quick and simple questionnaire. The topic generator goes deep on the topic with general questions. The individual transformations deepen the analysis targeting even personal and cultural aspects. It is known that maturity models tend to fail if they become too complex [9], for this reason, the structure that was chosen is the quick test. This choice is also mandated by the aim of the maturity model, considering it is supposed to be spread over a large population.

2.1 Maturity Model Preparation

Three main aspects need to be considered: the problem definition, the target of the assessment, and the analysis of defined models.

The analysis of the defined model has been presented in the previous sections. In our case, the problem definition is the assessment of the current knowledge and use of the ISO GPS language and the assessment of gaps between industry and research/education and the standards. To fulfil the problem definition statement the target population consists in technicians, academic researchers, and students that are involved/prospectively involved in the development of industrial products. Regarding technicians, the three main departments involved in product development, namely R&D/design, manufacturing, and quality control, are targeted. Both students from the university level (undergraduate and graduate level) and high school level are targeted aiming to assess whether the current training on ISO GPS-related content is adequate. It is also relevant to discern between people who read geometrical specifications and people who create geometrical specifications. This separation is also present in the Geometric Dimensioning and Tolerancing Professional (GDTP) Certification Program offered by the American Society of Mechanical Engineers (ASME) where two levels of assessment are possible: technologist and senior level [10].

2.2 Model Development

In [3] the maturity level was defined based on ISO GPS competence. Competence is usually defined as the ability to perform [11], and for this reason, it is difficult to assess in particular with a short questionnaire; the GDTP Certification Program uses 150 questions to assess the competency level [10]. This number of questions is too large to be implemented to feed data to the maturity model here described. For these reasons, in the proposed maturity model the level of maturity is defined based both on knowledge and usage of the ISO GPS language. Knowledge is one of the contributors of competence [11], and is here defined as the recognition of a ISO GPS operator. Therefore, the level of competence can only be less than or equal to the level of usage which can only be less than or equal to the level of knowledge. The level of competence is only estimated starting from the level of knowledge and usage based on questions applied to actual cases.

In the proposed maturity model, the overall ISO GPS language has been mapped into six distinct sectors defined as Key Performance Indicators (KPI) of the system: general concept, geometric tolerances, datum systems, dimensional tolerance, modifiers and indications, and tolerance stack-up. The general concepts section assesses awareness of key standards groups (e.g., ISO GPS, AMSE, Y14.5) and terms like MBD (Model Based Definition), envelope principle, and independence principle. The geometric tolerances section examines knowledge and usage of symbols defined in ISO 1101 [12]. The datum system section focuses on symbols for establishing a datum system, based on ISO 5459 [13]. The dimensional tolerances section covers knowledge and usage of dimensional tolerances, referring to ISO 14405-1 [14] and ISO 286-1 [15]. The Modifiers and Indications section explores additional symbology in the ISO GPS system. Lastly, the tolerance stack-up section evaluates the use of tolerance stack-up essential for tolerance analysis. Three different levels of assessment are defined: the single entry rating, the population distribution, and the population rating. The rating is defined on a scale from zero to ten mapping knowledge and usage in percentage. Every single entry in the questionnaire received a rating. To map the knowledge and usage over a population the first level of assessment is given by the distribution of knowledge and usage over the population, i.e., the percentage of the population knowing and/or using a specific percentage of ISO GPS language. The results are distribution curves over a cartesian plane, for reference Fig. 5 can be seen. The population rating is defined based on the integral of the distribution curves representing the area below the curves. In an ideal implementation, 100% of the population knows and uses 100% of the ISO GPS language, the marked area covers the whole graph, and the integral of the distribution is equal to 1; therefore, the rating is defined by multiplying the integral by ten.

2.3 Assessment Tool Development and Testing

As the assessment tool, a questionnaire is created and implemented through a google form. The structure of the questionnaire can be seen in Fig. 1. To comply with GDPR the questionnaire is designed to be completely anonymous.

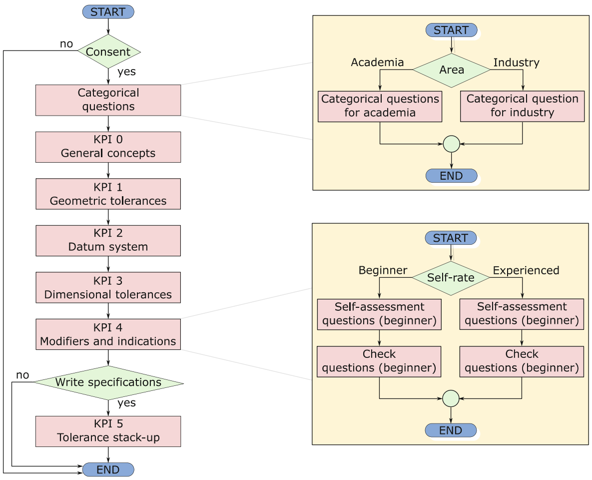

Fig. 1. General questionnaire scheme

The questionnaire is composed of eight sections. In the first one information about the questionnaire are present and consent is asked. The second section contains all the categorical questions that are useful for statistical analysis. This section is subdivided into two subsections: one for industry and one for academia.

For the industry subsections, it is asked to indicate the industrial sector (e.g., automotive, aerospace and defence, etc.), the area of work (design, manufacturing, quality control, and maintenance), and the years of experience. The industrial sector list was derived from the Global Industry Classification Standard (GICS®) [16] obtaining a list of fifteen possibilities. For the education subsection, it is asked to indicate whether the participant is a student or a teacher/researcher/technician, and the level of education (high school, university). For both subsections it is asked to indicate the use of geometric specifications (read or create), and whether the participant received ISO GPS training in the past.

The subsequent sections contain the questions for each KPI where three levels of assessment are provided. The first level asks for a self-rating between beginner and experienced; based on this first question, participants are divided into two adaptive subsections. The use of adaptive subsections allows for fewer questions to assess the overall knowledge and usage providing an adequate level of difficulty to the participants. In each of these subsections a second self-assessment is provided where participants are asked about specific ISO GPS symbology whether the symbol is “Known but not used/seen in actual specifications”, “Known and used/seen in actual specification”, or “Not Known”. An example of a self-assessment question relative to the beginner’s subsection of KPI 1 (Geometric tolerances) can be seen in Fig. 2 (left).

Self-rating questions are biased meaning that they could potentially fail in assessing the knowledge: answers may be given based on a self-perception of knowledge instead of proper knowledge. Consequently, an adaptive check layer of unbiased application-based questions is provided to validate the self-assessment. The option “I don’t know” is always available to provide a better evaluation as described in the next paragraph. An example of a check question relative to the advanced subsection of KPI 2 (Datum System) can be seen in Fig. 2 (right).

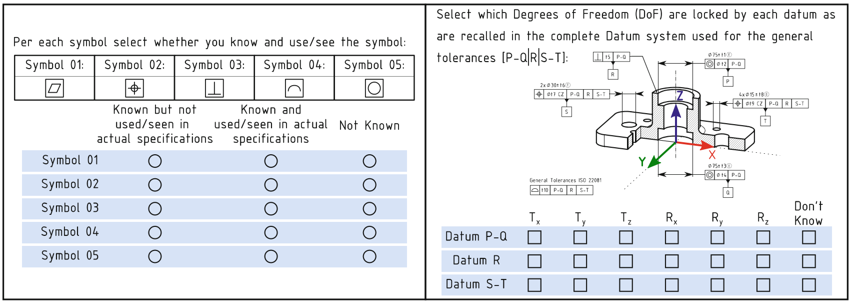

Fig. 2. Example of self-assessment questions from the beginner’s subsection of KPI 1 (Geometric tolerances) on the left, and of check question from the advanced subsection of KPI 2 (Datum systems) on the right.

Sections regarding KPI 0 (General concepts) and KPI 5 (Tolerance stack-up) are slightly different. For KPI 0 (General concepts) there are no differences between beginners and advanced; the evaluation is derived only on the self-assessment based on the awareness of specific areas of the ISO GPS system. For KPI 5, the self-assessment is based on the use of tools to compute tolerance stack-ups.

Questions are provided in Italian specifically for the Italian market to prevent any potential misinterpretations. However, an English version of the questionnaire has already been prepared for future international dissemination in the second phase.

2.4 Evaluation Model

The evaluation is performed using MS Excel. For KPI 0 a rating is given proportional to the percentage of known topics. A descriptive analysis of the result is also created.

For KPI 1, 2, 3, and 4 the percentage of "not known", "Known but not used/seen in actual specifications", and "Known and used/seen in actual specification" is computed. The knowledge percentage is given by the sum of the last two options; the percentage of usage is considered the last value. The percentage of correct, incorrect, and not answered in check questions is also computed. Per each entry, the knowledge and usage percentage are then scaled down based on incorrect answers to estimate the competence. Answers not given are not considered since they represent an honest expression of non-knowledge that does not imply a wrong application of the ISO GPS system. The evaluation of KPI 5 is based on a descriptive analysis of the entries. The aggregate rating for KPI 1, 2, 3, and 4 are found integrating the Knowledge and usage curve as described in Sect. 2.2. An overall rating is found by averaging the ratings of these KPIs.

3 Results and Discussion

In this section, an overview of the result obtained during the testing phase is presented to show the analysis performed. In this phase, twenty entries to the questionnaire were collected. It was determined that the time required to complete the questionnaire ranged from 10 to 15 min.

For each question, a descriptive analysis is done. The first interesting data is the percentage of people who already received ISO GPS training in the past, only three out of twenty did. If the percentage is that low, it means that something more on the training and education of professionals shall be done systematically. Figure 3 shows the descriptive analysis for the self-assessment of KPI 1 (Geometric tolerances) for the beginner level. At first glance the number and distribution of "not known" is important; for instance, in this example, it is noteworthy that some people do not know the symbol for location tolerance but all of them know the flatness and perpendicularity tolerance symbol. Furthermore, the circularity symbol is more known than the location one. This can be explained by the use of a linear positioning scheme rather than a geometrical one, introducing ambiguity [1].

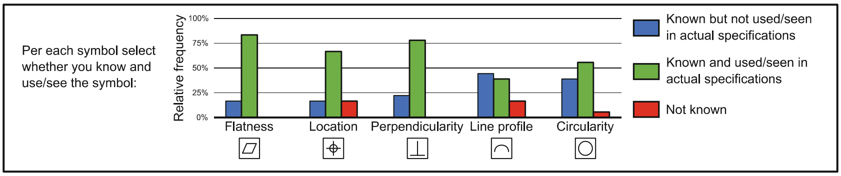

Fig. 3. Example of descriptive statistics for a self-assessment question (KPI 1: Geometric tolerances, beginner level)

Figure 4 shows the descriptive analysis for the check questions from the KPI 2 (Datum systems) at the beginner level; the correct answers are marked with *. The analysis of the "not know" and its distribution gives interesting insights; in this case, the cylindricity symbol seems to be not known by 35% of the interviewees. Then the analysis of the distribution of the answers compared to the correct one can shows three different behaviours: the correct answer is predominant (see symmetry, cylindricity, and perpendicularity), one specific wrong answer is predominant (no occurrence), and there is a balance between the correct and incorrect answers (see surface profile). In case of balance between the answers, communication between people becomes difficult because there are different interpretations both correct and incorrect. If one specific wrong answer is predominant it means that there is a fault in education.

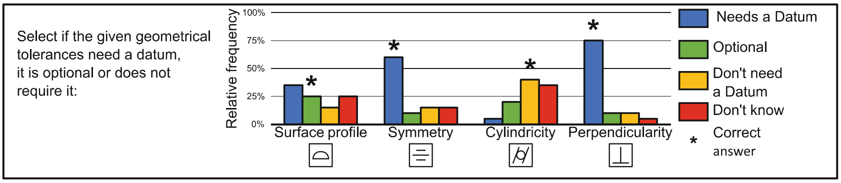

Fig. 4. Example of descriptive statistics for check question (KPI 2: Datum systems, beginner level)

Figure 5 shows the distribution of knowledge used across the population both according to the self-assessment (a) and according to the check questions (b) regarding KPI 1 (Geometric tolerances).

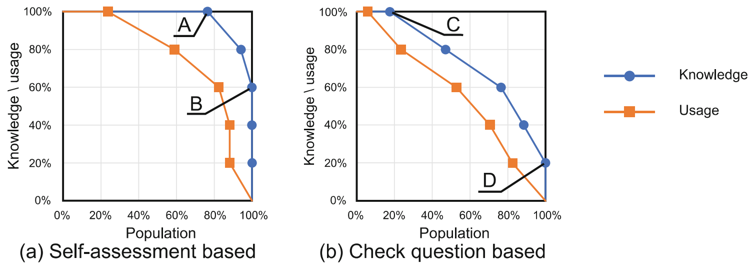

Fig. 5. Example of Knowledge and usage distribution across the population

Looking at Fig. 5(a), the graph can be read as: almost 80% of the interviewed declare to know 100% of the ISO GPS system related to the topic (Point A), while 100% of the interviewed know at least 60% (Point B). Looking at Fig. 5(b) which is based on the check questions it is possible to see how these percentages decrease: almost 20% is found to actually know 100% of the ISO GPS system (Point C), while 100% of the interview know at least 20% (Point D).

It is noteworthy that the difference between knowledge and usage, i.e., the horizontal distance between the two curves, increases as knowledge increases. This could describe a constraint within a particular supply chain: even if the professional knows how to properly use the symbols in the ISO GPS system, they cannot use them since they are not understood downstream. The gap between the two curves (knowledge and usage) compared across different industrial sectors may identify sectors that are struggling in the implementation because of the supply chain. Looking at Fig. 5(b) both curves drift to the left; worth noting that the shift increases as the self-assessment-based knowledge increases. This means that a high level of knowledge and usage was obtained based on a biased self-perception. The result is that the distance between the two curves is more uniform. Based on these graphs the rating is 9.6 for knowledge and 7.6 for usage; considering the application, it decreased to 7.4 for knowledge and 5.6 for usage.

It is important to note that these results are derived from a small sample size, and thus do not provide statistically significant information. However, they serve the purpose of illustrating an example of the outcomes that can be anticipated from the dissemination phase.

4 Conclusions

This contribution aims to present a tool to assess the knowledge and usage of the ISO GPS language in industry and academia. The questionnaire that was developed and tested proved to be a simple and usable tool to test the actual diffusion and knowledge of the ISO GPS language. The time requires to fill the questionnaire (see Sect. 3), allows its use in many different scenarios like during training, consulting, and diffusion by invitation. The different levels of analysis it provides are useful to picture many different funneling in the implementation of the ISO GPS system like education/industry gap or supply chain-related constraints.

At the time of writing, the questionnaire is commencing its official public distribution, initially within the Italian region. The data gathered during this phase will be utilized to offer the scientific and standardization community substantial statistical insights into the dissemination of the ISO GPS system. At this stage, distinct analyses will be conducted for various groups of respondents. Following this initial phase, the intention is to expand the distribution to an international level.

References

1. Chiabert, P., Lombardi, F., Orlando, M.: Benefits of geometric dimensioning and tolerancing. J. Mater. Process. Technol. **78**, 29–35 (1998). https://doi.org/10.1016/S0924-0136(97)00459-7
2. Schuldt, J., Hofmann, R., Gröger, S.: Introduction of a maturity model for the assessment of the integration of the GPS system in companies. Procedia CIRP. **92**, 129–133 (2020). https://doi.org/10.1016/j.procir.2020.05.188
3. Schuldt, J., Gröger, S.: The assessment of the ISO GPS system implementation with a GPS maturity model. Procedia CIRP **114**, 197–202 (2022). https://doi.org/10.1016/j.procir.2022.10.027
4. Morse, E.P., Shakarji, C.M., Srinivasan, V.: A brief analysis of recent ISO tolerancing standards and their potential impact on digitization of manufacturing. Procedia CIRP **75**, 11–18 (2018). https://doi.org/10.1016/j.procir.2018.04.080
5. Kong, C., et al.: The status of delivery of ISO GPS in China: a survey. Procedia CIRP **114**, 100–105 (2022). https://doi.org/10.1016/j.procir.2022.10.014
6. Walter, M.S.J., Klein, C., Heling, B., Wartzack, S.: Statistical tolerance analysis—a survey on awareness, use and need in German industry. Appl. Sci. **11**, 2622 (2021). https://doi.org/10.3390/app11062622

7. Wagire, A.A., Joshi, R., Rathore, A.P.S., Jain, R.: Development of maturity model for assessing the implementation of Industry 4.0: learning from theory and practice. Prod. Plan. Control. **32**, 603–622 (2021). https://doi.org/10.1080/09537287.2020.1744763
8. VDI, V.D.I.: VDI-Richtlinie 4000–1 - Entwurf: Systematische Transformation und Evaluaion von Produktionssystemen - Grundlagen (2021)
9. Schumacher, A., Erol, S., Sihn, W.: A maturity model for assessing industry 4.0 readiness and maturity of manufacturing enterprises. Procedia CIRP. **52**, 161–166 (2016). https://doi.org/10.1016/j.procir.2016.07.040
10. ASME: ASME - Geometric Dimensioning and Tolerancing Professional Certification - Applicant Information Handbook. https://www.asme.org/wwwasmeorg/media/resourcefiles/careereducation/certificationtraining/gdtp_applicationinformationhandbook.pdf. Accessed 20 Feb 2023
11. Wolf, A.: Can competence and knowledge mix? In: Competency Based Education and Training, pp. 34–46. Taylor & Francis Inc. (2005)
12. ISO International Organization for Standardization: ISO 1101:2017 - Geometrical product specifications (GPS). Geometrical tolerancing. Tolerances of form, orientation, location and run-out (2017)
13. ISO International Organization for Standardization: ISO 5459:2011 - Geometrical product specifications (GPS) - Geometrical tolerancing - Datums and datum systems (2011)
14. ISO International Organization for Standardization: ISO 14405–1:2016 Geometrical product specifications (GPS)—Dimensional tolerancing—Part 1: Linear sizes (2016)
15. ISO International Organization for Standardization: ISO 286–1:2010 - Geometrical product specifications (GPS) - ISO code system for tolerances on linear sizes - Part 1: Basis of tolerances, deviations and fits (2010)
16. MSCI Inc.: GLOBAL INDUSTRY CLASSIFICATION STANDARD (GICS®) METHODOLOGY - Guiding Principles and Methodology for GICS, https://www.msci.com/documents/1296102/11185224/GICS+Methodology+2022.pdf. Accessed 20 Feb 2023

Geometric Functional Specification for a Lifting Airfoil

Mattia Maltauro[1](✉), Marco Carraro[2], Roberto Meneghello[1], and Gianmaria Concheri[3]

[1] Department of Management and Engineering, University of Padova, Stradella San Nicola 3, 36100 Vicenza, Italy
mattia.maltauro@phd.unipd.it

[2] Department of Industrial Engineering, University of Padova, Via Venezia 1, 35131 Padova, Italy

[3] Department of Civil, Environmental and Architectural Engineering, Laboratory of Design Methods and Tools in Industrial Engineering, University of Padova, Via Venezia 1, 35131 Padova, Italy

Abstract. This paper presents a possible functional geometric specification for a lifting airfoil including the definition of functional tolerance limits (tolerance synthesis) and an associated inspection procedure. The proposed specification scheme is derived from the analogy between the mating of the airfoil with a fluid field and the consolidated example of the mating of a prismatic element in its site. The airfoil thickness is defined as a non-constant size with non-constant tolerances and the airfoil shape is prescribed with a non-constant profile of a line tolerance applied to the median airfoil line. The tolerance synthesis is based on XFLR5 software and Computational Fluid Dynamics (CFD) simulations. The inspection procedure uses the data acquired with a laser probe elaborated in Geomagic Wrap, GOM inspect and MATLAB. The overall process has been applied to a case study allowing to define limits and proposing a set of possible improvements regarding, particularly, the geometric specification of the leading and trailing edges of the airfoil.

Keywords: Geometric Specification · Airfoil · Tolerance Synthesis · Geometric Inspection

1 Introduction

Airfoils represent the cross-section of any object moving through a fluid aiming to generate lift. They can be divided into two main classes: blades, whose motion is determined by the mounting on a rotating shaft; and lifting airfoil that freely moves in the fluid.

For blades, the geometry influences the performance, meaning that a geometric deviation from its nominal – location, orientation, and form – will influence the fluid motion around the blade determining a change in performance. Furthermore, since they are physically mounted on a shaft a reference system for comparing the actual geometry with the nominal can be easily determined. For these reasons the golden standard to

M. Carfagni et al. (Eds.): ADM 2023, LNME, pp. 460–468, 2024.
https://doi.org/10.1007/978-3-031-52075-4_52

check blade conformity is the check for a line profile tolerance over the airfoil's upper and lower surface. At the same time, the literature provides a deep overview of the effect of geometric deviations on blades. Liu et al. statistically studied the effects of manufacturing deviations by performing CFD analysis based on the 3D scan of 35 actual blades [1]. However, the number of blades used in this study is limited; Garzon et al. suggest using the Principal Component Analysis (PCA) to model the geometric variations based on a limited sample simulating a larger sample with congruent deviations to statistically analyze the geometric effect on performances [2]. If a set of actual blades is not available, Melin et al. propose a method based on the perturbation of the Bézier curve control points for low-frequency deviations and perturbation of the actual curve coordinate for high-frequency deviations [3].

All these methodologies require high computational effort due to the high number of CFD analyses required; a solution is the use of surrogate models. Y. Wang et al. propose a surrogate model based on a multi-point Taylor expansion (MTE) using the Adjoint method [4]. X. Wang and Zou present a method based on the Non-intrusive Polynomial Chaos Expansion (NIPC) coupled with the Kriging surrogate model [5].

Other studies also investigate the effect of specific geometrical parameters, such as chord, stagger angle, leading-edge radius, etc., on the performances [6, 7].

These models create a relationship between the geometric variations and the performance, therefore can be used as a starting point for robust optimization methods aiming to obtain nominal designs non heavily influenced by the manufacturing deviations. Examples of applications based on the NSGA-II genetic algorithm [8, 9] and Gradient-Based method SQP (Sequential Quadratic Programming) [10] are proposed. Nevertheless, none of them answers the question of which is the admissible geometric deviation ensuring the targeted performance.

On the other hand, for lifting airfoils the performance influences the geometry: the airborne system is characterized by its flight envelope describing the admissible velocity-angle of attack configurations and, at a given velocity, the system will find its equilibrium (in steady flight) changing the angle of attack (α). Therefore, for lifting airfoils there is no intrinsic functional geometric alignment to check for geometric deviation, and the functional comparison among two different airfoils, e.g., the nominal and the actual one, can be only derived by its dynamic behaviour, as, for instance, the maximum lift that can be generated.

Even though robust optimization is a valuable design solution it requires a deep understanding of manufacturing deviation. For blades, literature can provide useful data to start with. For lifting airfoils, literature is lacking contributions regarding the geometric deviation effects. Therefore robust optimization is not a useful tool.

To fill this gap, this contribution aims to define admissible geometric deviations for lifting airfoils to fulfil functional requirements. To do so, the geometric characteristics to be geometrically and or dimensionally controlled will be identified, therefore determining a possible geometric specification scheme for lifting airfoils, a simplified procedure to assign tolerance values (tolerance synthesis) will be presented, and an inspection procedure to check for conformity will be proposed.

1.1 The Case Study

The overall procedure is applied to the airfoil of a fixed-wing drone designed and manufactured to compete in an international student competition, Air Cargo Challenge (ACC), by the Lift UP team from the University of Padua. The wing has a tapered planform with a total wingspan of 2.1 m. The wing section is based on a custom profile, called opt06v3, designed considering the following requirements:

- $C_{l,max} \geq 1.43$
- $f = 0.7C_{d,cruise} + 0.3C_{d,climb} \leq 1.025f_{nom}$
- $11\% < t_{max}/c < 14\%$

Where $C_{l,max}$ is the maximum lift coefficient according to the lift definition $L = 0.5\rho V^2 cC_l$ (with ρ = fluid density, V = fluid velocity, and c = airfoil chord). Similarly, the coefficient of drag C_d is defined according to the drag equation $D = 0.5\rho V^2 cC_d$. Finally f_{nom} is the nominal value of f therefore a constant and t_{max} is the maximum airfoil thickness.

2 Geometric Specification of Airfoils

When it comes to the geometric specification of airfoil the most used approach is the use of line profile (or surface profile, 3D) tolerances, according to ISO 1660:2017 [11], to both upper and lower surfaces. This type of geometric tolerance can effectively control the location, orientation and form of the airfoil. The standards call for a constant or linearly variable tolerance zone. Petitcuenot et al. present the application of these types of geometric tolerances to airfoils [12]. They suggest the introduction of variable tolerance zone with 3D variations and also with non-linear variability that is useful for aerodynamic requirements.

The use of such tolerances is common for blades where a functional reference system (Datum System) can be easily determined, in addition such tolerances well represent typical blades functional requirements, such as components' assemblability and proper clearance For lifting airfoils its use does not effectively represent the functional requirements: a local defect exceeding the tolerance limits may have a smaller impact on performance when compared to a global defect within limits. This implies that an actual airfoil with an out-of-tolerance local defect will be rejected even if it meets the required aerodynamic performance.

To support this statement a test case based on a NACA4412 airfoil assuming a constant line profile tolerance of 1.4% of the chord length is conducted. Two scenarios are studied: a global deviation implying a less curved camber line with a maximum deviation of 0.65% of the chord (therefore within tolerance) and a local deviation of 0.75% of the chord, therefore out of tolerance, Fig. 1a).

Using the XFLR5 software which implements the 2D Interactive Boundary Layer method (IBL) developed by M. Drela et al. [13], the aerodynamic performances of the two airfoils were computed, obtaining the C_l as a function of α in Fig. 1b). It can be seen that the global deviation has a greater impact on the performance (the graph is further away from the baseline), compared to the local one (the graph almost overlaps the NACA4412 baseline), confirming our statement. This result suggests not using the airfoil upper and lower surface to define a geometric specification scheme when aerodynamic performance requirements are involved but identifying other geometric characteristics that are more sensitive to the airfoil aerodynamic performance changes.

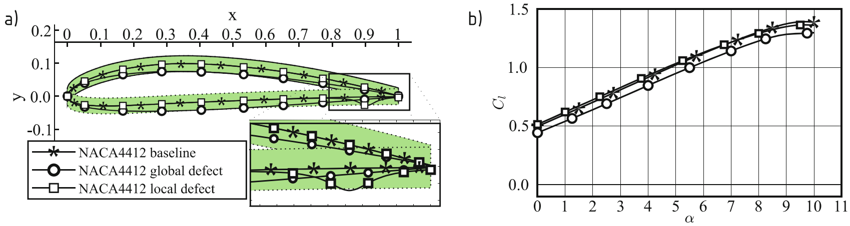

Fig. 1. Nominal NACA 4412 airfoil compared to the airfoil within tolerance with a global defect and the airfoil out of tolerance with a local defect (a), the deviations are magnified; the corresponding C_l over α graph for the three airfoil (b), it can be noted that the airfoil out-of-tolerance with a local defect is closer to the baseline compared to the one with a global defect.

3 Materials and Methods

3.1 Tolerance Specification

For lifting airfoils, given the functional requirements in Subsect. 1.1, the most important geometric characteristics are the camber line, affecting the coefficient of lift and its maximum value, and the thickness, conditioning the functional equation f. Moreover, any airfoil can be uniquely described by the camber line and thickness over the chord coordinate. For these reasons, the two geometric characteristics that are controlled by means of ISO GPS tolerances are the camber line and the thickness of the airfoil. To define the tolerance specification scheme for such geometries we start with a consolidated case: the mating of a prismatic element with its site (in 2D). To guarantee the assemblability, the width of the prismatic element is controlled by a size tolerance with the envelope modifier or a combination of a local size and a linearity tolerance to the median line. If we consider the second option, a local size can be defined as the distance between to opposite point (LP) or it can be defined by the size of a perfectly inscribed sphere (LS). The meaning of this specification can be seen in Fig. 2. The combination of a size and a linearity tolerance defines a boundary condition that can be used to assess the functional requirements. It is then possible to describe the actual geometry by graphing the actual thickness and the actual linearity deviation as a function of the axis' coordinate and comparing them to the tolerance zone, Fig. 2c).

Looking at the airfoil, we have a mating between the airfoil itself and a fluid field. Furthermore, the geometric characteristics that were chosen, resemble the ones used for the prismatic elements. For these reasons, we have opted to adapt the specification schemes in Fig. 2 to our case, see Fig. 3. The airfoil thickness, point by point, is defined through a linear size between the upper and lower surface, orthogonal to the chord. The camber line is, by definition, the derived geometry (median line) between the upper and

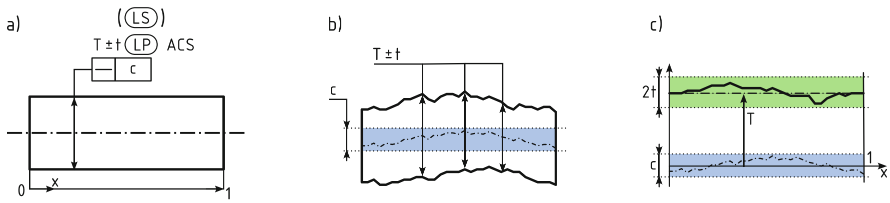

Fig. 2. Possible specification scheme for a prismatic element in 2D (a), its interpretation (b), and a possible interpretation with the thickness and median line division mapped into a cartesian plane (c).

lower surface of the profile, the same surfaces defining the thickness, therefore it can be considered as the median line of the prismatic element. The linearity tolerance has now no sense for the camber line and needs to be replaced by a "profile of a line" tolerance. According to ISO 1660:2017 "profile of a line" tolerances can be assigned also to derived geometries [11].

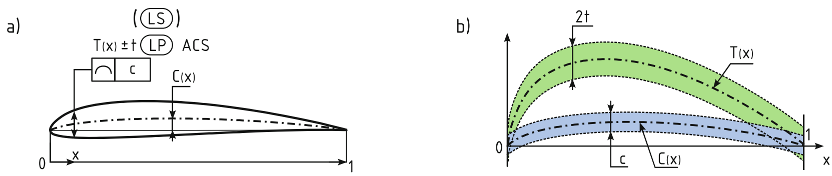

Fig. 3. Proposed specification scheme for a lifting airfoil with constant tolerances (a), and its interpretation (b).

The main difference between the two cases is that for the airfoil the thickness and the camber (which is the vertical coordinate of the camber line) have different nominal values along the chord coordinate. Therefore the nominal values need to be replaced by functions as in Fig. 3. Regarding tolerance zone type, the ISO GPS standards only address constant tolerance zones. When evaluating the geometrical deviations between the real and actual airfoils, however, the alignment of the leading and trailing edges is required. Consequently, the allowable deviations at the leading and trailing edges must be zero, which is not the case with constant tolerance zones. Therefore, it was determined to define a non-constant tolerance zone as also suggested in [12], which ensures that the leading and trailing edges have zero allowable deviations.

The two different modifiers, (LP) or (LS), can describe two different conventions for the thickness definition: the English convention that defines the thickness as the distance between the lower and upper surface perpendicularly to the chord, (corresponding to the (LP) modifier) and the American one where the thickness is defined as the size of an inscribing sphere [14] (resulting in the application of the (LS) modifier).

3.2 Tolerance Synthesis

The tolerance synthesis consists of the process of defining the tolerance limits that guarantee the fulfilment of functional requirements. To define the limits one way is to perform numerical simulation.

Different airfoils derived from the nominal one with different thickness distributions have been simulated with XFLR5 software to obtain C_d values in cruise and climb conditions so the functional equation f can be computed. Therefore, the tolerance limit for the thickness is determined by the modified airfoil that fulfils the functional requirement for f with the highest thickness increment compared to the nominal one. Similarly, the modified airfoil that fulfills the functional requirement for the maximum lift coefficient with the highest camber reduction determined the tolerance limit for the camber distribution. In this case the simulations were performed via CFD with the software Ansys Fluent using a structured mesh of $137'000$ elements with wall resolved flow, and a kw-SST turbulence model and second-order upwind scheme for the spatial interpolation. Based on XFLR5 and CFD simulations the limits for the thickness and camber line are defined.

3.3 Inspection Procedure

The actual wing manufactured by the LiftUP team was also inspected based on the geometric specification defined.

The geometry was acquired with a FARO® ScanArm 2 with a laser probe controlled by Geomagic Wrap®. The cloud of points was converted into a mesh and elaborated in GOM Inspect. Three different sections were sampled at 100 mm, 250 mm, and 400 mm from the wing root. The three sections were then elaborated in MATLAB® where the leading and trailing edges were geometrically defined and the profile oriented and scaled to have a unitary chord. The camber line was traced and the thickness was sampled along the chord. The actual values were then compared with the tolerance zones.

4 Results and Discussion

From the tolerance synthesis - Subsect. 3.2 - the tolerance limit for the thickness was found to be $+7\%$, while for the camber line -7%. Assuming symmetrical tolerances for both characteristics, both tolerances were set to be $\pm 7\%$ with respect to the nominal values. Therefore, the proposed geometric specification can be seen in Fig. 4a), and the corresponding tolerance zone in Fig. 4b). If the tolerance zone for the thickness is compared with the third functional requirement, Subsect. 1.1, no further restrictions are needed: the third functional requirement is always respected if the actual thickness is in tolerance.

The deviation of the actual thickness and camber for the three sections analyzed, obtained through the procedure described in Subsect. 3.3, overlapped with the tolerance zones can be seen in Fig. 5. Assuming x is the chord coordinate ($x = 0$ corresponds to the leading edge position), all three sections are within tolerance limits in the range $0.1 < x < 0.75$, except for the camber at $x = 0.7$ in Sect. 3. The cause of this violation

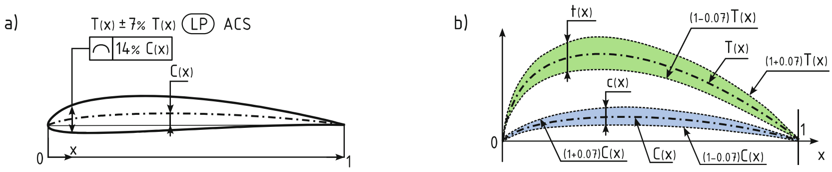

Fig. 4. Proposed specification scheme for the opt06v3 airfoil with the defined functional limits and non-uniform tolerance zones (a), and its interpretation (b).

is the presence of the hinge between the fixed and moving parts of the wing (namely the flaps), which causes a discontinuity in the wing surface. It shall be determined whether this single out-of-tolerance point precludes functional requirements fulfilment; if this is the case then it's necessary to improve the manufacturing quality of the flap hinge. Therefore the possibility to apply filters to the sampled data might be convenient and shall be explored. For $x > 0.75$ the deviations increase more and more getting closer to the trailing edge. This is because the nominal airfoil has a sharp trailing edge while the actual airfoil has a finite thickness at the trailing edge for manufacturing limitations.

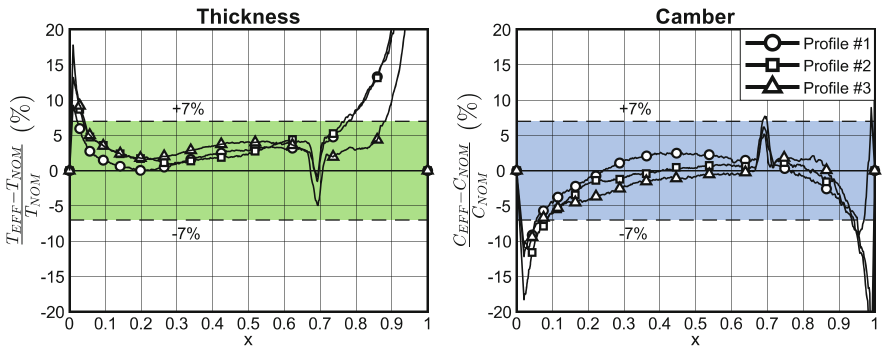

Fig. 5. Relative deviations for all three sections analized; thickness deviation on the left and camber deviation on the right.

Two possible solutions can be identified to overcome this issue. On the first hand during the design optimization process, a constraint to the trailing edge shape could be implemented to obtain a nominal airfoil that can be actually manufactured. On the other hand, the proposed verification process could be limited only at x lower than a certain value. Similar but less extreme behaviour is also seen near the leading edge. The reason behind this can be traced back to the tolerances definition as a percentage: near the leading and trailing edges both thickness and camber have near zero values meaning that the width of the tolerance zone is near zero too. A solution can be the definition of a more complex tolerance zone being wider near the leading edge or alternatively, applying the verification only at x higher than a certain value.

5 Conclusions

This paper proposes a possible functional geometric specification scheme for an airfoil section from a fixed-wing drone and an inspection procedure. The specification scheme is based on a size tolerance to the thickness and a line profile tolerance to the camber line. The size tolerance is mapped into a line profile as explained in Subsect. 3.1 to fit the purpose.

The tolerances are defined based on Panel Method and CFD simulations. One of the main limits of the proposed approach is that the camber and thickness impact on performance is considered independent, while a correlation may be present. Therefore, there is the possibility to have a airfoil within tolerance limits not fulfilling functional requirements and vice versa. A statistical analysis shall be performed to validate and eventually adjust the tolerance limits as a second-level refinement.

The application to an actual case study allowed to highlight the procedure limits and at the same time it gave the opportunity to suggest a set of possible improvements. In particular, the proposed procedure performs well only far from leading and trailing edges, so it can be used in a middle range of x, for example $0.1 < x < 0.9$. However, since the leading-edge shape greatly affects the stall characteristics of airfoils, the proposed specification scheme should be modified including, for example, the leading-edge radius as a geometric characteristic to be verified. The extension to a 3D case may also be considered for a more comprehensive aerodynamic analysis. To conclude, the proposed specification scheme can be considered a valid first step towards the functional geometric specification of lifting airfoils when functional requirements involved the coefficient of lift and drag. Thanks to the proposed improvements, the future effectiveness of the method will increase too.

References

1. Liu, J.-S., Zhu, D.X., Lew, B., Rodriguez, A.D.: Aerodynamic and mechanical analyses on manufacturing variations of a turbine blade row. In: Volume 2B: Turbomachinery. American Society of Mechanical Engineers (2018). https://doi.org/10.1115/GT2018-75536
2. Garzon, V.E., Darmofal, D.L.: Impact of geometric variability on axial compressor performance. J. Turbomach. **125**, 692–703 (2003). https://doi.org/10.1115/1.1622715
3. Melin, T., Jouannet, C., Krus, P.: Wing profile performance variations influenced by manufacturing tolerances. In: 51st AIAA Aerospace Sciences Meeting including the New Horizons Forum and Aerospace Exposition. American Institute of Aeronautics and Astronautics, Reston, Virigina (2013). https://doi.org/10.2514/6.2013-633
4. Wang, Y., Liu, S., Qin, N., Zhao, N.: Quantification of airfoil aerodynamics due to geometric uncertainties based on adjoint method. J. Chinese Inst. Eng. **44**, 618–626 (2021). https://doi.org/10.1080/02533839.2021.1940291
5. Wang, X., Zou, Z.: Uncertainty analysis of impact of geometric variations on turbine blade performance. Energy **176**, 67–80 (2019). https://doi.org/10.1016/j.energy.2019.03.140
6. Kolmakova, D., Baturin, O., Popov, G.: Effect of manufacturing tolerances on the turbine blades. In: ASME 2014 Gas Turbine India Conference. American Society of Mechanical Engineers (2014). https://doi.org/10.1115/GTINDIA2014-8253

7. Lange, A., Voigt, M., Vogeler, K., Schrapp, H., Johann, E., Gu¨mmer, V.: Probabilistic CFD simulation of a high-pressure compressor stage taking manufacturing variability into account. In: Volume 6: Structures and Dynamics, Parts A and B, pp. 617–628. ASMEDC (2010). https://doi.org/10.1115/GT2010-22484
8. Kamenik, J., et al.: Robust turbine blade optimization in the face of real geometric variations. J. Propuls. Power. **34**, 1479–1493 (2018). https://doi.org/10.2514/1.B37091
9. Ma, C., Gao, L., Cai, Y., Li, R.: Robust optimization design of compressor blade considering machining error. In: Volume 2C: Turbomachinery. American Society of Mechanical Engineers (2017). https://doi.org/10.1115/GT2017-63157
10. Garzon, V.E., Darmofal, D.L.: On the aerodynamic design of compressor airfoils for robustness under geometric uncertainty. In: Volume 5: Turbo Expo 2004, Parts A and B, pp. 191–202. ASMEDC (2004). https://doi.org/10.1115/GT2004-53581
11. ISO: ISO 1660:2017 - Geometrical product specifications (GPS) - Geometrical tolerancing - Profile tolerancing (2017)
12. Petitcuenot, M., Pierre, L., Anselmetti, B.: ISO specifications of complex surfaces: application on aerodynamic profiles. Procedia CIRP **27**, 16–22 (2015). https://doi.org/10.1016/j.procir.2015.04.037
13. Drela, M.: XFOIL: an analysis and design system for low reynolds number airfoils (1989). https://doi.org/10.1007/978-3-642-84010-4_1
14. Houghton, E.L., Carpenter, P.W., Collicott, S.H., Valentine, D.T.: Basic concepts and definitions. In: Aerodynamics for Engineering Students, pp. 1–68. Elsevier (2013). https://doi.org/10.1016/B978-0-08-096632-8.00001-1

Integrated Methods for Product and Process Design, Simulation, Analysis and Optimization

Modelling and Simulation of Conformal Biomimetic Scaffolds for Bone Tissue Engineering

Lorenzo Vaiani(✉), Antonio Emmanuele Uva, Michele Fiorentino, and Antonio Boccaccio

Dipartimento di Meccanica, Matematica e Management, Politecnico di Bari, Via Orabona 4, I-70125 Bari, Italy
lorenzo.vaiani@poliba.it

Abstract. In this work, a procedure for modelling and simulating conformal biomimetic scaffolds for bone tissue engineering is presented. Starting from a three-dimensional biomedical model of a real human mandible presenting a severe damage, a conformal shape was modelled and filled with an irregular beam network mimicking human trabecular bone. The material considered for the realization of the scaffold was hydroxyapatite derived from fish industry by-products, a material that is highly biocompatible to human bone. Several simulations were conducted on a beam-based wireframe model by varying the radius of the trabeculae, until reaching a stiffness of the scaffold equal to that of human bone. This represents a good design practice to avoid the stress shielding effect on growing bone tissue and functionality losses during bone regeneration. The resulting porosity and the average pore size, which are fundamental properties to ensure a proper vascularization of the growing tissue, were measured and compared to literature data, showing an acceptable agreement. The proposed beam-based approach for modelling and simulating conformal irregular scaffolds appeared as an interactive, fast, and versatile procedure that can be applied in the design stage of conformal biomimetic scaffolds for bone tissue regeneration.

Keywords: Bone Tissue Engineering · CAD Modelling · Mechanical Simulation

1 Introduction

Bone tissue engineering is an emerging multidisciplinary research field that studies the biomechanical properties of human bone tissues for reproducing and mimicking them in personalized biomedical implants. These devices are designed and optimized for restoring, maintaining, or improving the functionality of bone tissues in case of a severe damage, occurring as a consequence of an injury, a disease, a congenital defect or a surgical removal [1].

When a bone is subjected to a small fracture, colonies of healing cells can naturally fill the fracture site and regenerate the bone tissue, but when the fracture site presents void regions exceeding a critical size of about 2 cm, it is necessary to artificially guide the

M. Carfagni et al. (Eds.): ADM 2023, LNME, pp. 471–478, 2024.
https://doi.org/10.1007/978-3-031-52075-4_53

regeneration process [2]. This is because the cells that should generate new bone tissues can only migrate along random paths without any supervision for shape matching, and thus are capable of arranging themselves only in two-dimensional layers [1].

In order to correctly promote and guide bone regeneration in anatomical regions where large defects are present, biomimetic scaffolds can be employed. They consist in porous implants presenting conforming shapes, reproducing the void regions to fill with new bone tissue [3]. From a physiological point of view, these support structures represent a fundamental aid during fracture healing processes, since they behave as artificial extracellular matrices inducing a natural osteogenesis state and a controlled proliferation of adhered cells [1, 3].

From an engineering point of view, biomimetic scaffolds are commonly modelled as volumetric frameworks composed by a lattice of beam elements [4]. Generally speaking, lattice structures can be classified as regular (periodic) networks, or irregular (stochastic) networks. In the first case the lattices are generated by the repetition of a unitary cell containing a precise distribution of nodes and links [5]; in the second case the connections are distributed in the considered volumes with a controlled degree of randomness and can only be described through statistical parameters [6].

The materials employed for the realization of biomimetic porous scaffolds should possess the adequate strength to ensure load-bearing conditions and the maximum biocompatibility in terms of osteointegration, osteoinduction and osteoconduction. These are fundamental properties indicating respectively the capability of a material to create strong chemical linkages to the fracture site, to stimulate *in vitro* stem cell differentiation towards osteogenesis and to sustain cell growth through a series of biochemical interactions between the scaffold and the colonies of adhering cells [7, 8].

The primary materials used for the fabrication of biomimetic scaffolds can be subdivided in three main categories: polymers, metals, and ceramic materials. In the first group there are synthetic polymers as polyglycolic acid, polycaprolactone, hydrogels or natural macromolecules based on collagen or silk. In the second group the typically employed materials are stainless steels and titanium alloys, which ensure a reliable load bearing, and in the third group we can find ceramic materials as hydroxyapatite (which constitutes the higher percentage of human bone), tricalcium phosphate, aluminum or zirconium oxides and bioactive glasses [9–11].

In more detail, hydroxyapatite can be extracted in a sustainable way from waste compounds derived from by-products of fish industry, in particular from mussel shells, and can be successfully processed through direct foaming techniques, in order to obtain a porous matrix suitable for realizing conformal biomimetic scaffolds [12]. This material was considered, in the present work, as the starting point for the structural design of a highly biocompatible customized scaffold to be employed for the regeneration of a severely damaged region of a mandible, assumed as a case study. The workflow consisted in the acquisition of three-dimensional medical data represented by a triangulated mesh and the CAD modelling of the region corresponding to the void domain to fill with an irregular porous structure. In a mechanical simulation environment, several structural analyses were performed on a beam-based wireframe model in order to optimize the geometrical parameters of the lattice for a correct load bearing in a compressive state and to retrieve the porosity and the mean pore size, for ensuring a proper vascularization of the scaffold [13, 14].

2 Materials and Methods

2.1 Modelling of Conformal Shapes

The first step of the design process of the conformal biomimetic scaffold was the acquisition of the geometries of a severe damage on the mandible of an injured patient. Computed Tomography (CT) medical data were processed [15] to obtain a mesh representation of the bones. A remeshing operation was conducted on the original mesh, always keeping the deviations between original and final mesh within a reasonable tolerance. This was done to improve the general quality of the mesh and for reducing the overall number of triangles, thus achieving a lighter manipulation of the model into the CAD environments.

Once identified the boundaries of the fractured region, a three-dimensional CAD model conformal to the volume to fill with a porous scaffold was generated with Rhinoceros and Grasshopper software package, by using the bone fracture site boundaries as a driver for solid modelling. A freeform approach was adopted to sculpt the void volume in space, with a subdivision-surface logic based on the Catmull-Clark algorithm [16], as illustrated in Fig. 1.

The NURBS surface of the B-Rep model was exported to the open-source meshing software Gmsh 4.10.5 for filling the interior with a high-quality uniform and isotropic tetrahedral mesh, by using the Gmsh Delaunay algorithm.

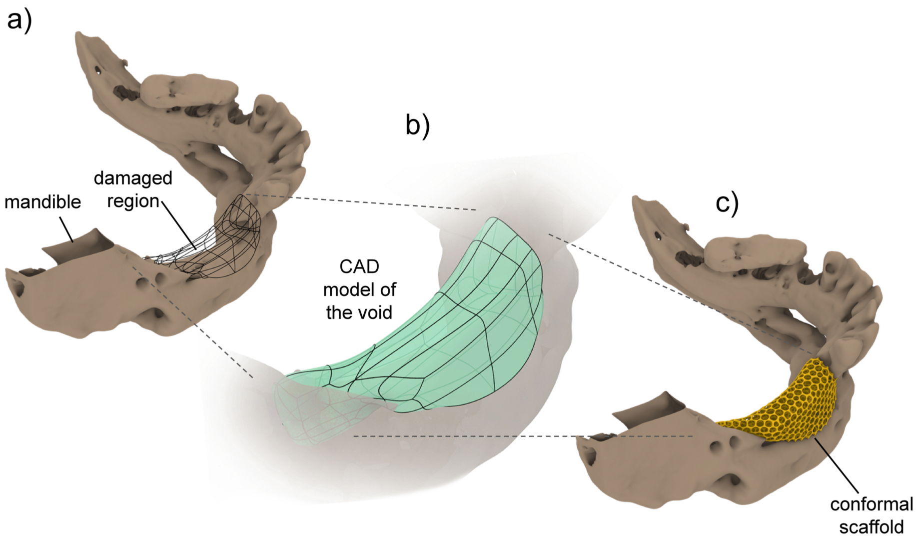

Fig. 1. Principal steps for the modelling procedure to generate a conformal scaffold: a) acquisition of the mesh generated by medical imaging; b) CAD modelling; c) creation of a conformal irregular lattice.

2.2 Generation of the Irregular Lattice

By using a custom script, the tetrahedral mesh was imported in Grasshopper and converted into a Voronoi dual graph. Each edge of the Voronoi graph was used as central axis for orienting the single beams and composing the lattice. The average edge length, coincident to the average length of the beams, was equal to 1 mm. As discussed in [6, 17], this dimension was considered as suitable for modelling a scaffold mimicking a human trabecular bone. The choice of a refined irregular topology was done for reproducing the natural randomness of bone tissue and for replicating at the same time the physics of direct foaming processes. This can be considered an advantage with respect to the regular topologies that can be employed in current medical applications, which can exhibit direction-dependent mechanical behaviors. Regarding the vertex valence of the generated lattice, defined as the number of beams departing from a single node, the value 4 was measured, which corresponds to a non-degenerate Voronoi tessellation of space. It is worthy to note that the original conformal surfaces of the CAD model were preserved in the lattice structure, and this is a necessary condition for enabling osteointegration of the implant. The final results are shown in Fig. 1.

After the modelling phase of the conformal lattice, a second lattice model (compression sample) with the same topology and sizing was generated, to perform a virtual compression test and retrieve the stiffness of the lattice [18, 19]. The model of the scaffold was enclosed into a bounding box and, following the same procedure described above, this box was filled with an identical lattice. This was done for gaining an affordable averaging during the subsequent mechanical characterization phase and for obtaining a CAD model presenting flat boundaries, a condition that is particularly useful in simulation steps. The dimensions of the compression sample were $10 \times 10 \times 20$ mm, and the proposed procedure is depicted in Fig. 2.

2.3 Simulation Setup

The simulation consisted in a “computer experiment”, reproducing the whole setup of a uniaxial compression test. The main objective was to design an ad-hoc scaffold from a structural point of view. The variable to optimize was the radius of the trabeculae, in order to design a beam network capable of bearing a pre-defined load. The target was to obtain an intrinsic stiffness of the lattice structure equal to the intrinsic stiffness of a human mandible.

The first simulation phase was the import of the CAD model of the lattice into Abaqus 6.14 environment, which has been treated as a “wireframe model”, i.e. a network of one-dimensional beam elements, connected by rigid interlockings at nodes.

Regarding the boundary conditions, pin constraints were imposed to the nodes in the lower part of the wireframe model, in order to lock their positions in space. Four symmetry constraints were set to the nodes lying on the vertical faces of the sample, since it was intended as a volume extracted from a wider lattice structure. A rigid plate was created to directly retrieve the reaction forces during the virtual compression test, and the upper nodes of the wireframe model were tied to it. In a subsequent step, a vertical displacement of 0.25 mm was imposed to the rigid plate in downward direction.

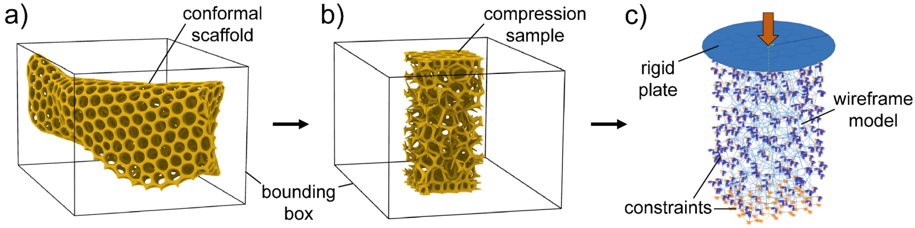

Fig. 2. Procedure for creating the "computer experiment": a) bounding box enclosing the scaffold; b) extraction of the sample for virtual compression test from the box; c) simulation setup for the wireframe model.

The material of the trabecular structure was assumed to be hydroxyapatite extracted from waste compounds produced from by-products of fish industry, i.e. mussel shells [12]. The elastic constants assumed for this mussel-derived sustainable hydroxyapatite were set equal to 35 GPa for Young's modulus and 0.27 for Poisson's ratio [8, 20, 21].

2.4 Structural Design of the Scaffold

To accomplish a correct load bearing condition, it was assumed as a design requirement that the Young's modulus of the whole scaffold should be equal to the average Young's modulus of human sponge bone. As discussed in [22], we assumed as a target parameter an intrinsic stiffness of 1.37 GPa. This condition represents a good design practice for avoiding the "stress shielding effect" and to promote load transfer to the growing bone tissue, which must be always subjected to some mechanical stimuli to stay healthy. If the Young's modulus of the artificial implant exceeds that proper of the bone, the growing tissue will be "stress shielded" and will lose its functionality [3, 23]. Since hydroxyapatite is slowly biodegradable, during the years the newly formed bone tissue will replace the scaffold and will gradually carry the load until establishing the natural physiological conditions [11, 17].

A series of virtual compression tests were performed in Abaqus environment, by varying the radius of the beams from 0.2 mm to 0.4 mm with equal steps of 0.05 mm. A corresponding set of load-displacement curves was retrieved, and the intrinsic stiffness of each beam network was extracted from the slope of the initial tangent of the stress-strain curve, before entering the non-linear regime. The optimal beam sizing allowing to obtain an intrinsic stiffness of the lattice structure comparable to the imposed target requirement was identified.

3 Results and Discussion

All the simulation results are presented, for variable beam radii, in the graph of Fig. 3. From this optimization emerged that the correct beam radius for the considered lattice topology and the considered requirements is 0.32 mm. In Fig. 3 is also reported the regression function allowing the design of biomimetic scaffolds presenting different targets for stiffness, to be eventually employed in other anatomical districts of human body. The law relating the overall stiffness of the lattice and the beam radius is a cubic law since the underlying mechanical response is driven by flexural and torsional stiffness of the interlocked beams constituting the volumetric framework of the scaffold.

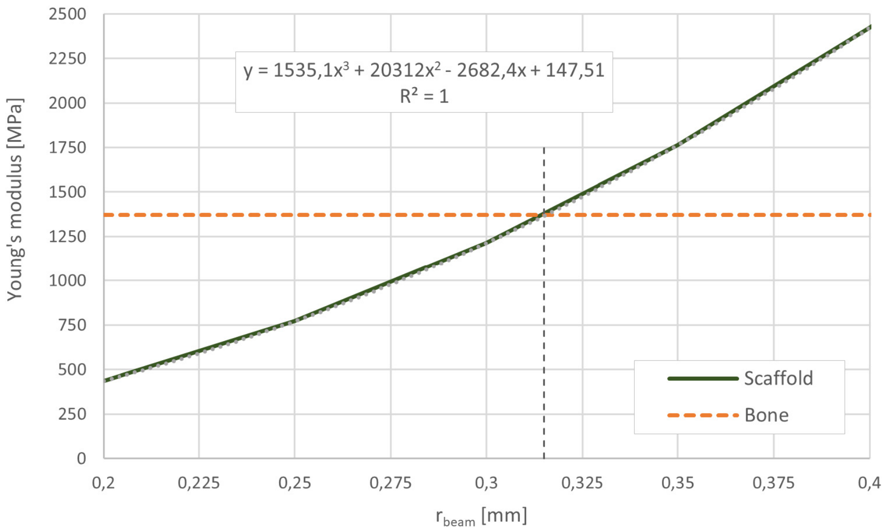

Fig. 3. Young's modulus of the irregular scaffold as a function of beam radius and regression function relating the variables.

After this identification phase, a geometrical analysis was performed on the designed scaffold, with the aim of retrieving the porosity and the pore size of the lattice. In Rhinoceros and Grasshopper environment, the wireframe structure was converted into a solid model presenting the identified sizing for beams. The volume of a cubic internal region in the compression sample and the effective volume occupied by the trabecular solid structure inside the same region were measured and utilized to calculate the porosity, defined as the ratio between the void region surrounding the solid lattice and the overall volume of the considered region. The computed value for porosity was equal to 70%. Then, within the same cubic region, a set of spheres was placed in the center of every Voronoi cell and expanded until colliding to the surfaces of the trabecular solid model [13, 18]. The pore size of the lattice structure was then computed as the average diameter of the above-mentioned spheres, and it was equal to 1.6 mm.

The obtained results for porosity and pore size were in acceptable agreement with the optimal ranges reported in scientific literature [13, 14, 24]. Furthermore, the beam-based approach based on a Voronoi tessellation ensured a full connectivity between adjacent cells, since the solid parts of the structure are concentrated only towards the beams. It is worthy to note that connectivity is a fundamental requirement for a biomimetic structure, in order to favor the vascularization of the growing bone tissue during regeneration. All the design data and all the results of the proposed procedure were reported in Table 1.

In conclusion, the proposed procedure for designing a conformal beam-based scaffold was: a) definition of the shape corresponding to the void region of the fracture site;

Table 1. Design data and simulation results.

Parameter	Bone	Scaffold
Material	HA-collagen comp. [3]	Mussel-derived HA [12]
Young's mod. [GPa]	1.37 [22]	1.37
Young's mod. HA [GPa]	35–120 [20]	35
Topology	Trabecular bone [17]	Gmsh Delaunay
Vertex valence	6 [6]	4
Connectivity [%]	100	100
Trabeculae length [mm]	0.5–2 [17]	1
Trabeculae radius [mm]	0.05–0.11 [24]	0.32
Porosity [%]	70–90 [24]	70
Pore size [mm]	0.7–1.2 [14]	1.6

b) filling with an irregular isotropic lattice generated by the Delaunay algorithm; c) conversion to a Voronoi tessellation (dual graph); d) structural simulations on a wireframe model. The adopted procedure resulted in an effective and reliable workflow for the structural design of conformal irregular scaffolds, because the wireframe model of the beam network, in which the composing elements are subjected to bending and torsion loads at nodes, can be easily studied in mechanical simulation packages, and a wide range of results can be obtained by simply varying topological, geometrical, and constitutive parameters. Therefore, the proposed procedure can be considered as an optimal practice to be employed in the conceptual design stages of a personalized, conformal, and highly biocompatible scaffold for bone tissue regeneration.

Acknowledgements. This work was supported by Regione Puglia under the project RIPARTI (assegni di RIcerca per riPARTire con le Imprese), Avviso pubblico n. 3/FSE/2021, POC PUGLIA FESR-FSE 2014/2020, Fondo Sociale Europeo.

References

1. Kundu, J., Pati, F., Shim, J.-H., Cho, D.-W.: Rapid prototyping technology for bone regeneration. In: Rapid Prototyping of Biomaterials, pp. 254–284. Woodhead Publishing, UK (2014)
2. Koons, G.L., Diba, M., Mikos, A.G.: Materials design for bone-tissue engineering. Nat. Rev. Mater. **5**, 584–603 (2020)
3. Alvarez, K., Nakajima, H.: Metallic scaffolds for bone regeneration. Materials **2**(3), 790–832 (2009). https://doi.org/10.3390/ma2030790
4. Boccaccio, A., Fiorentino, M., Uva, A.E., Laghetti, L.N., Monno, G.: Rhombicuboctahedron unit cell based scaffolds for bone regeneration: geometry optimization with a mechanobiology – driven algorithm. Mater. Sci. Eng. C **83**, 51–66 (2018)

5. Boccaccio, A., Uva, A.E., Fiorentino, M., Monno, G., Ballini, A., Desiate, A.: Optimal load for bone tissue scaffolds with an assigned geometry. Int. J. Med. Sci. **15**(1), 16–22 (2018). https://doi.org/10.7150/ijms.20522
6. Rodríguez-Montaño, Ó.L., et al.: Irregular load adapted scaffold optimization: a computational framework based on mechanobiological criteria. ACS Biomater. Sci. Eng. **5**(10), 5392–5411 (2019)
7. Albrektsson, T., Johansson, C.: Osteoinduction osteoconduction and osseointegration. Eur. Spine J. **10**(Suppl2), 96–101 (2001)
8. Eliaz, N., Metoki, N.: Calcium phosphate bioceramics: a review of their history, structure, properties, coating technologies and biomedical applications. Materials. **10**(4), 334 (2017)
9. Ma, P.X.: Scaffolds for tissue fabrication. Mater. Today **7**(5), 30–40 (2004)
10. Sprio, S., et al.: Composite biomedical foams for engineering bone tissue. In: Biomedical Foams for Tissue Engineering Applications, pp. 249–280. Woodhead Publishing, UK (2014)
11. Vaiani, L., et al.: Ceramic materials for biomedical applications: an overview on properties and fabrication processes. J. Func. Biom. **14**, 146 (2023)
12. Scialla, S., et al.: Mussel shell-derived macroporous 3D scaffold: characterization and optimization study of a bioceramic from the circular economy. Marine Drugs **18**(6), 309 (2020). https://doi.org/10.3390/md18060309
13. Barba, D., Alabort, E., Reed, R.C.: Synthetic bone: design by additive manufacturing. Acta Biomater. **97**, 637–656 (2019)
14. Caiazzo, F., Alfieri, V., Bujazha, B.D.: Additive manufacturing of biomorphic scaffolds for bone tissue engineering. Int. J. Adv. Manuf. Technol. **113**(9–10), 2909–2923 (2021)
15. Sun, W., Starly, B., Nam, J., Darling, A.: Bio-CAD modeling and its applications in computer-aided tissue engineering. Comput. Aided Des. **37**(11), 1097–1114 (2005)
16. Stam, J.: Exact evaluation of Catmull-Clark subdivision surfaces at arbitrary parameter values. In: Proceedings of the 25th Annual Conference on Computer Graphics and Interactive Techniques - SIGGRAPH 1998, pp. 395–404. Association for Computing Machinery, New York (1998)
17. Cowin, S.C.: Bone Mechanics Handbook, 2nd edn. CRC Press, US (2001)
18. Melchels, F.P., Bertoldi, K., Gabbrielli, R., Velders, A.H., Feijen, J., Grijpma, D.W.: Mathematically defined tissue engineering scaffold architectures prepared by stereolithography. Biomaterials **31**(27), 6909–6916 (2010)
19. Rodríguez-Montaño, Ó.L., et al.: An algorithm to optimize the micro-geometrical dimensions of scaffolds with spherical pores. Materials **13**, 4062 (2020)
20. Fiume, E., Magnaterra, G., Rahdar, A., Verné, E., Baino, F.: Hydroxyapatite for biomedical applications: a short overview. Ceramics **4**, 542–563 (2021)
21. Hamed, E., Lee, Y., Jasiuk, I.: Multiscale modeling of elastic properties of cortical bone. Acta Mech. **213**, 131–154 (2010)
22. Boccaccio, A., Lamberti, L., Pappalettere, C., Carano, A., Cozzani, M.: Mechanical behavior of an osteotomized mandible with distraction orthodontic devices. J. Biomech. **39**(15), 2907–2918 (2006)
23. Gerhardt, L.-C., Boccaccini, A.R.: Bioactive glass and glass-ceramic scaffolds for bone tissue engineering. Materials **3**(7), 3867–3910 (2010). https://doi.org/10.3390/ma3073867
24. Renders, G.A., Mulder, L., van Ruijven, L.J., van Eijden, T.M.: Porosity of human mandibular condylar bone. J. Anat. **210**(3), 239–248 (2007)

Leonardo da Vinci's Pendular Mill: Towards a Physical Model for Museum's Exhibits

Lorenzo Fiorineschi[1](✉), Federico Rotini[1], and Roberta Barsanti[2]

[1] Department of Industrial Engineering, University of Florence, Florence, Italy
lorenzo.fiorineschi@unifi.it
[2] Museo Leonardiano, Vinci, Italy

Abstract. Physical or virtual models of ancient machines often play a key role in museum's exhibits, as well as in cinematographic works somehow focused in technological heritage. To obtain such models, complex design activities are required, characterized by strict co-operations among different stakeholders (i.e. designers, historians, artisans, museum staff, etc.). In recent publications, the systematic design methods originally conceived for industrial purposes, have been considered as valid supports also for the reconstruction of ancient machines. In this paper, a specific systematic design procedure is applied to support the fuzzy front-end of the process, concerning the reconstruction of a machine devised by Leonardo da Vinci. The machine is the Pendular Mill, which is characterized by important criticalities such as the enormous size, the complexity of the mechanism, and the missing information about key details. The result obtained in this paper points out a set of different possibilities for the design of physical models for a museum's exhibit, highlighting the issues to be faced for each hypothesized direction. The obtained information constitutes the underpinning for the next planning and design activities of a brand new model of the machine.

Keywords: Leonardo da Vinci · Systematic Design · Ancient machines · Technological heritage · Engineering

1 Introduction

Ancient machines constitute one of the most fascinating attractions in museum's exhibits, as well as in documentaries or cinematographic works focused on technological heritage. Indeed, virtual or physical models re-built from original documents or remains of original machines, often constitute the key elements of the exhibit. In such a context, a strict co-operation between engineers and historians is required for the elicitation of design requirements, and to perform the design activities needed to obtain the reproduction of the original machine. As for usual engineering projects, the activity of designing models for ancient machines can benefit from the application of systematic approaches capable of guiding the designers from the definition of the first set of information to the final design. Accordingly, the same procedural (and iterative) steps of systematic design processes also characterize the design of models of ancient machines. By considering the well-known methods, and related definitions, proposed by Pahl and Beitz [1], the mentioned

M. Carfagni et al. (Eds.): ADM 2023, LNME, pp. 479–487, 2024.
https://doi.org/10.1007/978-3-031-52075-4_54

steps can be resumed in the clarification of the design task, the conceptual design, the embodiment design and the detail design of the model. During the clarification of the task, the designer (or the design team) operates by eliciting the information required to formulate both objectives and constraints that pave the way for the design process. In the conceptual design, the building blocks needed to implement each function of the system are conceived and combined together to obtain a set of preferred concepts. In the embodiment design step, the preferred concepts are developed in terms of size, materials, and performances, usually by exploiting Computer Aided Engineering (CAE) tools. Then, in the detail design, each single part of the system is defined in depth, and the production documents are provided.

This paper is focused on the task clarification step, within the specific context of the interpretation of ancient documents and the identification of the requirements for the design of museum models of ancient machines. In this case, the difficulties are twofold as, on the one hand, the design of models of ancient machines can be assimilated to a sort of re-design of an existing device, while, on the other hand, the available information is often fragmented and ambiguous. For these reasons, the stakeholders involved in this kind of activities (e.g. designers, historians, museum staff, manufacturers, etc.) are asked to face complex design issues by relying only on fragmented technical information. In particular, it is often difficult to identify the main functions that the machine (or part of it) was actually designed for, how it originally implemented the functions, and how it was intended to be manufactured (i.e. in terms of both materials and technological processes).

The machine considered in this paper was originally conceived by the well-known Italian polymath Leonardo da Vinci, who designed a plethora of different devices for a high variety of purposes [2, 3]. Sometimes, da Vinci realized quite detailed drawings and provided some textual information, which have been useful for reproducing a model of the original device (e.g. for the hydraulic saw [4]). Generally, Leonardo produced comprehensive illustrations about the devised machines, also suggesting alternatives for specific parts intended to be used to build the whole system [3]. However, the interpretation of Leonardo's sketches can often be not self-evident, since the early design undergoes successive integrations or even corrections (e.g. for the textile machines [5]). In other cases, except for the presence of rough sketches, the information is almost completely missing (e.g. for the Delta Wing [6]).

The objective of the work described in this paper is to obtain the first set of information needed to plan the reconstruction of a specific machine devised by Leonardo da Vinci, i.e. the Pendular Mill (see Subsect. 2.2). In particular, a tailored systematic procedure is considered, which has been recently proposed to support some critical tasks involved in the reconstruction process of ancient machines [6].

In Sect. 2, a description of the Pendular Mill is reported, according to the original sketches and notes of Leonardo. In the same section, the methodological approach is also described, and the steps considered in this work are highlighted. In Sect. 3, the results are presented, while Sect. 4 is dedicated to discussions and conclusions.

2 Materials and Methods

2.1 The Pendular Mill

In the renaissance era, the importance attributed to the research of novel sources of motion was relevant, as demonstrated by the number of different attempts that can be found in the documents of coeval engineers. For example, Francesco di Giorgio Martini conceived many milling systems where horses or humans were exploited as a source of motion, as can be seen in the Codex Ashburnham [7].

However, the interest toward the pendular mill of Leonardo is motivated by the originality of the solution proposed by the inventor, which is different from any other alternative proposed by coevals (e.g. wind mills, human-powered mills, animal-powered mills, etc.).

Leonardo in the Codex Atlanticus, folio 170r, represents the device (see Figs. 1 and 2). In Fig. 1, an early sketch of the system is provided. It was probably a first sketch made by Leonardo during the idea generation process, since the representation is very rough and approximate. Some textual notes are reported in the lower part of the sheet but are not referred to the mill. Indeed, the notes are focused on the hydraulic system represented near to the pendulum.

The information provided in Fig. 2 is more detailed and precise as well as the graphical representation. Indeed, thanks to this second representation, it has been possible to understand how Leonardo intended to realize (at least in term of working principles) the key part of the system.

The overall machine is a mill to produce wheat flour, which is intended to use a standard (for the era) rotational milling system. The concept, however, exploits a weird source of motion, i.e. a pendulum. Leonardo provided quite detailed information about dimensions and weight of the pendulum:

- Length: 30 "braccia" (or arms) intended here with the value considered in the renaissance era at Florence (i.e. about 0,583 m [8]).
- Weight: 20000 "Libbre" (or libbers), intended here with the value considered in the renaissance era at Florence (i.e. about 0,3395 kg [8]).

According to the information above, it is then clear that the sketches in Figs. 1 and 2 are not in scale. Indeed, the length of the pendulum, from the center of the oscillating mass to the center of the oscillating gear, is actually intended to be more than 17 m.

The weight of the oscillating mass (detail "d" in Fig. 2), converted in current units, is about 6800 kg.

An escapement (Detail "a" in Fig. 2) applied to two semi-gears is intend to allow the inversion of motion of the pendulum (see Detail "c" in Fig. 2), by preserving the same rotational direction for the mill. In addition, in order to "charge" the system (i.e. to move the mass of the pendulum in the starting position), a manual winch is considered (Detail "b" in Fig. 2).

In the detail "e" of Fig. 2 another device is reported, constituted by a sort of lever. Leonardo reported as it follows:

"Quando la pietra percote la contralieva a, tira indietro la lieva b".

Which can be translated as it follows:

"when the stone hits the counter lever a, it pulls back the lever b".

No additional information is reported about this detail, which actually constitutes the most ambiguous part, among those represented for the system.

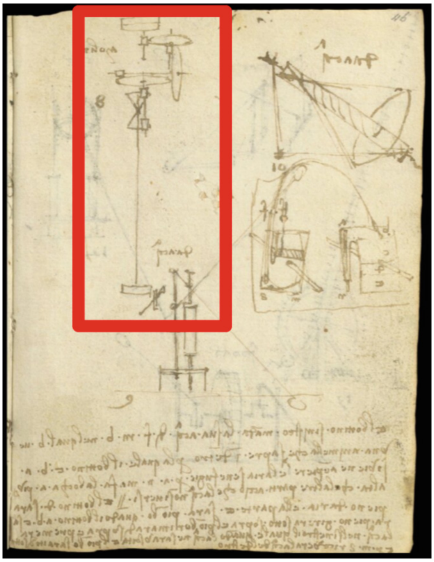

Fig. 1. Early sketch of the Pendular Mill of Leonardo da Vinci (Codex Forster I, folio 46r) [9]. The sketch is highlighted in red.

2.2 The Methodological Approach

In order to manage the different activities, from the planning of the task to production of the production documents, a schematic representation of the whole design process is considered. More specifically, the work described in this paper has been started by considering the systematic procedure recently proposed by Fiorineschi, Rotini and Barsanti [6] (see Fig. 3).

The first step of the process aims at analyzing the information available in the original documents. A preliminary set of technical data should be extracted for first discussions about the feasibility of the model.

In the second step, historians and designers are expected to identify the type and the fidelity level [11] of the model to be designed. Indeed, it can be possible to reproduce the system by using the technologies of the specific era (e.g. for high fidelity models), or to rebuild the model by exploiting modern technologies and materials.

In the third step, the technical analysis of the documents is performed to extract all the available information about each detail of the system (e.g., the purposes expected for

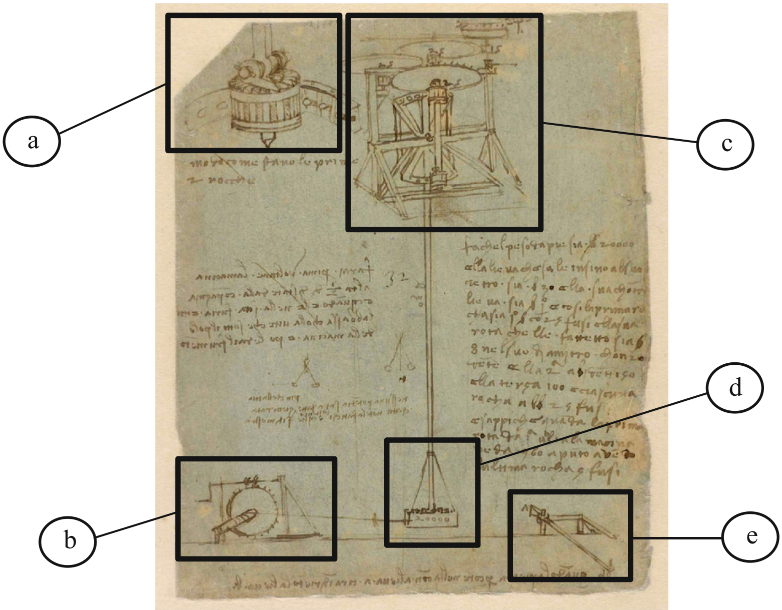

Fig. 2. Detailed sketch and description of the Pendular Mill of Leonardo da Vinci (Codex Atlanticus, folio 170r) [10]. The key elements of the system are indicated with letters.

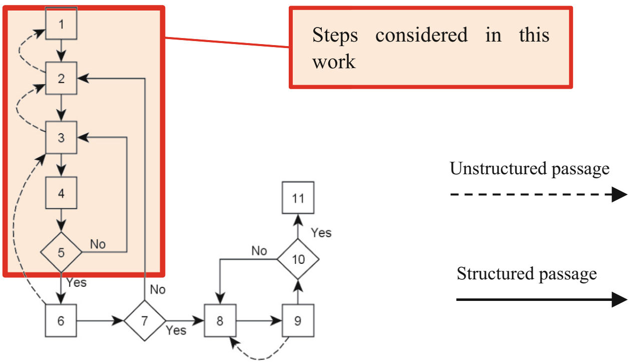

Fig. 3. Schematic representation of the systematic design procedure tailored for the reconstruction of ancient machines [6]. See Table 1 for the description of each step. The steps considered in this work are highlighted in red.

the designed artifact, the exploited energy types, the environment in which the device was expected to work, etc.).

The fourth step is devoted to the identification of the set of the main functions implemented by the ancient artifact. In particular, it is necessary to identify the functions that the system is expected to implement.

Table 1. Steps of the systematic procedure represented in Fig. 2.

Step number	Description
1	Preliminary analysis of the documents
2	Task clarification
3	Technical analysis of the documents
4	Main functions identification
5	Required information available?
6	Compilation of the Problem-Solution-Network
7	Solutions comply with requirements?
8	Selection of the preferred solutions
9	Embodiment design of the overall system
10	Does the system work or appear as expected?
11	Next steps (e.g. detail design, rendering, animations, etc.)

The fifth step considered in this work is a verification, which is used to verify if the available information is sufficient to proceed with the subsequent design steps (i.e. the conceptual design, the embodiment design and the detail design).

3 Results

The results obtained for each step are resumed here in the following paragraphs.

Concerning Step 1 (see Fig. 3), the information available in Fig. 2 reveals in a sufficient way how the system was intended to work. Except for the details of the mechanisms and the form of the structure that was intended to host the machinery, Leonardo has provided quite detailed data (i.e. the transmission rate, the weight, the length, and some reference to materials). Actually, the role of a part of the system is not explained (i.e. the detail "e" in Fig. 2), but similar issues are often present when facing this kind of activities.

Concerning Step 2 (see Fig. 3), after an in-depth reflection performed by engineers, historians and museum staff, it has been decided to consider the possibility of reproducing the machine with a high fidelity physical model. Due to the enormous dimensions considered by Leonardo, a scaled version is obviously needed. In a first hypothesis, a provisional encumbrance has been established to a volume spanning from 2 m^3 to 6 m^3, with a surface area spanning from about 1 m^2 to 2,5 m^2. The use of wood and forged iron (for metal parts) is required for the key parts of the mechanism, in order to obtain the desired fidelity level. For this reason, the hypothesis of an automated demonstrative model has been discarded, due to the low probability of obtaining a high-fidelity escapement system with a reasonable durability. Another reason resides in the additional complexities (and costs) related to safety requirements.

The in-depth technical analysis performed in Step 3 highlighted the criticalities that need to be carefully considered in future design activities. More precisely, it seems that the most complex part to be reproduced (as expected) is the escapement system for the inversion of the motion. However, the available representation reveals sufficient indications about its functioning, but it is difficult to understand if the suggested system will work as expected. The analysis of the ambiguous detail "e" in Fig. 2 left both historians and engineers with no exhaustive explanations for the moment. Several hypotheses can be made concerning the hosting structure. Perhaps, the system was intended to be hosted in a tower-like structure, which could be made by bricks and stones, or even by wooden trusses (e.g. like the structures conceived to attack bastions in war). In Step 4 (see Fig. 3) the main functions of the model to be designed have been identified as represented by the simplified IDEF0 diagram shown in Fig. 4.

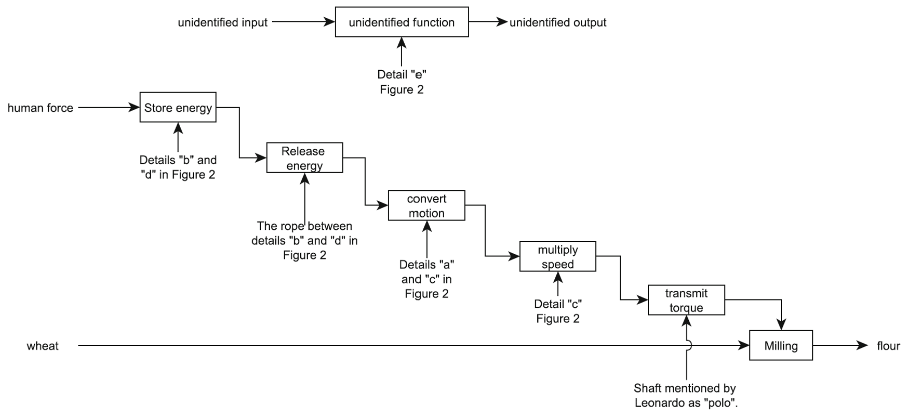

Fig. 4. Simplified IDEF0 diagram about the main functions identified for the system to be reproduced.

In the verification performed in the fifth step, therefore it emerged that the following set of information is still missing:

- The function implemented by the detail "e" in Fig. 2.
- The form of the hosting structure
- The actual dimensions of the mill
- The actual rotational speed of the mill
- Details about the mechanisms and the rest of the "milling plant" (e.g. bearings)

4 Discussions and Conclusions

The work presented in this paper applied the systematic design procedure to the early steps of the process related to the development of a high fidelity physical model for a museum. In particular, the fuzzy front-end of the process has been faced to provide a first provisional definition of the design task. The subsequent steps of the considered process revealed that some doubts are still present, which need to be carefully faced before starting the design activities. In particular, it is necessary to understand which function actually implements the device represented in the detail “e” of Fig. 2. An in-depth analysis of other documents from Leonardo and his coeval is needed in order to search for similar devices (if any), hopefully providing exhaustive information.

Concerning the hosting structure, it is important to decide whether it will be considered in the model or not, and in the first case, which kind of structure should be considered. Indeed, a wooden structure could be reproduced with real wood, while in case of a stonework structure, additive manufacturing technologies could be considered for convenience. Concerning details like bearings and other parts of the mechanisms, Leonardo conceived many variant of them (some of which already reproduced by the Museo Leonardiano), as reported in the same codex, as well as in other ones. Therefore, designers can consider them as “on the shelf” components in the future design activities. Concerning the escapement system, i.e. the most complex part to be designed for the model, further analysis are needed. Most importantly, it is necessary to discuss with the manufacturer about the possibility of realizing certain details by preserving the required fidelity level. This kind of discussion, however, is expected to be performed during the conceptual design process.

The impact expected for this work is first for society. Indeed, if the model will be manufactured and exhibited, people would have the possibility of observing this device of Leonardo, probably for the first time (as far as we know, this particular machine has never been reproduced at a high fidelity level). Another important impact is also expected for academia since design-science scholars. Indeed, this experience will demonstrate that engineering design methods born for the industrial field could be successfully applied also for improving the understanding of ancient technologies according to the historical context. Concerning historians, the data presented in this paper would allow them to perform independent studies about this device. Future developments of the works consist in the successive steps of the considered process, i.e. in designing the model across the three procedural stages usually acknowledged as conceptual design, embodiment design and detail design.

References

1. Pahl, G., Beitz, W., Feldhusen, J., Grote, K.H.: Engineering Design. 3rd edn. Springer-Verlag, London (2007). https://doi.org/10.1007/978-1-84628-319-2
2. Moon, F.C.: The Machines of Leonardo Da Vinci and Franz Reuleaux: Kinematics of Machines from the Renaissance to the 20th Century, vol. 2. Springer-Verlag, Dordrecht (2007). https://doi.org/10.1007/978-1-4020-5599-7
3. Galluzzi, P.: Leonardo da Vinci: from the “elementi macchinali” to the man-machine. Hist. Technol. **4**, 235–265 (1987). https://doi.org/10.1080/07341518708581700
4. Fiorineschi, L., Barsanti, R., Cascini, G., Rotini, F.: Application of systematic design methods to cultural heritage preservation. In: HERITECH 2020. IOP Conference Series (2020). https://doi.org/10.1088/1757-899X/949/1/012029
5. Hollister-Short, G.: Relating to Leonardo da Vinci’s work on textile machines. Le Journal de la Renaissance. **5**, 77–116 (2007). https://doi.org/10.1484/J.JR.2.303134
6. Fiorineschi, L., Rotini, F., Barsanti, R.: Systematic design of ancient machines’ models: Leonardo da Vinci’s glider. Heritage. **5**, 1593–1611 (2022). https://doi.org/10.3390/heritage5030083

7. Di Giorgio Martini, F.: Codex Ashburnham. https://www.leonardodigitale.com/sfoglia/codice-ashburnham-361/0001-r/. Accessed 18 Feb 2023
8. Cardarelli, F.: Encyclopaedia of Scientific Units, Weights and Measures. Springer, London (2003). https://doi.org/10.1007/978-1-4471-0003-4
9. da Vinci, L.: Codex Forster I. https://www.vam.ac.uk/articles/explore-leonardo-da-vinci-codex-forster-i#?c=&m=&s=&cv=92&xywh=857%2C-259%2C3140%2C2163. Accessed 10 Feb 2023
10. da Vinci, L.: Codex Atlanticus, folio 170r. https://codex-atlanticus.ambrosiana.it/#/Detail?detail=170. Accessed 17 Jan 2023
11. Fiorineschi, L., Rotini, F.: Unveiling the multiple and complex faces of fidelity. In: Proceedings of the Design Society: International Conference on Engineering Design, pp. 1723–1732. Delft, The Netherlands (2019). https://doi.org/10.1017/dsi.2019.178

CFD-Driven Shape Optimization of a Racing Motorcycle

Massimiliano Chillemi[1](✉), Filippo Cucinotta[1], Domenico Passeri[1], Lorenzo Scappaticci[2], and Felice Sfravara[1]

[1] Università degli Studi di Messina, Messina, Italy
massimiliano.chillemi@unime.it
[2] Allimep S.r.l., Perugia, Italy

Abstract. In motorsport applications the adoption of a Computational Fluid Dynamics (CFD) simulation is a well-established practice. This analysis is very useful to understand and optimize the aerodynamics performance of the prototypes.

By means of specific algorithms it's possible to define one or more control parameters and so changing the geometry of the fairing to optimize an engineering value.

These algorithms are largely used in other fields such as the hydrodynamics one but they are not largely used in motorsport, especially in motorcycles.

The motorcycle considered in this study is a prototype participating in the Moto2 World Championship, the middle class of the MotoGP World Championship.

Starting from tests, carried out in the wind tunnel, a baseline model was firstly created to get a correlation between experimental and numerical results and so used for a subsequent process of shape optimization. With the main objective of reducing the overall drag, a set of control points was defined on the existing geometry to deform the surface of the front fairing. These points have been used by the optimization algorithm to find the shape that reduces the overall drag.

The optimized geometry made it possible to obtain the desired drag reduction.

Keywords: CAE · CFD · Aerodynamics · Motorsport · Shape Optimization

1 Introduction

In the latest years Computational Fluid Dynamics (CFD) simulations have become an important tool to optimize the aerodynamics performance of vehicles and motorcycles.

CFD simulations are now more accessible, due to the development of computers with more calculation power and the relatively lower price of high-performance Central Processing Units. In motorsport, CFD is used to study both internal aerodynamics [1] or external aerodynamics [2]. In four-wheel prototypes, CFD simulations have been realized to improve the downforce [3], to study the influence of the front or rear wing [4] and to characterize the wake [5]. In motorcycles, these simulations techniques became

M. Carfagni et al. (Eds.): ADM 2023, LNME, pp. 488–496, 2024.
https://doi.org/10.1007/978-3-031-52075-4_55

more used in the recent years, it can be seen by the implementation of winglets in the fairing started in 2016. In the traditional aerodynamic design workflow, principally in the categories lower or equal than Moto2 championship, the teams test multiple solutions in the wind tunnel to select the most effective fairing or winglets. This procedure is time consuming and it is principally based on the experience of the team. The range of solutions that can be used are limited by the time and the costs. A method that can help to find new design solutions quickly and reliably is the shape optimization exploiting results from CFD simulations. Optimization algorithms have always been employed for ergonomics and structural optimization [6–13] and in the recent decades they have been used also for fluid-dynamics purposes [14–18], but rarely in motorsport applications. Utilizing optimization algorithms, an initial geometry is defined, along with the editable parts and the parameters to be optimized. The solver subsequently generates the optimal geometry, resulting in less computational resources and time used. A new design method is proposed, which consists in three different phases. The first phase is an experimental one, it consists in wind tunnel testing with a standard aerodynamic package. In the second phase, a correlation between the experimental data and the numerical results is reached. In the third and last phase, an algorithm calculates the optimal geometry and performs a simulation to extract the aerodynamics coefficients. These coefficients, due to the correlation work realized, can be compared with the original ones. If the results determine a good improvement, the optimized geometry can be realized and only the final design is manufactured avoiding the effort required by realizing different solutions and testing it one by one in the wind tunnel.

2 Materials and Methods

2.1 Original Geometry

The original geometry of the motorcycle was given by the manufacturer, which participates in the Moto2 Championship. The rider was modelled in Siemens NX and it was positioned on the motorcycle using the handlebars, the footrests and photos of the real rider in the aerodynamic position on track as guidelines. The overall length L (1960 mm), the maximum height H (2420 mm) and the maximum width W (550 mm) will be considered during the creation of the control volume. In CFD analysis, the control volume is a region of the space which encloses the flow domain of interest (Fig. 1).

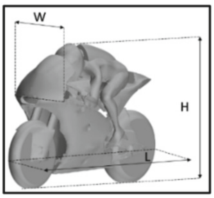

Fig. 1. Main dimensions of the motorcycle-rider assembly.

2.2 Wind Tunnel Setup

The wind tunnel tests were carried out at the “Raffaele Balli” wind tunnel in Perugia, which has an open-loop configuration (Fig. 2).

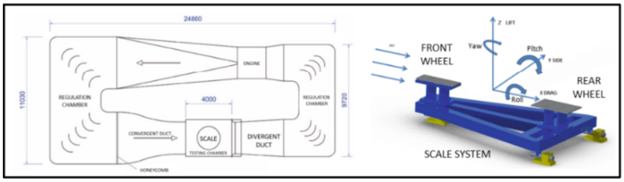

Fig. 2. Layout of the wind tunnel (on the left, all dimensions in mm) and measurement system setup (on the right).

The testing chamber is placed at the end of a converging duct, which allows to increase the flow velocity. The square section of the testing chamber is equal to 4.84 m^2. The diffuser then slows down the air flow and has an outlet section of 7.29 m^2. The motorcycle during the wind tunnel tests is positioned with the wheels on the corresponding scale. To maintain the motorcycle in position, the rear wheel is constrained with a wheel stop bracket. When the airflow impacts the motorcycle, the flow increases the downforce on the front, determining a bigger value of weight on the front scale and a lower value on the rear scale. Differential measurements are performed through the two scales positioned in the floor of the testing chamber to evaluate the aerodynamic coefficients (Fig. 2).

2.3 CFD Simulation Setup

2.3.1 Computational Domain and Boundary Conditions

The fluid domain considered in the simulation is represented in Fig. 3. The overall length of the block is 8L, distributed in 2L between the Velocity inlet 1 and the motorcycle and 5L between the motorcycle and the Pressure outlet. The height is 2H, while the depth is 7W. These dimensions were obtained from previous experiences of correlation studies in the “Raffaele Balli” wind tunnel.

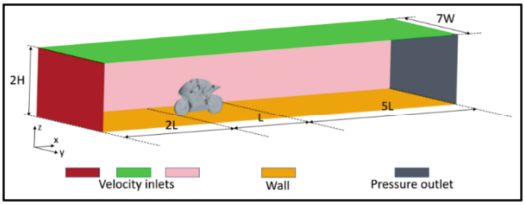

Fig. 3. Control volume and boundary conditions.

The velocity inlets are defined with a constant velocity of 160 kph along the x-direction (see Fig. 3). The pressure and density values in the control volume are set according to the values registered in the testing chamber during the run in Perugia (see Table 1).

Table 1. Atmospheric condition registered in the testing chamber.

Measured quantity	Dimension	Value
Air pressure	Pa	98852.664
Air density	kg/m^3	1.104

2.3.2 Mesh and Turbulence Model

The control volume has been meshed with a trimmed cell mesher. The transition between the outer cells and the surface of the motorcycle has been realized with the prism layer mesher. The first layer of cells in contact with the motorcycle have a dimension of 0.1 mm, then cells grow in 8 layers to the dimension of the cells in the Motorcycle Refinement Block (20 mm). The background mesh has a dimension of 120 mm, while in the Wake Refinement Block the dimension is 40 mm (Fig. 4).

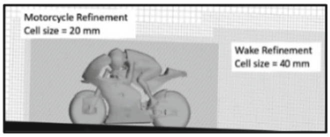

Fig. 4. Trimmed cell mesh with dimensions in the refinement blocks.

The chosen turbulence model, due to its robustness and reliability in this type of applications, is the Realizable Two-Layer k-ε. This model is based on the Standard K-Epsilon model, a two-equation model that involves transport equations for the turbulent kinetic energy k and its dissipation rate ε. The Realizable variant contains a transport equation for the turbulent dissipation rate ε which has been proposed by Shih et al. [19]. This model is substantially better than the Standard K-Epsilon model for many applications because it has a better treatment of anisotropy, which is important for flows with strong streamline curvature and it has an improved stability due to an implemented limiter that prevents unphysical results. The Realizable Two-Layer k-ε model combines the Realizable k-ε with the two-layer approach (which accepts mesh with y+ values of around 1 or values between 30 and 500).

2.4 Optimization Workflow

The CFD analysis was carried out on Simcenter STAR-CCM+. An integrated module, the Adjoint Solver, has been used for the optimization problem. The Adjoint Solver can predict the influence of one or more input parameters on the aerodynamics coefficients calculated by the simulation. In an adjoint analysis, a steady state simulation is realized with an initial mesh: this simulation is referred to as *primal*. In the primal simulation, the design parameters and the relationships between them and the resulting mesh are defined. When the solution of the primal simulation is obtained, all the reports are generated. An adjoint cost function is defined, and it corresponds to the engineering objective to optimize. In this case the cost function is related to the overall drag report.

Once the primal simulation is completed, the optimization process starts and follows the steps described in the diagram reported in Fig. 5.

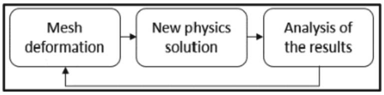

Fig. 5. Optimization loop.

This iterative process goes on until the mesh deformation doesn't influence significatively the results of interest.

The mesh is modified through the movement of the points on the intersection between the front fairing and the symmetry plane. These points can move along x and z, so the displacement is symmetrical. After every iteration, the solver evaluates the change in the cost function derivative and move the points of the mesh (Fig. 6).

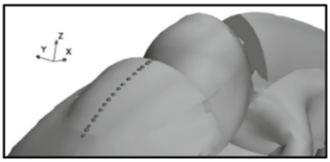

Fig. 6. Control points on the symmetry plane.

3 Results and Discussion

3.1 Wind Tunnel

Among all the values registered during the run in the wind tunnel, the most important ones to evaluate in this study are the Drag Force and the Drag Coefficient. These values will be compared with the ones calculated by CFD to validate the model (Table 2).

3.2 Baseline CFD Simulation

The Drag Force and the Drag Coefficient calculated by CFD are reported in Table 3. The differences between the numerical and the experimental values are possibly due to

Table 2. Values registered in the wind tunnel run.

Measured quantity	Dimension	Value
Drag Force	N	251.392
$C_D \cdot A$	m^2	0.227

a combination of different factors. Some of these could be due to the real motorcycle having some geometrical differences with the CAD model or due to the positioning of the rider in the wind tunnel not being exactly corresponding to the position of the CAD model of the rider. Though, it must be said that even wind tunnel tests can involve experimental errors. Precisely measuring aerodynamic forces on a motorcycle can be a technical challenge, and measurement errors or interferences can occur, affecting the results.

Table 3. Values calculated by CFD.

Measured quantity	Dimension	Value	Δ with experimental results
Drag Force	N	264.991	+ 5.13%
$C_D \cdot A$	m^2	0.225	-1.01%

The pressure distribution on the fairing and on the rider is reported in Fig. 7 from the frontal view. There are three main overpressure areas: the surface of the radiator, the inlet of the snorkel and the helmet of the rider. The first two areas are designed to work in overpressure conditions, while the helmet of the rider is in overpressure due to the shape of the fairing, which doesn't cover it. The goal is to minimize the drag produced by the helmet to reduce the overall drag keeping the same pressure in the other two overpressure zones.

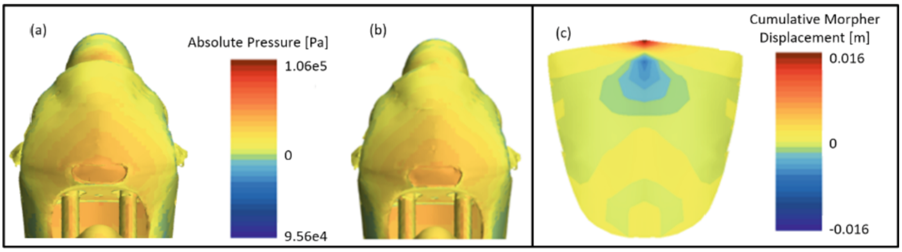

Fig. 7. Absolute pressure distribution on the original model (a), optimized model (b) and displacements of the optimized front fairing windshield (c).

3.3 Optimization

The optimizer reduced the drag, with the main goal of reducing the resistance caused by the interaction between front fairing and helmet. In Fig. 7a is represented the pressure distribution with the original fairing. It can be seen in Fig. 7b that the overpressure on the helmet is highly reduced with the new fairing and this is majorly caused by the appendix on the top that deviates flow around the rider.

Figure 7c shows the displacements of the mesh, in particular the optimized shape has an appendix on the top that goes outwards for 16 mm, while the middle part goes slightly inwards if compared to the original surface.

The percentual drag reduction is reported in Fig. 8a.

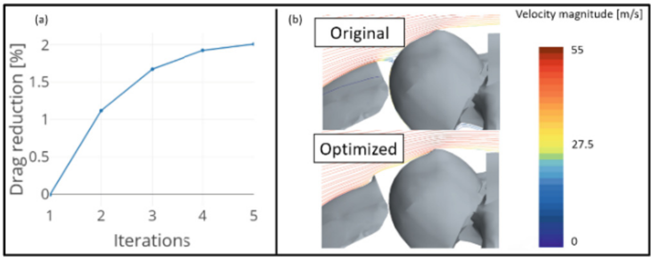

Fig. 8. Streamlines comparison.

The algorithm takes 5 steps until the drag reduction stabilizes at 2.01%. Supplementary computational effort would be not justified by a significative change in the drag value. The overall $C_D \cdot A$ obtained after the optimization is 0.220: comparing this value with the starting one reported in Table 3, a reduction of 2.24% is obtained.

In Fig. 8b the streamlines with the original fairing and the optimized one are compared. The flow doesn't impact anymore with the helmet as in the original case but it follows the curvature of the new appendix to go around it, reducing the drag.

4 Conclusions

The front fairing of a Moto2 prototype was optimized using an algorithm implemented in Simcenter STAR-CCM+. The goal was to optimize the drag reducing an unwanted overpressure zone on the helmet of the rider. After defining a set of control points on the symmetry plane, the algorithm modified the mesh in 5 iterations. Typically, in several days of work in the wind tunnel on the whole motorcycle, obtained $C_D \cdot A$ reductions go from 1% to 5% [20]. In this study, a 2.24% of $C_D \cdot A$ reduction was obtained working only on the front fairing and without having to pay for days of testing in a facility. Thus, the drag reduction achieved through the optimization process focused solely on the front fairing is an important result because it provides further evidence of the importance that CFD (Computational Fluid Dynamics) is gaining in the development of racing motorcycles. This applies both to achieving a more efficient development workflow and to containing the costs associated with wind tunnel rentals and equipment. The biomimetic appendix generated in the optimization process can be tested on the prototype by adding it to the existing fairing or replacing the plexiglass. This process can be extended to optimize other parts of the fairing or the air intake and exhaust system performance.

References

1. AbdHalim, M.A., NikMohd, N.A.R., MohdNasir, M.N., Dahalan, M.N.: Experimental and numerical analysis of a motorcycle air intake system aerodynamics and performance. Int. J. Autom. Mech. Eng. **17**(1), 7607–7617 (2020). https://doi.org/10.15282/ijame.17.1.2020.10.0565
2. Concli, F., Gobbi, M., Gorla, C.: Aerodynamic study of moto recycle racing wheels: a performance evaluation based on numerical CFD simulations. Int. J. Comput. Methods Exp. Measur. **7**(3), 275–284 (2019). https://doi.org/10.2495/CMEM-V7-N3-275-284
3. OmRaj, R.R., NaggariTharakaram, N., Prakash, N.: Design and CFD analysis of a rear wing of a motorsport car. Int. J. Veh. Struct. Syst. **14**(1), 217 (2022). https://doi.org/10.4273/ijvss.14.1.14
4. Knapik, J., Gallyamov, R.E., Ovchinnikov, V.A., Volkova, K.A., Avdeev, E.: F1 Car - front wing CFD analysis and optimization. In: 4th International Conference and Youth School “Information Technologies and Nanotechnologies” (2018)
5. Newbon, J., Dominy, R., Sims-Williams, D.: CFD investigation of the effect of the salient flow features in the wake of a generic open-wheel race car. SAE Int. J. Passenger Cars Mech. Syst. **8**(1), 217–232 (2015). https://doi.org/10.4271/2015-01-1539
6. Cucinotta, F., Raffaele, M., Salmeri, F.: A topology optimization of a motorsport safety device. In: Rizzi, C., Andrisano, A.O., Leali, F., Gherardini, F., Pini, F., Vergnano, A. (eds.) ADM 2019. LNME, pp. 400–409. Springer, Cham (2019). https://doi.org/10.1007/978-3-030-31154-4_34
7. Cucinotta, F., Raffaele, M., Salmeri, F.: A Topology Optimization Method for Stochastic Lattice Structures (2021). https://doi.org/10.1007/978-3-030-70566-4_38
8. Barberi, E., Cucinotta, F., Raffaele, M., Salmeri, F.: A hollowing topology optimization method for additive and traditional manufacturing technologies. In: Rizzi, C., Campana, F., Bici, M., Gherardini, F., Ingrassia, T., Cicconi, P. (eds.) Design Tools and Methods in Industrial Engineering II. LNME, pp. 422–430. Springer, Cham (2021). https://doi.org/10.1007/978-3-030-91234-5_43
9. Abdi, M., Ashcroft, I., Wildman, R.D.: Design optimisation for an additively manufactured automotive component. Int. J. Powertrains. **7**, 142–161 (2018). https://doi.org/10.1504/IJPT.2018.090371
10. Zhu, J.H., Zhang, W.H., Xia, L.: Topology optimization in aircraft and aerospace structures design. Arch. Comput. Methods Eng. **23**, 595–622 (2016). https://doi.org/10.1007/S11831-015-9151-2
11. Jia, D., Li, F., Zhang, C., Li, L.: Design and simulation analysis of trimaran bulkhead based on topological optimization. Ocean Eng. **191**, 106304 (2019). https://doi.org/10.1016/j.oceaneng.2019.106304
12. Gardan, N., Schneider, A.: Topological optimization of internal patterns and support in additive manufacturing. J. Manuf. Syst. **37**, 417–425 (2015). https://doi.org/10.1016/J.JMSY.2014.07.003
13. Cucinotta, F., Raffaele, M., Salmeri, F.: A stress-based topology optimization method by a Voronoi tessellation additive manufacturing oriented. Int. J. Adv. Manuf. Technol. **103**, 1965–1975 (2019). https://doi.org/10.1007/S00170-019-03676-4

14. Gao, T., Wang, Y., Pang, Y., Cao, J.: Hull shape optimization for autonomous underwater vehicles using CFD. Eng. App. Comput. Fluid Mech. **10**, 599–607 (2016). https://doi.org/10.1080/19942060.2016.1224735
15. Ghadimi, B., Nejat, A., Nourbakhsh, S.A., Naderi, N.: Shape optimization of a centrifugal blood pump by coupling CFD with metamodel-assisted genetic algorithm. J. Artif. Organs **22**, 29–36 (2019). https://doi.org/10.1007/s10047-018-1072-z
16. Yan, X., Zhu, J., Kuang, M., Wang, X.: Aerodynamic shape optimization using a novel optimizer based on machine learning techniques. Aerosp. Sci. Technol. **86**, 826–835 (2019). https://doi.org/10.1016/J.AST.2019.02.003
17. Kenway, G.K.W., Mader, C.A., He, P., Martins, J.R.R.A.: Effective adjoint approaches for computational fluid dynamics. Prog. Aerosp. Sci. **110**, 100542 (2019). https://doi.org/10.1016/J.PAEROSCI.2019.05.002
18. Jiao, Z., Yuan, S., Ji, C., Mannan, M.S., Wang, Q.: Optimization of dilution ventilation layout design in confined environments using computational fluid dynamics (CFD). J. Loss Prev. Process Ind. **60**, 195–202 (2019). https://doi.org/10.1016/J.JLP.2019.05.002
19. Shih, T.H., Liou, W.W., Shabbir, A., Yang, Z., Zhu, J.: A new k-ϵ eddy viscosity model for high reynolds number turbulent flows. Comput. Fluids **24**, 227–238 (1995). https://doi.org/10.1016/0045-7930(94)00032-T
20. Tarroni, A.: Aerodinamica della moto e del suo impianto di raffreddamento, 1st edn., EAI (2014). ISBN: 978-3-639-67347-0

Application of Physics-Based Modeling Techniques as a Tool to Help the Development of More Electrified Off-Highway Machinery

Daniele Beltrami(✉), Marco Ferrari, Paolo Giulio Iora, and Stefano Uberti

Department of Mechanical and Industrial Engineering, University of Brescia, 25123 Brescia, Italy
daniele.beltrami@unibs.it

Abstract. Environmental sustainability, greenhouse emissions, and air pollution reduction are among the major drivers for the electrification of the transport and mobility sector. In this regard, industry and academia have started developing electrified solutions for the off-highway industry, but it comes with high development costs. Modeling and simulation can greatly help system-level design but building the mathematical model of an entire machinery is not trivial. In this regard, using physics-based industrial-oriented modeling software like Simscape can simplify it, especially for small niche manufacturers, which usually have lower resources. In this paper, an electrified material handler is modeled using Simscape. The main movements of the machinery are compared with experimental data, and a good match is found for hydraulic pressure and flow. Even if the modeling of other subsystems is needed for more in-depth and accurate analysis, the paper already shows how modern industrial-oriented modeling software can be used to model complex subsystems and to get sensible results. Taking advantage of transient-state system design is indeed key to better assessing energy consumption and getting at a better overall system design, even for small and niche manufacturers.

Keywords: Electrification · Modeling · Simulation · Off-highway machinery

1 Introduction

The United Nations Sustainable Development Goals [1], as well as the increasingly stringent regulations on air quality and internal combustion engine (ICE) emissions, [2, 3] are clear examples of how environmental sustainability, greenhouse emission, and air pollution reduction are pushing for a more sustainable transport and mobility sector.

To this end, electrified passenger vehicles have already proven to be practical solutions [4], and many different electric and hybrid cars are available to end users. However, within the transport and mobility sector, there is also the off-highway machinery industry, which greatly differs from the automotive one. The tasks of these self-propelled machinery go indeed far beyond the transportation of people or goods, such as harvesting, digging, material lifting, external equipment power supplying, and many more [5].

M. Carfagni et al. (Eds.): ADM 2023, LNME, pp. 497–504, 2024.
https://doi.org/10.1007/978-3-031-52075-4_56

In this context, different manufacturers have been presenting prototypes, minimum viable products, and some final products [6–8], which is especially true for small battery electric machinery [9]. Small machinery have indeed lower energy-intensive duty cycles, and it is more likely that they are used in urban contexts, warehouses, or niches where pollution and emissions are a direct threat, like greenhouses [10].

The smaller the niche, the smaller is usually the company manufacturing the specialized machinery. In many cases, due to the limited size of these companies, they work more as system integrators than Original Equipment Manufacturers (OEM), thus, budget and timeframe are usually restricted.

Modeling and simulation are important resources for system designing to reduce costs, although building the mathematical model of entire machinery is not trivial. Indeed, it usually requires extensive knowledge of advanced mathematics.

In this paper, after a brief overview of the market and challenges for off-highway machinery electrification, a completely physics-based model of an electrified hydraulic material handler is created using MathWorks Simscape and compared to experimental data. The model is created using data found among datasheets, received by the manufacturer, or found in the literature, and Simscape components are filled with these data. A simplified CAD model is imported into Simscape, and much attention is given to the modeling of the hydraulics. The main movements of the material handler are then compared with experimental data and a good match is found for both pressure and flow. Finally, future works and improvements are presented.

2 Market and Challenges

Electrified machinery are usually more expensive to purchase with respect to ICE-powered ones, especially due to the high cost of battery packs and high-voltage equipment, but, because they can potentially reduce operating costs, their Total Cost of Ownership (TCO) can get competitive in the long term, as shown in [11]. Nonetheless, reasonable upfront costs are key to convince early-adopter clients.

Retrofitting traditional internal combustion engine machinery is a common approach: the original diesel-based power source is replaced by hybrid or totally electric powertrain with similar power, such that hydraulic system and actuators can remain the same. This relation is clearly visible in the Fig. 1, where it is shown that many battery-electric excavators and related ICE versions have very similar power-to-weight ratios [10].

Taking advantage of modeling and simulation is another smart approach to lower development costs, and it is exploited especially by the automotive industry. It can indeed exploit the presence of standard duty cycles, commercial software and libraries, and considerable scientific literature. However, due to many different machinery architectures and sizes, subsystems, duty cycles, etc., modeling and simulation of off-highway machinery is extremely challenging [12]. Any off-highway machinery can potentially be modeled using a data-driven and/or a physical modeling approach, but both need extensive knowledge of advanced mathematics, especially when considering non-linear domains.

To simplify this process, an industrial-oriented modeling software like Simscape offers libraries of pre-modeled components to be filled with technical data, such that to avoid the writing or the modeling of complex differential equations, but this software is not broadly used in industry and academia for off-highway machinery.

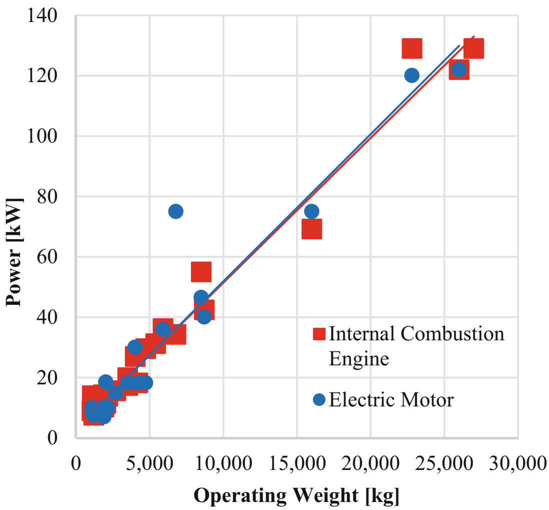

Fig. 1. Power-to-weight ratio of ICE excavators and battery-electric excavators. [10]

3 Methods and Tools

3.1 Hydraulics Material Handler

The modeled machinery is a 14ton material handler, the M15 produced by Officine Minelli s.r.l, which is a small specialized off-highway machinery manufacturer. The mechanical structure of this machinery is visible in the Fig. 2a, which is useful to show the main components of the machinery, as well as the nomenclature used throughout the paper. Intuitively, the mechanical structure is similar to an excavator, and so it is also its duty cycle. Indeed, the main duty cycle of a hydraulic material handler is based on the movements of boom, stick, and turret. The orange peel grab is the most common end-effector for the machinery sold by the manufacturer, but different end-effectors can be mounted upon request. In Fig. 2b the two angles of main importance alpha and beta are clearly represented.

The M15 is usually powered by a diesel engine connected to the main pump of the hydraulic system, and all the linear and rotational actuators are moved by hydraulics. Hydraulics, one of the main subsystems of the machinery, is commanded by the operator inside the cab and it relies on the load-sensing system logic/architecture.

The electric version of the same machinery is retrofitted from the diesel version: the diesel powertrain is replaced by an electric motor and a lead acid battery pack, but the mechanical structure is identical, as well as the hydraulics and actuators. While the introduction of an electric motor brings more flexibility in control and energy management of the machine without increasing excessively the upfront cost, the battery pack causes a big fraction of the higher cost of the entire machinery.

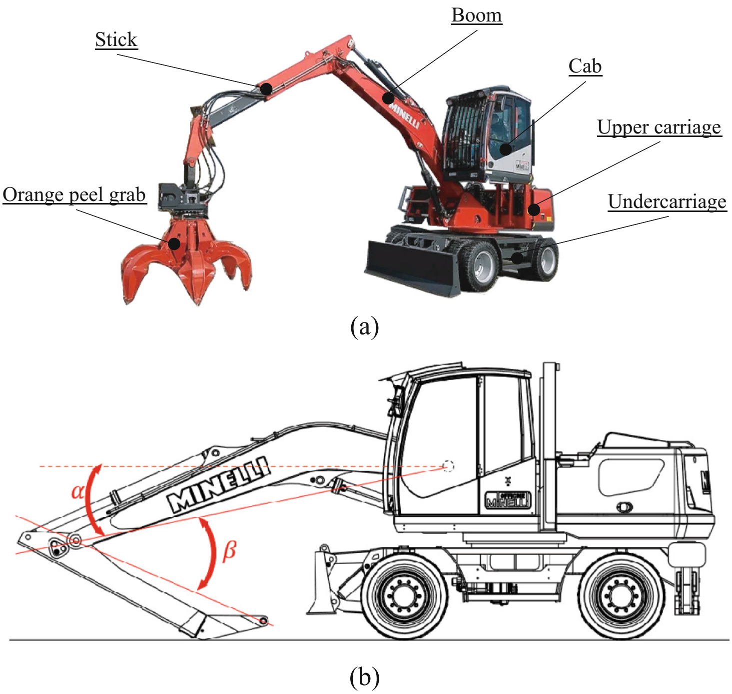

Fig. 2. Minelli M15 hydraulic material handler: substructures names (a), relevant angles of the arms (b).

3.2 Testing

To get experimental data from the machinery, two pressure sensors and two flow sensors are installed at the outlet ports of the main pump and of the directional control valves' manifold. These signals are managed by a data logger and sent to a PC used as acquisition system. The same PC also receives torque and frequency signals from the driver of the electric motor, as well as battery current and voltage (data are synchronized by means of a digital synchronism signal). A simplified scheme of the acquisition system is shown in the Fig. 3.

Different tests are performed, with or without an external load, at low or high motor speed, and with single or multiple actuator movements.

Pressure, flow and angular position of the arms during a run at low speed (1500 rpm) and no external loads are reported in the Fig. 6. At the beginning of the run the two arms are fully extended, and then they are lowered and raised one after the other.

3.3 Modeling

As visible from one subsystem in the Fig. 4, a simplified CAD model of the M15 is realized with SolidWorks and it is imported into Simscape. While the kinematics perfectly reproduces the ones of the real machinery, the values of masses, centers of

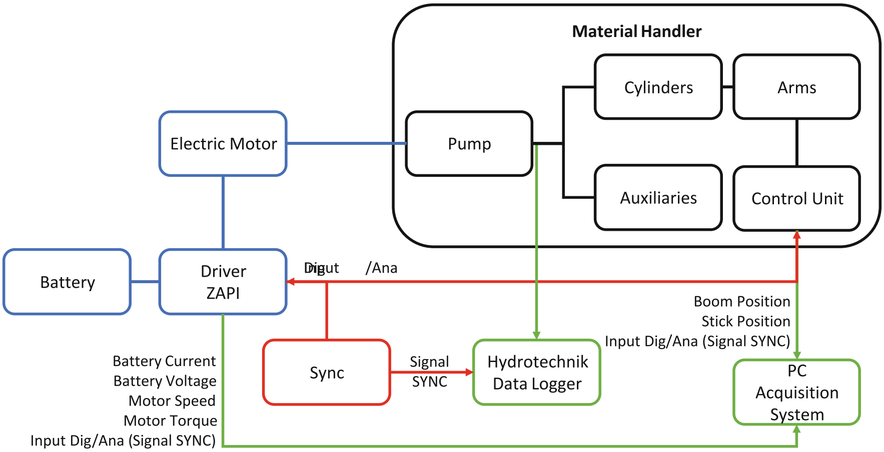

Fig. 3. Simplified scheme of the acquisition system.

mass, and moments of inertia are imported from a full assembly of the machinery and logged into the components using a MATLAB script.

As already said, also the hydraulic system of the M15 is modeled on Simscape. Pump and actuators are modeled by simply relying on technical data from datasheets sent by the manufacturer, while the modeling of the hydraulic valves requires more iterations and a profound understanding of the system. The variety of Simscape's hydraulic components is indeed limited and they can't represent every possible real valve, so some layout variations are needed and Simscape components must be properly connected to simulate a behavior as close as possible to the real one. For instance, a four-way post-compensated load sensing valve component does not exist among any Simscape library, so it is realized by combining multiple variable orifices with the related valve actuators.

Furthermore, the inputs and outputs of Simscape component can't be varied, as well as the data to fill out and characterize them. Regarding this latter need, as visible in the Fig. 5, a modeling tool is realized to translate the orifice-flow and orifice-pressure characteristics provided by the supplier to the spool-orifice characteristic requested by Simscape valve components. Behind the user interface, a Matlab script is used to compute the spool-orifice relation, while a Simscape model simulates a hydraulic bench test to ensure that the computed characteristic replicates the ones given by the supplier. This digital bench test takes into consideration both the intake flow "PA" and the outlet flow "BT" on the single distribution valve, while the load is composed of a simple linear actuator, whose cylinder ratio (ratio between cap side A and rod side B) can be varied by the user.

Regarding the electric system, a simple PI controls the dynamic and the torque of the electric motor by matching a constant input velocity, while a 0th-order equivalent circuit model simulates the battery.

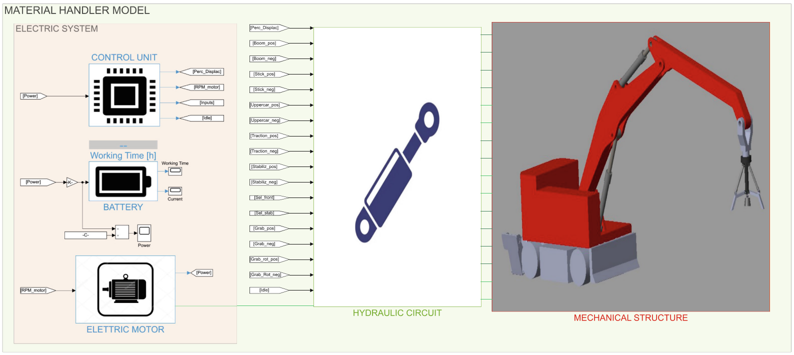

Fig. 4. General overview of the model of the machinery.

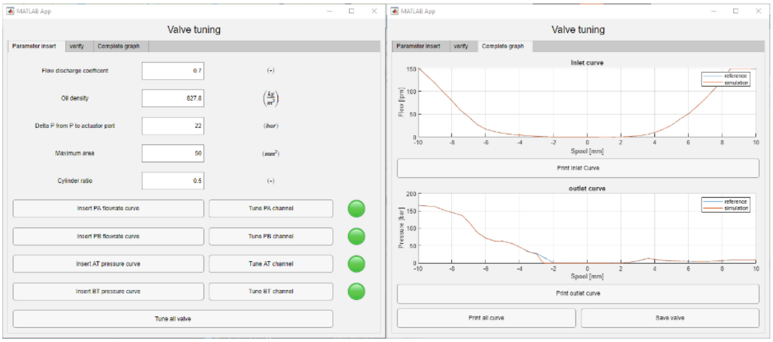

Fig. 5. Modeling tool for the spool of the directional control valve.

4 Results

The comparison between simulation and experimental data is visible in the Fig. 6. The model follows the behavior of the real machinery, apart from the low flow situation, where there is a constant bias caused by the minimum sensitivity of the flow sensor.

As previously mentioned, the real hydraulic system and the one modeled on Simscape are not identical: some components are indeed simplified, some secondary ones are missing, and some behaviors are recreated with slightly different hydraulic components, this causes many of the differences visible in the Fig. 6. For instance, around $t = 45s$, the stick's actuator correctly reaches its end of stroke, but in the real system there are compensation valves that are not included into the model, therefore, pressure and flow are slightly different. Similarly, the absence in the model of a hydraulic accumulator causes the different behavior around $t = 50s$.

The overall power consumption of the movements of the two arms is then well replicated, and in Table 1 four useful performance indexes of the model are visible: the average error $\overline{e}$, the standard deviation σ, the Integral Average Error IAE and its mean over time $\overline{\text{IAE}}$. In particular, this latter value shows how the average power over the cycle differs by only about 2.08 kW.

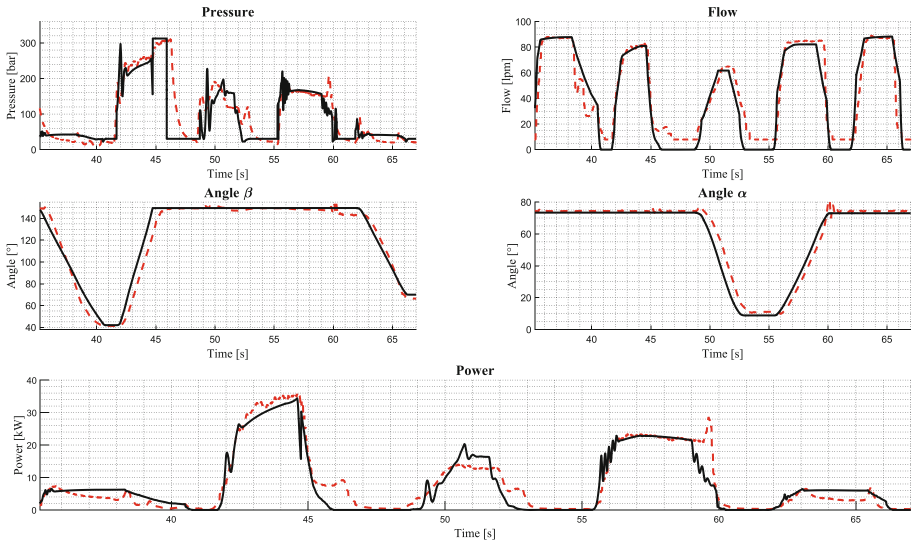

Fig. 6. Comparison of experimental data (dashed line) and simulation (solid line).

Table 1. Performance indexes of the model: $\bar{e}$ average error, σ standard deviation, IAE Integral Absolute Error, $\overline{\text{IAE}}$ average of Integral Absolute Error.

$\bar{e}$	σ	IAE	$\overline{\text{IAE}}$
0.50	3.21	66.08	2.08

5 Conclusion and Future Works

In this paper, an electrified hydraulic material handler is modeled on Simscape by only means of data found in datasheets, in literature or given by the manufacturer, and no complex equations are explicitly written while creating the model. The equations are indeed implicitly compiled by the software, greatly simplifying the modeling process. The simulated movements of the two main arms are compared to experimental data, and a good match is found between the two. Some differences are present due to the simplified hydraulic system, but the power consumption is very similar and compliant with experimental data.

The paper shows that physical-based industrial-oriented modeling and simulation software can be of great help for the system design of machinery, especially if retrofitted from an existing one, which is also shown to be common practice in industry. By evaluating the performance in a simulated environment, better system design choices can be potentially carried out for the selection of the electrified powertrain components, not relying only on steady-state analysis. Besides, with a more in-depth model, it would be possible to investigate and compare different control strategies.

References

1. United Nations: Transforming our world: the 2030 Agenda for Sustainable Development. New York, US (2015)
2. Emission Standards. Europe: Nonroad Engines. https://dieselnet.com/standards/eu/nonroad.php. Accessed 20 Jan 2021
3. United States Environmental Protection Agency Regulations for Emissions from Heavy Equipment with Compression-Ignition (Diesel) Engines | Regulations for Emissions from Vehicles and Engines | US EPA. https://www.epa.gov/regulations-emissions-vehicles-and-engines/regulations-emissions-heavy-equipment-compression#e-cfr. Accessed 20 Jan 2021
4. Lombardi, L., Tribioli, L., Cozzolino, R., Bella, G.: Comparative environmental assessment of conventional, electric, hybrid, and fuel cell powertrains based on LCA. Int. J. Life Cycle Assess. **22**, 1989–2006 (2017). https://doi.org/10.1007/S11367-017-1294-Y
5. Malavatu, J., Kandke, S.R., Gupta, S., Agrawal, B.: Design challenges in electrification of off-highway applications. In: 2019 IEEE Transportation Electrification Conference (ITEC-India), Bengaluru, India, pp. 1–5 (2019). https://doi.org/10.1109/ITEC-India48457.2019.ITECINDIA2019-247
6. Scolaro, E., Beligoj, M., Estevez, M.P., et al.: Electrification of agricultural machinery: a review. IEEE Access **9**, 164520–164541 (2021). https://doi.org/10.1109/ACCESS.2021.3135037
7. Lin, T., Lin, Y., Ren, H., et al.: Development and key technologies of pure electric construction machinery. Renew. Sustain. Energy Rev. **132**, 110080 (2020). https://doi.org/10.1016/j.rser.2020.110080
8. He, X., Jiang, Y.: Review of hybrid electric systems for construction machinery. Autom. Constr. **92**, 286–296 (2018). https://doi.org/10.1016/j.autcon.2018.04.005
9. J C Bamford Excavators Ltd. 1000th JCB Electric Mini (2022). https://www.jcb.com/en-gb/news/2022/12/award-winning-jcb-electric-mini-celebrates-big-milestone. Accessed 24 Jan 2023
10. Beltrami, D., Iora, P., Tribioli, L., Uberti, S.: Electrification of compact off-highway vehicles—overview of the current state of the art and trends. Energies (Basel) **14**, 5565 (2021). https://doi.org/10.3390/en14175565
11. Pihlatie M, Pippuri-Mäkeläinen J (2019) Electric Commercial Vehicles (ECV): Final Report
12. Briggs, I., Murtagh, M., Kee, R., et al.: Sustainable non-automotive vehicles: the simulation challenges. Renew. Sustain. Energy Rev. **68**, 840–851 (2017). https://doi.org/10.1016/j.rser.2016.02.018

A Methodology for Payload Design and Optimization of Autonomous Underwater Vehicles

Luigi Scarfone[1](✉), Antonio Lagudi[1], Umberto Severino[1], Andrea Caffaz[2], and Fabio Bruno[1]

[1] Department of Mechanical, Energy and Management Engineering (DIMEG), University of Calabria, Via Pietro Bucci 46C, 87036 Rende, CS, Italy
{luigi.scarfone,antonio.lagudi,umberto.severino, fabio.bruno}@unical.it

[2] Graal Tech S.r.l., Via Egidio Tagliolini 26, 16152 Genova, GE, Italy
andrea.caffaz@graaltech.it

Abstract. The development of an Autonomous Underwater Vehicle (AUV) is driven by careful design choices in order to obtain the best trade-off between mission performance and cost. Currently, several companies provide off-the-shelf solutions for a wide variety of operational scenarios offering highly modular systems. This allows users to customize the AUV integrating custom payloads tailored for specific applications. The factory customization has a strong impact on time and resources due to significant precautions to be taken. In particular, some design constraints must be respected for the mechanical integration ensuring, at the same time, the overall neutral buoyancy of the module to preserve the final trim of the AUV. Therefore, without a careful approach during the design phase, the risk of impairing the integrity and operation of the AUV could be high. This paper describes a design methodology for the proper development of custom payloads aimed to be integrated in AUVs. The proposed methodology has been applied in the manufacturing of a custom payload that has been integrated in the AUV X-300 of Graal Tech s.r.l. The methodology results as a useful tool for AUVs customization by providing detailed guidelines for the development of specific payloads for a wide range of applications.

Keywords: Autonomous Underwater Vehicle · Modular Payload Design · Balance Identification · Shape Optimization

1 Introduction

Applications of Autonomous Underwater Vehicles (AUVs) are rapidly spreading across a broad spectrum of underwater operations including oceanographic surveys, demining, pipeline monitoring and bathymetric data collection [1]. Most of these operations have been taking advantage of the versatility of commercially available systems, which is certainly a good option in terms of cost effectiveness [2]. Nevertheless, as user demands

M. Carfagni et al. (Eds.): ADM 2023, LNME, pp. 505–513, 2024.
https://doi.org/10.1007/978-3-031-52075-4_57

for specific applications become more stringent, the integration of dedicated components into the AUV becomes necessary. This aspect determines great customization effort, specially at factory, leading to a significant increase in delivery time and cost. However, the adoption of a modular approach in AUV design, as outlined in numerous works [3–5], can help mitigate these issues. This approach provides significant benefits in terms of adaptability to specific demands and product variety [6], facilitating the AUV customization for various applications. Although customization of AUVs is possible, it is typically constrained to specific manufacturers and their respective AUV models, with no universal methodology that can be applied to customize all underwater vehicles. This limitation arises due to the inherent complexity of customization, specifically the need to carefully consider precise physical constrains dictated by the mechanical characteristics of each AUV.

Neglecting a systematic approach when customizing an AUV can lead to a substantial increase in development effort, resulting in delays and higher costs. Hence, it is essential to include a methodical approach during the design phase, conducting a comprehensive analysis of the overall characteristics and their influence on the performance of the system [7].

In this context, the paper proposes a design methodology aimed to the development of custom payloads to be integrated in AUVs. The description of the individual steps of the methodology are presented in Sect. 2. Section 3 describes the application of the proposed methodology for the manufacturing of a custom payload for the AUV X-300, the evolution of Folaga AUV [8] manufactured by Graal Tech s.r.l. The results shows that, applying the proposed methodological approach, the manufactured payload has a minimal impact on AUV trim and navigation while reducing at the same time the overall cost and development resources.

2 Methodology Description

The proposed methodology for payload development is represented by a flowchart as shown in Fig. 1. The diagram depicts the overall manufacturing process for developing the custom payload. For each step several design choices are driven by specifics constrains to be respected, dictated by the mechanical and electrical characteristics of the AUV involved in the customization.

2.1 System Layout and Requirements

The shape and dimensions of the payload depend on the electronics that need to be housed in specific compartments; therefore, a preliminary analysis of the overall hardware requirements and dimensions is necessary.

The payload may consist of dry or wet compartments. In particular, dry compartments involve a hull housing of chosen length to accommodate electronic boards, sensors, battery packs and computer systems. Wet compartments encompass rearranging the hull module through protrusions or attaching a flooded external module to the hull. These compartments are designed to accommodate underwater sensors (Doppler velocity log,

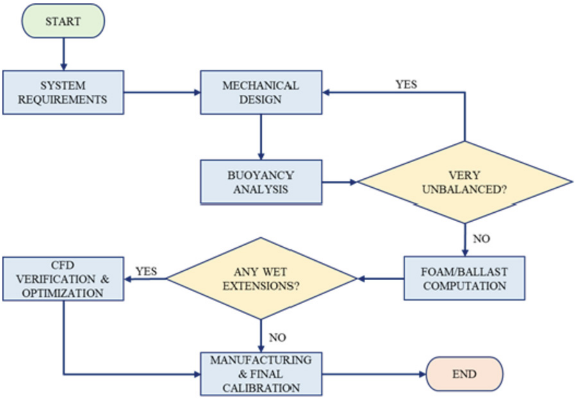

Fig. 1. Methodology flowchart description

acoustic systems, etc.) ensuring their functionality and impact protection. Additionally, the flooded external module should feature complementary carters to facilitate the integration of the payload in the AUV.

2.2 Mechanical Design

After defining the customized system, the next step is to proceed with mechanical design, carefully evaluating technical choices to mitigate critical aspects related to the harsh underwater environment. These choices include meticulous material selection, ensuring watertight sealing, and housing battery packs to guarantee reliability and safety. In this context, referring to guidelines provided by reputable associations such as the International Marine Contractors Association (IMCA) [9] and the American Bureau of Shipping (ABS) [10] can serve as valuable references for best practices.

A key consideration in the mechanical design is the shape of the payload, as it should not compromise the AUV navigation performance. Typically, AUVs have a torpedo shaped body with a circular cross section. Thus, the shape of the payload must conform to and align with the main body, ensuring seamless integration. This integration process is facilitated by using a male-female coupling system located at the end caps of the cylindrical modules. If strict conformity cannot be achieved, appropriate design consideration should be made to minimize resistance, especially in the case of protrusions or, in general, wet compartments. In particular, wet compartments need to be preliminary faired to reduce the drag, and the presence of asymmetric side protuberances has to be avoided to prevent asymmetric drag that could hinder AUV operation.

The external module must provide protection for the components and enough free space for foam or ballast integration, which is essential for payload balancing.

To ensure efficient hardware installation and maintenance, it is crucial to provide a dedicated internal chassis for organizing the hardware. One of the key considerations during this process is the reduction of electromagnetic interference (EMI) [11] by strategically placing sensitive hardware components away from potential sources of noise.

In terms of thermal management, it is important to locate electronic boards with high operating temperatures close to components that have direct contact with water. This arrangement promotes effective heat dissipation by utilizing water as a cooling medium. Additionally, it is recommended to position heavy components, like battery packs, at the bottom of the chassis. This arrangement effectively lowers the center of mass of the payload, resulting in improved stability for the AUV during navigation.

The internal chassis must also include an internal ballasting facility to effectively compensate for any imbalances of the payload before the integration in the AUV.

The final 3D CAD model of the custom payload has to be developed based on the aforementioned considerations. A static simulation is essential to assess the mechanical strength against hydrostatic pressure at the maximum operational depth. Additionally, thermal analysis could be performed to evaluate dissipation performance and assess the average temperature of the internal hull module during the operation.

2.3 Buoyancy Analysis and Foam/Ballast Computation

The custom payload must achieve balance when immersed in seawater. Hydrostatic simulations need to be conducted to evaluate its current balance and make necessary adjustments to ensure stability. This may involve integrating ballast or foam in the payload to achieve neutral buoyancy.

The position of the center of mass (CW) and the center of buoyancy (CB) significantly impact the static stability of the payload. It is necessary to align the CW and CB as vertically as possible to prevent instability caused by nonzero moments. Furthermore, maintaining metacentric stability is crucial for the payload to withstand inclinations caused by disturbances in heave, roll, and pitch [12]. The stability of the AUV relies on maintaining the metacentric height within an acceptable range, between 0 and 5 mm. By staying within this range, the AUV can avoid exhibiting excessive stiffness when subjected to external disturbances, thereby preserving its maneuverability performance.

Upon these considerations, it is necessary to calculate the total volume of foam and ballast required to achieve neutral buoyancy for the payload. If there is a significant imbalance in the payload, a considerable amount of foam and ballast may be needed, which may potentially results in integration difficulties. Therefore, it is crucial to review the mechanical design to address and minimize this imbalance effectively.

2.4 Hydrodynamic Assessment and Optimization

The presence of protuberances and external modules introduces an asymmetrical shape of the payload, which has a significant impact on AUV performance due to the increased drag. Therefore, an hydrodynamical assessment is essential to predict the dynamic behavior of the customized AUV under specific operating conditions.

Computational Fluid Dynamics (CFD) analysis provides a powerful tool for quantifying the hydrodynamic effects on the AUV after customization; in fact, it offers valuable insights for optimizing the payload shape, mitigating any adverse effect.

The CFD analysis involves using a precise 3D model of the customized AUV. Special attention should be given to the generation of the flow field mesh around the AUV and the definition of the boundary conditions such as flow velocity and pressure. Numerical simulations solve the Reynolds-Averaged Navier-Stokes (RANS) equations [13] witch describe the flow model. A k-ε turbulence model could be employed to make the equation set closure, enhancing prediction of AUV hydrodynamics [14]. Result analysis includes the visualization of the fluid flow around the AUV, the generation of the pressure maps and the evaluation of the resistant forces and moments. These analyses provide crucial insight of the overall performance during operation.

After analysis, it is necessary to perform payload optimization to minimize hydrodynamic resistance. This is achieved by selecting geometric variables that precisely describe the shape of the protuberances and external modules. Computing the optimal values for these parameters is essential to further refine the payload shape, resulting in performance benefits. The determination of these optimal values is guided by specific requirements, mechanical constraints, and objectives of the payload design.

2.5 Manufacturing and Final Calibration

After design assessment, the payload components can be manufactured. However, the integrity of the hull module should be verified using a hyperbaric pressure test prior to its mechanical integration in the AUV.

Finally, an additional calibration step in controlled environment must be performed to compute the mismatch between the simulated and actual AUV trim. During calibration, additional ballast or foam shall be integrated to compensate any mismatch keeping the overall trim parameters of the AUV unchanged.

3 Experimentation

The presented methodology has been applied for the customization of the X-300 vehicle from Graal Tech s.r.l., a torpedo-shaped AUV made up of a pair of carbon fiber cylinders connected to two terminating wet sections, with a maximum operational depth of 300 m [15] (Fig. 2).

Fig. 2. AUV X-300 from Graal Tech s.r.l.

Following the methodological approach, the payload layout was designed starting from the hardware/software requirements defined to fulfil specifics AUV missions. In particular, a dry compartment was designed for accommodating an IMU Xsens MTi-300, two CPUs Raspberry Pi 4, and an acoustic modem USBL Seatrac X150. Moreover, a wet compartment was designed for integrating a Doppler Acoustic Log (DVL) NavQuest Micro 600 and a Multibeam Sonar from Norbit.

After the finalization of the system layout, as shown in Fig. 3a,b, a mechanical design of the payload was conducted using Solidworks® 3D CAD software. Specifically, the payload consists of two main assemblies: the cylindrical hull and an external belly-like module. A dual configuration is presented to ensure system interoperability. The hull module (Fig. 3c) maintains the X-300 external diameter and includes bottom support for integrating an external flooded module. Inside the hull module, a longitudinal chassis composed of two planar plates is included for hardware arrangement. Special consideration was given to arranging noise sensitive sensors and high temperature working CPUs. The hull features a wet extensions for integrating the USBL, with a custom designed saddle to ensure proper sealing at the required depth. The external part is characterized by two complementary carters that provide impact protection for the compact sensors. Additionally, side wings were designed to offer further protections for the WBMS external protrusions.

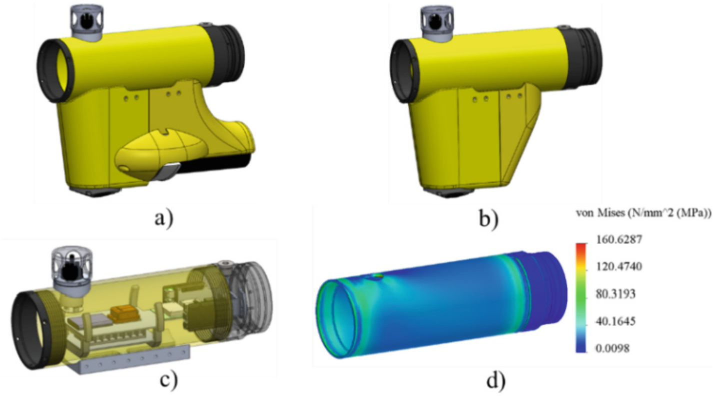

Fig. 3. On the top the payload dual configuration. On the bottom the hull module with electronics arrangement (c) and static pressure analysis (d).

Finally, a static pressure simulation was carried out on the hull module, as shown in Fig. 3d, to evaluate the payload structural integrity at the maximum specified depth.

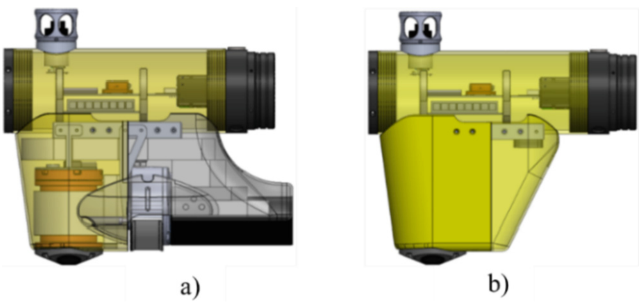

Fig. 4. On the left the buoyancy arrangement for DVL-WBMS payload configuration, on the right the ballast arrangement for the only DVL-configuration.

Subsequently, buoyancy analysis was performed on the 3D assembly to assess the balance and the trim of the vehicle. In particular, Solidworks® software was used due to its capability of providing accurate physical data of the materials, making it a powerful tool for achieving the desired payload balance.

The weight and final buoyancy were calculated by assuming material homogeneity for both payload configuration, aiming to evaluate the overall imbalance of the payload.

The volume of foam and ballast was determined and integrated in the payload as depicted in Fig. 4, to achieve the required system balance. HCP 50 material [16] was selected for the foam since it has the same operational depth of the AUV X-300.

For the shape optimization of the external module, a CFD simulation was conducted using the Flow Add-ins module of Solidworks®, analyzing the hydrodynamic properties of the customized AUV. In particular, Fig. 5 shows the fluid flow and pressure distribution surrounding the payload in DVL-WBMS configuration. The results indicate the presence of a compression dysfunction resulting from the pressure difference on the external module.

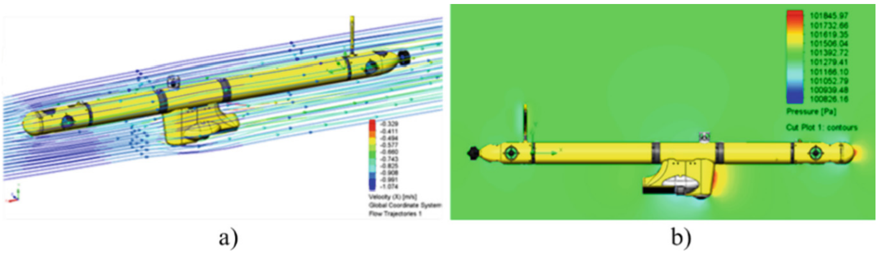

Fig. 5. On the left the fluid flow, on the right the surrounding pressure distribution.

Figure 6a,b depict the manufacturing process of the custom payload and the subsequent mechanical integration. The integrity of the hull module was verified through an hyperbaric pressure test at 30 bars, which corresponds to a depth range of 300 m.

The external module was manufactured by Stereolithography (SLA) 3D printing using the Somos EvoLVe 128 material, a durable stereolithography material with high strength and durability properties [17].

Figure 6c showcases the final calibration step for the AUV, conducted in saltwater, in only DVL configuration to verify the achievement of the neutral configuration. A slightly positive imbalanced with a mismatch of approximately 80 g was observed during the calibration. However, this mismatch was deemed tolerable within the methodology and was rectified by adding additional ballast in the AUV. In general, the acceptable degree of mismatch within the methodology depends on the available free volume capacity for compensation using ballast or foam.

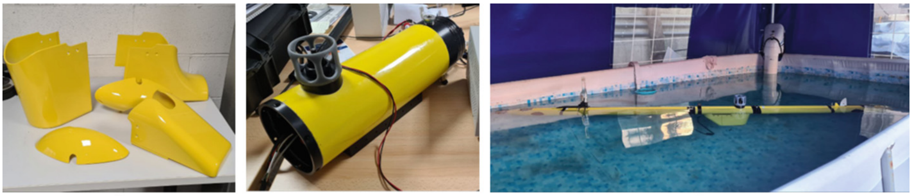

a) b) c)

Fig. 6. The payload manufacturing (a) (b) and the final calibration step performed (c).

4 Conclusions

The paper has proposed a design methodology for the proper development of custom payloads aimed to be integrated in AUVs. Specific design tricks have been provided for each step of the methodology, aiming to design and integrate these additional modules in the AUVs without affecting their trim. An application of the proposed methodology has been described for the customization of the AUV X-300. The results shown the effectiveness of the proposed methodological approach developing a specific reconfigurable payload for the required purposes.

Future development will focus on strengthening the presented methodology while additional experimentation will be carried out at sea to assess AUV trim and balance.

References

1. Nicholson, J., Healey, A.: The present state of autonomous underwater vehicle (AUV) applications and technologies. Marine Technol. Soc. J. **42**, 44–51 (2008)
2. Sahoo, A., Dwivedy, S.K., Robi, P.: Advancements in the field of autonomous underwater vehicle. Ocean Eng. **181**, 145–160 (2019)
3. Hiller, T., Steingrimsson, A., Melvin, R.: Expanding the small AUV mission envelope; longer, deeper & more accurate. In: 2012 IEEE/OES AUV), pp. 1–4, Southampton (2012)
4. Cruz, N.A., Matos, A.C., Ferreira, B.M.: Modular building blocks for the development of AUVs-from MARES to TRIMARES. In: Proceedings of International Symposium Und Technology, UT 2013, March 2013
5. Taylor, M., Wilby, A.: Design considerations and operational advantages of a modular AUV with synthetic aperture sonar. In: Proceedings of MTS/IEEE International Conference Oceans 2011 MTS/IEEE KONA, pp. 1–6, Waikoloa (2011)
6. Ulrich, K.: The role of product architecture in the manufacturing firm. Res. Policy **24**(3), 419–440 (1995)
7. Martin, M.V., Ishii, K.: Design for variety: developing standardized and modularized product platform architectures. Res. Eng. Des. **13**(3), 213–235 (2002)
8. Caffaz, A., Caiti, A., Casalino, G., Gualdesi, L., Turetta, A.: Folaga: a low cost AUV/glider for coastal environmental sampling. In: Underwater Technology, vol. 28, no. 4, pp. 151–157, Society for Underwater Technology (2009)
9. American Bureau for Shipping. https://ww2.eagle.org/en.html. Accessed 27 June 2023
10. International Marine Contractors Association. https://www.imca-int.com. Accessed 28 June 2023
11. Weston, D.A.: Electromagnetic Compatibility: Principles and Applications. CRC Press (2017). https://doi.org/10.1201/9781315214603

12. Fossen, T.I.: Handbook of Marine Craft Hydrodynamics and Motion Control. Wiley (2011). https://doi.org/10.1002/9781119994138
13. Anderson, J.D., Jr.: Computational Fluid Dynamics: The Basics with Applications. Mc Graw-Hill, New York (1995)
14. Jagadeesh, P., Murali, Idichandy, C.G.: Experimental investigation of hydrodynamic force coefficients over AUV hull form. Ocean Eng. **36**(1), 113–118 (2009)
15. Graal Tech. https://www.graaltech.com/products/x-300-auv. Accessed 18 Feb 2023
16. DIAB Divinycell® Homepage. https://www.diabgroup.com. Accessed 21 Feb 2023
17. Stratasys Homepage. https://www.stratasys.com. Accessed 24 Feb 2023

Numerical Modelling of Cryomodule Transportation with Nonlinear Wire Rope Isolators

Tommaso Aiazzi[1], Paolo Neri[1](✉), Francesco Bucchi[1], and Donato Passarelli[2]

[1] University of Pisa, 56122 Pisa, Italy
paolo.neri@unipi.it
[2] Fermi National Accelerator Laboratory, Batavia, IL 60510, USA

Abstract. Cryomodules for high-energy physics experiments are complex assemblies based on superconductive cavities aimed at particle beam acceleration. The assemblies are composed of many fragile and weak components, which are assembled in clean room environments and under a vacuum. Thus, a high risk of damage during transportation occurs, leading to huge costs in repairing and re-assembly both from an economical and timing point of view. For this reason, specific fixtures are designed to guarantee the safe transportation of cryomodules, named transportation tooling. These devices act as a mechanical filter, mitigating the vibration coming from road asperities. The key components of the transportation tooling are the wire rope isolators, which are compact and reliable nonlinear springs that provide stiffness and damping to the structure. This paper focuses on the numerical simulation of a cryomodule during transportation by exploiting a finite element and multi-body mixed approach. Two different models for the wire rope isolators are compared: the conventional linear spring-damper model, based on data provided by the manufacturer, and a purposely developed nonlinear model (enhanced Bouc-Wen), based on experimental characterization of the springs.

Keywords: Cryomodule transportation · Wire rope isolators · Vibration suppression · nonlinear vibrations

1 Introduction

Road transportation of complex large fragile items is a challenging topic and transportation tools, to be installed on commercial trucks, are designed for this sake. Due to the high complexity and cost of the structures to be transported, the experimental tuning of the transportation tool must be reduced or, ideally, avoided. Hence simulation tools have to be developed to numerically reproduce the dynamics and the stress of the transported goods. In the existing literature, several papers have been published focusing on different aspects of transportation analysis. Some papers investigate the qualitative analysis of damage during the transportation of fragile items [1–4], while others measured the on-road acceleration of truck loading beds under various operating conditions [5–7].

M. Carfagni et al. (Eds.): ADM 2023, LNME, pp. 514–521, 2024.
https://doi.org/10.1007/978-3-031-52075-4_58

Additionally, certain papers, develop multibody models to predict the acceleration and vibration levels of vehicles, passengers, and transported goods [8–10]. Lastly, some papers discuss the structural analysis of vehicle components during transportation [11, 12].

A representative case study in this field is the transportation of the SSR2 cryomodule in the framework of the PIP-II (Proton Improvement Plan-II) project carried out at Fermilab. PIP-II is a proton driver superconducting linac that exploits five different types of Superconducting Radio Frequency (SRF) cavities: half wave resonator (HWR) [13], 650 MHz multicell cavities (LB650, HB650) [14] and 325 MHz single spoke resonators (SSR1, SSR2) [15]. The SSR2 cryomodule has been developed by upgrading the previous design of the SSR1 prototype and will face internal transportation inside Fermilab facilities during the assembly stage. A Transportation Tool (TT) has been designed by the authors in previous activities [16] to transport the SSR1 prototype, and experimental tests demonstrated its capabilities in successfully filtering out road asperities. Simulations were performed in a multi-body environment, using a reduced order model for the flexible parts, and validation was carried out based on the data acquired during the preliminary transportation of dummy loads. Originally, the shock absorbers installed in the TT, i.e. wire rope isolators (WRI), were modeled using lamped stiffness and damping, exploiting the manufacturer's specification. Actually, laboratory tests showed that the non-linear Bouc-Wen model [17] was more suitable to reproduce the WRI characteristics. For this reason, in this research a numerical model of SSR2 was developed to assess if the existing TT is still effective in vibration mitigation for SSR2 cryomodule. The main novelty of the research consists in the application of the nonlinear WRIs model to the study of cryomodule transportation, and in the systematic comparison of the results obtained with the linear and nonlinear model of the WRIs. The numerical model of the cryomodule is presented in Sect. 2, along with the experimental characterization of the selected WRIs. Section 3 shows the results of the simulation carried out by applying to the model the inputs of a previously recorded transportation history. Finally, Sect. 4 discusses the comparison of the results obtained modeling WRIs as linear constant stiffness and damping or based on the nonlinear Bouc-Wen model.

2 Cryomodule Numerical Model

The estimation of the TT performances allows for assessing the filtering capabilities of the fixture. In particular, in this research, the TT designed for the transportation of the SSR1 cryomodule [16] is analyzed and adapted for the transportation of the cryomodule SSR2. This latter cryomodule has similar dimensions with respect to the previous version, but exploits some innovative design solutions concerning the insertion of the strongback into the structure. Thus, it is mandatory to check if the TT is still valuable for the transportation of SSR2, or if some changes are needed (e.g. different WRIs model or locations). To this extent, the numerical analysis of different configurations can help to choose the best solution. Previous research activity demonstrated the effectiveness of a mixed FE-MB approach in this simulation field. The main subassemblies are modeled through FE analysis, and the results are exported through the Craig-Bampton reduction method to be imported into an MB model. The full assembly is then prepared in the

MB environment, by adding the interconnections and, most importantly, the wire rope isolators. A full description of both the FE and the MB models is provided in the following sections. The model aims to compare different modeling strategies for WRIs, and to estimate the TT filtering capabilities for SSR2. Firstly, the simple conventional linear spring-damper model will be analyzed by using the WRIs parameters provided by the manufacturer (the device specification provides a reference value for static and dynamic stiffness and damping). Secondly, a nonlinear model specifically developed for WRI simulation will be exploited. The model is an enhanced version of the Bouc-Wen model [17], and the parameters are obtained through an experimental campaign on the actual WRI. The simulation effort aims to compare the results obtained with the same model, and the same input, by only changing the WRI modeling strategy.

2.1 FE Model

The cryomodule's FE model is divided into seven main parts. The vacuum vessel (4922 kg and 53738 shell elements) consists of a cylindrical shell in carbon steel. The vessel shell is closed at the upstream and downstream sides with endcaps. The strongback (788 kg and 52247 shell elements) consists of an aluminum alloy extrusion bolted to two carbon steel parallel rails and stiffened with two stainless steel I-beams. It lies inside the vessel to sustain the support posts (i.e. cavities supports). The thermal shield (306 kg and 88898 shell elements) is composed of sheets of different aluminum alloys connected with bonded connections. It aims at reducing the heat loads by providing thermal intercepts and stopping radiation from room-temperature components. The structure is connected to the aluminum rings of the support posts. To increase the stiffness some bumpers are introduced between the thermal shield and the vacuum vessel. The support posts (27 kg and 11341 brick elements each) are composed of a G-10 tube and different plates of aluminum and stainless steel. They sustain the cavities, the solenoids, and the thermal shield, and they are attached to the strongback with bolted connections. The cavities (158 kg and 72354 shell elements each) are divided into two parts, the actual niobium cavity and the helium vessel composed of stainless steel. The solenoids (35 kg each) are modeled as a point of mass since they are bulk and simple structures. Cavities and solenoids are used to control the particle beam. The two-phase pipe (118 kg and 610702 shell elements) is composed of stainless steel tubes connected by bellows to allow thermal deformation and by threaded roads (modeled as beams) to enhance the stiffness. The vacuum vessel, thermal shield, strongback, and support posts are combined into a single sub-model while the cavities and the two-phase pipe are exported on their own. The solenoids will be modeled within the MB model as lumped masses. The transporting tool's FE model was split into two parts that will be connected in the MB model: the inner frame (1330 kg and 63541 brick elements) that is attached to the vacuum vessel, and the outer frame (1340 kg and 38912 brick elements) that will be connected to the loading bed of the vehicle used for transport. The development of FE model must be developed considering the limitation imposed by the reduction method. First, all contacts should be bonded using the MPC formulation since other types of connection, such as joints, are not compatible with the reduction procedure (i.e. generation of modal neutral files, MNF). The aim is to minimize the number of MNF files to reduce the MB model computational time, since few larger MNF files rather are computationally more efficient than many smaller ones. To reduce the size of the MNF files the shells element were used every time possible, and the geometry was defeatured. The points reduction procedure requires the definition of interface points (i.e. master nodes) in all the locations where loads or connections are to be defined in the MB model. Thus, a remote point was defined in the needed locations. The more remote points that are added, the bigger the MNF file will be. During the creation of the MNF files, all modes in a range between 0 and 150 Hz have been considered.

2.2 MB Model

The MB model was developed by linking the various MNFs together. All the constraints can be applied to the interface points defined in the FE model through remote points. Most of the connections are defined through the fixed constraints, which are used to interface all the cavities and solenoids with the support posts, the cavities and the two-phase pipe, the vessel and the two-phase pipe, and the vessel and the inner frame. Each cavity is imported as an MNF and then made rigid into the Adams model, to represent its inertia properties with a low computational cost. The solenoids are modeled as rigid bodies. The vessel, thermal shield, strongback, and support posts are imported as a single MNF and connected with the inner frame, the cavities, the solenoids and the two-phase pipe with fixed constraints. The two-phase pipe has been imported as a single MNF file. The TT was divided into two MNF connected with the WRIs, which were modeled in two different ways. The first is using linear springs, considering a spring constant of 5.02e+05 N/m in the main direction and of 2.49e+05 N/m in the transversal directions, and a damping coefficient of 6000 Nm/s in all the directions. These values were provided by the manufacturer, with reference to dynamic conditions. The second way is a nonlinear model, considering the actual behavior of the WRIs. Here the values of the forces applied to the inner and outer frames are calculated using a *dll* file created with Matlab Simulink. The Simulink model is an input/output model, where the inputs are the displacement and the relative velocity between inner and outer frames, and the outputs are the values of the force (along the three directions). The Simulink model implements the BW equations using the constant parameters obtained from the experimental tests (described in the following section). Once one *dll* file is created, it can be used for every WRI in the MB model, provided that the inputs and outputs are defined consistently. Then six variables were created for every WRI, computing the relative displacement and velocity between the inner and outer frame as inputs. Three variables were defined as outputs of the controls, being the forces generated by the WRIs.

2.3 Wire Rope Experimental Characterization

The determination of the numerical values of the BW model parameters requires a specific experimental campaign. One of the adopted WRI (M32-850-08-[H]-B, IDC Shock & Vibration Isolation Products) was purchased and tested by exploiting hydraulic actuators along its three main directions as shown in Fig. 1(a). More details about the testing setup are presented in [17]. Since it was proven that the WRI behavior does not depend on deformation speed [18], a quasi-static test was performed by overlapping a large amplitude deformation cycle with small amplitude deformation loops in the higher load region, to improve the description of the displacement speed sign reversal. An optimization algorithm was adopted to retrieve the constant parameters of the BW model from experimental data, by nonlinear least square fit. To validate the effectiveness of the derived parameters in representing the WRI behavior, independent vibration tests were performed by sinusoidal and random excitation of the spring. The comparison between experimental and numerical data confirmed that the computed model can represent the WRI behavior, as shown in Fig. 1(b).

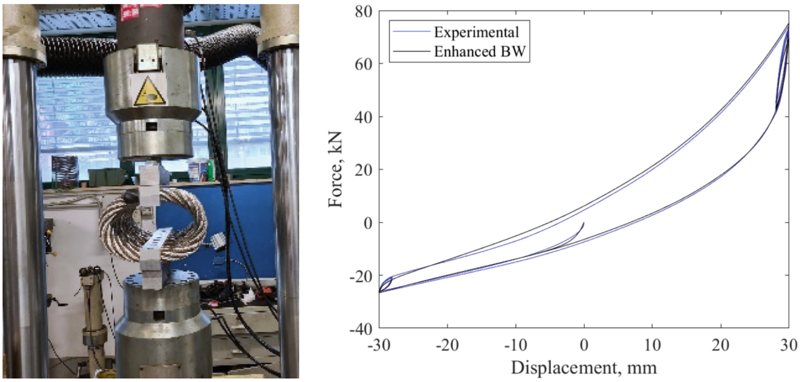

(a) (b)

Fig. 1. WRI test along the axial direction: (a) test setup and (b) model results.

3 Numerical Results

Two simulations were performed, one with the linear springs and one with the BW implementation. The excitation was applied to the outer frame, as an imposed displacement of three points of the outer frame. The data used in the simulation were gathered during the experimental transportation of the SSR1 cryomodule. Even if SSR1 and SSR2 are not identical, their main dimension and layout are comparable, thus SSR1 data were considered representative of realistic road transportation conditions. The vertical acceleration of the inner frame at the WRIs location was considered the simulation output. A transportation time of 60 s was considered, with a step size of 0.00125 s.

The results obtained with both the linear and the nonlinear model of the WRIs are reported in Fig. 2, in terms of vibration acceleration in the frequency domain. The region 0–60 Hz was highlighted in the graph, since it contains the highest contributions in terms of road asperities excitation. The black line refers to the outer frame acceleration, i.e. the road excitation. The red line is referred to the inner frame acceleration with the linear model, while the green curve is referred to the nonlinear model. As can be noted, both models feature a high response level in the frequency range lower than 5 Hz. These peaks are due to the excitation of rigid body motion of the structure (i.e. inner frame and cryomodule) bumping on the WRIs, thus in this region, a response amplification is observed. Since no internal resonances of the cryomodule are excited at these frequencies, these peaks are not considered dangerous for the assembly.

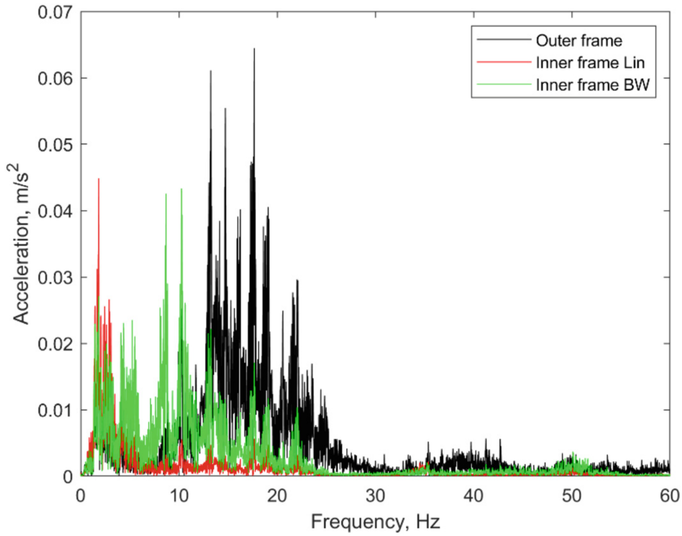

Fig. 2. Comparison between the linear and nonlinear model of the WRIs. (Color figure online)

Additionally, both models present a relevant vibration supression in the high-frequency range, i.e. above 20 Hz. This is due to the mechanical filtering effect of the WRIs, which reduces the excitation coming from the truck, thus avoiding the excitation of internal resonances of the cryomodule. Discrepancies can be noted between the two models in the range of 5–20 Hz. The linear model drastically attenuates the contribution above 5 Hz, thus representing an ideal behavior of the mechanical filter. On the other hand, the nonlinear model shows worse filtering performances in the range of 5–10 Hz, where the input peaks are almost not attenuated. Nevertheless, the filtering effect is evident in the range of 15–20 Hz, where the input peaks are reduced even if in this frequency region many modes of the cavities are predicted in the cryomodule model. These discrepancies are due to the different representations of the WRIs stiffness and damping of the two models. The linear model filters out almost completely all the contributions above a specific cutting frequency, thus overestimating the filtering capabilities of the TT. On the other hand, the nonlinear model provides a more conservative estimation of the TT performance, which is not able to completely suppress the vibration at higher frequencies. Anyway, both linear and nonlinear models demonstrate that the designed TT is still able to attenuate high-frequency vibrations, thus being suitable for SSR2 transportation. To assess which model provides the more realistic estimation, experimental transportation of the SSR2 cryomodule should be performed. Nevertheless, it is worth noting that previous experimental results obtained on SSR1 cryomodule (which is similar to SSR2 and can then be considered significant to this analysis) highlighted that some response peaks of the inner frame could be visible in the range of 10–20 Hz, in agreement with the BW model (i.e. green line in Fig. 2).

4 Conclusions

The present paper investigates the comparison between two different modeling strategies for the wire rope isolators, which are the key components in transportation tool design for cryomodules during on-road handling. A mixed finite element-multi body approach was adopted to obtain a transient simulation of a complex assembly in reasonable computational time. This approach, which has already demonstrated to be effective in this research field, allows for rapidly compare the results of different configurations. In particular, the TT designed for the SSR1 cryomodule was adapted to fit the SSR2 cryomodule, and the WRIs behavior (which impacts the filtering performance) was simulated with two different approaches: linear spring-damper model and nonlinear enhanced Bouc-Wen model. In the first case, the properties are retrieved by the component datasheet, while in the second case, the properties are retrieved by a specific experimental campaign. The two models (which only differ for the WRIs implementation) were used to simulate a time history experimentally measured during SSR1 transportation. The accelerations measured at the truck loading bed were applied as an input in the model, and the accelerations at the inner fame were monitored. The results showed that the conventional linear spring-damper model overestimates the TT filtering capabilities, since the cryomodule's response at higher frequencies results almost canceled. On the other hand, the nonlinear model provides a more reasonable estimation of the filtering capabilities, since high-frequency components results attenuated but not completely erased from the response. These results are in line with the findings obtained for experimental transportation of SSR1. Further research development consists of the experimental validation of the proposed models, to be performed on SSR2 cryomodule after assembly completion.

References

1. Singh, J., Singh, S.P., Joneson, E.: Measurement and analysis of US truck vibration for leaf spring and air ride suspensions, and development of tests to simulate these conditions. Packag. Technol. Sci. **19**, 309–323 (2006). https://doi.org/10.1002/pts.732
2. Singh, S.P., Xu, M.: Bruising in apples as a function of truck vibration and packaging. Appl. Eng. Agric. **9**, 455–460 (1993)
3. Jarimopas, B., Singh, S.P., Saengnil, W.: Measurement and analysis of truck transport vibration levels and damage to packaged tangerines during transit. Packag. Technol. Sci. **18**, 179–188 (2005). https://doi.org/10.1002/pts.687
4. Hinsch, R.T., Slaughter, D.C., Craig, W.L., Thompson, J.F.: Vibration of fresh fruits and vegetables during refrigerated truck transport. Trans. Am. Soc. Agric. Eng. **36**, 1039–1042 (1993). https://doi.org/10.13031/2013.28431
5. Cann, A.P., Salmoni, A.W., Eger, T.R.: Predictors of whole-body vibration exposure experienced by highway transport truck operators. Ergonomics **47**, 1436–1453 (2004). https://doi.org/10.1080/00140130410001712618
6. Lu, F., Ishikawa, Y., Shiina, T., Satake, T.: Analysis of shock and vibration in truck transport in Japan. Packag. Technol. Sci. **21**, 479–489 (2008). https://doi.org/10.1002/pts.841
7. Garcia-Romeu-Martinez, M.A., Paul Singh, S., Cloquell-Ballester, V.A.: Measurement and analysis of vibration levels for truck transport in Spain as a function of payload, suspension and speed. Packag. Technol. Sci. **21**, 439–451 (2008). https://doi.org/10.1002/pts.798

8. Yang, M., Gening, X., Qing, D., Han, X.: Vibration study of fork-lift truck based on the virtual prototype technology. Sens. Transducers **170**, 177–183 (2014)
9. Bucchi, F., Frendo, F., Bavaresco, F., Conte, G.: Multibody simulation of a rope-driven automated people mover. Proc. Inst. Mech. Eng. F J. Rail Rapid Transit. **232**, 2173–2185 (2018). https://doi.org/10.1177/0954409718764533
10. Bertini, L., Bucchi, F., Monelli, B.D., Neri, P.: Development of a simplified model for the vibration analysis of lawn mowers. Procedia Struct. Integrity **8**, 509–516 (2018). https://doi.org/10.1016/j.prostr.2017.12.050
11. Mi, C., Gu, Z., Yang, Q., Nie, D.: Frame fatigue life assessment of a mining dump truck based on finite element method and multibody dynamic analysis. Eng. Fail. Anal. **23**, 18–26 (2012). https://doi.org/10.1016/j.engfailanal.2012.01.014
12. Lee, S.H., Park, T.W., Park, J.K., Yoon, J.W., Jun, K.J., Jung, S.P.: A fatigue life analysis of wheels on guideway vehicle using multibody dynamics. Int. J. Precis. Eng. Manuf. **10**, 79–84 (2009). https://doi.org/10.1007/s12541-009-0097-x
13. Kim, S.H., et al.: Preservation of quality factor of half wave resonator during quenching in the presence of solenoid field. In: 6th International Particle Accelerator Conference, IPAC 2015 (2015)
14. Li, J., Harms, E.R., Hocker, A., Khabiboulline, T.N., Solyak, N., Wong, T.T.Y.: Development and integration testing of a power coupler for a 3.9-GHz superconducting multicell cavity resonator. IEEE Trans. Appl. Supercond. **21**, 21–26 (2011). https://doi.org/10.1109/TASC.2010.2089683
15. Passarelli, D., Wands, R.H., Merio, M., Ristori, L.: Methodology for the structural design of single spoke accelerating cavities at Fermilab. Nucl. Instrum. Meth. Phys. Res. A **834**, 1–9 (2016). https://doi.org/10.1016/j.nima.2016.07.013
16. Neri, P., Bucchi, F., Passarelli, D.: A multilevel finite element-multibody approach to design the suspension system for the road transportation of SSR1 cryomodule. Transp. Eng. **2**, 100017 (2020). https://doi.org/10.1016/j.treng.2020.100017
17. Neri, P., Holzbauer, J.: Experimental characterization and numerical modeling of wire rope isolators. In: Proceedings of the Nodycon: Third International Nonlinear Dynamics Conference, Rome (2023)
18. Wang, H.X., Gong, X.S., Pan, F., Dang, X.J.: Experimental investigations on the dynamic behaviour of o-type wire-cable vibration isolators. Shock. Vib. **2015**, 1–12 (2015). https://doi.org/10.1155/2015/869325

MBSE for Performance Analysis and Tracing in Preliminary Design Through SysML Diagrams

Castrese Di Marino[1], Agnese Pasquariello[2(✉)], Flavio Di Fede[1], and Stanislao Patalano[2]

[1] Leonardo Labs, Leonardo S.p.A., Corso Francia 426, 10146 Turin, Italy
[2] Fraunhofer J-Lab IDEAS, Department of Industrial Engineering, University of Naples Federico II, Naples, Italy
agnese.pasquariello@unina.it

Abstract. Nowadays, the high competitiveness in the global market pushes companies to pursue innovation with the aim of reaching profitable results. Even if the adoption of Model-Based System Engineering (MBSE) as an innovative approach for robust design is rapidly spreading in companies, there is still a lack of collaboration between system engineers involved in the requirements management and architectures modelling, and designers of specific systems. For this reason, the present work aims to better connect the system description process with the solving process through the adoption of specific SysML diagrams during preliminary design steps. A direct connection between requirements and design parameters is proposed by means of a well-defined process that fits into the wider V-Model for system development. The whole process enables (i) the rapid development of new models focusing on the connection between requirements and parameters, (ii) tracking of the designing process as well as (iii) the evaluation of performance requirements. This approach is applied to a case study of the Thermal Management System for a hybrid-electric aircraft, focusing on enabling the connection between system description and system development.

Keywords: Model-Based Systems Engineering (MBSE) · Requirements Management · Parametric Analysis · Sizing Modelling Framework · SysML

1 Introduction

The current trend for technological innovation, combined with a global market increasingly demanding, push production requirements and the need for new competitive products towards the adoption of innovative and integrated design processes. The Systems Engineering (SE) for systems development is spreading within this context since it promotes robust design for complex systems [1]. On another hand, SE as an approach still has potential improvement widely studied in scientific literature [2]. Especially, the concept of V-Model [3] is adopted as the

M. Carfagni et al. (Eds.): ADM 2023, LNME, pp. 522–529, 2024.
https://doi.org/10.1007/978-3-031-52075-4_59

basis for designing process compliant to SE. Special attention is given to design in the last stage of V-Model where a transition from conceptual representation to modelling is a critical aspect with potential loss of information and rising of non-compliant models.

However, since the top-down design process intrinsically included in SE positions the design phase after the architecture definition, the complexity management through a structured system decomposition [4] allows increasing the system preserving control and supervision. Indeed, the design definition process looks at technical solutions for abstract elements stated in logical architecture and defines their characteristics at different levels of detail. Therefore, system analysis supports the decision-making process at each level of design through the adoption of modelling as stated by MBSE. Furthermore, as Pahl and Beitz [5] divide the design process into three steps which are still relevant today i.e., conceptual design, embodiment design and detailed design, physical modelling should be better detailed to consider the increase of information during the modelling. Considering that the first stage of design is "sizing", it involves the setting of parameters, constraints, and their relations to produce systems performances that will meet requirements. However, since very often design models appear before the architectures are defined, it occurs the bridge between the two stages of the system development process is not established. This gap could lead to errors, loss of time due to redesigns and a lack of tracking requirements that need to be verified and validated continuously.

In [6], the authors fill the gap between representative tools and simulation tools by means of Parametric Diagrams of SysML (System Modeling Language). SysML, as a general-purpose graphical modelling language, is widely adopted by MBSE practitioners. It is made up of graphical notations with specific meanings that allow the construction of several diagrams with different modelling purposes. In particular, SysML supports system analysis through a Parametric Diagram, where "constraint block" represents a set of equations, with parameters to be analysed [7]. The resolution of these equations is exploited for both dimensioning and trade-off. On the same trend, Yvars et al. [8] characterize the sizing task in the design process by translating it into a constraint satisfaction problem. Given the logical decomposition of a system, the needs are modelled as equations relating design variables, behaviour variables and performance indicators associated with system components. However, traceability between logical architecture and sizing elements is not established. On the other hand, Bagdatli et al. [9] pursue the goal of traceability by using constraint blocks of SysML language. Bijam et al. [10] adopt SysML parametric diagram for the formalization of requirements and constraints enabling their verification during the system development process. Leserf et al. [11] also adopt the SysML parametric diagram to set model variants and to prepare the trade-off analysis by means of objective functions.

The present work aims to contextualize the aspects highlighted in the related works through a development process as a bridge between the generation of architectures and system design. We want to make the sizing process the natural continuation of system architecture development, giving value to the latter as a starting point for the design process together with the requirements. The proposal pushes toward an innovative approach for (i) rapid development of new models focusing on the connection between requirements and parameters, (ii) tracking of the designing process and choices alongside RFLP (Requirements, Functional, Logical, Physical) and (iii) the evaluation of performance requirements connected to the System of Interest (SoI). Indeed, anchoring global parameters from a System of Systems (SoS) to requirements and external constraints of SoI by means of Validation Criteria, enables parametric modelling not only about physical models but also about symbolic representations on a high-level, before implementing technical solutions on design.

2 MBSE Design Framework According to V-Model

The proposed approach relies on V-Model for Systems Engineering with the descending branch of system decomposition performed through the RFLP modelling method. The current proposal distinguishes the design phase into a preliminary design (PD) and a detailed design (DD) (see Fig. 1). Both phases embed the set of modelling activities that support the design at different levels of detail. Since the sizing model is commonly used during the preliminary design phase, its parametric nature allows for pursuing the goal of better integration with the logical architecture model. For this reason, the proposed framework introduces the parametric analysis besides the logical one with the aim to (i) prepare the basis for numerical sizing (in preliminary design), (ii) enable the connection with requirements and elements of logical architecture at the same level of system decomposition and (iii) pose the basis for stakeholder requirements definition at the next lower level. Parametric Analysis aims to define a sizing frame for functions. To this purpose, a set of items is introduced to define the frame and trace the sizing process. The output of this analysis is exploited for verification and validation according to the Preliminary Design stage. At higher levels, system elements are still black boxes that become new systems of interest if they cannot be immediately implemented and need to be deepened at lower levels. The sizing modelling and parametric analysis at a higher level support the derivation of new stakeholder requirements at a lower level allowing systems decoupling. Consequently, three cycles of Verification and Validation are proposed. The first one relies on preliminary design results or sizing, the second one

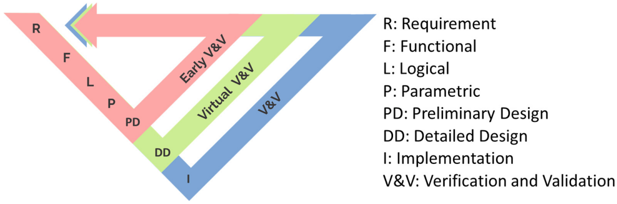

Fig. 1. Multi-level V-Model for Preliminary Design, Detailed Design and Implementation of Physical Modelling.

follows the detailed design or performance design, and the last one comes after the hardware/software implementation.

The designing process that executes the proposal follows six stages alongside descending and ascending branches of V-model, expanding the common version by means of intermediate steps and recursive cycles. In the following, the main stages are introduced and argued:

1. Context: analysis of the SoI goals and interaction. It is composed of:
   (a) Requirements Analysis: elicitation of needs, constraints and requirements, from Stakeholders Requirements to System Requirements.
      i. Stakeholders Requirements: problem-oriented issues about stakeholder needs connecting to validation criteria.
      ii. System Requirements: solution-oriented issues about "how the system shall work".
   (b) Validation criteria are specifications needed to instantly verify Stakeholder Requirements and assure system performance compliance.
2. Behaviour: analysis about all actions the SoI shall carry out, given the requirements analysis. It can be executed by means of:
   (a) Operational Analysis to define actions and sequence of operations the SoI shall perform.
   (b) Functional Analysis to define the functions the SoI shall implement to achieve the required purpose.
3. Architecture: logical representation of elements belonging to the SoI, with ports, interfaces, properties and flows. It is composed of two stages:
   (a) Logical Analysis and decomposition of the System to define the subsystems and components that implement the functions.
   (b) Logical Architecture to define relations among subsystems and components and their interactions (i.e., ports, interfaces, connections).
4. Parametric: preliminary analysis about the sizing of the SoI (inputs, outputs and parameters) where functions are intended as a black box. It is composed of:
   (a) Parametric Analysis to identify functions as a black box and global and local parameters to contextualize the sizing frame.
   (b) Attributes definition to relate parameters to Stakeholder Requirements and Validation Criteria.
5. Design: Physical Modelling for preliminary and detailed design, as well as implementation.
   (a) Preliminary and Sizing Design to estimate values for features and parameters as internal parameters and outputs towards other systems.
   (b) Detail and Performance Design to perform advanced modelling for dynamics simulations to evaluate how the system performs.
6. Post-processing: Verification and Validation process connected to Stakeholder Requirements:
   (a) Verification process is related to post-processing and assures that SoI executes what is established respecting system requirements.
   (b) Validation process poses attention to stakeholder requirements, assuring the SoI executes what stakeholders request.

3 Use Case: Thermal Management System of Electrical Motor on a Hybrid Aircraft

This section presents a case study of a system dedicated to the disposal of heat and control of the temperature of a heat source (i.e. Electrical Motor) installed on a hybrid aircraft. The SoI is a Thermal Management System (TMS) that keeps the temperature of the heat source within a certain range, by giving heat to a heat sink (i.e. external air) by means of a coolant mass flow. The coolant (fluid used as heat transfer) passes through the heat source, increases temperature, and releases heat to a secondary fluid towards a heat sink. Therefore, since the thermal power passes from the heat source to the heat sink, the context has a fundamental role in the design and defines possible design choices that lead to the development of the final architecture. According to the purpose of the paper, the case study is used for the definition of the problem and context, as well as for tracking of validation criteria. However, the modelling and sizing stage of SoI is out of the topic of this work. Therefore, only a few stages of the proposed workflow (Sect. 2) are highlighted: Logical and Parametric Analysis of the SoS where SoI is inserted and Requirement Analysis of the SoI during the step into the lower level. The development process starts with the analysis of the context where the TMS works. Figure 2a and Fig. 2b illustrate the logical architecture and the parametric network of the SoS. Logical Architecture defines ports and flows of the SoI, whereas Parametric Diagram specifies inputs and outputs for sizing. Given the low Technology Readiness Level adopted, and since this system interacts only with the heat source and heat sink, a simplified architecture is reported. Logical Architecture and Parametric Diagram provide the context; Stakeholder Requirements and Validation Criteria are used by the designer to develop and validate the SoI.

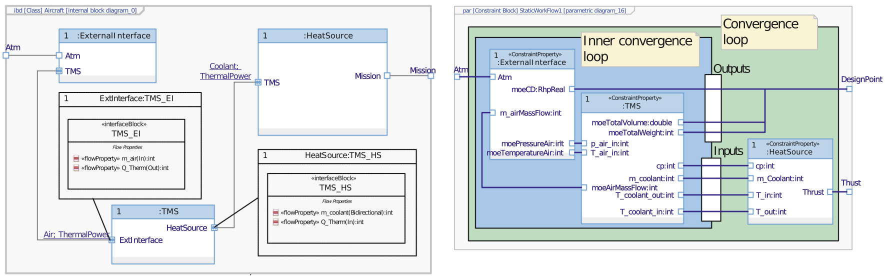

(a) (b)

Fig. 2. (a) Simplified Logical Architecture of Aircraft (SoS) and (b) Parametric Diagram at Aircraft level

TMS takes as inputs a coolant flow mass rate with a certain temperature and shall provide the same mass flow rate with updated thermodynamics conditions. In this application, TMS collects air mass flow rate from the external environment as a heat sink. Once considering the design of a specific system, all information is not needed, but just the context it belongs, and information exchanged, such as heat power produced and air mass flow from the external environment. In this way, it is possible to obtain a decoupling of the system from all the other systems. The problem is presented in a parametric and agnostic way. The parameters and values are reported as referenced variables. As "Global Mission", the TMS shall provide a variable flow rate ($\dot{m}$) of a specific fluid (c_p,viscosity) within precise thermal conditions (T_{in}, T_{out}) to the propulsion system in order to remove a certain quantity of heat power ($\dot{Q}$), respecting space (V) and weight (W) limits. The heat power produced follows a certain function or law that depends on the mission profile, atmosphere and power source. Since the attention is on sizing, only the design point ($\dot{Q}_{max}$) is considered. Consequently, the system estimates the air mass flow given the external conditions (T_{air}, P_{air}). The sizing process needs to perform a recursive process where the heat source, thermal management system and external interface are mutually influenced, as shown in Fig. 2b. Therefore, the designing process of TMS, intended as a "black box" starts by deriving System Requirements and Constraints from Stakeholder Requirements. Then, inputs and outputs are defined and included as attributes within the block representing the SoI. A set of constraints (from outside) and estimated parameters (towards the outside) are defined and connected to requirements and validation criteria. Finally, in Fig. 3, the relationship that connects the sizing block and logical block by means of connectors between attributes and parameters is reported. As seen, the global values of the logical block, are connected to the global parameters of the corresponding sizing function.

Given the Global Mission of the system, and known the context, a set of Stakeholder Requirements is given and associated to Validation Criteria to prove the SoI meets the stakeholder needs. In Fig. 4a, three Stakeholder Requirements are reported as main needs to be satisfied in combination with assigned validation criteria:

1. The SoI shall keep the coolant within a precise thermal range (T_{it}, T_{out})
   – $T_{in} > T > T_{out}$
2. The SoI shall provide a variable mass flow rate ($\dot{m}$) of a specific fluid (water) in a specific phase (liquid)
   – Heat capacity of coolant falls within $c_{p,max}$ and $c_{p,min}$
   – Coolant Mass Flow Rate = $\dot{m}$
3. The SoI shall respect weight (W) and space (V) limits imposed by context and surrounding environment
   – Total Weight $< W$
   – Heat Exchanger Volume $< V$

Afterwards, the designer team derives a first level of System Requirements that aim to "satisfy" Stakeholder Requirements. In the Requirements Diagram (Fig. 4b), requirements are reported and managed as a tree using different kinds of items and connections. In particular, "containment" is used to decompose plural requirements, whereas "satisfy" and "derivereq" trace connections among the

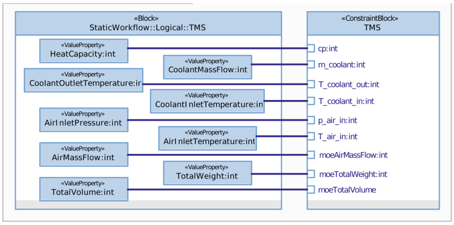

Fig. 3. Correlations between System Attributes and Global Variable of Sizing Functions.

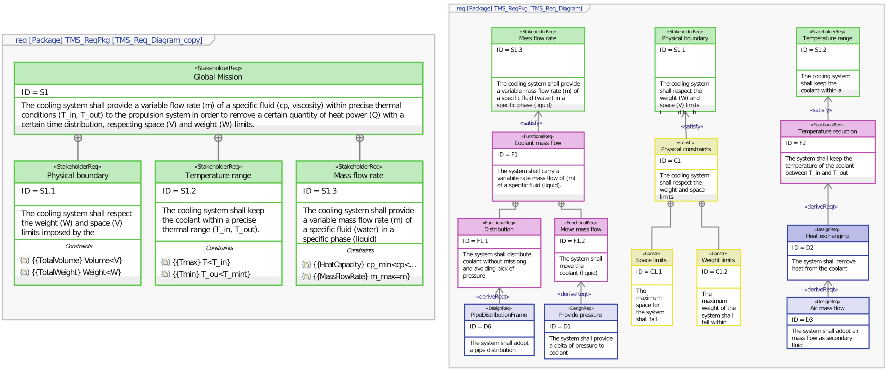

(a) (b)

Fig. 4. (a) Stakeholder Requirements of SoI (b) System Requirements of SoI

requirements chain. Main System Requirements verify Stakeholder Requirements whereas Validation Criteria are allocated as SysML constraints. Furthermore, three different kinds of System Requirements are adopted: Functional Requirements, Constraints and Design Choices. The last one traces technical solutions implemented and removes degrees of freedom from the system.

Once the context for the TMS has been defined thanks to the parametric analysis at the aircraft level, the functional and logical analysis will be developed in the following phases according to the approach proposed in Sect. 2. The outcomes of this analysis lead to the identification of sub-systems and parts as the basis for detailed design, clarifying the SoI architecture. Consequently, each element belonging to TMS shall be sized and analyzed by re-applying the proposed process.

4 Conclusions

The present paper reports a possible innovative approach to support the designing process alongside context, definition, analysis, and development of a complex system, taking into account the System Engineering approach and SysML as representing language. A particular focus is given to Parametric Analysis as a frame for sizing functions development and Validation Criteria connected to Stakeholder Requirements for designing process support. Indeed, Parametric Analysis and Validation criteria represent the starting point for the implementation of a system during the designing stage and certificate that the system meets the requirements at the upper level. The advantages of this approach are the management of requirements and traceability for a quick and precise implementation whenever a change occurs.

References

1. Pasquariello, A., Vitolo, F., Patalano, S.: Systems and requirements engineering: an approach and a software tool for the interactive and consistent functional requirement specification. In: Gerbino, S., Lanzotti, A., Martorelli, M., Mirálbes Buil, R., Rizzi, C., Roucoules, L. (eds.) Advances on Mechanics, Design Engineering and Manufacturing IV JCM 2022, pp. 491–502. LNME, Springer, Cham (2023)
2. Vitolo, F., Rega, A., Di Marino, C., Pasquariello, A., Zanella, A., Patalano, S.: Mobile robots and cobots integration: a preliminary design of a mechatronic interface by using MBSE approach. Appl. Sci. **12**(1), 419 (2022)
3. Graessler, I., Hentze, J., Bruckmann, T.: V-Models for Interdisciplinary Systems Engineering. In: Marjanović, D., Štorga, M., Škec, S., Bojčetić, N., Pavković, N. (eds.) DS 92: Proceedings of the DESIGN 2018 15th International Design Conference, pp. 747–756. Design (2018)
4. Systems and software engineering - System life cycle processes ISO/IEC/IEEE 15288:2015 (2015)
5. Pahl, G., Beitz, W., Feldhusen, J., Grote, K.-H.: Engineering Design. Springer, London (2007). https://doi.org/10.1007/978-1-84628-319-2
6. Mhenni, F., Choley, J., Penas, O., Plateaux, R., Hammadi, M.: A SysML-based methodology for mechatronic systems architectural design. Adv. Eng. Inform. **28**(3), 218–231 (2014)
7. Friedenthal, S., Moore, A., Steiner, R.: Chapter 8 - Modeling constraints with parametrics. In: Friedenthal, S., Moore, A., Steiner, R. (eds.) A Practical Guide to SysML (Third Edition), pp. 185–203. Morgan Kaufmann, Boston (2015)
8. Yvars, P., Zimmer, L.: System sizing with a model-based approach: application to the optimization of a power transmission system. Math. Probl. Eng. **2018**(5), 1–14 (2018)
9. Bagdatli, B., Karagoz, F., Reilley, K., Mavris, D.N.: MBSE-enabled Interactive Environment for Aircraft Conceptual Sizing & Synthesis. In: AIAA Scitech 2019 Forum. AIAA, San Diego, California (2019)
10. Bijan, Y., Yu, J., Graves, H., Stracener, J., Woods, T.: 6.6.1 Using MBSE with SysML Parametrics to Perform Requirements Analysis. In: INCOSE International Symposium, Denver, CO, vol. 21, pp. 769–782 (2011)
11. Leserf, P., de Saqui-Sannes, P., Hugues, J.: Trade-off analysis for SysML models using decision points and CSPs. Softw. Syst. Model. **18**(6), 3265–3281 (2019)

Toward a Framework for Virtual Testing of Complex Machine Tools

Andrea Rega[1](✉), Alessandro Genua[1,2,3], Ferdinando Vitolo[1], Stanislao Patalano[1], Giuseppe Sanseverino[3], Lars Penter[2], Frank Arnold[2], Steffen Ihlenfeldt[2], and Antonio Lanzotti[1]

[1] Fraunhofer J-Lab IDEAS, Department of Industrial Engineering, University of Naples Federico II, Naples, Italy
andrea.rega@unina.it

[2] Chair of Machine Tool Development and Adaptive Controls, Technische Universität Dresden, Dresden, Germany

[3] Department of Sports Equipment and Technology, Chemnitz University of Technology, Chemnitz, Germany

Abstract. Virtual prototyping is a strategic practice in the research and development of innovative products and machine tools. Virtual prototyping allows the integration of multidomain simulations into the designing process to replicate and analyze the impact of design choices on the overall system performance, reducing time-to-market while simultaneously improving quality. The current paper provided a methodological approach to model complex machine tools and perform virtual testing. As a use case for this study, a parallel kinematic machine (Pentapod P800, METROM Mechatronische Maschinen GmbH, Germany) is investigated. The adoption of these complex machine tools within the industrial context and the design of parallel kinematic machines can be eased by the implementation of methodologies capable of reducing efforts and risks during the analysis and the testing phases, prior to actual commissioning. In this scenario, virtual testing guarantees generality, completeness, and quick response. Therefore, the multibody model of the Pentapod P800 was developed following the proposed framework. Then, the simulation of a test trajectory was successfully carried out. The results show that this approach might lead to the design and implementation of a parallel kinematics machine reducing risks, time, and costs.

Keywords: Digital modelling · Virtual prototyping · Multibody modelling · Parallel kinematic machines

1 Introduction

Virtual prototyping is an advanced engineering technique that allows industrial systems to be tested and optimized before physical construction [1]. By creating a digital model of the physical system and running simulations, potential design flaws and operational issues can be detected and corrected early in the development process. This can result in significant cost savings, faster time-to-market, and reduced risks associated with

M. Carfagni et al. (Eds.): ADM 2023, LNME, pp. 530–536, 2024.
https://doi.org/10.1007/978-3-031-52075-4_60

commissioning and start up. Virtual prototyping has important implications for various industries, including manufacturing, automotive, aerospace, and energy. Recent studies have demonstrated the effectiveness of virtual commissioning in improving the design and performance of complex systems, such as robotic work cells [2] and production engineering [3].

By using digital modelling, it is possible to develop virtual tests thus enabling the opportunity to test different approaches avoiding the need of physical tests. Many applications, particularly those involving serial machines, have been discussed in literature [4, 5]. A parallel kinematic machine (PKM) [6] belongs to a class of machines with multiple links and joints that offer superior performance in terms of speed and rigidity, due to the comparatively low moving masses. Virtual prototyping of PKM offers advantages in terms of cost, time and safety [7, 8]. One of the key challenges in virtual prototyping of these machines is the development of accurate models that can be used to predict their behaviour under several operating conditions [9, 10]. To develop such models, it is possible to use different approaches: (i) analytical methods; (ii) experimental methods. The first involve developing mathematical models based on the kinematics and dynamics of the machine, this can result in complex models. The second methods involve measuring the dynamic response of the machine under different operating conditions and using these data to develop a model. This approach requires significant experimental setup and very accurate data acquisition.

Alternatively, computational techniques, such as multibody modelling [11], can be used to simulate and virtually analyse the kinematics and dynamics of complex mechanical systems [12, 13]. A multibody model consists of a representation of a mechanical systems by means of several rigid or flexible bodies interconnected with joints and constraints to specify the relative motion that can occur between two bodies. Once developed, a multibody model, can be used to support design choices or for simulation-based optimization.

As mentioned above, the accurate modelling requires extensive knowledge of the geometric and process-specific parameters. Determining these through practical testing represents a considerable human and financial effort for the machine supplier for planning, implementation and evaluation. The use of multibody modelling and simulation represents a promising approach for examining the static and dynamic behaviour of the machine behaviour for the most diverse application scenarios and load cases without having to map these in reality and accompany them with measurements.

In this paper, using multibody modelling, a framework towards virtual testing and prototyping of complex machine tools is presented. As a proof of concept, a multibody model of the Pentapod P800 (METROM Mechatronische Maschinen GmbH, Hartmannsdorf, Germany) [14, 15] has been developed in order to simulate the calibration process before the actual process. Figure 1 shows the actual machine under investigation. The calibration process involves comparing the intended trajectory to the simulated trajectory of the Pentapod end-effector. The presented activity is carried out by using Simscape Multibody (MathWorks Inc., Natick, USA) to develop a digital model of the Pentapod P800 machine tool and to solve the inverse kinematic issue to perform virtual testing. This approach might lead to savings in terms of time and resources needed in the process of design and implementation of a PKM.

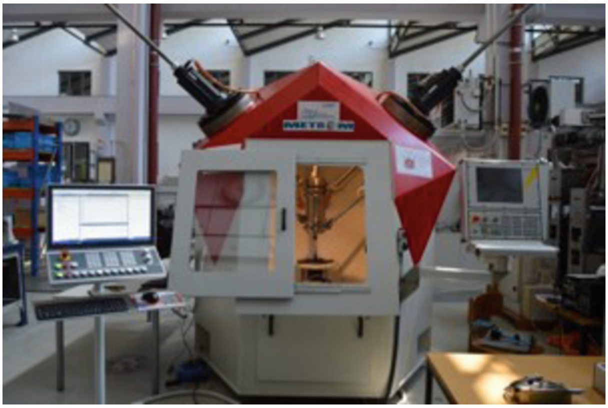

Fig. 1. Pentapod P800 machine tool (METROM Mechatronische Maschinen GmbH, Hartmannsdorf, Germany) at Technische Universität Dresden workshop.

The paper is organized as follows: Sect. 2 presents the proposed methodology, while Sect. 3 shows a use case consisting in the development of a multibody model of the Pentapod machine. Finally, a brief discussion on results and conclusions of this activity is reported in Sect. 4.

2 Method

No available multibody models of the Pentapod P800 were found in literature. In order to obtain digital models of complex machine tools for virtual testing and prototyping, the following steps are necessary: information collection, CAD modelling, multibody modelling, model finishing, and simulation.

- Information collection: gather information about the machine tool. In example: intended use, forces and torques acting on it, and materials used in its construction. This information can be obtained from design specifications, engineering drawings, and operating manuals.
- CAD modelling: create a 3D CAD model of the machine tool using software such as SolidWorks (Dassault Systèmes, Vélizy-Villacoublay, France). This model serves as basis for developing the multibody model.
- Multibody Modelling: this step can be realized with two different approaches, i.e., (i) the CAD model of the machine tool is converted into a.xml file and imported to Simscape Multibody. Then, subsystems, frames, and joints are automatically generated based on the geometry and topology of the CAD model; (ii) the multibody model is developed by manually import each meaningful CAD component. Each component can be imported to Simscape Multibody from neutral file format such as STEP, IGES, or STL. Joints between the components (e.g., prismatic, revolute, spherical) are defined and characterized by defining the origin of acting forces and torques; reference frames to position and orient components relative to one another are also manually defined.

- Model finishing: following the first of the multibody modelling approaches above-mentioned can be fast and convenient. However, the imported CAD model needs to be refined to ensure that it is suitable for simulation. Physical properties such as mass, inertia, and geometry need to be added to each component using adequate Simscape Multibody blocks. Joints interconnecting different components can be defined using Simscape Multibody blocks, and forces and torques acting on the components can be added using Simscape Physical Signal blocks.
- Simulation: after finishing the model, simulations can be run to analyze its behavior under different operating conditions. The results of the simulations can be used to optimize the design of the machine tool and identify potential problems or areas for improvement.

Proposed methodology for multibody modelling of complex machine tools provides a structured approach for accurately predicting their behavior and improving their design. The methodology ensures that all the necessary information is gathered, the CAD model is created and imported correctly, the model is finished for simulation, and the results are validated through simulation. Proposed framework can be generalized and applied to different types of complex machine tools to improve their design or perform virtual testing for process optimization.

3 Use Case

Pentapod P800 produced by Metrom© is the machine tool under investigation. The PKM is composed of five extensible legs forming a closed kinematic chain. The five legs, moving thanks to five independent drives, carry the main spindle which is used for milling. In addition to use as a milling machine, such kinematics can also be used for other machining processes such as welding, additive manufacturing and hammer peening. By using a rotary table as a redundant axis, the Pentapod P800 can realize complete 5-sided machining. Through digital modelling of the Pentapod machine tool, followed by a virtual testing phase, the executability of some trajectories was simulated in order to evaluate the kinematic behavior of the machine tool.

As previously discussed, after a preliminary phase consisting in gathering information, a CAD model is created using SolidWorks 2020. Then, crucial components are identified and exported to an STL file to be used in the multibody model.

Parts that had no significant impact on the movement analysis (e.g., bolts, doors, supports, and frame parts that obstruct visibility) were removed. This reduces the computational load, enabling to focus only on critical components while ensuring the model's fidelity.

In this study both the multibody modelling approaches introduced in the previous section were used. Since the use of the first approach resulted in a complex and non-controllable model, the second approach was used for this application. Figure 2 shows the block diagram including joints, reference frames and components of the multibody model of a single leg of the machine tool under investigation.

Figure 3 shows the entire model of the machine tool. The block model shows the five legs organized into five subsystems each of which is connected to the main spindle. The developed multibody model consists of rigid-bodies and allows for analyzing the

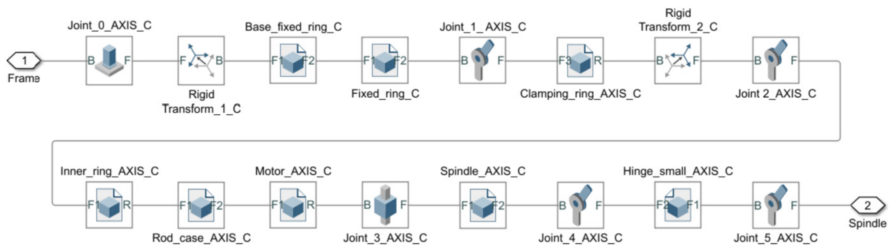

Fig. 2. Multibody model of a single leg.

motion of the Pentapod with the movement limits of the components by simulating its kinematic behavior given any trajectory to be followed by the end effector. Solution of the inverse kinematic problem to carry out virtual tests was obtained by leveraging the potentiality of the MATLAB KinematicSolver (MathWorks Inc., Natick, USA). In brief, using the KinematicSolver and custom scripts it is possible to show the execution of the virtual test by importing the created multibody model, the selected trajectory, defining the end effector frame and the global reference frame.

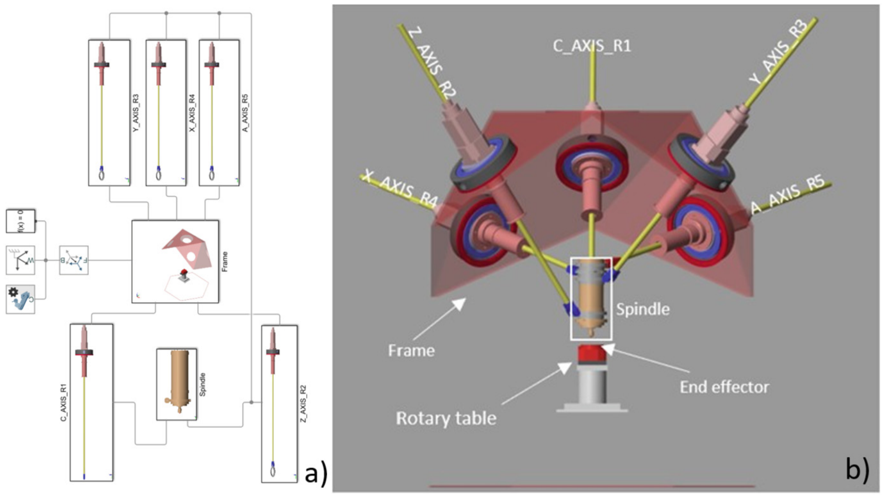

Fig. 3. Multibody model of Pentapod P800 in the Simscape environment: a) block model; b) 3D model.

The virtual test allows to check the kinematic behaviour of the Pentapod while moving along the loaded trajectory. Figure 4 shows a configuration of the Pentapod machine while following a test trajectory.

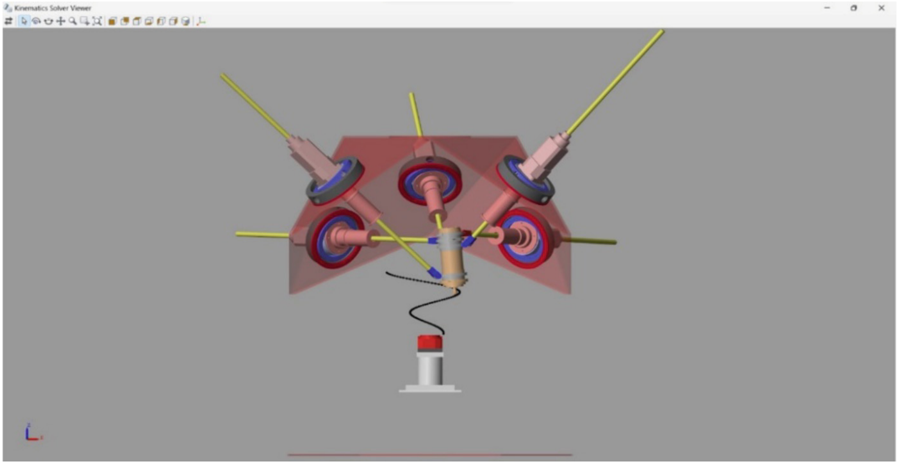

Fig. 4. The model of the machine tool during the following of a test trajectory.

4 Concluding Remarks and Future Developments

This paper provided a methodological approach to model complex machine tools and perform simulation for virtual testing or prototyping. As a proof of concept, multibody model of a PKM (Pentapod P800) was developed following proposed framework, and simulation of a test trajectory was successfully carried out showing the potential of this approach. It is noteworthy that the development of a multibody model of such a complex machine might require considerable amount of time. Nevertheless, this leads to the possibility to carry out virtual tests for investigating the kinematic behaviour of the machine or the design choices. In example, when testing trajectories of the tool central point, virtual testing ensures a reduction of physical tests to be carried out, leading to a reduction of time and costs and limiting potential damage to personnel or equipment. In fact, simulation of the test trajectory reported in Fig. 4 required a computational time of about 10 min (using a windows machine with 1.8 GHz clock speed and 16 GB ram), a physical test of the same trajectory would require programming of the trajectory, preparation and operation of the PKM by specialized personnel which would result in increased costs. In addition, models obtained with the framework objective of this study can be used to investigate collisions, permeations, and unexpected movements to determine their causes. Moreover, this paper demonstrated the possibility to perform virtual testing using commercially available software (e.g., Simscape Multibody; SolidWorks).

In conclusion, although this activity focused mainly on the study of the kinematics of a PKM, proposed methodological approach can be generalized laying good foundations for future investigations of the behaviour of complex machine tools with reduced time and efforts. It is worth to mention that proposed proof of concept still suffers from limitations such as increased computational times (up to 30 min) for testing of more complex trajectories and lack of validation of the digital model with regards to the physical machine. Future studies should address these issues by improving digital models and reducing computational times associated with the KinematicSolver from MATLAB.

Acknowledgments. The present work is carried out in the context of the Erasmus agreement among the University of Naples Federico II and the LWM TU Dresden.

References

1. Wang, G.G.: Definition and review of virtual prototyping. J. Comput. Inf. Sci. Eng. **2**(3), 232–236 (2002)
2. Raffaeli, R., Neri, F., Peruzzini, M., Berselli, G., Pellicciari, M.: Virtual prototyping as a supporting tool for the design of complex robotic cells. In: Rizzi, C., Campana, F., Bici, M., Gherardini, F., Ingrassia, T., Cicconi, P. (eds.) ADM 2021. LNME, pp. 675–682. Springer, Cham (2022). https://doi.org/10.1007/978-3-030-91234-5_68
3. Hauf, D., Süß, S., Strahilov, A., Franke, J.: Multifunctional use of functional mock-up units for application in production engineering. In: 2017 IEEE 15th International Conference on Industrial Informatics (INDIN), Emden, Germany, pp. 1090–1095. IEEE (2017)
4. Netto, A.V., Ferreira de Oliveira, M.C.: Virtual reality for machine tool prototyping. In: ASME International Mechanical Engineering Congress and Exposition, New Orleans, Louisiana, USA, vol. 3641, pp. 15–22. ASME (2002)
5. Coman, G.C., Serban, C., Ivan, A.M., Nicolescu, A.F.: Virtual prototyping, physical structure development and PC control of a double arm (five link) SCARA robot. IOP Conf. Ser. Mater. Sci. Eng. **591**(1), 012075 (2019)
6. Boër, C.R., Molinari-Tosatti, L., Smith, K.S. (eds.): Parallel Kinematic Machines. Theoretical Aspects and Industrial Requirements. Springer, London (2012). https://doi.org/10.1007/978-1-4471-0885-6
7. Bianchi, G., Fassi, I., Tosatti, L.M.: PKM Analysis and design in a virtual prototyping environment. J. Adv. Manuf. Syst. **1**(02), 211–226 (2002)
8. Munzinger, C., Krauße, M., Kipfmüller, M.: Simulation of parallel kinematic machine tools with minimal effort. Prod. Eng. Res. Devel. **4**, 491–499 (2010)
9. Zhang, H., Fang, H., Zhang, D., Zou, Q., Luo, X.: Trajectory tracking control study of a new parallel mechanism with redundant actuation. Int. J. Aerosp. Eng. **01**(2020), 1–14 (2020)
10. Sayed, A.S., Mohamed, N.A., Salem, A.A., Ammar, H.H.: Modeling of nonlinear 3-RRR planar parallel manipulator: kinematics and dynamics experimental analysis. Int. J. Mech. Mechatron. Eng **20**, 175–185 (2020)
11. Shabana, A.A.: Dynamics of Multibody Systems, 3rd edn. Cambridge University Press, Ne York (2005)
12. Tolun, O.C., Tutsoy, O.: 3D modeling and justification of an electrical vehicle with multibody modeling softwares. In: ICOLES 2022, vol. 115, Antalya, Turkey (2022)
13. Ratiu, M., Rus, A., Balas, M.L.: Dynamics of a 6R industrial robot. IOP Conf. Ser. Mater. Sci. Eng. **898**(1), 012013 (2020)
14. Metrom Homepage. https://metrom.com/. Accessed 20 Mar 2023
15. Bär, G.F., Weiß, G.: Kinematic analysis of a pentapod robot. J. Geom. Graph. **10**(2), 173–182 (2006)

A Structured Methodology for New Product Development Combining QFD and MCDM: Case Study on Router Bits

Giulia Polensig[1], Domenico Marzullo[2(✉)], Iacopo Bodini[1], Elio Padoano[2], and Massimo Tolazzi[1]

[1] Freud S.p.A, Via Remigio Solari, 7, 33050 Pavia di Udine, Italy
[2] Department of Engineering and Architecture, University of Trieste, Via Alfonso Valerio, 6/1, 34127 Trieste, Italy
dmarzullo@units.it

Abstract. An integrated approach to product development methods is necessary to connect and rationalize in a single framework the different design phases. Moreover, it allows to map and facilitate the decision-making process, especially when many stakeholders are involved. This paper presents a methodology for the design and development of a new product or component that integrates Quality Function Deployment (QFD) and Multi Criteria Decision Making (MCDM) methods, from the definition of the user requirements to the generation and simulation of the concept models. The evaluation of the results is carried out at different stages of the process with a customer-driven approach. Initially QFD, combined with the Analytic Hierarchic Process (AHP), is applied to define the product requirements from the customer needs. Thereby, the focus of the subsequent development is identified. The concept generation phase is therefore implemented throughout a series of brainstorming sessions. A first selection among the generated solutions is conducted using a summarizing function, according to the level of requirement satisfaction. Several refinements of the chosen concepts are then derived from manufacturability considerations and Finite Element Analyses. Finally, according to the Technique for Order Preference by Similarity to Ideal Solution (TOPSIS) a ranking of the developed products is obtained following the performance specifications. The presented methodology was applied to the development of a new router bit with insert knives, allowing to report the decision-making reasoning and to consider the user needs throughout the product design.

Keywords: Quality Function Deployment QFD · Multi Criteria Decision Making MCDM · Concept design

1 Introduction

Product development includes a series of activities that begins with the perception of a market opportunity and ends with production, sale and delivery of a product [1]. It is an interdisciplinary process that involves design, manufacturing and marketing. In the

M. Carfagni et al. (Eds.): ADM 2023, LNME, pp. 537–545, 2024.
https://doi.org/10.1007/978-3-031-52075-4_61

majority of product development projects, the process can be divided into several phases [2, 3]. The first is the *project definition and planning* phase. A project usually starts with the identification of an opportunity, which can be motivated by market demands or driven by the availability of a new technology. The scope should be clearly reported and the product mandatory requirements, e.g. related to safety, are considered. Afterwards, the *conceptual design* phase can begin with the identification of the target market needs. Several alternatives of product concepts with different working principles are generated and evaluated to select one or few for further development. It is the most crucial phase in the product development lifecycle since the main cause of failure in projects relates to the early design stage. This usually depends on unclear and imprecise design requirements [4]. During the subsequent stage of *embodiment design*, or *system-level design*, the product components, materials, all the specifications and an initial manufacturing plan are defined. To support this activity, simulations are usually run on the generated CAD models according to the problem in exam. The *detailed design stage* is consequently implemented and followed by further testing and refinement.

In such design process, a structured methodology is beneficial to drive the design requirements identification and analysis, as well as the concept development and evaluation. According to the main notions of the Concurrent Engineering, all activities connected with product development should be assessed in a unified and simultaneous way. Several combinations of Quality Function Deployment (QFD) and different methods of Multi-Criteria Decision Making (MCDM), which aim to support many product development phases and the related service and supply selections, can be found in the literature [5, 6]. However, it is commonly found that this process should be adapted to the project and the organization context.

This paper proposes an integrated methodology that combines QFD and MCDM methods, following the main steps of the design and development of a new product. It aims to incorporate the whole product life cycle and the tasks of different business units to optimize all these relative aspects from the early stages. A suitable MCDM method is used according to both the current development phase and the progress status of the product design. The selection criteria respectively consider different evaluation perspectives. Firstly, they are based only on the customer needs, then the organization and manufacturing requirements are introduced and finally more technical factors are considered. In Sect. 2, the employed methods are briefly described and their proposed integration is presented in a structured design process. Section 3 involves the application of this process to the case study of an innovative router bit for wood milling, carried out as industrial case at Freud S.p.A. Final considerations and further developments are then reported in Sect. 4.

2 Structured Methodology

The proposed integrated methodology was developed combining QFD and MCDM methods (Fig. 1). This structured approach allows to rationalize and map all the decision-making process, from the definition of the user requirements for the new product, to the generation and simulation of the concept models. The evaluation of the outcomes is carried out with a customer-driven approach at different stages of the process.

Initially, the QFD permits the interpretation of the customer needs and the identification of the related technical characteristics of the product, constructing a framework as a base for further design. QFD allows to transform subjective needs and requirements of customers into objective and technical criteria, and then to discover product characteristics that are most critical and important to quality. The Voice of Customers (VOCs) are hence translated in Critical to Quality specifications (CTQs). Finally, the level of quality of the product is quantified and verified with a set of testable specifications with measurable targets [7]. In this context, the prioritization of the customer requirements is made applying the Analytic Hierarchy Process (AHP) [8, 9]. Eventually, the technical characteristics can be classified in terms of importance, related to the capacity to bring quality and satisfy the customer needs, and in terms of difficulty in reaching the target values. A threshold on the maximum acceptable level of difficulty and a minimum limit on the relevance can be applied, defining thereby the development focus.

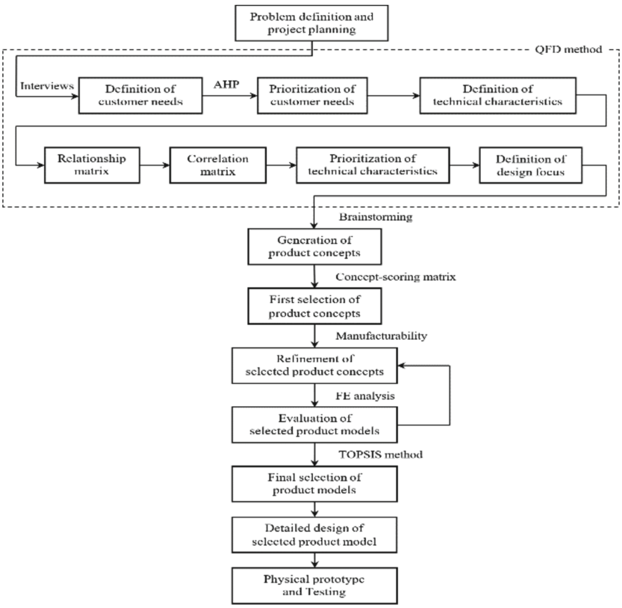

Fig. 1. Methodology structure for new product development

All the information and data collected with QFD are used as input in the concept generation phase, with the aim of developing a new product and defining the solutions to satisfy the engineering requirements. In this paper, the concept solutions are focused on the customer's most relevant engineering specifications that do not require excessive resources. A series of structured brainstorming sessions are therefore conducted with an interdepartmental team, that should include design engineering and manufacturing functions [10]. The first selection among the generated solutions is based on the level of requirement satisfaction and made using a summarizing function on the concept scoring matrix [1]. In this way a smaller number of concepts will be further studied, thus avoiding waste of resources on an excessive number of ideas.

The next step is a detailed refinement of the model that transforms the concept into a proper product. Several modifications of the chosen concepts are derived following the notions of Design for Manufacturing (DFM) and Design for Assembly (DFA). A first manufacturing workflow is created, defining the required machinery and tools. The evaluation of the manufacturing tasks performed at the predevelopment stage, in fact, allows to reduce the production costs and to introduce any alterations without impact.

The product concepts are then analysed in depth to ensure the functionality and compare their characteristics. For instance, Finite Element Analyses are performed to assess the response of the model to certain loads. The model geometry is consequently adapted, establishing an iterative process of refinement and verification. Moreover, some important parameters can be extracted and used to compare the different concepts in further phases.

The final product evaluation is made using the Technique for Order Preference by Similarity to Ideal Solution (TOPSIS) with technical criteria [11]. TOPSIS allows the ranking of the developed products, which make up the selection set, according to their overall performance on the criteria. To this end, the method defines two hypothetical alternatives: a positive ideal solution, which presents the best performance in all criteria, and a negative ideal solution, with the worst performances. The best alternative in the selection set is the one closest to the positive ideal solution, according to a measure of closeness defined in the method. To compute the distance between the alternatives the Euclidean distance is usually employed: this requires that all the criteria be expressed with numerical values [12].

3 Methodology Application: Case Study on a New Clamping System for Router Bit Knives

The presented methodology was applied to the development of a new clamping system for router bit knives with a particular focus on the end-user friendliness of the knife exchange and assembly process. The possibility to change only the worn-out cutting part has several environmental and economic benefits. The overall product can have a longer lifetime, reducing waste and allowing to easily separate materials for recycling. The user needs are considered throughout all the product design phases and the decision-making reasoning can be consequently reported to the company organization.

3.1 Project Planning and Product Requirements Definition with QFD and AHP

The main phases of the project are laid out in a schematic plan, which includes the project milestones and the estimated due dates. The project can be visualised in a Gantt chart. In order to define the quality and so the value-adding elements starting from the design conception phase, the customer is chosen as the final user of the Router Bit (RB).

Several interviews are conducted, principally with sales and marketing representatives, to gather the necessary information and define the customer requirements. During the meetings, a particular attention is paid to the latent needs and the reasons behind the statements. The outcome is a list with more than 100 voices. These sentences are then analysed according to QFD and summarized in a smaller and more manageable Demanded Quality chart with about 30 VOCs, clustered into different categories. A prioritization of the VOCs is then realized with the AHP. Each interviewee filled a pairwise comparison matrix using the 9-point scale of Saaty [8]. This process is also useful to have a VOCs review directly from the interviewees and understand if the list is accurate and complete. A global pairwise comparison matrix is eventually obtained where each element is the geometric mean of the pairwise assessments performed by all the interviewees. Both the singular and the final matrices have a consistency ratio below 0.2 and mainly lower than 0.1; given the large matrix size the ratings are accepted [9].

Fig. 2. House of Quality of the project

An interdisciplinary team is composed by many product and manufacturing engineers, to carry out the rating activities about technical topics during the implementation of QFD. Afterwards, the team defines the CTQs from the VOCs according to the what-not-how principle [1], since solution independent CTQs provide more creative freedom in a new product concept generation. Hence 32 CTQs are eventually clustered into different categories with a measurement standard and the respective units for each one.

The Relationship Matrix, that displays the connection intensities between each VOC and each CTQ characteristic, is created with grades in a 1-3-9 scale from no correlation to strong correlation. In an analogue way, the team creates the Correlation Matrix according to four intensity levels (strong positive, positive, negative, strong negative), in order to clearly understand how the technical specifications influence each other and to manage the possible trade-offs. The prioritization of the CTQs is then calculated through the weighted sum, combining the ranking of the VOCs and the relationship matrix values. Thus, they are ordered according to their ability to influence the customer satisfaction on the most important requirements. A target value for each CTQ is also decided, nevertheless it can be modified afterwards if necessary. Eventually, each member of the team individually votes the target difficulty level according to a predefined scale. In case of outliers, the values are mediated after a brief discussion.

All the charts and matrices are composed into the House of Quality, the multifunctional tool used as a guide for all the future product development. For the sake of brevity, among all the matrixes generated only the House of Quality is reported in this paper in Fig. 2, where the main VOCs and CTQs developed as described above are listed.

Finally, to better visualise the level of importance and the difficulty of each CTQ, these are plotted in a graph including a threshold on the difficulty level according to the resources available in terms of people and time (Fig. 3). The team identifies the CTQs that will be the future development focus based on the area where they are located and it evaluates the possible trade-offs.

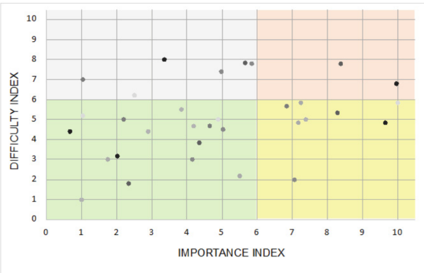

Fig. 3. Importance and Difficulty Index of the CTQs

3.2 Conceptual Design and Evaluation

The concept generation starts individually and the people, mainly part of the core team, attempt to find solutions to the selected CTQs. Then several brainstorming sessions are performed with different teams, composed by design engineer, product engineer, product expert and manufacturing engineer. Starting from the most important CTQs, the team tries to find solutions that permit to reach the targets. Initially, the selected technical requirements are related to technical solutions, as a feature, a partial product concept or a design characteristic (Fig. 4). A first group of partial features of the product is therefore obtained. Then, during the discussions, more complex solutions and product concepts emerge. Whiteboards with markers or post-it are widely used to sketch, write and visualise the ideas with a gallery method that incentive debate. All the observations and comments are also written down by a designated record keeper. The collected data, a series of drawings and notes, are elaborated after the brainstorming. Ideas and partial solutions are combined to form complete concepts, firstly as sketches, then as CAD models. During the modelling process, some problems, inconsistencies or missing features of the concept emerge and are resolved. A 3D model in this early stage is therefore very useful to better understand the working principle of the idea. A total of 16 concepts with different clamping system of the knives were conceived and modelled.

Once the RB concepts are defined, a MCDM selection is performed with the concept scoring matrix, where the performance of every concept is rated according to various criteria. The criteria used are the CTQs, obtained from the customer needs during QFD, and the requirements of the manufacturing and the organization. The final ranking of the concepts is calculated with a weighted sum where the rating of the concept performance in each criterion is multiplied by the importance index of the criterion. The first four concepts are selected to be developed forward according to the available resources. Afterwards, the people involved in the requirement definition phase of QFD are interviewed to validate the choice.

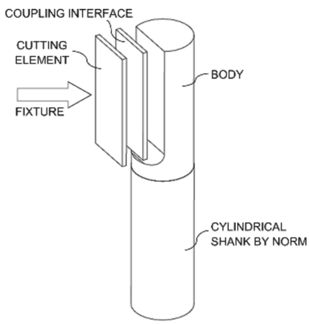

Fig. 4. Conceptual elements of a RB system

3.3 Embodiment Design and Selection

The RB models are refined according to DFM and DFA considerations, setting the final geometry of every part, the sequence of manufacturing operations, machinery and set of tools. FEA are then conducted to evaluate each RB until the components are verified.

Finally, the performances of the refined product concepts are compared according to the new available information and a final selection is carried out. The final RB concepts present similar characteristics according to the CTQs used in the first selection, in terms of ease of use and customer requirements. Therefore, a different MCDM approach is implemented with TOPSIS method, using the data obtained from FEA on the models and other technical aspects. The weights of the criteria are calculated using two ‘objective’ methods based on their information content, the Standard Deviation Method (SDM) [13] and the Entropy Method (EM) [14], and the stakeholders' subjective assessments. The RBs are therefore sorted according to their performances in the criteria, weighted with the different importance values. The two objective weights from SDM and EM provide the same ranking. Comparing the objective rankings with the one obtained from the subjective weights, the first and second place do not change, while the third and fourth ranked concepts are reversed.

4 Conclusions

Overall, the structured approach aided and supported the decision-making process, improving its transparency. The explication of the decision rationale was in fact mapped, ensuring that the important topics were addressed, and reducing the possibility of proceeding with unsupported decisions. Moreover, the implementation of QFD was found significantly beneficial by all team members during the whole process and it facilitated the design activities, although it required non negligible time and resources. The case study topic was in fact already preliminary addressed, but the results at such pre-conceptual design stage were considered negative, probably due to a non-structured and supported design approach. During the first stages, QFD allowed to comprehend and reflect about the development project with a customer perspective. Having already thought about the product in terms of requirements and being familiar with the problem facilitate the design activities. In further stages, the information about customer needs and their correlations with the technical product requirements are well organized and could be retrieved rapidly, due to the composition of the House of Quality matrix. The elaboration itself of all the data to arrive to the matrix helped each designer and the extended team to better understand the design conditions and what the product should do. Therefore, it is important to underline that the utility of QFD in product development resides largely in the process, rather than in the results alone.

The next phases of the product development correspond to the detailed design, which should be implemented on the selected concept. A functional prototype can therefore be manufactured, tested and evaluated according to the CTQs criteria, which are already defined with a measurement standard and a target value.

References

1. Ulrich, K.T., Eppinger, S.D.: Product Design and Development, 6th edn. McGraw-Hill, New York (2016)
2. Pahl, G., Beitz, W., Feldhusen, J., Grote, K.-H.: Engineering Design. Springer, London (2007). https://doi.org/10.1007/978-1-84628-319-2
3. Di Gironimo, G., Lanzotti, A., Marzullo, D., Esposito, G., Carfora, D., Siuko, M.: Iterative and participative axiomatic design process in complex mechanical assemblies: case study on fusion engineering. Int. J. Interact. Des. Manuf. **9**, 325–338 (2015)
4. Marzullo, D., Di Gironimo, G., Lanzotti, A., Mazzone, G., Mozzillo, R.: Design progress of the DEMO divertor locking system according to IPADeP methodology. Procedia CIRP **34**, 56–63 (2015)

5. Marini, C.D., Fatchurrohman, N., Azhari, A., Suraya, S.: Product development using QFD, MCDM and the combination of these two methods. 2016 IOP Conf. Ser. Mater. Sci. Eng. **114**(1), 012089 (2016)
6. Mohammadshahi, Y.: A state-of-art survey on TQM applications using MCDM techniques. Decis. Sci. Lett. **2**, 125–134 (2013)
7. ISO 16355-1, Application of statistical and related methods to new technology and product development process - Part 1: General principles and perspectives of quality function deployment (QFD), pp. 1–61 (2021)
8. Saaty, T.L.: The Analytic Hierarchy Process. McGraw-Hill, New York (1980)
9. Saaty, T.L.: Some mathematical concepts of the analytic hierarchy process. Behaviormetrika **18**(29), 1–9 (1991). https://doi.org/10.2333/bhmk.18.29_1
10. Goldenberg, J., Mazursky, D.: Creativity in Product Innovation, pp. 45–51. Cambridge University Press, Cambridge (2002)
11. Hwang, C.L., Yoon, K.: Multiple Attribute Decision Making: Methods and Applications. Springer-Verlag, New York (1981)
12. Hwang, C.L., Lai, Y.J., Liu, T.Y.: A new approach for multiple objective decision making. Comput. Oper. Res. **20**(8), 889–899 (1993)
13. Wang, Y., Luo, Y.: Integration of correlations with standard deviations for determining attribute weights in multiple attribute decision making. Math. Comput. Model. **51**(1–2), 1–12 (2010)
14. Zhu, Y., Tian, D., Yan, F.: Effectiveness of entropy weight method in decision-making. Math. Prob. Eng. **2020**, 1–5 (2020). https://doi.org/10.1155/2020/3564835

Computer-based Design and Manufacturing for the Reproduction of Classic Car Spare Parts

Paolo Bertoncelli[1], Francesco Gherardini[1](✉), Enrico Dalpadulo[1], Amaury Lorient[2], Alberto Vergnano[1], and Francesco Leali[1]

[1] Department of Engineering "Enzo Ferrari", University of Modena and Reggio Emilia, Modena, Italy
francesco.gherardini@unimore.it
[2] ICAM Engineering School, Site de Vendée, La Roche-sur-Yon, France

Abstract. The supply of automotive spare parts, especially for historic vehicles, is not guaranteed by car manufacturers. Usually, car restorers look for original components at flea markets and fairs, but often they have to produce replicas from broken parts or, worse, without information about the original parts. A possible support in mechanical craftsmanship comes from digital tools commonly used in industry today. With the goal of replicating a component that no longer exists, this paper provides a workflow that integrates traditional manufacturing technologies with computer-based tools. The core is the digital model, which is used to prototype and test the replica for functionality as well as simulate its manufacturing process.

An engine valve cover of a historic racing car was chosen as a case study, for which information sources were practically unobtainable. Firstly, a 3D model and a 3D printed prototype were developed. Sand casting was chosen based on the original process and computer simulations allowed to reconstruct the casting equipment and define the best part design. A faithful and functional replica is then manufactured and assembled with the original engine, respecting the original part in terms of form, materials and production. The proposed design approach can be further adopted in different contexts requiring on-demand, one-off or small-batch production.

Keywords: Component reproduction · Computer-Aided Engineering · Sand casting · Additive Manufacturing · 3D modelling · Car restoration

1 Introduction

Despite the current high level of industrialization of modern countries, the mechanical craft sector shows interesting prospects for development also thanks to the support of modern technologies [1]. In this context, car restoration is playing a leading role, since it is rapidly expanding and currently represents one of the sectors that provides the highest return on investment [2]. However, even if the number of potential classic vehicles is increasing, the supply of spare parts is actually guaranteed for a limited number of years. This implies that there is no shortage of rare, hard-to-find or lost spare parts that need to be reproduced [3]. In some cases, component reproduction can take advantage of

M. Carfagni et al. (Eds.): ADM 2023, LNME, pp. 546–553, 2024.
https://doi.org/10.1007/978-3-031-52075-4_62

digital tools such as Reverse Engineering (RE) and Additive Manufacturing (AM) to get functional parts quickly and effectively [4, 5]. On the one hand, this work summarizes the key stages of such digital process chains [6]. On the other hand, it provides an approach for reproducing components where, conversely, the use of the original manufacturing technology is demanding [7]. In this case, computer-based tools such as rapid prototyping (RP), computer-aided manufacturing (CAM) process preparation, and computer-aided engineering (CAE) process simulation may be involved to support the redesign of product and process. In particular, computer-aided technologies (CAX) can be used to test and simulate digital models and provide reliable and error-free manufacturing and assembly processes. The paper aims to define a design approach capable of supporting today part manufacturers and car restorers in the reproduction of spare parts while complying with the principle of preservation and responsible use of historic vehicles. This will lead to a "newly built" part, defined as "an accurate as possible copy in terms of form, materials and make, reproduced directly from a documented original" in [7]. The paper is structured as follows. The next section describes the workflow for the reconstruction of spare parts, relying on product and process design tasks based on CAX tools. Section 3 describes the case study for the implementation of the approach and the related design and manufacturing results. Finally, Sect. 4 provides a conclusive discussion, opening to possible further developments.

2 Materials and Methods

Similarly to other industrial applications, the reproduction of spare parts involves tasks as design, production and test operations. Considering cases where technical data lacks completeness and, in particular, technical data and drawings are missing, structured approaches involving CAX tools become relevant. Product and process design must be supported both by retrieving information from existing documentation and by introducing models to refine and validate the geometry. Figure 1 illustrates the workflow for the reproduction of spare parts by sand casting, integrating design and manufacturing tasks.

The preliminary collection of sources and the study of the existing documentation allows setting the inputs for the reproduction of the spare part. Additionally, measurements on existing parts and geometry capture are required to define the design constraints. 3D modelling based on parametric CAD tools leads to a digital representation of the part, which can be reproduced in a physical prototype to preliminarily verify assembly and functional requirements, checking for any issues and improving the 3D model. An accessible and affordable RP process such as the Fused Filament Fabrication (FFF) is well suited for this purpose. Once the functional model is achieved, the design of production equipment is required for simulating the casting process, using specific CAE tools [8]. The simulation improves the product layout and its production, also obtaining the parameters for the primary foundry process [9]. Since the cast product requires subsequent machining, CAM tools can be used to prepare for CNC milling operations. After machining, final post-processing treatments such as finishing and polishing are performed; then, the final spare part undergoes assembly and testing operations.

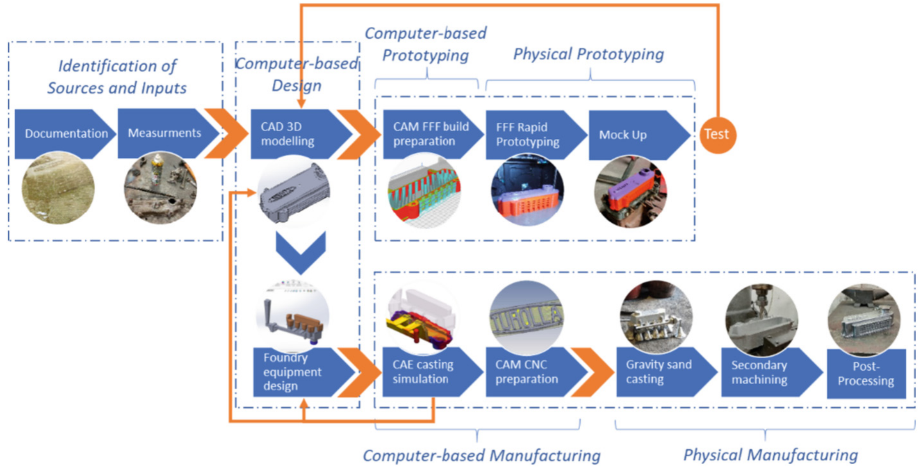

Fig. 1. Workflow for the reproduction of a spare part made by sand-casting.

3 Results

3.1 Case Study

The case study concerns the reconstruction of a valve cover for the Fiat 750 Turolla, a racing car produced between the 1940s and 1950s by the Turolla brothers in their mechanical workshop (Ferrara, Italy) dedicated to the preparation and assembly of sports cars [10]. In those years, the racing car manufacturers took up the standard mechanics of road vehicles and redesigned most of their components to improve performance. Turolla started from the engine of a Fiat Topolino C and designed a tuning kit made up of the intake and exhaust manifolds, the oil pan and the valve cover. The engine, as well as all the customised mechanics, was housed in an original chassis and bodywork to participate in the Mille Miglia from 1947 to 1951. Unfortunately, all the few existing cars were crashed and dismantled after the races, or were lost, apart from a frame that was recovered by an Italian restorer. Retracing Turolla's steps, the original engine of a Fiat Topolino C is taken as the basis for redesigning all the tuned components, including the valve cover.

3.2 Source Identification and Input Phase

The input definition started from the identification of historical sources: Based on books, historical documents relating to the races in which the car participated, notes, photographs and the know-how of the still-alive mechanics of the time, the customised components belonging to the original tuning kit were identified. The recovered sources are limited since Turolla belongs to the so-called 'Etceterini', i.e. the group of the minor car manufacturers of the past. Among these, a blurred black and white photo showing the valve cover geometry.

Since the valve cover was originally mounted on a tuned engine of a Fiat Topolino C, we recovered and disassembled this engine into its components to get the dimensions and geometry of the coupling interfaces. The base flange of the valve cover must mate with the engine head and must not cause oil leaks or infiltration. In addition, the base flange must be compatible with the original cover gasket. A common characteristic for all tuners at the time is that the valve covers were cast from an aluminium alloy. Therefore, by combining data from photos, direct measurements and still-existing valve covers from Turolla's competitors, we have reconstructed a geometry consistent with the historical and functional characteristics of a Fiat 750 Turolla.

The valve cover was originally produced by sand casting, so we went with the same technology, which involves resin models (originally wooden models, called "patterns") in order to create the sand mould with the shape of the casting. This technology is more expensive than modern sintered moulds, but leads to superior surface quality and appearance.

3.3 Computer-Based Design Phase

A parametric 3D CAD model (Fig. 2a) was developed using Dassault Systèmes SolidWorks, including two configurations: the casting model and the final machined model, both designed according to the rules of Design for Manufacturing.

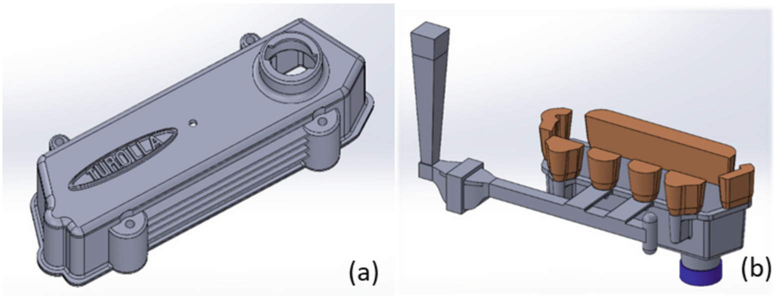

Fig. 2. Output of the computer-based design phase: (a) the machined model of the valve cover; (b) the casting equipment.

As for the casting, after defining the division plane, we set a draft angle of 3° on all the vertical surfaces, the minimum thickness was set at 3 mm, a machining allowance of 3 mm was added to all the coupling surfaces, and all edges were rounded. Finally, the entire casting model has been scaled by 4% to compensate for shrinkage. This 3D model is the input for the computer-based manufacturing phase (see Subsect. 3.5) and for the production of the patterns (see Subsect. 3.6).

To complete the mould, the pouring basin, sprue, filter, runner, gates and feeders were designed. The mould was designed to be as simple as possible, with a single sprue with a square section (18 × 18 mm, Fig. 2b). A 20 × 20 mm filter was placed between the sprue and the runner. The transition from sprue to filter up to the runner was particularly modelled in order to improve the fluid dynamics of the molten alloy. From the runner, two gates reach the upper feeders. In fact, this position let the casting system to be easily removed from the casting with a straight simple cut. A knurled block of cast iron was also positioned in the bottom cap area. A trap at the end of the runner prevents unwanted waves or ram effect during alloy pouring.

3.4 Computer-Based and Physical Prototyping Phases

Ultimaker Cura - FFF CAM was used for part build preparation (Fig. 3a). A first prototype (Fig. 3b) of the final machined model was made to test the final geometry of the valve cover with the engine head. A second refined prototype limited to the contact interface of the base flange (Fig. 3c) was 3D printed to test further small refinements to improve the coupling. Both prototypes were 3D printed by a Kentstrapper Verve printer in PolyLactic Acid (PLA) polymer for its affordability and ease of printing.

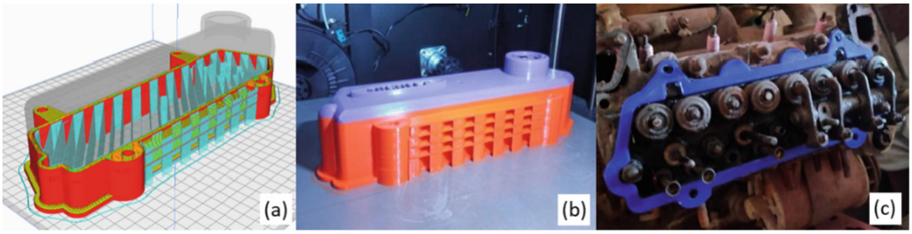

Fig. 3. Output of the prototyping phases: (a) computer-based part build preparation; physical prototypes of the (b) machined model and (c) base flange.

3.5 Computer-Based Manufacturing Phase

All the components of the casting system (foundry equipment, described in Subsect. 3.2) were optimised recurring to casting process simulations with Magma software (Fig. 4a). The presence of porosity in particular was reduced to an acceptable low level by providing a number of feeders on top of the casting. The size of the feeders was optimised through genetic algorithms in Magma. The final height of 30 mm was in the search range from 20 mm to 50 mm. The material solidification was carefully modelled by setting the long freezing range, which resulted more reliable than the short one in our past experience.

The following parameters were used for the casting model:

- Material: AlSi7Mg (also known as EN 42100), with 524 °C Liquidus temperature and 613 °C Solidus temperature.
- Cast iron coolers set at 30 °C initial temperature.
- Sand moulds set as green sand, a classic sand composed of sand, water and an inorganic binder (in our case bentonite) at 30 °C initial temperature.
- Heat Transfer Coefficient (HTC) at alloy-sand contact specified as temperature dependent, specifically as 1000 W/(m^2K) above the Liquidus temperature and 400 W/(m^2K) below the Solidus one, in order to model the air gap formation during the casting shrinkage.

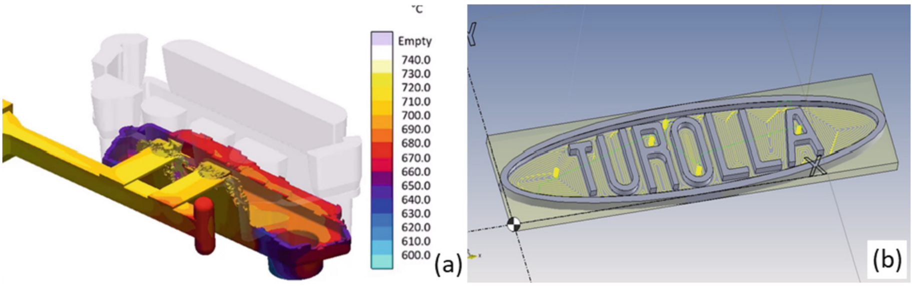

Fig. 4. Output of the computer-based manufacturing phase: (a) casting process and (b) CAM milling simulations.

Originally, the Turolla logo was applied in a second time, and the original component was forged. However, modern CNC machining is the cheapest technology to build a single component, so the CNC process of the Turolla logo was designed using TopSolid CAM milling software (Fig. 4b).

3.6 Physical Manufacturing Phase

The manufacturing steps for the production of the valve cover can be summarized as follows:

- Fabrication of the mould box and of the pattern/core in epoxy resin (which can last up to 400 moulds) (Fig. 5a).
- Secure the pattern into the mould box, fill the mould box with green sand and compact it by vibration.
- Coupling of the two green sand moulds.
- Aluminium casting and cooling phase for solidification of the part.
- Opening of the sand moulds for extracting the cast part (Fig. 5b).
- Post-processing treatments (cutting of the casting system, deburring, grinding, etc.).
- T6 heat treatment of the casting, which involves quenching followed by artificial aging to improve the mechanical properties of the material.
- Secondary machining (milling and drilling, Fig. 5c). High-density wood was pre-inserted into the part to prevent wall flexing during clamping, and suitably shaped wooden wedges were used for the sloping lid walls in contact with the fixture. To create the four holes for the fixing screws, the contact surfaces of the screws were milled by removing 3 mm of allowance and then drilled. Four rectangular section fins were made, equally spaced 7 mm apart, with a thickness of 3 mm and a height of 13.5 mm. The inclined wall where the fins were to be made was levelled to avoid sharp edges.
- Finally, the valve cover was finished with manual processing and subjected to surface abrasion with various sandpapers up to 1000 grit.
- The Turolla logo was machined with a very thin cutter tip (1.5 mm diameter) and glued with a two-component resin to ensure better adhesion to the valve cover. In order to make it very similar to the original, the logo was aged in appearance and sandblasted, to have a matte background and polished letters.

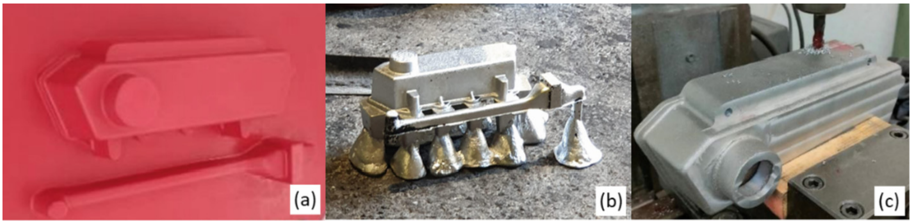

Fig. 5. Output of the physical manufacturing phase: (a) epoxy resin pattern; (b) cast part after mould extraction; (c) machining operations.

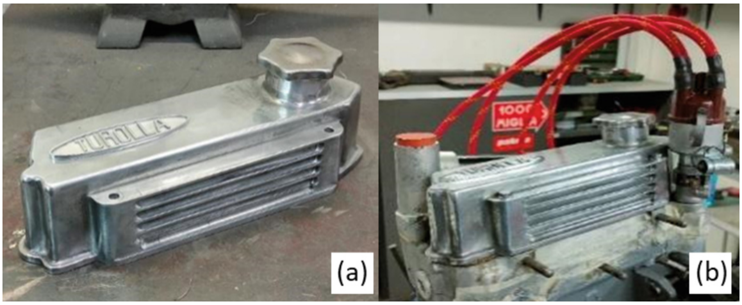

Fig. 6. The final valve cover (a) and its assembly on the engine head (b).

The final geometry and appearance of the valve cover is shown in Fig. 6a.

4 Discussion and Conclusion

The component reproduction approach using traditional foundry technology, supported by CAX tools, is fully applied to define the part design and the related manufacturing process. A functional replica for end-use is then produced and assembled with the original engine (Fig. 6b).

The proposed design approach can be further adopted in similar contexts requiring on-demand, one-off or small batch production of lost or hard-to-find part. On the one hand, this type of approach takes time and requires technical know-how to combine traditional manufacturing with new technological tools. On the other hand, this approach is consistent with the original process, resulting in a handcrafted valve cover like in the 1940s/1950s; leads to an accurate result in terms of piece functionality and constructive effectiveness; leads to a digital model of the part that can be stored, modified and reused when required.

Further design and manufacturing processes will be explored, e.g. direct modelling of the part on the 3D scanned interface of the engine head and metal additive manufacturing of the entire valve cover as a possible manufacturing alternative.

Acknowledgment. The authors acknowledge Gruppo Promotor srl (Ferrara, Italy) and Capricorn Fonderia srl (Modena, Italy) for their valuable support.

References

1. Scheepers, L., Angerer, P., Dragano, N.: Digitalisation in craft enterprises: perceived technostress, readiness for prevention and countermeasures - a qualitative study. Int. J. Environ. Res. Pub. Health **19**, 11349 (2022)
2. Johnson, S.: Classic cars: keep motoring heritage alive. Eng. Technol. **16**, 1–6 (2021)
3. Khajavi, S.H., Salmi, M., Holmström, J.: Additive manufacturing as an enabler of digital spare parts. In: Eyers, D. (eds.) Managing 3D Printing, pp. 45–60. Palgrave Macmillan, Cham, Switzerland (2020)
4. Dalpadulo, E., Petruccioli, A., Gherardini, F., Leali, F.: A review of automotive spare-part reconstruction based on additive manufacturing. J. Manuf. Mater. Process. **6**(6), 133 (2022)
5. Petruccioli, A., Gherardini, F., Leali, F.: Assessment of close-range photogrammetry for the low cost development of 3D models of car bodywork components. Int. J. Interact. Des. Manuf. **16**(2), 703–713 (2022)
6. Otto, K.N., Wood, K.L.: Product Design: Techniques in Reverse Engineering and New Product Development. Prentice Hall, Upper Saddle River, NJ, USA (2006)
7. Fédération Internationale des Véhicules Anciens (FIVA): Turin Charter Handbook (2019). https://fiva.org/download/turin-charter-handbook-updated-2019-english-version/
8. Vergnano, A., Brambilla, E., Bonfiglioli, G.: Efficiency and reliability of gravity die casting models for simulation based design. In: Cavas-Martínez, F., Eynard, B., Fernández Cañavate, F.J., Fernández-Pacheco, D.G., Morer, P., Nigrelli, V. (eds.) Advances on Mechanics, Design Engineering and Manufacturing II. LNME, pp. 3–12. Springer, Cham (2019). https://doi.org/10.1007/978-3-030-12346-8_1
9. Vergnano, A., Salvati, E., Magistrelli, A., Brambilla, E., Veronesi, P., Leali, F.: A method for yield and cycle time improvements in Al alloy casting with enhanced conductivity steel for die construction. Manuf. Rev. **9**, 9–18 (2022)
10. Nonato, M.: Dalle nebbie nasce una scintilla: le Officine Turolla. Marco Nonato self editing, Ferrara, Italia (2020)

Knowledge and Product Data Management

Interoperability Between AR and CAD Systems for Industrial Applications

Emanuele Marino(✉), Loris Barbieri, Fabio Bruno, Marino Mangeruga, and Maurizio Muzzupappa

Department of Mechanical, Energy and Management Engineering (DIMEG), University of Calabria, Pietro Bucci 46C, 87036 Rende, CS, Italy
{emanuele.marino,loris.barbieri,fabio.bruno,marino.mangeruga, maurizio.muzzupappa}@unical.it

Abstract. Augmented Reality (AR) has been widespread over the years in different areas, especially in the manufacturing field, to facilitate the digitization of production processes, and increase productivity and product quality. While AR has grown in popularity, significant barriers exist to its adoption in industry, including high development costs and ineffective interoperability, which limit high flexibility and rapid adaptability required for competitive production systems. Therefore, handling interoperability properly is a key issue in this scenario, especially between AR technology and existing IT systems, widely adopted throughout the product lifecycle. Many of those challenges are related to the compatibility of data representation across these different systems, resulting in data loss or sharing of unusable information. Based on these considerations, this paper first analyzes the main issues related to the interoperability between AR and CAD systems, including data exchange, AR content authoring, and virtual data specifications. To bridge the gap between AR and CAD interoperability, a CAD automation tool is then presented that can support unskilled operators in preparing AR content for industrial applications. Preliminary experimentation is carried out to evaluate the main potentialities due to its adoption, which provides the basis for further implementation and investigation in a real industrial setting.

Keywords: CAD-AR interoperability · Augmented Reality · CAD systems

1 Introduction

Although AR has attracted the interest of many researchers for its huge benefits and has experienced unprecedented growth in recent years, significant barriers exist to its adoption in industry, including high development costs and ineffective interoperability, which limit the high flexibility and rapid adaptability required for competitive production systems [1]. Therefore, handling interoperability properly is a key issue in this scenario, especially between AR technology and existing IT systems, such as CAx, PDM, and PLM systems, which are widely used throughout the product lifecycle. Many of those challenges are related to the compatibility of data representation across these different systems, resulting in data loss or sharing of unusable information [1].

M. Carfagni et al. (Eds.): ADM 2023, LNME, pp. 557–564, 2024.
https://doi.org/10.1007/978-3-031-52075-4_63

Because of these considerations, this paper focuses on some critical factors of AR-CAD interoperability, including data exchange, AR content authoring, and the specifications of virtual information with respect to the industrial activity to be supported. The paper presents also a CAD automation tool that can assist users in creating AR content within a CAD environment and effectively transferring it toward AR systems reducing the gap between these two different environments. A preliminary evaluation is carried out by involving experienced AR developers to assess the potentialities of the proposed CAD automation tool in assisting users in AR content authoring for industrial scenarios.

2 AR Interoperability Issues

Nowadays, the efficient and effective integration of AR in industry is still an open issue. In fact, existing literature has reported on a variety of challenges in implementing AR solutions related to AR interoperability [1, 2], which refers to the ability of different systems and devices to work together seamlessly [3]. From a general point of view, AR interoperability is a complex concept that encompasses many different aspects of AR technology, including compatibility between heterogeneous hardware and software, standardization, data sharing, device and sensor integration, content handling, user input, and AI integration. All these factors are essential for the advancement and wide-scale adoption of AR technology in industrial contexts [2, 4]. Among these factors, data exchange, AR content authoring, and the specifications of virtual information are critical factors as they can significantly limit the efficient and effective applicability of AR in industry if not properly addressed.

2.1 Data Exchange Between CAD and AR Platforms

Data exchange between CAD and AR platforms is of paramount importance to ensure the effective and efficient reuse of engineering data by AR technology for industrial purposes [5]. Unfortunately, there are still several issues in AR data exchange, which originate from the fact that CAD software use a proprietary file format that might be not compatible with AR platforms. They are usually not supported by AR systems natively and, as a consequence, they require further conversions before importing. One common approach is to use neutral file formats, such as .stl, .step, .iges, or .jt [5]. These formats keep geometric data and, some of them, can also contain non-geometric data such as materials, hierarchical structure, manufacturing tolerances, and other types of metadata. Nevertheless, external tools are necessary for importing neutral file formats into common AR platforms, as direct import is not yet supported [1]. These tools may have limitations and may require payment. Therefore, custom development of external tools by qualified developers with specific software development skills may be necessary. A more effective alternative to neutral formats is the use of 3D file formats, such as .fbx, .obj, .dae, .vrml, or .gLTF, as they can be easily imported into AR platforms such as Unity and Unreal Engine [6]. Similarly, computer graphics software, such as Autodesk Maya, Blender or 3D Studio Max can be used to convert neutral file formats into 3D types. At the same time, it is worth noting that the conversion process could result in loss of data or accuracy, so it is fundamental to check the final file to ensure that it has the level of quality and details needed for the intended use. A summary of the main file formats utilized for data exchange between CAD and AR applications, along with their relevant characteristics is shown in Table 1.

In addition to the file format, another important aspect of AR data exchange is the size and complexity of files. Regarding size, AR data can be large because of the high resolution and detailed nature of visual information it contains. This can create challenges for storage, transmission, and processing as the data may take a significant amount of space and require high-performance hardware to handle. At the same time, large files can make it difficult to transmit AR data over networks, especially when dealing with limited bandwidth or high latency. Similarly, the complexity of data can limit their processing in real time, which is often a requirement for AR applications, especially in industry. To overcome some of these issues, optimization and compression techniques are usually adopted. For instance, CAD models are subject to a tessellation process, which translates a B-rep model into a lightweight triangular mesh. Then, this mesh can be also decimated, reducing the number of polygons, and as a consequence, its size and complexity [1]. This allows the model to be rendered more efficiently and smoothly on AR devices. Finally, also scalability represents a factor to be considered as it refers to the fact that AR and CAD environments can have different scales, and this can make it difficult to match the size of the virtual models with the real-world objects.

Table 1. 3D data exchange file formats and their main characteristics.

File type	Geometry	Hierarchy	Material	Metadata (PMI, GD&T, ...)	CAD compatibility	AR compatibility
STL	Yes	No	No	No	Yes	No
STEP	Yes	Yes	Yes	Yes	Yes	No
IGES	Yes	No	Yes	No	Yes	No
JT	Yes	Yes	Yes	Yes	Yes	No
WMRL	Yes	No	Yes	No	Limited	Yes
FBX	Yes	Yes	Yes	No	No	Yes
OBJ	Yes	Limited	Yes	No	Limited	Yes
DAE	Yes	No	Yes	No	No	Yes
glTF	Yes	Yes	Yes	Limited	Limited	Yes

● Yes ● No ● Limited

2.2 AR Content Authoring

AR content authoring [7, 8] refers to the process of creating content using AR authoring tools such as 3D models, animations, and interactive elements, for use in AR applications [9]. A common operation in AR authoring process is the definition of markers, including their position and orientation, which are used to register AR content in the real world during AR visualization. AR authoring tools can be grouped into programmers and non-programmers ones [10]. The former are typically code libraries that require advanced programming skills to users, whereas the latter provide visual scripting functionalities, with a timeline and drag-and-drop functionalities, for creating AR content without writing code. More specifically, the first ones involve using specialized tools and software which require a significant amount of training, and specific programming skills, with the consequence that they are time-consuming and typically used only by expert users [11]. Conversely, the second ones are more recent and allow non-programmer users for selecting from predefined libraries of 3D models and built-in scripts to animate and build interactive AR applications. Although these tools are designed to be user-friendly and require no programming skills, it may still be necessary to possess some technical knowledge and creativity to produce AR content of high quality. These, in fact, are adequate for implementing basic applications with elementary functionalities, and the development of custom or more complex applications still requires specific software development and programming skills. In summary, the level of complexity and technical skill required to use AR authoring tools vary depending on the specific tool and the complexity of the AR content being created [12]. In the industrial context, where operators are trained to use CAx tools, the skills required to use authoring tools represent a limiting factor to the diffusion of AR. Often, in fact, the development and programming of AR applications are outsourced to third parties. This is a solution that may help with demonstration applications but is not effective from the perspective of an integrated use of AR in the product development process, and thus from Industry 4.0 viewpoint. In fact, some custom solutions have been developed for specific activities carried out in the industrial context. For example, Pham and Xiao [13] presented an automatic system capable of creating assembly tasks from analysis of mechanical assembly video. Van Lopik et al. [14] proposed an AR authoring tool for supporting users in creating AR content for repair training operations. Lorenz et al. [15] presented an approach for a 3D-content editor to assist technicians in preparing AR instructions for maintenance of machines.

2.3 AR Content Specifications for Industrial Activities

AR-assisted industrial applications are revolutionizing technical communication since they offer the possibility of making such communication more efficient through the augmentation of digital data and new ways of interacting with it. This trend reflects the growing recognition of the benefits AR can offer in terms of improving communication effectiveness and facilitating a higher level of user engagement and understanding [16]. In this regard, among the open issues limiting AR applicability, there is how AR content should be defined, which information it must provide to the user, to effectively support and simplify an industrial activity, based on its specifics, in order to improve performance and safety of workers, and increase overall productivity. In fact, based on the specific industrial activity that is meant to be supported, it is necessary to identify the appropriate amount and type of information to be displayed in AR in order to make the user's operability more effective and to prevent the AR tool from being counterproductive [17]. For example, in the case of the assembly of components, AR technology can guide human operators with various types of digital information superimposed on a real scene such as

3D models that appear in a specific animated assembly order, text instructions, pictures or videos, and general guidelines for using assembly tools. In the case of maintenance activities, operators can be supported by AR through overlaid digital instructions and schematics on physical equipment, real-time data such as operating parameters and performance metrics, and maintenance procedures. Similarly, inspection activities can also benefit from the adoption of AR by augmenting 3D models, 2D or 3D annotations, including dimensions, tolerances, PMI (product manufacturing information), etc. Of all the possible applications of AR content in an industrial scenario, this paper focuses on the use of 3D CAD models for supporting visual inspection of products through a visual comparison between virtual and real objects.

3 CAD2AR: A CAD Automation Tool

The following shows an exemplification of a CAD automation tool that simplifies interoperability between CAD and AR authoring systems. CAD2AR tool has been developed to be used for industrial applications, specifically to support operators during the authoring of AR content for inspection activities that require the augmentation and alignment of 3D CAD models onto their physical counterparts. Unlike traditional authoring tools, which often involve specific programming skills, the proposed CAD2AR tool can assist CAD operators who lack coding expertise. It allows them to accomplish AR authoring stages directly in the CAD environment, including importing CAD models, defining markers positioning, generating and exporting AR data in a compatible format for AR systems. The tool has been programmed by using the CAD software's API (Application Programming Interface) with a modular architecture, enabling the integration of specific features for other industrial domains without any restrictions. The following figure (Fig. 1) depicts the data workflow that consists of two different stages: preparation and data export. Both stages allow the user to perform AR content authoring within the CAD environment and generate AR data compatible with AR systems for inspection activities.

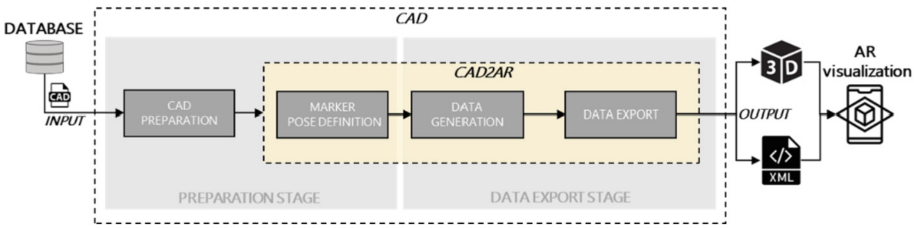

Fig. 1. Data workflow of the proposed CAD automation tool.

In the first stage, i.e. the preparation one, CAD models (single components or assemblies) are modelled or retrieved from the database and imported into the CAD environment. In the context of AR-assisted industrial activities, in fact, CAD models are usually overlaid on top of real world and, in the case of inspection of products, superimposed onto their physical counterparts. In this way, operators can visually inspect real products by comparing virtual and real objects. This activity can be carried out at different stages throughout the manufacturing process, serving different purposes. For instance, it can be used to verify the absence of components or whether their geometries and assembly positions are correct. The second operation of the first stage involves modelling of markers that act as reference systems for the alignment of virtual content into the real environment during the AR visualization when a marker-based approach is adopted. In general, the larger the size of the product, the more markers the user defines to improve the accuracy of AR content registration. Therefore, the user then attaches physical markers into real world at the same locations occupied by the virtual ones in the CAD environment to achieve this alignment during AR visualization. Markers' pose is calculated based on the absolute reference coordinate system of the CAD environment by exploiting specific functions provided by CAD's API. In the last stage, i.e. the data export one, two main operations are carried out: converting CAD models into a lightweight compatible 3D file format, such as .gLTF, and generating an XML file that contains all the data about markers in terms of position and orientation. These two outputs, i.e., the converted 3D models and the XML file, are finally exported from the CAD software that can be used for the inspection of products during AR visualization. In this scenario, two main operations are performed: augmentation of 3D virtual models onto real objects through AR capabilities and the alignment achieved through the recognition of physical markers.

3.1 Experiments and Results

A preliminary evaluation has been conducted by involving 8 male experienced AR developers with an average age of 30.5 (SD = 4.5) to assess the benefits due to the adoption of the CAD automation tool. The study has consisted of comparing the proposed tool with an AR authoring platform, i.e. Unity, in the creation of AR content for the industrial inspection context. More specifically, the participants have been invited to model virtual markers and export AR data needed for the augmented visualization using functionalities provided by the two authoring tools. As objective metrics, the completion time to perform the task has been taken into account to evaluate the efficiency of both tools. A total of five different assemblies of increasing complexity, in terms of geometries and number of components, have been considered as shown in Fig. 2. This was justified by the fact that an ever-increased number of markers have been modelled onto virtual

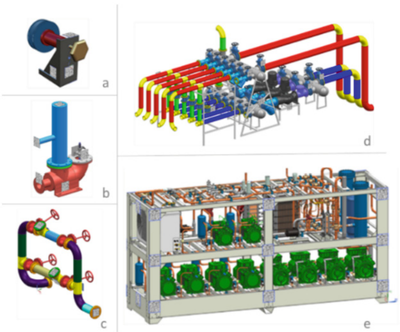

assembly	n° of components	n° of markers
a	8	4
b	14	7
c	32	8
d	87	20
e	215	22

Fig. 2. 3D model assemblies used for the experimentation and related number of markers.

components in the same positions with the two authoring tools as the complexity of assemblies increased.

Figure 3 shows the results of the preliminary evaluation, considering the average time needed to prepare the augmented scenario by using both authoring tools.

In particular, what emerged is that the use of the proposed CAD automation tool reduces the mean time required to complete the authoring task with respect to the other AR authoring tool. This is more evident when the complexity of assembly and, in turn, the number of markers to be modelled increases. Another aspect that emerged from this analysis was that utilizing the proposed CAD automation tool resulted in more precise placement of virtual markers compared to relying solely on the authoring tool. This is because the CAD environment leverages the geometric features of CAD models, which cannot be fully replicated in the case of tessellated models. Although this preliminary evaluation has produced interesting findings, it is worth noting that the study's narrow focus on a single case study limits the generalizability of the results. Furthermore, the experimentation was limited to one group of AR experts without considering users with different levels of technical expertise and background knowledge.

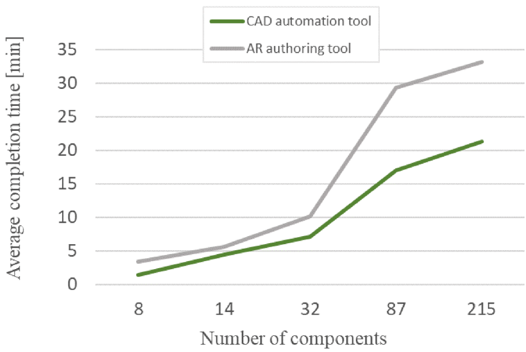

Fig. 3. Average completion time of AR content authoring.

4 Conclusions

This paper has presented an overview of main interoperability challenges that can hinder the effective adoption and integration of AR in industrial environments. Specifically, the paper addressed three critical issues: data exchange, AR content authoring, and AR data specifications, which if not properly addressed, can significantly limit the widespread adoption of AR technology in industry. In this regard, the paper proposed a CAD automation tool that can be used to prepare AR content to assist operators in performing inspection activities on real products. A preliminary evaluation was conducted to compare the proposed tool with another authoring tool, resulting in interesting findings that warrant further experimentation in different use cases. Future research directions will involve the use of both objective and subjective metrics to evaluate not only potential enhancements in user performance but also user satisfaction and cognitive workload required to complete the authoring task.

Acknowledgments. This research has been partially funded by the project SMILE, funded by the Italian MISE under the PON "Imprese e Competitività" program. Project n. F/190084/03/X44 – CUP: B21B19000530008 COR: 1679960.

References

1. Vernica, T., Lipman, R., Bernstein, W.Z.: Visualizing model-based product definitions in augmented reality. In: International Design Engineering Technical Conferences and Computers and Information in Engineering Conference, vol. 85376. ASME (2021)
2. Masood, T., Egger, J.: Augmented reality in support of Industry 4.0-implementation challenges and success factors. Robot. Comput. Integr. Manuf. **58**, 181–195 (2019)
3. Arena, F., Collotta, M., Pau, G., Termine, F.: An overview of augmented reality. Computers **11**(2), 28 (2022)
4. Masood, T., Egger, J.: Adopting augmented reality in the age of industrial digitalisation. Comput. Ind. **115**, 103–112 (2020)
5. Han, Y.S., Lee, J., Lee, J., Lee, W., Lee, K.: 3D CAD data extraction and conversion for application of augmented/virtual reality to the construction of ships and offshore structures. Int. J. Comput. Integr. Manuf. **32**(7), 658–668 (2019)
6. Mohan, S.G., Bhat, D., Hegde, A., Madguni, A.: Refined interiors using augmented reality. In: 2022 IEEE 2nd Mysore Sub Section International Conference, pp. 1–7. IEEE (2022)
7. Salonen, T., Sääski, J., Woodward, C., Korkalo, O., Marstio, I., Rainio, K.: Data pipeline from CAD to AR based assembly instructions. In: ASME World Conference on Innovative Virtual Reality, vol. 43376, pp. 165–168. ASME (2009)
8. Syed, T.A., et al.: In-depth review of augmented reality: tracking technologies, development tools, AR displays, collaborative AR, and security concerns. Sensors **23**(1), 146 (2022)
9. Gimeno, J., Morillo, P., Orduña, J.M., Fernández, M.: A new AR authoring tool using depth maps for industrial procedures. Comput. Ind. **64**(9), 1263–1271 (2013)
10. Wang, Y., Langlotz, T., Billinghurst, M., Bell, T.: An authoring tool for mobile phone AR environments. In: Proceedings of New Zealand Computer Science Research Student Conference, vol. 9, pp. 1–4 (2009)
11. Bhattacharya, B., Winer, E.H.: Augmented reality via expert demonstration authoring (AREDA). Comput. Ind. **105**, 61–79 (2019)
12. Gonzalez, A.V., et al.: A comparison of desktop and augmented reality scenario-based training authoring tools. In: 2019 IEEE International Symposium on Mixed and Augmented Reality (ISMAR), pp. 339–350. IEEE (2019)
13. Pham, T A., Xiao, Y.: Unsupervised workflow extraction from first-person video of mechanical assembly. In: Proceedings of the 19th International Workshop on Mobile Computing Systems & Applications, pp. 31–36 (2018)
14. van Lopik, K., Sinclair, M., Sharpe, R., Conway, P., West, A.: Developing augmented reality capabilities for industry 4.0 small enterprises: lessons learnt from a content authoring case study. Comput. Ind. **117**, 103208 (2020)
15. Lorenz, M., Knopp, S., Kim, J., Klimant, P.: Industrial augmented reality: 3D-content editor for augmented reality maintenance worker support system. In: 2020 IEEE International Symposium on Mixed and Augmented Reality Adjunct, pp. 203–205. IEEE (2020)
16. Egger, J., Masood, T.: Augmented reality in support of intelligent manufacturing – a systematic literature review. Comput. Ind. Eng. **140**, 106195 (2020)
17. Gattullo, M., Evangelista, A., Uva, A.E., Fiorentino, M., Gabbard, J.L.: What, how, and why are visual assets used in industrial augmented reality? A systematic review and classification in maintenance, assembly, and training (from 1997 to 2019). IEEE Trans. Vis. Comput. Graph. **28**, 1443–1456 (2022)

VQR Scores Estimation Based on PCA Analysis

Paolo Neri(✉)

University of Pisa, 56122 Pisa, Italy
paolo.neri@unipi.it

Abstract. The "Research Quality Assessment" is a procedure promoted by ANVUR in the academic field, aimed at evaluating the paper quality in academics. Even if the main evaluation criteria are public, the final score of each paper is not directly obtained through an algorithm based on quantitative data, but can be affected by the peer review process and qualitative considerations. Thus, it is not possible to a priori know the outcome of each specific publication. In the present research activity, the VQR results of an Italian Department in the industrial engineering field were analyzed through a PCA approach. Additionally, a score estimation algorithm was developed, based on numerical evaluation parameters, which can quantitatively describe the paper's quality. Even if the actual final score is not deterministic because of the peer review process, a strong correlation between the predicted and the actual scores was found in the analyzed data. The estimation for the specific paper can be faulty, nevertheless, the developed algorithm demonstrated consistency in terms of overall Department performance, especially for the higher scores.

Keywords: VQR scores estimation · PCA analysis · Regression algorithm · Quality assessment

1 Introduction

The evaluation of scientific publications is a challenging task, since many factors can be taken into account. Several different quality indexes were defined in the literature: an overview and an analysis of the main proposal are reported in [1], and a study about the importance of quantity or quality of publications is provided in [2]. In this broad field, the Italian National Agency for the Evaluation of Universities and Research Institutes (ANVUR) promoted the so called Research Quality Assessment (VQR, from the Italian translation of *Valutazione della Qualità della Ricerca*) starting in 2004 [3, 4]. The evaluation is referred to public universities and research institutes, and it is also extended to volunteer private institutions. VQR is repeated periodically, covering the scientific production of the previous five years. The evaluation is based on three main aspects, i.e. rigors, originality and impact of the papers. Each aspect receives a score in the range of 0–10, which is then summed to obtain the final paper outcome in the range of 0–30. The papers are divided into Scientific Areas, and the score of each paper is assessed by the groups of experts for evaluation (GEV). The group is composed of highly qualified

M. Carfagni et al. (Eds.): ADM 2023, LNME, pp. 565–572, 2024.
https://doi.org/10.1007/978-3-031-52075-4_64

Italian and foreign scholars, who are experts in each area. The evaluation is obtained by combining quantitative data (e.g. Journal metrics or paper citations) and qualitative aspects (e.g. scientific soundness and novelty). Additionally, the evaluation criteria are mostly devoted to publication quality instead of quantity, since each scholar could submit a maximum of four papers published in the considered period.

In this paper, the results of the third VQR exercise, which was recently completed and covered the papers between 2015 and 2019, are analyzed. No comments nor conclusions are drawn about the strength and weaknesses of the VQR approach, which are outside the aim of the present research. This paper instead analyses the correlation between specific quantitative parameters of a Department in the industrial engineering field (referred to as Institution, in the following) and the VQR scores. The statistical analyses of the evaluation outcomes allowed the development of a regression algorithm, based on principal component analysis (PCA) which can estimate the average expected VQR outcome of the Institution, provided a pool of presented papers. In other words, the developed algorithm is not able to precisely predict the score of a single paper, but it demonstrated to be reliable in statistically estimating the overall performance of the studied Institution.

2 Data Set Description

The studied dataset was composed of the publications which were submitted by the Institution for the third VQR exercise. The evaluation procedure allowed the submission of a maximum of four publications for each researcher, imposing a limitation on the total number of presented papers equal to three times the number of employees. For these reasons, the Institution presented a total number of 306 papers. Since the final VQR outcome of each paper is confidential, the analysis was based on a subset of 217 papers, whose VQR scores were voluntarily provided by the authors. The selection was limited to Area 09: Industrial engineering and information technology only, thus excluding the contribution belonging to other areas of the Institution. For each paper, many qualitative and quantitative data were available. The present analysis was limited to the quantitative numerical variables, to simplify the algorithm development. In particular, more than 20 indexes were taken into account, including the number of authors, the publication year, the number of citations on the Scopus database (both total and excluding self-citations), the number of citations on Web of Science (WoS) database, Scimago Journal Ranking (SJR), Source Normalized Impact per Paper (SNIP), publication year, Impact Factor (IF) and five years IF. Additionally, four different scores were considered as the papers' VQR outcome: rigors, originality, impact, and total score. In the present analysis, the VQR evaluation system is studied following a black box approach, considering the paper metrics as input and the scores as output. All the numerical variables (both input and outputs) were normalized along the dataset, so that each variable resulted to have zero mean value and unitary standard deviation. This normalization allowed obtaining a robust comparison between different variables with different orders of magnitude. It is worth noting that the adopted procedure impairs the possibility to recover the absolute score of each paper starting from the normalized score.

3 VQR Results Analysis

3.1 Single Index Analysis

A first attempt to analyze VQR results was performed by considering the correlation between single relevant indexes and the different scores of the paper. In particular, two indexes were considered in this stage: IF and total citation number. A plot could be drawn having on the horizontal axis one of the indexes, and on the vertical axis the total score of the paper. Figure 1 shows the results of this analysis, highlighting that using a single index allows drawing a lower bound of the score. In other words, provided the value of the index, it is possible to estimate the minimum expected score, but not the maximum. Indeed, the left side of the plots shows that even papers with really low IF or citation numbers could receive high scores.

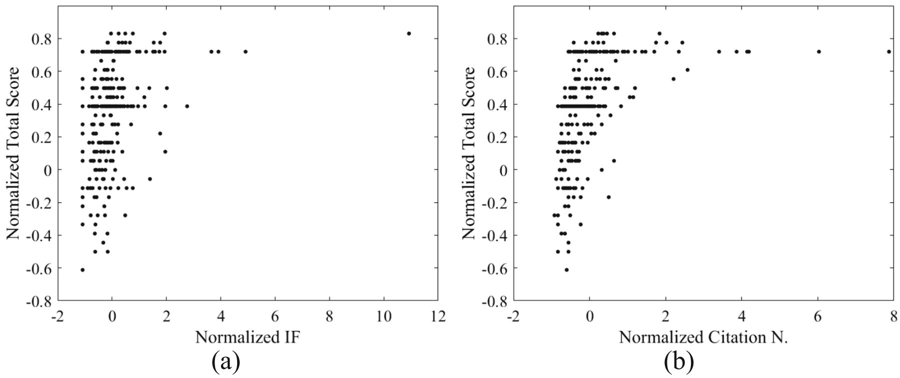

Fig. 1. Single parameter influence: (a) IF and (c) total number of citations.

The plots also highlight that the outliers, i.e. papers with extremely high values of the index, also received the maximum score. This is a trivial conclusion, but only applies to a really small number of papers. The same analysis was repeated for other indexes (e.g. SJR), also considering rigors, originality and impact scores singularly, providing really similar results. This allowed concluding that, for the majority of the papers, the final score cannot be directly related to the value of a single index.

3.2 PCA Analysis

To investigate the possible correlation between the scores and the papers' indexes, a multivariable analysis was conducted. Many possible indexes are to be considered, and the definition of the proper combination is not trivial. Thus, to obtain an objective evaluation of the population, a Principal Component Analysis approach was used, and the data were processed through the Partial Least Squares Regression (PLSR) algorithm [5–7]. Based on single value decomposition, the algorithm can compute a linear least square fit of the data. The results depend on the number of eigenvectors to be considered, thus the algorithm also provides the percentage of variance explained by the regression model if additional eigenvectors are progressively added. The eigenvectors do not directly correspond to single indexes of the analysis, but rather to a combination of more inputs. It is possible to plot the explanation percentage with respect to the number of considered eigenvectors: the higher the percentage, the higher the correlation between inputs and outputs. The results of this analysis for the whole population are reported in Fig. 2(a), with reference to the total VQR score.

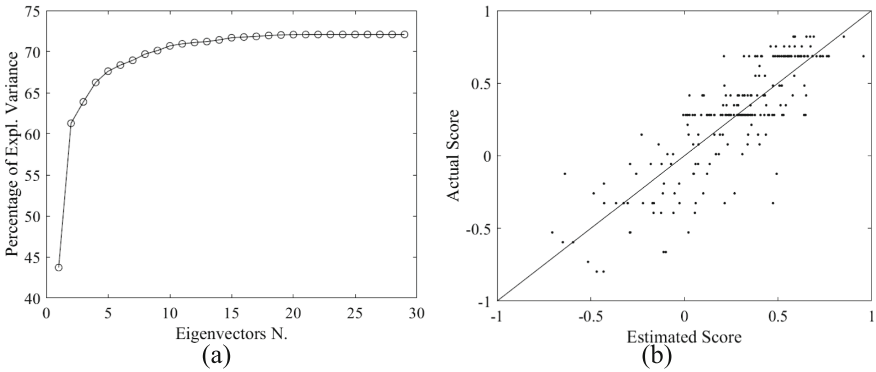

Fig. 2. PLSR results for total score: (a) percentage of explained variance and (b) linear fit.

The total score provides a reasonable percentage of explained variance close to 70%, thus allowing to estimate the possible VQR outcome of the papers. It is worth noting that, selecting nine eigenvectors, the algorithm reaches the plateau in explanation percentage, thus nine eigenvectors were used for the following analysis. This allowed using the PSLR algorithm to compute a reliable linear fit of the population, i.e. compute an estimation of the VQR total score starting from the considered indexes. The results are reported in Fig. 2(b) for the total score. The black dots represent the studied population, while the black line represents the theoretical line corresponding to a perfect correspondence between estimated and actual scores. As can be seen, the estimated values are reasonably correlated with the actual score, showing a Pearson correlation coefficient [8] $r = 0.838$. The dispersion in the data is coherent with the results of Fig. 2(a), which shows that a relevant percentage of unexplained variance is still present in the population.

3.3 Correlation with Different Scores

A similar analysis was repeated for the single scores, i.e. originality, rigors and impact. The PLSR algorithm was used to assess the percentage of explained variance and to predict the scores through linear regression. Figure 3 shows the results in terms of explained variance: the green, red and blue curves are referred to originality, rigors and impact scores, respectively.

As can be noted, the impact score provides the highest explanation percentage (close to 75%), while the originality and rigors scores provide lower percentages (close to 50%). This can be ascribed to the fact that the impact can be more objectively related to the papers' indexes, while the other scores are more subjective during the review process.

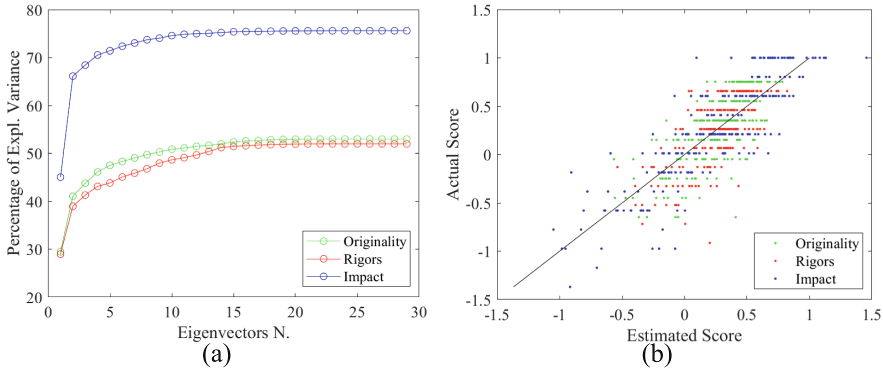

Fig. 3. PLSR results for single scores: (a) percentage of explained variance and (b) linear fit.

The linear regression results, reported in Fig. 3(b), confirm that the impact (blue dots, $r = 0.861$) estimation performs better with respect to the originality (green dots, $r = 0.709$) and rigors (red dots, $r = 0.693$) estimations. The comparison between Fig. 3 and Fig. 2 shows that the algorithm performance for the total scores is much closer to the impact estimation than to the other scores, meaning that the higher aleatory levels of the originality and rigors scores are balanced in the total score computation.

4 Estimation of Actual VQR Results

4.1 Estimation Reliability

The estimation performance was further investigated by a deeper result analysis. The linear regression algorithm of course provides a real number, while the actual VQR evaluation procedure was discretized with a step of 0.5 points. For this reason, the same discretization was applied to the estimated values. Then, it was possible to divide the data by grouping all the papers having the same estimated score. For each group, the mean value and the standard deviation of the actual VQR scores of the papers belonging to the group were computed. The results are reported in Fig. 4. The plot shows the papers with blue dots, where the scores are discretized with the 0.5 steps (before the normalization). The mean value of each score group is reported with a red cross, while the black dashed lines represent the mean value of each group plus and minus the standard deviation (σ) of the same group.

As can be noted, the plot shows some differences between the higher scores region and the lower scores region. In the higher scores region, the mean value of the actual VQR scores is perfectly aligned with the 45° line, meaning that the score estimation is reliable on average. Additionally, the standard deviation in this region is approximately constant for any paper group. The only exception is represented by the papers with the maximum scores, where a really small number of papers was present and, thus, mean value and standard deviation are not representative. On the other hand, the lower scores region shows more noise in the mean value of the scores (i.e. difference with respect to the 45° line) and in the standard deviation, thus proving a less reliable estimation.

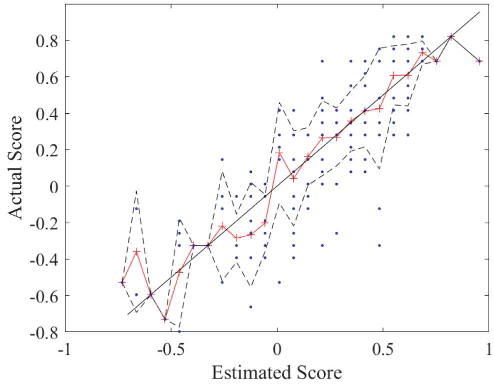

Fig. 4. Algorithm estimation: mean value and standard deviation.

This can be ascribed to the fact that the evaluation of higher quality papers is more objective, based on Journal metrics and citation performances, while the evaluation of lower quality papers is more subjective during peer review.

4.2 Estimation Validation

To validate the proposed approach, it is crucial to estimate the score of papers that were not used to set up the regression algorithm. This allows to avoid bias in the algorithm. Additionally, the estimation quality can be assessed only if the actual VQR score of the paper is known. Thus, the data set was divided into two subsets, called training and test. The training set is then used to set up the regression algorithm, while the test set (which is not used in the algorithm setup) is used to assess the reliability of the evaluated scores. Random indexing was used to define the two subsets, choosing 160 papers for the training set and the remaining 57 papers for the test set. The results are reported in Fig. 5, which is drawn as done for Fig. 4, with reference to the training set. Additionally, the test set was added to the plot with magenta dots.

The plot confirms the comments raised for Fig. 4, with the higher scores region providing a more reliable estimation of the scores, at least on average. Additionally, the distribution of the test papers (i.e. magenta dots) is perfectly included in the training set distribution, having just a few papers outside the $\pm\sigma$ confidence region. This allows concluding that the proposed method can estimate the actual VQR scores of the papers, at least in terms of mean value at the Institution level. In other words, the score estimation of a single paper can be fallacious, but the overall Institution's performance considering the whole set of available papers is reliable. Hence, the method can provide an estimation of the Institution's performance, allowing comparing different papers sets while selecting the best papers for VQR evaluation.

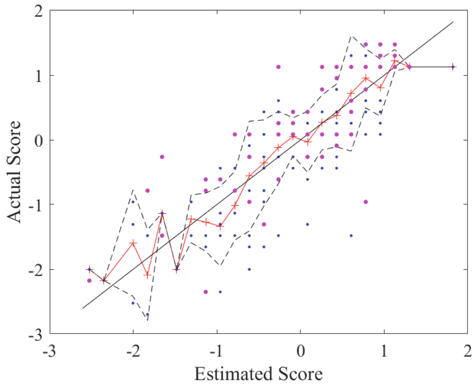

Fig. 5. Algorithm estimation: comparison between training and test sets.

5 Conclusions

This paper describes a statistical analysis of VQR results for a specific Institution. The actual VQR scores of most of the evaluated papers were voluntarily provided by the authors, thus allowing studying possible correlations between papers' indexes and VQR outcomes. The scores and the indexes were normalized to have a zero mean value and unitary standard deviation. In this research, the analysis is limited to quantitative numerical indexes, such as Journal impact factor, total number of citations, etc. The preliminary analysis allowed concluding that a single index can only provide a lower bound of the scores, thus it is not possible to directly estimate the actual score by considering a single index. For this reason, the investigation was extended by considering the combined effect of different parameters, by exploiting principal component analysis and singular value decomposition approach, thus applying a linear regression algorithm. The whole dataset (composed of 217 papers from the same Institution, Area 09) was first analyzed with the proposed algorithm to assess if the method is reliable in VQR scores estimation, proving that a strong correlation between the estimated scores and the mean value of the actual VQR scores exists, especially in the higher scores region. Furthermore, the proposed approach was validated by dividing the dataset into two subsets: training and test. The algorithm was updated by considering the training set only, and then it was used to estimate the scores of the test set, which was not used for algorithm setup. The results confirmed that the algorithm can provide a reliable estimation of the actual VQR outcomes, at least in terms of the average for the whole Institution. Thus, the proposed approach can be considered a reliable tool to select the papers to be presented for future VQR evaluation.

Further research development could be carried out by considering further indexes (e.g. ratio between existing indexes), which could provide a deeper insight into the explainable variance. Additionally, the results could benefit from the analysis of a wider dataset, i.e. adding more papers from different Institutions (provided that they are referred to the same scientific Area, which can impact the VQR evaluation criteria).

References

1. Santos, A.A.D., Dutra, M.L.: Indexes for evaluating research groups: challenges and opportunities. In: Bisset Álvarez, E. (ed.) DIONE 2021. LNICSSITE, vol. 378, pp. 41–53. Springer, Cham (2021). https://doi.org/10.1007/978-3-030-77417-2_3
2. Kaur, J., Ferrara, E., Menczer, F., Flammini, A., Radicchi, F.: Quality versus quantity in scientific impact. J. Informetr. **9**, 800–808 (2015)
3. ANVUR. https://www.anvur.it/en/activities/vqr/. Accessed 06 Mar 2023
4. Zanon, B.: Research quality assessment and planning journals. The Italian perspective. Ital. J. Plann. Pract. **2**, 96–123 (2012)
5. Chong, I.G., Jun, C.H.: Performance of some variable selection methods when multicollinearity is present. Chemom. Intell. Lab. Syst. **78**, 3–112 (2005)
6. Rosipal, R., Krämer, N.: Overview and recent advances in partial least squares. In: Saunders, C., Grobelnik, M., Gunn, S., Shawe-Taylor, J. (eds.) SLSFS 2005. LNCS, vol. 3940, pp. 34–51. Springer, Heidelberg (2006). https://doi.org/10.1007/11752790_2
7. de Jong, S.: SIMPLS: An alternative approach to partial least squares regression. Chemometr. Intell. Lab. Syst.Intell. Lab. Syst. **18**, 251–263 (1993)
8. Pearson, K.: VII. Note on regression and inheritance in the case of two parents. Proc. Roy. Soc. London **58** (1895). https://doi.org/10.1098/rspl.1895.0041

Data Handling of 3D Geometric Model with Augmented Information for Cultural Heritage

Luca Di Angelo[1,2](✉), Paolo Di Stefano[1,2], Emanuele Guardiani[1,2], Antonio Mancuso[3], and Giuseppe Marannano[3]

[1] Department of Industrial and Information Engineering, and of Economics, University of L'Aquila, Via G. Gronchi 18, 67100 L'Aquila, Italy
luca.diangelo@univaq.it

[2] University of L'Aquila, Piazzale Pontieri 1, 67040 HeritechneMonteluco Di Roio, AQ, Italy

[3] Department of Engineering, University of Palermo, Viale Delle Scienze 90128, Palermo, Italy

Abstract. In a digital world where technological development allows the implementation of computer-based methods that can objectively support human activities, it is no more conceivable that activities such as the analysis, classification, and reconstruction of archaeological ceramics are made manually. This determines that expert operators are involved in time-consuming, tedious, poorly repeatable, and reproducible activities whose results depend on his/her experience. This problem concerns the need for robust and reliable automatic methods supporting the operator in these activities. To address these problems, in the last years, the University of L'Aquila research group published robust and reliable methods based on the codification of archaeologists' knowledge in recognizing the most significant geometric and morphological features of sherds. With such tools now available, producing more objective knowledge referring to a huge amount of sherds, the need arises to develop computer-based systems capable of sharing this knowledge.

For this purpose, in this paper, a dedicated database is proposed. Particular efforts were made to implement an intuitive and interactive web interface with commands that co-determine the essential interaction of the archaeologist with the fragments in the traditional method.

Keywords: Computer methods in archaeology · Automatic features recognition · Innovative representation scheme · Semantic annotations · Web-based application

1 Introduction

The "UNESCO, ICCROM, ICOMOS (1994)" (Nara Document on Authenticity, article 13. http://www.international.icomos.org/charters/nara e.html) recommends that an essential aim of the cultural heritage (CH) is the preservation of the authenticity and integrity of archaeological excavations and finds through the following activities:

- Archaeological excavation, including field and underwater excavations;

M. Carfagni et al. (Eds.): ADM 2023, LNME, pp. 573–580, 2024.
https://doi.org/10.1007/978-3-031-52075-4_65

- Archaeological research, devoted to finding the historical, artistic, and scientific value of relics and investigating the historical process, the state of civilization, and the technological level;
- Archive management, making it possible to collect, record, organize, add, delete, and modify information about relics;
- Conservation, monitoring, storing safely, and restoring heritage items;
- Exhibition, including exhibitions in museums, onsite, or on the Web;
- Utilization of cultural heritage through film, television, game production, imitation, printing, and publications.

Despite the scientific community's efforts, these goals must be satisfactorily achieved. This condition is common to all artifacts, including ceramics, most found in archaeological excavations, and essential to getting information about the site's history, economy, and art. The traditional techniques concerning archeological research, archive management, conservation, exhibition, and utilization are based on manual activities performed by skilled operators. Typically, archaeologists assign attributes to the ceramic material by analyzing shape, dimensions, decoration, technological elements, color, and material [1]. Decoration, technological features, and color are examined through visual analysis, whereas shape and dimensions characterization is primarily based on the findings' graphical representation [2]. Since the results of the previous studies are stored in paper catalogs, the operator, by visual comparison with known classifications, assigns each analyzed sherd to a specific ceramic typology.

The traditional method for ceramics analysis presents limitations in the study of the find and knowledge sharing. As to the first aspect, in a previous paper [3], the authors demonstrated that the traditional method for shape and dimensional characterization is neither reproducible nor repeatable for the graphical representation of sherds, even for "indicative" ones. In archaeology, the term "indicative" refers to fragments having features such as pieces of rim, base, and presence of grooves that help the archaeologists orient the sherd. So, in the archaeology practice, the non-indicative fragments (walls without pieces of rim, base, or groove), since archaeologists cannot orient them, they are not analyzed, although they are most parts of the finds and have essential information about the shape of the original pottery profile. Among all these approaches, the only one capable of recognizing the geometric and morphological features analyzed by archaeologists is the one proposed by the research group of the University of L'Aquila and published in ([4, 5], and [6]). The segmentation method analyzes the differential geometrical properties and topological invariants. Starting from the discretized models of the sherds, the published methods automatically segment axially-symmetric features (the rim, internal and external wall, and base) and non-axially symmetric ones (handles and constant radius features such as decorations). The method applied by the authors to hundreds of real archaeological fragments (most of which were "not indicative") produced results following skilled archaeologist evaluations.

To achieve the goals set by UNESCO, tools must be developed to share the knowledge derived from these new tools. Since these tools must support the archaeologists' activities, rather than sharing their use that requires specific skills, the aim should be to share the results by implementing 3D information systems with intuitive and interactive interfaces that allow archaeological pottery visualization and documentation.

The cataloging of this information in a structured way that allows quick access, clustering, and comparison providing adequate support for the classification and interpretation, is not trivial [7]. The solution to this problem proposed in the literature is using relational databases management systems (RDBMS) that can manage heterogeneous sources, data structures, content, and formats. By analyzing the published databases/structures managing the shape and morphology of sherds, they have a variety of structures and formats; as a direct consequence, this makes it difficult to exchange data among researchers [8]. Furthermore, none of them has an intuitive and interactive web interface with which the operator can interact with the pottery and add information to help the scientific community add knowledge ([9–11], and [12]).

To contribute significantly to this field, the paper proposes a semantic scheme for cataloging digital finds of ceramics that includes the information necessary for correct and accurate documentation of resources, according to the most accredited methodologies for digital libraries. A web client will use this semantic scheme to catalog, visualize, manipulate, and semantic annotate 3D digital objects and transfer annotations between models. The website will give users (archeologists, researchers, etc..) a place to discuss the research: it will be possible to manipulate the 3D object obtained by the feature recognition process and, also, it will be possible to contribute to enrich and refine existing information provided by other experts on the objects displayed in the web browser and stored in the database. The procedure will be applied and tested for real sherds from different archeological sites.

2 Computer-Based Method

The database presented in the paper is fed with the results of the automatic methodologies proposed in ([3–5], and [9]) and implemented in *Keramodeo V1*. Starting from the parameters shown in Fig. 1a), for each 3D discretized model, *Keramodeo V1* performs the evaluations of:

- the differential geometric properties (normal and curvatures at each mesh vertex) [13];
- the axis of symmetry [13];
- the segmentation of the geometric and morphological features [5];
- the segmentation and characterization of the dimensional features [4];
- the construction of the representative 2d profile of the sherd [3].

Readers can find more details in the corresponding papers cited above. Once the processing is complete, after an expert archaeologist has supervised and accepted the processing, the data are saved from being imported into the database (Fig. 1 b).

The structure of the website is shown below. Figure 2 shows the login page where the user must enter the credentials to access (if already available) or create a new user account.

Once logged in, Fig. 3 shows the website's home page (dashboard) architecture. Figure 3(a) show, on the left side, the main menu allows the navigation between the different sections (collections), i.e., between the macro-categories of already cataloged archaeological pottery finds. In the central part of the body page (Fig. 3b) is shown a

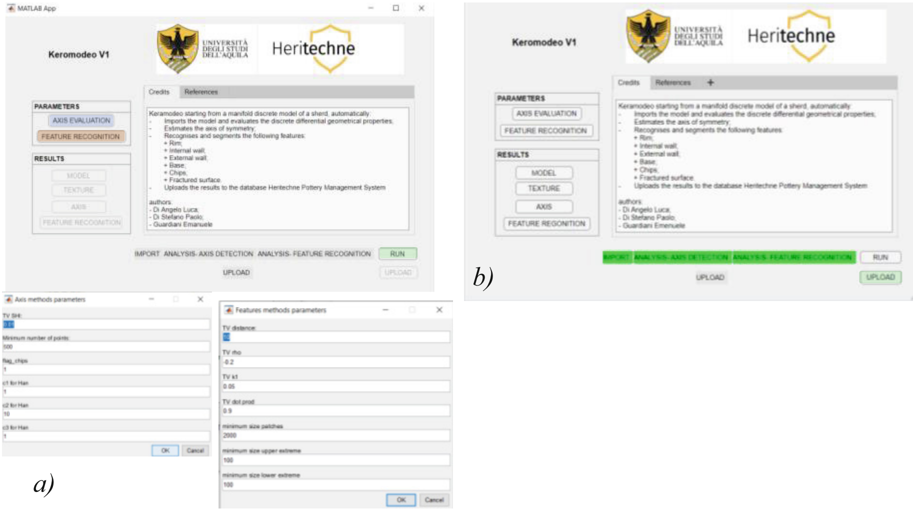

Fig. 1. The Keramodeo GUI used to generate the data for the database.

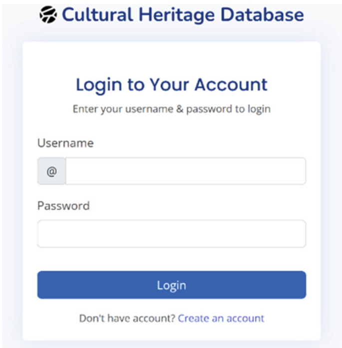

Fig. 2. Website login page

table with the latest objects already stored in the database, with information on views and the number of comments. The comments, ordered by descending date, are shown in the right section of the home page (Fig. 3c).

In the dashboard (or using the search menu on the header), the user can select a single object (model) to obtain the information stored in the database. Figure 4 shows the object viewer module. The user interface provides all the working tools for interacting effectively and immediately with the 3D CAD model. In particular, the "menu icons" on the right side of the interface allow easy access to various display functions and features. In more detail, these buttons enable making user interacting with the web interface, changing the display options or the set of features to display.

The button (C) of Fig. 3 allows the complete display of the 3D CAD model (see Fig. 4a), with that it is possible to interact dynamically using the mouse keys (see Fig. 4b). The required model is loaded into the browser in the form of an.obj or.stl file.

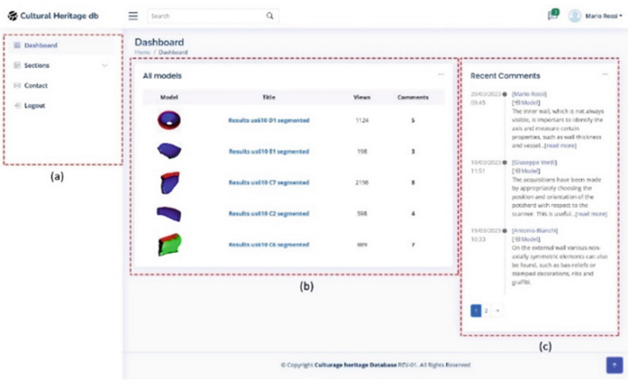

Fig. 3. Website structure.

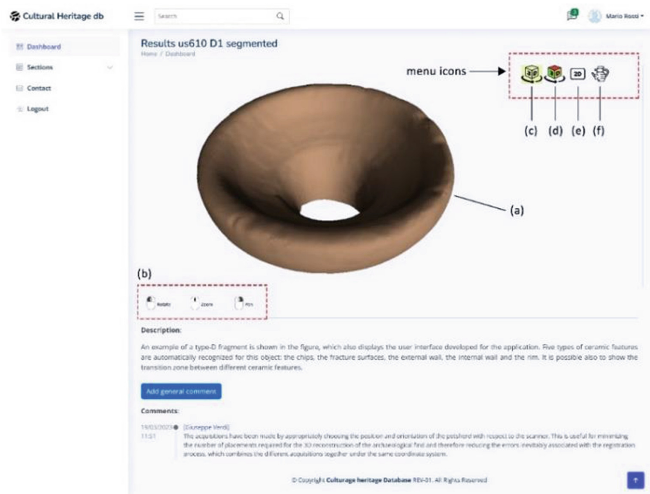

Fig. 4. Structure of the object viewer module

The button (d) of Fig. 4 allows the ceramic features to be displayed directly on the three-dimensional cad model. As shown in Fig. 5, five ceramic features are automatically recognized for the represented object: the chips, the fracture surfaces, the external wall, the internal wall, and the rim. It is also possible to show the transition zone between different ceramic features. An interactive legend displayed on the right side of the 3D object (Fig. 5a), in addition to showing the color of the features, also shows the number of comments entered by users for the given feature. Selecting a feature on the legend makes it possible to highlight the feature extension on the CAD model and simultaneously show the comments users enter (Fig. 5b).

The button (e) of Fig. 4 allows the visualization of the 2D model profile and the archaeological sherd model's main geometrical and dimensional properties (see Fig. 6).

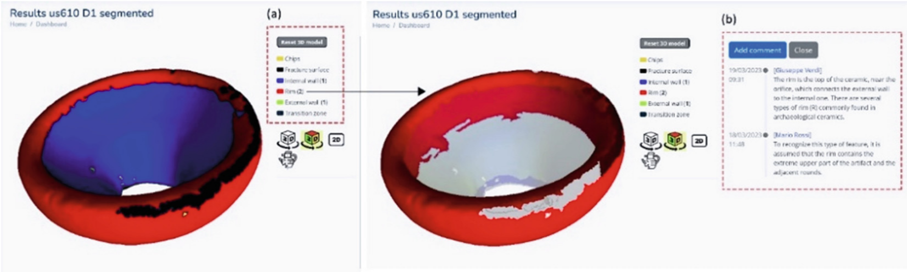

Fig. 5. Ceramic features recognized for the represented object

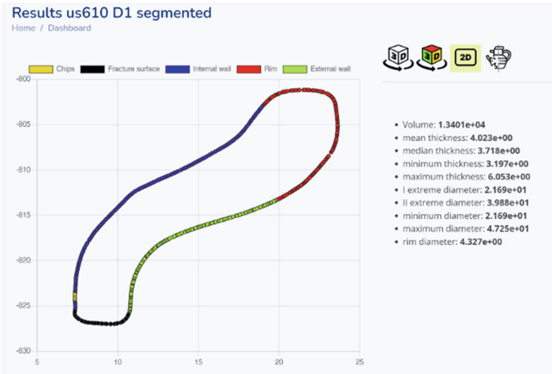

Fig. 6. 2D profile and main geometrical and dimensional properties of the object.

Finally, button (f) of Fig. 4 allows the visualization of the reconstructed 3D CAD model (see Fig. 7).

3 Discussion and Conclusion

Today, despite the scientific community's efforts, the recommendations of "UNESCO, ICCROM, ICOMOS (1984)" for preserving the authenticity and integrity of archaeological finds are not yet been completely achieved. Regarding archaeological ceramics, this is because their analysis, classification, and reconstruction are still made by manual methods based on the operator's experience. This implies that the operator is involved in time-consuming, tedious, poorly repeatable, and reproducible activities whose results depend on his/her experience. This modus operandi is no longer sustainable in a digital world where technological development allows the implementation of computer-based methods that can objectively support human activities. Developing an automatic method to support/replace the operator in the above-mentioned routine activities must be based on expert operators' encoding knowledge. This is the only way to implement it in algorithmic rules for analyzing 3D discrete models. In the last ten years, the University of L'Aquila research group published methods based on the codification of archaeologists' knowledge in recognizing the most significant geometric and morphological features of sherds. Methods applied by the authors to hundreds of real archaeological fragments (produced results following skilled archaeologist evaluations. With such tools now available, to achieve the objectives set by "UNESCO, ICCROM, ICOMOS (1984)", the need arises to develop computer-based systems capable of sharing the knowledge and methods developed with archeologists.

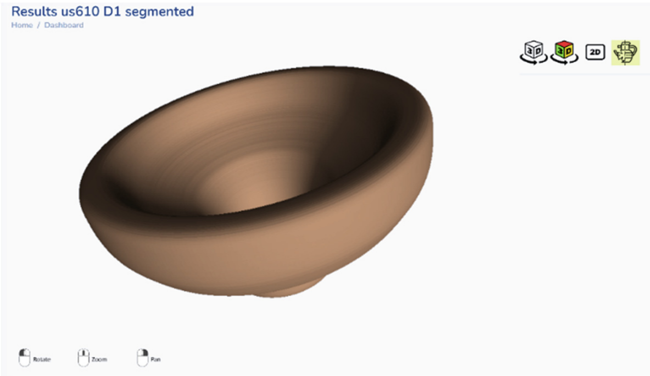

Fig. 7. Visualization of the reconstructed 3D CAD model

In this paper, these systems are identified as a special database from which the archaeologist will be able to view the material, study it also thanks to the support of the "augmented" information provided by the feature recognition system (morphological, geometric, etc.). In the proposed first version, particular efforts were made to develop an intuitive and interactive web interface with the commands that co-determine the essential interaction of the archaeologist with the fragments in the traditional method: 3D manipulation, displaying results of segmentation and dimensional characterization, adding labels and annotations.

Once these main commands were defined, together with archaeologists, the interface was designed regarding the shape and position of menus, tables, legends, and icons. Once the design and implementation of the interface were finished, it was submitted to archaeologists working with the research team. The learning ramp was steep, and the archaeologists became skilled in using the interface after a few interactions. Having verified the effectiveness of the developed system, future efforts will be directed toward three different topics:

- implementing new functionalities that handle other information that can be taken from 3D model analyses (thicknesses, textures, etc.);
- implementing methods for querying the database for the classification and cataloging of sherds;
- using the database to create and share knowledge of hundreds of sherds from an archeological site;
- implementing mobile augmented reality applications to share information high-level information from 3D models to improve also the exhibition activities

References

1. Orton, C., Hughes, M., Hughes, M.: Pottery in Archaeology. Cambridge University Press, Cambridge (2013)
2. Martinez Carrillo, A.L.: Computer application in archaeological pottery: a review and new perspective, on the road to reconstructing the past. In Proceeding of the 36th Computer Application and Quantitative Method in Archaeology Conference, pp. 397–401. Archaeolingua Foundation, Budapest, Hungary (2008)
3. Di Angelo, L., Di Stefano, P., Pane, C.: An automatic method for pottery fragments analysis. Measurement **128**, 138–148 (2018)
4. Di Angelo, L., Di Stefano, P., Pane, C.: Automatic dimensional characterisation of pottery. J. Cult. Herit. **26**, 118–128 (2017)
5. Di Angelo, L., Di Stefano, P., Guardiani, E., Pane, C.: Automatic shape feature recognition for ceramic finds. J. Comput. Cult. Herit. (JOCCH) **13**(3), 1–21 (2020)
6. Di Angelo, L., Di Stefano, P., Morabito, A.E., Pane, C.: Measurement of constant radius geometric features in archaeological pottery. Measur. J. Int. Measur. Confederat. **124**, 138–146 (2018)
7. Soler, F., Melero, F.J., Luzón, M.V.: A complete 3D information system for cultural heritage documentation. J. Cult. Herit. **23**, 49–57 (2017)
8. Di Angelo, L., Di Stefano, P., Guardiani, E.: A review of computer-based methods for classification and reconstruction of 3D high-density scanned archaeological pottery. J. Cult. Herit. **56**, 10–24 (2022)
9. Smith, N.G., Karasik, A., Narayanan, T., Olson, E.S., Smilansky, U., Levy, T.E.: The pottery informatics query database: a new method for mathematic and quantitative analyses of large regional ceramic datasets. J. Archaeolog. Method Theory **21**(1), 212–250 (2014)
10. Gattiglia, G., Holly, W.: ArchAIDE: archaeological automatic interpretation and documentation of cEramics. In: CEUR Workshop Proceedings, pp. 60–65 (2018)
11. Stergioulas, A., Ioannakis, G., Koutsoudis, A., Chamzas, C.: The orion pottery repository – a publicly available 3D objects' benchmark database with texture information. In: Ioannides, M. (ed.) EuroMed. LNCS, vol. 11196, pp. 174–187. Springer, Cham (2018). https://doi.org/10.1007/978-3-030-01762-0_15
12. Di Angelo, L., Di Stefano, P., Guardiani, E., Morabito, A.E.: 3D informational database for automatic archiving of archaeological pottery finds. Sensors **21**(3), 978 (2021)
13. Di Angelo, L., Di Stefano, P.: Experimental comparison of methods for differential geometric properties evaluation in triangular meshes. Computer-Aided Design and Applications **8**, 193–210 (2011)
14. Di Angelo, L., Di Stefano, P.: Axis estimation of thin-walled axially symmetric solids. Pattern Recogn. Lett. **106**, 47–52 (2018)

Design for Manufacturing and Assembly

Development of an Assembly Procedure to Reduce the Uncertainty Propagation by Geometric Tolerance Stackup Analysis of a Complex Ion Source for Nuclear Physics Applications

Alberto Girotto[1(✉)], F. Leccia[1], L. Sibilia[1], Ileana Bodini[1], Diego Paderno[1], M. Ballan[2], P. Rebesan[3], Stefano Uberti[1], Gabriele Baronio[1], M. Manzolaro[2], and Valerio Villa[1]

[1] Department of Mechanical and Industrial Engineering, University of Brescia, Brescia, Italy
a.girotto@unibs.it

[2] National Institute for Nuclear Physics (INFN) - Laboratori Nazionali di Legnaro, Legnaro, Italy

[3] National Institute for Nuclear Physics (INFN) - Padova Division, Padua, Italy

Abstract. At Legnaro National Laboratories of the Italian National Institute for Nuclear Physics, Design for Assembly principles were applied to ease and improve the assembly procedure of the Forced Electron Beam Induced Arc Discharge ion source for the SPES Isotope Separation On-Line facility. Such device is a key component for the whole system, as its correct functioning is fundamental to provide the radioactive ion beam to the experimental users; furthermore, its reliability and performance stability are directly affected by the construction and placement accuracy of the parts that compose the assembly.

A deep critical analysis of the current assembly procedure was performed to identify the main issues that affect the mounting accuracy of the ion source components. Consequently, a new assembly procedure was developed to fix the identified issues without applying relevant modification to the ion source parts; specifically, a custom assembly tool was designed not only for an easier coupling of the components, but also to improve the accuracy of the functional surfaces positioning to increase the device performance stability during operation. To achieve this, a custom assembly tool was designed to reduce the number of the elements of the tolerance stackup and, therefore, the uncertainty propagation. The proposed assembly procedure results significatively less time consuming than the current one, moreover it improves the accuracy of the FEBIAD ion source components position once assembled, as confirmed by Coordinate Measuring Machine measures.

Keywords: Design for assembly · assembly tool · Tolerance analysis · Geometrical Product Specifications

M. Carfagni et al. (Eds.): ADM 2023, LNME, pp. 583–591, 2024.
https://doi.org/10.1007/978-3-031-52075-4_9

1 Introduction

The Selective Production of Exotic Species (SPES) facility at Legnaro National Laboratories (LNL) of the Italian Institute of Nuclear Physics (INFN) is an Isotope Separation On-Line (ISOL) facility having the purpose to produce Radioactive Ion Beams (RIBs) for research in different branches of science, from nuclear physics to nuclear medicine [1].

In the case of the SPES facility (Fig. 1), such RIBs are produced by the interaction of a production target, usually made of fissile material with a high-intensity and high energy proton beam produced by a cyclotron [1]. Depending on the impinging beam energy and the target composition, specific nuclear reactions are activated, leading to the production of a characteristic range of isotopes of different elements. Most of the nuclear reaction products can be released by the target thanks to diffusion and effusion processes, allowed by the high working temperature of the system, generally around 2000 °C; additionally, the target operates under high vacuum (10^{-6} mbar) to avoid both oxidation and the presence of external contaminants.

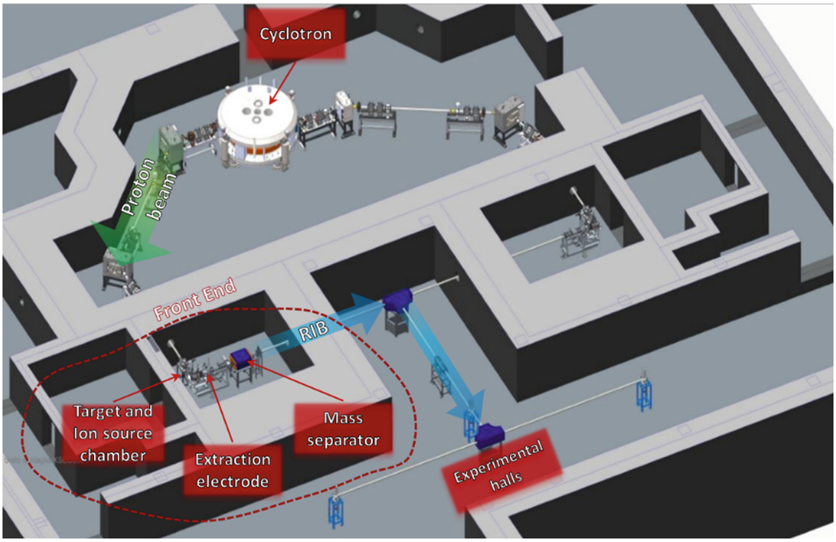

Fig. 1. SPES facility layout

The released particles effuse through a transfer line towards the ion source, where the incoming neutral radionuclides are ionized, fundamental step for the subsequent extraction and acceleration of the radionuclides as a Radioactive Ion Beam (RIB) allowing its transport and manipulation by the subsequent electrostatic devices. Afterwards, an electromagnetic mass separator allows the mass-selection and purification of the transported ions. The resulting isobaric RIB can be directly delivered to experimental users or further accelerated up to the energy level required for specific research activities.

1.1 The Case Study

The ion source is a key component for an ISOL facility, as its performance stability and reliability are fundamental for ensuring the availability of the requested RIBs to the experimental users. Indeed, a malfunctioning of the ion source, causes the interruption of the beam delivery and down-times required for the substitution of the entire Target-Ion Source unit (Fig. 2), that has to be handled as nuclear waste regardless of the cumulated operational time reached. Currently, the standard operational timespan of a Target-Ion Source unit is 15 days, mostly because the ion source performances degrade over time.

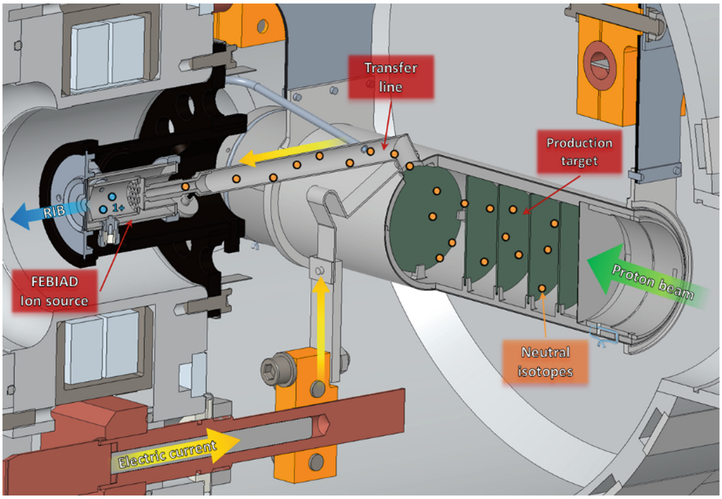

Fig. 2. Target and ion source chamber

Among the different types of ion sources, the Forced Electron Beam Induced Arc Discharge (FEBIAD) ion source is the most used because of its flexibility since it can be used to potentially ionize any element of the periodic table. Such a device is composed by several components produced in refractory metals (e.g., Molybdenum and Tantalum) and ceramics (Alumina and Graphite) which are represented in Fig. 3. Indeed, the occurrence of the ionization process requires extreme working conditions: working temperature levels in the range 1500 °C–2000 °C, achieved by Joule effect heating, and high vacuum (10^{-6} mbar) necessary to minimize the presence of contaminants in the produced beam and prevent components oxidation [2].

From a geometrical point of view, the accurate alignment of the FEBIAD anode and cathode, namely the two main components of the ion source, strongly affects the performance repeatability. In particular, the assembly of the anode is critical, since such component has to be electrically insulated from the rest of the ion source, and it is fixed through a support system, which foresees three Alumina cylindrical insulators supported by pins and retainer nuts radially disposed at 120° to each other.

With the aim to ensure acceptable ion source performances, restricted geometric limitations related to the functional facing surfaces of the anode and the cathode (called anode grid and cathode front surface) are required [2]:

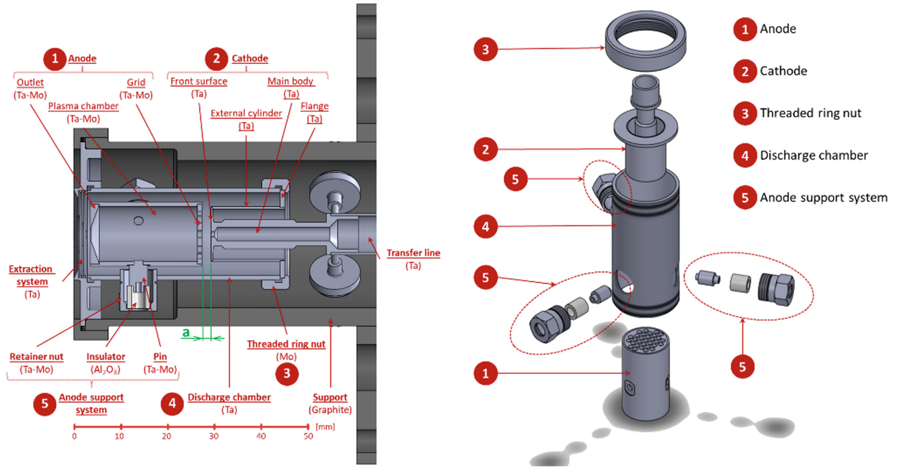

Fig. 3. FEBIAD ion source main components

- They should be positioned at a distance (“*a*” in Fig. 3) between 0.9 and 1.2 mm;
- Their parallelism is desired.

Currently, the SPES FEBIAD ion source is constituted by more than 20 components that are manually assembled with a complex operator-dependent procedure resulting in a lack of both accuracy and repeatability of the functional surfaces positioning. The aim of this work is to propose an alternative anode assembly procedure (AP), capable of limiting the positioning uncertainty of the two functional ion source surfaces. Such procedure was identified after a critical analysis of the current assembly method.

2 Materials and Methods

The development of an improved assembly strategy for the FEBIAD ion source, according to Design for Assembly (DFA) approach [3], became necessary to reduce the elements that were considered as a source of uncertainty for the positioning of each part of the assembly. However, before modifying the current alignment procedure, it was carefully examined and evaluated by performing a critical analysis.

2.1 Critical Analysis of the Current Alignment Procedure

The current assembly procedure foresees an alignment tool to manually center the anode within the discharge chamber (Fig. 4), nevertheless the results in terms of the accuracy of such an operation are dependent on the ability of the operator.

The main issues and sources of uncertainty for the positioning of the ion source components by performing the current assembly strategy were identified by a critical analysis:

1. The anode is not properly blocked by the alignment tool allowing its sliding along the z axis, as represented in Fig. 5;

2. The clearance fits between the alignment tool and the other components were not suitable for an accurate positioning of the parts; Because of the small dimensions of the anode support system components, they were particularly difficult to be manually handled. Moreover, the fixing of the retainer nuts was problematic as it compromises the position of the anode since it was not blocked.

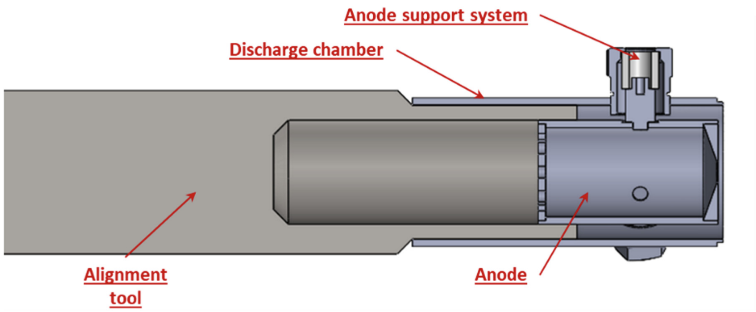

Fig. 4. The alignment tool used to perform the current assembly procedure

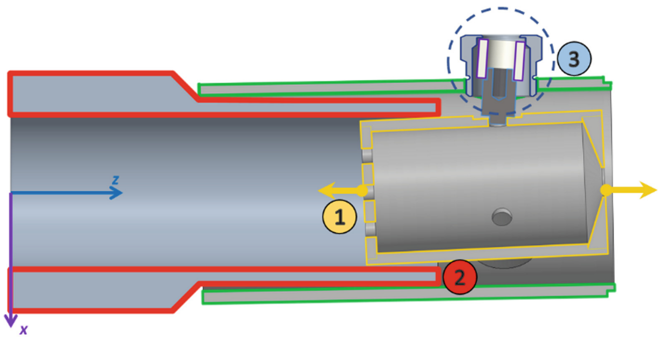

Fig. 5. Representation of the critical issues identified for the current assembly procedure

The uncertainty propagation due to the several elements of the tolerance stackup, as a consequence of the unconstrained degrees of freedom of both the anode and its support system, have a detrimental effect on the assembly repeatability [4]. Therefore, a control of the position and inclination of the anode grid was not feasible. In addition, the assembly operations were extremely time consuming, as the entire assembly procedure required several hours to be completed.

2.2 The Proposed Assembly Procedure

The identified issues were solved without relevant modifications of the ion source parts geometry since a new assembly procedure based on a custom support tool was developed. The assembly tool is constituted by the components represented in Fig. 6.

The main body (called *base tool*) foresees a housing to properly constrain the anode in order to maintain its own correct position during the assembly operation. In addition, the anode support system components are sustained by the sliding rods that are radially oriented toward the anode holes. To achieve this, the pin holes were threaded as well as the end of the sliding rods.

A tolerance stackup analysis [5] allowed to properly design the assembly tool: for the anode grid position was considered a different tolerance stackup constituted by less elements with respect to the one related to the current assembly procedure.

Reducing the number of the tolerance stackup elements for the anode allowed to limit the uncertainty propagation of the anode grid position. In fact, the anode was accurately blocked as aforementioned, moreover the distance *d* was controlled by allocating a symmetric dimensional tolerance of ± 0.01 mm to the tool's dimensions, as highlighted in Fig. 7.

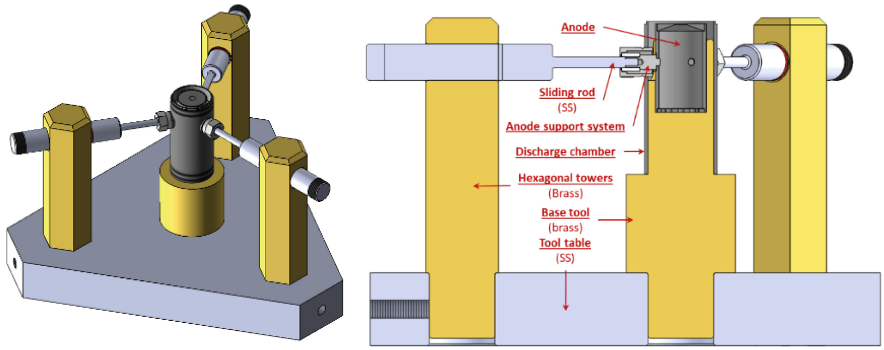

Fig. 6. The assembly tool designed to improve the anode mounting procedure. The main component that directly affects the anode grid position is the *base tool*

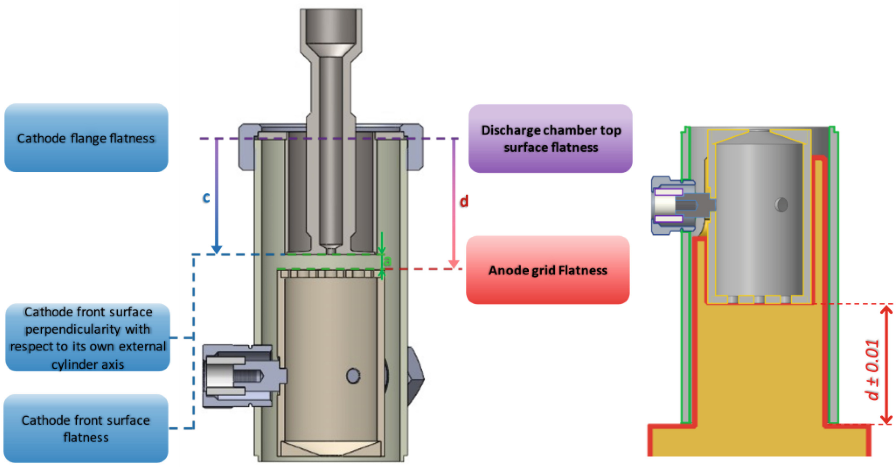

Fig. 7. FEBIAD ion source tolerance stackup elements by considering the assembly tool to perform the mounting strategy

3 Results and Discussion

A prototype of such a proposed assembly tool was produced at LNL and it was successfully tested. The improvement of such an assembly strategy allowed to simplify the mounting operations of the anode and to reduce the time required to complete the fixing of the ion source parts to few minutes. Different assemblies were prepared by performing the different assembly procedures, afterwards the distance *d* was measured through CMM (Coordinate Measuring Machine) measurements as shown in Fig. 8.

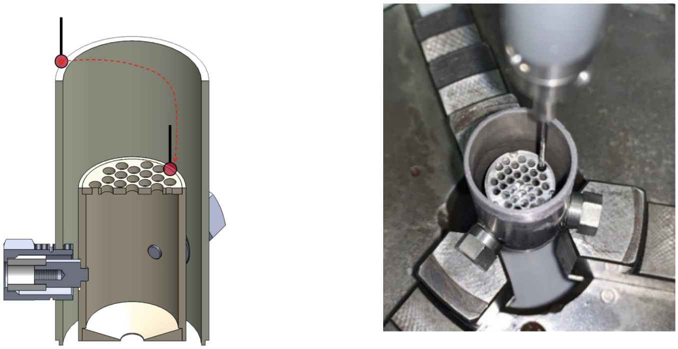

Fig. 8. CMM strategy to measure the distance *d*

3.1 Assembly Procedures Comparison

The CMM measures were performed on four different assemblies each one characterized by a set of different FEBIAD ion source components (four different sets, one for each assembly) prepared using the aforementioned mounting strategies. The results are resumed in Table 1 and Table 2.

Table 1. CMM measures on four assemblies prepared by the current mounting strategy

	$d_{nominal}$ [mm]	$d_{measured}$ [mm]	Δ [mm]
Average	17,000	16.763	−0.237
Max		17.134	0.134
Min		16.578	−0.422

It has been observed that the assemblies realized by the proposed assembly procedure were characterized by an average *d* value closer to the nominal dimension, while the larger deviation from the nominal value (Δ) was measured for an assembly performed by the current assembly strategy. Furthermore, in Table 3 reports the comparison between the same set of components mounted following the two different assembly procedures.

Table 2. CMM measures on four assemblies prepared by the proposed mounting strategy

	$d_{nominal}$ [mm]	$d_{measured}$ [mm]	Δ [mm]
Average	17,000	17.075	0.075
Max		17.247	0.247
Min		16.951	−0.049

Table 3. CCM measures comparison between assemblies having the same FEBIAD ion source components prepared by the two different assembly procedures

	$d_{nominal}$ [mm]	$d_{measured}$ [mm]	Δ [mm]
Proposed AP	17.000	16.991	−0.009
Current AP		16.736	−0.264

As a result of the CMM measurements, it was observed that the proposed assembly procedure ensures a lower deviation for the *d* distance from the nominal value with respect to the current assembly procedure.

4 Conclusions

CMM measurements were used to compare the different assembly procedures: the assemblies prepared through the proposed assembly procedure confirm that the custom assembly tool prototype ensures a more accurate anode positioning with respect to the current manual mounting method. This result was achieved by minimizing the elements of the tolerance stackup of the FEBIAD ion source, which is an approach that can be extended to all applications that require improvements in the positioning accuracy of assembled components.

A further enhancement can be reached if a new assembly tool will be designed allocating the proper tolerances needed to improve the quality of the assembly. Moreover, additional repeatability test will be necessary to validate the new assembly procedure.

References

1. Marchi, T., et al.: The SPES facility at Legnaro National Laboratories. J. Phys.: Conf. Ser.. IOP Publishing Ltd (2020).https://doi.org/10.1088/1742-6596/1643/1/012036
2. Manzolaro, M., Meneghetti, G., Andrighetto, A., Vivian, G.: Electrical-thermal-structural finite element simulation and experimental study of a plasma ion source for the production of radioactive ion beams. Rev. Sci. Instrum. **87**(3) (2016).https://doi.org/10.1063/1.4943209
3. Formentini, G., Rodríguez, N.B., Favi, C.: Design for manufacturing and assembly methods in the product development process of mechanical products: a systematic literature review. Int. J. Adv. Manuf. Technol. **120**(7–8), 4307–4334 (2022). https://doi.org/10.1007/s00170-022-08837-6

4. Vetturi, D., Lancini, M., Bodini, I.: How geometrical tolerances affect the measurement of reciprocal alignment of two different assemblies: a case study. In: Proceedings of the ASME 2010 10th Biennial Conference on Engineering Systems Design and Analysis. ASME 2010 10th Biennial Conference on Engineering Systems Design and Analysis. Vol. 2, pp. 227-232. Istanbul, Turkey. July 12–14, ASME (2010). https://doi.org/10.1115/ESDA2010-24759
5. Chen, H., Jin, S., Li, Z., Lai, X.: A comprehensive study of three dimensional tolerance analysis methods. Comput.-Aid. Design **53**, 1–13 (2014). https://doi.org/10.1016/j.cad.2014.02.014

Author Index

M. Carfagni et al. (Eds.): ADM 2023, LNME, pp. 593–595, 2024.
https://doi.org/10.1007/978-3-031-52075-4